

**NEGATIVE ION PHOTOELECTRON SPECTROSCOPY: ANTIOXIDANTS,
ACTINIDE CLUSTERS, MOLECULAR ACTIVATION, AND SUPERATOMS**

by

Zhaoguo Zhu

A dissertation submitted to Johns Hopkins University in conformity with the
requirements for the degree of Doctor of Philosophy

Baltimore, Maryland

October 2022

© 2022 Zhaoguo Zhu

All rights reserved

Abstract

Negative ion photoelectron spectroscopy (PES) utilizes photons to examine the electronic and geometric properties of negative ions and their corresponding neutrals. A diverse range of topics spanning biology, chemistry, physics, and material science were investigated, including antioxidation abilities of antioxidants, electronic structure of actinide-containing clusters, mechanism of activation reactions, design of superatoms, multiple Rydberg anions, and electron induced proton transfer. The insight acquired from anion photoelectron spectroscopy has provided understanding into the above-mentioned topics at a molecular level.

After briefly introducing the PES technique, Chapters II to VI present these studies in detail. In Chapter II, the antioxidation abilities of two famous antioxidants in the body and food, ascorbic acid and gallic acid, were measured spectroscopically and compared to computations. In Chapter III, we studied the interactions of hydrogen, oxygen, or gold atoms with thorium or uranium atoms; chemical bonding between thorium and thorium atoms in clusters; and electron affinity of the uranium atom. Chapter IV discusses the small molecule activation, such as water, carbon dioxide, methane, or hydroxylamine, by single metal anions or metal hydride anions. With the help of high-level quantum chemistry calculations, reaction mechanisms were revealed at a molecular level. Finally, Chapter V shows that the electronic spectra in cobalt sulfide superatomic clusters are tunable via ligand substitution, shedding light on novel material designs.

Advisor: Dr. Kit H. Bowen, Jr.

Committee: Dr. Paul J. Dagdigian

Dr. Cheng Lan

Acknowledgements

First and foremost, I would like to express my sincere appreciation to my advisor, Prof. Kit. H. Bowen, for giving me the opportunity to join his world-leading team. Dr. Bowen has been offering his consistent support at a level beyond my imagination. His knowledge, motivation, passion, patience, and great taste in science have always been an inspiration to me. I've gained immense knowledge of experimental physical chemistry and instrument engineering in this lab. Everything would not be possible without his sterling guidance in looking for projects, doing experiments, writing research papers, attending conferences, and, most important, being a critical thinker.

I would like to thank Dr. Paul J. Dagdigian and Dr. Lan Cheng for serving on my thesis advisory committee and being readers of this dissertation. I am also grateful to other scientists and professors who have helped me at Hopkins.

I would like to acknowledge our theoretical collaborators, Prof. David A. Dixon, Prof. Kirk A. Peterson, Prof. Evangelos Miliordos, Prof. A. N. Alexandrova, Prof. Lan Cheng, and their group members. This dissertation would not have been possible without them.

I would like to give my special thanks to Prof. Xinxing(Colin) Zhang at Nankai University for recommending me to Dr. Bowen. I treasure all suggestions he provided to me.

During my graduate career, I've had the opportunity to work with numerous intelligent and competent colleagues. I divide my Ph.D. into three stages. In the first two years (2016-2018), I spent half of my time taking classes, finishing teaching assistant tasks, and the other half shadowing in the lab. Thank you to Dr.

Evan L. Collins, Dr. Sara Marquez, and Dr. Sandra M. Ciborowski for guiding me in the early days. They taught me how to be a good graduate student in the Bowen lab.

I want to thank Dr. Gaoxiang Liu for being my first mentor in the lab and a real friend in my daily life. He educated me to be meticulous and responsible. From him, I've learned so much about instrument operation and maintenance, problem-solving, data analysis, and result presentation. Our daily conversations spanned many topics, from experimental results to calculation skills, sports to movies, and bubble tea to hot pot. He took me and friends to Hershey Park for fun. There were too many memories I will never forget. I could not find my feet so quickly in the US without his help. Best wishes to him and his wife.

In the second stage, I started working with Dr. Mary Marshall, who was my partner for three years (2018-2021). We accomplished our first independent project, troubleshoot and fixed the instrument issues by ourselves for the first time, wrote our first paper, and so on. There were so many first-time letting us grow fast and become mature. Like in a quest story, we believed we can conquer every difficulty we met, and we did! I am fortunate to have her as a partner for over half of my Ph.D. career. The most productive days of those six years were spent with her. I wish her all the best.

In the last stage (2021-2022), I would like to thank Dr. Rachel M. Harris and Burak A. Tufekci. We did many exciting projects together. History is a loop. I also switched my role to a mentor. Rachel is a great mother, a fixer of everything, and an excellent experimental scientist. She struggled in tough times but finally walked out. We had a good time drinking beers and throwing axes:). I really felt happy for her from the bottom of my heart when she defended last year. Burak is a young talent. Although he only has worked with me since

last year, he has already shown ambitions and potential to be a good graduate student. I like chatting with him about news, international relations, and everything. I have no doubt that he will earn well-deserved success in his future endeavors. Go, Team PIPES!

I want to thank other lab members and visiting students, Dr. Nicolas Blando, Dr. Zachary Hicks, Dr. Linjie Wang, Dr. Mike A. Denchy, Lucas Hansen, Benjamin R. Bilik, Chalynette Martinez- Martinez, Moritz Blankenhorn, Marica Dipalo, Tatsuya Chiba, Kathryn Foreman, Yinlin Chen, Yulu Cao, Haojun Jia, Jinheng Xu, and all other scholars.

I would like to thank Boris Steinberg for solving problems in the lab and the machine shop. I would like to thank John Kidwell, Joseph Russel, Jasmine Harris, and Meghan Carter for administrative assistance throughout six years.

I would like to thank Dr. Yuyang Ji for preparing the case competition together and sharing valuable job-hunting information with me. I thank Qifeng Jiang, Bing Xu, Xuechen Zheng, Yi Zhuang, Yinhan Wang, Yinong Zhao, Qingchu Jin, Sixuan Li, Zhenhui Liu, Beiun Shen, Zhuowan Li, Zhongtian Shen, Jiyang Wen, and all other buddies for making my life colorful at Hopkins.

I would like to thank my kind roommates, Dr. Liangyu Guan, Dr. Bin Ren, Dr. Junzi Liu, Dr. Huang Chen, Dr. Dan Zhu, and Xiangyu Xie. I will miss our chats, road trips, and every Diet Coke we drank together. I also want to thank Tiny, Beibei, and Feifei for bringing me joy. You are all excellent cats! I thank their owners, Dr. Ren, Beijun Shen, and Zhuowan Li as well.

I would like to thank all my friends on either side of the Pacific Ocean for providing me with an escape when I felt exhausted. Specifically, I want to thank JOY4, a group of 4 like the main characters in “*Friends*”. I am grateful Pengpeng Ji, Qianying Zhao, and Xiangyu Luo always stay with me when I need emotional support. Phone calls from LA, Suzhou, and Shanghai are conciliating and encouraging every time. Without your help, I could not have defeated all the anxiety and depression. I hope our friendship lasts to the end of eternity.

I would like to thank Shun Yao for accompanying me on this adventure. I cherish every moment with you.

Finally, I thank my parents for their unconditional and continued love. Their selfless support allowed me to choose “the one less traveled by”. And that has made all the difference.

Contents

Abstract.....	ii
Acknowledgements	iii
List of Figures.....	x
List of Tables	xxvi
I. Introduction	1
II. Antioxidants.....	13
II.A.1. A Photoelectron Spectroscopic Study of Ascorbate and Deprotonated Ascorbate Anions Using an Electrospray Ion Source and a Cryogenically Cooled Ion Trap	15
II.A.2. Photoelectron Spectroscopic and Computational Study of the Deprotonated Gallic Acid and Propyl gallate Anions	28
III. Actinide Clusters.....	43
III.A. Thorium.....	44
III.A.1. ThH ₅ , An Actinide-Containing Superhalogen Molecule.....	46
III.A.2. Photoelectron Spectroscopic and <i>Ab Initio</i> Computational Studies of the Anion, HThO ⁻ ..	55
III.A.3. ThAu ₂ ⁻ , ThAu ₂ O ⁻ and ThAuOH ⁻ anions: Photoelectron Spectroscopic and Theoretical Characterization.....	73
III.A.4. The Th ₂ O ⁻ , Th ₂ Au ⁻ and Th ₂ AuO _{1,2} ⁻ Anions: Photoelectron Spectroscopic and Computational Characterization of Energetics and Bonding	106

III.B.	Uranium	142
III.B.1.	The Electron Affinity of the Uranium Atom.....	143
III.B.2.	Anion Photoelectron Spectroscopic and Relativistic Coupled- Cluster Studies of Uranyl Dichloride Anion, UO_2Cl_2^-	158
III.B.3.	Au as a surrogate for F: The case of UAu_6 vs UF_6	172
III.B.4.	The transition from halogen-like to metallic-like bonding of gold in Uranium-Auride Clusters (U@Au_n), ($n = 3 - 7$).....	179
IV.	Small Molecule Activation	198
IV.A.	Small molecule activation by single atomic anions	199
IV.A.1.	Water activation and splitting by single anionic iridium atoms	200
IV.A.2.	Study of the Reaction of Hydroxylamine with Iridium Cluster Anions, ($n = 1 - 5$)	215
IV.A.3.	Selective Activation of the C-H Bond in Methane by Single Platinum Atomic Anions ...	236
IV.A.4.	Simultaneous Functionalization of Methane and Carbon Dioxide Mediated by Single Platinum Atomic Anions	246
IV.A.5.	Molecular-Level Electrocatalytic CO_2 Reduction Reaction Mediated by Single Platinum Atoms	257
IV.B.	CO_2 Hydrogenation by Metal Hydride Cluster Anions	269
IV.B.1.	CO_2 Activation and Hydrogenation by Palladium Hydride Cluster Anions	270

IV.B.2.	CO ₂ Hydrogenation to Formate and Formic Acid by Bimetallic Palladium-Copper Hydride	
Clusters		283
V.	Superatoms	295
V.A.1.	Tuning the Electronic Properties of Hexanuclear Cobalt Sulfide Superatoms via Ligand Substitution	297
V.A.2.	Ligand Effect on the Electronic Structure of Cobalt Sulfide Clusters: A Combined Experimental and Theoretical Study	310
VI.	Appendix	324
VI.A.	Preliminary data	324
VI.A.1.	Relevant Complexes of Metal Tetraphenyl Porphyrins Studied via Photoelectron Spectroscopy	324
VI.A.2.	Photoelectron Spectroscopic Study of ThPtO ₂ ⁻ and ThPtC ⁻ anions	331
VI.A.3.	Internal Proton Transfer in the Radical Anion of Cytidine Prevents Dissociative Electron Attachment.	334
VI.A.4.	Uranium Containing Clusters	339
VI.A.5.	Multiple Rydberg Anions	343
VI.A.6.	Molecular-Level CO ₂ Reduction Reaction Mediated by Ni and Pd Atomic Anions	357
VI.A.7.	Parent Anions of Diiodobenzene	364
	Curriculum Vitae	370

List of Figures

Figure I.A.1.1 Potential energy diagram detailing the transitions that occur during anion photoelectron spectroscopy.	3
Figure II.A.1.1 The structures of the different anions, radicals, and neutral molecules associated with vitamin C. The structures represent those that are most stable in the gas phase.	18
Figure II.A.1.2. The schematic view of the electrospray ionization source that was incorporated into the preexisting pulsed ion photoelectron spectrometer.	20
Figure II.A.1.3. The mass spectrum of an ascorbic acid solution with a pH of 8 generated by ESI.	21
Figure II.A.1.4 The photoelectron spectrum of the ascorbate anion (AscH^-) taken with the ion trap at ambient temperature using the 4th harmonic of a Nd:YAG laser (266 nm, 4.66 eV).	22
Figure II.A.1.5 The photoelectron spectrum of deprotonated ascorbate (Asc^{2-}) taken at an ion trap temperature of 77K using the 3 rd harmonic of a Nd:YAG laser (355 nm, 3.49 eV).	22
Figure II.A.1.6 The photoelectron spectrum of deprotonated ascorbate taken at room temperature using the 4 th harmonic of a Nd:YAG laser (266 nm, 4.66 eV).	23
Figure II.A.2.1. The HAT and SET Mechanisms of radical scavenging process.....	29
Figure II.A.2.2 Photoelectron spectra of $[\text{GA-H}]^-$ recorded with (a) 3.49 eV photons at room temperature, (b) 3.49 eV photons at 77 K, (c) 4.66 eV photons at room temperature, and (d) 4.66 eV photons at 77 K.	33

Figure II.A.2.3 Photoelectron spectra of $[\text{PG-H}]^-$ recorded with (a) 3.49 eV photons at room temperature, (b) 4.66 eV photons at room temperature, (c) 3.49 eV photons at 77 K, and (d) an expanded view of (c), beginning at $\text{EBE} = 2.5$ eV.	34
Figure II.A.2.4 Optimized geometries of $[\text{GA-H}]^-$ and $[\text{PG-H}]^-$ with their respective HOMO and HOMO-1 molecular orbitals.	36
Figure III.A.1.1 The mass spectrum obtained from the pulsed arc cluster ion source using thorium powder pressed into an aluminum rod with H_2 backing gas.	48
Figure III.A.1.2 Photoelectron spectrum of ThH_5^- measured with a 266 nm laser.	49
Figure III.A.1.3 Geometrical structures and bond lengths (in Å) of the $\text{ThH}_5^{-/0}$ molecules optimized at the B3LYP/aug-ccpVT/ECP60MDF level of theory. The thorium atom is blue, and the hydrogen atoms are white.	50
Figure III.A.1.4 Summary of AdNDP analysis of the ThH_5^- anion at the B3LYP/aug-ccpVTZ/ECP60MDF level of theory.	52
Figure III.A.2.1 The mass spectrum obtained by expanding H_2 gas over a laser ablated thorium rod. The peak at 249 amu corresponds to the HThO^- anion.	61
Figure III.A.2.2 The photoelectron spectra of the anion HThO^- collected at a) 532 nm, b) 355 nm, and c) 266 nm.	62
Figure III.A.2.3 Computed equilibrium structures and electronic energies for low-lying electronic states of HThO^- , HThO , and ThOH	64

Figure III.A.2.4 The photoelectron spectrum of HThO^- collected with 532 nm wavelength photons of an Nd:YAG laser compared with the computational simulation. The computed electronic spectrum is blue-shifted by 0.03 eV to account for the net zero-point vibrational correction.....	65
Figure III.A.2.5 Valence HF orbitals of HThO^- involved in photodetachment processes or bonding.	68
Figure III.A.3.1 The mass spectrum of anions generated by PACIS when using (a) 1:1 Thorium-gold mixture and helium gas and (b) 3:1 Thorium-gold mixture and hydrogen gas.	103
Figure III.A.3.2 Photoelectron spectra of ThAu_2^- , ThAu_2O^- and ThAuOH^- measured with 355nm (3.49 eV) photons.....	104
Figure III.A.3.3 Lowest energy isomeric structures. Thorium in blue, Gold in yellow, Oxygen in red, and Hydrogen in gray.	105
Figure III.A.3.4 Bonding NBOs of the ground state of ThAuOH (C_1).	105
Figure III.A.4.1 The mass spectra of anions generated by PACIS when using (a) thorium powder and helium gas and (b) a 3:1 thorium-gold powder mixture and helium gas.....	112
Figure III.A.4.2 Photoelectron spectra of (a) Th_2O^- , (b) Th_2Au^- , (c) Th_2AuO^- and (d) $\text{Th}_2\text{AuO}_2^-$ measured with 3.49 eV photons. Lowest energy isomeric structures are displayed for each species, with thorium in blue, gold in yellow and oxygen in red. Calculated vertical detachment energies (VDE) (eV) at CCSD(T)/aT level for each structure are indicated by colored bars.	113
Figure III.A.4.3 Lowest energy isomeric structures. Thorium in blue, Gold in yellow, and Oxygen in red.	114
Figure III.A.4.4 Trendline in Th-Th Bond Order from MO analysis vs the Th-Th bond distance in Å	135

Figure III.B.1.1 Mass spectrum resulting from laser vaporization of a depleted uranium target.	148
Figure III.B.1.2 Photoelectron spectrum of the uranium atomic anion (U^-) measured with the third harmonic of an Nd:YAG laser (355 nm, 3.49 eV) and our magnetic bottle (MB) electron energy analyzer.....	150
Figure III.B.1.3 Photoelectron spectrum of the uranium atomic anion (U^-) measured with the first harmonic of an Nd:YAG laser (1064 nm, 1.16 eV) and our velocity-map imaging (VMI) electron energy analyzer.	151
Figure III.B.2.1 The mass spectrum obtained from laser ablating a uranium rod in the presence of a 0.5% HCl and 0.5% O_2 in a He gas mixture. The UO_2Cl_2^- anion mass peaks occur at 340, 342, and 344 amu.	160
Figure III.B.2.2 Molecular orbitals in which the unpaired electrons in the lowest scalar-relativistic states of UO_2Cl_2^- are located. The O, Cl, and U atoms are colored in red, green, and cyan, respectively. The vertical electronic energy difference with respect to the neutral molecule obtained from SFX2C-1e- EOMEA-CCSD/cc-pVTZ calculations are enclosed in the brackets.	162
Figure III.B.2.3 Vibrational progression for the transition from the vibronic ground state of UO_2Cl_2^- to vibrational states of the ground electronic state of UO_2Cl_2 obtained from Franck–Condon (FC) simulation using the harmonic approximation. The x axis denotes vibrational energies (in eV) with the origin set as the value of the origin transition. simulation convoluted to the experimental resolution. The broad curve is obtained by convoluting the stick spectrum with a half width at half maximum value of 0.1 eV. A value of 0.397 eV for the difference between EA_a and ADE was obtained as the shift between the threshold and the maximum peak position in this FC progression.	165

Figure III.B.2.4 The photoelectron spectra of UO_2Cl_2^- obtained using (a) the third harmonic (355 nm, 3.49 eV) and (b) the fourth harmonic of an Nd:YAG laser (266 nm, 4.66 eV). The arrows designate the position of the computed value of 3.15 eV for the adiabatic electron affinity.	166
Figure III.B.3.1 Photoelectron Spectrum of UAu_6^- taken with the 3.49 eV, 4.66 eV, and 6.42 eV photons	174
Figure III.B.3.2 Optimized ground state geometries of nearly isoenergetic isomers: (a) Ring isomer (I), (b) Quasi-octahedral isomer (II), and (c) Butterfly isomer (III) of neutrals, i.e., UAu_6 (top row) and anions, i.e., UAu_6^- (bottom row). Relative energies, ΔE , are given at the DFT level of theory.	175
Figure III.B.4.1 Mass Spectrum resulting from laser vaporization of Au and U rods, pulsed with a 10% Ar in He gas mixture. Gold clusters are marked with a red star, starting with Au_2^- . The peaks observed 41 amu after a gold cluster peak, labelled with blue hash marks, are UAu_n^- peaks. Other peaks located in the low mass region are uranium oxides.	183
Figure III.B.4.2 Photoelectron Spectrum of UAu_n^- ($n=3-7$) taken with the third (3.49 eV) and fourth harmonic (4.66 eV) of a Nd:YAG photodetachment laser, as well as an excimer (6.42 eV) photodetachment laser.	184
Figure III.B.4.3 Optimized ground state geometries of neutral and anionic $[\text{UAu}_n]$, $n=3-5$ at B3LYP/cc-PV-DZ-PP level of theory. Blue and metallic green spheres represent the U and Au atoms, respectively.	186
Figure III.B.4.5 Electronic structure and bonding analysis of neutral and anionic UAu_3 cluster.	189
Figure III.B.4.4 Electronic structure and bonding analysis of UAu_4 cluster.....	189

Figure III.B.4.6 Electronic structure and bonding analysis of UAu_5 cluster.....	193
Figure III.B.4.7 Electronic structure and bonding analysis of UAu_6 cluster.....	195
Figure III.B.4.8 AdNDP analysis on 3-centered 2-electron bonding pattern in the neutral and mono-anion of UAu_n , $n= 5,6$, and 7. The ON values represent the occupation number.	196
Figure IV.A.1.1 Mass spectra of Ir^- with water. Mass spectrum (a) was recorded under low ablation laser power (b) under high ablation laser power.	203
Figure IV.A.1.2. Photoelectron spectra of the atomic metal anions, Ir^- , (in the top panel) and $[\text{Ir}(\text{H}_2\text{O})]^-$ anions (in the lower panels). All of these anion photoelectron spectra were measured using the fourth harmonic (4.66 eV/photon) of an Nd:YAG laser. Blue arrows link Ir^- peaks to the corresponding blue-shifted peaks in $\text{Ir}^-(\text{H}_2\text{O})$ anion-molecule complexes. Red dots mark additional structural isomers.	204
Figure IV.A.1.3 Optimized structures of $[\text{Ir}(\text{H}_2\text{O})]^-$ categorized in three types. (i) Ir anion is solvated by a water molecule; (ii) only one O-H bond is broken; (iii) two O-H bonds are broken. The relative energies of $[\text{Ir}(\text{H}_2\text{O})]^-$ and their calculated VDEs are listed below each structure. Bond lengths are also shown in each structure.	205
Figure IV.A.1.4 Comparison between the experimental photoelectron spectra and the simulated DOS (density of states) spectra of the low-lying isomers of $[\text{Ir}(\text{H}_2\text{O})]^-$ clusters. The simulated spectra were obtained by fitting the distribution of the transition lines with unit-area Gaussian functions of 0.2 eV full width at half maximum (FWHM). The vertical lines are the transitions obtained based on the theoretical calculated VDEs and excitation energies.	208

Figure IV.A.1.5 Calculated reaction pathway for H₂O with Ir anion. Energies are given in eV. The total energy of isolated Ir(triplet) and H₂O is set at 0 eV. IN for reaction intermediate, TS for transition state, and labeled with a superscript t and s, for triplet and singlet, respectively. The Minimum Energy Crossing Points (MECPs), are schematically indicated with bicolor at the crossings of the two potential energy surfaces.208

Figure IV.A.1.6 NBO net charges of all atoms in lowest intermediates and transition states in energy along the reaction pathway (upper panels). Two-dimensional electron localization functions (ELF) for the species above (lower panels). Atoms are labeled and numbered in the ELF contour. The ELF distributions are shown on the Ir-H-O plane and are described chromatically. A large ELF value means that electrons are greatly localized.....210

Figure IV.A.2.1 Mass spectrum of the interaction of laser-ablated anionic iridium clusters, Ir_n⁻, with helium seeded with hydroxylamine (H₂NOH), resulting in a variety of Ir_n⁻, Ir_nO⁻, and Ir_n(NOH)⁻ clusters, indicated by o, x, and #, respectively.....221

Figure IV.A.2.2 Photoelectron spectra of the Ir_n(NOH)⁻ clusters (*n* =1-4) taken with the fourth harmonic of the Nd:YAG laser (266 nm, 4.66 eV). The marked peak in the Ir(NO⁻H)⁻ spectrum comes from IrO₂⁻.222

Figure IV.A.2.3 Lowest Energy Isomers of Ir_n(NOH)⁻; *n*=1-5. Free energies are at 298.15K, relative to separated Ir_n⁻ + NH₂OH - H₂; i.e., Δ*G* for the reaction (Ir_n⁻ + NH₂OH → Ir_n(NOH)⁻ + H₂). *M* denotes the spin multiplicity.225

Figure IV.A.2.4 (a) Hydrogen-bonded complex between Ir^- and NH_2OH . (b) N-H fragmentation product. (c)

O-H fragmentation product. (d) N-O fragmentation product. Free energies are at 298.15K, relative to

$\text{Ir}^- + \text{NH}_2\text{OH}$. M denotes the spin multiplicity229

Figure IV.A.2.5 $[\text{Ir}(\text{NH})\cdots\text{H}_2\text{O}]^-$ structures at (a) the triplet state local minimum, (b) the singlet-triplet

minimum energy crossing point, and (c) the singlet state local minimum. ΔE_{rel} denotes the relative

electronic energies and M denotes the spin multiplicity.230

Figure IV.A.2.6 Potential energy diagram, not to scale, summarizing the key reaction steps leading to the

formation of $\text{Ir}(\text{O})(\text{NH})^- + \text{H}_2$ and $\text{Ir}(\text{O})^- + \text{NH}_3$. Free energies, in kJ/mol, are relative to $\text{Ir}^- + \text{NH}_2\text{OH}$.

Unshaded boxes correspond to triplet states, whereas the blue-shaded boxes are singlet states.....231

Figure IV.A.3.1 The mass spectra of Pt^- without methane (A), with methane (B), and with deuterated

methane (C).238

Figure IV.A.3.2 Photoelectron spectra of Pt^- (A), $[\text{PtCH}_4]^-$ (B), and $[\text{PtCD}_4]^-$ (C) all measured with 355 nm

(3.496 eV) photons.240

Figure IV.A.3.3 Optimized structures for $[\text{PtCH}_4]^-$ and their relative energies compared to its GM. The

relative energies of $[\text{PtCD}_4]^-$ are shown in parenthesis. Energies are given in eV. Bond lengths are

given in Å.241

Figure IV.A.3.4 Calculated reaction pathway for methane activation by Pt^- . Zero-point energy corrected

energies are given in eV. Bond lengths of the transition states are given in Å.243

Figure IV.A.3.5 Selected molecular orbitals of the GM H-Pt-CH_3^- depicting the Pt-C and Pt-H bonds and

the nearly intact valence Pt orbitals.244

Figure IV.A.4.1 The mass spectra of Pt^- with methane (A), with deuterated methane (B), with methane and carbon dioxide (C), and with deuterated methane and carbon dioxide (D).....	248
Figure IV.A.4.2 Photoelectron spectra of $[\text{H}_3\text{C-Pt-H}(\text{CO}_2)]^-$ (A) and $[\text{D}_3\text{C-Pt-D}(\text{CO}_2)]^-$ (B), both measured with 266 nm (4.661 eV) photons. The stick spectrum overlay represents the calculated VDEs of different $[\text{H}_3\text{C-Pt-H}(\text{CO}_2)]^-$ structures in Figure 3.	249
Figure IV.A.4.3 Optimized structures for $\text{H}_3\text{C-Pt-H}^-$, CO_2 , and $[\text{H}_3\text{C-Pt-H}(\text{CO}_2)]^-$. The relative energies of $[\text{H}_3\text{C-Pt-H}(\text{CO}_2)]^-$ and their calculated VDEs to singlet and triplet neutrals are shown below each structure. The Natural Bond Orbital (NBO) charge on each atom is also provided. The charge besides the methyl groups shows the total charge on $-\text{CH}_3$	250
Figure IV.A.4.4 Profile of the tandem reaction between Pt^- , CH_4 , and CO_2 . Zero-point corrected energies are given in eV. The numbers in parentheses indicate the activation barriers compared to the entrance channel of CO_2 functionalization. ¹⁴ The letters in parentheses correspond to their labels in Figure 3. The potential energy surface is referenced to the total energy of isolated Pt^- , CH_4 , and CO_2	251
Figure IV.A.5.1 (A) Mass spectra of Pt^- reacting with H_2O (top panel) and with H_2O and CO_2 (bottom panel). (B) The mass spectrum of Pt^- with H_2O and CO_2 is bisected into the lower (top panel) and higher (bottom panel) mass regions for a closer view of the reaction products.	261
Figure IV.A.5.2 Photoelectron spectra of $[\text{H-Pt-OH}(\text{CO}_2)]^-$ measured with 266 nm (4.661 eV) photons. The stick spectrum overlay represents the calculated VDEs of the different $[\text{H-Pt-OH}(\text{CO}_2)]^-$ structures in Figure 3. The dotted line represents the simulated spectrum.	261

Figure IV.A.5.3 Optimized structures for H-Pt-OH^- , CO_2 , and $[\text{H-Pt-OH}(\text{CO}_2)]^-$. The relative energies of $[\text{H-Pt-OH}(\text{CO}_2)]^-$ and their calculated VDEs to singlet and triplet neutrals are shown below each structure. The Natural Bond Orbital (NBO) charge on each atom is also provided.....	262
Figure IV.A.5.4 Profile of the molecular-level CO_2RR mediated by anionic Pt atoms. Zero-point corrected energies are given in eV. The letters in parentheses correspond to their labels in Figure 3. The potential energy surface is referenced to the total energy of isolated Pt^- , H_2O , and CO_2	263
Figure IV.B.1.1 The mass spectra of anions generated by PACIS without (top panel) and with (bottom panel) CO_2 injection into the cell.....	273
Figure IV.B.1.2 Simulated and experimental mass spectra of PdHCO_2^- and $\text{PdH}_2\text{CO}_2^-$. The peaks marked by a cross indicates peaks consisting of only PdHCO_2^- , while peaks marked with a circle indicates peaks consisting of only $\text{PdH}_2\text{CO}_2^-$	274
Figure IV.B.1.3 Photoelectron spectrum of PdHCO_2^- measured with 266nm (4.66 eV) photons. The stick spectrum overlay represents the calculated VDE values of the different PdHCO_2^- structures in Figure 4.	275
Figure IV.B.1.4 The optimized structures of PdHCO_2^- . The relative energies of PdHCO_2^- and their calculated VDEs are listed below each structure. Bond lengths are also shown in each structure.	276
Figure IV.B.1.5 Calculated reaction pathway for CO_2 hydrogenation by PdH^- . Zero-point energy corrected energies are given in eV. The total energy of isolated PdH^- and CO_2 is set at 0 eV.....	277
Figure IV.B.1.6 Charges on different moieties of PdHCO_2^- intermediates along the reaction pathway of CO_2 activation by PdH^-	278

Figure IV.B.1.7 Photoelectron spectrum of $\text{PdH}_2\text{CO}_2^-$ measured with 266nm (4.66 eV) photons. Lowest

energy isomeric structures are displayed for each isomer. The relative energies of $\text{PdH}_2\text{CO}_2^-$ and their

calculated VDEs are listed below each structure. Bond lengths are also shown in each structure. ...279

Figure IV.B.2.1 (A) The mass spectrum of PdCuH_4^- cluster anions. (B) Simulated and experimental mass

spectra of PdCuH_4^- . (C) Mass spectrum of PdCuH_4^- reacting with CO_2 . (D) Simulated and experimental

mass spectra of $\text{PdCuCO}_2\text{H}_4^-$. *F* indicates formate. *FA* indicates formic acid.....285

Figure IV.B.2.2 Photoelectron spectra of PdCuH_4^- (A) and $\text{PdCuCO}_2\text{H}_4^-$ (B) measured with 266 nm (4.66

eV) photons.....286

Figure IV.B.2.3 The calculated relevant lowest energy structures of PdCuH_4^- (A and B), $\text{PdCuCO}_2\text{H}_4^-$ (C,

D, and E), and PdCuH_2^- (F). Symmetry, spectroscopic label, and energy relative to the global minimum

structure of the same stoichiometry are shown below each structure. The charge on each atom is also

shown.....287

Figure IV.B.2.4 Profile for the reaction of CO_2 with PdCuH_4^- . Zero-point energy corrected energies are

given in eV. 0 eV is set as the total energy of structure **A** and an isolated CO_2289

Figure V.A.1.1 (a) Structure of $\text{Co}_6\text{S}_8(\text{PEt}_3)_{6-x}(\text{CO})_x^-$. (b) Anion mass spectrum of

$\text{Co}_6\text{S}_8(\text{PEt}_3)_{6-x}(\text{CO})_x^-$ generated using IR/PE anion source. This work focuses on the red peaks in the

mass spectrum.....301

Figure V.A.1.2 Negative ion photoelectron spectra of $\text{Co}_6\text{S}_8(\text{PEt}_3)_{6-x}(\text{CO})_x^-$ ($x = 0-3$) anions collected using

355 nm (3.49 eV) photons from a Nd:YAG laser. The arrows point to the experimental values of AEA

and VDE; the red lines correspond to theoretical AEA, and the blue lines correspond to vertical transitions from the anion to the singlet and triplet neutral states.....	303
Figure V.A.1.3 Optimized ground state structure of anionic $\text{Co}_6\text{S}_8(\text{PEt}_3)_{6-x}(\text{CO})_x^-$ ($x = 0-3$) clusters. The red superscript indicates the spin multiplicity ($2S+1$) of each cluster.	304
Figure V.A.1.4 (a) The absolute energy values of the HOMO and LUMO for neutral $\text{Co}_6\text{S}_8(\text{PEt}_3)_{6-x}(\text{CO})_x$ ($x = 0-3$). (b) Incremental differences in the experimental AEA values, the theoretical AEA values, and the LUMO values of $\text{Co}_6\text{S}_8(\text{PEt}_3)_{6-x}(\text{CO})_x$, each with respect to $\text{Co}_6\text{S}_8(\text{PEt}_3)_6$. (c) Molecular orbital isosurfaces of the HOMO and LUMO in $\text{Co}_6\text{S}_8(\text{PEt}_3)_{6-x}(\text{CO})_x$ ($x=0-3$) clusters.	306
Figure V.A.2.1 Anion mass spectrum of $\text{Co}_6\text{S}_8(\text{PEt}_3)_x^-$ generated using IR/PE anion source.	314
Figure V.A.2.2 Negative ion photoelectron spectra of $\text{Co}_6\text{S}_8(\text{PEt}_3)_x^-$ ($x = 2 - 5$) anions collected using 355 nm (3.49 eV) photons from a Nd:YAG laser. The red arrows indicate the AEA, the blue arrows indicate the VDE and the VDE*.....	315
Figure V.A.2.3 Optimized ground state geometry of anionic $\text{Co}_6\text{S}_8(\text{PEt}_3)_x$ ($x = 0-5$) clusters. Superscripts in red text show the multiplicity of the clusters.	316
Figure V.A.2.4 The experimental and theoretical adiabatic and vertical detachment energy of $\text{Co}_6\text{S}_8(\text{PEt}_3)_x$ ($x = 0 - 6$) clusters. The plus symbol (+) indicates the AEA^T and VDE^T values of cluster's isomers at $x=2, 3$, and 5. The results of $\text{Co}_6\text{S}_8(\text{PEt}_3)_6$ are taken from Ref. 38.	317
Figure V.A.2.5 One electron-energy levels of $\text{Co}_6\text{S}_8(\text{PEt}_3)_x$ ($x = 0-5$) clusters. The solid blue and red bars represent the singly and doubly occupied energy levels, respectively. Unoccupied energy levels are	

shown by dashed gray lines. The energy of LUMO (in eV) is indicated for each cluster. The α -spin and β -spin channel are represented by up and down arrows.....	319
Figure V.A.2.6 (a) One-electron energy levels with their symmetry labels for Co_6S_8 in octahedron symmetry. The solid and dashes lines represent occupied and unoccupied energy levels. (b) One-electron energy levels along with their iso-surfaces for $\text{Co}_6\text{S}_8(\text{PET}_3)$. The solid blue and red bars represent the singly and doubly occupied energy levels, respectively. Unoccupied energy levels are shown by dashed gray lines. The α -spin and β -spin channel represented by up and down arrows.	320
Figure VI.A.1.1: The mass spectra obtained when ablating 5, 10, 15, 20- tetraphenyl-21H,23H- porphine iron (III) chloride in the presence of He, 5% CO_2 in He, and 5% O_2 in He.	326
Figure VI.A.1.2 The mass spectra obtained when ablating 5, 10, 15, 20- tetraphenyl-21H,23H- porphine nickel (II) in the presence of He, 5% N_2O in He, 5% CO_2 in He, and 5% O_2 in He.	327
Figure VI.A.1.3 The photoelectron spectra of $(\text{FeTPP})\text{O}^-$ taken with the 3 rd (355 nm, 3.49 eV) and 4 th (266 nm, 4.66 eV) harmonics of a Nd:YAG laser.....	328
Figure VI.A.1.4 The photoelectron spectra of $(\text{NiTPP})^-$, $(\text{NiTPP})\text{O}^-$, and $(\text{NiTPP})\text{O}_2^-$ taken with the 4 th (266 nm, 4.66 eV) harmonics of a Nd:YAG. Calculations are needed to confirm the EA and VDE values of the different complexes, as well as determine the connectivity.	329
Figure VI.A.2.1 The mass spectrum of anions generated by PACIS with a 1:1 thorium-platinum powder mixture and helium gas.....	332
Figure VI.A.2.2 Photoelectron spectra of ThPtC^- and ThPtO_2^- measured with 3.49 eV photons.	333

Figure VI.A.4.1 The mass spectrum obtained from ablating a depleted uranium rod in the presence of HCl and O ₂ .	339
Figure VI.A.4.2 The photoelectron spectra of UOCl ₂ ⁻ collected with the third (355 nm, 3.49 eV) and fourth (266 nm, 4.66 eV) harmonics of a Nd:YAG laser.	340
Figure VI.A.4.3 Mass spectrum of UCD _n ⁻ , n=0-4.	341
Figure VI.A.4.4 Photoelectron spectra of UCD _n ⁻ , n=0-4 collected with with the third (355 nm, 3.49 eV) harmonics of a Nd:YAG laser.	341
Figure VI.A.4.5 Mass spectrum of U _m Ar _n ⁻ . Right panel: zoomed-in view.	342
Figure VI.A.4.6 Photoelectron spectrum of UAr ⁻ with 355 nm photons.	342
Figure VI.A.5.1 The mass spectrum obtained when ablating a Mg rod in the presence of trace amounts of NH ₃ . The isotopic pattern of Mg is observed for Mg(NH ₃) ₅ ⁻ and Mg(NH ₃) ₆ ⁻ .	345
Figure VI.A.5.2 The photoelectron spectra obtained when photodetaching the TRA Mg(NH ₃) ₄ ⁻ , Mg(NH ₃) ₅ ⁻ and Mg(NH ₃) ₆ ⁻ .	346
Figure VI.A.5.3 The mass spectra obtained when ablating a La rod in the presence of He (top) and trace amounts of NH ₃ (bottom).	347
Figure VI.A.5.4 The photoelectron spectra of La ⁻ , La(NH ₃) ₅ ⁻ , and La(NH ₃) ₆ ⁻ .	348
Figure VI.A.5.5 The mass spectrum obtained when ablating a vanadium rod in the presence of helium and trace amounts of NH ₃ . With pure He, vanadium carbide clusters form. With trace amounts of NH ₃ in the backing gas, vanadium ammonia clusters are observed.	349

Figure VI.A.5.6 The photoelectron spectra of $V(NH_3)_6^-$ and $V(NH_3)_7^-$ obtained with the 3 rd harmonic (355 nm, 3.49 eV) of a Nd:YAG laser.	350
Figure VI.A.5.7 The photoelectron spectrum of $Y(NH_3)_6^-$ obtained using the 3 rd harmonic (355 nm, 3.49 eV) harmonic of a Nd:YAG laser.	350
Figure VI.A.5.8 The mass spectrum obtained when ablating a U rod in the presence of trace amounts of NH_3	351
Figure VI.A.5.9 The photoelectron spectrum of $Th(NH_3)_{5-9}^-$ obtained using the 2 nd harmonic (532 nm, 2.33 eV) harmonic of a Nd:YAG laser.	352
Figure VI.A.5.10 The mass spectrum obtained when ablating a U rod in the presence of trace amounts of NH_3	352
Figure VI.A.5.11 Zoomed in mass spectrum obtained when ablating a U rod in the presence of trace amounts of NH_3	353
Figure VI.A.5.12 The photoelectron spectrum of $U(NH_3)_{3-10}^-$ obtained using the 2 nd harmonic (532 nm, 2.33 eV) harmonic of a Nd:YAG laser.	353
Figure VI.A.5.13 Photoelectron spectra of smaller uranium ammonia clusters.	354
Figure VI.A.5.14 Photoelectron spectra of some dehydrogenation products and $U(NH_3)_7(NH_4)^-$	354
Figure VI.A.6.1 Mass spectra of Pd^- reacting with H_2O (top panel) and with H_2O and CO_2 (bottom panel).	359
Figure VI.A.6.2 Photoelectron spectra of $[Pd(H_2O)(CO_2)]^-$ measured with 355 nm (3.49 eV) photons. ...	360

Figure VI.A.6.3 Mass spectra of Ni^- reacting with H_2O (top panel) and with H_2O and CO_2 (bottom panel).	361
Figure VI.A.6.4 Photoelectron spectra of $[\text{Pd}(\text{H}_2\text{O})(\text{CO}_2)]^-$ measured with 355 nm (3.49 eV) photons. ..	362
Figure VI.A.7.1 Mass spectrum of clusters generated from 1,3-DIB using a closed housing photoemmission source.....	365
Figure VI.A.7.2 Photoelectron spectra of $1,2\text{-C}_6\text{H}_4^-$ and $1,3\text{-C}_6\text{H}_4^-$ with 355 nm and 266 nm photons.	365
Figure VI.A.7.3 Photoelectron spectra of $1,2\text{-C}_6\text{H}_4\text{I}^-$ and $1,3\text{-C}_6\text{H}_4\text{I}^-$ with 355 nm and 266 nm photons. .	365
Figure VI.A.7.4 Photoelectron spectra of $1,2\text{-C}_6\text{H}_4\text{I}_2^-$ and $1,3\text{-C}_6\text{H}_4\text{I}_2^-$ with 355 nm and 266 nm photons.	366
Figure VI.A.7.5 Photoelectron spectra of $1,2\text{-C}_6\text{H}_4\text{I}_3^-$ and $1,3\text{-C}_6\text{H}_4\text{I}_3^-$ with 266 nm photons.....	366
Figure VI.A.7.6 Mass spectrum of clusters generated from 1,2-DIB using a open housing photoemmission source.....	367
Figure VI.A.7.7 Photoelectron spectra of $1,2\text{-C}_6\text{H}_4\text{I}_2^-$ and $(1,2\text{-C}_6\text{H}_4\text{I}_2)_2^-$ with 355 nm and 266 nm photons.	367
Figure VI.A.7.8 Comparison between closed housing and open housing conditions. Left: closed, right: open.	367
Figure VI.A.7.9 Photoelectron spectra of I^- , $1,2\text{-C}_6\text{H}_4\text{I}_3^-$, and $(1,2\text{-C}_6\text{H}_4\text{I}_2)_2\text{I}^-$ with 266 nm photons.	368

List of Tables

Table II.A.2.1. Experimentally and computationally determined values for deprotonated propyl gallate and gallic acid anions and their corresponding neutral radicals. (eV)	35
Table III.A.1.1 Experimental and theoretical vertical detachment energies (VDE) values (eV) for ThH_3^- and ThH_5^- at the different levels of theory. The aug-ccpVTZ/ECP60MDF basis sets are used for all methods.....	50
Table III.A.2.1. Electron configurations of low-lying electronic states of HThO^- and HThO as well as their vertical electronic energies relative to the electronic ground state of the HThO^- anion, $1^1\text{A}'$, in its equilibrium geometry. The valence molecular orbitals shown here comprise Th 6s, 6p, 6d, 7s, O 2s, 2p, and H 1s orbitals.	59
Table III.A.2.2 The electron binding energy (eV) values of the observed transitions in the photoelectron spectra of HThO^- . ^a The photon wavelength used in each case to collect the spectrum. ^b The EBE values correspond to the intensity maxima for each peak. ^c The approximate peak position.	63
Table III.A.2.3 Harmonic vibrational frequencies (cm^{-1}) of the electronic ground states of HThO^- and HThO computed at the SFX2C-1e-CCSD(T)/cc-pVTZ level of theory.	64
Table III.A.3.1 CCSD(T) equilibrium geometries (\AA and deg.) and CCSD(T) harmonic frequencies (cm^{-1}) of the molecules of this work ^{a,b}	94
Table III.A.3.2 Contributions (in kcal/mol) to the FPD adiabatic electron affinity, EA_0 , and VDE of ThAu_2 . Values in parentheses are in eV.	95

Table III.A.3.3 Electronic excited states of ThAu ₂ calculated at the X2C-mmfc DCG-EOM-CCSD level of theory using the linear ThAu ₂ ⁻ CCSD(T)/aVQZ equilibrium geometry. Values are in eV.	96
Table III.A.3.4 Contributions (in kcal/mol) to the FPD adiabatic electron affinity, EA ₀ , and VDE of ThAu ₂ O. Values in parentheses are in eV ^a This work.	96
Table III.A.3.5 Contributions (in kcal/mol) to the FPD adiabatic electron affinity, EA ₀ , and VDE of ThAuOH, as well the 0K isomerization energy of ThAuOH ⁻ (ΔE _{isom}). Values in parentheses are in eV.	97
Table III.A.3.6 EOM-CCSD (X2C-mmfc) excited electronic states (in eV) for the C _s isomer of ThAuOH at the anion geometry.....	98
Table III.A.3.7 Calculated contributions to the FPD 0K atomization energies (AE ₀) and resulting heats of formation (all in kcal/mol).	99
Table III.A.3.8 Natural charges of ThAu ₂ , ThAu ₂ O, and ThAuOH and their anions.	100
Table III.A.3.9 NBOs of the Lewis structure for ¹ A ₁ ThAu ₂ . ^a	100
Table III.A.3.10 NBOs of the Lewis structure for ¹ A' ThAu ₂ O. ^a	101
Table III.A.3.11 NBOs of the Lewis structure for ¹ A ThAuOH (C ₁). ^a	102
Table III.A.4.1 Relative Energies of Th ₂ Au and Th ₂ Au ⁻ in kcal/mol at different level of theory. ^a	114
Table III.A.4.2. Relative Energies of Th ₂ AuO, Th ₂ AuO ⁻ Th ₂ AuO ₂ and Th ₂ AuO ₂ ⁻ in kcal/mol at different level of theory. ^a	117
Table III.A.4.3 Th ₂ O and Th ₂ O ⁻ relative energies in kcal/mol at different level of theory. ^a	118
Table III.A.4.4 Th ₂ and Th ₂ ⁻ Relative energies in kcal/mol at different level of theory. ^a	118

Table III.A.4.5 Th-Th Bond Order (BO) analysis from NBO (Natural Bond Orbital) and MO (Molecular Orbital) analysis.	119
Table III.A.4.6 CCSD(T) Adiabatic electron affinities (eV) (ΔH_{0K}).	124
Table III.A.4.7 Vertical detachment energies (VDE) (eV) at CCSD(T)/aT level.	126
Table III.A.4.8 Heats of formation and Bond Dissociation Energies in kcal/mol at 0 K.	129
Table III.B.1.1 CMRCI+Q calculations of the electron affinities of Th and U (in kcal/mol with meV in parentheses).	152
Table III.B.1.2 Calculated contributions to the electron affinities (in kcal/mol) within the coupled cluster FPD scheme. See Eq. (3) for details. Values in meV are given in parentheses.	154
Table III.B.2.1 Structural parameters (bond lengths in Å and bond angles in degree) computed at the SFX2C-1e-CCSD(T)/cc-pVTZ level for UO_2Cl_2 and UO_2Cl_2^-	163
Table III.B.2.2 Harmonic vibrational frequencies (in cm^{-1}) computed at SFX2C-1e-CCSD(T)/cc-pVTZ level for the ground state of UO_2Cl_2 and the ground state of UO_2Cl_2^-	163
Table III.B.2.3 The computed adiabatic electron affinity (EA_a) and vertical detachment energy (VDE) values (in eV) of UO_2Cl_2^- . The HF values for EA_a were obtained using the cc-pVQZ-unc basis sets. The correlation contributions were obtained using the cc-pVTZ-unc and cc-pVQZ-unc basis sets and extrapolated to estimate the basis-set-limit value.	165
Table III.B.3.1 Experimental and calculated electron affinities (EA) of UAu_6 and vertical detachment energies (VDE) of UAu_6^- clusters.	176

Table III.B.4.1 The data include the spin-multiplicity of neutral and mono-anions of UAu_n , $n = 3-7$. Also given are the singly(?) occupied Lewis lone pairs in the spin up and down state along with the natural bond order (NBO) charges on U and Au atoms. The Mayer bond order (MBO) between the U and Au atoms, and the HOMO-LUMO gap (HL) is provided for the studied U@Au_n cluster.	193
Table III.B.4.2 Experimental and calculated electron affinities (EA) and vertical detachment energies (VDE) of UAu_n^- ($n = 3-7$) clusters.....	194
Table IV.A.1.1 Computed VDEs for each structure from figure 3 and their corresponding experimental values (eV).....	206
Table IV.A.2.1 Measured VDEs and predicted VDEs and ADEs of $\text{Ir}_n(\text{NOH})^-$, in eV.....	223
Table IV.A.3.1 Experimental and calculated VDE/VPTE values for the GM structure, H-Pt-CH_3^-	241
Table IV.B.2.1 Computed VDEs for each structure from Figure 3 and their corresponding experimental values. All VDE values are given in eV.	288
Table V.A.1.1 Theoretical and experimental adiabatic and vertical detachment energies (1 st and 2 nd peak) of $\text{Co}_6\text{S}_8(\text{PEt}_3)_{6-x}(\text{CO})_x^-$ ($x = 0-3$) clusters. The superscripts T and E indicate theoretical and experimental values, respectively.....	305
Table V.A.2.1 Theoretical and experimental adiabatic and 1 st and 2 nd vertical detachment energies (VDE and VDE*) of $\text{Co}_6\text{S}_8(\text{PEt}_3)_x^-$ ($x = 0-5$) clusters.....	318
Table VI.A.5.1 List of the VDE (eV) of the multiple Rydberg anions.....	354

I. Introduction

Photoelectron spectroscopy (PES) is an appealing experimental technique to probe electronic structures of matter. The principle of PES is based on the photoelectric effect, which raised puzzling questions about the nature of light—particle versus wavelike behaviour—that were finally resolved by Albert Einstein in 1905,¹ Albert Einstein's annus mirabilis (miracle year). Later in 1921, the law of photoelectric effect was recognized by the Nobel Prize in Physics. Einstein discovered this effect from the experimental observation made by Heinrich Hertz.² In Hertz's experiment, light of a specific wavelength is incident upon a bulk material. Electrons are emitted from the material after they absorb energy from the light if and only if that light energy is above the work function of the material. The total energy of the light is conserved by distribution to the kinetic and binding energies of the photo-emitted electrons. These photo-emitted electrons are referred to as photoelectrons. The difference between the energy of the ejected photoelectrons and the incident light is the work function of the material. Using this methodology, a PES experiment measures the kinetic energies of photoelectrons ejected from surfaces, liquids, or gas phase molecules after being exposed to a photon beam used as a probe.

Depending on the photon energy, PES can be divided mainly into three categories: X-ray photoelectron spectroscopy (XPS), extreme-ultraviolet photoelectron spectroscopy (EUPS), and ultraviolet photoelectron spectroscopy (UPS). XPS was developed by Kai Siegbahn in 1957.^{3,4} XPS utilizes soft-X-rays with photon energies of 200-2000 eV to study core-level electrons. The core levels will have chemical shifts when the chemical environment of the atom that is ionized changes, allowing the determination of the chemical structures. It is widely used for solid materials.

UPS was first developed by Feodor I. Vilesov in 1961⁵ and David W. Turner in 1962.^{6,7} Compared to XPS, UPS can only probe valence electrons due to the relatively low photon energies. However, the photoelectrons emitted carry smaller kinetic energies, resulting in better resolution. In the following years, UPS has been extensively improved and advanced for various applications in chemistry and physics.

PES was first implemented in the study of negatively charged (anionic) species in 1967 for the direct measurement of the electron affinity (EA) of helium.⁸ The low valence electron binding energies of anionic species allows PES to probe both the ground and excited states of the less negative species. Later, in the 1980's, the anion PES technique was first well developed by Lineberger,⁹ Smalley,¹⁰ and Meiwesbroer,¹¹ et al. The groups led by Neumark,¹² Cheshnovsky,¹³ Kaya,¹⁴ Wang,¹⁵ Ganteför,¹⁶ Haberland, Issendorff,¹⁷ and my supervisor, Bowen¹⁸ have also made substantial and extensive contributions to the PES studies of cluster anions in the following years.

The brief experimental procedures of anion PES are explained as follows: A size-selected anion cluster is photodetached by a detachment laser beam with a fixed photon energy ($h\nu$) to generate photoelectrons with different kinetic energies (EKE). The energies of the emitted photoelectrons are characteristics of their original electronic energy states. These photoelectrons are collected and analyzed by an electron energy analyzer based on their kinetic energies to produce the photoelectron spectrum. The photodetachment process is governed by the energy conservation relationship in Equation 1, where $h\nu$ is the photon energy, EBE is the electron binding energy, and EKE is the electron kinetic energy.

$$h\nu = \text{EBE} + \text{EKE} \quad (\text{Equation 1})$$

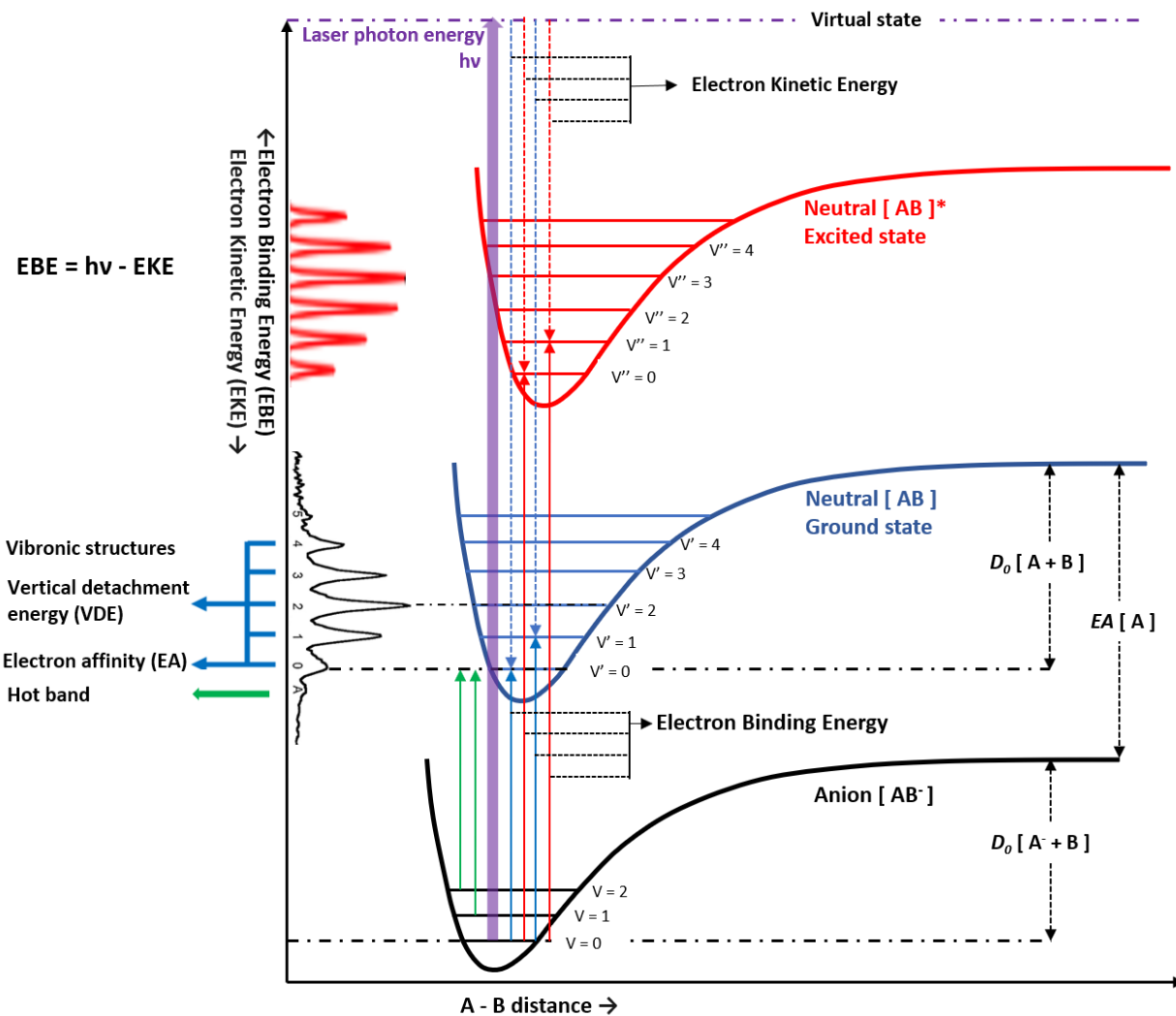


Figure II.A.1.1 Potential energy diagram detailing the transitions that occur during anion photoelectron spectroscopy.

The photon energy is known, and the EKE is measured experimentally using an energy analyzer; therefore, the EBE can be calculated. The main benefit of PES is there are no forbidden transitions. In optical spectroscopy, spin selection rules limit the possible transitions. The vibronic transitions in PES do not possess these selection rules. The spectroscopic data provides structural information of the neutral molecule. To understand the experimental PES spectrum, there are several spectral features we need to pay special attention to.

Adiabatic electron affinity (EA). The adiabatic electron affinity (EA) is the energy difference between the ground state of the neutral and the ground state of the anion, shown in Equation 2 and Figure I.A.1.1.

$$EA = E(\text{Neutral at Neutral Ground Geo.}) - E(\text{Anion at Anion Ground Geo.}) \quad \text{Equation 2}$$

The EA can be determined experimentally if there is a high Franck-Condon overlap between the ground state of the neutral and the ground state of the anion; however, if there are significant geometrical changes between the anion and the neutral, the Franck-Condon overlap is poor and the EA will not be visible in the PES. If there is a good Franck-Condon overlap, the EA is the threshold of the spectrum.

How to determine the EA from the PES is a long-time topic in this lab. We met questions from reviewers almost every time we tried to estimate the EA of a molecule or a cluster. I try to make it as clear as I can. By definition, EA is a 0-0 transition from a theoretical picture. However, locating the 0-0 transition in a spectrum is not straightforward. There are several hindrances. First, the clusters/molecules we made in the beam are not cold enough. Unless at 0K, some vibrationally excited states will be populated following the Boltzmann distribution. The population at excited states will cause the hot bands which are the features lower than the 0-0 transition. As shown in figure I.A.1.1, the feature at the lowest EBE side is not the EA. Cooling the systems can eliminate the hot bands. Supersonic expansion, ion trap with buffer gas, and their combinations are the most common ways. Second, the spectrum is not resolved enough to identify the EA. Traditional PES has its resolution limit. Depending on the detectors, the best resolution of the PES is about $50 \text{ cm}^{-1}/6 \text{ meV}$. If one can use a tunable laser, zero kinetic energy electron (ZEKE) and slow velocity map imaging (SEVI) can achieve around $0.1 \text{ cm}^{-1} / 0.01 \text{ meV}$ resolution or better.²⁴ To accurately determine the EA, the higher resolution is better. For most systems, we don't care about the 4th or 5th effective numbers after the digit. Obtaining a valuable number of EA with reasonable uncertainty is sometimes more important. To extract an EA from

a spectral band threshold, one can extrapolate the rising curve and intersect the baseline. And then add the resolution correction (half width of the half maximum) to the intersection. Another rough estimation our lab used in some published papers is locating the 5% of the rising feature/peak. Third, the co-existence of different species/isomers/states with the same mass will cause the misinterpretation of the spectrum. According to the discussions above, the lowest feature is the EA if the hot band is eliminated. However, if two species have the same mass, both will be observed in the PES spectrum. Another example is weakly bound states. If dipole (or multiple) bound anions and valence bound anions co-exist in the beam, photodetachment from the weakly bound anions will show features at the lower EBE range. All in all, we need to consider all possible factors when assigning the EA.

Vertical detachment energy (VDE). The vertical detachment energy (VDE) of the neutral system can also be determined. The VDE stems from the transition from the anion ground state to that of a vibrational state of the neutral system that has the highest Franck-Condon overlap with the anion. This transition is highlighted in Figure I.1 and explained in Equation 3.

$$\text{VDE} = E(\text{Neutral at Anion Ground Geo.}) - E(\text{Anion at Anion Ground Geo.}) \quad \text{Equation 3}$$

Since this transition has a high Franck-Condon overlap, it is the most intense photoelectron transition in the PES spectrum. VDE is the most straightforward concept and is easy to locate in each spectrum.

Peak spacings. Two factors affect the peak spacings: energy gaps between electronic states and gaps between vibrational levels of the molecule. Energy gaps between electronic states are normally in the eV level, and vibrational gaps are 1-3 orders of magnitude smaller than eV. Also, vibrational states often show consecutive peaks with the same binding energy intervals. When the temperature of a studied system is low enough and the structural difference

between the anion and the neutral is big enough, one could also observe vibrational progressions of the neutral.

Sometimes vibrational frequencies can be used as a way of isotope tagging to detect the structure of the molecules.

For electronic states, if the neutral is a closed-shell system, the spacing between the first and the second PES peaks corresponds to the HOMO-LUMO gap based on Koopmans' theorem. Note that the energy spacing of the peaks is not equivalent to the HOMO-LUMO gap. More accurately, the energy spacing observed between the first and the second peak in the spectrum is equal to the gap between the ground state and the first excited state of the neutral. In some systems, the lowest excitation process is dominated by the HOMO to LUMO transition. However, there is always an exciton binding energy difference between the excitation energy and the HOMO-LUMO gap. Moreover, multi-electron process will cause the failure of Koopmans' theorem. I will discuss it in the part of *advanced features* later.

Spectral band intensity. The spectral intensity corresponds to the number of electrons counts within certain kinetic energy window. Reproducing the band intensity is very tricky but intriguing. The intensity of the photoelectron spectrum at a particular electron kinetic energy depends on the angle (θ) between the polarization vector of the laser light and the electron collection direction according to

$$I(\theta) = \frac{\sigma_{tot}}{4\pi} [1 + \beta(E)P_2(\cos\theta)] \quad \text{Equation 4}$$

where σ_{tot} is the total photodetachment cross section, $\beta(E)$ is the anisotropy parameter, and $P_2(\cos\theta)$ is the second Legendre polynomial. Lineberger and co-workers collected spectra with the laser polarization at the "magic" angle of $54^\circ 44'$, so that $P_2(\cos\theta) = 0$, and the intensity is that of the average photodetachment cross section. Therefore, they can obtain meaningful relative intensities without the necessity of measuring photoelectron angular distributions. Relative intensity among the features directly indicates the cross-section of the anion MOs.²³ In reality, one band or peak is often contributed by multiple photodetachment transitions. Due to the limitation of the instrument resolution

and peak broadening, near peaks will convolute to a bigger one. Some systems with complex electronic structures like transition metal or actinides have dense electronically excited states. If the energy spacing between the electronic states is smaller than gap of vibrational levels, electronic states and vibrational states will both contribute to the band intensity. In this case, to roughly reproduce the band intensity, one can assume all the cross-sections of the anion MOs are the same and then do gaussian broadening for each transition.

Advanced features. In addition to the direct features discussed above, more indirect and deeper information can be obtained from the PES.

1) Isomers. As discussed in the EA part, isomers close in energy might co-exist in the ion beam; however, they cannot be identified by mass spectrometry or separated by a mass gate. One can distinguish the isomers by photoelectron spectrum. In Chapter IV.A.1, two different PES of $\text{Ir}(\text{H}_2\text{O})^-$ anions were seen in the experiment, indicating different isomers were made under different experimental conditions. Furthermore, isomers of Ir-H₂O complex anion suggest water molecule being activated by single Iridium anions.

2) Photodissociation. One can sometimes observe photodetachment transitions from fragments of the anion in the spectrum. For example, in the spectrum of PtHCO_2^- collected by our group, the feature from PtH^- is clearly present. Our diiodobenzene experiment, discussed in Chapter VI.A.7, I^- peak at 3 eV appeared in the 3rd harmonic PES of 1,2- $\text{C}_6\text{H}_4\text{I}_2^-$ but vanished in the 4th harmonic PES. Photodissociation features are photon energy dependent. From a potential surface model, the first photon pumps the anion to an excited unbound state, and the excited intermediate will break into fragments spontaneously. A second photon will continue to detach the anionic fragment, thus yielding EBE features in the spectrum of the parent anion.

3) Autodetachment. Autodetachment is sometimes observed in anion PES if an anion that absorbs a photon is excited to a temporary excited state in the detachment continuum.¹⁹ When the anion has resonance (either shape resonance or Feshbach resonance) with the photon energy used for photodetachment, the anion will be pumped to its excited states and undergo an autodetachment process. Feshbach resonances are long-lived anion excited states, usually involving two-electron transitions, whereas shape resonances are short-lived anion states, which involve one-electron transition and are characterized by an angular momentum barrier. Autodetaching resonances were first observed by Lineberger and co-workers in atomic anions and in small molecular anions with tunable lasers.²⁰ In principle, the autodetachment processes can be accessed by PES upon optical excitation to an anion resonant state. Schiedt and Weinkauff performed resonant PES following optical excitations to both Feshbach resonances and shape resonances in the p-benzoquinone anion. They observed significant variations of the observed Franck-Condon (FC) profiles.²¹ A resonant PES of Au_2^- via a Feshbach state using high-resolution imaging conducted by Wang group is an easy example to understand autodetachment.²² Nevertheless, very few resonant PES experiments have been conducted deliberately because most anion PES experiments are performed with fixed wavelength detachment lasers.

4) Multielectron process. Based on Koopmans' theorem, the first EBE peak corresponds to the detachment from HOMO/SOMO; the second corresponds to HOMO/SOMO-1. But it cannot explain all transitions. PES mainly involves single-electron processes where each spectral band corresponds to single-electron detachment from one molecular orbital (MO). However, when an electron from a deeper orbital is emitted, the relaxation energy can excite a second electron filling an empty orbital. The new transition caused by the second electron is called "shake-up transition" in XPS. The multielectron process is also very common in PES. One can easily find examples in the

spectrum of transition metal anion like Pd^- .²³ The lowest EBE transition corresponds to $\text{Pd}^- (4d^9 5s^2)^2D_{5/2} \rightarrow \text{Pd} (4d^{10})^1S_0$, which means two-electron process occurs. The shake-up peaks intensities are relatively weak due to the electron correlation effect.

5) Selection rules. There is no simple selection rule between the initial state of the anion and the final states of the neutral because of the multielectron process. For one electron process in single atomic anions with term symbol $^{2S+1}L_J$, photoelectron selection rules are $|\Delta L| \leq 1$, $|\Delta S| \leq 1/2$, $|\Delta J| \leq 1+1/2$, where l is the angular momentum of the orbital shell from which the electron was detached.²³ With the help of first-order time-dependent perturbation theory, one can determine the transition probability of a system from an initial state $|i\rangle$ to an energetically higher lying final state $|f\rangle$ (i.e., absorption of a photon $\hbar\omega$). This results in Fermi's golden rule for the transition. For an ionization process, the initial state corresponds to the bound electron in the cluster, and the final state corresponds to an electron detached from the cluster and escapes to infinity after the ionization process at time $t = 0$. Via the interactions between the polarized light field and the Schrodinger equation of the initial bound state, one can construct the wave functions of the outgoing photoelectron with certain angular momentum. By substituting the initial and final states into the cross-section formula, an explicit formula for the photoelectron angular distribution (PAD) can be obtained. Selection rules can be derived from the condition that the angular matrix in the PAD formula is not zero. For all formulas and mathematical details, please refer to Bartels' thesis.²⁵

6) Others. There are other possible reasons for extra features in PES, such as photodetachment angle distribution (PAD), spin-orbital splitting, resonant transitions, lower harmonic photon leakage, etc.

In summary, PES is a powerful tool for studying clusters and reactions in the gas phase. With various ion sources and laser techniques, PES has become a highly versatile technique capable of addressing fundamental problems in chemistry, physics, material science, and even life science, such as electronic structures, chemical bonding, reaction mechanism, electron-molecule interactions, and so on. The isolated systems we study in the vacuum also build a bridge between experiments and theoretical calculations. Details will be discussed in the main body of this thesis.

Chapter II to Chapter V is mainly a selected collection of my published work on applying PES to study antioxidants (Chapter II), thorium and uranium containing systems (Chapter III), molecular activation (Chapter IV), and superatomic clusters (Chapter V). The appendix contains majorly unpublished results. The full publication list is on the curriculum vitae.

References:

1. Einstein, A. (1905). Über einen die Erzeugung und Verwandlung des Lichtes betreffenden heuristischen Gesichtspunkt. *Ann Physik* 17:132–148. Translated into english in: Einstein, A. (1965). Concerning an heuristic point of view toward the emission and transformation of light. *American Journal of Physics*, 33(5), 1–16.
2. Hertz, H. (1887). Ueber einen Einfluss des ultravioletten Lichtes auf die elektrische Entladung. *Annalen der Physik*, 267(8), 983-1000.
3. Siegbahn, K., & Edvarson, K. (1956). β -Ray Spectroscopy in the Precision Range of 1: 105. *Nuclear physics*, 1(8), 137-159.
4. Nordling, C., Sokolowski, E., & Siegbahn, K. (1957). Precision method for obtaining absolute values of atomic binding energies. *Physical Review*, 105(5), 1676.
5. Vilesov, F. I., Kurbatov, B. L., & Terenin, A. N. (1961). Electron distribution over energies in the photoionization of aromatic amines in the gaseous phase. In *Doklady Akademii Nauk* (Vol. 138, No. 6, pp. 1329-1332). Russian Academy of Sciences.
6. Al-Joboury, M. I., & Turner, D. W. (1963). 985. Molecular photoelectron spectroscopy. Part I. The hydrogen and nitrogen molecules. *Journal of the Chemical Society (Resumed)*, 5141-5147.
7. Turner, D. W., & Jobory, M. A. (1962). Determination of ionization potentials by photoelectron energy measurement. *The Journal of Chemical Physics*, 37(12), 3007-3008.

8. Brehm, B., Gusinow, M. A., & Hall, J. L. (1967). Electron affinity of helium via laser photodetachment of its negative ion. *Physical Review Letters*, 19(13), 737.
9. Corderman, R. R., & Lineberger, W. C. (1979). Negative ion spectroscopy. *Annual Review of Physical Chemistry*, 30(1), 347-378.
10. Cheshnovsky, O., Yang, S. H., Pettiette, C. L., Craycraft, M. J., & Smalley, A. R. (1987). Magnetic time-of-flight photoelectron spectrometer for mass-selected negative cluster ions. *Review of Scientific Instruments*, 58(11), 2131-2137.
11. Ganteför, G., Meiwes-Broer, K. H., & Lutz, H. O. (1988). Photodetachment spectroscopy of cold aluminum cluster anions. *Physical Review A*, 37(7), 2716.
12. Metz, R. B., Kitsopoulos, T., Weaver, A., & Neumark, D. M. (1988). Study of the transition state region in the $\text{Cl} + \text{HCl}$ reaction by photoelectron spectroscopy of ClHCl^- . *The Journal of chemical physics*, 88(2), 1463-1465.
13. Markovich, G., Giniger, R., Levin, M., & Cheshnovsky, O. (1991). Photoelectron spectroscopy of iodine anion solvated in water clusters. *The Journal of chemical physics*, 95(12), 9416-9419.
14. Nakajima, A., Taguwa, T., Hoshino, K., Sugioka, T., Naganuma, T., Oho, F., Watanabe, K., Nakao, K., Konishi, Y., Kishi, R. and Kaya, K., 1993. Photoelectron spectroscopy of $(\text{C}_6\text{F}_6)^-n$ and $(\text{Au-C}_6\text{F}_6)^-$ clusters. *Chemical physics letters*, 214(1), pp.22-26.
15. Wang, L. S., Cheng, H. S., & Fan, J. (1995). Photoelectron spectroscopy of size-selected transition metal clusters: Fe^-n , $n = 3-24$. *The Journal of chemical physics*, 102(24), 9480-9493.
16. Ganteför, G., & Eberhardt, W. (1996). Localization of 3 d and 4 d Electrons in Small Clusters: The “Roots” of Magnetism. *Physical review letters*, 76(26), 4975.
17. G. Wrigge, M. Astruc Hoffmann, B. von Issendorffa, and H. Haberland Ultraviolet photoelectron spectroscopy of Nb_4^- to Nb_{200}^- . *Eur. Phys. J. D* 24, 23–26 (2003)
18. Coe, J. V., Snodgrass, J. T., Freidhoff, C. B., McHugh, K. M., & Bowen, K. H. (1985). Negative ion photoelectron spectroscopy of the negative cluster ion $\text{H}-(\text{NH}_3)_1^-$. *The Journal of chemical physics*, 83(6), 3169-3170.
19. K. R. Lykke, K. K. Murray, D. M. Neumark, and W. C. Lineberger, *Philos. Trans. A. Math. Phys. Eng. Sci.* 324, 179 (1988).
20. Patterson, T. A., Hotop, H., Kasdan, A., Norcross, D. W., & Lineberger, W. C. (1974). Resonances in alkali negative-ion photodetachment and electron affinities of the corresponding neutrals. *Physical Review Letters*, 32(5), 189.
21. Schiedt, J., & Weinkauff, R. (1999). Resonant photodetachment via shape and Feshbach resonances: p-benzoquinone anions as a model system. *The Journal of chemical physics*, 110(1), 304-314.
22. León, I., Yang, Z., & Wang, L. S. (2013). Resonant photoelectron spectroscopy of Au_2^- via a Feshbach state using high-resolution photoelectron imaging. *The Journal of Chemical Physics*, 139(19), 194306.
23. Feigerle, C. S., Corderman, R. R., Bobashev, S. V., & Lineberger, W. C. (1981). Binding energies and structure of transition metal negative ions. *The Journal of Chemical Physics*, 74(3), 1580-1598.

24. Osterwalder, A., Nee, M. J., Zhou, J., & Neumark, D. M. (2004). High resolution photodetachment spectroscopy of negative ions via slow photoelectron imaging. *The Journal of chemical physics*, 121(13), 6317-6322.
25. Bartels, C. (2008). *Angular distributions of photoelectrons from cold, size-selected sodium cluster anions* (Doctoral dissertation, Verlag nicht ermittelbar).

II. Antioxidants

The importance of oxidation in the body and foodstuffs has been widely recognized. The term ROS (reactive oxygen species) is used for short-lived diffusible entities such as hydroxyl ($\cdot\text{OH}$), alkoxyl ($\text{RO}\cdot$), or peroxy ($\text{ROO}\cdot$) radicals and some radical species of medium lifetime such as superoxide ($\text{O}_2\cdot^-$) or nitroxyl radical ($\text{NO}\cdot$). It also includes the non-radicals: hydrogen peroxide (H_2O_2), organic hydroperoxides (ROOH), and hypochlorous acid (HOCl). ROS are generated by inflammatory cells, which accumulate in both allergic¹ and non-allergic² inflammations, as well as through interactions of tissues with ultraviolet and ionizing radiation and other toxins. When an excess of free radicals is formed, they can overwhelm protective enzymes such as superoxide dismutase, catalase and peroxidase and cause destructive and lethal cellular effects (*e.g.*, apoptosis) by oxidizing membrane lipids, cellular proteins, DNA and enzymes, thus shutting down cellular respiration.

Antioxidants play an important role in food preservation by inhibiting oxidation processes and contributing to health promotion rendered by many dietary supplements, nutraceuticals, and functional food ingredients. The antioxidants react with ROS faster than relevant biological targets react with ROS, thus protecting lipids, fats, and proteins from the attack of free radicals. Methods of assessing antioxidant behavior fall into two broad categories reflecting the focus on bioactivity in humans or activity in foods.³ In this chapter, I will present one example in each category.

The first example is the most famous antioxidant, ascorbic acid, also known as Vitamin C. At physiological pH, ascorbic acid is predominately present as the ascorbate anion, $\text{C}_6\text{H}_7\text{O}_6^-$. In Section II.A.1, the photoelectron spectra of the ascorbate anion, $\text{C}_6\text{H}_7\text{O}_6^-$, and the deprotonated ascorbate anion, $\text{C}_6\text{H}_6\text{O}_6^{2-}$, are presented. The ionization energy of the ascorbate anion is determined to be 3.85 eV, which is lower than other biological molecules found in the body.

The ascorbate anion will readily donate an electron to reactive oxygen species and detrimental radicals in the body and, therefore, protect potential biological targets.

The example for the second category (activity in foods) is gallic acid and its derivative, propyl gallate. Gallic acid, also known as 3,4,5-trihydroxybenzoic acid, is widely present in the plant kingdom and found in various food sources, such as tea, grapes, and red wine. Propyl gallate, commonly used as an antioxidant in food, is a synthetic derivative of gallic acid. In section II.A.2, photoelectron spectra of the deprotonated gallic acid anion, $[\text{GA-H}]^-$, and the deprotonated propyl gallate anion, $[\text{PG-H}]^-$, were measured at both ambient temperature and at 77 K. Electron affinities of the dehydro-gallic acid radical, $[\text{GA-H}]^\cdot$, as well as of the dehydro-propyl gallate radical, $[\text{PG-H}]^\cdot$, were determined to be 2.90 ± 0.05 eV and 2.85 ± 0.05 eV, respectively. DFT calculations on the deprotonated anions and corresponding radicals showed that intra-molecule bonding could effectively stabilize the molecules, thus enhancing the antioxidant ability.

References:

1. Simon, H. U., Yousefi, S., Schranz, C., Schapowal, A., Bachert, C., & Blaser, K. (1997). Direct demonstration of delayed eosinophil apoptosis as a mechanism causing tissue eosinophilia. *The Journal of Immunology*, 158(8), 3902-3908.
2. Dibbert, B., Weber, M., Nikolaizik, W. H., Vogt, P., Schöni, M. H., Blaser, K., & Simon, H. U. (1999). Cytokine-mediated Bax deficiency and consequent delayed neutrophil apoptosis: a general mechanism to accumulate effector cells in inflammation. *Proceedings of the National Academy of Sciences*, 96(23), 13330-13335.
3. Lindley, M. G. (1998). The impact of food processing on antioxidants in vegetable oils, fruits and vegetables. *Trends in Food Science & Technology*, 9(8-9), 336-340.

II.A.1. A Photoelectron Spectroscopic Study of Ascorbate and Deprotonated Ascorbate Anions Using an Electrospray Ion Source and a Cryogenically Cooled Ion Trap

Reprinted by permission from J. Phys. Chem. A 2021, 125, 35, 7699–7704. Copyright 2021 American Chemical Society

Mary Marshall, Zhaoguo Zhu, Rachel Harris, Evan Collins,[‡] Kit H. Bowen*

Department of Chemistry, Johns Hopkins University, Baltimore, MD 21218, USA

Abstract

Reactive oxygen species (ROS) in biological systems are formed through a variety of mechanisms. These species are very reactive and have been associated with many diseases, including cancer and cardiovascular disease. One way of removing ROS from the body is through the use of radical scavengers, which are compounds capable of giving up an electron to neutralize the ROS yet form a stable radical species themselves. A common radical scavenger is ascorbic acid, also known as vitamin C. At physiological pH, ascorbic acid is predominately present as the ascorbate anion, $C_6H_7O_6^-$. The ascorbate anion, as well as the dianion ($C_6H_6O_6^{2-}$), is an effective antioxidant due to its ability to donate an electron from a lone pair generated by deprotonation. An electrospray ionization source was added to our pulsed anion photoelectron spectrometer to study the ascorbate anions and deprotonated ascorbate dianions via photoelectron spectroscopy. The antioxidant behavior of the ascorbate anion and the deprotonated ascorbate dianion was confirmed based on the experimental vertical detachment energy (VDE), and, therefore, the ionization energy of the anions, 3.85 eV and 2.68 eV, respectively.

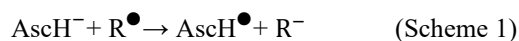
Introduction

Reactive oxygen species (ROS) are free radicals, or free radical initiators, that are generated through a range of both normal metabolic processes, as well as through interactions of tissues with ultraviolet and ionizing radiation and other

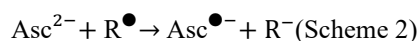
toxins.¹ These highly unstable, very reactive species damage important biological molecules, including DNA, lipids and proteins. The subsequent radical chain reactions resulting from ROS interactions are capable of causing significant tissue damage due to oxidative stress. This process is often proposed as the cause of many diseases, such as cancer and cardiovascular and neurodegenerative diseases.²⁻⁴ Additionally, it has been proposed that these radical reactions are major contributors to aging in organisms.⁵

Biological systems have several defensive processes for removing excessive ROS from the body. A common method is through the employment of antioxidants. These radical scavengers are able to neutralize free radicals into stable molecules through electron or hydrogen atom donation.⁶ The scavengers become stable, radical species and are degraded through different established pathways.^{2,3} Ascorbic acid, also known as vitamin C, is an excellent, water-soluble radical scavenger due to its ability to react with a wide range of biologically relevant ROS, e.g., hydroxyl radicals and superoxide anion, in the blood and cytoplasm.^{2,7,8}

Although not produced within the body, ascorbic acid can be easily consumed, as it is naturally present in many common fruits and vegetables.⁹ It is an important nutrient that is attributed to many biological functions beyond its usefulness as an antioxidant, including the production of collagen, enzyme activity and iron absorption.^{10,11} At physiological pH, ascorbic acid (AscH_2) is mostly present in the form of the ascorbate anion (AscH^-), since the pK_a of the most acidic hydrogen is 4.24 (Figure II.A.1.1).¹² The ascorbate anion is one of the most active antioxidant forms of vitamin C. It is classified as a donor antioxidant due to its ability to donate an electron from the lone pair generated by deprotonation, i.e., Scheme 1, where R is the ROS.^{3,12}



AscH[•] is transient; the second hydrogen has a pKa of -0.9 and will rapidly deprotonate to Asc^{•-}.¹² Although not present in high concentrations in biological systems, since AscH[•] has a pKa of 11.8, the doubly deprotonated form of ascorbic acid, Asc²⁻, is also an effective antioxidant. The dianion transfers an electron to a free radical species to form the stable radical anion, Asc^{•-}, e.g., Scheme 2.



Asc^{•-} is a stable radical species that can convert back into the ascorbate anion as well as into dehydroascorbic acid (DHA) in biological systems, as shown in Figure II.A.1.1.¹² Additionally, Asc^{•-} can be a source of hydrated electrons, which are considered a universal reductant.¹³

The most stable structures of ascorbic acid, the ascorbate anion, and deprotonated ascorbate have been determined using X-ray crystallography with the aid of calculations.^{14,15} The vertical ionization energies and electron affinities have been theoretically calculated for ascorbic acid and the ascorbate anion, as well as deprotonated ascorbate and their radicals in both the gas phase and when solvated by water.¹⁶⁻¹⁸ Another radical scavenger, vitamin E, has previously been studied via photoelectron studies.¹⁹ In this work, we report the anion photoelectron spectra of the ascorbate anion (AscH⁻) and deprotonated ascorbate (Asc²⁻) generated by an electrospray ionization source. The photoelectron study of AscH⁻ and Asc²⁻ sheds light on energetic aspects of vitamin C as an antioxidant.

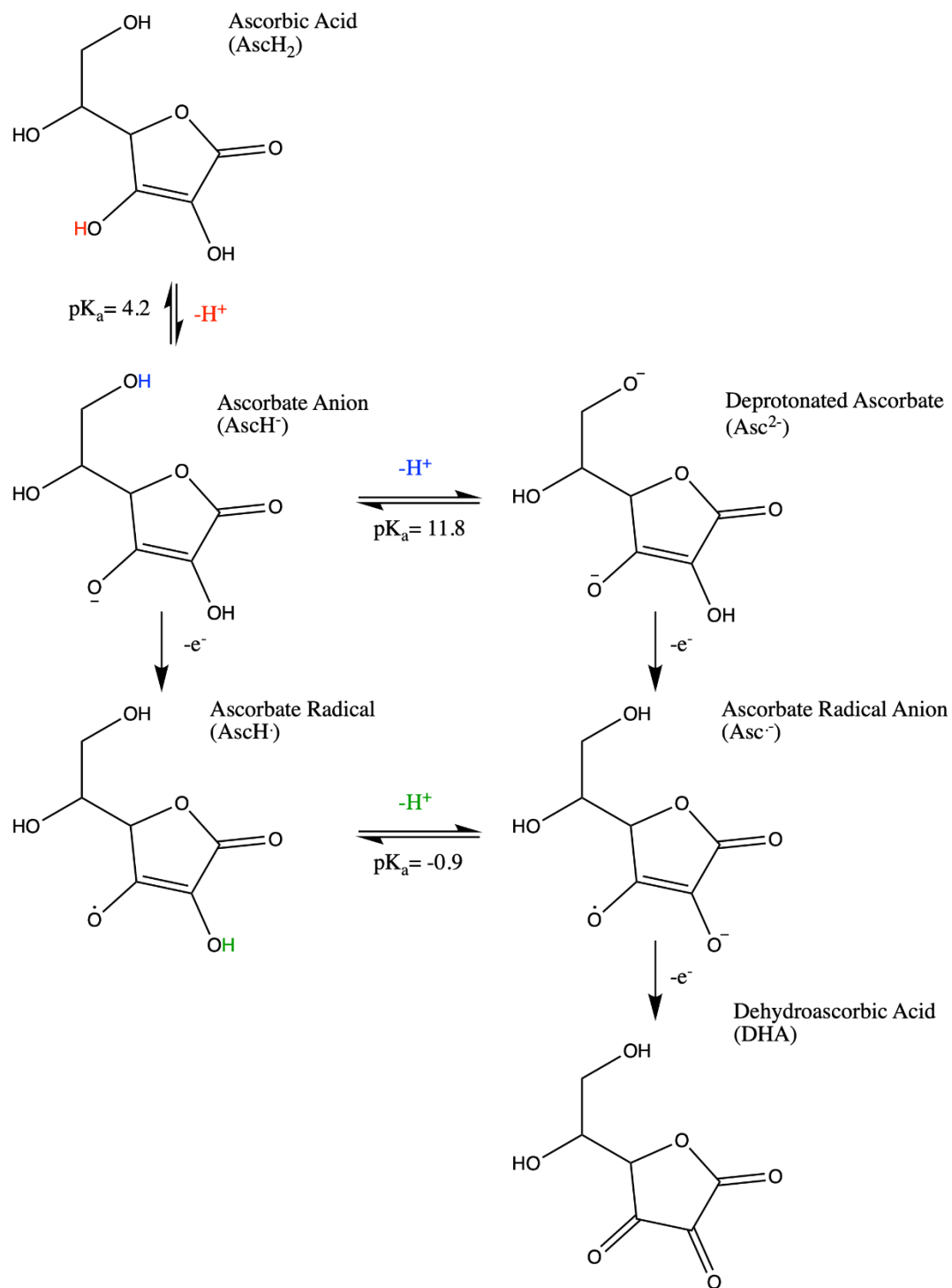


Figure II.A.1.1 The structures of the different anions, radicals, and neutral molecules associated with vitamin C. The structures represent those that are most stable in the gas phase.

Experimental

The ascorbate anion (AscH^-) and the deprotonated ascorbate dianion (Asc^{2-}) were generated via electrospray ionization; a source recently added to one of our pulsed anion photoelectron spectrometers. This system is highly amenable to ionization by ESI due to water solubility and facile tuning of the pH conditions in solution. The electrospray ionization source is modeled on the previous designs of Lai-Sheng Wang, Xue-Bin Wang, and Mark Johnson.^{20–22} Millimolar solutions of L(+)-ascorbic acid (Sigma-Aldrich, BioXtra, $\geq 99.0\%$) diluted in 3:1 MeOH:H₂O in a range of pH values ($5 < \text{pH} < 12$) were prepared. The ascorbic acid solution was sprayed through a $\sim 10\ \mu\text{m}$ pulled silica capillary floated at negative 3–5 kV into a humidity controlled, ambient atmosphere chamber. The ions entered a stainless steel desolvation capillary, which was heated to help remove solvent from the droplets formed via the ionization process. After exiting the capillary, the anions were guided through differentially pumped chambers by ion guides and ion optics into an ion trap. The ion trap has the capability to be cooled to 77 K by a liquid nitrogen flow cryostat (Advanced Research Systems, Inc.), and the temperature is monitored via a silicon diode. A buffer gas of 20% H₂ with a balance of He was used in the ion trap to facilitate the cooling of the ions, as well as collisional focusing.²⁰ The ions were accumulated and cooled in the trap for 100 ms before being pulsed out of the trap into a time of flight mass spectrometer. The ions from the electrospray ionization source enter into that time of flight mass spectrometer, which has been described elsewhere,^{23,24} on the opposite side of the Wiley-McLaren extraction plates as compared to our tradition pulsed anion sources, as shown in Figure II.A.1.2.

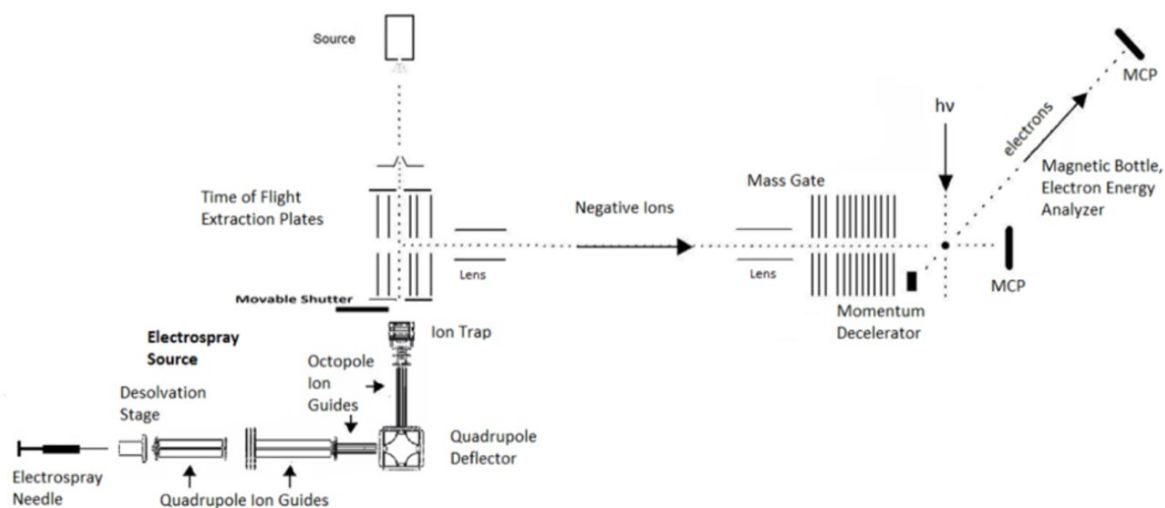


Figure II.A.1.2. The schematic view of the electrospray ionization source that was incorporated into the preexisting pulsed ion photoelectron spectrometer.

Anion photoelectron spectroscopy was conducted by crossing a mass-selected packet of negative ions with a fixed frequency photon beam and energy-analyzing the resultant photodetached electrons. These photoelectrons are governed by the energy-conserving relationship: $h\nu = \text{EBE} + \text{EKE}$, where $h\nu$ is the photon energy, EBE is the electron binding energy, and EKE is the measured electron kinetic energy. The anion photoelectron spectrometer consists of an magnetic bottle electron energy analyzer and a Nd:YAG laser. The magnetic bottle has a resolution of ~ 50 meV at an EKE of 1 eV. The spectra were collected with the 3rd and 4th harmonic of the Nd:YAG laser (355 nm, 3.49 eV and 266 nm, 4.66 eV, respectively). The photoelectron spectrometer was calibrated against the known transitions of I⁻.²⁵

Photoelectron spectra were obtained with the ion trap at room temperature as well as when cooled to 77 K.

Results

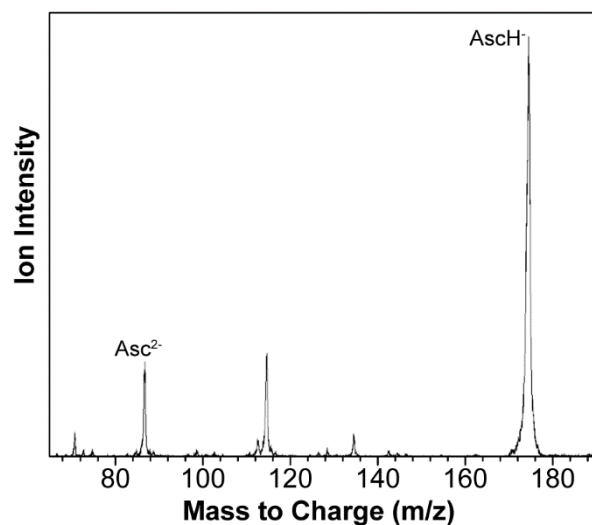


Figure II.A.1.3. The mass spectrum of an ascorbic acid solution with a pH of 8 generated by ESI.

The ascorbate anion (AscH^-), deprotonated ascorbate (Asc^{2-}), and fragments of ascorbate were seen in the mass spectrum, as presented in Figure II.A.1.3. The relative intensities of the ascorbate anion versus deprotonated ascorbate were strongly dependent on the pH of the solution. In line with the pK_a of ascorbate and deprotonated ascorbate, deprotonated ascorbate was favored at pH higher than 11.8.¹² The other fragments in the spectrum were likely generated in the ionization process or during the ion transport through the ion guide system via collisions with background gas molecules.

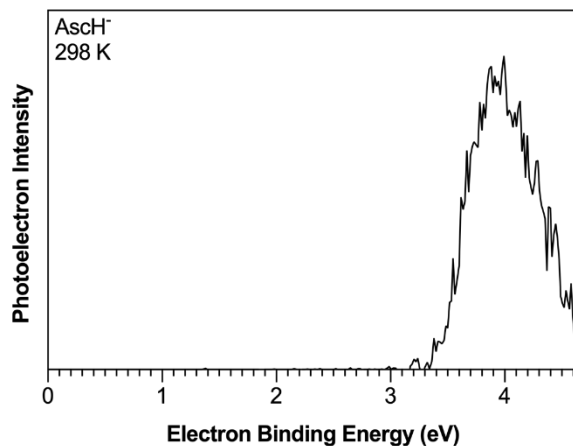


Figure II.A.1.4 The photoelectron spectrum of the ascorbate anion (AscH^-) taken with the ion trap at ambient temperature using the 4th harmonic of a Nd:YAG laser (266 nm, 4.66 eV).

The photoelectron spectrum (PES) of the ascorbate anion (AscH^-) was obtained using the fourth harmonic of a Nd:YAG laser (266 nm, 4.66 eV) with the ion trap at ambient temperature (Figure II.A.1.4). The broad feature has an onset at EBE ~ 3.5 eV, corresponding to the electron affinity (EA) of the ascorbate radical, AscH^\bullet , with a vertical detachment energy (VDE) value of 3.85 eV. While there appear to be vibrational bands, they are not well resolved in the spectrum.

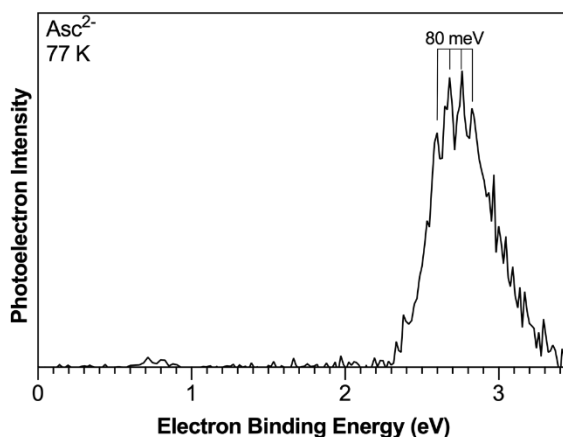


Figure II.A.1.5 The photoelectron spectrum of deprotonated ascorbate (Asc^{2-}) taken at an ion trap temperature of 77K using the 3rd harmonic of a Nd:YAG laser (355 nm, 3.49 eV).

The deprotonated ascorbate (Asc^{2-}) was photodetached at an ion trap temperature of 77 K using the 3rd harmonic of a Nd:YAG laser (355 nm, 3.49 eV), as well as at ambient temperature in the ion trap using the 4th harmonic of a Nd:YAG laser (266 nm, 4.66 eV); Figures II.A.1.5 and II.A.1.6, respectively. The observed VDE value, when photodetachment was conducted with 355 nm photons, is 2.68 eV. The vibrational structure, 80 meV, is easily discernable under these cold anions conditions. The spectrum collected using higher energy photons and with the ion trap at room temperature

displays two broad bands. The VDE value of the first peak appears to have shifted to slightly higher electron binding energy under these circumstances. Instead of the 2.68 eV VDE value observed in the 3rd harmonic spectrum, the VDE value was fitted to be 2.97 eV in the 4th harmonic spectrum. The next higher EBE feature exhibits an onset at an EBE of ~3.75 eV.

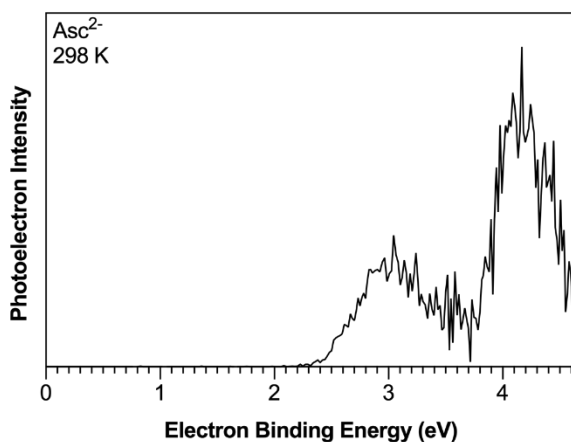


Figure II.A.1.6 The photoelectron spectrum of deprotonated ascorbate taken at room temperature using the 4th harmonic of a Nd:YAG laser (266 nm, 4.66 eV).

Discussion

The vertical detachment energy (VDE) is equal to the energy difference between the electronic ground state configuration of the anion and the anion's neutral counterpart in the same configuration. In terms of the ascorbate anion, the anion's neutral counterpart is the ascorbate radical. The VDE value of the ascorbate anion corresponds to its ionization energy, which is also correlated to its efficiency as an antioxidant. Low ionization energy means that the molecule is readily oxidized and can easily donate an electron.²⁶ In the presence of molecules with various ionization energies, the molecule or compound with the lower ionization energy will more readily give up an electron. When neutralizing a ROS, an antioxidant donates an electron and becomes oxidized.^{2,3} A successful antioxidant will more

readily donate an electron than the biological target in the body, such as DNA. We observed that the ionization energy of ascorbate, i.e., the VDE of AscH^\cdot , to be 3.85 eV, compared to the calculated ionization energy of 3.755 eV.¹⁷ Using the P3 method, Ortiz et al. also calculated the ionization energies and electron affinities of nucleosides, i.e., 2-deoxyadenosine, 2-deoxycytidine, 2-deoxyguanosine, 2-deoxythymidine, and 2-deoxyuridine, and of three common free radicals, e.g., OH, OOH, OCl. The free radicals had higher electron affinities (0.350- 3.549 eV) than the ascorbate anion (-3.507 eV) and the nucleosides (-0.330- -0.506 eV). The positive electron affinity of the free radicals indicates the willingness of the radicals to accept an electron. Furthermore, at 3.755 eV, the ascorbate anion had a dramatically lower ionization energy than the nucleosides (7.978- 9.176 eV).¹⁷ Thus, the reaction of ascorbate with free radicals is more favorable than the radical-nucleoside reaction. This is consistent with the spectroscopic data presented here. The ascorbate anion will donate an electron to the free radical to reduce it and thus become a more stable radical, AscH^\cdot , itself. It should be noted the gas phase ionization energy, 3.85 eV, is over one eV lower than the ionization energy of AscH^\cdot in an aqueous solution.¹⁶ In either phase, the ascorbate anion will readily donate an electron to free radicals.

Based on the photoelectron spectrum obtained using 355 nm photons, the observed VDE value of Asc^{2-} is 2.68 eV for detachment of its second excess electron. Although the deprotonated ascorbate dianion, Asc^{2-} , is not seen in high concentration in the human body, it is a better antioxidant than the ascorbate anion because it has a lower VDE value and will more readily donate an electron. This is supported by the fact that the radical anion, $\text{Asc}^{\cdot-}$, formed by removing an electron from deprotonated ascorbate, is more stable than the dianion; the radical anion is calculated to be lower in energy by 3.24 eV in the gas phase.¹⁶ Since $\text{Asc}^{\cdot-}$ is lower in energy than Asc^{2-} , the observed Asc^{2-} photodetachment transitions terminate on the excited states of the radical anion. This implies that the highest EBE peak in the 4th

harmonic photoelectron spectrum of Asc^{2-} , i.e., the one with an onset at an EBE of ~ 3.75 eV, is a transition from Asc^{2-} to a still higher energy excited state of $\text{Asc}^{\bullet-}$.

As mentioned above, the observed VDE value in the Asc^{2-} spectrum, i.e., due to its lowest EBE peak, shifted to a slightly higher EBE value when measured with higher energy photons; the VDE value obtained when using 4.66 eV photons is 2.97 eV (Figure 6) compared with 2.68 eV when using 3.49 eV photons (Figure 5). Although the 355 nm photons have higher photon energy than 2.97 eV, the shifted peak intensity was not observed in the third harmonic photoelectron spectrum. This shift was likely due to the repulsive Coulomb barrier that led to multiple detachment channels. At higher photon energy, more detachment channels are accessible, leading to different excited state transitions. This is consistent with the photoelectron spectrum of the doubly charged citric acid anion, the lower EBE photodetachment channel continued to be observed in the higher photon energy photoelectron spectra of the deprotonated ascorbate.²⁷

The potential minimum of the dianion corresponds to the equilibrium distance between the two excess electrons. In order for the dianion to be stable, these charges need to have sufficient separation.²⁷ Previously, it has been proposed that the excess electrons in Asc^{2-} are positioned on an oxygen located on the furan ring and on an alkyl oxygen (Figure II.A.1.1).¹⁵ In the condensed phase, solvation helps stabilize these charges, whereas in the gas phase these charges render the dianion metastable. In order for an electron to escape the deprotonated ascorbate dianion resulting in the more stable radical anion, $\text{Asc}^{\bullet-}$, energy is needed to overcome the intervening repulsive Coulomb barrier.

Conclusion

An electrospray ionization source was added to an existing anion photoelectron spectrometer to study the anions related to ascorbic acid. The photoelectron spectra of the ascorbate anion, $\text{C}_6\text{H}_7\text{O}_6^-$, and the deprotonated ascorbate anion, $\text{C}_6\text{H}_6\text{O}_6^{2-}$, are presented. The antioxidant behavior of both anions is confirmed through the photoelectron spectra. The ionization energy of the ascorbate anion is determined to be 3.85 eV, which is lower than other biological molecules found in the body. The ascorbate anion will readily donate an electron to reactive oxygen species and detrimental radicals in the body and, therefore, protect potential biological targets. Although deprotonated ascorbate anion is not present at biological pH, the ionization energy, 2.68 eV, is lower than the ascorbate anion and is a better antioxidant.

References

- (1) Carr, A.; Maggini, S. Vitamin C and Immune Function. *Nutrients*, **2017**, 9 (11), 1211.
- (2) Winterbourn, C. C. Reconciling the Chemistry and Biology of Reactive Oxygen Species. *Nat. Chem. Bio.* **2008**, 4, 278-286.
- (3) Nimse, S. B.; Pal, D. Free Radicals, Natural Antioxidants, and Their Reaction Mechanisms. *RSC Adv.* **2015**, 5(35), 27986-28006.
- (4) Lichtenberg, D.; Pinchuk, I. Oxidative Stress, the Term and the Concept. *Biochem. Biophys. Res. Commun.* **2015**, 461, 441-444.
- (5) Harman, D. Free Radical Theory of Aging. *Mutat. Res.* **1992**, 275 (3-6), 257-266.
- (6) Haya, L.; Mainar, A. M.; Pardo, J. I.; Urieta, J. S. A New Generation of Cysteine Derivatives with Three Active Antioxidant Centers: Improving Reactivity and Stability. *Phys. Chem. Chem. Phys.* **2014**, 16 (4), 1409-1414.
- (7) Frei, B.; England, L.; Ames, B. N. Ascorbate Is an Outstanding Antioxidant in Human Blood Plasma. *Proc. Natl. Acad. Sci.* **1989**, 86, 6377-6381.
- (8) Cross, C. E.; Van der Vliet, A.; O'Neill, C. A.; Louie, S.; Halliwell, B. In *Environmental Health Perspectives*; Public Health Services, US Dept of Health and Human Services, 1994; Vol. 102, pp. 185-191.
- (9) Smirnoff, N. L-Ascorbic Acid Biosynthesis, *Vitamins and Hormones*, **2004**, 61, 241-266.
- (10) Vinishdharma, T.; Don, K. R. Vitamin C as a Therapeutic Healing Agent. *Drug Intervention Today.* **2019**, 12, 554-558.
- (11) Daud, Z. A. M.; Ismail, A.; Sarmadi, B. In *Encycl. Food Heal.* **2016**; pp. 266-274.
- (12) Du, J.; Cullen, J. J.; Buettner, G. R. Ascorbic Acid: Chemistry, Biology and the Treatment of Cancer. *Biochimica et Biophysica Acta - Reviews on Cancer.* 2012.

- (13) Brautzsch, M.; Kerzig, C.; Goez, M. Sustainable, Inexpensive and Easy-to-Use Access to the Super-Reductant $E^{\cdot-}$ -aq through 355 Nm Photoionization of the Ascorbate Dianion—an Alternative to Radiolysis or UV-C Photochemistry. *Green Chem.* **2016**, 18 (17), 4761–4771.
- (14) Carlson, G. L.; Cable, H.; Pedersen, L. G. An Ab Initio Study of Ascorbic Acid. *Chem. Phys. Lett.* **1976**, 38 (1), 75–78.
- (15) Allen, R. N.; Shukla, M. K.; Reed, D.; Leszczynski, J. Ab Initio Study of the Structural Properties of Ascorbic Acid (Vitamin C). In *International Journal of Quantum Chemistry*, 2006; Vol. 106, pp. 2934-2943.
- (16) Herrmann, N.; Heinz, N.; Dolg, M.; Cao, X. Quantum Chemical Study of the Autoxidation of Ascorbate. *J. Comput. Chem.* **2016**, 37, 1914-1923.
- (17) Pérez-González, A.; Galano, A.; Ortiz, J. V. Vertical Ionization Energies of Free Radicals and Electron Detachment Energies of Their Anions: A Comparison of Direct and Indirect Methods versus Experiment. *J. Phys. Chem. A* **2014**, 118, 34, 6125-6131.
- (18) Martínez, A.; Rodríguez-Girones, M. A.; Barbosa, A.; Costas, M. Donator Acceptor Map for Carotenoids, Melatonin and Vitamins. *J. Phys. Chem. A* **2008**, 112, 38, 9037-9042.
- (19) Anstöter, C. S.; West, C. W.; Bull, J. N.; Verlet, J. R. R. The Vitamin E Radical Probed by Anion Photoelectron Imaging. *J. Phys. Chem. B* **2016**, 120, 29, 7108-7113.
- (20) Wang, X. Bin; Wang, L. S. Development of a Low-Temperature Photoelectron Spectroscopy Instrument Using an Electrospray Ion Source and a Cryogenically Controlled Ion Trap. *Rev. Sci. Instrum.* **2008**, 79, 073108.
- (21) Wang, L. S.; Ding, C. F.; Wang, X. Bin; Barlow, S. E. Photodetachment Photoelectron Spectroscopy of Multiply Charged Anions Using Electrospray Ionization. *Rev. Sci. Instrum.* **1999**, 70, 1957.
- (22) Kamrath, M. Z.; Relph, R. A.; Guasco, T. L.; Leavitt, C. M.; Johnson, M. A. Vibrational Predissociation Spectroscopy of the H_2 -Tagged Mono- and Dicarboxylate Anions of Dodecanedioic Acid. *Int. J. Mass Spectrom.* **2011**, 300, 2, 91-98.
- (23) Thomas, O. C.; Zheng, W.; Bowen, K. H. Magic Numbers in Copper-Doped Aluminum Cluster Anions. *J. Chem. Phys.* **2001**, 114, 5514.
- (24) Stokes, S. T.; Li, X.; Grubisic, A.; Ko, Y. J.; Bowen, K. H. Intrinsic Electrophilic Properties of Nucleosides: Photoelectron Spectroscopy of Their Parent Anions. *J. Chem. Phys.* **2007**, 127.
- (25) Kruit, P.; Read, F. H. Magnetic Field Paralleliser for 271 Electron-Spectrometer and Electron-Image Magnifier, *J. Phys. E: Sci. Instr.* **1983**, 16, 313-324.
- (26) Martínez, A.; Rodríguez-Girones, M. A.; Barbosa, A.; Costas, M. Donator Acceptor Map for Carotenoids, Melatonin and Vitamins. *J. Phys. Chem. A* **2008**, 112, 38, 9037-9042.
- (27) Wang, X. Bin; Ding, C. F.; Wang, L. S. Photodetachment Spectroscopy of a Doubly Charged Anion: Direct Observation of the Repulsive Coulomb Barrier. *Phys. Rev. Lett.* **1998**, 81, 3351.

II.A.2. Photoelectron Spectroscopic and Computational Study of the Deprotonated Gallic Acid and Propyl gallate Anions

Reprinted with permission from *J. Am. Soc. Mass Spectrom.* 2022, 33, 8, 1355–1361

Copyright 2022 American Society for Mass Spectrometry.

Zhaoguo Zhu,[†] Mary Marshall,[†] Rachel Harris,[†] Evan Collins,[‡] Kit H. Bowen^{†,*}

[†]Department of Chemistry, Johns Hopkins University, Baltimore, MD 21218, USA

[‡]Current Address: Intel Corporation, Hillsboro, OR 97124, USA

***Corresponding Author** K.H.B.: kbowen@jhu.edu

Abstract

Antioxidants play important roles in eliminating reactive oxygen species (ROS), which have been associated with various degenerative diseases, such as cancer, aging and inflammatory diseases. Gallic acid (GA) and propyl gallate (PG) are well-known antioxidants and have been widely studied *in vitro* and *in vivo*. GA and PG's biological antioxidant abilities are related to the electronic structure of their dehydro-radicals. In this work, we report a combined photoelectron spectroscopic and computational study of the deprotonated gallic acid anion, [GA-H]⁻, and deprotonated propyl gallate anion, [PG-H]⁻. Adiabatic electron affinities of the dehydro-gallic acid radical, [GA-H][·] and of the dehydro-propyl gallate radical, [PG-H][·], are measured to be 2.90 ± 0.05 eV and 2.85 ± 0.05 eV, respectively, and compared to computational results.

Abbreviations:

GA: gallic acid, PG: propyl gallate

[GA-H][·]: dehydro-gallic acid radical, [PG-H][·]: dehydro-propyl gallate radical

[GA-H]⁻: deprotonated gallic acid anion, [PG-H]⁻: deprotonated propyl gallate anion

Introduction

Reactive oxygen species (ROS), primarily generated in the mitochondria of cells, have been regarded as toxic byproducts resulting from metabolism processes involved in cancer and other diseases.¹⁻⁴ Common ROS exist in the form of hydroxyl radicals ($\text{OH}\cdot$), alkoxyl radicals ($\text{RO}\cdot$), peroxy radicals ($\text{ROO}\cdot$), and hydrogen peroxide (H_2O_2).⁵ Excessive levels of these species are thought to have destructive consequences on cellular macromolecules, e.g., lipids, proteins and DNA, resulting in cell and tissue injury that is often associated with degenerative diseases.⁶⁻¹² Nutritional and medical studies have identified several antioxidants that prevent the oxidative stress caused by ROS.^{13,14} The antioxidants react with ROS faster than relevant biological targets react with ROS, thus protecting lipids, fats, and proteins from the attack of free radicals.

Among the various antioxidants, gallic acid (GA) and its derivative propyl gallate (PG) are thought to possess strong abilities to scavenge ROS.^{15,16} Gallic acid, also known as 3,4,5-trihydroxybenzoic acid, is widely present in the plant kingdom and found in various food sources, such as tea, grapes, and red wine.¹⁷⁻²¹ Propyl gallate, commonly used as an antioxidant in food, is a synthetic derivative of GA.^{22,23} Both of them act as antioxidants, antibacterial agents,

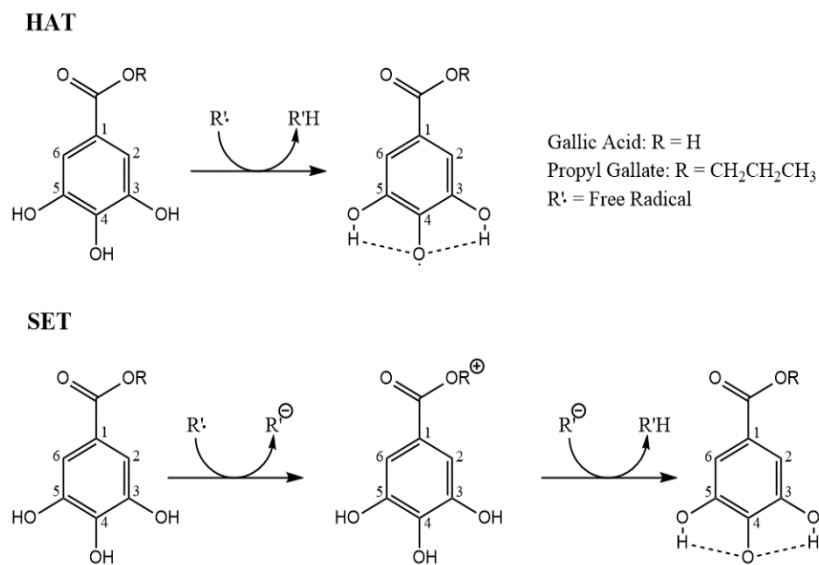


Figure II.A.2.1. The HAT and SET Mechanisms of radical scavenging process

antitumor agents and anti-inflammatories in the body.²⁴⁻²⁷ The mechanism of action among phenolic antioxidants has been extensively investigated²⁸⁻³¹. For polyphenols, hydrogen atom transfer (HAT) and single electron transfer (SET) are the two dominant mechanistic pathways.^{32,33} They are represented in Figure II.A.2.1. Via HAT, GA and PG react with free radicals as hydrogen donors and form the relatively stable dehydro-gallate, [GA-H]·, and dehydro-propyl gallate, [PG-H]·, radicals. In the case of SET, antioxidants lose an electron to the radical first and then undergo the proton transfer process. Previous DFT computational analysis suggested that GA in the gas phase reacts by HAT.²⁹ In aqueous and lipid media at physiological pH, PG reacts with ·OOH, ·OOCH₃ and ·OOCHCH₂ radicals by transferring the hydrogen from the phenolic hydroxyl(s) group.³⁴ In particular, the bond dissociation enthalpy (BDE) of O-H bonds has been shown to be a good indicator of antioxidant activity due to the HAT mechanism.³⁵ The BDE values of O-H bonds for GA and PG are estimated to be 347.4 kJ/mol and 334.6 kJ/mol, respectively, based on the experimentally measured rate constants of reactions of the antioxidants with the lipid peroxy radicals.^{36,37} Also, computational investigations of BDE values for GA and PG in different environments have been carried out. The computed BDE values range from 318 kJ/mol to 385 kJ/mol for GA and from 297 kJ/mol to 371 kJ/mol for PG.^{28,37-43}

However, despite results from decades of spectroscopic and theoretical studies on the antioxidant capabilities and stabilities of GA and PG, the electron affinity (EA) values of the [GA-H]· and the [PG-H]· radicals had not been measured.⁴⁴⁻⁴⁸ These EA values would be particularly useful, however, since they could be used to determine O-H BDE values in the acidity/electron affinity thermochemical cycle proposed by Blanksby and Ellison.⁴⁹ Knowledge of O-H BDE values can provide insight into the antioxidant nature of GA and PG, as they have for other radical scavengers, such as vitamin E and vitamin C. Here, we present our experimental and computational studies of the

electronic structure of [GA-H] \cdot and [PG-H] \cdot . The experimental part of this work involved forming their anions through electrospray ionization and measuring their anion photoelectron spectra. This led to the determination of the electron affinities and excitation energies of the [GA-H] \cdot and [PG-H] \cdot radicals, which were then compared to results from our computations. This work takes its place along-side previous anion photoelectron spectroscopic studies of vitamin E and vitamin C.^{50,51}

Methods

Experimental

Deprotonated gallate anions, [GA-H] $^-$, and deprotonated propyl gallate anions, [PG-H] $^-$, were generated via electrospray ionization, one of the anion sources on our existing pulsed anion photoelectron spectrometer. Details of the electrospray ionization source have been described elsewhere previously.⁵¹ Millimolar solutions of propyl gallate (Sigma-Aldrich, $\geq 98.0\%$) in 3:1 MeOH: H₂O were prepared over a range of pH values (9 < pH < 11). These solutions were injected through a $\sim 10\ \mu\text{m}$ pulled silica capillary, floated at negative 3-5 kV, into a humidity controlled, ambient atmosphere chamber. A buffer gas comprised of 20% H₂ with a balance of He was employed in the ion trap to facilitate cooling of the ions, as well as promoting collision focusing. The ions were accumulated and cooled in the trap for 100 ms before being pulsed into a time-of-flight mass spectrometer to be mass-analyzed. The mass spectrum is displayed in the figure S1 in the supporting materials. The time-of-flight mass spectrometer portion of our apparatus has also been previously described elsewhere.⁵²

The anions of interest were then mass-selected and decelerated before entering a magnetic bottle region of our anion photoelectron spectrometer. Anion photoelectron spectroscopy is conducted by crossing the mass-selected beam of

negative ions with a fixed frequency photon beam and energy-analyzing the resultant photodetached electrons. These photoelectrons are governed by the energy-conserving relationship: $h\nu = \text{EBE} + \text{EKE}$, where $h\nu$ is the photon energy, EBE is the electron binding (photodetachment transition) energy, and EKE is the measured electron kinetic energy. Our magnetic bottle, electron energy analyzer has a resolution of ~ 50 meV at an EKE of 1 eV. The photoelectron spectra were collected with both the 3rd and 4th harmonic light from a Nd:YAG laser (355 nm, 3.49 eV and 266 nm, 4.66 eV photons, respectively) and with the ion trap at both ambient (~ 300 K) temperature and 77 K. The photoelectron spectra were calibrated against the well-known transitions of I⁻.^{53,54}

Computational

All calculations were performed using the Gaussian 09 program package.⁵⁵ DFT calculations were conducted by applying the M06-2X functional with the D3 dispersion correction.^{56,57} All geometries, including that of the anions and their corresponding neutral molecules, were fully optimized without any geometrical constraints while using the aug-cc-pVDZ basis set.^{58,59} Frequency analyses were carried out for all optimized structures to ensure the absence of imaginary frequencies. The electronic energies were improved by single-point calculations with a larger basis set, i.e., aug-cc-pVTZ, at the optimized geometries. The excitation energies of the neutral radicals were obtained by TD-DFT method. Frank-Condon simulations were carried out using the tools available in the PESCAL2016 package.^{60,61} The temperature (~ 77 K) was adjusted to obtain the best match to the experimental spectra.

Results

Gallic acid

The photoelectron spectra of the deprotonated gallic acid anion, $[\text{GA-H}]^-$, are shown in Figure II.A.2.2. These spectra were measured at 77 K to reduce the presence vibrational hot bands, i.e., photoelectrons from vibrationally excited anions. A broad EBE band, beginning at $\text{EBE} = 2.90$ eV and reaching its maximum at $\text{EBE} = 3.32$ eV, was

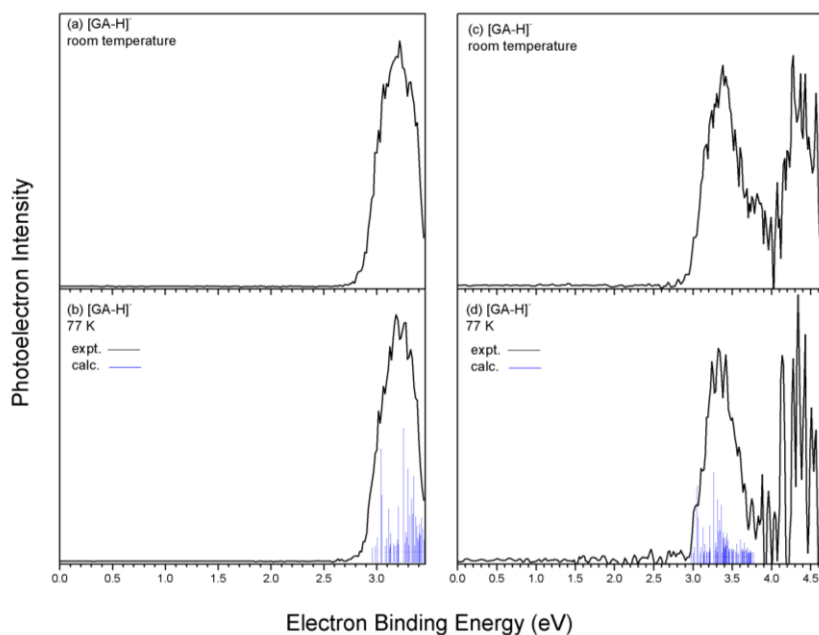


Figure II.A.2.2 Photoelectron spectra of $[\text{GA-H}]^-$ recorded with (a) 3.49 eV photons at room temperature, (b) 3.49 eV photons at 77 K, (c) 4.66 eV photons at room temperature, and (d) 4.66 eV photons at 77 K.

observed in all of the spectra. The vertical detachment energy (VDE) is the transition energy, i.e., EBE, at which the Franck-Condon overlap between the wavefunctions of the anion and its neutral counterpart is greatest. The EBE value corresponding to this maximum intensity in the observed band, i.e., 3.32 eV for the $[\text{GA-H}]^-$ anion, is its vertical detachment energy. When significant Franck-Condon overlap exists between $v = 0$ of the anion and $v' = 0$ of its corresponding neutral (the origin transition) and no vibrational hot bands are present, the EBE of the spectrum's threshold value corresponds to the adiabatic electron affinity (EA). The EA is the energy difference between the lowest energy, relaxed geometry of the anion and the lowest energy isomer (global minimum) of its neutral counterpart. By extrapolating the lowest EBE edge, we determine the EA value to be 2.90 ± 0.05 eV. As illustrated in Table II.A.2.1,

our calculated EA = 2.96 eV and VDE = 3.20 eV agree well with the experimental values. In the 266 nm (4.66 eV) spectrum, a second band appears approximately 1.2 eV above the first one. This transition represents photoelectron detachment from an inner molecular orbital. In other words, the second EBE band is also the transition from the ground state of anion to the first excited state of the neutral radical. After cooling to 77 K, vibrational features spaced by 0.1 eV were also observed at both photon energies. In Figure II.A.2.2(b) and Figure II.A.2.2(d), blue stick spectra represent transitions from $v = 0$ of the anion to all of the vibrationally excited states of its corresponding neutral, these being the result of a Franck-Condon analysis.

Propyl gallate

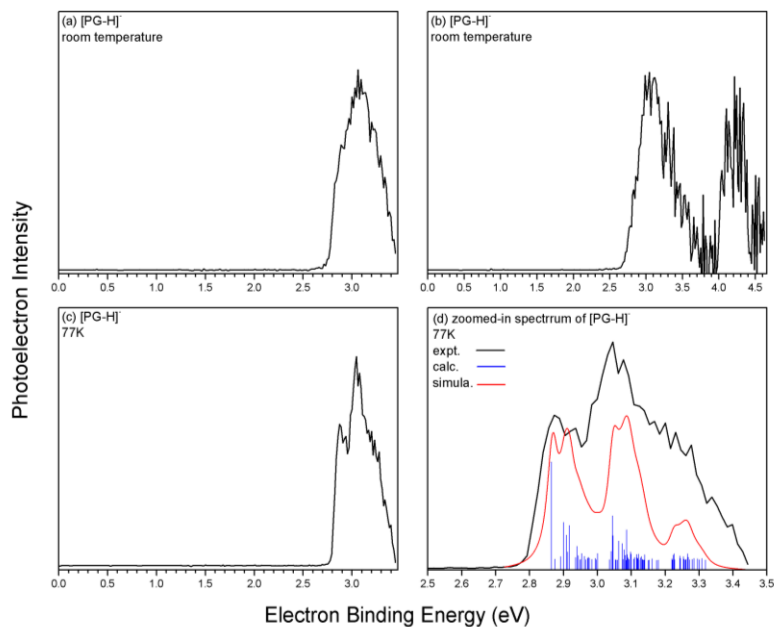


Figure II.A.2.3 Photoelectron spectra of $[\text{PG-H}]^-$ recorded with (a) 3.49 eV photons at room temperature, (b) 4.66 eV photons at room temperature, (c) 3.49 eV photons at 77 K, and (d) an expanded view of (c), beginning at EBE = 2.5 eV.

The photoelectron spectra of the deprotonated propyl gallate anion, $[\text{PG-H}]^-$, are presented in Figure II.A.2.3.

These spectra were obtained at the ambient temperature of the ion trap using both 355 nm (3.49 eV) and 266 nm (4.66

eV) photons and at an ion trap temperature of 77 K (to eliminate vibrational hot bands) using 355 nm photons. The ambient temperature 355 nm spectrum consists of a single broad band with a maximum at EBE = 3.06 eV. The ambient temperature 266 nm spectrum reveals a second band, representative of electron detachment from an inner molecular orbital. Upon cooling the ion trap to 77 K, as shown in Figure II.A.2.3(c), a strong EBE peak at 2.85 eV and its vibrational features are revealed. Figure II.A.2.3(d) presents an expanded view of Figure 3(c). Displayed under Figure II.A.2.3(d) is a Franck-Condon simulation-based stick spectrum (in blue) which depicts transitions from $v = 0$ of the anion to all vibrational ground and excited states of its corresponding neutral. The red curve is the simulated spectrum with its features having been subjected to Gaussian broadening of 400 cm^{-1} FWHM. The overall profiles of the experimental and simulated spectra are in good agreement. Additionally, due to the negligible geometrical structure difference between the [PG-H]⁻ anion and its corresponding neutral radical, [PG-H][•], the Franck-Condon overlap between their ground vibrational wavefunctions is significant, resulting in a strong EA-determining (origin) peak in the spectrum at EBE = 2.85 eV. Our calculated EA = 2.87 and VDE = 3.08 eV values are in excellent agreement with the experimental values, i.e., 2.85 ± 0.05 eV and 3.06 ± 0.05 eV, respectively.

Table II.A.2.1. Experimentally and computationally determined values for deprotonated propyl gallate and gallic acid anions and their corresponding neutral radicals. (eV)

	Expt. EA	Calc. EA	Expt. VDE	Calc. VDE	Expt. first excitation energy ^a	Calc. first excitation energy
[GA-H] [•] / [GA-H] ⁻	2.90 ± 0.05	2.96	3.32 ± 0.05	3.20	~1.25	1.40
[PG-H] [•] / [PG-H] ⁻	2.85 ± 0.05	2.87	3.06 ± 0.05	3.08	~1.30	1.39

^aThis value was obtained by subtracting the VDE from the EBE value of the second peak in the spectrum.

Discussion

Deprotonation of gallic acid can yield three kinds of deprotomers which are carboxylate ion, para-phenoxide ion, and ortho-phenoxide ion. Even if the carboxylate isomer had been present, it would not have been observed in the photodetachment spectrum, because its calculated VDE is 4.87 eV and photon energy is 4.66 eV. While it is

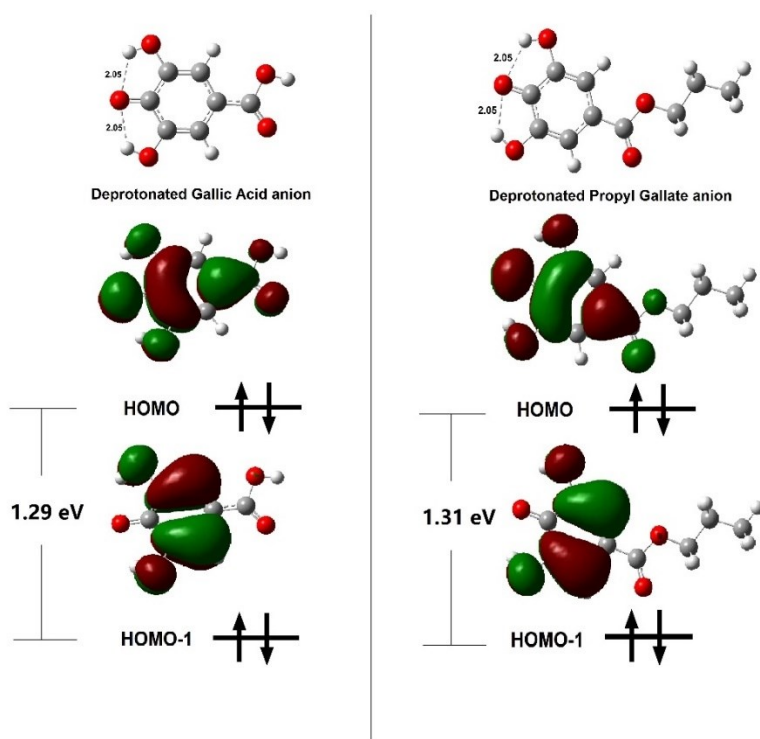


Figure II.A.2.4 Optimized geometries of $[\text{GA-H}]^-$ and $[\text{PG-H}]^-$ with their respective HOMO and HOMO-1 molecular orbitals.

conceivable that both ortho- and para- phenoxide ions can be made by ESI, Boltzmann distribution favors the population of para-phenoxide ion of deprotonated gallic acid because para-phenoxide ion lies 0.39 eV lower than the ortho one in energy. Additionally, the measured and calculated VDE favors the para-phenoxide of gallic acid deprotomer, too. Para-phenoxide ion of deprotonated propyl gallate is also thermodynamically preferred due to the

large energy gap (0.37 eV) between para- and ortho- isomers. The geometry and energetics of the isomers are provided in the figure S2. Figure II.A.2.4 presents the calculated structures of the most stable conformers of the [GA-H]⁻ and [PG-H]⁻ anions, i.e., *para*-phenoxide ions of deprotonated gallic acid and propyl gallate, along with their highest occupied molecular orbitals (HOMO) and their second highest occupied molecular orbitals (HOMO-1). In the left panel of figure 4, the optimized [GA-H]⁻ anion structure reveals a singlet ground state and a planar geometry due to conjugation effects. Additionally, two intramolecular hydrogen bonds, each 2.05 Å in length, are formed between two ortho hydroxyl groups and the central oxygen atom on the benzene ring. The neutral [GA-H][•] radical also shares a similar geometry with two 2.16 Å intramolecular hydrogen bonds. Intramolecular hydrogen bonds have an enhancing effect on the antioxidant ability, because they stabilize the structure of the [GA-H][•] radical and lower the bond dissociation enthalpy of the center O-H bond.^{29,49}

The [PG-H]⁻ anion also forms two intramolecular hydrogen bonds between hydroxyl groups and an oxygen atom of the same length as in the [GA-H]⁻ anion, i.e., 2.05 Å. However, the neutral [PG-H][•] radical has two hydrogen bonds with lengths of 2.16 Å each, which are longer and weaker than its anionic counterpart. We assigned the EBE = 2.85 eV peak to the 0-0 transition, and the VDE = 3.06 eV peak to the transition from the ground state of the anion to a vibrationally excited state in its neutral counterpart, 1262 cm⁻¹ above its vibrational ground state. In the 1262 cm⁻¹ vibrational mode, two intramolecular hydrogen bonds are stretched, leading to a smaller geometric difference between the anion and neutral, and a larger Franck-Condon overlap.

The HOMO and HOMO-1 molecular orbital structures of [GA-H]⁻ are both delocalized over the benzene ring and show strong π -like orbital features (Figure II.A.2.4). The calculated energy difference between these molecular orbitals

is 1.29 eV, closely matching the observed interval in the experimental spectrum. The direct detachment feature at EBE values ranging from 2.9 to 3.6 eV corresponds to the loss of an electron from the doubly occupied HOMO in the anion, while the second band, i.e., from 4.0 to 4.5 eV, corresponds to that from HOMO-1. For the [PG-H]⁻, the energy difference between the HOMO and HOMO-1 is 1.31 eV, which is in accordance with the spacing observed between the two bands in the spectrum taken at 266 nm (Figure II.A.2.3b). Our TD-DFT calculations also show that the first excited state for both [GA-H][•] and [PG-H][•] radicals corresponds to the promotion of an electron from HOMO-1 to singly occupied HOMO. The calculated excitation energies of the first excited state are 1.40 eV and 1.39 eV for [GA-H][•] and [PG-H][•] radicals, respectively. Additionally, the modest difference in EA values between the [GA-H][•] radical (2.90 eV) and the [PG-H][•] radical (2.85 eV) is attributed to the small electron density of the HOMO on the propyl group.

Conclusion

In this work, the photoelectron spectra of the deprotonated gallic acid anion, [GA-H]⁻, and the deprotonated propyl gallate anion, [PG-H]⁻, were measured at both ambient temperature and at 77 K. Electron affinities of the dehydro-gallic acid radical, [GA-H][•], as well as of the dehydro-propyl gallate radical, [PG-H][•], were determined to be 2.90 ± 0.05 eV and 2.85 ± 0.05 eV, respectively. Our DFT calculations and Frank Condon analyses confirm the electron affinities and the excitation energies of these two radicals. The measured electron affinity values of these two important antioxidant radicals together with properties, such as acidity and BDE, can provide further insight into their antioxidant natures.

References

1. Apel, K.; Hirt, H. Reactive oxygen species: metabolism, oxidative stress, and signal transduction. *Annu. Rev. Plant Biol.* **2004**, *55*, 373-399.
2. Murphy, M. P. How mitochondria produce reactive oxygen species. *Biochem. J.* **2009**, *417*(1), 1-13.
3. Turrens, J. F. Mitochondrial formation of reactive oxygen species. *J. Physiol.* **2003**, *552*(2), 335-344.
4. Yu, B. P. Cellular defenses against damage from reactive oxygen species. *Physiol. Rev.* **1994**, *74*(1), 139-162.
5. Simon, H. U.; Haj-Yehia, A.; Levi-Schaffer, F. Role of reactive oxygen species (ROS) in apoptosis induction. *Apoptosis.* **2000**, *5*(5), 415-418.
6. Braekke, K.; Harsem, N. K.; Staff, A. C. Oxidative stress and antioxidant status in fetal circulation in preeclampsia. *Pediatr. Res.* **2006**, *60*(5), 560.
7. Valko, M.; Rhodes, C.; Moncol, J.; Izakovic, M. M.; Mazur, M. Free radicals, metals and antioxidants in oxidative stress-induced cancer. *Chem.-biol. Interact.* **2006**, *160*(1), 1-40.
8. Hracsko, Z.; Orvos, H.; Novak, Z.; Pal, A.; Varga, I. S. Evaluation of oxidative stress markers in neonates with intra-uterine growth retardation. *Redox Rep.* **2008**, *13*(1), 11-16.
9. Harman, E. Protein oxidation in aging and age-related diseases. *J. Gerontology.* **1956**, *11*, 298-300.
10. Harman, D. The aging process. *Proc. Natl. Acad. Sci.* **1981**, *78*(11), 7124-7128.
11. Ozawa, T. Genetic and functional changes in mitochondria associated with aging. *Physiol. Rev.* **1997**, *77*(2), 425-464.
12. Beckman, K.B.; Ames, B.N. The free radical theory of aging matures. *Physiol. Rev.* **1998**, *78*(2), 547-581.
13. Amarowicz, R.; Pegg, R. B.; Rahimi-Moghaddam, P.; Barl, B.; Weil, J. A. Free-radical scavenging capacity and antioxidant activity of selected plant species from the Canadian prairies. *Food Chem.* **2004**, *84*(4), 551-562.
14. Halliwell, B.; Aeschbach, R.; Löliger, J.; Aruoma, OI. The characterization of antioxidants. *Food Chem. Toxicol.* **1995**, *33*, 601-617.
15. Aruoma, O. I.; Murcia, A.; Butler, J.; Halliwell, B. Evaluation of the antioxidant and prooxidant actions of gallic acid and its derivatives. *J. Agric. Food Chem.* **1993**, *41*(11), 1880-1885.
16. Badhani, B.; Sharma, N.; Kakkar, R. Gallic acid: a versatile antioxidant with promising therapeutic and industrial applications. *RSC Adv.* **2015**, *5*(35), 27540-27557.
17. Damiani, E.; Bacchetti, T.; Padella, L.; Tiano, L.; Carloni, P. Antioxidant activity of different white teas: comparison of hot and cold tea infusions. *J. Food Compos. Anal.* **2014**, *33*(1), 59-66.
18. Samanidou, V.; Tsiagiannidis, A.; Sarakatsianos, I. Simultaneous determination of polyphenols and major purine alkaloids in Greek Sideritis species, herbal extracts, green tea, black tea, and coffee by high-performance liquid chromatography-diode array detection. *J. Sep. Sci.* **2012**, *35*(4), 608-615.
19. Schmitzer, V.; Slatnar, A.; Veberic, R.; Stampar, F.; Solar, A. Roasting affects phenolic composition and antioxidative activity of hazelnuts (*Corylus avellana* L.). *J. Food Sci.* **2011**, *76*(1), S14-S19.
20. Shahrzad, S.; Aoyagi, K.; Winter, A.; Koyama, A.; Bitsch, I. Pharmacokinetics of gallic acid and its relative bioavailability from tea in healthy humans. *J. Nutr.* **2001**, *131*(4), 1207-1210.

21. Burns, J.; Gardner, P. T.; O'Neil, J.; Crawford, S.; Morecroft, I.; McPhail, D. B.; Lister, C.; Matthews, D.; MacLean, M.R.; Lean, M.E.; Duthie, G. G. Relationship among antioxidant activity, vasodilation capacity, and phenolic content of red wines. *J. Agric. Food Chem.* **2000**, *48*(2), 220-230.
22. Garrido, J.; Garrido, E. M.; Borges, F. Studies on the food additive propyl gallate: synthesis, structural characterization, and evaluation of the antioxidant activity. *J. Chem. Educ.* **2011**, *89*(1), 130-133.
23. Becker, L. Final report on the amended safety assessment of propyl gallate. *Int. J. Toxicol.* **2007**, *26*, 89-118.
24. Ji, B. C.; Hsu, W. H.; Yang, J. S.; Hsia, T. C.; Lu, C. C.; Chiang, J. H.; Yang, J.L.; Lin, C.H.; Lin, J.J.; Suen, L.J.W.; Gibson Wood, W. Gallic acid induces apoptosis via caspase-3 and mitochondrion-dependent pathways in vitro and suppresses lung xenograft tumor growth in vivo. *J. Agric. Food Chem.* **2009**, *57*(16), 7596-7604.
25. Kroes, B. V., Van den Berg, A. J. J., Van Ufford, H. Q., Van Dijk, H., Labadie, R. P. Anti-inflammatory activity of gallic acid. *Planta medica.* **1992**, *58*(06), 499-504.
26. Lee, D. S.; Je, J. Y. Gallic acid-grafted-chitosan inhibits foodborne pathogens by a membrane damage mechanism. *J. Agric. Food Chem.* **2013**, *61*(26), 6574-6579.
27. Pandurangan, A. K.; Mohebal, N.; Norhaizan, M. E.; Looi, C. Y. Gallic acid attenuates dextran sulfate sodium-induced experimental colitis in BALB/c mice. *Drug Des. Devel. Ther.* **2015**, *9*, 3923.
28. Lu, Z.; Nie, G.; Belton, P. S.; Tang, H.; Zhao, B. Structure–activity relationship analysis of antioxidant ability and neuroprotective effect of gallic acid derivatives. *Neurochem. Int.* **2006**, *48*(4), 263-274.
29. Wright, J. S., Johnson, E. R., DiLabio, G. A. Predicting the activity of phenolic antioxidants: theoretical method, analysis of substituent effects, and application to major families of antioxidants. *J. Amer. Chem. Soc.* **2001**, *123*(6), 1173-1183.
30. Leopoldini, M.; Pitarch, I. P.; Russo, N.; Toscano, M. Structure, conformation, and electronic properties of apigenin, luteolin, and taxifolin antioxidants. A first principle theoretical study. *J. Phys. Chem. A.* **2004**, *108*(1), 92-96.
31. Marino, T.; Galano, A.; Russo, N. Radical scavenging ability of gallic acid toward OH and OOH radicals. Reaction mechanism and rate constants from the density functional theory. *J. Phys. Chem. B.* **2014**, *118*(35), 10380-10389.
32. Mendes, R. A.; Almeida, S. K.; Soares, I. N.; Barboza, C. A.; Freitas, R. G.; Brown, A.; de Souza, G. L. A computational investigation on the antioxidant potential of myricetin 3, 4'-di-O- α -L-rhamnopyranoside. *J. Mol. Model.* **2018**, *24*(6), 1-8.
33. Santos, J. L.; Kauffmann, A. C.; da Silva, S. C.; Silva, V. C.; de Souza, G. L. Probing structural properties and antioxidant activity mechanisms for eleocarpanthraquinone. *J. Mol. Model.* **2020**, *26*(9), 1-8.
34. Medina, M. E.; Iuga, C.; Alvarez-Idaboy, J. R. Antioxidant activity of propyl gallate in aqueous and lipid media: a theoretical study. *Phys. Chem. Chem. Phys.* **2013**, *15*(31), 13137-13146.
35. Kalita, D.; Kar, R.; Handique, J. G. A theoretical study on the antioxidant property of gallic acid and its derivatives. *J. Theor. Comput. Chem.* **2012**, *11*(02), 391-402.
36. Roginsky, V. Chain-breaking antioxidant activity of natural polyphenols as determined during the chain oxidation of methyl linoleate in Triton X-100 micelles. *Arch. Biochem. Biophys.* **2003**, *414*(2), 261-270.

37. Denisova, T. G.; Denisov, E. T. Dissociation energies of OH bonds in natural antioxidants. *Russ. Chem. Bull.* **2008**, 57(9), 1858-1866.
38. de Souza, G. L.; Peterson, K. A. (2021). Benchmarking antioxidant-related properties for gallic acid through the use of DFT, MP2, CCSD, and CCSD (T) approaches. *J. Phys. Chem. A*. **2021**, 125(1), 198-208.
39. Ji, H.-F.; Zhang, H.-Y.; Shen, L. Proton dissociation is important to understanding structure-activity relationships of gallic acid antioxidants. *Bioorg. Med. Chem. Lett.* **2006**, 16, 4095–4098.
40. Rajan, V. K.; Muraleedharan, K. A computational investigation on the structure, global parameters and antioxidant capacity of a polyphenol, gallic acid. *Food Chem.* **2017**, 220, 93–99.
41. Škorňa, P.; Michalík, M.; Klein, E. Gallic acid: Thermodynamics of the homolytic and heterolytic phenolic O–H bonds splitting-off. *Acta Chim. Slov.* **2016**, 9, 114–123.
42. Đorovic, J.; Markovic, J. M. D.; Stepanic, V.; Begovic, N.; Amic, D.; Markovic, Z. Influence of different free radicals on scavenging potency of gallic acid. *J. Mol. Model.* **2014**, 20, 2345-1–2345-9.
43. Kalita, D.; Kar, R.; Handique, J. G. A theoretical study on the antioxidant property of gallic acid and its derivatives. *J. Theor. Comput. Chem.* **2012**, 11, 391–402.
44. Masoud, M. S.; Hagagg, S. S.; Ali, A. E.; Nasr, N. M. Synthesis and spectroscopic characterization of gallic acid and some of its azo complexes. *J. Mol. Struct.* **2012**, 1014, 17-25.
45. Eslami, A. C.; Pasanphan, W.; Wagner, B. A.; Buettner, G. R. Free radicals produced by the oxidation of gallic acid: An electron paramagnetic resonance study. *Chem. Cent. J.* **2010**, 4(1), 15.
46. Mohammed-Ziegler, I.; Billes, F. Vibrational spectroscopic calculations on pyrogallol and gallic acid. *J. Mol. Struct.: THEOCHEM.* **2002**, 618(3), 259-265.
47. Billes, F.; Mohammed-Ziegler, I.; Bombicz, P. Vibrational spectroscopic study on the quantum chemical model and the X-ray structure of gallic acid, solvent effect on the structure and spectra. *Vib. Spectrosc.* **2007**, 43(1), 193-202.
48. Badhani, B.; Kakkar, R. DFT study of structural and electronic properties of gallic acid and its anions in gas phase and in aqueous solution. *Struct. Chem.* **2017**, 28(6), 1789-1802.
49. Blanksby, S. J.; Ellison, G. B. Bond dissociation energies of organic molecules *Acc. Chem. Res.* **2003**, 36 (4) 255– 263
50. Anstöter, C. S.; West, C. W.; Bull, J. N.; Verlet, J. R. The vitamin e radical probed by anion photoelectron imaging. *J. Phys. Chem. B*. **2016**, 120(29), 7108-7113.
51. Marshall, M.; Zhu, Z.; Harris, R.; Collins, E.; Bowen, K. H. A Photoelectron spectroscopic study of the ascorbate and deprotonated ascorbate anions using an electrospray ionization source and a cryogenically cooled ion trap. *J. Phys. Chem. A*. **2021**, 125, 7699-7704.
52. Gerhards, M.; Thomas, O. C.; Nilles, J. M.; Zheng, W.-J. Bowen, K. H. Cobalt-benzene cluster anions: mass spectrometry and negative ion photoelectron spectroscopy. *J. Chem. Phys.* **2002**, 116, 10247.
53. Peláez, R. J.; Blondel, C.; Delsart, C.; Drag, C. Pulsed photodetachment microscopy and the electron affinity of iodine. *J. Phys. B-At. Mol. Opt.* **2009**, 42(12), 125001.
54. Luckoenig, E.; Morillon, C.; Vergès, J. Experimental and theoretical studies in atomic iodine-infrared arc spectrum observations, classification and hyperfine-structure. *Phys. Scr.* **1975**, 12(4), 199-219.

55. Frisch, M. J.; Trucks, G. W.; Schlegel, H. B.; Scuseria, G. E.; Robb, M. A.; Cheeseman, J. R.; Scalmani, G.; Barone, V.; Mennucci, B.; Petersson, G. A.; Nakatsuji, H.; Caricato, M.; Li, X.; Hratchian, H. P.; Izmaylov, A. F.; Bloino, J.; Zheng, G.; Sonnenberg, J. L.; Hada, M.; Ehara, M.; Toyota, K.; Fukuda, R.; Hasegawa, J.; Ishida, M.; Nakajima, T.; Honda, Y.; Kitao, O.; Nakai, H.; Vreven, T.; Montgomery, J. A., Jr.; Peralta, J. E.; Ogliaro, F.; Bearpark, M.; Heyd, J. J.; Brothers, E.; Kudin, K. N.; Staroverov, V. N.; Keith, T.; Kobayashi, R.; Normand, J.; Raghavachari, K.; Rendell, A.; Burant, J. C.; Iyengar, S. S.; Tomasi, J.; Cossi, M.; Rega, N.; Millam, J. M.; Klene, M.; Knox, J. E.; Cross, J. B.; Bakken, V.; Adamo, C.; Jaramillo, J.; Gomperts, R.; Stratmann, R. E.; Yazyev, O.; Austin, A. J.; Cammi, R.; Pomelli, C.; Ochterski, J. W.; Martin, R. L.; Morokuma, K.; Zakrzewski, V. G.; Voth, G. A.; Salvador, P.; Dannenberg, J. J.; Dapprich, S.; Daniels, A. D.; Farkas, O.; Foresman, J. B.; Ortiz, J. V.; Cioslowski, J.; Fox, D. J. Gaussian 09, Revision D.01; Gaussian, Inc.: Wallingford, CT, 2013.
56. Zhao, Y.; Truhlar, D. G. The M06 suite of density functionals for main group thermochemistry, thermochemical kinetics, noncovalent interactions, excited states, and transition elements: two new functionals and systematic testing of four M06-class functionals and 12 other functionals. *Theo. Chem. Acc.* **2008**, *120*(1-3), 215-241.
57. Grimme, S.; Antony, J.; Ehrlich, S.; Krieg, H. A consistent and accurate ab initio parametrization of density functional dispersion correction (DFT-D) for the 94 elements H-Pu. *J. Chem. Phys.* **2010**, *132*(15), 154104.
58. Dunning Jr, T. H. Gaussian basis sets for use in correlated molecular calculations. I. The atoms boron through neon and hydrogen. *J. Chem. Phys.* **1989**, *90*(2), 1007-1023.
59. Kendall, R. A.; Dunning Jr, T. H.; Harrison, R. J. Electron affinities of the first-row atoms revisited. Systematic basis sets and wave functions. *J. Chem. Phys.* **1992**, *96*(9), 6796-6806.
60. Ervin, K. M.; Ho, J.; Lineberger, W. C. Ultraviolet photoelectron spectrum of nitrite anion. *J. Phys. Chem.* **1988**, *92*(19), 5405-5412.
61. Ervin, K. M.; Ramond, T. M.; Davico, G. E.; Schwartz, R. L.; Casey, S. M.; Lineberger, W. C. Naphthyl Radical: Negative ion photoelectron spectroscopy, Franck-Condon simulation, and thermochemistry. *J. Phys. Chem. A* **2001**, *105*(48), 10822-10831.

III. Actinide Clusters

Chemists have been fascinated by actinides, mainly due to their importance in the nuclear industry, environmental science, and even life's origin.¹⁻⁴ Interrupting the 6d transition elements in the last row of the periodic table, the actinides result as electrons fill the 5f orbitals. Among the actinides, the chemical bonding behaviors of actinium and thorium resemble those of the transition metals; the 5f-electrons of protactinium, uranium, neptunium, and plutonium often play important roles in their bonding; and among the still heavier elements, their bonding tends to mimic the lanthanide elements in terms of electron shielding and their f-electron contributions. While the 4f orbitals of lanthanides are considered core orbitals, strong relativistic effects enable the 5f orbitals of actinide elements to be more involved in chemical bonding than expected without including these effects in a theoretical treatment of the species.

Thorium and uranium are the most abundant actinide elements on the earth and among the largest elements occurring in nature. Investigations on thorium and uranium are twofold: analytical and spectroscopic studies and theoretical calculations performed with relativistic computational methods. We have fruitful collaborative relationships with different computational groups, all of which have expertise in computational actinide chemistry. They are Lan Cheng, David Dixon, and Kirk Peterson. This chapter presents anion spectroscopic studies on small thorium- and uranium-containing clusters. In section A, interactions between Th and H, Th and O, and Th and Au will be discussed. In section B, the measurement of the electron affinity of the uranium atom, the electronic structure of the uranyl dichloride, and interactions of U with Au will be presented.

References

1. Adam, Z. (2007). Actinides and life's origins. *Astrobiology*, 7(6), 852-872.
2. Gascoyne, M. (1992). Geochemistry of the actinides and their daughters. In *Uranium-series disequilibrium: applications to earth, marine, and environmental sciences*. 2. ed.
3. Ewing, R. C. (1999). Nuclear waste forms for actinides. *Proceedings of the National Academy of Sciences*, 96(7), 3432-3439.
4. Freeman, A. J., & Darby, J. B. (Eds.). (2013). *The Actinides: Electronic Structure and Related Properties*.

III.A. Thorium

The chemist Jöns Jacob Berzelius received an unusual ore for inspection in 1828. The material was named thoria, after Thor, the Scandinavian god of thunder and war. Later, the element isolated from the ore, thorium, has persisted to the present day, and the original ore has changed its name slightly to thorite. Being the first true actinide, thorium still has an empty 5f orbital; therefore, Th(IV) is the most stable and plentiful oxidation state. Although thorium comprises roughly 8.1 ppm of the Earth, its chemical characteristics and properties have been relatively underexplored.

This section presents studies on the interactions between Th and other atoms with combined photoelectron spectroscopic and high-level quantum theoretical methods. In section III.A.1, ThH_5^- , which exhibits a C_{4v} structure with five Th-H single bonds, possesses the largest known H/M ratio among the actinide elements(M).

In section III.A.2, I will present our study on the stoichiometry of the product of Th reacts with H_2O . The reaction of thorium atoms with water or hydrogen/oxygen mixtures differs significantly from that of the other actinides. While HThO is the favored product of $\text{Th} + \text{H}_2\text{O}$ reactions, MOH has been observed as the reaction product of other actinides (M) with water. We measured and calculated both the electron affinity of HThO and the energy separations between the ground state of neutral HThO and its low-lying electronically excited states.

In section III.A.3, I present the studies on the interactions between Th and Au atoms. Recent research has led to promising thorium-based materials — such as Gold-thoria catalysts — to catalyze the activation of small molecules.

These materials could eventually replace the more traditional chromium- and copper-doped magnetite catalysts used to form carbon dioxide and hydrogen from carbon monoxide and water. Also, Au displays very interesting properties when meeting thorium. Au can be analogous to a halogen in some cases. Our studies discuss it from both geometry and energy perspectives.

In section III.A.4, Th-Th bonding characters in Th_2O^- , Th_2Au^- , $\text{Th}_2\text{AuO}_1^-$, and $\text{Th}_2\text{AuO}_2^-$ were studied by a synergy between anion photoelectron spectroscopy and ab initio electronic structure calculations. The bond distances encompass bond orders of Th-Th bonds from 4 to 0. The bonding character between thorium and gold is significantly influenced by oxygen, evolving from metallic toward ionic bonding when oxygen is present.

III.A.1. ThH₅, An Actinide-Containing Superhalogen Molecule

Reprinted with permission from John Wiley and Sons. *ChemPhysChem* 22, 5-8 (2021). DOI: 10.1002/cphc.202000918

Mary Marshall, Zhaoguo Zhu, Rachel Harris, Kit H. Bowen,* Wei Wang, Jie Wang, Chu Gong, and Xinxing Zhang*

Abstract:

Thorium and its compounds have been widely investigated as important nuclear materials. Previous research focused on the potential use of thorium hydrides, such as ThH₂, ThH₄, and Th₄H₁₅, as nuclear fuels. Here, we report studies of the anion, ThH₅⁻, by anion photoelectron spectroscopy and computations. The resulting experimental and theoretical vertical detachment energies (VDE) for ThH₅⁻ are 4.09 eV and 4.11 eV, respectively. These values and the agreement between theory and experiment facilitated the characterization of the structure of the ThH₅⁻ anion and showed its neutral counterpart, ThH₅ to be a superhalogen. ThH₅⁻, which exhibits a C_{4v} structure with five Th-H single bonds, possesses the largest known H/M ratio among the actinide elements, M. The adaptive natural density partitioning (AdNDP) method was used to further analyze the chemical bonding of ThH₅⁻ and to confirm the existence of five Th-H single bonds in the ThH₅⁻ molecular anion.

Article:

In the 1960's, Neil Bartlett carried out the reaction between the noble gas, xenon, and the powerful oxidizing agent, PtF₆, demonstrating that the once-believed inert gas can be reactive. With an electron affinity of ~6.8 eV, the PtF₆ molecule had behaved like an ultra-halogen.^[1] Gutsev and Boldyrev later coined the term “superhalogen” to describe the class of compounds that behave chemically like halogens yet possess much higher electron affinities. Generally, superhalogens are molecules or clusters having electron affinities that are greater than that of chlorine, the element with the highest electron affinity in the periodic table. Superhalogens are of the form, MX_{k+1}, where the ligand, X, is

a halogen atom and k is the nominal valence of the central electropositive metal M .^[2] Jena later extended the definition of superhalogens, showing that they can exist without halogen atoms.^[3-5] Thus, some hydrides, e.g., AlH_4 , came to be classified as superhalogens, since as such, they readily formed their anionic counterparts, i.e., AlH_4^- .^[6] Superhalogens have been reported for both main group elements and transition metals, but to the best of our knowledge, they have not been extended to Th.

Interest in thorium hydrides stems not only from their potential as fuels for nuclear reactors, but also from indications that they are superconducting materials. Relative to thorium oxides, thorium hydrides possess higher thorium metal densities, this being an attribute in power reactors.^[7] The superconductivity parameters of ThH_2 and Th_4H_{15} , both of which are metallic solids, are well known^[8,9] and both compounds have been characterized by nuclear magnetic resonance.^[10,11] Several computational studies have also predicted that the superhydrides XH_n ($n > 5$) possess high superconducting transitions.^[12-15] Furthermore, given their high hydrogen-to-metal ratio, some thorium hydrides have been considered as candidate materials for hydrogen storage.^[16] Because of the radioactivity and toxicity of some actinides, the ability to conduct accurate theoretical calculations is quite important. Owing to electron correlation and relativistic effects, accurate calculations on actinides and actinide compounds are still very challenging. While thorium is only mildly radioactive and modestly toxic compared to trans-uranium actinides, calculations on thorium compounds provide valuable benchmarks for computations on heavier actinides. Theoretical calculations on thorium hydride systems have included ThH_4 ^[17-19] and $HThCl_3$.^[20]

The present work investigates the thorium penta-hydride anion, ThH_5^- , using anion photoelectron spectroscopy (PES) and quantum chemical calculations. ThH_5 is shown to be a superhalogen, whose anion, ThH_5^- , exhibits the highest

H/M ratio among other actinide compounds. Detailed experimental and theoretical methods are provided in the supporting information (SI).

Figure III.A.1.1 shows the mass spectrum containing ThH_5^- . No other hydrides ThH_x^- ($x \neq 5$) were observed. This phenomenon is uncommon for mass spectrometric studies of metal hydrides, since there are almost always diverse combinations of hydrogen atoms attached to the metal atoms as shown in previous reports.^[21-23] When a cluster ion exhibits unusually high intensity relative to its neighbors in the mass spectrum, it might well possess some particular property that facilitates its abundance and by implication, its stability. Clusters of this type are often declared the “magic clusters”,^[24] and examples of such clusters include the famous discovery of C_{60} .^[25]

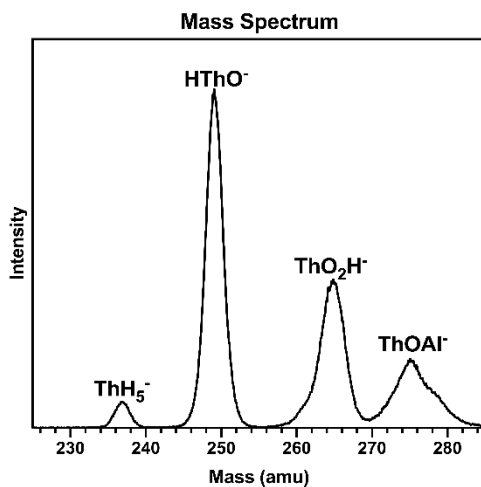


Figure III.A.1.1 The mass spectrum obtained from the pulsed arc cluster ion source using thorium powder pressed into an aluminum rod with H_2 backing gas.

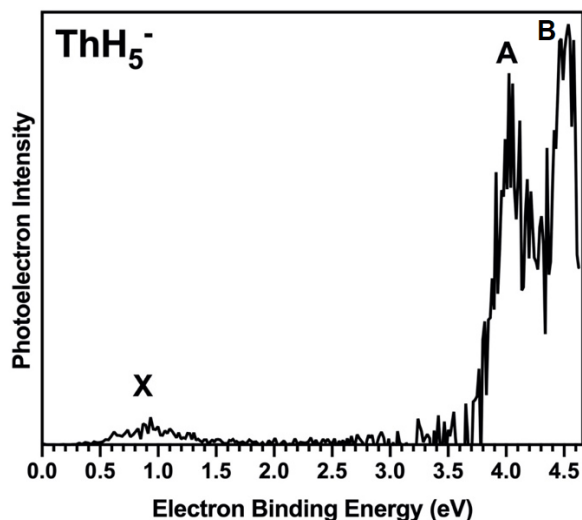


Figure III.A.1.2 Photoelectron spectrum of ThH_5^- measured with a 266 nm laser.

Figure III.A.1.2 shows the photoelectron spectrum for ThH_5^- taken with a 266 nm (4.66 eV) laser. Three features marked as A, B and X are observed in the spectrum. Feature A has an onset at an electron binding energy (EBE) of 3.71 eV ranging up to 4.35 eV, with an intensity maximum at 4.09 eV. The vertical detachment energy (VDE) is the transition at which the Franck-Condon overlap between the wave function of the ground state and that of its neutral counterpart in the structure of the anion is maximal. The VDE value for ThH_5^- is determined to be 4.09 eV. In addition, feature B peaks at 4.52 eV. There is also a weaker EBE band, feature X, which begins at $\text{EBE} = 0.58$ eV, reaching its maximum at $\text{EBE} = 0.88$ eV. This feature corresponds to ThH_3^- . The 4.66 eV photons have enough energy to photodissociate ThH_5^- into $\text{ThH}_3^- + \text{H}_2$, with a second photon photodetaching an electron from ThH_3^- . This is a two-photon phenomenon, which was also seen in the spectrum PtH_5^- .^[21] These values are tabulated in Table III.C.1.1, where they are compared with corresponding theoretical values.

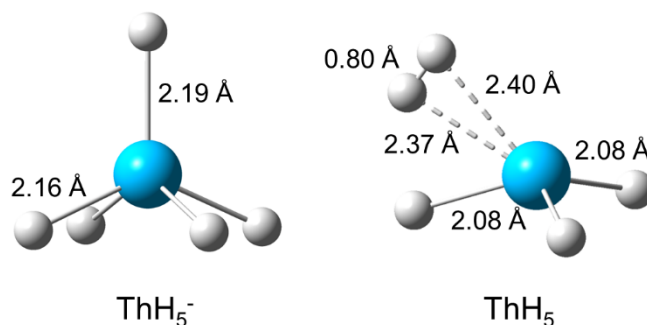


Figure III.A.1.3 Geometrical structures and bond lengths (in Å) of the $\text{ThH}_5^{-/0}$ molecules optimized at the B3LYP/aug-ccpVT/ECP60MDF level of theory. The thorium atom is blue, and the hydrogen atoms are white.

To better understand the ThH_5^- anion, we used quantum theoretical methods to compare with the experimental results (details provided in the SI). Figure III.A.1.3 presents the calculated geometric structures and bond lengths of ThH_5^- . The anion geometry converged to C_{4v} symmetry. The optimization of the singlet and triplet states of ThH_5^- determined that the singlet state is more stable. The Cartesian coordinates of the calculated structures are shown in Table S1. The ThH_5^- anion was optimized at several density theory functionals including PBE, PBE0, B3LYP, TPSS, TPSSh, as well as CCSD(T) level of theory. The aug-ccpVTZ basis set was applied to the hydrogen atoms, and the relativistic pseudopotential ECP60MDF was used for Th in all calculations. The VDE values calculated at different levels for ThH_5^- are presented in Table III.A.1.1.

Table III.A.1.1 Experimental and theoretical vertical detachment energies (VDE) values (eV) for ThH_3^- and ThH_5^- at the different levels of theory. The aug-ccpVTZ/ECP60MDF basis sets are used for all methods.

System	Expt. VDE	Theo. VDE	Expt. 2 nd VDE	Theo 2 nd VDE
ThH_3^-	0.88 (X)	0.72 ^[a]	-	-

ThH ₅ ⁻⁰ (singlet)	4.09 (A)	4.11 ^[a] , 3.82 ^[b] , 4.06 ^[c] , 3.89 ^[d] , 3.97 ^[e] , 4.34 ^[f]	4.52 (B)	4.66 ^[a]
ThH ₅ ⁻⁰ (triplet)	-	1.32 ^[a]	-	-

[a] B3LYP, [b] PBE, [c] PBE0, [d] tpss, [e] tpssh, [f] CCSD(t)

The calculated VDE values of ThH₅⁻ agree well among each other and are also in good agreement with the experimental results (4.09 eV, peak A). To identify the weaker peak observed at 0.88 eV (peak X), we optimized both the singlet ThH₃⁻ anion and the triplet state of ThH₅⁻. The calculated VDE value of the ThH₃⁻ anion is 0.72 eV, which is close to what is observed experimentally. The calculated structure of ThH₃⁻ is presented as Figure S1. However, the VDE value of the triplet state of ThH₅⁻ is 1.32 eV, drastically different from the peak X. Peak X in the photoelectron spectrum is therefore assigned to the ThH₃⁻ anion. The agreement between the calculated and experimental VDE values of ThH₃⁻ (0.72 eV and 0.88 eV, respectively) and that of the singlet state of ThH₅⁻ (4.11 and 4.09 eV, respectively) indicate that both anions are present in the PES. Photodissociation of ThH₅⁻ by the photodetachment laser after mass selection is the likely source of ThH₃⁻ anions in the ion beam. The dissociation energy for the reaction ThH₅⁻ → ThH₃⁻ + H₂ is calculated to be 1.76 eV, well below the photon energy used for photodetachment. Photodissociation of hydrides and loss of H₂ during the photoelectron spectroscopy is not uncommon in our experiments.^[21] In addition, the high-energy (peak B) transition for ThH₅⁻ (peak B, 4.66 eV) is also in good agreement with the experimental second VDE transition (4.52 eV), further confirming the presence of ThH₅⁻.

The calculated VDE depends on the computational methods and basis sets, and they range from 3.82 to 4.34 eV in the methods that we used. The experimental VDE value of 4.09 eV for the ThH₅⁻ anion is within the range of our theoretical estimates. The VDE value obtained at the B3LYP (4.11 eV) and PBE0 (4.06 eV) levels of theory are the

closest to the experimental value. Based on reasonable agreement between experiment and theory, we conclude that the theoretical methods used are reliable.

We have also presented the structure of the neutral ThH_5 molecule in Figure III.A.1.3, which displays a H_2 molecule weakly attached to ThH_3 . Since there is a large structural difference between the neutral and the anion, the Franck-Condon overlap between these two states is not sufficient enough to facilitate the experimental observation of the adiabatic electron affinity (AEA), therefore, here we could only report the calculated value, 2.23 eV.

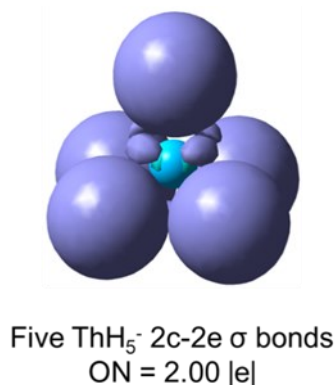


Figure III.A.1.4 Summary of AdNDP analysis of the ThH_5^- anion at the B3LYP/aug-ccpVTZ/ECP60MDF level of theory.

To further investigate the chemical bonding of ThH_5^- , we performed the adaptive natural density partitioning (AdNDP)^[23] analysis of ThH_5^- (Figure III.A.1.4) at the B3LYP/aug-ccpvtz/ ECP60MDF level of theory. Five Th-H σ bonds in ThH_5^- with occupation number (ON) values of 2.00 |e| are observed. According to Gutsev and Boldyrev, the general formula for a typical superhalogen anion is MX_{k+1}^- , where k is the number of valence electrons of M.^[2] Since the Th atom has a $[\text{Rn}]6d^2 7s^2$ electronic configuration with 4 valence electrons, ThH_5 , with five Th-H σ bonds, is a

superhalogen. The high VDE of ThH_5^- also confirms the superhalogen nature of ThH_5 . The frontier molecular orbitals and their corresponding energy levels of ThH_5^- involving the Th-H bonds are presented in Figure S2. It is apparent that the s and d orbitals of Th participate in the formation of the Th-H bonds. There is no clear evidence of the involvement of f orbitals.

To conclude, we have investigated the structural and electronic properties, as well as the chemical bonding, of the ThH_5^- anion by anion photoelectron spectroscopy and computational studies. ThH_5^- has C_{4v} structure with five Th-H single bonds contributing to the experimentally observed photoelectron spectrum. Both the singlet ThH_5^- anion and the photodissociation product ThH_3^- are observed in the photoelectron spectrum. The AdNDP analysis reveals five Th-H single bonds with occupation numbers of almost 2.0. Based on the current study, we extend superhalogens to the actinide element, Th, and the ThH_5^- anion has the greatest H/M ratio among all actinide compounds.

References

- [1] K. F. Edwards, J. F. Liebman, in ACS Symp. Ser., American Chemical Society, **2017**, pp. 261–281.
- [2] G. L. Gutsev, A. I. Boldyrev, *Chem. Phys.* **1981**, *56*, 277–283.
- [3] P. Jena, Q. Sun, *Chem. Rev.* **2018**, *118*, 5755–5870.
- [4] S. Giri, S. Behera, P. Jena, *Angew. Chemie Int. Ed.* **2014**, *53*, 13916–13919.
- [5] H. Fang, P. Jena, *Angew. Chemie Int. Ed.* **2019**, *58*, 11248–11252.
- [6] J. D. Graham, A. M. Buytendyk, X. Zhang, E. L. Collins, B. Kiran, G. Gantefoer, B. W. Eichhorn, G. L. Gutsev, S. Behera, P. Jena, K. H. Bowen, *J. Phys. Chem. A* **2014**, *118*, 8158–8162.
- [7] C. B. Satterthwaite, I. L. Toepke, *Phys. Rev. Lett.* **1970**, *25*, 741–743.
- [8] H. Winter, G. Ries, *Zeitschrift für Phys. B Condens. Matter Quanta* **1976**, *24*, 279–284.
- [9] J. F. Miller, R. H. Caton, C. B. Satterthwaite, *Phys. Rev. B* **1976**, *14*, 2795–2800.
- [10] K. F. Lau, R. W. Vaughan, C. B. Satterthwaite, *Phys. Rev. B* **1977**, *15*, 2449–2457.
- [11] M. Peretz, D. Zamir, Z. Hadari, *Phys. Rev. B* **1978**, *18*, 2059–2065.
- [12] H. Wang, J. S. Tse, K. Tanaka, T. Iitaka, Y. Ma, *Proc. Natl. Acad. Sci. U. S. A.* **2012**, *109*, 6463–6466.
- [13] X. Feng, J. Zhang, G. Gao, H. Liu, H. Wang, *RSC Adv.* **2015**, *5*, 59292–59296.
- [14] Y. Li, J. Hao, H. Liu, J. S. Tse, Y. Wang, Y. Ma, *Sci. Rep.* **2015**, *5*, 9948–9955.

- [15] Z. M. Geballe, H. Liu, A. K. Mishra, M. Ahart, M. Somayazulu, Y. Meng, M. Baldini, R. J. Hemley, *Angew. Chem. Int. Ed.* **2018**, *57*, 688–692.
- [16] I. R. Shein, K. I. Shein, N. I. Medvedeva, A. L. Ivanovskii, *Phys. B Condens. Matter* **2007**, *389*, 296–301.
- [17] P. Pyykko, J. P. Desclaux, in *J. Phys. Colloq.*, EDP Sciences, **1978**, pp. C4-222-C4-223.
- [18] P. Pyykkö, J. P. Desclaux, *Chem. Phys.* **1978**, *34*, 261–280.
- [19] P. Pyykkö, *Chem. Rev.* **1988**, *88*, 563–594.
- [20] T. Ziegler, V. Tschinke, in *Density Funct. Methods Chem.*, Springer New York, **1991**, pp. 139–154.
- [21] X. Zhang, G. Liu, K.-H. Meiwes-Broer, G. Ganteför, K. H. Bowen, *Angew. Chem. Int. Ed. Engl.* **2016**, *55*, 9644–9647.
- [22] X. Zhang, H. Wang, E. Collins, A. Lim, G. Ganteför, B. Kiran, H. Schnöckel, B. Eichhorn, K.H. Bowen, *J. Chem. Phys.* **2013**, *138*, 124303.
- [23] X. Zhang, P. Robinson, G. Ganteför, A. Alexandrova, K. H. Bowen, *J. Chem. Phys.* **2015**, *143*, 094307.
- [24] I. A. Solov'yov, A. V. Solov'yov, W. Greiner, A. Koshelev, A. Shutovich, *Phys. Rev. Lett.* **2003**, *90*, 053401.
- [25] H. W. Kroto, J.R. Heath, S. C. O'Brien, R. F. Curl, R. E. Smalley, *Nature* **1985**, *318*, 162–163.
- [26] D. Y. Zubarev, A. I. Boldyrev, *Phys. Chem. Chem. Phys.* **2008**, *10*, 5207–5217.

III.A.2. Photoelectron Spectroscopic and *Ab Initio* Computational Studies of the Anion, HThO⁻

Reprinted (adapted) with permission from *J. Phys. Chem. A* 2021, 125, 9, 1903-1909. Copyright 2021 American Chemical Society. <https://doi.org/10.1021/acs.jpca.0c11539>

Mary Marshall, Zhaoguo Zhu, Junzi Liu, Lan Cheng,* and Kit H. Bowen*

Department of Chemistry, Johns Hopkins University, Baltimore, MD 21218, USA

Abstract

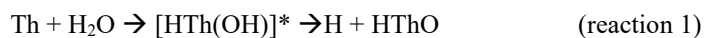
The synergetic combination of anion photoelectron spectroscopy and high-level relativistic coupled-cluster calculations was employed to study the anion, HThO⁻. The atomic connectivity of this anion was found to be HThO⁻ and not ThOH⁻. Vibrational and electronic energy spacings in the HThO⁻ photoelectron spectrum were measured and calculated, with good agreement between them being found. Computations yielded electronic energies and equilibrium structures as well as enabling orbital analyses. The adiabatic electron affinity (EA_a) of HThO was determined to be 1.297 ± 0.035 eV.

Introduction

Nuclear energy offers a high-energy-density alternative to greenhouse gas-emitting fossil fuels; however, radiological waste disposal and proliferation risks remain significant issues. Currently, most nuclear reactors utilize isotopically-enriched uranium-235 as their fuel, but the possibility of instead using thorium as the fuel has attracted attention.¹⁻⁴ This is largely because thorium is over three times more abundant than uranium, and thorium reactors are reputed to be safer to operate, to produce less radioactive waste, and to have a reduced proliferation threat. Thorium reactors are inherently breeder reactors, converting natural, non-fissile thorium-232 (with the aid of neutrons provided by a seeded fissile material, e.g., uranium-235 or plutonium-239) into the fissile isotopes, uranium-233 and uranium-232.

Therefore, thorium reactors are comparable to uranium breeder reactors, which convert uranium-238 into fissile plutonium-239. In these, as well as in all nuclear reactors, fission results in heat, which in turn is used to generate electricity.

Thorium is the only actinide element not to possess 5f electrons in its atomic ground state. Due to its [Rn]6d²7s² electronic configuration, thorium is normally present in its tetravalent state. In aqueous solutions, for example, thorium forms numerous hydroxides, e.g., Th(OH)₃⁺, Th(OH)₂²⁺, Th(OH)₃⁺, and Th₂(OH)₂⁶⁺.⁵⁻¹⁰ However, in matrix isolation studies, where laser-ablated thorium atoms and water molecules were co-deposited on an argon ice, HTh(OH) and HThO were found to be the major intermediates and reaction products, with only residual amounts of H₂ThO, HThO(OH), HTh(OH)₃, and OTh(OH)₂ detected. Interestingly, there was no evidence of thorium hydroxide, ThOH, having been formed. The formation of the intermediate, [HTh(OH)]*, (see reaction 1) was favored over the direct dissociation of water (see reaction 2).¹¹



The same result was found when reacting Th atoms with a H₂/O₂ mixture.¹¹ The reaction of thorium atoms with hydrogen peroxide generated Th(OH)₂ and Th(OH)₄, but it did not yield ThOH.¹² Water activation was also observed in guided ion beam studies, where Th⁺ cations reacted with D₂O to form DThO⁺.¹³ Several Fourier transform, ion cyclotron resonance mass spectrometric studies had reported the reactions of Th⁺ and Th²⁺ with H₂O to form ThO⁺ and ThOH⁺.¹⁴⁻¹⁶ However, subsequent calculations found these reactions preferred HThO^{+/2+} over the ThOH^{+/2+} isomer.¹⁷

The reaction of thorium atoms with water or with hydrogen/oxygen mixtures differs significantly from that of the other actinides. Based on density-functional theory (DFT) calculations, the reaction between U^+ and water favors the dehydration product, UO^+ , although small amounts of UOH^+ are also predicted to be formed.¹⁸ Uranium metal exhibits a highly exothermic reaction with water, generating uranium hydride as an intermediate before yielding the final UO_2 product.¹⁹ Plutonium metal reacts with water to produce PuOH and H_2 , although, upon heating, these initial products react to yield PuO_2 and PuH_2 .²⁰ Thus, while HThO is the favored product of $\text{Th} + \text{H}_2\text{O}$ reactions, HMO has not been observed as the reaction product of other actinides (M) with water. The $\text{HM}'\text{O}$ stoichiometry is, however, a known product of reactions between Group IV metals (M') and water. Matrix infrared spectroscopic studies with TiO_2 reacting with H_2O formed HTiO , although the main product was $\text{OTi}(\text{OH})_2$.²¹ The formation of HThO as a product of the $\text{Th} + \text{H}_2\text{O}$ reaction underscores thorium's kinship with the Group IV transition metals, both because of its four valence electrons and its lack of f-electrons.

In the present work, we utilized anion photoelectron spectroscopy in synergetic conjunction with high-level relativistic coupled-cluster calculations, finding the principle thorium-containing anionic species observed to be HThO^- and not ThOH^- . We then measured and calculated both the electron affinity of HThO and the energy separations between the ground state of neutral HThO and its low-lying electronically excited states.

Methods

Experimental

Anion photoelectron spectroscopy (PES) is conducted by crossing a mass-selected anion beam with a fixed energy photon beam and energy analyzing the resulting photodetached electrons. The photodetachment process is governed

by the energy conserving relationship, $h\nu = EBE + EKE$, where $h\nu$ is the photon energy, EBE is the electron binding (photodetachment transition) energy, and EKE is the electron kinetic energy. Our photoelectron apparatus has been described previously.²² Briefly, it consists of an ion source, a time-of-flight mass spectrometer, a Nd:YAG photodetachment laser, and a magnetic bottle electron energy analyzer. The second (532 nm, 2.33 eV), third (355 nm, 3.49 eV), and fourth (266 nm, 4.66 eV) harmonics of an Nd:YAG laser were used to photodetach the $HThO^-$ anion. The resolution of the energy analyzer is ~ 35 meV at $EKE = 1$ eV. Photoelectron spectra were calibrated against the well-known transitions of Cu^- .²³ The $HThO^-$ anions were generated in a laser vaporization ion source. A translating, rotating, surface-oxidized thorium rod was ablated using the second harmonic photon energy of a different Nd:YAG laser (532 nm, 2.33 eV), while 20 psi of UHP H_2 gas expanded over the rod.

Computational

All calculations were performed using the CFOUR program package.²⁴⁻³⁰ Equilibrium structures for the ground state ($1^1A'$) and the first excited state ($1^3A''$) of the $HThO^-$ anion were calculated using coupled-cluster singles and doubles with noniterative triples [CCSD(T)]³¹ method. Throughout our calculations, scalar-relativistic effects were taken into account using the spin-free exact two-component theory in its one-electron variant (SFX2C-1e)^{32,33} and correlation-consistent triple-zeta basis sets (cc-pVTZ)^{34,35} recontracted for the SFX2C-1e scheme. The 1s, 2s, 2p, 3s, 3p, 3d, 4f, 4p, 4d, 4f, 5s, 5p, 5d electrons and O 1s electrons were frozen in all CC calculations. The equilibrium structure for the electronic ground state ($1^2A'$) of the neutral $HThO$ molecule was also obtained at the SFX2C-1e-CCSD(T)/cc-pVTZ level. The equation-of-motion electron attachment coupled-cluster singles and doubles (EOMEA-CCSD)³⁶ method was used to obtain the equilibrium structures for three electronically excited states of $HThO$, namely, the $1^2A''$, $2^2A'$

and $2^2A''$ states. For comparison, we also carried out a geometry optimization for the electronic ground state, $X^2\Delta$, of ThOH. Geometry optimizations performed here exploited the availability of analytic gradients for the SFX2C-1e scheme²⁸ and the coupled-cluster methods.^{26,27} Table III.A.2.1 presents the electron configurations of these six states as well as the vertical electronic energies between them and the electronic ground state of the HThO⁻ anion in its equilibrium geometry.

	Leading electron configuration	Vertical electronic energy (eV)
HThO ⁻ $1^1A'$	$1a'^2 2a'^2 3a'^2 1a''^2 4a'^2 5a'^2 2a''^2 6a'^2 7a'^2 8a'^2$	0
HThO ⁻ $1^3A''$	$1a'^2 2a'^2 3a'^2 1a''^2 4a'^2 5a'^2 2a''^2 6a'^2 7a'^2 8a'^1 3a''^1$	0.73
HThO $1^2A'$	$1a'^2 2a'^2 3a'^2 1a''^2 4a'^2 5a'^2 2a''^2 6a'^2 7a'^2 8a'^1$	1.27
HThO $1^2A''$	$1a'^2 2a'^2 3a'^2 1a''^2 4a'^2 5a'^2 2a''^2 6a'^2 7a'^2 3a''^1$	2.15
HThO $2^2A'$	$1a'^2 2a'^2 3a'^2 1a''^2 4a'^2 5a'^2 2a''^2 6a'^2 7a'^2 9a'^1$	2.47
HThO $2^2A''$	$1a'^2 2a'^2 3a'^2 1a''^2 4a'^2 5a'^2 2a''^2 6a'^2 7a'^2 4a''^1$	2.85

Table III.A.2.1. Electron configurations of low-lying electronic states of HThO⁻ and HThO as well as their vertical electronic energies relative to the electronic ground state of the HThO⁻ anion, $1^1A'$, in its equilibrium geometry. The valence molecular orbitals shown here comprise Th 6s, 6p, 6d, 7s, O 2s, 2p, and H 1s orbitals.

In the present calculations, the electronic energies of the $1^3A''$ state of HThO⁻ and the $1^2A'$ state of HThO relative to the $1^1A'$ state of HThO⁻ were calculated as the difference of the corresponding SFX2C-1e-CCSD(T)/cc-pVTZ energies. The electronic energies of the $1^2A''$, $2^2A'$, and $2^2A''$ states of HThO relative to the $1^1A'$ state of HThO⁻ were obtained using an indirect scheme. We computed the difference between SFX2C-1e-EOMEA-CCSD/cc-pVTZ energies of these three states and that for the $1^2A'$ state of HThO, and then added the CCSD(T) relative energy between the HThO $1^2A'$ state and the HThO⁻ $1^1A'$ state.

A Franck-Condon (FC) simulation was also carried out to obtain the vibrational progression for the $\text{HThO}^- 1^1\text{A}' \rightarrow \text{HThO}^- 1^2\text{A}'$ transition. The harmonic vibrational frequencies and normal coordinates of the $\text{HThO}^- 1^1\text{A}'$ state were obtained by means of numerical differentiation²⁹ of analytic SFX2C-1e-CCSD(T)/cc-pVTZ gradients. The potential energy surface of the $\text{HThO}^- 1^2\text{A}'$ state was then represented as a Taylor expansion using the equilibrium structure of the $\text{HThO}^- 1^1\text{A}'$ state as the origin, in which SFX2C-1e-CCSD(T)/cc-pVTZ energies in 125 grid points were fit into a quartic function of displacements in terms of the normal coordinates of the $\text{HThO}^- 1^1\text{A}'$ state. The vibrational Schrödinger equation was solved on this potential energy surface using products of harmonic oscillator functions of the $\text{HThO}^- 1^1\text{A}'$ state as basis functions to represent the vibrational wave functions.³⁰ The FC overlap integrals with the vibrational ground state of the $\text{HThO}^- 1^1\text{A}'$ state were then obtained in a straightforward manner.

Results

Together with H_2 , the residual oxygen on the thorium rod introduced enough oxygen into the system to produce HThO^- . The resulting mass spectrum is presented in Figure III.A.2.1. The dominant peak at mass 249 amu is HThO^- . It was present only when H_2 was utilized as the expansion gas. The mass peak at 248 amu is ThO^- . Both ThO^- and ThO_2^- were observed with no expansion gas and with H_2 as the expansion gas, but HThO^- and HThO_2^- were only seen when H_2 was employed.

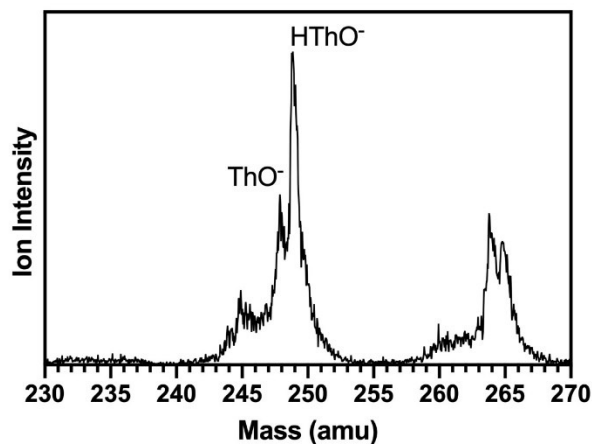


Figure III.A.2.1 The mass spectrum obtained by expanding H_2 gas over a laser ablated thorium rod. The peak at 249 amu corresponds to the HThO^- anion.

Figure III.A.2.2 presents the photoelectron spectra of HThO^- , i.e., the anion at mass 249 amu. These were collected using the 532 nm, 355 nm, and 266 nm wavelengths of the Nd:YAG photodetachment laser. The electron binding energies (EBE) corresponding to various peak positions are listed in Table III.A.2.2. The peak positions taken from Figure III.A.2.2(a) are the EBE values of the intensity maxima of peaks A, X, X', X'', and B. The peak positions for spectral feature, X, in Figures III.A.2.2(b) and (c) are approximate origin transition EBE values. These estimates have accounted for their vibrational progression profiles. The peak positions for features, B and C, in Figures III.A.2.2(b) and 2(c) are the EBE values of their intensity maxima.

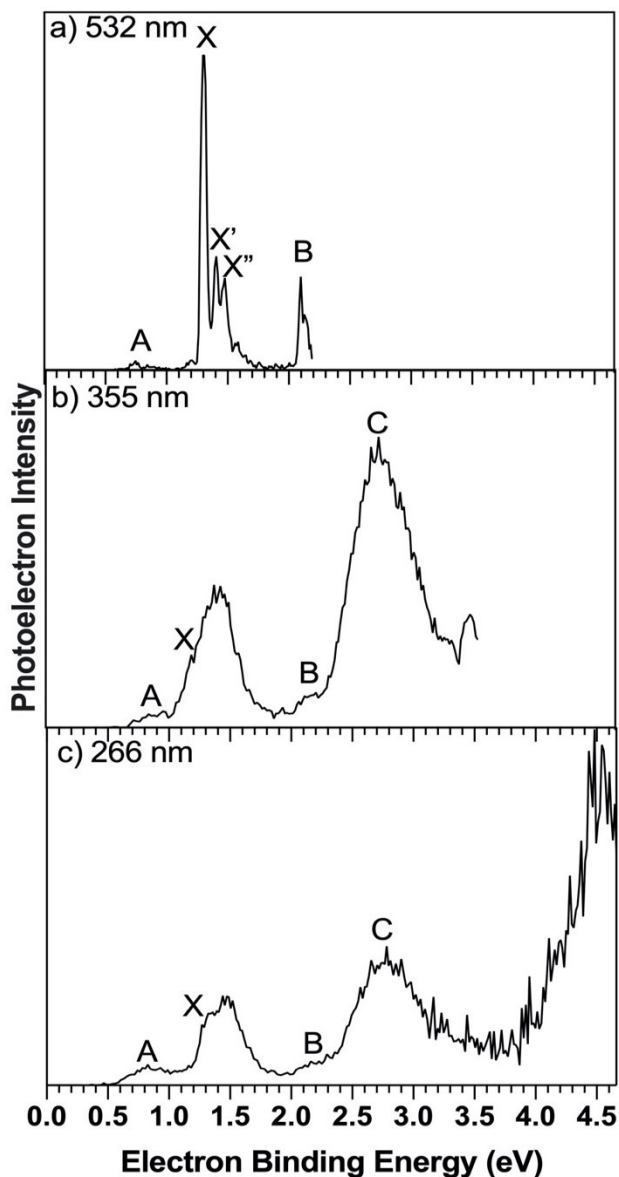


Figure III.A.2.2 The photoelectron spectra of the anion HThO^- collected at a) 532 nm, b) 355 nm, and c) 266 nm.

The electronic ground state for HThO^- is the $1^1\text{A}'$ state, and the electronic ground state for HThO is the $1^2\text{A}'$ state. As shown in Table III.A.2.1, the photodetachment of HThO^- that results in HThO involves detachment of an $8\text{a}'$ electron. Since the molecular orbital $8\text{a}'$ receives most of its contribution from the Th 7s orbital, the detachment reduces the repulsion between the Th-H and Th-O bonding orbitals and hence shortens the Th-O bond by 0.03 \AA and the Th-H

bond by as much as 0.07 Å. The computed equilibrium structures and electronic energies are summarized in Figure III.A.2.3. The relativistic coupled-cluster Th-H and Th-O bond lengths of 2.099 Å and 1.864 Å and H-Th-O bond angle of 105.7° for HThO compare reasonably well with previous DFT results of 2.054 Å, 1.869 Å, and 100.2°, respectively.¹¹ The present coupled-cluster results are expected to be higher quality than previous DFT ones. We note that the DFT Th-H and Th-O bond lengths of 2.034 and 1.820 Å for the HThO⁺ cation are shorter than those in the neutral molecule.¹⁷ This may indicate that a removal of a Th 7s electron in HThO further shortens the bond lengths, which is consistent with the present observation that the bond lengths of HThO are shortened compared to HThO⁺ with removal of a Th 7s electron.

	Electron Binding Energy (eV)		
Labeled Peaks	532 nm ^a	355 nm ^a	266 nm ^a
A	0.747 ^b	0.799 ^c	0.809 ^c
X	1.297 ^b	1.234 ^c	1.279 ^c
X'	1.407 ^b	-	-
X''	1.476 ^b	-	-
B	2.097 ^b	2.131 ^c	2.139 ^c
C	-	2.737 ^b	2.780 ^b

Table III.A.2.2 The electron binding energy (eV) values of the observed transitions in the photoelectron spectra of HThO⁺. ^aThe photon wavelength used in each case to collect the spectrum. ^bThe EBE values correspond to the intensity maxima for each peak. ^cThe approximate peak position.

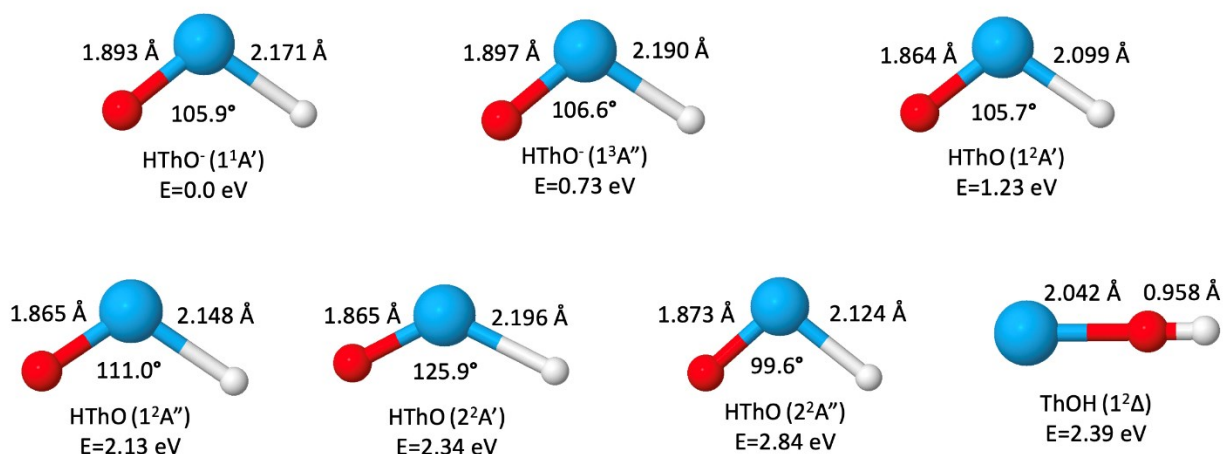


Figure III.A.2.3 Computed equilibrium structures and electronic energies for low-lying electronic states of HThO^- , HThO , and ThOH .

The electronic energy difference between the $1^2\text{A}'$ state of HThO in its equilibrium geometry and the $1^1\text{A}'$ state of HThO^- in its equilibrium geometry is calculated to be 1.23 eV. This together with the net zero-point vibrational correction of ~ 0.03 eV, deduced from the harmonic vibrational frequencies in Table III.A.2.2, leads to a computed adiabatic electron affinity, EA_{as} , of 1.26 eV, which is in good agreement with the measured value of $\text{EBE} = 1.297$ eV for feature, X, seen in Figure III.A.2.2(a) and Table III.A.2.2.

	$\text{HThO}^- 1^1\text{A}'$	$\text{HThO} 1^2\text{A}'$
H-Th-O bending	374	378
Th-O stretching	811	860
Th-H stretching	1259	1446

Table III.A.2.3 Harmonic vibrational frequencies (cm^{-1}) of the electronic ground states of HThO^- and HThO computed at the SFX2C-1e-CCSD(T)/cc-pVTZ level of theory.

Figure III.A.2.4 presents the vibrationally-resolved photoelectron spectrum of HThO^- (peaks, X, X', and X''), measured with 532 nm photons along with the computational simulation of those peaks. Not only does the profile of the stimulated spectrum resemble that of the experimental spectrum, but the computed vibrational energy spacings of 0.106 eV for Th=O stretching and 0.176 eV for Th-H stretching are in nearly quantitative agreement with the respective values of 0.110 eV and 0.179 eV, measured in the photoelectron spectrum of HThO^- . These values are in accord with Th=O and Th-H stretching frequencies of 0.105 eV and 0.176 eV, obtained via the combination of matrix-infrared spectroscopy and relativistic calculations.^{11,12} The excellent agreement between experiment and theory firmly establishes feature, X, as the origin transition from the ground electronic state of HThO^- to the ground electronic state of HThO . With this additional evidence, the adiabatic electron affinity (EA_a) of HThO is determined to be 1.297 ± 0.035 eV.

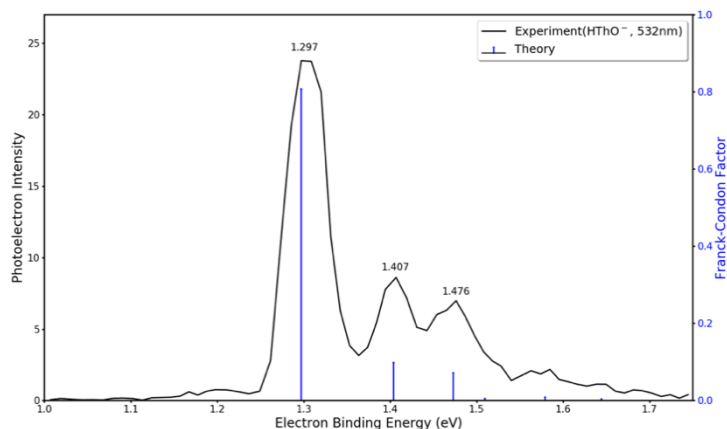


Figure III.A.2.4 The photoelectron spectrum of HThO^- collected with 532 nm wavelength photons of an Nd:YAG laser compared with the computational simulation. The computed electronic spectrum is blue-shifted by 0.03 eV to account for the net zero-point vibrational correction.

In addition to the origin-containing vibrational progression (observed as peaks X, X', and X''), we now consider the nature of peaks A, B, and C, in the photoelectron spectra of HThO⁻ (Figure III.A.2.2). Peak A is a low intensity feature located at EBE = 0.747 eV. This broad, weak peak is likely due to a small amount of ThO⁻ in the ion beam due to mass leakage (see Figure III.A.2.1). The spectral position of this feature is consistent with the previously-measured, ground state ThO⁻ → ground state ThO photodetachment transition at EBE ~0.7 eV.³⁷ Both peaks B and C likely correspond to transitions from the ground electronic state of HThO⁻ to an electronically excited state of the neutral HThO. These photoelectron spectral features are located at EBE values of ~2.1 eV and ~2.7 eV, respectively. Our calculations found that the vertical electronic energies for transitions from the HThO⁻ 1¹A' state to the 1²A'', 2²A', and 2²A'' excited electronic states of HThO are 2.15 eV, 2.47 eV, and 2.85 eV, respectively (see Table III.A.2.1). Thus, transitions to these final (neutral) states are expected to contribute to features, B and C, in the range, EBE = 2.0-3.0 eV. Peak C is mostly likely due to the 1¹A' → 2²A'' anion to neutral transition. Nevertheless, the broad profiles of these two features insinuate underlying spectral complexity. The leading configuration of these three neutral states differ from that of the 1¹A' state of HThO⁻ by more than one electron. Some of the intensity in these transitions may tentatively be attributed to strong electron correlation in the 1¹A' state of HThO⁻. Similar observations of multiple electron processes have been reported for other heavy-metal-containing molecules, including ThO⁻.³⁷

The first excited state of HThO⁻, i.e., 1³A'', is predicted to lie 0.73 eV above the HThO⁻ ground state, 1¹A'. However, the 1³A'' state is unlikely to be significantly populated in our anion source, and the lifetime of the 1³A'' is short relative to production in the anion source and photodetachment. If the 1³A'' state of the anion was to have met these challenges, it would have produced an observed transition at EBE ~ 2.0 / 2.1 eV. We mention this outlying possibility only because

there are very weak vibrational hot bands at EBE = 1.20 eV and 1.17 eV in the photoelectron spectrum of HThO^- in Figure III.A.2.2(a) and Figure III.A.2.4, implying that the nascent HThO^- anions were not completely cold.

Despite the absence of computational or experimental evidence of the formation of the anion, ThOH^- , our theoretical results show that the neutral thorium hydroxide isomer, ThOH , lies around 2.39 eV above the $1^1\text{A}'$ ground state of HThO^- , as shown in Figure III.A.2.3. Since photodetachment is a vertical ultra-fast process, there would not have been time for HThO neutral products of photodetachment to have isomerized into ThOH . Forming the ThOH isomer from HThO would involve the breaking and reforming of bonds. Although the Th-O-H atomic connectivity of ThOH no doubt occurs on the potential energy surfaces of the neutral photodetachment products, the ThOH potential well must be far from that of HThO and thus is not accessible by photodetachment.

Orbital Analysis

Orbitals $2a''$ and $6a'$ represent Th-O bonding orbitals (Figure III.A.2.5). These orbitals are largely transferable from ThO (or ThO^-) to HThO (or HThO^-). Orbital $7a'$ appears to be responsible for the Th-H bond and consists of around 70% H 1s orbital and 30% Th 6d orbital. These three orbitals are doubly occupied in HThO^- and in all electronic states of HThO studied here. Calculations show that detachment of an electron from these orbitals requires photon energies higher than 4 eV. Since the electronegative oxygen atom in ThO^- already has an appreciable negative charge, it is less energetically favorable for hydrogen to donate its electron to oxygen to form an O-H bond. The addition of hydrogen to ThO^- thus favors the thorium site, in which hydrogen atom plays the role as an acceptor of an electron from Th 6d orbitals.

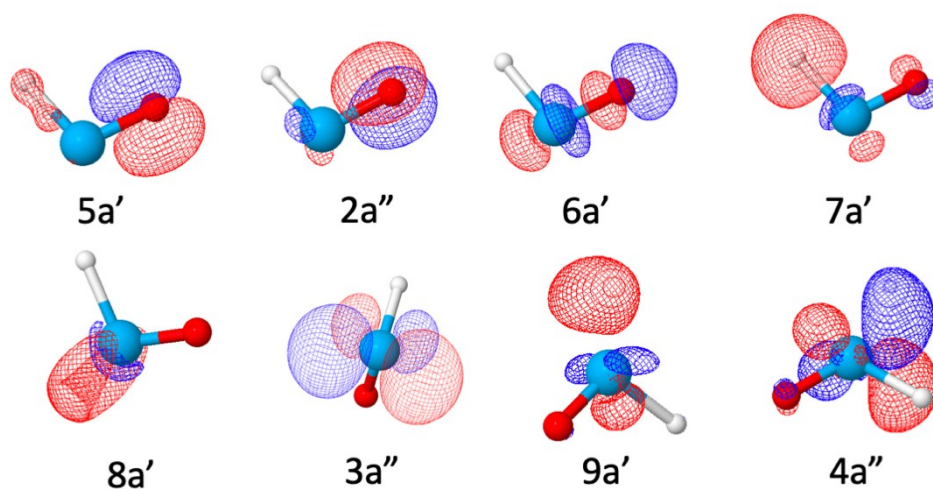


Figure III.A.2.5 Valence HF orbitals of HThO⁻ involved in photodetachment processes or bonding.

As shown in Figure III.A.2.5, orbital 8a' is by and large a polarized Th 7s orbital and is doubly occupied in HThO⁻.

Detachment of an electron in this orbital leads to the electronic ground state of the neutral molecule. The detachment to generate the $1^2A''$, $2^2A'$, or $2^2A''$ state of HThO involves detachment of an 8a' electron accompanied by an excitation from the 8a' orbital to the 3a'', 9a', or 4a'' orbital, respectively, which as shown in Figure III.A.2.5 receives most of the contributions from the Th 6d orbitals.

Conclusions

In this paper, we present a combined experimental and high-level computational study of the connectivity and electronic structure of the HThO molecule and the HThO⁻ anion. The present experiment uses the reaction of ThO⁻ with H₂ gas to produce HThO⁻. Since the oxygen atom in ThO⁻ already possesses a substantial negative charge, it is not energetically favorable for hydrogen to donate an electron to oxygen to form an O-H bond and ThOH⁻. Instead, a hydrogen atom accepts an electron from the Th 6d orbital to form HThO⁻. Photodetachment of the ground state of

anion HThO^- ($1^1\text{A}'$) to form the electronic ground state of the neutral HThO ($1^2\text{A}''$) ejects a thorium 7s electron. This reduces the repulsion with the Th-H and Th-O bonding orbitals and causes their bond lengths to shorten. The adiabatic electron affinity of HThO is accurately determined by resolving the vibrational progression for this transition. In addition, transitions from the ground state of HThO^- to electronically excited states of HThO are characterized to provide valuable information about the electronic structure of HThO .

Corresponding Authors

*K.H.B.: kbowen@jhu.edu and L. C.: lcheng24@jhu.edu

Author Contributions

The experimental work was done at Johns Hopkins University by Mary Marshall and Zhaoguo Zhu. Kit H. Bowen supervised the experiments. The computational work was done at Johns Hopkins University by Junzi Liu and Lan Cheng. The manuscript was written as a collaborative effort.

ABBREVIATIONS

EA_{a} , adiabatic electron affinity; DFT, density-functional theory; M, actinides; M', Group IV metals; PES, anion photoelectron spectroscopy; Nd:YAG, neodymium-doped yttrium aluminum garnet; EBE, electron binding energy; EKE, electron kinetic energy; UHP, ultra-high purity; CFOUR, coupled-cluster techniques for computational chemistry; CCSD(T), coupled cluster singles and doubles with non-iterative triples; SFX2C-1e, spin-free exact two-component theory in its one-electron variant; cc-pVTZ, correlation consistent-polarized valence triple zeta; EOMEA-

CCSD, equation-of-motion electron attachment coupled-cluster singles and doubles; FC, Franck-Condon; eV, electron volt.

REFERENCES

1. Morss, L. R. *The Chemistry of the Actinide and Transactinide Elements*; Springer: Netherlands, 2010.
2. Lung, M.; Gremm, O. Perspectives of the Thorium Fuel Cycle. *Nucl. Eng. Des.* **1998**, *180*, 133–146.
3. Lombardi, C.; Luzzi, L.; Padovani, E.; Vettriano, F. Thorium and Inert Matrix Fuels for a Sustainable Nuclear Power. *Prog. Nucl. Energy* **2008**, *50*, 944–953.
4. Bae, K.-M.; Kim, M.-H. Core Design for Heterogeneous Thorium Fuel Assemblies for PWR (I)- Nuclear Design and Fuel Cycle Economy. *Nucl. Eng. Technol.* **1978**, *37*, 91–100.
5. Ekberg, C.; Albinsson, Y.; Comarmond, M. J.; Brown, P. L. Studies on the Complexation Behavior of Thorium (IV). 1. Hydrolysis Equilibria. *J. Solution Chem.* **2000**, *29*, 63–86.
6. Engkvist, I.; Albinsson, Y. Hydrolysis Studies of Thorium Using Solvent Extraction Technique. *Radiochim. Acta* **1992**, *58–59*, 109–112.
7. Moulin, C.; Amekraz, B.; Hubert, S.; Moulin, V. Study of Thorium Hydrolysis Species by Electrospray-Ionization Mass Spectrometry. *Anal. Chim. Acta* **2001**, *441*, 269–279.
8. Baes, C. F.; Meyer, N. J.; Roberts, C. E. The Hydrolysis of Thorium(IV) at 0 and 95°. *Inorg. Chem.* **1965**, *4*, 518–527.
9. Kafle, A.; Armentrout, P. B. Mechanism and Energetics of the Hydrolysis of Th^+ to form $\text{Th}(\text{OD})_3^+$: Guided Ion Beam and Theoretical Studies of ThO^+ , ThO_2^+ , and OThOD^+ reacting with D_2O . *J. Phys. Chem. A* **2019**, *123*, 5893–5905.
10. Kafle, A.; Nwokolo, C.; Sanchez, L.; Armentrout, P. B. Threshold Collision-Induced Dissociation of Hydrated Th(IV) Trihydroxide Cation: Experimental and Theoretical Investigation of the Binding Energies for $\text{Th}(\text{OH})_3^+(\text{H}_2\text{O})_n$ Complexes ($n = 1-4$). *J. Phys. Chem. A* **2020**, *124*, 3090 – 3100.
11. Liang, B.; Andrews, L.; Li, J.; Bursten, B. E. Experimental and Theoretical Studies of the Products of Laser-Ablated Thorium Atom Reactions with H_2O in Excess Argon. *J. Am. Chem. Soc.* **2002**, *124*, 6723–6733.
12. Wang, X.; Andrews, L. Infrared Spectra and Structures of the $\text{Th}(\text{OH})_2$ and $\text{Th}(\text{OH})_4$ Molecules. *Phys. Chem. Chem. Phys.* **2005**, *7*, 3834–3838.
13. Cox, R. M.; Armentrout, P. B., Activation of Water by Thorium Cation: A Guided Ion Beam and Quantum Chemical Study, *J. Am. Soc. Mass Spectrom.* **2019**, *20*, 1835–1849.
14. Santos, M.; Marçalo, J.; De Matos, A. P.; Gibson, J. K.; Haire, R. G. Gas-Phase Oxidation Reactions of Neptunium and Plutonium Ions Investigated via Fourier Transform Ion Cyclotron Resonance Mass Spectrometry. *J. Phys. Chem. A* **2002**, *106*, 7190–7194.
15. Cornehl, H. H.; Wesendrup, R.; Diefenbach, M.; Schwarz, H. A Comparative Study of Oxo-Ligand Effects in the Gas-Phase Chemistry of Atomic Lanthanide and Actinide Cations. *Chem.-A Eur. J.* **1997**, *3*, 1083–1090.

16. Gibson, J. K.; Haire, R. G.; Santos, M.; Marçalo, J.; De Matos, A. P. Oxidation Studies of Dipositive Actinide Ions, An^{2+} ($An = Th, U, Np, Pu, Am$) in the Gas Phase: Synthesis and Characterization of the Isolated Uranyl, Neptunyl, and Plutonyl Ions $UO_2^{2+}(g)$, $NpO_2^{2+}(g)$, and $PuO_2^{2+}(g)$. *J. Phys. Chem. A* **2005**, *109*, 2768–2781.
17. Mazzone, G.; Michelini, M. D. C.; Russo, N.; Sicilia, E. Mechanistic Aspects of the Reaction of Th^+ and Th^{2+} with Water in the Gas Phase. *Inorg. Chem.* **2008**, *47*, 2083–2088.
18. del Carmen Michelini, M.; Russo, N.; Sicilia, E. How Can Uranium Ions (U^+ , U^{2+}) Activate the O-H Bond of Water in the Gas Phase? *Angew. Chem.* **2006**, *118*, 1113–1117.
19. Delegard, C. H.; Schmidt, A. J. Uranium Metal Reaction Behavior in Water, Sludge, and Grout Matrices. Pacific Northwest National Laboratory, **2008**.
20. Haschke, J. M. Reactions of Plutonium and Uranium with Water: Kinetics and Potential Hazards. Los Alamos, **1995**.
21. Shao, L.; Zhang, L.; Chen, M.; Lu, H.; Zhou, M. Reactions of Titanium Oxides with Water Molecules. A Matrix Isolation FTIR and Density Functional Study. *Chem. Phys. Lett.* **2001**, *343*, 178–184.
22. Gerhards, M.; Thomas, O. C.; Nilles, J. M.; Zheng, W.-J.; Bowen, K. H. Cobalt-Benzene Cluster Anions: Mass Spectrometry and Negative Ion Photoelectron Spectroscopy. *J. Chem. Phys.* **2002**, *116*, 10247–10252.
23. Ho, J.; Ervin, K. M.; Lineberger, W. C. Photoelectron Spectroscopy of Metal Cluster Anions: Cu_n^- , Ag_n^- , and Au_n^- . *J. Chem. Phys.* **1990**, *93*, 6987–7002.
24. Matthews, D. A.; Cheng, L.; Harding, M. E.; Lipparini, F.; Stopkiewicz, S.; Jagau, T.-C.; Szalay, P. G.; Gauss, J.; Stanton, J. F. Coupled-Cluster Techniques for Computational Chemistry: The CFOUR Program Package. *J. Chem. Phys.* **2020**, *152*, 214108.
25. CFOUR. *Coupled-Cluster Techniques for Computational Chemistry*, a quantum-chemical program package by Stanton, J. F.; Gauss, J.; Cheng, L.; Harding, M. E.; Matthews, D. A.; Szalay, P. G.; with contributions from Auer, A. A.; Bartlett, R. J.; Benedikt, U.; Berger, C.; Bernholdt, D. E.; Bomble, Y. J.; Christiansen, O.; Engel, F.; Faber, R.; Heckert, M.; Heun, O.; Hilgenberg, M.; Huber, C.; Jagau, T.-C.; Jonsson, D.; Jusélius, J.; Kirsch, T.; Klein, K.; Lauderdale, W.J.; Lipparini, F.; Metzroth, T.; Mück, L.A.; O'Neill, D.P.; Price, D.R.; Prochnow, E.; Puzzarini, C.; Ruud, K.; Schiffmann, F.; Schwalbach, W.; Simmons, C.; Stopkiewicz, S.; Tajti, A.; Vázquez, J.; Wang, F.; Watts, J. D.; and the integral packages MOLECULE (Almlöf, J.; Taylor, P. R.), PROPS (Taylor, P. R.), ABACUS (Helgaker, T.; Jensen, H. J. A.; Jørgensen, P.; Olsen, J.), and ECP routines by Mitin, A. V.; van Wüllen, C. For the current version, see <http://www.cfour.de>.
26. Watts, J. D.; Gauss, J.; Bartlett, R. J. Coupled-cluster Methods with Noniterative Triple Excitations for Restricted Open-Shell Hartree–Fock and Other General Single Determinant Reference Functions. Energies and Analytical Gradients. *J. Chem. Phys.* **1993**, *98*, 8718.
27. Stanton, J. F.; Gauss, J. Analytic Energy Gradients for the Equation-of-Motion Coupled-Cluster Method: Implementation and Application to the HCN/HNC System. *J. Chem. Phys.* **1994**, *100*, 4695.
28. Cheng, L.; Gauss, J. Analytic Energy Gradients for the Spin-Free Exact Two-Component Theory using an Exact Block Diagonalization for the One-Electron Dirac Hamiltonian. *J. Chem. Phys.* **2011**, *135*, 084114.
29. Stanton, J. F.; Lopreore, L.; Gauss, J. The Equilibrium Structure and Fundamental Vibrational Frequencies of dioxirane. *J. Chem. Phys.* **1998**, *108*, 7190.

30. Matthews, D. A.; Vazquez, J.; Stanton, J. F. Calculated Stretching Overtone Levels and Darling- Dennison Resonances in Water: A triumph of Simple Theoretical Approaches. *Mol. Phys.* **2007**, *105*, 2659- 2666.
31. Raghavachari, K.; Trucks, G. W.; Pople, J. A.; Head-Gordon, M. A Fifth-Order Perturbation Comparison of Electron Correlation Theories. *Chem. Phys. Lett.* **1989**, *157*, 479-483.
32. Dyall, K. G. Interfacing relativistic and nonrelativistic methods. IV. One- and Two-Electron Scalar Approximations. *J. Chem. Phys.* **2011**, *115*, 9136.
33. Liu, W.; Peng, D. Exact Two-Component Hamiltonians Revisited. *J. Chem. Phys.* **2009**, *131*, 031104.
34. Peterson, K. A. Correlation Consistent Basis Sets for Actinides. I. The Th and U Atoms. *J. Chem. Phys.* **2015**, *142*, 074105.
35. Dunning, T. H. Gaussian Basis Sets for Use in Correlated Molecular Calculations. I. The Atoms Boron through Neon and Hydrogen. *J. Chem. Phys.* **1989**, *90*, 1007-1023.
36. Nooijen, M.; Bartlett, R. J. Equation of Motion Coupled Cluster Method for Electron Attachment. *J. Chem. Phys.* **1996**, *102*, 3629.
37. Li, Y.; Zou, J.; Xiong, X.-G.; Su, J.; Xie, H.; Fei, X.; Tang, Z.; Liu, H. Probing Chemical Bonding and Electronic Structures in ThO⁻ by Anion Photoelectron Imaging and Theoretical Calculations. *J. Phys. Chem. A* **2017**, *121*, 2108–2113.

III.A.3. ThAu_2^- , ThAu_2O^- and ThAuOH^- anions: Photoelectron Spectroscopic and Theoretical Characterization

Reproduced with permission from AIP Publishing. *J. Chem. Phys.* **156**, 054305 (2022)

Zhaoguo Zhu,¹ Mary Marshall,¹ Kit H. Bowen^{1,*}, and Kirk A. Peterson^{2,*}

¹ Department of Chemistry, Johns Hopkins University, Baltimore, MD 21218, USA

² Department of Chemistry, Washington State University, Pullman, WA 99164, USA

Abstract

The thorium-gold negative ions ThAu_2^- , ThAu_2O^- , and ThAuOH^- have been observed and experimentally characterized by anion photoelectron spectroscopy. These experiments are accompanied by extensive ab initio electronic structure calculations using a relativistic composite methodology based primarily on coupled cluster CCSD(T) calculations. The theoretical electron affinities (EAs) at 0 K agree with the experimental adiabatic EAs to within 0.02 eV for all species. Two separate isomers were located in the calculations for ThAuOH^- and detachment from both of these appear to be present in the photoelectron spectrum. Excited electronic states of the neutral molecules are reported at the EOM-CCSD level of theory. Atomization energies and heats of formation are also calculated for each neutral species and have expected uncertainties of 3 and 4 kcal/mol, respectively. The σ bonds between Th and Au are determined by natural bond orbital (NBO) analysis to consist of predominately sd hybrids on Th bonding with the Au 6s orbital. In order to investigate the correspondence between the bonding in Th-Au and Th-F molecules, a limited number of calculations were also carried out on most of the F-analogs of this study. These results demonstrate that Au does behave like F in these cases, although the Th-F σ bonds are much more ionic compared to Th-Au. This results in an EA for ThF_2 that is 10 kcal/mol smaller than that of ThAu_2 . The EA values for the Th(IV) species, i.e., ThX_2O and ThXOH , only differed however by 3-4 kcal/mol.

I. Introduction

The chemistry of actinides (An) has received prodigious attention in recent years due to the wide applications of uranium and plutonium in nuclear energy development.¹ The renewed research on the thorium-based molten salt fast reactors (MSFR) shows that thorium, the second element in the An series, is a potential nuclear fuel to complement uranium-based reactors.²⁻⁴ Also, the high natural abundance of thorium (9.6 ppm) in the Earth's crust compared to that of uranium (2.7 ppm) is an economic stimulus to the development of the next-generation nuclear reactor.⁴ Thorium is an early An element without 5f electrons and has an atomic, ground-state electron configuration of $[\text{Rn}]6d^27s^2$, analogous to group IV transition metals. Owing to the significant relativistic and non-negligible electron correlation effects, electronic structures of thorium-containing compounds are complicated and challenging for theoretical calculations.⁵⁻¹⁰ The combination of experimental data and calculations is vital to interpreting and understanding thorium chemistry.

Gold-thoria catalysts, which are ThO_2 -supported on gold clusters or a single gold atom, showed extremely high catalytic activity for carrying out the water-gas shift reaction (WGS) and the process of CO oxidation.¹¹⁻¹³ Tabakova et al. (2006) suggested the WGS activity is related to the gold clusters interacting with thoria.¹¹ Notably, an OH group probably at the boundary of the gold-thoria catalyst may interact with CO resulting in a formate intermediate toward the formation of CO_2 , which means the $\text{Au}_x\text{-Th}_y\text{O}_n\text{H}$ ($x, y, n=0, 1, 2, 3 \dots$) moiety in the catalyst plays a critical role in the CO oxidation reaction. Although several first principle calculations were performed to study the mechanism of CO oxidation by gold-thoria catalysts, the function of the OH group is unexplored at the molecular level.^{12,13} To

give a better understanding of the structure of the gold-thoria catalyst, it is essential to study the chemical bonding in thorium-gold, thorium-gold oxide, and thorium-gold hydroxide species.

In addition to the bulk thorium-gold containing species, small thorium-gold and thorium-gold oxide clusters are also of great interest to theorists. Barysz and Pyykkö performed a first principle theoretical study of the ThAu^+ cation, identified its $^1\Sigma^+$ ground state, and showed it has a single bond with a bond dissociation energy of 3.5 eV.¹⁴ In 2006, Pyykkö's theoretical work reported that ThAu_2^{2+} and OThAu^+ have $D_{\infty h}$ and $C_{\infty v}$ symmetry, respectively.¹⁵ In both ThAu_2^{2+} and OThAu^+ clusters, Au^+ is an analogue to oxygen. Additionally, Gagliardi predicted a tetrahedral ThAu_4 cluster in which gold carries a formal charge of -1 |e| and behaves like a halogen.¹⁶ The unique properties of Au have been summarized on Cs^+Au^- and $[\text{Au}=\text{C}=\text{Au}]^{2+}$ as well as many other systems.¹⁷⁻¹⁹ However, experimental studies of thorium-gold clusters are scarce. Recently the photoelectron spectra of Th_2Au^- and $\text{Th}_2\text{AuO}_{1,2}^-$ were reported by some of the current authors.²⁰ Those experiments were also accompanied by ab initio calculations similar to those of this study. To the best of our knowledge, no experimental or theoretical data have been reported on the structures and bonding of $\text{ThAu}_2^{0/-}$, $\text{ThAu}_2\text{O}^{0/-}$ or $\text{ThAuOH}^{0/-}$ clusters.

In this paper, we report the first investigation on ThAu_2^- , ThAu_2O^- and ThAuOH^- anions in the gas phase using photoelectron spectroscopy combined with high level theoretical calculations. Experimental and theoretical results are compared and utilized to characterize the electronic structures and chemical bonding of all three species.

II. Methods

A. Experimental

The present work utilized anion photoelectron spectroscopy (aPES) as its primary probe. The experimental technique, aPES, is conducted by crossing a mass-selected beam of negative ions with a fixed-energy photon beam and energy analyzing the resulting photodetached electrons. This technique is governed by the energy-conservation relationship, $h\nu = \text{EBE} + \text{EKE}$, where $h\nu$, EBE, and EKE are the photon energy, electron binding (transition) energy, and the electron kinetic energy, respectively. Our photoelectron spectrometer, which has been described previously,²¹ consists of one of several ion sources, a linear time-of-flight (TOF) mass spectrometer, a mass gate, a momentum decelerator, a neodymium-doped yttrium aluminum garnet (Nd:YAG) laser for photodetachment, and a magnetic bottle electron energy analyzer. Photoelectron spectra were calibrated against the well-known photoelectron spectrum of Cu.²²

The anions of interest were generated using a pulsed-arc (discharge) cluster ionization source (PACIS), which has been described in detail elsewhere.^{23,24} This cluster anion source has been used to generate a variety of bimetal cluster anions.^{25,26} During PACIS operation, a 30 μs long, 150-volt electrical pulse applied across the Cu anode and the Th-Au sample cathode in the discharge chamber vaporizes the Th and Au atoms. The sample cathode had been prepared in a nitrogen glove box, where a Th-Au powder mixture was firmly pressed onto a copper rod. Another layer of Cu powder was pressed onto the top of the Th-Au layer to prevent contact between the thorium powder and air. Almost simultaneously with the electrical discharge, 150 psi of ultrahigh purity helium gas was injected into the discharge region to make the ThAu_2^- and ThAu_2O^- anions, while 150 psi of pure hydrogen gas was used to make the ThAuOH^- anion. The resulting mixture of atoms, ions, and electrons then reacted and cooled as it expanded through the PACIS housing and nozzle. The resultant anions were further analyzed by TOF mass spectroscopy and aPES.

B. Computational

Equilibrium geometries of all six species ($\text{ThAu}_2/\text{ThAu}_2^-$, $\text{ThAu}_2\text{O}/\text{ThAu}_2\text{O}^-$, $\text{ThAuOH}/\text{ThAuOH}^-$) were optimized at the coupled cluster singles and doubles with perturbative triples, CCSD(T), level of theory.²⁷ For the open-shell anion species, restricted open-shell Hartree-Fock (ROHF) orbitals were used in CCSD(T) calculations where the spin restriction is relaxed in the CCSD solutions, i.e., R/UCCSD(T).²⁸ For these geometry optimizations the 3rd-order Douglas-Kroll-Hess (DKH3) scalar relativistic Hamiltonian²⁹⁻³² was used throughout with diffuse-augmented correlation consistent basis sets from double- to triple-zeta ($n=\text{D, T}$), i.e., aug-cc-pVnZ-DK for O and H,^{33,34} the newly developed aug-cc-pVnZ-DK3 for Au,³⁵ and the cc-pVnZ-DK3 sets^{36,37} for Th augmented by a diffuse function in each angular symmetry obtained via even-tempered extension. Throughout this text these basis sets will be denoted as aVnZ ($n=\text{D, T, Q}$). In these calculations only the valence electrons were correlated (6s6p6d7s for Th, 6s5d for Au, 2s2p for O, and 1s for H), i.e., the standard frozen-core (FC) approximation was employed.

The CCSD(T) equilibrium geometries calculated at the triple-zeta level were then used in subsequent Feller-Peterson-Dixon (FPD) composite calculations³⁷⁻⁴⁰ of the electron affinities and atomization energies, with the latter leading to heats of formation. Specifically, the FPD energy is defined in this work to be:

$$E_{\text{FPD}} = E_{\text{FC-CCSD(T)/aVQZ}} + \Delta E_{\text{CBS}} + \Delta E_{\text{CV}} + \Delta E_{\text{QED}} + \Delta E_{\text{SO}} + \Delta E_{\text{ZPE}} \quad (1)$$

On the right-hand-side of Eq. (1), $E_{\text{FC-CCSD(T)/aVQZ}}$ is the frozen-core DKH3 CCSD(T) energy calculated with the aVQZ basis set. The complete basis set (CBS) limits were obtained using core-valence basis sets, aug-cc-pwCVQZ-DK3 on Au,³⁵ aug-cc-pwCVQZ-DK on O,⁴¹ aug-cc-pVQZ-DK on H,⁴² and diffuse augmented cc-pwCVQZ-DK3 on Th.^{36,37} These sets will be denoted aCVnZ below ($n=\text{T, Q}$). Using FC DKH3 CCSD(T) calculations with aCVTZ and aCVQZ basis sets, the HF energies were extrapolated to the HF limit via⁴³ ($n=3$ and 4 for T and Q, respectively)

$$E_n = E_{CBS} + A(n+1)e^{-6.57\sqrt{n}} \quad (2)$$

while the CCSD(T) correlation energies were extrapolated with^{44,45}

$$E_n = E_{CBS} + \frac{B}{\left(n + \frac{1}{2}\right)^4} \quad (3)$$

The second term on the right-hand-side of Eq. (1), ΔE_{CBS} , is the difference between the extrapolated CBS limit [sum of the results of Eqs. (2) and (3)] and the aVQZ energy. The term ΔE_{CV} is the effect of correlating the outer-core electrons, i.e., 5s5p5d on Th, 5s5p on Au, and 1s on O. This is calculated as the difference between DKH3 CCSD(T) calculations with outer-core correlated and frozen core, both with the same aCVTZ and aCVQZ basis sets. These differences were then extrapolated to the CBS limit via Eq. (3). Small effects due to the leading contribution of QED, the Lamb shift ΔE_{QED} , were obtained using the local model potential approach proposed by Pyykkö and Zhao for the self-energy term, including a fit to the Ueling potential for the vacuum polarization.^{37,46} These calculations were carried out at the frozen-core DKH3-CCSD(T) level of theory with aCVDZ basis sets. The spin-orbit correction, ΔE_{SO} , was calculated using four- (4-c) or two- (2-c) component CCSD(T) using orbitals/spinors from average of configuration Dirac Hartree Fock (AoC-DHF) calculations. The Dirac-Coulomb-Gaunt (DCG) Hamiltonian, as well as Dyall's spin-free (SF) Hamiltonian,⁴⁷ were used throughout using the same aVDZ basis sets defined above but completely uncontracted and with a finite-nucleus model.⁴⁸ It should be noted that the Gaunt term was only implemented at the DHF level of theory. Only valence electrons were correlated in these coupled cluster calculations with virtual orbital cutoffs of 20 E_h . In the cases of ThAu₂/ThAu₂⁻ and ThAuOH/ThAuOH⁻, the SO correction was calculated as the difference between a 4-c CCSD(T) calculation⁴⁹ with the DCG Hamiltonian and one with Dyall's SF

Hamiltonian. For the larger $\text{ThAu}_2\text{O}/\text{ThAu}_2\text{O}^-$ pair, the exact 2-c molecular mean field (X2C-mmF) CCSD(T) method⁵⁰ (originating from a DHF calculation with the DCG Hamiltonian) was utilized in place of 4-c CCSD(T). In all cases the spin-orbit corrections were calculated at the DKH3 CCSD(T)/aVTZ geometries. The SO contribution for the O atom was obtained from its experimental energy levels,⁵¹ with its Gaunt contribution calculated at the AoC-DHF/aVDZ level of theory. Excited electronic states for the neutral molecules were calculated using the Equation-of-Motion CCSD method with the X2C-mmF Hamiltonian (both SF and DCG).^{52,53}

For the calculation of adiabatic electron affinities and atomization energies, zero-point energy (ZPE) corrections were obtained from harmonic vibrational frequencies calculated at the DKH3 CCSD(T) level of theory with the aVDZ basis set throughout except for $\text{ThAu}_2/\text{ThAu}_2^-$ which utilized aVTZ. Heats of formation at 298 K were calculated by combining FPD atomization energies using the contributions of Eq. (1) for the molecules and atoms, including thermal corrections via standard gas phase partition function expressions, with the known 298 K enthalpies of formation for the gaseous elements: $\Delta H_f(\text{H}) = 52.1028 \pm 0.0000$ kcal/mol, $\Delta H_f(\text{O}) = 59.5672 \pm 0.0005$ kcal/mol,⁵⁴⁻⁵⁶ $\Delta H_f(\text{Au}) = 88.05 \pm 0.26$ kcal/mol,⁵⁷ and $\Delta H_f(\text{Th}) = 143.9 \pm 1.4$ kcal/mol.^{58,59}

Natural Bond Orbital (NBO) analysis,⁶⁰ including natural population analysis (NPA),⁶¹ was carried out with the NBO7 program⁶² using DKH3 Hartree-Fock/aVTZ wave functions. In these calculations the Th 6s and 6p orbitals were included in the valence space. Nearly all the calculations of this work were carried out with MOLPRO 2020.2,⁶³⁻⁶⁵ except for the SO calculations, which were completed with DIRAC19.⁶⁶

III. Results and Discussion

A. Experimental results

Figure III.A.3.1(a) presents the mass spectrum of anionic products ranging from 100 amu to 900 amu using a 1:1 thorium-gold mixture and helium backing gas. Three major series of clusters are observed. The first series starting from 254 amu consists of ThC_xO_y^- ($x=0,1,2$, $y=1,2$) anion clusters, and the second series beginning from 457 amu is composed of the ThAuAl^- anion and its oxides. ThAu_2^- anion appears at 626 amu at the beginning of the third series in which we also observe ThAu_2O^- and ThAu_2Al^- anions. Aluminum as well as carbon and oxygen, are from the surface of the cathode and surroundings in the PACIS source housing. From Figure III.A.3.1(b), the ThAuOH^- anion is observed when using 3:1 thorium-gold mixture and hydrogen gas. We see a variety of thorium hydride anions, thorium hydroxide, thorium-gold hydride, and thorium-gold hydroxide anions in the spectrum in Figure III.A.3. 1(b).

We then applied anion photoelectron spectroscopy with a 355 nm laser to characterize the ThAu_2^- , ThAu_2O^- and ThAuOH^- anions. The resulting photoelectron spectra of ThAu_2^- , ThAu_2O^- and ThAuOH^- are presented in Figure III.A.3. 2. In each spectrum, we observe several peaks corresponding to transitions from the ground state of the anion to different states of its corresponding neutral. For ThAu_2^- , two broad electron binding energy (EBE) bands range from ~ 1.3 eV to 3.49 eV; they reach their intensity maximum at 1.53 eV and 2.71 eV. For ThAu_2O^- , the spectrum displays three EBE bands starting from ~ 1.3 eV, ~ 2.0 eV, and 2.5 eV, with these attaining their maxima at 1.65 eV, 2.21 eV, and 2.73 eV, respectively. In ThAuOH^- 's spectrum, the first feature X, with its threshold occurring at EBE of ~ 0.7 eV, is peaked at 1.03 eV. Band A, which is the most intense feature in the spectrum, exhibits an onset of signal at 1.23 eV and reaches maximum intensity at 1.43 eV. Band B, which ranges from EBE ~ 2.7 to 3.4 eV, is relatively broad and weak, suggesting that it contains multiple transitions, some of which may be due to multi-electron processes with low transition efficiencies. In the anion photoelectron spectra, the intensity maxima of these peaks represent transitions

from the ground state of anion to the ground and excited states of the neutral counterpart. Among these transitions, the electron binding energy (EBE) value at the peak position in the lowest EBE spectral feature (labeled as X) is the vertical detachment energy (VDE), which is the energy difference between the ground state anion and its neutral counterpart at the geometry of the anion. Thus, VDEs of ThAu_2^- , ThAu_2O^- and ThAuOH^- are 1.53 eV, 1.65 eV, and 1.03 eV, respectively. When there is sufficient Franck–Condon overlap between the ground state of the anion and the ground state of the neutral, and when vibrational hot bands are absent, the threshold EBE (E_T) is the value of the electron affinity (EA). Nevertheless, since vibrational temperatures for anions are difficult to estimate and since some degree of vibrational excitation is not uncommon (giving rise to hot bands), the EA value often lies between the threshold and the VDE value. As a reasonable approximation, one can estimate the EA as that corresponding to the EBE value at $\sim 10\%$ of the rising photoelectron intensity. Therefore, EAs of ThAu_2^- , ThAu_2O^- and ThAuOH^- are evaluated to be 1.30 eV, 1.35 eV, and 0.80 eV, respectively. The EA values of ThAu_2^- and ThAu_2O^- are relatively similar to each other, while the EA and VDE value of ThAuOH^- is significantly lower than the other two species.

B. Computational Results

1. Assignment of low-lying detachment energies

$\text{ThAu}_2/\text{ThAu}_2^-$ As shown graphically in Figure III.A.3. 3 and more specifically in Table III.A.3.1, the ThAu_2 molecule, which has a closed-shell 1A_1 ground state in the absence of SO coupling effects (more on this below), has a bent, symmetrical structure with a CCSD(T)/aVQZ bond angle of 136.6° . Initial calculations also investigated the presence of low-lying triplet states which uncovered 3A_1 and 3B_1 states that arise from single excitations from the 7s orbital on Th to 6d orbitals that correspond to $6d_{\delta}$ at linear geometries. At the CCSD(T)/aVTZ level of theory these triplets lie

just 2.54 and 2.25 kcal/mol, respectively, above the singlet state at their respectively equilibrium geometries (which are qualitatively very similar to that of the singlet). Most of the FPD calculations then proceeded assuming a 1A_1 ground state for ThAu_2 , but subsequent X2C-mmF-EOM-CCSD calculations with the DCG Hamiltonian demonstrated that SO coupling was sufficient to yield a triplet ground state for ThAu_2 . Combining the SO effect on the state splitting at the EOM-CCSD level with the vertical triplet-singlet splitting at the CCSD(T)/aVTZ level of theory yields a singlet-triplet correction of -1.43 kcal/mol. The ground state of the anion has a linear equilibrium geometry with a Th-Au bond length that has lengthened by 0.134 Å upon electron attachment. Relative to the closed-shell 1A_1 state of the neutral, the additional electron occupies the degenerate $6d_8$ orbital on the Th atom, yielding a $^2\Delta_g$ ground state. The results of the FPD treatment for both the adiabatic EA (EA_0) and VDE are shown in Table III.A.3.2. It can be noted that correlation of the outer-core electrons has a non-negligible effect on the EAs, decreasing EA_0 and VDE by 0.8 and 0.6 kcal/mol, respectively. Including the effects of spin-orbit coupling increases both values by about 4 kcal/mol (0.17 eV). The final FPD value for the adiabatic EA, 29.5 kcal/mol (1.28 eV), which is relative to the triplet ground state of ThAu_2 , is in excellent agreement with experiment (1.30 eV).

For ThAu_2^- the calculation of the VDE is complicated by the fact that the lowest state of neutral ThAu_2 even at the linear anion geometry is a $^3\Delta_{1g}$ state and not the $^1\Sigma^+_{0g}$. At the scalar relativistic DKH3-CCSD(T)/aVTZ level of theory, the $^3\Delta_g$ state lies above the $^1\Sigma^+_g$ by 1.99 kcal/mol, but including spin-orbit coupling as the difference between X2C-mmF EOM-CCSD with DCG and SF Hamiltonians favors the $\Omega=1_g$ over the 0_g spin-orbit state by 3.89 kcal/mol, yielding a final singlet-triplet separation at the anion geometry of -1.90 kcal/mol (the triplet being lower). As shown in Table III.A.3.2., this results in a final FPD VDE of 33.6 kcal/mol (1.45 eV), which is in very good agreement with

the experimental result (1.53 eV) extracted from the spectrum shown in Figure III.A.3. 2. The full results of the X2C-mmfc DCG-EOM-CCSD calculations at the anion geometry are shown in Table III.A.3.3. All of these excited states are dominated by a single excitation from the highest occupied MO of closed-shell ThAu₂, which is predominately Th 7s in character. As shown in Table III.A.3.3, there are many even (g) parity states that can contribute to the PES, particularly the lowest $\Omega=2g$ and $0g$ states that arise from the $^3\Delta_g$ and $^1\Sigma_g^+$, respectively. In particular, the first 4 Ω states are related to the anion ground electronic state by just a single electron detachment, and as such might be expected to have relatively strong intensity. From these calculations it is not clear which of these gerade states could be assigned to the PES feature marked "A" at about 2.7 eV. The first ungerade state lies at a VDE of about 3.2 eV.

ThAu₂O/ThAu₂O⁻ As seen in Figure 3, the equilibrium geometries of the ThAu₂O and ThAu₂O⁻ molecules have a pyramidal structure with a central Th atom, corresponding to C_s symmetry. The neutral molecule has a closed-shell MO configuration and the ground electronic state of the anion involves the attachment of the electron into an MO localized on Th with predominately Th 7s character with contributions from the Th 6d and 7p orbitals. As shown in Table III.A.3.1, the largest change in the ThAu₂O structure upon electron attachment is in the Th-Au bond length, which lengthens by 0.112 Å. The other internal coordinates only involve minor changes. Table III.A.3.4 shows the FPD results for EA₀ and the VDE. In this case all of the FPD contributions on top of the FC-CCSD(T)/aVQZ values are relatively small. The largest is the effect of including SO coupling, but even this is just -0.90 and -0.59 kcal/mol for the EA₀ and VDE, respectively. This is not surprising since the additional electron occupies primarily a Th 7s orbital. The final FPD result for the EA₀ is 31.3 kcal/mol (1.36 eV), which is in excellent agreement with the experimental value of 1.35 eV. The VDE obtained by FPD, 35.1 kcal/mol (1.52 eV) is, however, lower than the

experimental result (1.65 eV) by 0.13 eV. In regard to the features A and B shown in the spectrum of Figure III.A.3.

2, it is not clear at present what these might correspond to. The results of EOM-CCSD calculations on ThAu₂O (at the anion geometry) show the first two excited states to be triplets and lie about 3 eV above the ground state. The corresponding singlets are higher in energy by about another 0.1 eV. These excitation energies correspond to detachment energies of 4.5 eV and above, which are far above the highest energy portion of the measured PES.

ThAuOH/ThAuOH⁻ Initial work on ThAuOH/ThAuOH⁻ assumed a bent molecule with a central Th atom in analogy to bent ThF₂ (or ThAu₂). A planar structure with C_s symmetry was readily found and its structural parameters are given in Table III.A.3.1. As in the ThAu₂ case, the closed-shell neutral molecule has a highest occupied molecular orbital (HOMO) that is primarily Th 7s in character. The anion is formed by attaching an electron in a Th 6d orbital, yielding a ²A' electronic state. As in the previous cases considered in this study, the largest change in the neutral structure upon electron attachment is in the Th-Au bond length, which lengthens by 0.172 Å. Some lengthening of the Th-O distance is also observed, 0.051 Å, and the Au-Th-O bond angle opens up by about 30°. As shown in Table III.A.3.5, the calculated EA₀ value is smaller than that of ThAu₂, but the FPD contributions are rather similar with outer-core correlation decreasing the EA by about 1 kcal/mol and SO increasing it by about 3. The final FPD result for EA₀, 20.4 kcal/mol (0.89 eV), is in good agreement with the experimental result of 0.80 eV. The calculated VDE of 24.6 kcal/mol (1.06 eV) is also in very good agreement with the experimental value of 1.03 eV. Both of these results seem to accurately account for the feature marked X in the spectrum of Figure III.A.3.2.

In regards to features A and B of the PES shown in Fig. 2, excited states of the C_s form of ThAuOH were calculated at the CCSD(T)/aVTZ equilibrium geometry of the anion using the X2C-mmEOM-CCSD level of theory. These

results are shown in Table III.A.3.6. Without the inclusion of SO coupling, the low-lying excited states are composed of various singlets and triplets, all of which originate from an excitation from the HOMO of the neutral that has primarily Th 7s character. It is easily seen that the near-linear structure used in these calculations leads to many excited states that are nearly degenerate. The first excited state is calculated to be a $^3A''$ and lies within 0.2 eV of the singlet ground state. The next state, a $^1A''$, is separated by 1 eV and then there are many singlet and triplet states separated by only a few tenths of an eV. With the inclusion of SO coupling, one of the components of the lowest $^3A''$ state is now isoenergetic with the closed-shell $^1A'$ state. The next two components of the triplet lie within 0.14 and 0.35 eV of the SO ground state. As in the SF case, the next states then begin about 1 eV higher in energy and are all relatively closely spaced. Referring to the PES of Fig. 2, the width of peak X can now be attributed in part to the contributions from up to 3 electronic states. Peak A could be due in part to the excited state with a VDE of 1.4 eV. It is not clear what peak B could be attributed to except perhaps high-lying excited states of ThAuOH.

The relatively large intensity of peak A, however, is difficult to easily rationalize. This led to a search for alternative structures, which led to the C_1 symmetry molecule shown in Fig. 3, which has a central Th atom bonded directly to Au, O, and H. For this isomer, which like ThAu₂O is also formally a Th(IV) species, the anion is formed by attaching an electron to the empty Th 7s orbital of the closed-shell neutral. From the structural parameters given in Table III.A.3.1, electron attachment again leads to large changes in the Th-Au distance (+0.136 Å) and modest elongation of the Th-O distance (+0.030 Å). Most importantly, as shown in Table III.A.3.5, the C_1 isomer of the anion is *more* stable than the C_s form by 41.4 kcal/mol (1.80 eV). As also shown in Table III.A.3.5, the electron affinity is slightly larger for the C_1 isomer as compared to the C_s one. Just as in ThAu₂O, all the contributions beyond the FC

CCSD(T)/aVQZ values are relatively small. The FPD result for the EA_0 , 30.2 kcal/mol (1.31 eV), and the VDE, 33.2 kcal/mol (1.44 eV), seem to be good matches for peak A in the PES of Fig. 2. The relatively large intensity could be due to the higher population of the C_1 form relative to the C_s isomer (since it is significantly more stable), but also due to excited state contributions from the latter isomer as mentioned above. Also as in the $ThAu_2O$ case, excited states arising from the C_1 isomer are not predicted to play a role in the PES of Fig 2 since the first excited state (at the anion geometry) is calculated to lie 3.0 eV above the electronic ground state (without SO), which corresponds to a VDE of about 4.5 eV.

2. Thermochemistry

Atomization energies at 0K (AE_0) have been calculated with the FPD method for the neutral molecules of this work to provide additional insights in their bonding. These results, including the breakdown of the FPD contributions, are shown in Table III.A.3.7. Most of the contributions are relatively large, particularly the effects due to the CBS extrapolation (~ 3 kcal/mol), outer-core correlation (~ 5.5 kcal/mol), and SO coupling (~ 6.5 kcal/mol). The contribution due to the Lamb shift is calculated to be particularly large for $ThAu_2$, -1.4 kcal/mol, which is about twice as large as the value calculated for $ThAu_2O$. Generally this quantity is larger when the change in valence s-orbital occupation is large, which naively would point towards a larger value for $ThAu_2O$ compared to $ThAu_2$ (see Sec. 3 below). Confirmation of the present results with a more rigorous treatment would be very interesting. The final FPD atomization energy for $ThAu_2$, 154.1 kcal/mol, which includes a correction for the triplet ground state (see above), is nearly half the AE_0 value of ThF_2 .⁶⁷ Curiously the AE_0 value calculated for $ThAu_2O$ is nearly identical to the sum of the experimental ThO bond dissociation energy (207.6 kcal/mol)⁶⁸ and the $ThAu_2$ atomization energy. Utilizing

experimental heat of formation values for the elements (see Sec. II.B), heats of formation at 298K have been calculated and are also shown in Table III.A.3.7. The atomization energies have estimated uncertainties of ± 3 kcal/mol, while the heats of formation are estimated at ± 4 kcal/mol due to the uncertainty in the experimental heat of formation of atomic Th (± 1.4 kcal/mol).⁵⁸

3. Electronic structure analysis

Table III.A.3.8 lists the atomic charges for all the molecules of the present work from natural population analysis. The neutral species are characterized by a positively charged Th atom (between +0.95 and +2.4) with all other atoms negatively charged. In these cases the charge on Au is about -0.5 while that of O is generally -1.3. Somewhat surprisingly, in the C_1 isomer of ThAuOH the H atom is strongly negative with a charge of -0.6. In the anions, the extra electron is localized on Th, so this reduces the positive charge on Th by 0.6 (ThAu₂O) to 0.8 (ThAu₂). The remaining additional negative charge is distributed over the Au and O atoms, although preferentially more on the Au atoms. The bonding given by NBO analysis is given in Table III.A.3.9, 10, and 11 for ThAu₂, ThAu₂O, and ThAuOH (C_1), respectively. The bonding NBOs of ThAuOH (C_1) are shown in Figure III.A.3. 4 as representative examples. In all three cases, full sets of 5d lone pairs (10 for ThAu₂ and ThAu₂O and 5 for ThAuOH) are not shown but are also present on the Au atoms. As shown in Table III.A.3.9 for ThAu₂, two σ -type NBOs arise from couplings of Th 7s and 6d natural atomic orbitals (NAOs) with Au 6s and 5d. The two Th NAOs mix, along with some 7p and 5f character, to form two 6d-rich hybrids (71%) directed toward Au. The Au 7s NAOs remain essentially unhybridized and combine with the Th hybrids to form two σ bonds that are strongly polarized toward the Au atoms with percent ionicities of 58%. The 3rd hybrid on Th is an s-rich (68%) lone pair that arises from mixing the Th 7s and 6d NAOs. For the

negative ion, the additional electron occupies an unhybridized 6d orbital on Th and the Th lone pair remains essentially unchanged. The σ bonds become only slightly less d-rich (66%) compared to those of the neutral (71%) with a very similar percent ionicity (55%).

The NBO analysis of the Lewis structure for ThAu_2O shown in Table III.A.3.10 consists of one Th-Au bond and three Th-O bonds. The σ bond between Th and Au arises from a hybrid on Th consisting primarily of 7s and 6d NAOs in nearly equal amounts with essentially an unhybridized 6s orbital on Au. This bond is slightly more strongly polarized towards Au than in the ThAu_2 case, as judged by the percent ionicity, 63%. The 3 bonds between Th and O arise from couplings of Th 6d and 5f NAOs with 2s and 2p NAOs of O. The σ bond involves a d-rich (63%) hybrid on Th mixing with p-rich hybrid (76%) on O. The two π bonds also involve d-rich hybrids on Th (61% and 73%) but mix with unhybridized 2p orbitals on O. All three bonds are more strongly polarized toward the O atom compared to the Th-Au bond, particularly in the case of the π bonds. In the case of the anion of ThAu_2O , the additional electron occupies a Th s-rich (54%) hybrid lone pair orbital that arises from coupling Th 7s, 7p (22%), and 6d (22%) NAOs. The other NBOs are similar to those of the neutral except that the Th-Au σ bond is a bit more rich in d character (66%) compared to the neutral. An NBO analysis of the bonding in the C_1 isomer of ThAuOH is shown in Table III.A.3.11. A total of 5 bonds are formed, σ bonds between Th, Au, and H with σ and π bonds between Th and O. In this sense the bonding is similar to ThAu_2O . The σ bond between Th and Au is from the couplings of 7s and 6d NAOs on Th mixing with primarily an unhybridized 6s on Au. The resulting hybrid on Th has nearly equal parts of 7s (47%) and 6d (44%) with small contributions of 7p and 5f. Not surprisingly the bond is polarized towards the more electronegative Au atom with a percent ionicity of 61%. The Th-H σ bond involves a d-rich (63%) hybrid on Th mixing with the 1s of H. This

bond is also very polarized towards H (% ionicity of 63%). Last, the σ and π bonds between Th and O are very similar to those described previously for ThAuO₂ although one of the bonds designated as π is actually a mixture of both σ and π character. The unpaired electron in the negative ion of ThAuOH (C₁) occupies an s-rich (54%) lone pair orbital on Th with strong contributions from p-type (24%) and d-type (19%) NAOs. The other NBOs are very similar to those of the neutral except that the Th-Au and Th-H σ bonds become more d-rich and more polarized away from the Th.

4. Correspondence of Th-Au and Th-F species

As noted in the Introduction, it has been previously noted that Au⁺ and Au can behave as analogs of O and halogens, respectively. In order to investigate this further, DKH3-CCSD(T)/aVTZ calculations have been carried out on the F-analogs of some of the present molecules, i.e., ThF₂/ThF₂⁻, ThF₂O/ThF₂O⁻, and ThFOH/ThFOH⁻ (C₁). In each of these cases the ground electronic states were identical to the Au-analogs, and the equilibrium structures were remarkably similar outside of the expected shorter Th-F bond compared to Th-Au. In regard to the equilibrium electron affinities, the F-containing molecules have CCSD(T)/aVTZ EA values (ThF₂: 17.1 kcal/mol, ThF₂O: 28.8 kcal/mol, ThFOH (C₁): 26.4 kcal/mol) smaller than the analogous Au-containing ones (27.1, 32.5 and 29.7 kcal/mol for ThAu₂, ThAu₂O, and ThAuOH, respectively) by 3-10 kcal/mol, with the largest difference observed for ThF₂. On inspection of the NBOs, the Th-O bonds in ThF₂O and ThFOH are nearly identical in character to those of ThAu₂O and ThAuOH. The Th-F bonds, however, are much more polarized towards F in comparison to Au and the hybrid orbitals on Th involved in these σ -type bonds have substantial 6d and 5f character with very little s or p contributions. This is particularly true for ThF₂ where the % ionicity of the σ_{ThF} bond is 89.0% compared to 58.1% for σ_{ThAu} , and the % of 5f character is

25% compared to just 4% for the ThAu₂ case. In the negative ion, ThF₂⁻, the addition of the extra electron into a Th 6d orbital results in the bonding becoming sufficiently ionic that no formal bonds were discovered in the NBO analysis.

IV. Conclusions

The ThAu₂⁻, ThAu₂O⁻, and ThAuOH⁻ negative ions were characterized both experimentally by anion photoelectron spectroscopy and by ab initio calculations based on relativistic coupled cluster theory. Excellent agreement between experiment and theory was observed, to within 0.02 eV, for the adiabatic electron affinities (0 K from theory and the threshold EBE from experiment). In particular, the spectrum of ThAuOH⁻ was interpreted as arising from two isomers, one corresponding to Th(IV) and the other (less stable) to Th(II). The bonds of Th to Au were calculated to be fairly ionic but were not nearly as ionic as Th-F bonds, as indicated by analogous calculations on the F analogs of these three Au-containing molecules. Atomization energies and heats of formation were calculated for the neutral species using the same composite relativistic coupled cluster methodology as the EAs, yielding expected accuracies of 3-4 kcal/mol.

References

- ¹ D. Lecarpentier and J. Vergnes, Nucl. Eng. and Des. **216**, 43 (2002).
- ² V. Jagannathan, Int. J. Energy Res. **42**, 117 (2018).
- ³ Lombardi, C, L. Luzzi, E. Padovani, and F. Vettraino, Prog. Nucl. Energy **50**, 944 (2008).
- ⁴ D. Heuer, E. Merie-Lucotte, M. Allibert, M. Brovchenko, V. Ghetta, and P. Rubiolo, Ann Nuc. Energy **64**, 421 (2014).
- ⁵ Y. L. Li, X. G. Xiong, and H. T. Liu, Nucl. Sci. Tech. **30**, 70 (2019).
- ⁶ J. B. Liu, X. Chen, J. B. Lu, H. Q. Cui, and J. Li, J. Comp. Chem. **39**, 2432 (2018).
- ⁷ Y. Gong, L. Andrews, V. E. Jackson, and D. A. Dixon, Inorg. Chem. **51**, 11055 (2012).

- ⁸ Y. Li, J. Zou, X. G. Xiong, J. Su, H. Xie, Z. Fei, Z. Tang, and H. Liu, *J. Phys. Chem. A* **121**, 2108 (2017).
- ⁹ Y. Li, J. Zou, X. G. Xiong, H. Xie, Z. Tang, M. Ge, Y. Zhao, and H. Liu, *J. Chem. Phys.* **148**, 244304 (2018).
- ¹⁰ R. M. Cox, A. Kafle, P. B. Armentrout, and K. A. Peterson, *J. Chem. Phys.* **151**, 034304 (2019).
- ¹¹ T. Tabakova, V. Idakiev, K. tenchev, F. Boccuzzi, M. Manzoli, and A. Chiorino, *App. Cat. B* **63**, 94 (2006).
- ¹² Y. Tang, S. Zhao, B. Long, J. C. Liu, and J. Li, *J. Phys. Chem. C* **120**, 17514 (2016).
- ¹³ B. Long, Y. Tang, and J. Li, *Nano Research* **9**, 3868 (2016).
- ¹⁴ M. Barysz and P. Pyykkö, *Chem. Phys. Lett.* **368**, 538 (2003).
- ¹⁵ P. Hrobárik, M. Straka, and P. Pyykkö, *Chem. Phys. Lett.* **431**, 6 (2006).
- ¹⁶ L. Gagliardi, *J. Am. Chem. Soc.* **125**, 7504 (2003).
- ¹⁷ M. Gerhards, O. C. Thomas, J. M. Nilles, W. J. Zheng, and K. H. Bowen Jr., *J. Chem. Phys.* **116**, 10247 (2002).
- ¹⁸ J. Ho, K. M. Ervin, and W. C. Lineberger, *J. Chem. Phys.* **93**, 6987 (1990).
- ¹⁹ S. Burkart, N. Blessing, B. Klipp, J. Müller, G. Ganteför, and G. Seifert, *Chem. Phys. Lett.* **301**, 546 (1999).
- ²⁰ Z. Zhu, M. Marshall, R. M. Harris, K. H. Bowen, M. Vasiliu, and D. A. Dixon, *J. Phys. Chem. A* **125**, 258 (2021).
- ²¹ H. R. Siekmann, C. Lüder, J. Faehrmann, H. O. Lutz, and K. H. Meiwes-Broer, *Z. Phys. D* **20**, 417 (1991).
- ²² X. Zhang, Y. Wang, H. Wang, A. Lim, G. Gantefoer, K. H. Bowen Jr., J. U. Reveles, and S. N. Khanna, *J. Am. Chem. Soc.* **135**, 4856 (2013).
- ²³ Y. J. Ko, A. Shakya, H. Wang, A. Grubisic, W. Zheng, M. Götz, G. Ganteför, K. H. Bowen Jr., P. Jena, and B. Kiran, *J. Chem. Phys.* **133**, 124308 (2010).
- ²⁴ X. Zhang, G. Ganteför, K. H. Bowen Jr., and A. N. Alexandrova, *J. Chem. Phys.* **140**, 164316 (2014).
- ²⁵ H. Wang, Y. Jae Ko, X. Zhang, G. Gantefoer, H. Schnoeckel, B. W. Eichhorn, P. Jena, B. Kiran, A. K. Kandalam, and K. H. Bowen Jr., *J. Chem. Phys.* **140**, 124309 (2014).
- ²⁶ H. Wang, X. Zhang, Y. J. Ko, A. Grubisic, X. Li, G. Ganteför, H. Schnöckel, B. W. Eichhorn, M. Lee, P. Jena, A. K. Kandalam, B. Kiran, and K. H. Bowen Jr., *J. Chem. Phys.* **140**, 054301 (2014).
- ²⁷ K. Raghavachari, G. W. Trucks, J. A. Pople, and M. Head-Gordon, *Chem. Phys. Lett.* **157**, 479 (1989).
- ²⁸ P. J. Knowles, C. Hampel, and H. J. Werner, *J. Chem. Phys.* **99**, 5219 (1993).
- ²⁹ M. Douglas and N. M. Kroll, *Ann. Phys.* **82**, 89 (1974).
- ³⁰ B. A. Hess, *Phys. Rev. A* **33**, 3742 (1986).
- ³¹ T. Nakajima and K. Hirao, *J. Chem. Phys.* **113**, 7786 (2000).

- ³² M. Reiher and A. Wolf, J. Chem. Phys. **121**, 10945 (2004).
- ³³ T. H. Dunning, J. Chem. Phys. **90**, 1007 (1989).
- ³⁴ R. A. Kendall, T. H. Dunning, and R. J. Harrison, J. Chem. Phys. **96**, 6796 (1992).
- ³⁵ R. Feng, E. D. Glendening, and K. A. Peterson, J. Phys. Chem. A **125**, 5335 (2021).
- ³⁶ R. L. Feng and K. A. Peterson, J. Chem. Phys. **147**, 084108 (2017).
- ³⁷ K. A. Peterson, J. Chem. Phys. **142**, (2015).
- ³⁸ D. A. F. Dixon, D.; Peterson, K. A. , in *Annual Reports in Computational Chemistry*, edited by A. W. Ralph (Elsevier, 2012), Vol. 8, pp. 1.
- ³⁹ D. Feller, K. A. Peterson, and D. A. Dixon, J. Chem. Phys. **129**, 204105 (2008).
- ⁴⁰ K. A. Peterson, D. Feller, and D. A. Dixon, Theor. Chem. Acc. **131**, 1079 (2012).
- ⁴¹ K. A. Peterson and T. H. Dunning, Jr., J. Chem. Phys. **117**, 10548 (2002).
- ⁴² W. A. de Jong, R. J. Harrison, and D. A. Dixon, J. Chem. Phys. **114**, 48 (2001).
- ⁴³ A. Karton and J. M. L. Martin, Theor. Chem. Acc. **115**, 330 (2006).
- ⁴⁴ D. Feller, K. A. Peterson, and J. G. Hill, J. Chem. Phys. **135**, 044102 (2011).
- ⁴⁵ J. M. L. Martin, Chem. Phys. Lett. **259**, 669 (1996).
- ⁴⁶ P. Pykkö and L.-B. Zhao, J. Phys. B **36**, 1469 (2003).
- ⁴⁷ K. G. Dyall, J. Chem. Phys. **100**, 2118 (1994).
- ⁴⁸ L. Visscher and K. G. Dyall, Atom Data Nucl Data **67**, 207 (1997).
- ⁴⁹ L. Visscher, T. J. Lee, and K. G. Dyall, J. Chem. Phys. **105**, 8769 (1996).
- ⁵⁰ J. Sikkema, L. Visscher, T. Saue, and M. Iliaš, J. Chem. Phys. **131**, 124116 (2009).
- ⁵¹ C. E. Moore, *Atomic Energy Levels*. Vol. 1, (NSRDS-NBS 35; Office of Standard Reference Data, National Bureau of Standards, Washington DC, 1971).
- ⁵² A. Shee, T. Saue, L. Visscher, and A. Severo Pereira Gomes, J. Chem. Phys. **149**, 174113 (2018).
- ⁵³ J. F. Stanton and R. J. Bartlett, J. Chem. Phys. **98**, 7029 (1993).
- ⁵⁴ B. Ruscic and D. H. Bross.
- ⁵⁵ B. Ruscic, R. E. Pinzon, G. v. Laszewski, D. Kodeboyina, A. Burcat, D. Leahy, D. Montoy, and A. F. Wagner, J. Phys: Conf. Ser. **16**, 561 (2005).

- ⁵⁶ B. Ruscic, R. E. Pinzon, M. L. Morton, G. von Laszewski, S. J. Bittner, S. G. Nijsure, K. A. Amin, M. Minkoff, and A. F. Wagner, *J. Phys. Chem. A* **108**, 9979 (2004).
- ⁵⁷ J. W. Arblaster, *J. Phase Equil. Diff.* **37**, 229 (2016).
- ⁵⁸ J. D. Cox, D. D. Wagman, and V. A. Medvedev, *CODATA Key Values for Thermodynamics*, (Hemisphere Publishing Corp., New York, 1989).
- ⁵⁹ R. J. M. Konings and O. Beneš, *J. Phys. Chem. Ref. Data* **39**, 043102 (2010).
- ⁶⁰ F. Weinhold and C. L. Landis, *Valency and Bonding: A Natural Donor–Acceptor Perspective*, (Cambridge University Press, 2005).
- ⁶¹ A. E. Reed, R. B. Weinstock, and F. Weinhold, *J. Chem. Phys.* **83**, 735 (1985).
- ⁶² NBO 7.0, Theoretical Chemistry Institute, University of Wisconsin, Madison, WI (2018).
- ⁶³ MOLPRO, version 2020.2, a package of ab initio programs, H.-J. Werner, P. J. Knowles, G. Knizia, F. R. Manby, M. Schütz, P. Celani, W. Györffy, D. Kats, T. Korona, R. Lindh, A. Mitrushenkov, G. Rauhut, K. R. Shamasundar, T. B. Adler, R. D. Amos, S. J. Bennie, A. Bernhardsson, A. Berning, D. L. Cooper, M. J. O. Deegan, A. J. Dobbyn, F. Eckert, E. Goll, C. Hampel, A. Hesselmann, G. Hetzer, T. Hrenar, G. Jansen, C. Köppl, S. J. R. Lee, Y. Liu, A. W. Lloyd, Q. Ma, R. A. Mata, A. J. May, S. J. McNicholas, W. Meyer, T. F. Miller III, M. E. Mura, A. Nicklass, D. P. O'Neill, P. Palmieri, D. Peng, T. Petrenko, K. Pflüger, R. Pitzer, M. Reiher, T. Shiozaki, H. Stoll, A. J. Stone, R. Tarroni, T. Thorsteinsson, M. Wang, and M. Welborn, see <https://www.molpro.net>.
- ⁶⁴ H. J. Werner, P. J. Knowles, G. Knizia, F. R. Manby, and M. Schutz, *Wires Comput Mol Sci* **2**, 242 (2012).
- ⁶⁵ H. J. Werner, P. J. Knowles, F. R. Manby, J. A. Black, K. Doll, A. Hesselmann, D. Kats, A. Köhn, T. Korona, D. A. Kreplin, Q. Ma, T. F. Miller, III, A. Mitrushchenkov, K. A. Peterson, I. Polyak, G. Rauhut, and M. Sibaev, *J. Chem. Phys.* **152**, 144107 (2020).
- ⁶⁶ DIRAC, a relativistic ab initio electronic structure program, Release DIRAC19 (2019), written by A. S. P. Gomes, T. Saue, L. Visscher, H. J. Aa. Jensen, and R. Bast, with contributions from I. A. Aucar, V. Bakken, K. G. Dyall, S. Dubillard, U. Ekström, E. Eliav, T. Enevoldsen, E. Faßhauer, T. Fleig, O. Fossgaard, L. Halbert, E. D. Hedegård, T. Helgaker, B. Helmich-Paris, J. Henriksson, M. Iliaš, Ch. R. Jacob, S. Knecht, S. Komorovský, O. Kullie, J. K. Lærdahl, C. V. Larsen, Y. S. Lee, H. S. Nataraj, M. K. Nayak, P. Norman, G. Olejniczak, J. Olsen, J. M. H. Olsen, Y. C. Park, J. K. Pedersen, M. Pernpointner, R. Di Remigio, K. Ruud, P. Sałek, B. Schimmelpfennig, B. Senjean, A. Shee, J. Sikkema, A. J. Thorvaldsen, J. Thyssen, J. van Stralen, M. L. Vidal, S. Villaume, O. Visser, T. Winther, and S. Yamamoto (available at <http://dx.doi.org/10.5281/zenodo.3572669>, see also <http://www.diracprogram.org>).
- ⁶⁷ D. L. Hildenbrand and K. H. Lau, *Pure Appl. Chem.* **64**, 87 (1992).
- ⁶⁸ R. J. M. Konings, O. Beneš, A. Kovacs, D. Manara, D. Sedmidubský, L. Gorokhov, V. S. Iorish, V. Yungman, E. Shenyavskaya, and E. Osina, *J. Phys. Chem. Ref. Data* **43**, 013101 (2014).

Table III.A.3.1 CCSD(T) equilibrium geometries (Å and deg.) and CCSD(T) harmonic frequencies (cm⁻¹) of the molecules of this work ^{a,b}

$C_{2v}/C_{\infty v}$	ThAu ₂ (¹ A ₁)	ThAu ₂ ⁻ (² Δ _g)
$r(\text{ThAu})$	2.7510	2.8845
θ	136.58	180.00
ω_i	166 (b ₂), 121 (a ₁), 21 (a ₁)	137 (b _{1u}), 89 (a _g), 8 (b _{2u}), 8 (b _{3u})
C_s	ThAu ₂ O (¹ A')	ThAu ₂ O ⁻ (² A')
$r(\text{ThO})$	1.8693	1.8959
$r(\text{ThAu})$	2.8065	2.9185
$\theta(\text{AuThO})$	113.41	109.88
$\phi(\text{AuOThAu})$	132.19	130.07
ω_i	824 (a'), 161 (a''), 127 (a'), 119 (a''), 55 (a'), 25 (a')	780 (a'), 138 (a''), 109 (a'), 90 (a''), 72 (a'), 22 (a')
C_1	ThAuOH (¹ A)	ThAuOH ⁻ (² A)
$r(\text{ThO})$	1.8729	1.9028
$r(\text{ThAu})$	2.8081	2.9443
$r(\text{ThH})$	2.1221	2.1841
$\theta(\text{AuThO})$	112.61	111.18
$\theta(\text{HThAu})$	106.96	112.68
$\phi(\text{OAuThH})$	117.21	118.76
ω_i	1454, 822, 472, 226, 142, 79	1281, 770, 374, 242, 119, 88
C_s	ThAuOH (¹ A')	ThAuOH ⁻ (² A')
$r(\text{ThO})$	2.0703	2.1216
$r(\text{ThAu})$	2.7808	2.9530
$r(\text{OH})$	0.9598	0.9564

$\theta(\text{AuThO})$	134.76	165.65
$\theta(\text{ThOH})$	162.59	169.18
ω_i	3880 (a'), 627 (a'), 383 (a'), 346 (a''), 137 (a'), 78 (a')	3922 (a'), 563 (a'), 326 (a'), 320 (a''), 102 (a'), 50 (a')

^a Structures calculated with aVTZ basis sets except for $\text{ThAu}_2/\text{ThAu}_2^-$ which used aVQZ. Harmonic frequencies were calculated with aVDZ basis sets except for $\text{ThAuOH}/\text{ThAuOH}^-$ which used aVTZ.

^b See also Figure III.A.3. 3

Table III.A.3.2 Contributions (in kcal/mol) to the FPD adiabatic electron affinity, EA_0 , and VDE of ThAu_2 . Values in parentheses are in eV.

	aVQZ	ΔCBS	ΔCV	ΔQED	ΔSO	$\Delta(\text{triplet})^a$	ΔZPE	FPD	Expt ^b
EA_0	27.37	+0.14	-0.81	+0.22	+3.91	-1.43	+0.10	29.49 (1.28)	(1.30)
VDE	31.46	+0.29	-0.60	+0.14	+4.15	-1.90	---	33.55 (1.45)	(1.53)

^a Singlet-triplet excitation energy using CCSD(T)/aVTZ and X2C-mmEOM-CCSD since the rest of the FPD calculations assumed a singlet ground state for ThAu_2 . See the text.

^b This work

Table III.A.3.3 Electronic excited states of ThAu₂ calculated at the X2C-mmf DCG-EOM-CCSD level of theory

using the linear ThAu₂⁻ CCSD(T)/aVQZ equilibrium geometry. Values are in eV.

Ω state	dE	dE (relative to VDE)	Ω state	dE	dE (relative to VDE)
(1) 1 _g	0.00	1.45	(1) 2 _u	1.768	3.223
(1) 2 _g	0.15	1.60	(1) 3 _u	1.853	3.308
(1) 0 _g	0.23	1.68	(1) 0 _u	1.904	3.359
(1) 3 _g	0.38	1.84	(1) 1 _u	1.949	3.404
(2) 0 _g	0.84	2.30	(2) 2 _u	1.969	3.424
(3) 0 _g	0.87	2.32	(2) 0 _u	2.023	3.478
(2) 1 _g	0.90	2.36	(2) 1 _u	2.099	3.554
(2) 2 _g	1.12	2.58	(3) 0 _u	2.336	3.790
(3) 1 _g	1.24	2.70	(3) 2 _u	2.380	3.835
(3) 2 _g	1.33	2.78	(3) 1 _u	2.401	3.856

Table III.A.3.4 Contributions (in kcal/mol) to the FPD adiabatic electron affinity, EA₀, and VDE of ThAu₂O. Values

in parentheses are in eV ^a This work.

	aVQZ	Δ CBS	Δ CV	Δ QED	Δ SO	Δ ZPE	FPD	Expt ^a
EA ₀	32.40	-0.02	-0.30	-0.06	-0.90	+0.14	31.26 (1.36)	(1.35)
VDE	35.37	+0.12	+0.38	-0.16	-0.59	---	35.12 (1.52)	(1.65)

Table III.A.3.5 Contributions (in kcal/mol) to the FPD adiabatic electron affinity, EA_0 , and VDE of $ThAuOH$, as well the 0K isomerization energy of $ThAuOH^-$ (ΔE_{isom}). Values in parentheses are in eV.

Isomer a		aVQZ	Δ CBS	Δ CV	Δ QED	Δ SO	Δ ZPE	FPD	Expt ^b
C_1	EA_0	29.58	-0.04	-0.18	-0.04	+0.42	+0.46	30.21 (1.31)	
	VDE	32.12	+0.09	+0.44	-0.11	+0.69	---	33.23 (1.44)	(1.43)
C_s	EA_0	17.96	+0.10	-1.16	+0.24	+3.04	+0.24	20.41 (0.89)	(0.80)
	VDE	21.64	+0.23	-0.90	+0.20	+3.37	---	24.55 (1.06)	(1.03)
	ΔE_{isom}	39.07	+0.41	+0.44	+0.30	-2.24	+3.44	41.43 (1.80)	

^a See Figure III.A.3. 3.

^b This work.

Table III.A.3.6 EOM-CCSD (X2C-mm) excited electronic states (in eV) for the C_s isomer of ThAuOH at the anion geometry.

without SO			with SO		
State	dE (relative to		State	dE (relative to	
	dE	VDE)		dE	VDE)
¹ A'	0.00	1.06	1	0.00	1.06
³ A''	0.16	1.22	2 ^a	0.00	1.07
³ A'	0.16	1.22	3	0.14	1.20
¹ A''	1.16	2.22	4	0.35	1.41
¹ A'	1.16	2.23	5	1.20	2.27
³ A''	1.42	2.48	6	1.33	2.39
³ A'	1.45	2.52	7	1.37	2.43
¹ A''	1.58	2.64	8	1.59	2.65
¹ A'	1.61	2.68	9	1.69	2.75
³ A''	2.16	3.22			
³ A'	2.16	3.22			
³ A''	2.22	3.28			
³ A'	2.24	3.30			

^a This state corresponds to the closed-shell reference state.

Table III.A.3.7 Calculated contributions to the FPD 0K atomization energies (AE_0) and resulting heats of formation (all in kcal/mol).

Species	aVQZ	Δ CBS	Δ CV	Δ QED	Δ SO	Δ ZPE	AE_0	$H_f(298-0)^a$	$\Delta H_f(298K)$
ThAu ₂	153.82	+0.83	+5.64	-1.38	-5.83	-0.44	154.1 ^b	+0.67	165.3
ThAu ₂ O	358.55	+2.95	+6.31	-0.71	-7.12	-1.87	358.1	+1.30	20.2
ThAuOH (C ₁)	347.78	+2.87	+4.17	-0.12	-6.68	-4.57	343.5	+2.25	-2.1

^a Thermal correction to the atomization energy.

^b This also includes a +1.43 kcal/mol contribution from the singlet-triplet splitting. See the text.

Table III.A.3.8 Natural charges of ThAu₂, ThAu₂O, and ThAuOH and their anions.

Species	Th	Au	O	H
ThAu ₂ ^a	0.953	-0.477		
ThAu ₂ ⁻	0.129	-0.565		
ThAu ₂ O	2.289	-0.517	-1.255	
ThAu ₂ O ⁻	1.668	-0.661	-1.347	
(C _i) ThAuOH	2.391	-0.520	-1.247	-0.624
(C _i) ThAuOH ⁻	1.729	-0.695	-1.348	-0.686
(C _s) ThAuOH	1.340	-0.564	-1.296	0.520
(C _s) ThAuOH ⁻	0.561	-0.760	-1.293	0.492

^a These results are for the singlet state of ThAu₂.

Table III.A.3.9 NBOs of the Lewis structure for ¹A₁ ThAu₂.^a

NBO	occ	energy	% ion	c _A	Th hybrid (A)				c _B	Au/O hybrid (B)		
					% s	% p	% d	% f		% s	% p	% d
<i>n</i> _{Th}	1.994	-0.215		1.000	68	2	30	0				
σ _{ThAu}	1.963	-0.349	58.1	0.458	15	9	71	4	0.889	91	0	9

^a There are also ten lone pairs corresponding to the Au 5d orbitals at energies around -0.46 a.u. Columns include orbital type, occupancy, and energy (in au), percent ionicity ($=c_B^2 - c_A^2$), polarization coefficients (c_A and c_B), and percent hybrid character. Bonding NBOs are superpositions of hybrid pairs, $\Omega_{AB} = c_A h_A + c_B h_B$.

Table III.A.3.10 NBOs of the Lewis structure for ¹A' ThAu₂O.^a

NBO	occ	energy	% ion	c_A	Th hybrid (A)				c_B	Au/O hybrid (B)		
					% s	% p	% d	% f		% s	% p	% d
σ_{ThAu}	1.969	-0.332	62.6	0.4323	38	7	49	6	0.9017	93	1	6
π_{ThO}	1.983	-0.468	81.6	0.3033	0	1	61	37	0.9529	0	99	1
π_{ThO}	1.999	-0.485	77.6	0.3344	0	0	73	26	0.9424	1	99	1
σ_{ThO}	1.995	-0.816	69.9	0.3877	2	6	63	29	0.9218	23	76	1

^a There are also ten lone pairs corresponding to the Au 5d orbitals at energies around -0.46 a.u. The 2s lone pair on O is at -0.92 a.u. Columns include orbital type, occupancy, and energy (in au), percent ionicity ($=c_B^2 - c_A^2$), polarization coefficients (c_A and c_B), and percent hybrid character. Bonding NBOs are superpositions of hybrid pairs, $\Omega_{AB} = c_A h_A + c_B h_B$.

Table III.A.3.11 NBOs of the Lewis structure for ¹A ThAuOH (C_i).^a

NBO	occ	energy	% ion	c _A	Th hybrid (A)				c _B	Au/O hybrid (B)		
					% s	% p	% d	% f		% s	% p	% d
σ _{ThAu}	1.987	-0.334	61.3	0.4398	47	5	44	4	0.8981	92	1	7
σ _{ThH}	1.990	-0.409	62.6	0.4323	25	2	63	10	0.9017	100	0	0
π _{ThO}	1.998	-0.476	78.0	0.3314	1	0	73	26	0.9435	1	99	1
σ _{ThO}	1.990	-0.589	73.6	0.3635	2	4	65	29	0.9316	15	84	1
π _{ThO} ^b	1.990	-0.688	76.6	0.3418	1	2	68	28	0.9398	8	91	1

^a There are also five lone pairs corresponding to the Au 5d orbitals at energies around -0.46 a.u. Columns include orbital type, occupancy, and energy (in au), percent ionicity ($=c_B^2 - c_A^2$), polarization coefficients (c_A and c_B), and percent hybrid character. Bonding NBOs are superpositions of hybrid pairs, $\Omega_{AB} = c_A h_A + c_B h_B$.

^b This hybrid has a mixture of both σ and π character.

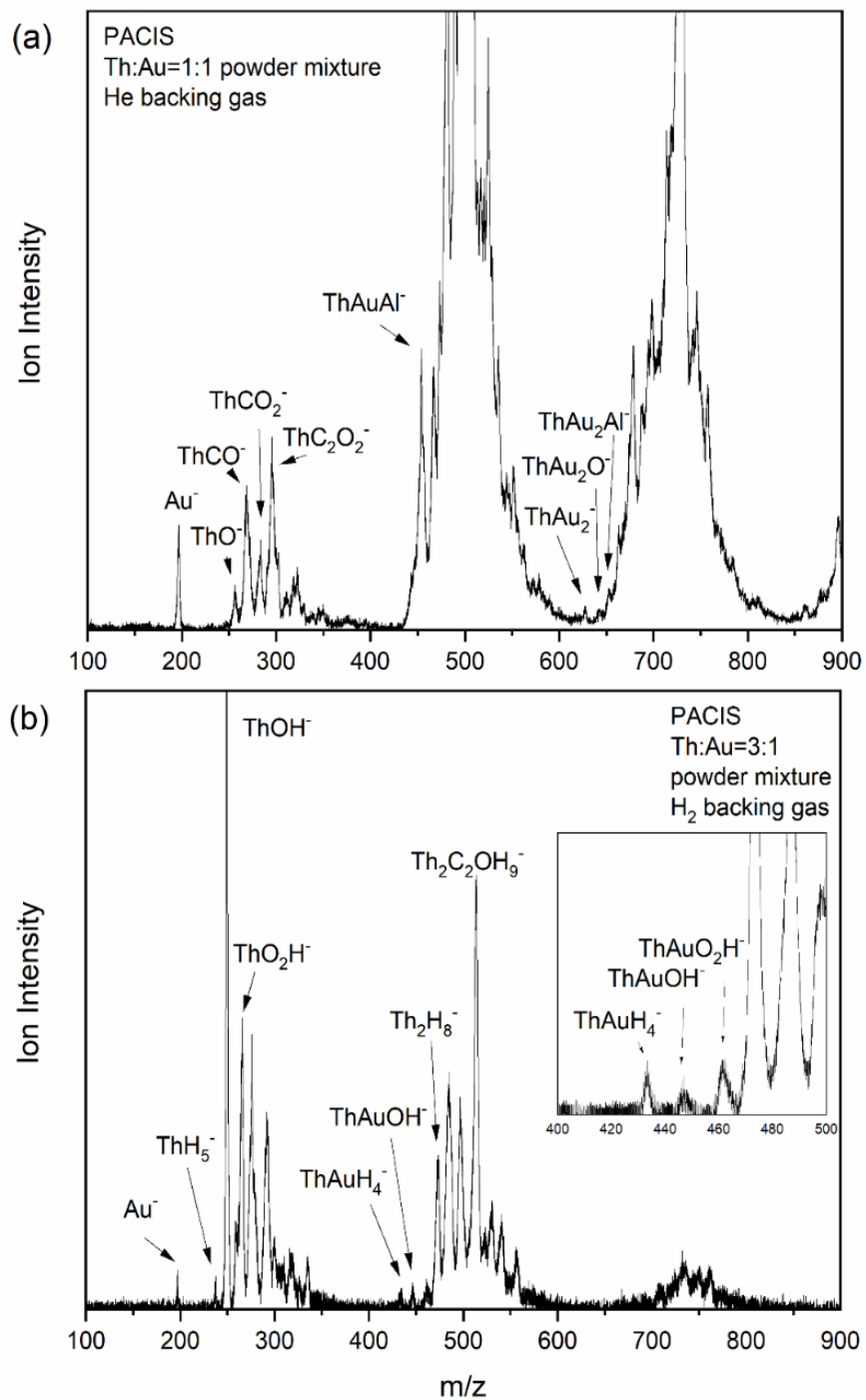


Figure III.A.3.1 The mass spectrum of anions generated by PACIS when using (a) 1:1 Thorium-gold mixture and helium gas and (b) 3:1 Thorium-gold mixture and hydrogen gas.

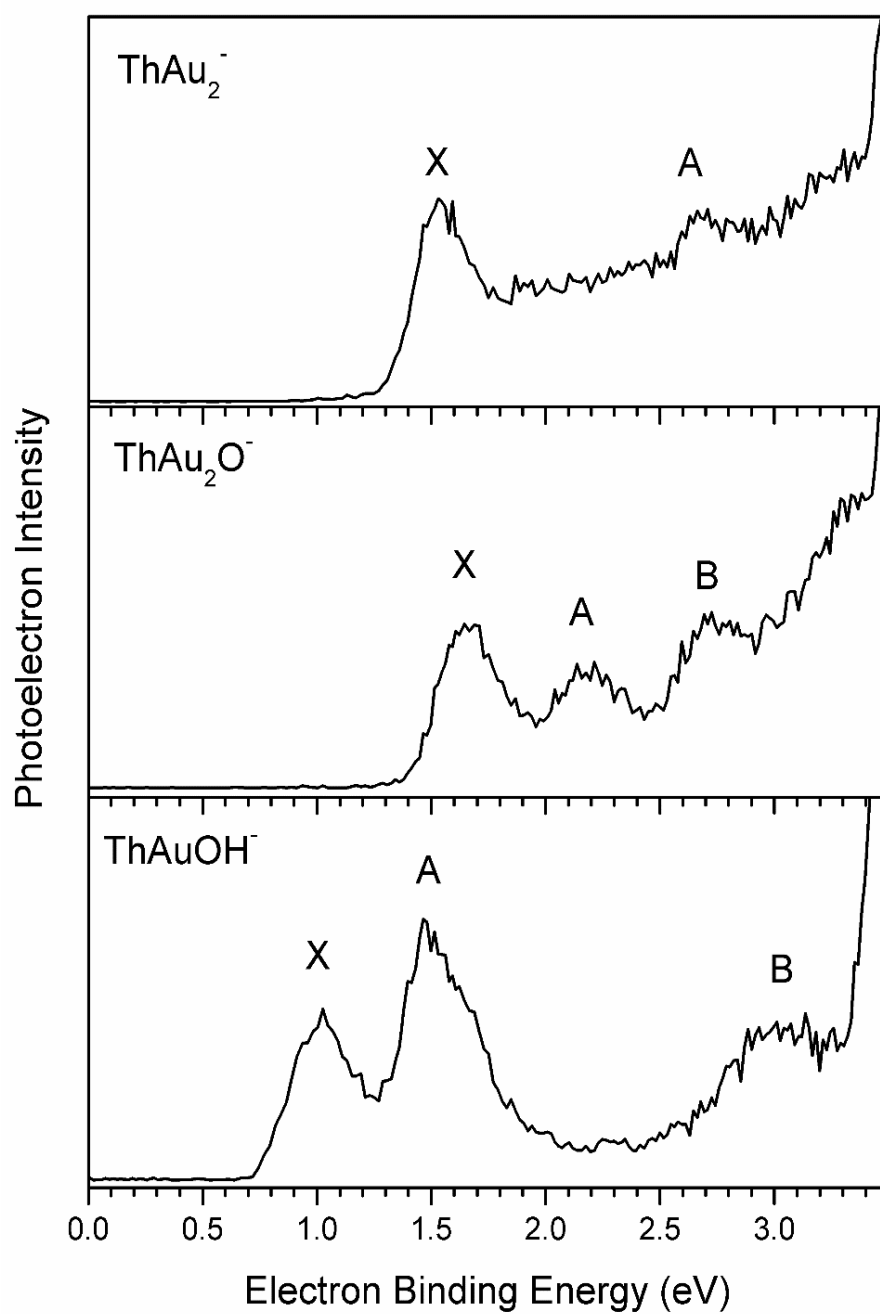


Figure III.A.3.2 Photoelectron spectra of ThAu_2^- , ThAu_2O^- and ThAuOH^- measured with 355nm (3.49 eV) photons.

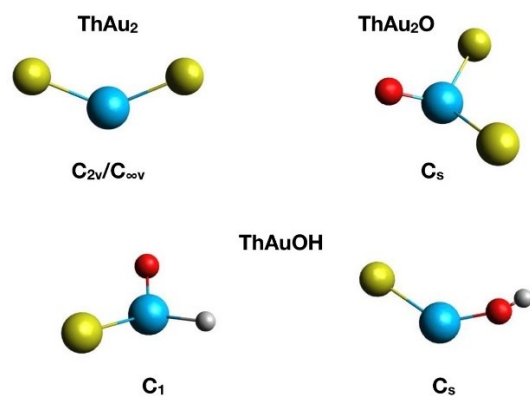


Figure III.A.3.3 Lowest energy isomeric structures. Thorium in blue, Gold in yellow, Oxygen in red, and Hydrogen in gray.

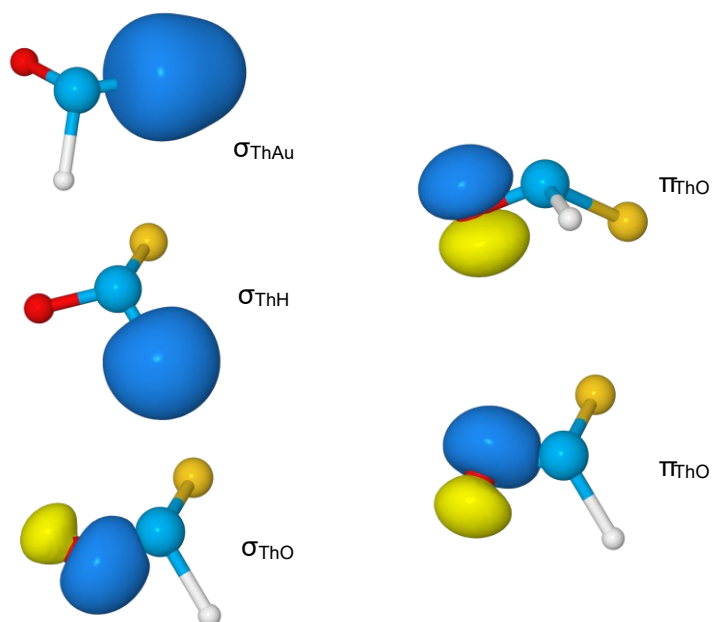


Figure III.A.3.4 Bonding NBOs of the ground state of ThAuOH (C_1).

III.A.4. The Th_2O^- , Th_2Au^- and $\text{Th}_2\text{AuO}_{1,2}^-$ Anions: Photoelectron Spectroscopic and Computational Characterization of Energetics and Bonding

Reprinted (adapted) with permission from *J. Phys. Chem. A* 2021, 125, 1, 258-271.

Copyright 2021 American Chemical Society. <https://doi.org/10.1021/acs.jpca.0c09766>

Zhaoguo Zhu,¹ Mary Marshall,¹ Rachel M. Harris,¹ Kit H. Bowen^{1,*} Monica Vasiliu² and David A. Dixon^{2,*}

¹Department of Chemistry, Johns Hopkins University, Baltimore, MD 21218, USA

²Department of Chemistry and Biochemistry, University of Alabama, Tuscaloosa, Alabama 35401, USA

ABSTRACT:

The observation and characterization of the anions: Th_2O^- , Th_2Au^- and $\text{Th}_2\text{AuO}_{1,2}^-$ is reported. These species were studied through a synergetic combination of anion photoelectron spectroscopy and *ab initio* correlated molecular orbital theory calculations at the CCSD(T) level with large correlation-consistent basis sets. To better understand the energetics and bonding in these anions and their corresponding neutrals, a range of smaller diatomic to tetratomic species were studied computationally. Correlated molecular orbital theory calculations at the CCSD(T) level showed that in most of these cases there are close lying anion and neutral clusters with different geometries and spin states that can explain and are consistent with the experimental observed spectra. Thus, comparison of experimentally determined and computationally predicted vertical detachment energies and electron affinities for different optimized geometries and spin states shows excellent agreement to within 0.1 eV. The structures for both the neutrals and anions have a significant ionic component to the bonding due to the large electron affinity of the Au atom and modest ionization potentials for Th_2 , Th_2O , and Th_2O_2 . The analysis of the bonding for the Th-Th bonds from the molecular orbitals is consistent with this ionic model. The results show that there is a wide variation in bond distance from 2.7 to 3.5 Å for the Th-Th bonds all of which are less than twice the atomic radius of Th of 3.6 Å. The bond distances encompass bond orders from 4 to 0. There can be different bond orders for the same bond distance depending on the nature of the ionic bonding suggesting that one may not be able to correlate bond order with bond distance in these types of clusters. In addition, the presence of an Au atom may provide a unique probe of the bonding in such clusters due to its ability to accept an electron from clusters with modest ionization potentials.

INTRODUCTION

Most of the actinides have valence electrons residing in 5f-orbitals, giving them chemical properties that are unlike those of other families in the periodic table. The actinides can also have multiple oxidation states, ranging from +2 to

+7, leading to diverse molecular geometries. Due to their electronic configurations, the actinides are capable of bonding that is not typically observed in transition metal chemistry. Bonding in the actinides can often follow different trends, for example, bond lengths decreasing with increasing atomic number.¹ This is the result of the well-known actinide contraction, by which their 5f orbitals become more stable (and more contracted) with increasing atomic number.² Also, whereas metal-metal bonds are common among the d-block metals, very few such bonds have been observed in the actinide series.³ Even so, actinides can form multiple covalent molecular bonds.⁴⁻⁶ A better understanding of the electronic structure and bonding behavior of the actinides is necessary in order to advance the development of nuclear energy-related applications, generally and the management of its resulting waste products, in particular.

Thorium is the second element in the actinide series with the electronic configuration, $[\text{Rn}]6d^27s^2$, with four valence electrons. Due to the fact that it uses its 7s and 6d orbitals for bonding, thorium's chemistry often resembles that of the transition metals. Metal-metal bonds between thorium atoms have been investigated extensively through quantum chemistry. Straka et al. performed a quasi-relativistic density functional (B3LYP) calculation on the HThThH molecule, predicting that the $^1\Sigma_g$ ground state has a triple Th-Th bond with a bond length of 2.71 Å.⁷ In 2006, Th₂ was predicted to have quadruple bond character with a $^3\Delta_g$ ground state. Twelve low-lying excited states within an energy range of less than 1 eV were predicted with the first excited $^1\Sigma_g^+$ state only 400 cm⁻¹ above the ground state. It was predicted that a quadruple bond is present in both its ground and first excited states.⁵ Also through computations, a variety of ligands have been used to probe the Th-Th bond length in LThThL molecules (L = C₈H₈,⁸ C₅(CH₃)₅,⁹ and NH₃, PH₃, PMe₃, PCy₃, PPh₃, AsH₃, NHC, CO, and NO).³ To date, the H₃AsThThAsH₃ molecule has been predicted to have the shortest Th-Th quadruple bond length (2.590 Å).³ Ligand substitutions can tune the Th-Th bond order from quadruple (H₃AsThThAsH₃), to triple (H₃NThThNH₃), to double (OCThThCO), to single (ONThThNO). Th-Th bonds confined in carbon cages have also been modeled. Ge et al. predicted a stable Th(III)-based dimetallofullerene, Th₂@I_h-C₈₀, which consists of a Th₂⁶⁺ core and an I_h-C₈₀⁶⁻ cage.¹⁰ The two remaining valence electrons in the Th₂⁶⁺ core form open-shell, 2-fold, one-electron-two-center bonds with the electronic configuration of (6d7s7p)σ¹(5f6d)π¹. These authors further predicted that the Th-Th distance can be changed from 3.803 Å to 2.843 Å by replacing the I_h-C₈₀ cage with the I_h-C₆₀ cage. Correlated molecular orbital theory calculations have been reported for ThO₂, ThO₂⁻, Th₂O₂, and Th₂O₄.¹¹

In sharp contrast to the relatively extensive computational work on Th-Th bonding, experimental studies have been scarce. The only molecule to have been synthesized with a direct Th-Th bond appears to be the Th₂ molecule. This gas-phase Th₂ dimer was produced by laser ablation and detected by mass spectrometry.¹² In 2015, it was studied in the gas phase via 2-D fluorescence spectroscopy; there, the vibrational frequencies for two of its electronically excited states (169 and 212 cm⁻¹) were compared to that of the ground state (135 cm⁻¹).¹³ These results suggest that Th₂ excited states have stronger Th–Th bonds than its ground state.

In addition to metal dimer and ligand-supported molecules, such as LMML (M = metal, L = ligand), heterometallic clusters with three or more metals in close proximity also contain metal-metal bonds.¹⁴ Several examples of M_nAu (M = metal, n ≥ 2) clusters with short metal-metal bonds have been reported, these including those with M = Na,¹⁵ Ti,¹⁶ Cr,¹⁷ Cu,¹⁸ Ag,¹⁹ Pt,²⁰ and La, T, and Sc.²¹ Nevertheless, despite the abundance of data on these heterometallic clusters, the literature is moot on M_nAu species in which M = Th. In the present study, however, we report the observation of the anions, Th₂O⁻, Th₂Au⁻, Th₂AuO₁⁻, and Th₂AuO₂⁻, in the gas phase. These anions were characterized by time-of-flight mass spectrometry, anion photoelectron spectroscopy, and *ab initio* electronic structure calculations. The synergetic combination of anion photoelectron spectroscopy and computations showed that Th-Th metal-metal bonds are formed in all four of these species. Additionally, this work revealed that the bonding character between thorium and gold is significantly influenced by oxygen, evolving from metallic toward ionic bonding when oxygen is present.

METHODS

Experimental

This work utilized anion photoelectron spectroscopy (aPES) as its primary experimental tool. The aPES technique is conducted by crossing a mass-selected beam of negative ions with a fixed-energy photon beam and energy analyzing the resulting photodetached electrons. This technique is governed by the energy-conservation relationship, $h\nu = \text{EBE} + \text{EKE}$, where $h\nu$, EBE, and EKE are the photon energy, electron binding (photodetachment transition) energy, and the electron kinetic energy, respectively. Our photoelectron spectrometer, which has been described previously,²² consists of an ion source, a linear time-of-flight (TOF) mass spectrometer, a mass gate, a momentum decelerator, a neodymium-doped yttrium aluminum garnet (Nd:YAG) laser for photodetachment, and a magnetic bottle electron energy analyzer. Photoelectron spectra were calibrated against the well-known photoelectron spectrum of Cu.²³

The anions of interest were generated using a pulsed-arc (electric discharge) cluster ionization source (PACIS), which has been described in detail elsewhere.^{24,25} This cluster anion source has been used to generate a variety of bimetal cluster anions.^{26–30} During PACIS operation, a 30 μ s long, 150-volt electrical pulse applied between a copper anode and the sample cathode vaporizes the sample atoms. The sample cathode was prepared in a nitrogen glove box, where the sample powder was firmly pressed onto an aluminum rod. Both pure thorium powder and a 3:1 Th:Au powder mixture were used in the experiment. To prevent contact between the thorium powder and air, a thin sacrificial layer of aluminum powder was pressed onto the top of the sample layer. During operation of the PACIS source and almost simultaneously with the firing of its electric discharge pulses, \sim 150 psi of ultrahigh purity helium gas was injected into the source's discharge region through a pulsed valve, these actions together resulting in the generation of a variety of cluster sizes and compositions. The Th_2O^- anions were generated using pure thorium powder sample, while the thorium-gold-containing clusters anions were formed using a thorium-gold mixed powder sample. The resulting plasma, containing ions, neutrals, and electrons was cooled as it expanded through the PACIS source's housing and nozzle. The resultant anion mixture was mass-analyzed by TOF mass spectroscopy, after which the chosen mass-selected anion compositions were photodetached and their resultant electrons energy analyzed.

Computational Methods

All cluster geometries were initially optimized at the DFT level³¹ with the hybrid B3LYP exchange correlation functional.^{32,33} The aug-cc-pVDZ basis sets^{34,35} were used for O, the cc-pVDZ-PP basis sets with effective core potentials were used for Th,^{36,37} and the aug-cc-pVDZ-PP basis sets with effective core potentials were used for Au.³⁸ Vibrational frequencies were calculated to confirm that the structures were minima. These calculations were performed using the Gaussian16 program system.³⁹

The DFT geometries were then used as starting points for high accuracy CCSD(T)^{40–43} (coupled cluster theory with single and double excitations with perturbative triples correction) calculations to predict the structural characteristics for the lower energy isomers and the energetics. The aug-cc-pVnZ basis sets were used for O; the cc-pVnZ-PP basis sets were used for Th, and aug-cc-pVnZ-PP were used for Au for $n = \text{D, T and Q}$. These basis sets are abbreviated as an for $n = \text{D, T and Q}$. The CCSD(T) energies were extrapolated to the CBS limit by fitting to a mixed Gaussian/exponential (Eq. 1):^{44,45}

$$E(n) = E_{\text{CBS}} + A \exp[-(n - 1)] + B \exp[-(n - 1)^2] \quad (1)$$

where $n = 2, 3$, and 4 (DZ through QZ). Values obtained from this procedure are denoted as CBS.

The lower energy isomers were optimized at the CCSD(T) at up to $n = T$, except for $\text{Th}_2\text{AuO}_2^{0/+}$ clusters which were optimized at $n = D$ level. For the diatomics, a 7-point Dunham expansion was used.^{46,47} Their harmonic frequencies (ω_e) and anharmonic constants ($\omega_e x_e$) were also calculated. The thermodynamic properties were predicted using the CCSD(T)/aT (or aD for the largest ones) optimized geometries at the CCSD(T) level of theory including core-valence (CV) correlation corrections with the aug-cc-pwCVnZ(O)/cc-pwCVnZ-PP(Th)/aug-cc-pwCVnZ-PP(Au) basis sets for $n = D, T$, and Q (abbreviated as awn for $n = D, T$ and Q). The calculations included the correlation of the valence electrons (5s, 5p, 5d, 6s and 6p core-shell electrons for Th, 5s, and 5p core-shell electrons for Au and the 1s core-shell electrons of O).

Total atomization energies (TAEs or ΣD_0) at 0 K were calculated from the following expression (Eq. 2) with Δ referring to the difference between the molecule (reactant) and the atomic products for each energy component using aug-cc-pwCVnZ(O)/cc-pwCVnZ-PP(Th)/ aug-cc-pwCVnZ-PP(Au) basis sets for $n = D, T$, and Q and the CBS extrapolation:

$$\Sigma D_0 = \Delta E_{\text{CBS}} + \Delta E_{\text{ZPE}} + \Delta E_{\text{SO}} \quad (2)$$

Additional corrections to the CCSD(T)/CBS energy (ΔE_{CBS}) are necessary to reach chemical accuracy (± 1 kcal/mol). The unscaled vibrational frequencies from the B3LYP/aD calculations were used to calculate the vibrational zero point energies (ZPEs) for all the molecules except the diatomic where the harmonic frequencies (ω_e) and anharmonic constants ($\omega_e x_e$) at CCSD(T)/awQ level were used to calculate the ZPEs. The atomic spin-orbit corrections were used to calculate the spin orbit corrections of the molecules (ΔE_{SO}) with the O atom from Moore's tables⁴⁸ ($\Delta E_{\text{SO}}(\text{O}) = 0.22$ kcal/mol), and the Th atom from Sansonetti and Martin⁴⁹ ($\Delta E_{\text{SO}}(\text{Th}) = 8.81$ kcal/mol).

Heats of formation at 0 K were calculated by combining our computed ΣD_0 values with the known enthalpies of formation at 0 K for the elements with $\Delta H_{f,0\text{K}}(\text{O}) = 59.00 \pm 0.00$ kcal/mol, from the Active Thermochemical Tables (ATcT),⁵⁰⁻⁵² $\Delta H_{f,0\text{K}}(\text{Au}) = 88.0 \pm 0.5$ kcal/mol⁵³ and $\Delta H_{f,0\text{K}}(\text{Th}) = 143.9 \pm 1.4$ kcal/mol.⁵⁴ Note that there is another value reported for $\Delta H_{f,0\text{K}}(\text{Th})$ 142.1 ± 1.5 kcal/mol.⁵⁵ Heats of formation at 298 K were calculated by following the procedures outlined by Curtiss et al.⁵⁶ using 1.3 kcal/mol thermal corrections for Au and Th, respectively, and 1.04 kcal/mol thermal corrections for O.

The open-shell calculations were done with the R/UCCSD(T) approach where a restricted open shell Hartree-Fock (ROHF) calculation was initially performed and the spin constraint was then relaxed in the coupled cluster calculation.^{42,57–59} The CCSD(T) calculations were performed with the MOLPRO 2018 program package.^{60,61} The Natural Population Analysis (NPA) results based on the Natural Bond Orbitals (NBOs)^{62,63} using NBO7^{64,65} are calculated using MOLPRO 2018.

The calculations were done on our local UA Opteron- and Xeon-based Linux computation clusters as well as on using resources in the Molecular Sciences Computing Facility (MSCF) in the Environmental Molecular Science Laboratory (EMSL) at Pacific Northwest National Laboratory (PNNL) and the DMC computer at the Alabama Supercomputer Center.

RESULTS AND DISCUSSION

Experimental Results

Figure III.A.4.1(a) presents the mass spectrum of cluster anions generated using thorium metal powder and helium expansion gas in a PACIS source. There, we observe the anionic clusters: $\text{Th}_2\text{O}_{1-3}^-$, $\text{Th}_2\text{AlO}_{0-3}^-$, $\text{Th}_2\text{Al}_2\text{O}_{0-2}^-$ and $\text{Th}_2\text{Al}_3\text{O}^-$. Figure III.A.4.1(b) shows the mass spectrum of Th_2Au -containing cluster anions made from a thorium-gold powder mixture and helium expansion gas in a PACIS source. There, one observes the $\text{Th}_2\text{AuO}_{0-2}^-$ series, the $\text{Th}_2\text{AuCO}_2^-$ anion, and the $\text{Th}_2\text{AuAlC}_{2,3}\text{O}_{0-3}^-$ cluster anion series. This mass spectrum is simplified by the fact that thorium and gold each have only one naturally-occurring isotope. The contaminant elements: aluminum, carbon and oxygen, seen in these spectra originated from the surface of the cathode and the surroundings in the PACIS source housing. Since there were no mass-coincident species present at masses: 480 amu, 661 amu, 677 amu, and 693 amu, these anions were identified as: Th_2O^- , Th_2Au^- , Th_2AuO^- , and $\text{Th}_2\text{AuO}_2^-$. Each of these were mass-selected and their photoelectron spectra measured using third harmonic photons (355 nm, 3.49 eV/photon) from a Nd:YAG laser.

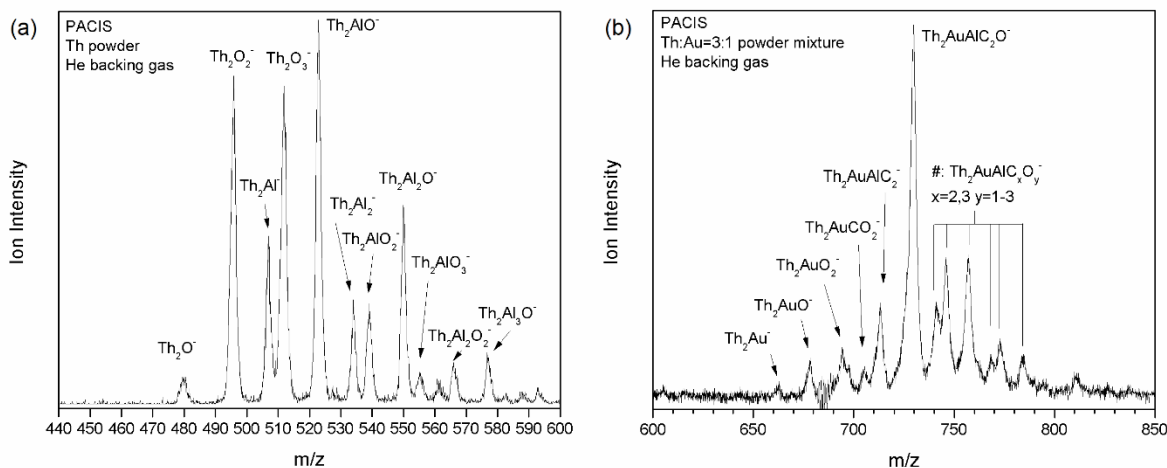


Figure III.A.4.1 The mass spectra of anions generated by PACIS when using (a) thorium powder and helium gas and (b) a 3:1 thorium-gold powder mixture and helium gas.

The photoelectron spectra of Th_2O^- , Th_2Au^- , Th_2AuO^- and $\text{Th}_2\text{AuO}_2^-$ are presented in Figure III.A.4.2. The photoelectron spectrum of Th_2O^- [see Figure III.A.4.2(a)] exhibits a peak with an onset at EBE = 1.30 eV and an intensity maximum at EBE = 1.49 eV. An unresolved band has a shoulder ranging from EBE = 2.0 eV to 2.7 eV and a peak centered at EBE = 3.30 eV. The photoelectron spectrum of Th_2Au^- , [see Figure III.A.4.2(b)] exhibits a peak with an onset at EBE = 1.34 eV and an intensity maximum at EBE = 1.60 eV. The series of poorly resolved peaks beyond EBE = 1.7 eV correspond to transitions from the ground state of the anion to the various electronically-excited states of the Th_2Au^- anion's neutral counterpart. The photoelectron spectrum of Th_2AuO^- , [see Figure III.A.4.2(c)] displays a peak which is centered at EBE = 1.59 eV. The fact that this peak is narrower than the lowest EBE peak in the photoelectron spectrum of Th_2Au^- suggests that the geometric structures of Th_2AuO^- and Th_2AuO are more similar to each other than are the geometric structures of Th_2Au^- and Th_2Au . The second band in the Th_2AuO^- spectrum ranges from EBE = 1.85 eV to EBE = 2.05 eV and reaches its maximum intensity at EBE ~ 2.0 eV. Beyond EBE = 2.3 eV, a broad band appears that rises steadily attaining its maximum intensity at EBE ~ 3.3 eV. The photoelectron spectrum of $\text{Th}_2\text{AuO}_2^-$ [see Figure III.A.4.2(d)] exhibits two broad peaks with intensity maxima at EBE = 1.56 eV and EBE = 2.50 eV.

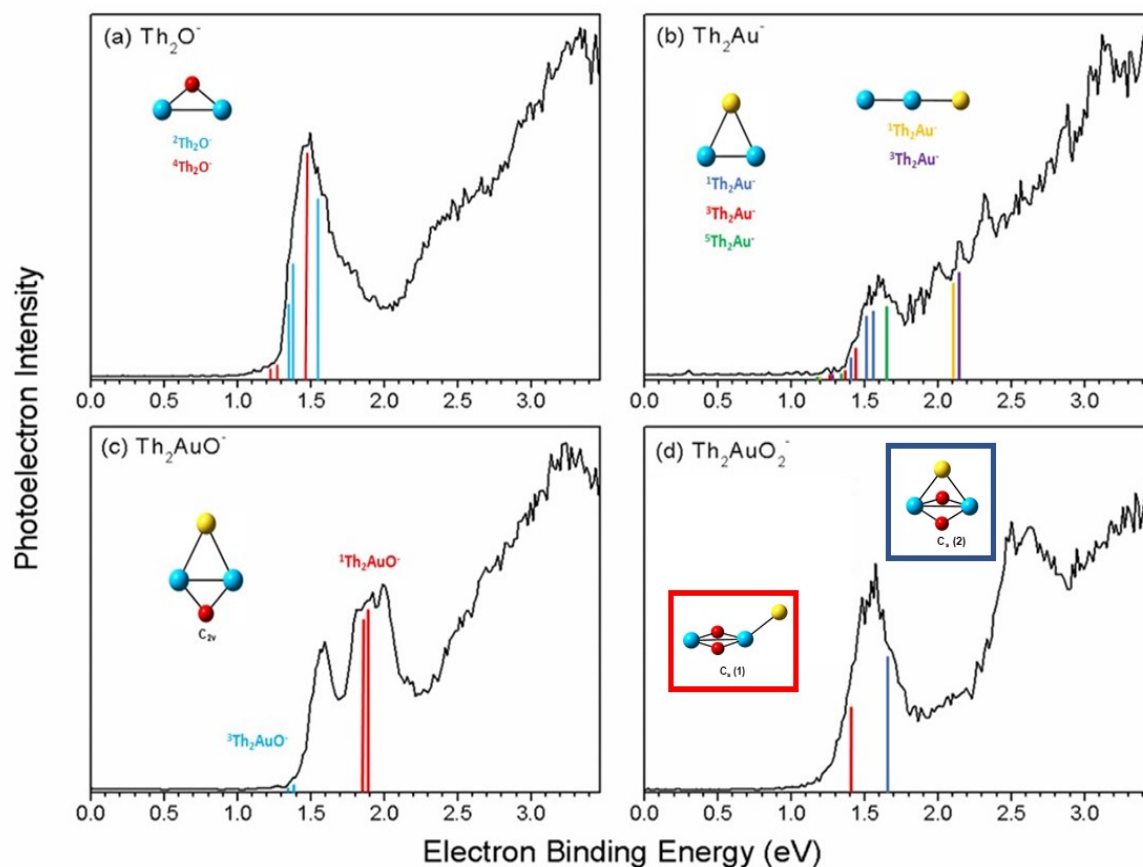


Figure III.A.4.2 Photoelectron spectra of (a) Th_2O^- , (b) Th_2Au^- , (c) Th_2AuO^- and (d) $\text{Th}_2\text{AuO}_2^-$ measured with 3.49 eV photons. Lowest energy isomeric structures are displayed for each species, with thorium in blue, gold in yellow and oxygen in red. Calculated vertical detachment energies (VDE) (eV) at CCSD(T)/aT level for each structure are indicated by colored bars.

The vertical detachment energy (VDE) is the photodetachment transition at which the Franck-Condon overlap between the wave function of the ground state of the anion and that of the ground state of its neutral counterpart is maximal. Thus, the VDE value corresponds to the EBE value of the intensity maximum of the lowest EBE peak. The VDE values of Th_2O^- , Th_2Au^- , Th_2AuO^- , $\text{Th}_2\text{AuO}_2^-$ are therefore 1.49 eV, 1.60 eV, 1.59 eV and 1.56 eV, respectively. The adiabatic (thermodynamic) electron affinity (EA) is the energy difference between the lowest energy state of the anion and the lowest energy state of its neutral counterpart. When sufficient Franck-Condon overlap exists between $v = 0$ of the anion and $v' = 0$ of its neutral counterpart (the origin transition) and there are no vibrational hot bands (photoelectrons from vibrationally excited anions) present, the EA value corresponds to the EBE value at the intensity

threshold of the lowest EBE peak or band. We have assigned EA values by extrapolating the low EBE side of the lowest EBE bands to zero. The EA values for Th_2O , Th_2Au , Th_2AuO , Th_2AuO_2 are therefore 1.30 eV, 1.34 eV, 1.38 eV and 1.25 eV, respectively. The EA values of these four species, as well as their VDE values, are relatively similar to one another.

Computational Results

A variety of structures and spin states were examined for the anions: Th_2Au^- , Th_2AuO^- and $\text{Th}_2\text{AuO}_2^-$ and their corresponding neutrals. In addition, we also predicted the properties of Th_2 , ThAu , ThAuO , ThAuO_2 , AuO , AuO_2 , Th_2O , Th_2O_2 and ThO_2 and their anions for comparison as well as the electron affinities of atomic Th and Au. Selected low energy structures are shown in Figure III.A.4.3.

Geometries and isomer energies

Relative energies of various isomers and in different spin states are given in Tables III.A.4.1 - 4. The optimized geometric parameters for the Th-Th bonds are given in Table III.A.4.5 with the remaining data in the Supporting Information.

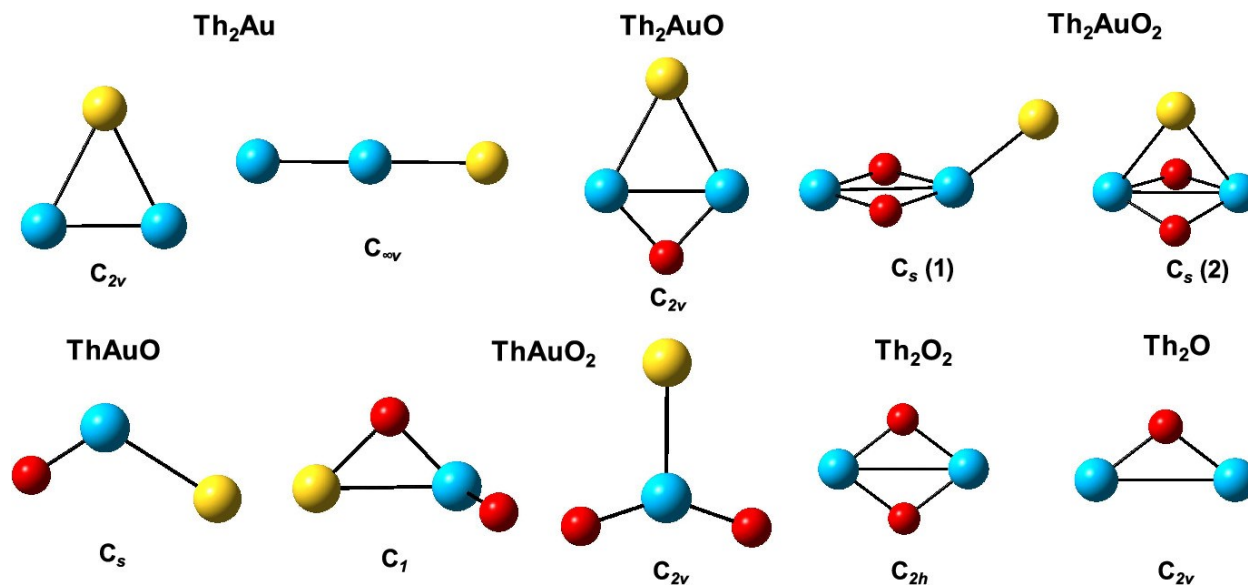


Figure III.A.4.3 Lowest energy isomeric structures. Thorium in blue, Gold in yellow, and Oxygen in red.

Table III.A.4.1 Relative Energies of Th_2Au and Th_2Au^- in kcal/mol at different level of theory.^a

Isomer	B3LYP/ aD	CCSD(T)/ aD (sp)	CCSD(T)/ aD (opt)	CCSD(T)/ aT (sp)	CCSD(T)/ aT(opt)	CCSD(T)/ aQ (sp)	CCSD(T)/ CBS	CCSD(T)/ aW/T/Q/CBS ^b
² Th ₂ Au (C _{2v})	13.4	0.2	0.0	0.0	0.0	0.0	0.0	0.0/0.3/0.6/0. 7
⁴ Th ₂ Au (C _{2v})	11.2	1.1	1.3	2.9				
⁶ Th ₂ Au (C _{2v})	10.4	3.6		6.1				
² Th ₂ Au (C _{∞v})	0.0	0.0	0.1	0.2	0.4	0.7	0.8	0.0
⁴ Th ₂ Au (C _{∞v})	11.8	20.8						
² Th ₂ Au (D _{∞h})	67.2							
¹ Th ₂ Au -(C _{2v})	1.6	0.0	0.0	0.0	0.0	0.0	0.0	0.0
³ Th ₂ Au -(C _{2v})	5.8	2.9		3.5				
⁵ Th ₂ Au -(C _{2v})	4.7	3.0		2.1				

¹ Th ₂ Au - (C _{∞v})	0.0	1.7	2.6	1.1	1.1	0.4	0.0	3.1/2/1/1.2/0. 6
³ Th ₂ Au - (C _{∞v})	0.3	3.7		2.3				
¹ Th ₂ Au - (D _{∞h})	52.9							

^a sp = single point calculations (no geometry optimization); opt = geometry optimization. ^b CCSD(T)/aT optimized geometries were used.

Table III.A.4.2. Relative Energies of Th_2AuO , Th_2AuO^- , Th_2AuO_2 and $\text{Th}_2\text{AuO}_2^-$ in kcal/mol at different level of theory.^a

Isomer	B3LYP/ aD	CCSD(T)/ aD (sp)	CCSD(T)/ aD (opt)	CCSD(T)/ aT ^b	CCSD(T)/ aQ	CCSD(T)/ CBS	CCSD(T) awD/T/Q/CBS ^c
$\text{Th}_2\text{AuO}/\text{Th}_2\text{AuO}^-$							
$^2\text{Th}_2\text{AuO}$ (C_{2v})	4.1	0.7	0.3	0.0	0.0	0.0	0.5/0.0/0.0/0.0
$^4\text{Th}_2\text{AuO}$ (C_{2v})	0.0	0.0	0.0	1.7	3.0	3.8	0.0/0.6/1.7/2.3
$^1\text{Th}_2\text{AuO}^-$ (C_{2v})	0.0	0.0	0.0	0.0	0.0	0.0	0.0
$^3\text{Th}_2\text{AuO}^-$ (C_{2v})	3.1	3.8	4.8	3.6	2.4	1.7	5.6/5.6/4.3/3.4
$\text{Th}_2\text{AuO}_2/\text{Th}_2\text{AuO}_2^-$							
$^2\text{Th}_2\text{AuO}_2$ (C_s) (1)	0.0	0.0		0.0			
$^4\text{Th}_2\text{AuO}_2$ (C_s) (1)	18.1	22.1		22.4			
$^2\text{Th}_2\text{AuO}_2$ (C_s) (2)	21.0	21.0		21.0			
$^4\text{Th}_2\text{AuO}_2$ (C_s) (2)	23.1	28.6		27.6			
$^1\text{Th}_2\text{AuO}_2^-$ (C_s) (1)	0.0	0.0	0.0	0.0	0.0	0.0	0.0
$^1\text{Th}_2\text{AuO}_2^-$ (C_s) (2)	6.8	3.8	3.9	4.0	4.1	4.2	2.4/2.9/3.7/4.2

$^3\text{Th}_2\text{AuO}_2^-$ (C _s) (1)	8.0	13.2		12.6			
$^3\text{Th}_2\text{AuO}_2^-$ (C _s) (2)	23.2	22.4		21.8			

^a sp = single point calculations (no geometry optimization); opt = geometry optimization. ^b CCSD(T)/aT (opt) for Th₂AuO and CCSD(T)/aT (sp) for Th₂AuO₂; ^c CCSD(T)/aT optimized geometries were used for Th₂AuO and CCSD(T)/aD optimized geometries were used for Th₂AuO₂

Table III.A.4.3 Th₂O and Th₂O⁻ relative energies in kcal/mol at different level of theory.^a

Isomer	B3LYP/ aD	CCSD(T)/ aD (opt)	CCSD(T)/ aT (opt)	CCSD(T)/ aQ	CCSD(T)/ CBS	CCSD(T)/ awD/T/Q/CBS ^b
$^3\text{Th}_2\text{O}$ (C _{2v})	0.0	0.0	0.0	0.0	0.0	0.0
$^5\text{Th}_2\text{O}$ (C _{2v})	2.5	2.2	1.2	0.5	0.0	1.7/2.2/1.4/0.8
$^1\text{Th}_2\text{O}$ (C _{2v})	7.4	4.4	4.1	4.0	3.8	4.4/4.1/4.1/4.0
$^3\text{Th}_2\text{O}$ (C _s) (ThThO)	25.3					
$^2\text{Th}_2\text{O}^-$ (C _{2v})	0.0	0.0	0.0	0.0	0.0	0.0
$^4\text{Th}_2\text{O}^-$ (C _{2v})	0.4	2.0	3.0	3.5	3.9	2.2/3.0/3.4/3.7
$^6\text{Th}_2\text{O}^-$ (C _{2v})	16.5	20.6(sp)	21.6(sp)			

^a sp = single point calculations (no geometry optimization); opt = geometry optimization. ^b CCSD(T)/aT optimized geometries were used

Table III.A.4.4 Th₂ and Th₂⁻ Relative energies in kcal/mol at different level of theory.^a

Isome r	B3LY P/ aD	CCSD(T))/ aD	CCSD(T))/ aT	CCSD(T))/ aQ	CCSD(T))/ CBS	CCSD(T))/ awD	CCSD(T))/ awT	CCSD(T))/ awQ	CCSD(T))/ CBS
$^3\text{Th}_2$	0.0	0.5	0.0	0.0	0.0	0.4	0.0	0.0	0.0
$^1\text{Th}_2$	3.8	0.0	0.3	0.5	0.7	0.0	0.3	0.5	0.6

$^5\text{Th}_2$	11.8	5.9	9.2						
$^2\text{Th}_2^-$	6.2	2.3	0.0	0.0	0.0	2.2	0.6	0.0	0.0
$^4\text{Th}_2^-$	0.0	6.8	3.8	3.6	3.5	6.6	4.6	3.6	3.0
$^6\text{Th}_2^-$	8.9	0.0	0.2	1.5	2.3	0.0	0.0	0.1	0.5

^a All CCSD(T)/aT optimized geometry.

Table III.A.4.5 Th-Th Bond Order (BO) analysis from NBO (Natural Bond Orbital) and MO (Molecular Orbital) analysis.

Molecule	r(Th-Th) (Å)	NBO BO	MO BO
$^2\text{Th}_2\text{Au}$ (C_{2v})	2.765	3.48	3.5
$^2\text{Th}_2\text{Au}$ ($C_{\infty v}$)	2.720	2.93	3.5
$^1\text{Th}_2\text{Au}^-$ (C_{2v})	2.990	1.92	3.0
$^1\text{Th}_2\text{Au}^-$ ($C_{\infty v}$)	2.773	2.92	4.0
$^2\text{Th}_2\text{AuO}$ (C_{2v})	2.888	2.48	2.5
$^4\text{Th}_2\text{AuO}$ (C_{2v})	3.057	1.48	2.0
$^1\text{Th}_2\text{AuO}^-$ (C_{2v})	3.443	0.97	1.0
$^3\text{Th}_2\text{AuO}^-$ (C_{2v})	2.972	1.98	2.5
$^2\text{Th}_2\text{AuO}_2$ (C_s) (1)	3.383	0.00	0.0
$^1\text{Th}_2\text{AuO}_2^-$ (C_s) (1)	3.419	0.00	0.0
$^1\text{Th}_2\text{AuO}_2^-$ (C_s) (2)	3.342	0.00	0.0
$^3\text{Th}_2\text{O}$ (C_{2v})	3.324	0.50	2.0
$^5\text{Th}_2\text{O}$ (C_{2v})	3.056	1.97	2.0
$^1\text{Th}_2\text{O}$ (C_{2v})	3.364	1.00	2.0
$^2\text{Th}_2\text{O}^-$ (C_{2v})	3.170	1.48	2.5
$^4\text{Th}_2\text{O}^-$ (C_{2v})	3.144	1.47	1.5
$^1\text{Th}_2\text{O}_2$ (C_{2h})	3.350	0.00	0.0
$^2\text{Th}_2\text{O}_2^-$ (C_{2v})	3.382	0.00	0.0
$^3\text{Th}_2$	2.694	4.00	4.0

$^1\text{Th}_2$	2.736	4.00	4.0
$^2\text{Th}_2^-$	2.683	4.50	3.5
$^4\text{Th}_2^-$	2.680	4.50	4.0
$^6\text{Th}_2^-$	2.782	3.50	4.0

Th₂AuO₀₋₂

Th₂Au and its anion have a complicated set of states and geometries. The lowest energy state for Th₂Au[−] is either $^1\text{A}_1$ in C_{2v} symmetry or the linear singlet ThThAu; these two isomeric structures being different by less than 1 kcal/mol. At the highest computational level, i.e., CCSD(T)/CBS with weighted core basis sets, the linear singlet is 0.6 kcal/mol above the C_{2v} singlet. The triplet and quintet states for the C_{2v} isomer are, at most, 3.5 kcal/mol higher in energy. The triplet state for the linear ThThAu isomer is also close in energy. Thus, there will be a significant number of species observed in the experiment, which have comparably low energies.

For neutral Th₂Au, there are again two very low energy doublet structures within 1 kcal/mol of each other. Linear ThThAu is 0.7 kcal/mol less stable than the C_{2v} structure at the CCSD(T)/CBS limit with weighted core basis sets. There are also low energy quartet and sextet states for the C_{2v} isomer of the neutral. Thus, the vertical detachment energies and the adiabatic electron affinities will be complicated by the number of low-lying species in both the neutral and its anion, as will the geometries of the various species.

The Th-Th bond distances for Th₂Au[−] and Th₂Au are given in Table III.A.4.5 (See Figure III.A.4.3 for structures). For the C_{2v} geometries of both the anion and its neutral, the Th-Th bond length is very sensitive to the apical angle at the Au; a slight increase in the $\angle\text{ThAuTh}$ angle can lead to a significant increase in the Th-Th bond distance. For the C_{2v} geometry of the neutral, the Th-Th bond distance increases as the spin state increases, but no such trend is observed for the anion. For the linear ThThAu geometry, the Th-Th bond distance decreases as the spin state increases in its anion, whereas in its neutral, the Th-Th bond distance increases as the spin state increases, although to a lesser extent. The Th-Au bond distances are not strongly dependent on spin states for both the anion and its neutral in all the isomeric structures. The Th-Au bond distances are slightly longer in the anionic structures compared to their corresponding neutrals.

The addition of a single oxygen atom to Th_2Au leads to a wide range of structures. The O atom can bridge the Th-Th bond, leading to different structures or it can add directly to a Th or Au atom external to the ring of metal atoms. The lowest energy structures all involve the O atom interacting with Th, since the interaction of O with Au is a very high energy species. This is consistent with the high bond energy for ThO at 208.5 kcal/mol and the much lower BDE (bond dissociation energy) for AuO at 53.5 ± 5 kcal/mol. The lowest energy structure for the anion is the singlet C_{2v} structure with the O atom bridging the Th-Th bond and with the Au atom bridging Th-Th bond opposite to the O atom. The triplet is less than 6 kcal/mol higher in energy, depending on the level of the theory. The lowest energy structure for the neutral is also a C_{2v} structure with the O atom bridging the Th-Th bond and the Au atom bridging the same Th-Th bond opposite to the O atom. The exact spin state depends on the level of the calculation with the quartet slightly higher in energy than the doublet (< 4 kcal/mol) at the highest computational levels. The next higher energy isomeric neutral doublet structure has the O atom bridging the Th-Th bond and the Au atom binding only one Th atom. This structure could not be optimized for the anion.

The addition of an O atom bridging the Th-Th bond does not substantially change the geometry of the Th_2Au core for the neutral. Thus, Th-Au is essentially unchanged, and the Th-Th bond is ~ 0.17 Å longer in Th_2AuO as compared to Th_2Au . For the anion, Th_2AuO^- , the Th-Au bond is ~ 0.11 Å shorter and the Th-Th bond is 0.45 Å longer than for the corresponding lowest energy Th_2Au^- structure. As observed for Th_2Au , the Th-Th bond is the most sensitive to Th-Au-Th angle as well as the Th-O-Au angle. Thus, for the $\text{Th}_2\text{AuO}^- C_{2v}$ structure, as the Th-Au-Th and Th-O-Au angles decrease from the lowest energy singlet to the triplet state, the Th-Th bond shortens by 0.47 Å, the Th-Au bond increases by 0.15 Å, and the Th-O bond stays almost the same. For neutral Th_2AuO , both Th-Au-Th and Th-O-Au angles increase from the doublet to the quartet state and the Th-Th bond increases by ~ 0.10 Å, although both the Th-Au and Th-O bonds change by less than 0.01 Å.

Addition of a second oxygen atom to Th_2AuO leads to formation of a Th_2O_2 core with the Au now bonded to just one of the Th atoms and no longer bridging them as in the lowest energy structure. This structure for the anion is lower in energy by 4 kcal/mol. than the one with the Au atom bridging the two Th atoms. For the neutral, the C_s (1) structure with two ThOTh bridges and the Au atom bonded to only one Th atom is clearly the most stable structure. The structure with the Au atom bridging both Th atoms, i.e., C_s (2), is more than 20 kcal/mol higher in energy. For both anionic and neutral Th_2AuO_2 structures, the Th-Th bonds are much longer than predicted for Th_2Au and Th_2AuO and are

comparable to the Th-Th bond in Th_2AuO^- . The Th-Th-Au angle for the lowest energy Th_2AuO_2 anion is almost linear, but in the corresponding neutral, it bends to 138° . For the lowest energy anionic and neutral Th_2AuO_2 structures, there are two different Th-O bonds, a longer one to the Th atom which binds the Au atom and a shorter one which links to the other Th atom.

Thorium oxygen species

For Th_2O , we cannot determine if the ground state is the triplet or the quintet, since they have essentially the same energy; they are less than 1 kcal/mol apart at the CCSD(T)/CBS with weighted core basis set level of theory. Furthermore, the singlet is only 4 kcal/mol higher in energy. For the anion, the doublet is the ground state with the quartet being 4 kcal/mol higher in energy. The Th_2O anion and neutral have C_{2v} symmetry with the O atom bridging the Th-Th bond. For Th_2O^- , the Th-Th bond distance is 3.17 Å and Th-O-Th angle is 97° ; for Th_2O the Th-Th bond distance is 0.15 Å longer and the angle is 105° . The Th-Th bonds become shorter as the Th-O-Th angle becomes smaller in going to the higher spin states, this being the case for both anions and neutrals. The Th-O bonds do not change as much as the Th-Th bond with the spin state, and they are slightly shorter for the neutrals compared to their corresponding anions.

While they were not studied experimentally in this work, it is nevertheless instructive to consider the related anions, Th_2O_2^- and $\text{ThAuO}_{0.2}^-$ together with their neutral counterparts computationally. The lowest energy Th_2O_2^- anion and corresponding neutral have two O atom bridges on Th-Th bond. The lowest energy Th_2O_2^- anion is a doublet state in C_{2v} symmetry with two shorter (2.07 Å) and two longer (2.21 Å) Th-O bonds. The quartet spin state is 14 kcal/mol higher in energy at the CCSD(T)/aT level of theory. The lowest energy neutral, Th_2O_2 has a C_{2h} symmetry with four equivalent Th-O bonds of 2.11 Å length each. The triplet state neutral is 20 kcal/mol higher in energy at the CCSD(T)/aT level of theory. The Th-Th bond distance is 3.38 Å for the lowest energy anion and 0.03 Å shorter for the neutral.

The ThO_2^- anion is a doublet in C_{2v} symmetry with a Th-O bond length of 1.95 Å and an O-Th-O angle of 114° at the CCSD(T)/aT level. The Th-O bond distances for the singlet neutral ThO_2 are ~ 0.04 Å shorter. ThO is predicted to be a singlet and ThO^- is predicted to be a doublet. The bond distance is predicted to increase from 1.85 Å in the neutral to 1.89 Å in the anion.

ThAuO_{0.2}

The dimer anion ThAu^- is predicted to have a triplet ground state, whereas neutral ThAu is predicted to have a doublet ground state. The ThAu^- singlet and quintet states are 10 kcal/mol and 13 kcal/mol, respectively, higher in energy. The neutral ThAu quartet is about 6 kcal/mol higher in energy. The bond distance is predicted to increase from 2.71 Å in the neutral to 2.82 Å in the anion at the CCSD(T)/aQ level of theory. The Th-Au bond for both the neutral and the anion is not significantly dependent on the spin state, exhibiting changes less than 0.02 Å. The Th-Au bond distances in the anion and neutral ThAu dimer are ~ 0.20 Å and ~ 0.30 Å, respectively, these being shorter than in the corresponding Th_2Au structures.

The lowest energy structures of both the ThAuO^- anion and its neutral are bent. They have C_s symmetry, with Th serving as the central atom and with Au binding to the ThO moiety. The ThAuO^- anion is a ground state singlet, with its triplet state residing at least 26 kcal/mol higher in energy. Neutral ThAuO is a doublet ground state, with its other spin states sitting much higher in energy. The Th-Au bond distance for the anion is 2.93 Å, i.e., ~ 0.13 Å longer than for the neutral. The Th-O bond distance is almost unchanged, i.e., 1.89 Å for the anion vs 1.86 Å for the neutral. The Th-Au bond distances for ThAuO^- and ThAuO are 0.05 Å longer and 0.21 Å shorter than for corresponding Th_2AuO^- and Th_2AuO species. The Th-O bond distances for both ThAuO^- and ThAuO are much shorter than those of anionic and neutral Th_2AuO structures, where an O atom bridged both Th atoms; they are in fact similar to Th-O bonds in ThO dimers.

ThAuO_2^- has a singlet ground state in C_{2v} symmetry and a structure where an Au atom binds a ThO_2 -like molecule with an O-Th-O angle of 121° . The neutral, lowest energy ThAuO_2 isomer is a doublet in C_1 symmetry, with one of the O atoms bridging Th-Au bond and the other O atom bonding only to Th. The ThAuO_2 isomer corresponding to the anion's lowest energy structure is about 8 kcal/mol higher in energy with an O-Th-O angle of $\sim 144^\circ$. The Th-Au bond distance is 3.08 Å in the anion and ~ 0.1 Å shorter in the neutral. The Th-O bond distance for the anion is similar to the Th-O bond distance in ThO_2^- .

Th₂ dimer

The Th_2 dimer is complicated. The triplet is predicted to be the ground state for the neutral, but the singlet is only 0.6 kcal/mol higher in energy at the CCSD(T)/CBS level with the weighted core basis sets. At our best computational level, CCSD(T)/CBS level with the weighted core basis sets, the Th_2^- anion is predicted to be a doublet ground state with the sextet and the quartet only 0.5 kcal/mol and 3.0 kcal/mol, respectively, higher in energy. At the CCSD(T)/aQ

level of theory, triplet Th_2 is predicted to have a bond distance of 2.694 Å, which is 0.042 Å shorter than in the singlet. For the doublet Th_2^- anion, the bond distance is 2.683 Å, ~ 0.01 Å shorter than the bond distance in the lowest energy ground state triplet neutral. The sextet Th_2^- anion has a longer bond distance of 2.782 Å, almost 0.10 Å longer than in the doublet anion ground state. The quartet anion is predicted to have almost same bond distance as the doublet ground state.

Au oxygen species

AuO is predicted to have a singlet ground state and AuO^- is predicted to be a doublet. The bond distance in AuO^- is predicted to decrease to 1.88 Å from 1.89 Å in the neutral. AuO_2 is predicted to be linear with the doublet clearly being the ground state at the CCSD(T) level of theory. Its anion is a linear triplet with the singlet ~ 11 kcal/mol higher in energy. The Au-O distance is predicted to decrease from 1.85 Å in the anion to 1.80 Å in the neutral.

Calculated electron affinities (EA) and vertical detachment energies (VDE)

The adiabatic electron affinities are summarized in Table III.A.4.6 at the CCSD(T) level of theory with the DFT/B3LYP values reported in the Supporting Information. The calculated adiabatic electron affinity for Th_2Au is 0.08 eV lower than the experimental value at the weighted core CCSD(T)/CBS level and 0.12 eV lower without the weighted core basis sets at the CCSD(T)/CBS level. The electron affinity for Th_2AuO is 0.07 eV higher than the experimental value at the weighted core CCSD(T)/CBS level and 0.02 eV lower without the weighted core basis sets at the CCSD(T)/CBS level. The calculated CCSD(T)/CBS electron affinity for Th_2AuO_2 is the same as the experimentally determined value. The calculated adiabatic electron affinity for Th_2O at the CCSD(T)/CBS level with and without weighted core basis sets is 0.04 eV and 0.08 eV, respectively, greater than experiment. The agreement between computational and experimental values confirms the spectral assignments of the adiabatic electron affinities.

As additional benchmarks of our approach, the experimental electron affinities of AuO and Au are also known, with the calculated values falling within 0.04, and 0.01 eV of the experimental values. The calculated value for Th is within 0.01 eV of the recently reported experimental value. This good agreement with experiment further confirms that our calculated results should be valid to better than ± 0.1 eV. Note that for ^4Th there are two states very close in energy, $(6d\sigma)^1(6d\delta)^1(6d\pi)^1$ and $(6d\delta)^1(6d\pi)^2$, with the first one of these just 1.3 kcal/mol higher in energy.

Table III.A.4.6 CCSD(T) Adiabatic electron affinities (eV) (ΔH_{0K}).

Neutral	Anion	aD/awD ^a	aT/awT ^a	aQ/awQ ^a	CBS/CBS ^a	Expt.
² Th ₂ Au	¹ Th ₂ Au ⁻	1.35/1.36	1.26/1.32	1.23/1.28	1.22/1.26	1.34
² Th ₂ AuO	¹ Th ₂ AuO ⁻	1.51/1.55	1.45/1.55	1.39/1.49	1.36/1.45	1.38
² Th ₂ AuO ₂	¹ Th ₂ AuO ₂ ⁻	1.24/1.24	1.23/1.23	1.24	1.25	1.25
² ThAu	³ ThAu ⁻	0.96/0.92	1.02/0.96	1.05/0.99	1.07/1.01	
¹ Th ₂ O ₂	² Th ₂ O ₂ ⁻	0.50/0.47	0.50/0.45	0.52/0.47	0.54/0.49	
³ Th ₂ O	² Th ₂ O ⁻	1.21/1.22	1.28/1.25	1.34/1.30	1.38/1.34	1.30
¹ ThO ₂	² ThO ₂ ⁻	1.20/1.22	1.17/1.19	1.17/1.19	1.18/1.19	
² AuO ₂	³ AuO ₂ ⁻	3.35/3.32	3.42/3.40	3.47/3.46	3.50/3.49	
¹ ThO	² ThO ⁻	0.44/0.43	0.53/0.47	0.57/0.51	0.60/0.53	
² AuO	¹ AuO ⁻	2.15/2.20	2.28/2.33	2.34/2.38	2.37/2.41	2.3740±0.0070 ⁶⁶
³ Th ₂	² Th ₂ ⁻	0.72/0.70	0.77/0.74	0.80/0.76	0.82/0.77	
³ Th	⁴ Th ⁻	0.45/0.44	0.53/0.51	0.60/0.56	0.64/0.59	0.607690(60) ⁶⁷
² Au	¹ Au ⁻	2.09/2.19	2.17/2.26	2.21/2.29	2.23/2.30	2.30860±0.00070 ⁶⁸

^a Basis sets: cc-pVnZ-PP (Th), aug-cc-pVnZ-PP (Au), aug-cc-pVnZ (O) /aug-cc-pwCVnZ (O), cc-pwCVnZ-PP (Th), aug-cc-pwCVnZ-PP (Au).

The vertical detachment energies are given in Table III.A.4.7. For Th₂Au⁻, the VDE values are complicated by the similarity in the energies of the linear and C_{2v} isomers of the anion and by the fact that different spin states in the neutral have different overlaps with the geometry of the anion. Thus, we expect that the ¹Th₂Au⁻ (C_{2v}) structure will give rise to transitions ranging from 1.41 to 1.55 eV, these encompassing the experimental with an intensity maximum EBE of 1.60 eV and an EBE onset at of 1.34 eV. The higher energy C_{2v} spin states of the anion will give rise to lower VDE values. The linear ThThAu anion would have a VDE of 1.28 eV, this lying at the low intensity side of the observed EBE value. Thus, the results point to the observation of the C_{2v} structure as the dominant one in the EBE spectrum of Th₂Au for the first peak. It is possible that higher binding energies could involve electron detachment from the linear structure.

For Th₂AuO⁻, there is a low-lying triplet state along with a singlet ground state for the C_{2v} structure. For the neutral, the optimized doublet and quartet states are essentially isoenergetic. The low energy VDE is consistent with removal of an electron from the triplet to form either the doublet or quartet neutral with respective VDE values of 1.34

and 1.39 eV in comparison with the experimental EBE peak value of 1.59 eV and an EBE onset of 1.30 eV. The higher energy EBE band is consistent with a transition from the ground state singlet to the doublet and quartet neutral states with calculated values of 1.84 and 1.89 eV; these predicted values fall in the middle of the experimental EBE range of 1.85-2.05 eV.

For ${}^1\text{Th}_2\text{AuO}_2^-$ (C_s) (1), the higher energy ${}^1\text{Th}_2\text{AuO}_2^-$ (C_s) (2) structure with the O atom bridging two Th atoms is 4 kcal/mol higher in energy and may be present in the experiment. The calculated VDE value is 1.40 eV without the outer core electrons correlated and 1.42 eV with the outer core electrons correlated for ${}^1\text{Th}_2\text{AuO}_2^-$ (C_s) (1). The VDE value for the higher energy anion structure ${}^1\text{Th}_2\text{AuO}_2^-$ (C_s) (2) is 1.65 eV. These calculated VDE values fall under the band in the experimental EBE spectrum centered at 1.56 eV.

For Th_2O^- , the quartet state is slightly higher in energy than the doublet. The ground state of the Th_2O neutral can be either the triplet or the quintet. The calculated VDE values for the triplet and quintet states are essentially the same and in good agreement with the experimental EBE values with an EBE onset at 1.30 eV and a maximum intensity in the EBE peak at 1.49 eV.

Table III.A.4.7 Vertical detachment energies (VDE) (eV) at CCSD(T)/aT level.

Anion	Neutral	VDE
${}^1\text{Th}_2\text{Au}^-$ (C_{2v})	${}^2\text{Th}_2\text{Au}$ (C_{2v})	1.51
	${}^4\text{Th}_2\text{Au}$ (C_{2v})	1.41
	${}^6\text{Th}_2\text{Au}$ (C_{2v})	1.55
${}^3\text{Th}_2\text{Au}^-$ (C_{2v})	${}^2\text{Th}_2\text{Au}$ (C_{2v})	1.43
	${}^4\text{Th}_2\text{Au}$ (C_{2v})	1.26
	${}^6\text{Th}_2\text{Au}$ (C_{2v})	1.37
${}^5\text{Th}_2\text{Au}^-$ (C_{2v})	${}^2\text{Th}_2\text{Au}$ (C_{2v})	1.19
	${}^4\text{Th}_2\text{Au}$ (C_{2v})	1.35
	${}^6\text{Th}_2\text{Au}$ (C_{2v})	1.65
${}^1\text{Th}_2\text{Au}^-$ ($C_{\infty v}$)	${}^2\text{Th}_2\text{Au}$ ($C_{\infty v}$)	1.28
	${}^4\text{Th}_2\text{Au}$ ($C_{\infty v}$)	2.14

$^3\text{Th}_2\text{Au}^- (\text{C}_{\infty\text{v}})$	$^2\text{Th}_2\text{Au} (\text{C}_{\infty\text{v}})$	1.19 ^a
	$^4\text{Th}_2\text{Au} (\text{C}_{\infty\text{v}})$	2.10 ^a
$^1\text{Th}_2\text{AuO}^- (\text{C}_{2\text{v}})$	$^2\text{Th}_2\text{AuO} (\text{C}_{2\text{v}})$	1.84
	$^4\text{Th}_2\text{AuO} (\text{C}_{2\text{v}})$	1.87
$^3\text{Th}_2\text{AuO}^- (\text{C}_{2\text{v}})$	$^2\text{Th}_2\text{AuO} (\text{C}_{2\text{v}})$	1.34
	$^4\text{Th}_2\text{AuO} (\text{C}_{2\text{v}})$	1.39
$^2\text{Th}_2\text{O}_2^-$	$^1\text{Th}_2\text{O}_2$	0.68
$^1\text{Th}_2\text{AuO}_2^- (\text{C}_s) (1)$	$^2\text{Th}_2\text{AuO}_2 (\text{C}_s) (1)$	1.40 ^b
$^1\text{Th}_2\text{AuO}_2^- (\text{C}_s) (2)$	$^2\text{Th}_2\text{AuO}_2 (\text{C}_s) (2)$	1.65
$^2\text{ThO}_2^-$	$^1\text{ThO}_2$	1.23
$^3\text{AuO}_2^-$	$^2\text{AuO}_2$	2.29
$^3\text{ThAu}^-$	$^2\text{ThAu}$	1.06
	$^4\text{ThAu}$	1.34
$^1\text{ThAu}^-$	$^2\text{ThAu}$	0.63
	$^4\text{ThAu}$	0.90
$^5\text{ThAu}^-$	$^2\text{ThAu}$	0.51
	$^4\text{ThAu}$	0.78
$^2\text{ThO}^-$	^1ThO	0.56
$^2\text{Th}_2\text{O}^- (\text{C}_{2\text{v}})$	$^3\text{Th}_2\text{O} (\text{C}_{2\text{v}})$	1.37
	$^5\text{Th}_2\text{O} (\text{C}_{2\text{v}})$	1.38
	$^1\text{Th}_2\text{O} (\text{C}_{2\text{v}})$	1.56
$^4\text{Th}_2\text{O}^- (\text{C}_{2\text{v}})$	$^3\text{Th}_2\text{O} (\text{C}_{2\text{v}})$	1.29
	$^5\text{Th}_2\text{O} (\text{C}_{2\text{v}})$	1.23
	$^1\text{Th}_2\text{O} (\text{C}_{2\text{v}})$	1.48
$^1\text{AuO}^-$	^2AuO	2.29
$^2\text{Th}_2^-$	$^3\text{Th}_2$	0.77
	$^1\text{Th}_2$	0.80

	⁵ Th ₂	1.34
⁴ Th ₂ ⁻	³ Th ₂	0.61
	¹ Th ₂	0.64
	⁵ Th ₂	1.17
⁶ Th ₂ ⁻	³ Th ₂	0.81
	¹ Th ₂	0.79
	⁵ Th ₂	1.20

^a aD basis set. ^b 1.42 eV with the awT basis set.

Heats of formation and Bond Dissociation Energies

Calculated heats of formation and selected bond dissociation energies are reported in Table III.A.4.8 and compared with the experimental values when available. The experimental heat of formation of ThO has been reported as -5.0 ± 2.4 kcal/mol⁶⁹ and -6.4 ± 3.3 kcal/mol.⁵⁵ In comparison with these, our calculated value is more negative ($\Delta H_{f,298K} = -8.3$ kcal/mol) and falls essentially within the experimental error bars. The experimental heat of formation of ThO₂ has been reported as -108.8 ± 3.0 kcal/mol⁶⁹ and -104.8 ± 10 kcal/mol⁵⁵ and our calculated value ($\Delta H_{f,298K} = -108.7$ kcal/mol) is in excellent agreement with these values. The experimental heat of formation of Th₂ has been reported to be 217.0 and 216.2 ± 5.8 (0K) kcal/mol⁵⁵ and our calculated heat of formation, $\Delta H_{f,298K} = 220.5$ kcal/mol, is slightly more positive and within the reported experimental error bars. For the remaining molecules for which experimental data is not available, the current values represent the best available thermodynamic data.

Bond dissociation energies (BDEs) are valuable parameters for understanding the bonding in these species. The BDE of AuO has been reported to be 53.3 ± 5 kcal/mol, and whereas our calculated value of 48 kcal/mol is slightly smaller than that, it is likely to be more reliable.⁵³ Roos et al.⁵ report a CASPT2 BDE for Th₂ of 3.28 eV (75.6 kcal/mol), which is 8 kcal/mol larger than our value but is not consistent with the experimental heats of formation.

The BDE values of diatomic ThAu and Th₂ are very similar to one another, with the BDE value of ThAu being 2 kcal/mol larger. At 211 kcal/mol, the BDE value of the ThO diatomic is much larger, while at 48 kcal/mol, the BDE of AuO is much smaller, suggesting that ThO bonds will govern over AuO bonds in the structures that are formed.

For Th₂Au, we find that the C_{2v} and C_{∞v} ThThAu isomers have comparable energies, which is being consistent with the similar BDE values for Th-Th and Th-Au. The Th-Th and Th-Au BDE values in the Th₂Au cluster are larger than

in the diatomics, suggesting metallic character in these species. This is consistent with the Th-Th bond distances ranging only from 2.71 to 2.76 Å in the structures and in diatomic Th₂. By contrast, the ThAu bond distances in the trimer species are significantly longer than in diatomic ThAu. It is also important to note that the Th-Th interaction is key to the stability of the species, as the D_{∞h}, ThAuTh, species is much higher in energy. In this D_{∞h} structure, there can be no overlap of the Th 6d orbitals with each other. The only bonding utilizes the valence s-orbitals, leading to a total bond order of 0.5, caused by placing five electrons into the three valence s-orbitals, i.e., a bonding orbital, a non-bonding orbital and an anti-bonding orbital. Although the first Th-O BDE in Th₂O is only 50 kcal/mol, the second Th-O BDE is much higher. In contrast, the ThO BDE in ThO₂ is 159 kcal/mol. The AuO BDE is much smaller, at 48 kcal/mol. The large Th-O BDE and the lower AuO BDE means that Th₂O and Th₂O₂ can be considered as core structural units. This is consistent with the relative energies of the isomers discussed above, where the Au is best described as complexing to Th₂O or to Th₂O₂. There is still a significant interaction of the Au with the cluster with a binding energy of 88 kcal/mol for Th₂AuO where the Au can bridge the two Th atoms connected by an oxygen. This Au-cluster interaction decreases by 20 kcal/mol when the Au can only bind to a Th or bridge across the Th₂O₂ cluster as in Th₂AuO₂. The binding of Au⁻ to the cluster is about 20 kcal/mol smaller for Th₂O and Th₂O₂. Note that the Th-cluster BDE in Th₂AuO₂ is quite high due to breaking two Th-O bonds when Th is liberated. Note also that when a Th is removed, the oxygen binding energy to the cluster is substantially decreased, again consistent with the conclusion that the ThO bonds are controlling the energetics of cluster formation.

Table III.A.4.8 Heats of formation and Bond Dissociation Energies in kcal/mol at 0 K.

Molecule	$\Delta H_{f,0K}$	$\Delta H_{f,298K}$	Bond		
			Th-Au	Th-Th	M-O
² ThAu	162.5	162.4	69.4		
³ ThAu ⁻	139.2	139.1	39.5 Th + Au ⁻		
² Th ₂ Au (C _{2v})	227.2	227.1	81.4 Th ₂ + Au	79.2 ThAu + Th	
² Th ₂ Au (C _{∞v})	226.6	226.7	82.0 Th ₂ + Au	79.8 ThAu + Th	
¹ Th ₂ Au ⁻ (C _{2v})	197.5	197.4	58.6	85.6	

			$\text{Th}_2 + \text{Au}^-$	$\text{ThAu}^- + \text{Th}$	
$^1\text{Th}_2\text{Au}^- (\text{C}_{2v})$	198.2	198.3	57.2 $\text{Th}_2 + \text{Au}^-$	84.9 $\text{ThAu}^- + \text{Th}$	
$^2\text{Th}_2\text{AuO} (\text{C}_{2v})$	80.2	79.7	93.9 $\text{Th}_2\text{O} + \text{Au}$	75.4 $\text{ThAuO} + \text{Th}$	141.3 $\text{Th}_2\text{Au} + \text{O}$
$^1\text{Th}_2\text{AuO}^- (\text{C}_{2v})$	46.8	46.5	74.1 $\text{Th}_2\text{O} + \text{Au}^-$	74.4 $\text{ThAuO}^- + \text{Th}$	209.7 $\text{Th}_2\text{Au}^- + \text{O}$
$^2\text{Th}_2\text{AuO}_2 (\text{C}_s) (1)^a$	-74.6	-75.3	77.5 $\text{Th}_2\text{O}_2 + \text{Au}$	171.3 $\text{ThAuO}_2 + \text{Th}$	213.8 $\text{Th}_2\text{AuO} + \text{O}$
$^1\text{Th}_2\text{AuO}_2^- (\text{C}_s) (1)$	-103.4	-104.1	53.1 $\text{Th}_2\text{O}_2 + \text{Au}^-$	118.3 $\text{ThAuO}_2^- + \text{Th}$	209.2 $\text{Th}_2\text{AuO}^- + \text{O}$
$^2\text{ThAuO} (\text{C}_s)$	11.7	11.4	68.3 $\text{ThO} + \text{Au}$		209.8 $\text{ThAu} + \text{O}$
$^1\text{ThAuO}^- (\text{C}_s)$	-22.7	-23.0	90.3 $\text{ThO}^- + \text{Au}$		211.0 $\text{ThAu} + \text{O}^-$
$^2\text{ThAuO}_2 (\text{C}_1)$	-47.1	-47.6	26.9 $\text{ThO}_2 + \text{Au}$		117.8 $\text{ThAuO} + \text{O}$
$^1\text{ThAuO}_2^- (\text{C}_{2v})$	-129.0	-129.3	55.6 $\text{ThO}_2 + \text{Au}^-$		166.5 $\text{ThAuO} + \text{O}^-$
$^3\text{Th}_2\text{O} (\text{C}_{2v})$	86.1	85.6		49.8 $\text{ThO} + \text{Th}$	
$^2\text{Th}_2\text{O}^- (\text{C}_{2v})$	55.2	54.7		67.3 $\text{ThO} + \text{Th}^-$	
$^1\text{Th}_2\text{O}_2 (\text{C}_{2h})$	-85.1	-86.1			230.2 $\text{Th}_2\text{O} + \text{O}$
$^2\text{Th}_2\text{O}_2^- (\text{C}_{2v})$	-96.3	-97.3			208.2 $\text{Th}_2\text{O} + \text{O}^-$
^2AuO	99.1	99.0			47.9
$^1\text{AuO}^-$	43.7	43.5			50.1 $\text{Au}^- + \text{O}$

$^2\text{AuO}_2 (\text{D}_{\infty\text{h}})$	88.6	88.1			69.5 AuO + O
$^3\text{AuO}_2^- (\text{D}_{\infty\text{h}})$	7.2	6.7			95.5 AuO $^-$ + O
^1ThO	-8.0	-8.3			210.9
$^2\text{ThO}^-$	-20.2	-20.4			189.9 Th + O $^-$
$^1\text{ThO}_2 (\text{C}_{2\text{v}})$	-108.2	-108.7			159.2 ThO + O
$^2\text{ThO}_2^- (\text{C}_{2\text{v}})$	-135.6	-136.1			153.4 ThO + O $^-$
$^3\text{Th}_2$	220.7	220.5		67.2	
$^2\text{Th}_2^-$	202.9	202.8		71.4	

^a Calculated using EA and the heats of formation of the anion, $^1\text{Th}_2\text{AuO}_2^- (\text{C}_s)$ (1).

Bonding

The bond orders (BOs) for the Th-Th bonds are calculated based on analyses of the MOs and of the NBOs. The values are reported in Table III.A.4.5 and the orbital diagrams are shown in the Supporting Information. We first discuss the bonding in the core fragments.

Th₂

The bonding of the clusters containing Au can be best described by first examining the structures containing Th and O. $^3\text{Th}_2$ has the electron configuration $(7s\sigma_g)^2(6d\delta_g)^1(6d\sigma_g)^1(6d\pi_u)^4$, consistent with a bond order (BO) of 4 as noted by Roos et al.⁵ The electron configuration for the corresponding $^1\text{Th}_2$ is $(7s\sigma)^2(6d\sigma)^2(6d\pi)^4$ with a BO of 4.0 as well. From the NBO analysis, the lowest energy $^3\text{Th}_2$, with two unpaired electrons in $d\delta$ and $d\sigma$, has two bonds formed by only d orbitals, while the other two bonds possess both mixed d- and s-orbital character. For $^2\text{Th}_2^-$, the bond order calculated using an analysis of the MOs is 3.5 with an electron configuration of $(7s\sigma)^2(6d\delta)^1(6d\pi)^4$. There is also a $(6d\pi)^2$ non-bonding lone pair. From the NBO analysis, the bond order should be 4.5 with two bonds, having mostly d character and with the other 2.5 bonds exhibiting mixed d- and s-character. The slightly higher in energy isomers, $^6\text{Th}_2^-$ and $^4\text{Th}_2^-$ should have bond orders of 4.0 from MO analysis, with the electronic configurations

$(7s\sigma)^2(6d\sigma)^1(6d\delta)^1(6d\delta)^1(6d\pi)^3(6d\pi \text{ lone pair})^1$ and $(7s\sigma)^2(6d\sigma)^1(6d\delta)^1(6d\pi)^4(6d\pi \text{ lone pair})^1$, respectively. From the NBO analysis, ${}^6\text{Th}_2^-$ and ${}^4\text{Th}_2^-$ have BOs of 3.5 and 4.5, respectively.

Th oxygen clusters

Th_2O can be envisioned as being held together by ionic bonding between an O^{2-} and two Th^+ ions, consistent with a ground state triplet with a $(7s\sigma)^2(6d\delta)^1(6d\pi)^1$ configuration and a $(6d\pi)^2$ lone pair, resulting in a BO of 2.0. (We use the same labels for describing the types of bonding as in the linear Th_2 configuration, although these are not the correct symmetry labels in lower symmetry.) ${}^5\text{Th}_2\text{O}$ and ${}^1\text{Th}_2\text{O}$ have a BO of 2.0 as well based on an analysis of the MOs. The quintet has a $(7s\sigma)^2(6d\pi)^1(6d\delta)^1$ configuration with two $(6d\pi, 6d\delta)$ unpaired lone pair electrons and the singlet has a $(7s\sigma)^2(6d\pi)^2$ configuration with a $(6d\pi)^2$ lone pair. The NBO analysis gives a different BO of only 0.5 for the Th-Th bond. The Th-O ‘bonds’ in all three neutral electronic states have a BO of 1.96 from the NBO analysis; these Th-O bonds are mostly localized on the O atom. The O atom has a charge of *ca.* -1.5 |e|, confirming the ionic character of the Th-O bond. ${}^2\text{Th}_2\text{O}^-$ has an extra $(6d\pi)$ electron and ${}^4\text{Th}_2\text{O}^-$ has an extra $(6d\delta)$ lone pair electron with resulting BOs of 2.5 and 1.5, respectively. Th_2O can be considered as an ionically bonded species built on O^{2-} and Th^+ ions, since the charge on the O atom remains the same; the Th-O bonds are again localized mostly on the O atom.

Th_2O_2 can be envisioned as an ionically bonded species with two Th^{2+} and two O^{2-} . There is no Th-Th bonding in this case, but there is a lone pair on each Th atom consistent with a non-bonding $(6d\pi)^4$ configuration and with loss of the 7s electrons to form the +II formal oxidation state. Th_2O_2^- can also be considered as being held together by ionic bonding with two O^{2-} ions and with a Th^+ ion and a Th^{2+} ion. As with the neutral, there is no Th-Th bonding, and there is a lone pair on each Th atom with a non-bonding $(6d\pi)^4$ and an extra electron lone pair on one of Th atoms. From the NBO analysis, the O atoms’ charges remain unchanged at *ca.* -1.5 |e| for both the neutral and the anion; the Th-O ‘bonds’ are highly polarized, with most of the electron density being mostly localized the O.

Th₂Au

It is possible to describe Th_2Au with an ionic model as $\text{Au}^-(\text{Th}_2)^+$. The Au atom has a high electron affinity and could abstract an electron from the Th_2 moiety. The Th_2 bond in C_{2v} Th_2Au would then be $(7s\sigma)^2(6d\delta)^1(6d\pi)^4$, resulting in a bond order of 3.5, based on the MO analysis. ${}^2\text{Th}_2\text{Au}(\text{C}_{\infty v})$ has an $(7s\sigma)^2(6d\sigma)^1(6d\pi)^4$ electronic configuration with a bond order of 3.5, based on the MO analysis, where the unpaired electron resides in a $6d\sigma$ orbital which is different

from the C_{2v} isomer, where the unpaired electron is a $6d\delta$. ${}^2\text{Th}_2^+$ has the electronic configuration, $(7s\sigma)^2(6d\sigma)^1(6d\pi)^4$ so the linear conformer has the same electron configuration for the Th-Th bond.

In the simple ionic model, the anion Th_2Au^- should have the Th_2 MO scheme of $(7s\sigma_g)^2(6d\delta_g)^1(6d\sigma_g)^1(6d\pi_u)^4$ for neutral ${}^3\text{Th}_2$ or the MO scheme $(7s\sigma)^2(6d\sigma)^2(6d\pi)^4$ for ${}^1\text{Th}_2$ configuration as the singlet Th_2 is just 0.5 kcal/mol higher in energy; the Th-Th bond order would thus equal 4.0. In fact, the linear structure of singlet ThThAu^- does have the bonding pattern of the singlet. Note that the ${}^3\text{Th}_2\text{Au}^-$ which would give the ionic species, $({}^3\text{Th}_2)(\text{Au}^-)$, is 2.3 kcal/mol higher in energy at the CCSD(T)/aT level of theory. However, the Th-Au bonds in Th_2Au^- C_{2v} structure are more elongated by the additional electron repulsion from the Au^- than in the linear anion. For Th_2Au^- C_{2v} , the bonding is best described as $(7s\sigma_g)^2(6d\pi_u)^4$, with a non-bonding orbital composed of lone pairs on the Th atom, giving a Th-Th bond order of 3.0.

The NBO analysis for ${}^1\text{Th}_2\text{Au}^-$ (C_{2v}) has a Th-Th BO of 1.92, with the Th 6d orbitals as the main contributors. Linear, $C_{\infty v}$, ${}^1\text{Th}_2\text{Au}^-$ has a Th-Th BO of 2.92 with a shorter Th-Th bond than the C_{2v} isomer. Two of the Th-Th bonds are shared about equally by both Th atoms through their 6d orbitals, and the third bond is more localized on the Th atom, which is directly bonded to the Au atom through a mixture of s-d orbitals. ${}^2\text{Th}_2\text{Au}$ ($C_{\infty v}$) has a Th-Th bond order of 2.93 as well. The unpaired α spin is mostly on the Th atom (0.74 e) that is not bound to the Au atom, with the remaining spin (0.26 e) on the Th atom that binds the Au atom. ${}^2\text{Th}_2\text{Au}$ (C_{2v}) is predicted to have a BO which is artificially high due to the presence of open shells (different α and β spins) and the presence of multicentered bonds.

Th₂AuO₁₋₂

In the simple ionic model, the addition of an Au atom to Th_2O would generate an Au^- ion and a ${}^2\text{Th}_2\text{O}^+$ ion. ${}^2\text{Th}_2\text{O}^+$ is generated by the removal of an electron from the neutral ${}^3\text{Th}_2\text{O}$'s lone pair electron on the Th atoms to give a $(7s\sigma)^2(6d\delta)^1(6d\pi)^2$ configuration. The Th-Th bond order for ${}^2\text{Th}_2\text{O}^+$ as well as for ${}^2\text{Th}_2\text{AuO}$ of 2.5 does not change from that in ${}^3\text{Th}_2\text{O}$. The slightly higher energy ${}^4\text{Th}_2\text{AuO}$ is described as $({}^4\text{Th}_2\text{O})^+\text{Au}^-$, with a configuration of $(7s\sigma)^2(6d\delta)^1(6d\pi)^1$ and with a $(6d\pi)^1$ lone pair configuration, resulting in a BO of 2.0. Addition of the electron as part of a lone pair to form ${}^1\text{Th}_2\text{OAu}^-$ adds enough electron repulsion to elongate the Th-Th bond relative to the neutral, so that there are then 2 lone pairs and a Th-Th π -bond with a bond order of 1.0. This Th-Th bond in ${}^1\text{Th}_2\text{OAu}^-$, which can be considered as $({}^1\text{Th}_2\text{O})\text{Au}^-$, is 0.08 Å longer than in ${}^1\text{Th}_2\text{O}$, with a BO of 2.0. In ${}^1\text{Th}_2\text{O}$, there is a $(6d\pi)^2$ lone pair and a $(7s\sigma)^2(6d\pi)^2$ configuration for the Th-Th interaction. The Th-Th bond distance for the higher energy anion,

$^3\text{Th}_2\text{OAu}^-$, is much closer to the Th-Th bond distance of the neutral structure; moreover, $^3\text{Th}_2\text{OAu}^-$ has a BO of 2.5 with $(7s\sigma)^2(6d\pi)^3$ and a $(6d\pi)^1$ lone pair electronic configuration. The $^3\text{Th}_2\text{O}$ ground state with a Th-Th bond is 0.35 Å longer than the Th-Th bond in $^3\text{Th}_2\text{OAu}^-$ and has a $(7s\sigma)^2(6d\delta)^1(6d\pi)^1$ configuration with a $(6d\pi)^2$ lone pair and a BO of 2.0.

From the NBO analysis, the lowest energy neutral, $^2\text{Th}_2\text{OAu}$, and the anion, $^1\text{Th}_2\text{OAu}^-$ have the same bond orders of 2.48 and 0.97 as found from the MO analysis (2.5 and 1.0, respectively) given above. In addition, the NBO analysis shows a 3 center-2 electron (3c-2e) AuThTh bond for both lowest energy Th_2OAu neutral and anion structures. This 3c-2e bond is a s-d bond with the most contribution from the Au atom's s-orbitals and can be explained by an Au atom contribution to the Th-Th π bonds from the MO analysis. Also, the NBO analysis confirms that the unpaired electron is mostly a $6d\delta$ and is equally shared by both Th atoms. The Th-O bonds in these Th_2OAu molecules are highly polarized. The charges on O and Au atoms of *ca.* -0.5 |e| and *ca.* -1.5 |e|, respectively, remain almost unchanged for Th_2OAu neutral and anion and are the same as for the Th_2Au and Th_2O molecules, respectively.

Addition of an Au atom to Th_2O_2 abstracts a lone pair electron from the Th atom to generate $\text{Au}^-(\text{Th}_2\text{O}_2)^+$. As there is no Th-Th bond in Th_2O_2 , there is not one in Th_2AuO_2 . The location of the Au atom on one of the Th atoms is consistent with the formation of this ionic bonded structure. The addition of an electron to form $(\text{Th}_2\text{O}_2)\text{Au}^-$ replaces the lone pair on the Th atom and the Au atom does not change its position. Note that in all cases, there are a number of low-lying isomers consistent with the lack of directional bonding in an ion pair. The similarity in the electron affinities is also consistent with the ion pair bonding model, since one is removing an electron from a lone pair on the Th atoms in Th_2OAu^- and $\text{Th}_2\text{O}_2\text{Au}^-$ or from a higher energy Th-Th bonding orbital in Th_2Au^- .

Conclusions

Anion photoelectron spectroscopy of Th_2O^- , Th_2Au^- and $\text{Th}_2\text{AuO}_{1,2}^-$ yielded vertical detachment energies in the range of 1 to 2 eV. Correlated molecular orbital theory calculations at the CCSD(T) level gave values that are consistent with the experimental data and showed that in many cases there are close lying anion and neutral clusters with different geometries and spin states that can account for the observed spectra. The calculations are in agreement with the vertical detachment energies within 0.10 eV. The results suggest that there is a wealth of information for even such simple triatomic through penta-atomic species.

A plot of the Th-Th bond orders from an analysis of the molecular orbitals vs Th-Th bond distances is shown in Figure III.A.4.4 (the corresponding results for the bond order from the NBOs is given in the Supporting Information). We focus on the Th-Th bonds as the highly polarized Th-O and Th-Au bonds and their bond orders do not change as significantly with the bond distance. The Th-Th bond distances range from about 2.7 to 3.5 Å and the bond orders range from 4 to 0. There is a qualitative trend of a decrease in bond order with increasing bond distance, but it is interesting to note that there can be a significant difference in the bond order for a given distance especially for longer distances.

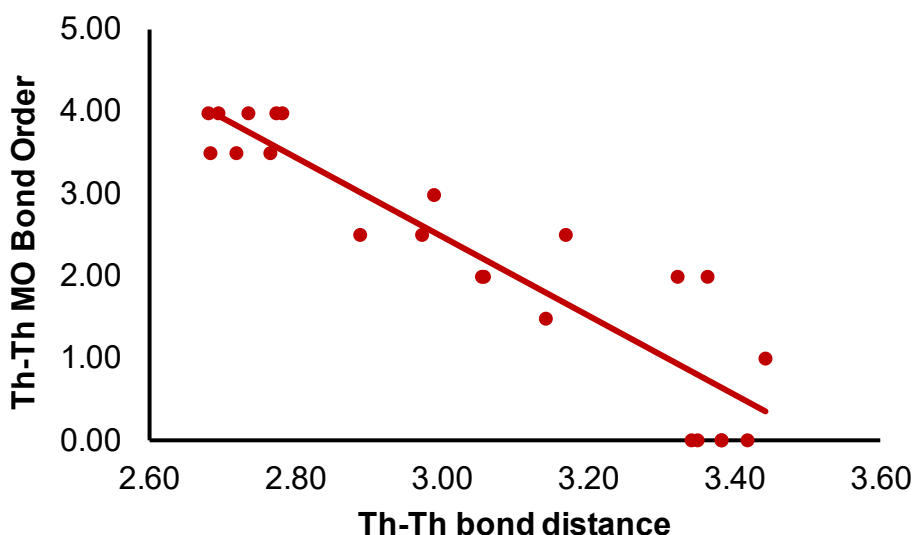


Figure III.A.4.4 Trendline in Th-Th Bond Order from MO analysis vs the Th-Th bond distance in Å

We find that a simple ionic model provides insights into the bonding in these species due to the large electron affinity (EA) of Au, the strong Th-O bond, the weak AuO bond, and the low ionization potentials (IPs) of the Th₂O_{0,1,2} clusters. The EA of Au is 2.3 eV and the IPs of Th₂, Th₂O, and Th₂O₂ are 4.90, 5.04, and 5.42 eV calculated at the CCSD(T)/awT level. Thus, the difference in the IP-EA that needs to be overcome by an attractive ionic interaction ranges from 2.6 to 3.1 eV. A simple Coulombic model with the Au⁻ at a distance of 3.0 Å (an approximate average of the Th-Au distances) from the positive charge gives 4.8 eV in terms of the Coulombic interaction so there is a sufficient Coulombic attraction energy for these charge transfer processes to occur leading to ion pair formation. As shown by the values in Table III.A.4.8, the ionic component contributes a significant amount to the BDEs. Even ThAu can have a significant ionic component as the IP of Th is 6.31 eV⁷⁰ and the ThAu distance is 2.70 Å (see Supporting Information).

In this case, the Coulombic attraction energy is 5.3 eV and the IP-EA difference is 4.0 eV so the Coulombic bond energy is 1.3 eV out of the total BDE of 3.0 eV (Table III.A.4.8).

The neutral Th_2Au structure is quite flexible as would be expected of a species with a closed shell Au^- bonded to a Th_2^+ core with a strong Th-Th bond in the ionic model. The Au^- can then effectively move around the Th_2^+ core with low barriers. The BDEs and bond distances analysis Th_2Au relative to the their diatomics suggest metallic character in these species. We prefer this ionic model for the bonding rather than a metal-metal bonding model as would be appropriate for Au_3 which exhibits similar flexibility but for a different reason.⁷¹ The anion is prepared by adding the electron to the Th_2^+ core. There are a number of low-lying spin states when only the metals are present due to the different ways of coupling the spins in $\text{Th}_2^{+/0}$ as the Au^- is closed shell in the neutral and in the anion. Thus, the Th-Th bond order is dominated by what happens in the diatomic $\text{Th}_2^{+/0}$ moiety. The interaction of the Au^- with the $\text{Th}_2^{+/0}$ group can impact the Th-Th bond distances; for example, the Th-Th bond distance lengthens in the C_{2v} neutral structure due to electron repulsion from the Au^- with both Th atoms.

In the presence of oxygen, the energetics are dominated by the presence of strong Th-O bonds as the Au-O bond is quite weak. The Th-O interactions have a dominant ionic component and we treat the O as a formal O^{2-} . Thus, for Th_2O , we would expect to have two Th(I), each of which has a ground state $7s^26d^1$ electron configuration; the $7s^16d^2$ and $7s^25f^1$ excited states of the ion are not that high in energy.⁷⁰ Thus, we expect a number of low-lying spin states for Th_2O as is predicted. In addition, the ThOTh bond angle is quite flexible ranging from 90 to 110° depending on the spin state. The Th-Th bond is longer than in $\text{Th}_2\text{Au}^{0/-}$ ranging from 3.0 to 3.4 Å depending on the spin state but is still substantially less than twice the atomic radius of 1.80 Å.⁷² Thus, there is always some metal-metal Th bonding present in these Th clusters held together by a single O atom. Addition of an electron to Th_2O tends to make the Th-Th bond distances about the same, near 3.20 Å. The Th-Th bond order in Th_2O is 2.0 in the neutral and 1.5 to 2.5 in the anion depending on the spin state. The addition of Au to Th_2O can be described as a charge transfer process leading to the formation of the $[\text{Th}_2\text{O}^+][\text{Au}^-]$ ion pair due to the large EA of Au and the modest IP of Th_2O . The Th-Th bond length shortens on addition of the Au, consistent with the ionic model. The addition of the electron to form Th_2AuO^- leads to Au^- bonded to a neutral ThOTh unit as the additional negative charge goes onto the metal oxide. Although the energy differences between the singlet and triplet states are small in Th_2AuO^- , the Th-Th bond distance has a surprisingly large variation with the longer bond distance by 0.4 Å corresponding to the more stable species with a bond order of

1.0. The triplet has a bond order of 2.5. Again, there is a balance in the electron repulsion so that the singlet minimizes electron repulsion by formation of lone pairs on the Th.

The bonding in Th₂O₂ is dominated by the ion pairing of the two O²⁻ with the two Th(II). The Th-Th bond distance is still between 3.3 and 3.4 Å, and in principle, could retain some metal-metal character. However, in this case, the electrons that are on the Th localize as lone pairs and it is best to describe Th₂O₂ as not having a metal-metal bond. Addition of Au to Th₂O₂ again leads to formation of an ion pair [Th₂O₂⁺][Au⁻] and the Th-Th distance does not significantly change on addition of the Au. This is consistent with the charge of +2 on the metal.

Overall, the results show that what one might consider as a cluster with metal-metal bonds between Th and Au may have a significant ionic component to the bonding and that an ion pair model can account for the MOs. The results show, in the presence of moieties with moderately large electron affinities such as Au and moderate ionization potentials such as the Th species, that one cannot ignore the possibility of significant ionic character even for interactions between metals. As a metal, Au with its quite high electron affinity may prove to have unique interactions and serve as a different type of probe for the properties of the metal and metal oxide clusters. The results also suggest that one must go beyond just using the bond distance to obtain the bond order to describe the types of bonding that are present in these thorium metal clusters and oxides.

Supporting Information

Complete citation for References 30, 39 and 60. Additional relative energies and geometry parameters at different level of theory for all isomers and their spin states. Total energies in atomic units. Components for calculating the total atomization energies and calculated heats of formation in kcal/mol. Adiabatic electron affinities (eV) (ΔH_0K) at the B3LYP/aD level. Ionization potentials of Th₂, Th₂O, and Th₂O₂ in eV at 0 K. NBO Bond Orders vs bond distances in angstroms. Trendlines in Th-Th Bond Order from NBO and MO analysis vs the Th-Th bond distance. Isomeric structure pictures. MO pictures. XYZ optimized coordinates for the larger molecules.

References

- (1) Kelley, M. P.; Popov, I. A.; Jung, J.; Batista, E. R.; Yang, P. δ and ϕ Back-Donation in AnIV Metallacycles. *Nat. Commun.* **2020**, *11* (1), 1–10. <https://doi.org/10.1038/s41467-020-15197-w>.
- (2) Denning, R. G. Electronic Structure and Bonding in Actinyl Ions and Their Analogs. *J. Phys. Chem. A* **2007**, *111* (20), 4125–4143. <https://doi.org/10.1021/jp071061n>.
- (3) Hu, H.-S.; Kaltsoyannis, N. The Shortest Th–Th Distance from a New Type of Quadruple Bond. *Phys. Chem. Chem. Phys.* **2017**, *19* (7), 5070–5076. <https://doi.org/10.1039/C7CP00113D>.

- (4) Philip F. Souter, †; Gary P. Kushto, †; Lester Andrews, *, † and; Neurock‡, M. Experimental and Theoretical Evidence for the Formation of Several Uranium Hydride Molecules. *J. Am. Chem. Soc.* **1997**, *119* (7), 1682–1687. <https://doi.org/10.1021/JA9630809>.
- (5) Björn O. Roos, *, †; Per-Åke Malmqvist, † and; Gagliardi‡, L. Exploring the Actinide–Actinide Bond: Theoretical Studies of the Chemical Bond in Ac₂, Th₂, Pa₂, and U₂. *J. Am. Chem. Soc.* **2006**, *128* (51), 17000–17006. <https://doi.org/10.1021/JA066615Z>.
- (6) Knecht, S.; Jensen, H. J. A.; Saue, T. Relativistic Quantum Chemical Calculations Show That the Uranium Molecule U₂ Has a Quadruple Bond. *Nat. Chem.* **2018**, *11* (1), 40–44. <https://doi.org/10.1038/s41557-018-0158-9>.
- (7) and, M. S.; Pyykkö, P. Linear HThThH: A Candidate for a Th–Th Triple Bond. *J. Am. Chem. Soc.* **2005**, *127* (38), 13090–13091. <https://doi.org/10.1021/JA052723U>.
- (8) Zhou, J.; Sonnenberg, J. L.; Schlegel, H. B. Theoretical Studies of AnII₂(C₈H₈)₂ (An = Th, Pa, U, and Np) Complexes: The Search for Double-Stuffed Actinide Metallocenes. *Inorg. Chem.* **2010**, *49* (14), 6545–6551. <https://doi.org/10.1021/IC100427T>.
- (9) Wang, C.-Z.; Gibson, J. K.; Lan, J.-H.; Wu, Q.-Y.; Zhao, Y.-L.; Li, J.; Chai, Z.-F.; Shi, W.-Q. Actinide (An = Th–Pu) Dimetallocenes: Promising Candidates for Metal–Metal Multiple Bonds. *Dalt. Trans.* **2015**, *44* (39), 17045–17053. <https://doi.org/10.1039/C5DT02811F>.
- (10) Ge, X.; Dai, X.; Zhou, H.; Yang, Z.; Zhou, R. Stabilization of Open-Shell Single Bonds within Endohedral Metallofullerene. *Inorg. Chem.* **2020**, *59* (6), 3606–3618. <https://doi.org/10.1021/ACS.INORGCHEM.9B03089>.
- (11) Andrews, L.; Gong, Y.; Liang, B.; Jackson, V. E.; Flamerich, R.; Li, S.; Dixon, D. A. Matrix Infrared Spectra and Theoretical Studies of Thorium Oxide Species: ThO_x and Th₂O_y. *J. Phys. Chem. A* **2011**, *115* (50), 14407–14416. <https://doi.org/10.1021/jp208926m>.
- (12) Heaven, M. C.; Barker, B. J.; Antonov, I. O. Spectroscopy and Structure of the Simplest Actinide Bonds. *J. Phys. Chem. A* **2014**, *118* (46), 10867–10881. <https://doi.org/10.1021/jp507283n>.
- (13) Steimle, T.; Kokkin, D. L.; Muscarella, S.; Ma, T. Detection of the Thorium Dimer via Two-Dimensional Fluorescence Spectroscopy. *J. Phys. Chem. A* **2015**, *119* (35), 9281–9285. <https://doi.org/10.1021/ACS.JPCA.5B06608>.
- (14) Sculfort, S.; Braunstein, P. Intramolecular D10–D10 Interactions in Heterometallic Clusters of the Transition Metals. *Chem. Soc. Rev.* **2011**, *40* (5), 2741–2760. <https://doi.org/10.1039/C0CS00102C>.
- (15) Baruah, T.; Blundell, S. A.; Zope, R. R. Electronic and Structural Properties of Small Clusters of Clusters of Nan Au and Nan Ag (N=1-10). *Phys. Rev. A* **2001**, *64* (4), 043202. <https://doi.org/10.1103/PhysRevA.64.043202>.
- (16) Britto Hurtado, R.; Cortez-Valadez, M.; Gámez-Corrales, R.; Flores-Acosta, M. Structural and Vibrational Properties of Gold-Doped Titanium Clusters: A First-Principles Study. *Comput. Theor. Chem.* **2018**, *1124*, 32–38. <https://doi.org/10.1016/J.COMPTC.2017.12.008>.
- (17) Lu, P.; Liu, G. H.; Kuang, X. Y. Probing the Structural and Electronic Properties of Bimetallic Chromium–Gold Clusters Cr_mAu_n (m + n ≤ 6): Comparison with Pure Chromium and Gold Clusters. *J. Mol. Model.* **2014**, *20* (8). <https://doi.org/10.1007/S00894-014-2385-3>.
- (18) Bishea, G. A.; Arrington, C. A.; Behm, J. M.; Morse, M. D. Resonant Two-photon Ionization Spectroscopy of Coinage Metal Trimers: Cu₂Ag, Cu₂Au, and CuAgAu. *J. Chem. Phys.* **1998**, *95* (12), 8765. <https://doi.org/10.1063/1.461212>.
- (19) Bonačić-Koutecký, V.; Burda, J.; Mitrić, R.; Ge, M.; Zampella, G.; Fantucci, P. Density Functional Study of Structural and Electronic Properties of Bimetallic Silver–Gold Clusters: Comparison with Pure Gold and Silver Clusters. *J. Chem. Phys.* **2002**, *117* (7), 3120. <https://doi.org/10.1063/1.1492800>.

- (20) Yuan, H. K.; Kuang, A. L.; Tian, C. L.; Chen, H. Structural and Electronic Properties of $Aun-XPt_x$ ($n = 2-14$; $X \leq n$) Clusters: The Density Functional Theory Investigation. *AIP Adv.* **2014**, *4* (3). <https://doi.org/10.1063/1.4869019>.
- (21) Zhang, H.-R.; Zhao, Y.-R.; Gao, R.; Hu, Y.-F. Insights into the Structures, Stabilities, Electronic and Magnetic Properties of X_2Aun ($X = La, Y, \text{ and } Sc$; $n = 1-9$) Clusters: Comparison with Pure Gold Clusters. *Mol. Phys.* **2016**, *115* (3), 308–319. <https://doi.org/10.1080/00268976.2016.1259666>.
- (22) Gerhards, M.; Thomas, O. C.; Nilles, J. M.; Zheng, W.-J.; Bowen, K. H. Cobalt–Benzene Cluster Anions: Mass Spectrometry and Negative Ion Photoelectron Spectroscopy. *J. Chem. Phys.* **2002**, *116* (23), 10247–10252. <https://doi.org/10.1063/1.1477924>.
- (23) Ho, J.; Ervin, K. M.; Lineberger, W. C. Photoelectron Spectroscopy of Metal Cluster Anions: Cun^- , Ag_n^- , and Au_n^- . *J. Chem. Phys.* **1990**, *93* (10), 6987–7002. <https://doi.org/10.1063/1.459475>.
- (24) Burkart, S.; Blessing, N.; Klipp, B.; Muller, J.; Gantefor, G.; Seifert, G.; Germany, G. Experimental Verification of the High Stability of AlH : 13 a Building Block of a New Type of Cluster Material? *Chem. Phys. Lett.* **1999**, *301* (4), 546–550.
- (25) Siekmann, H. R.; Lüder, C.; Faehrmann, J.; Lutz, H. O.; Meiwes-Broer, K. H. The Pulsed Arc Cluster Ion Source (PACIS). *Zeitschrift für Phys. D Atoms, Mol. Clust.* **1991**, *20* (1), 417–420. <https://doi.org/10.1007/BF01544026>.
- (26) Zhang, X.; Wang, Y.; Wang, H.; Lim, A.; Gantefor, G.; Bowen, K. H.; Reveles, J. U.; Khanna, S. N. On the Existence of Designer Magnetic Superatoms. *J. Am. Chem. Soc.* **2013**, *135* (12), 4856–4861. <https://doi.org/10.1021/JA400830Z>.
- (27) Ko, Y. J.; Shakya, A.; Wang, H.; Grubisic, A.; Zheng, W.; Götz, M.; Ganteför, G.; Bowen, K. H.; Jena, P.; Kiran, B. Electronic Structure and Properties of Isoelectronic Magic Clusters: $Al_{13}X$ ($X = H, Au, Li, Na, K, Rb, Cs$). *J. Chem. Phys.* **2010**, *133* (12), 124308. <https://doi.org/10.1063/1.3490401>.
- (28) Zhang, X.; Ganteför, G.; Bowen, K. H.; Alexandrova, A. N. The $PtAl^-$ and $PtAl_2^-$ Anions: Theoretical and Photoelectron Spectroscopic Characterization. *J. Chem. Phys.* **2014**, *140* (16), 164316. <https://doi.org/10.1063/1.4873160>.
- (29) Wang, H.; Zhang, X.; Ko, Y. J.; Grubisic, A.; Li, X.; Ganteför, G.; Schnöckel, H.; Eichhorn, B. W.; Lee, M.-S.; Jena, P.; Kandalam, A. K.; Kiran, B.; Bowen, K. H. Aluminum Zintl Anion Moieties within Sodium Aluminum Clusters. *J. Chem. Phys.* **2014**, *140* (5), 054301. <https://doi.org/10.1063/1.4862989>.
- (30) Wang, H.; Ko, Y. J.; Zhang, X.; Gantefor, G.; Schnoeckel, H.; Eichhorn, B. W.; Jena, P.; Kiran, B.; Kandalam, A. K.; Jr., K. H. B. The Viability of Aluminum Zintl Anion Moieties within Magnesium-Aluminum Clusters. *J. Chem. Phys.* **2014**, *140* (12), 124309. <https://doi.org/10.1063/1.4869104>.
- (31) Parr, R. G.; Yang, W. Density-Functional Theory of Atoms and Molecules. Oxford University Press: Oxford, U.K.: New York 1989.
- (32) Becke, A. D. Density-functional Thermochemistry. III. The Role of Exact Exchange. *J. Chem. Phys.* **1998**, *98* (7), 5648. <https://doi.org/10.1063/1.464913>.
- (33) Lee, C.; Yang, W.; Parr, R. G. Development of the Colle-Salvetti Correlation-Energy Formula into a Functional of the Electron Density. *Phys. Rev. B* **1988**, *37* (2), 785. <https://doi.org/10.1103/PhysRevB.37.785>.
- (34) Jr., T. H. D. Gaussian Basis Sets for Use in Correlated Molecular Calculations. I. The Atoms Boron through Neon and Hydrogen. *J. Chem. Phys.* **1998**, *90* (2), 1007. <https://doi.org/10.1063/1.456153>.
- (35) Kendall, R. A.; Jr., T. H. D.; Harrison, R. J. Electron Affinities of the First-row Atoms Revisited. Systematic Basis Sets and Wave Functions. *J. Chem. Phys.* **1998**, *96* (9), 6796. <https://doi.org/10.1063/1.462569>.
- (36) Peterson, K. A. Correlation Consistent Basis Sets for Actinides. I. The Th and U Atoms. *J. Chem. Phys.* **2015**, *142* (7), 074105. <https://doi.org/10.1063/1.4907596>.

- (37) Weigand, A.; Cao, X.; Hangele, T.; Dolg, M. Relativistic Small-Core Pseudopotentials for Actinium, Thorium, and Protactinium. *J. Phys. Chem. A* **2014**, *118* (13), 2519–2530. <https://doi.org/10.1021/JP500215Z>.
- (38) Peterson, K. A.; Puzzarini, C. Systematically Convergent Basis Sets for Transition Metals. II. Pseudopotential-Based Correlation Consistent Basis Sets for the Group 11 (Cu, Ag, Au) and 12 (Zn, Cd, Hg) Elements. *Theor. Chem. Accounts* **2005**, *114* (4), 283–296. <https://doi.org/10.1007/S00214-005-0681-9>.
- (39) Frisch, M. J.; Trucks, G. W.; Schlegel, H. B.; Scuseria, G. E.; Robb, M. A.; Cheeseman, J. R.; Scalmani, G.; Barone, V.; Petersson, G. A.; Nakatsuji, H.; et al. Gaussian 16, Revision A.03. Gaussian, Inc.: Wallingford, CT 2016.
- (40) III, G. D. P.; Bartlett, R. J. A Full Coupled-cluster Singles and Doubles Model: The Inclusion of Disconnected Triples. *J. Chem. Phys.* **1998**, *76* (4), 1910. <https://doi.org/10.1063/1.443164>.
- (41) Raghavachari, K.; Trucks, G. W.; Pople, J. A.; Head-Gordon, M. A Fifth-Order Perturbation Comparison of Electron Correlation Theories. *Chem. Phys. Lett.* **1989**, *157* (6), 479–483. [https://doi.org/10.1016/S0009-2614\(89\)87395-6](https://doi.org/10.1016/S0009-2614(89)87395-6).
- (42) Watts, J. D.; Gauss, J.; Bartlett, R. J. Coupled-cluster Methods with Noniterative Triple Excitations for Restricted Open-shell Hartree–Fock and Other General Single Determinant Reference Functions. Energies and Analytical Gradients. *J. Chem. Phys.* **1998**, *98* (11), 8718. <https://doi.org/10.1063/1.464480>.
- (43) Bartlett, R. J.; Musiał, M. Coupled-Cluster Theory in Quantum Chemistry. *Rev. Mod. Phys.* **2007**, *79* (1), 291. <https://doi.org/10.1103/RevModPhys.79.291>.
- (44) Feller, D.; Peterson, K. A.; Hill, J. G. On the Effectiveness of CCSD(T) Complete Basis Set Extrapolations for Atomization Energies. *J. Chem. Phys.* **2011**, *135* (4), 044102. <https://doi.org/10.1063/1.3613639>.
- (45) Peterson, K. A.; Woon, D. E.; Jr., T. H. D. Benchmark Calculations with Correlated Molecular Wave Functions. IV. The Classical Barrier Height of the $H+H_2\rightarrow H_2+H$ Reaction. *J. Chem. Phys.* **1998**, *100* (10), 7410. <https://doi.org/10.1063/1.466884>.
- (46) Dunham, J. L. The Energy Levels of a Rotating Vibrator. *Phys. Rev.* **1932**, *41* (6), 721. <https://doi.org/10.1103/PhysRev.41.721>.
- (47) Dunham, J. L. The Wentzel-Brillouin-Kramers Method of Solving the Wave Equation. *Phys. Rev.* **1932**, *41* (6), 713. <https://doi.org/10.1103/PhysRev.41.713>.
- (48) Moore, C. E. *Atomic Energy Levels as Derived from the Analysis of Optical Spectra, Volume 1, H to V*; U.S. National Bureau of Standards Circular 467; U.S. Department of Commerce, National Technical Information Service: Washington, D.C., 1949.
- (49) Sansonetti, J. E.; Martin, W. C. Handbook of Basic Atomic Spectroscopic Data. *J. Phys. Chem. Ref. Data* **2005**, *34* (4), 1559. <https://doi.org/10.1063/1.1800011>.
- (50) ATcT Thermochemical Values ver. 1.122g <https://atct.anl.gov/ThermochemicalData/version1.122g/index.php> (accessed Sep 9, 2021).
- (51) Branko Ruscic; Reinhardt E. Pinzon; Melita L. Morton; Gregor von Laszewski; Sandra J. Bittner; Sandeep G. Nijssure; Kaizar A. Amin; Michael Minkoff, and; LastNameWagner, A. F. Introduction to Active Thermochemical Tables: Several “Key” Enthalpies of Formation Revisited†. *J. Phys. Chem. A* **2004**, *108* (45), 9979–9997. <https://doi.org/10.1021/JP047912Y>.
- (52) PB, C.; TL, N.; JH, B.; GB, E.; JF, S.; DH, B.; B, R. Active Thermochemical Tables: The Adiabatic Ionization Energy of Hydrogen Peroxide. *J. Phys. Chem. A* **2017**, *121* (46), 8799–8806. <https://doi.org/10.1021/ACS.JPCA.7B06221>.
- (53) Luo, Y.-R. *Comprehensive Handbook of Chemical Bond Energies*; CRC Press, Taylor and Francis Group, 2007.
- (54) Cox, J.; Wagman, D. D.; Medvedev, V. A. *CODATA Key Values for Thermodynamics*; Hemisphere Publishing Corp: New York, 1989.

- (55) Thermal Constants of Substances,; Yungman, V. S.; Glushko, V. P.; Medvedev, V. A.; Gurvich, L. V., Ed.; New York, 1999.
- (56) Marçalo, J.; Gibson, J. K. Gas-Phase Energetics of Actinide Oxides: An Assessment of Neutral and Cationic Monoxides and Dioxides from Thorium to Curium †. <https://doi.org/10.1021/jp904862a>.
- (57) Deegan, M. J. O.; Knowles, P. J. Perturbative Corrections to Account for Triple Excitations in Closed and Open Shell Coupled Cluster Theories. *Chem. Phys. Lett.* **1994**, 227 (3), 321–326. [https://doi.org/10.1016/0009-2614\(94\)00815-9](https://doi.org/10.1016/0009-2614(94)00815-9).
- (58) Rittby, M.; Bartlett, R. J. An Open-Shell Spin-Restricted Coupled Cluster Method: Application to Ionization Potentials in Nitrogen. *J. Phys. Chem.* **2002**, 92 (11), 3033–3036. <https://doi.org/10.1021/J100322A004>.
- (59) Knowles, P. J.; Hampel, C.; Werner, H.-J. Erratum: “Coupled Cluster Theory for High Spin, Open Shell Reference Wave Functions” [*J. Chem. Phys.* 99, 5219 (1993)]. *J. Chem. Phys.* **2000**, 112 (6), 3106. <https://doi.org/10.1063/1.480886>.
- (60) Werner, H.-J.; Knowles, P. J.; G. Knizia, Manby, F. R.; Schütz, M.; Celani, P.; Györfy, W.; Kats, D.; Korona, T.; Lindh, R. . et al. MOLPRO, A Package of Ab Initio Programs (<https://www.molpro.net>). 2019.
- (61) Werner, H.-J.; Knowles, P. J.; Manby, F. R.; Black, J. A.; Doll, K.; Heßelmann, A.; Kats, D.; Köhn, A.; Korona, T.; Kreplin, D. A.; Ma, Q.; MillerIII, T. F.; Mitrushchenkov, A.; Peterson, K. A.; Polyak, I.; Rauhut, G.; Sibaev, M. The Molpro Quantum Chemistry Package. *J. Chem. Phys.* **2020**, 152 (14), 144107. <https://doi.org/10.1063/5.0005081>.
- (62) Reed, A. E.; Curtiss, L. A.; Weinhold, F. Intermolecular Interactions from a Natural Bond Orbital, Donor-Acceptor Viewpoint. *Chem. Rev.* **2002**, 88 (6), 899–926. <https://doi.org/10.1021/CR00088A005>.
- (63) Weinhold, F.; Landis, C. R. *Valency and Bonding: A Natural Bond Orbital Donor-Acceptor Perspective*; Cambridge University Press, 2005; Vol. 9780521831284. <https://doi.org/10.1017/CBO9780511614569>.
- (64) Weinhold, F.; Glendening, E. D.; Weinhold, F.; Glendening, E. D. *NBO 7.0 Program Manual Natural Bond Orbital Analysis Programs*; 1996.
- (65) Glendening, E. D.; Landis, C. R.; Weinhold, F. NBO 7.0: New Vistas in Localized and Delocalized Chemical Bonding Theory. *J. Comput. Chem.* **2019**, 40 (25), 2234–2241. <https://doi.org/10.1002/JCC.25873>.
- (66) Takatoshi Ichino, *; Adam J. Gianola; Django H. Andrews, and; Lineberger*, W. C. Photoelectron Spectroscopy of AuO⁻ and AuS⁻. *J. Phys. Chem. A* **2004**, 108 (51), 11307–11313. <https://doi.org/10.1021/JP045791W>.
- (67) Tang, R.; Si, R.; Fei, Z.; Fu, X.; Lu, Y.; Brage, T.; Liu, H.; Chen, C.; Ning, C. Candidate for Laser Cooling of a Negative Ion: High-Resolution Photoelectron Imaging of Th. *Phys. Rev. Lett.* **2019**, 123 (20), 203002. <https://doi.org/10.1103/PhysRevLett.123.203002>.
- (68) Hotop, H.; Lineberger, W. C. Dye-laser Photodetachment Studies of Au⁻, Pt⁻, PtN⁻, and Ag⁻. *J. Chem. Phys.* **2003**, 58 (6), 2379. <https://doi.org/10.1063/1.1679515>.
- (69) Königs, R. J. M.; Morss, L. R.; Fuger, J. Thermodynamic Properties of Actinides and Actinide Compounds in The Chemistry of the Actinide and Transactinide Elements; Morss, L. R.; Edelstein, N. M.; Fuger, J., Ed.; J. Springer Dordrecht, 2006; pp 2113–2224.
- (70) Atomic Spectra Database | NIST <https://www.nist.gov/pml/atomic-spectra-database> (accessed Sep 9, 2021).
- (71) RR, P.; M, C.; KA, P.; DA, D. Potential Energy Surface of Group 11 Trimers (Cu, Ag, Au): Bond Angle Isomerism in Au₃. *J. Phys. Chem. A* **2019**, 123 (6), 1198–1207. <https://doi.org/10.1021/ACS.JPCA.8B11219>.
- (72) Emsley, J. The Elements; Clarendon Press: Oxford, UK, 1994.

III.B. Uranium

In 1789, The oxide uraninite, rather than the uranium element, was first discovered in the mineral pitchblende by Martin Heinrich Klaproth while working in his experimental laboratory in Berlin.¹ He believed then that UO_2 was an elemental species and named it after the planet Uranus (named after the primordial Greek deity of the Heaven), which had been discovered eight years earlier by William Herschel.

Before 2021, the fundamental and intrinsic property, electron affinity, of the uranium atom had not been measured experimentally. Due to the strong spin-orbit and relativistic effects, theorists also had difficulty in predicting the EA accurately. In section III.B.1, the experimentally determined value of the electron affinity of the uranium atom was determined to be 0.309 ± 0.025 eV. The computationally predicted electron affinity of uranium based on composite coupled cluster calculations and full 4-component spin-orbit coupling calculations was found to be 0.232 eV.

The valence electron configuration of U is $5f^3 6d^2 7s^1$ and exhibits oxidation states ranging from +3 to +6. The comprehensive mixing of these three valence orbitals gives rise to the complicated chemical bonding properties of all uranium complexes. The primary contribution of uranium based nuclear waste is from the uranyl (UO_2^{2+}) complex, the most stable form of uranium in nature. The Uranium-ligand interactions can significantly influence the electronic structure and bonding properties of UO_2^{2+} . In section III.B.2, A joint relativistic coupled-cluster and experimental photoelectron (PE) spectroscopic study of the uranyl dichloride anion, UO_2Cl_2^- , is reported. The experimentally measured EA was assigned to the feature at 3.2 ± 0.20 eV, consistent with the computed value, 3.15 eV.

In sections III.B.3 and III.B.4, I present the studies on the interactions between U and Au atoms. The transition from halogen-like to metallic-like bonding of gold in UAu_n^- clusters ($n=3-7$) is discussed. We also compared the UAu_6 to UF_6 , the most important molecule in the nuclear industry.

References

1. L. R. Morss, N. M. Edelstein, J. Fuger, *The Chemistry of the Actinide and Transactinide Elements* (Springer: Dordrech, NLD, 2006).

III.B.1. The Electron Affinity of the Uranium Atom

Reproduced with permission from AIP Publishing. *J. Chem. Phys.* **154**, 224307 (2021); DOI: 10.1063/5.0046315

Sandra M. Ciborowski,¹ Gaoxiang Liu,¹ Moritz Blankenhorn,¹ Rachel M. Harris,¹ Mary A. Marshall,¹ Zhaoguo Zhu,¹ and Kit H. Bowen^{1,*} and Kirk A. Peterson,^{2,*}

¹Department of Chemistry, Johns Hopkins University, Baltimore, MD 21218 USA

²Department of Chemistry, Washington State University, Pullman, WA 99162 USA

Abstract

The results of a combined experimental and computational study of the uranium atom are presented with the aim of determining its electron affinity. Experimentally, the electron affinity of uranium was measured via negative ion photoelectron spectroscopy of the uranium atomic anion, U⁻. Computationally, the electron affinities of both thorium and uranium were calculated by conducting relativistic coupled-cluster and multi-reference configuration interaction calculations. The experimentally determined value of the electron affinity of the uranium atom was determined to be 0.309 eV ± 0.025 eV. The computationally predicted electron affinity of uranium based on composite coupled cluster calculations and full 4-component spin-orbit coupling calculations was found to be 0.232 eV. Predominately due to a better convergence of the coupled cluster sequence for Th and Th⁻, the final calculated electron affinity for Th, 0.565 eV, was in much better agreement with the accurate experimental value of 0.608 eV. In both cases the ground state of the anion corresponds to electron attachment to the 6d orbital.

Introduction

The actinides comprise the elements from actinium through lawrencium in the Periodic Table. In broad terms, the chemical bonding behaviors of actinium and thorium resemble those of the transition metals; the *5f* valence electrons of protactinium, uranium, neptunium, and plutonium play important roles in their bonding; and among the still heavier elements, their bonding tends to mimic the lanthanide elements in terms of electron shielding and their *f* electron contributions.¹⁻¹³

The present work focuses on uranium and, in particular, on the electron affinity (EA) of its atom. There have been many studies of uranium, often focusing on its radioactivity, its natural decay products, the ability of certain of its isotopes to undergo nuclear fission, and their resulting fission products. Some of these aspects lead to long-term health and environmental concerns, regarding the storage and disposition of nuclear waste, which is generated by power

reactors and production facilities, as well as the handling of natural uranium in mines and isotopically-depleted uranium projectiles on battlefields.¹⁴⁻¹⁷ Important physical properties, which have been measured include uranium's melting point, boiling point, ionization potential, and half-life, the latter being approximately the age of the earth in the case of uranium's 238 isotope.¹⁸⁻²¹

Because uranium exhibits metallic bonding character under most conditions, its chemical reactions can proceed without 6*d* electron promotion, leading to its facile reactivity.¹¹ The chemistry of uranium is thus the chemistry of its oxidation products. With a ground state electron configuration of [Xe]5*f*³6*d*¹7*s*², uranium exhibits oxidation states ranging from +3 and +6, and given the itinerant nature of uranium's 5*f* electrons, its chemical bonds often involve their significant contribution.²²

Surprisingly, despite widespread interest in uranium, its electron affinity (EA) has not been measured experimentally. Computationally, however, there have been several predictions of the uranium atom's electron affinity, all of which have had to contend with strong spin-orbit and relativistic effects. These calculated electron affinities of uranium (in meV) are 175,²⁷ 290,²³ 300,²⁴ 373,²⁸ 531,²³ and 702,²³ with publication dates ranging from 1984 to 2009. All of these studies predict electron attachment to either the 7*p* or 6*d* orbitals of U atom.

The work herein presents the results of a combined experimental and computational study aimed at determining the electron affinity of the uranium atom. This involved experimentally measuring the electron affinity of the uranium atom by using anion photoelectron spectroscopy and computationally predicting the EA value of uranium by conducting coupled cluster and multi-reference configuration interaction calculations. Since an accurate experimental measurement of the electron affinity of the thorium atom has recently become available,²⁹ we also carried out benchmark calculations of the EA value of thorium in order to help validate our computational methods.

Methods

Experimental

Anion photoelectron spectroscopy is conducted by crossing a beam of mass-selected negative ions with a fixed-frequency photon beam and energy-analyzing the resultant photodetached electrons. The photodetachment process is governed by the energy-conserving relationship: $h\nu = \text{EBE} + \text{EKE}$, where $h\nu$ is the photon energy, EBE is the electron binding (photodetachment transition) energy, and EKE is the electron kinetic energy. Our apparatus consists of a laser

vaporization anion source, a time-of-flight mass spectrometer, a Nd:YAG photodetachment laser, a magnetic bottle (MB) electron energy analyzer, and a velocity-map imaging (VMI) electron energy analyzing spectrometer.³⁰ The magnetic bottle photoelectron spectrometer's resolution is ~ 35 meV at $EKE = 1$ eV, and the VMI spectrometer resolution is $\Delta E/E \sim 0.03$.³⁰ The first (1064 nm, 1.16 eV) and third (355 nm, 3.49 eV) harmonic outputs of a Nd:YAG laser were both used to photodetach electrons from mass-selected, atomic uranium anions, U^- , with the first harmonic photoelectron spectrum being energy-analyzed by the VMI spectrometer and with the third harmonic photoelectron spectrum being energy-analyzed by the MB spectrometer. The well-known atomic transitions of Cu^- and the molecular transitions of NO^- were used to calibrate the MB-measured and VMI-measured photoelectron spectra, respectively.^{31,32} The atomic uranium anions were generated by a laser vaporization ion source. This device consisted of a rotating, translating depleted, i.e., pure U-238, uranium rod, which was being ablated by second harmonic (532 nm, 2.33 eV) photon pulses from a Nd:YAG laser, while being bathed by synchronous high pressure pulses of high purity helium gas.

Computational

Initial studies were carried out to calculate the electron affinities of both the thorium and uranium atoms by using the full internally contracted multi-reference configuration interaction (CMRCI) level of theory³³ in order to facilitate the study of both 7p and 6d electron attachments. These calculations employed orbitals from complete active-space, self-consistent field (CASSCF) calculations, using the same active-space for Th and U, i.e., the 6d, 7s, 7p, and 5f orbitals. The lower-lying orbitals were optimized but constrained to be doubly-occupied. These same CAS configurations were used as the reference functions in the subsequent CMRCI calculations, where all the valence electrons were correlated (6s,6p,6d,7s,5f). The multi-reference Davidson correction was used throughout,³⁴ i.e., CMRCI+Q. The basis sets employed corresponded to the all-electron cc-pVXZ-DK3 sets ($X = D, T, Q$)^{16,35} extended with an even-tempered set of diffuse functions in each angular momentum (denoted VXZ-DK+ below) in order to provide more accurate electron affinities. The third order Douglas-Kroll-Hess (DKH3) scalar relativistic Hamiltonian^{36,37} was used throughout. The CASSCF energies were extrapolated to the complete basis set (CBS) limit using³⁸

$$E_n^{HF} = E_{CBS}^{HF} + A(n+1)e^{-6.57\sqrt{n}} \quad (1)$$

with VTZ-DK+ and VQZ-DK+ basis sets ($n=3, 4$), and the analogous correlation energies were extrapolated to their CBS limits using³⁹

$$E_n^{corr} = E_{CBS}^{corr} + \frac{B}{(n+1/2)^4} \quad (2)$$

The results of these two extrapolations were combined to yield the total CMRCI+Q/CBS limit energies. The lowest-lying electronic terms for Th^- were found to be the ^4F and $^4\text{G}^\circ$, corresponding to the electron configurations $[\text{Rn}]6\text{d}^37\text{s}^2$ and $[\text{Rn}]6\text{d}^27\text{s}^27\text{p}^1$, respectively. For the U^- atomic anion, the analogous terms were the $^6\text{M}^\circ$ and ^6M for the electron configurations $[\text{Rn}]5\text{f}^36\text{d}^27\text{s}^2$ and $[\text{Rn}]5\text{f}^36\text{d}^17\text{s}^27\text{p}^1$, respectively. The neutral atom ground states correspond to ^3F ($[\text{Rn}]6\text{d}^27\text{s}^2$) and $^5\text{L}^\circ$ ($[\text{Rn}]5\text{f}^36\text{d}^17\text{s}^2$) for Th and U, respectively.

In the context of these multi-reference calculations, spin-orbit (SO) effects were included using the state-interacting approach at the CASSCF level of theory using the full Breit-Pauli operator.⁴⁰ The neutral atoms and anions were treated separately and for the anion calculations both the d- and p-attached electronic states were treated simultaneously. State-averaged orbitals were used throughout these calculations. In addition for the Th^- case the quartet G, F, D, and P states associated with the 7p^1 configuration were all included.

The Feller-Peterson-Dixon (FPD)⁴¹⁻⁴⁶ composite method was also used to determine the electron affinities for both the Th and U atoms. This approach has previously been successfully applied to the first few ionization potentials of lanthanide⁶⁷ and actinide³⁵ atoms, as well as the electron affinities of the heavy p-block elements.⁶⁸ The present calculations only focused on the lowest energy states of the negative ions, which involved electron attachment to the 6d orbitals; the numerous contributions to the electron affinities are described in detail below. The majority of these calculations were carried out at the CCSD(T) level of theory with the DKH3 Hamiltonian, also utilizing the diffuse-augmented VXZ-DK3+ basis sets ($X = \text{D, T, Q}$)^{16,35}. Core-valence correlation, i.e., $5\text{s}5\text{p}5\text{d}$ on Th and U, was also considered, and in these cases, wCVXZ-DK+ basis sets were used, i.e., cc-pwCVXZ-DK3 sets^{16,35} with a series of even-tempered diffuse functions. The coupled cluster calculations employed restricted open-shell HF orbitals (ROHF), although the spin restriction was relaxed in the CCSD(T) calculations, i.e., the R/UCCSD(T) method.⁴⁷⁻⁴⁹ All of the CCSD(T) calculations, as well as the CMRCI calculations described above, were carried out using the MOLPRO quantum chemistry package.⁵⁰

The final FPD electron affinities were constructed based on the following contributions to the energies:

$$E_{\text{FPD}} = E_{\text{wCVQZ-DK+}} + \Delta E_{\text{CBS}} + \Delta E_{\text{CV}} + \Delta E_{\text{SO}} + \Delta E_{\text{Gaunt}} + \Delta E_{\text{Lamb}} + \Delta E_T + \Delta E_Q \quad (3)$$

where $E_{\text{wCVQZ-DK+}}$ is the total energy at the frozen-core (FC) CCSD(T)/wCVQZ-DK+ level of theory. The HF energies were then extrapolated to the CBS limit using Eq. (1) with wCVTZ-DK+ and wCVQZ-DK+ basis sets, and the analogous correlation energies were extrapolated to their CBS limits using Eq. (2). The results of these two extrapolations were combined to yield the total FC-CCSD(T)/CBS energies, with the difference between the latter values and $E_{\text{wCVQZ-DK+}}$ yielding ΔE_{CBS} . ΔE_{CV} is the core correlation contribution, $E_{\text{CV}} - E_{\text{valence}}$, both in the same wCVXZ-DK+ basis sets (X = T and Q), extrapolated to the CBS limit using Eq. (2).

Spin orbit (SO) contributions, ΔE_{SO} , were calculated using full 4-component Dirac-Hartree-Fock (DHF) Kramers-restricted configuration interaction (KRCI)⁵¹ with the Dirac-Coulomb Hamiltonian and uncontracted VTZ-DK3+ basis sets. The spin-free Hamiltonian of Dyall⁵² in an analogous multireference CI (MRCI)⁵³ was used for comparison. The contributions from the 2-electron Gaunt term, ΔE_{Gaunt} , were obtained at the 4-component DHF/VTZ-DK3+ level with the Dirac-Coulomb-Gaunt Hamiltonian. The DHF calculations utilized average-of-configuration DHF orbitals involving 2-3 electrons in the 10 spinors arising from the 6d orbitals for Th/Th⁻ and 4-5 electrons in the 24 spinors arising from the 5f and 6d orbitals for U/U⁻. The KRCI/MRCI calculations for Th and Th⁻ utilized three GAS (generalized active-space) spaces involving single excitations from the 6p and singles and doubles from the 7s and 6d orbitals. In the cases of U and U⁻, an additional GAS space was added that included singles and doubles from the 5f orbitals. A virtual orbital cutoff of 10.0 au. was used throughout. All SO and Gaunt calculations for Eq. (3) were carried out using the DIRAC program.⁵⁴

ΔE_{Lamb} is a contribution for the Lamb shift or quantum electrodynamic effects (QED). In this work, the local potential approach of Pyykkö has been used for both the vacuum polarization and self-energy contributions.^{35,55} These calculations were carried out with the MOLPRO program at the FC-CCSD(T) level of theory with the wCVDZ-DK+ basis sets and DKH3 Hamiltonian.

The next two terms, ΔE_T and ΔE_Q , account for valence electron correlation effects beyond the CCSD(T) level of theory. The ΔE_T term is defined as the difference between CCSDT and CCSD(T) in the VTZ-DK3+ basis set with the DKH3 Hamiltonian.^{56,57} The effect of quadruple excitations, ΔE_Q , was defined as the difference between CCSDT(Q)^{58,59} and CCSDT using truncated VTZ-DK+ basis sets, where the diffuse g and h functions were not included. Calculations were also carried out on Th/Th⁻ using full iterative CCSDTQ with the smaller VDZ-DK3+ basis set, and this yielded

an EA smaller by just 0.05 kcal/mol (0.002 eV) compared to CCSDT(Q) with the same basis. In the case of thorium, it was possible to also include the approximate effects of pentuple excitations, ΔE_P , as the difference between CCSDTQ(P)⁶⁰ and CCSDTQ^{61,62} calculations with a truncated VDZ-DK3+ basis set (the diffuse g was deleted). The MRCC program⁶³ as interfaced to MOLPRO was used for all the higher-order electron correlation calculations.

Results and Discussion

Experimental

The negative ions observed due to laser ablation of a depleted uranium target rod are presented in the mass spectrum shown in Figure III.B.1.1. In addition to anions of the various uranium oxides, a weak intensity of the uranium atomic anion, U^- , was also observed.

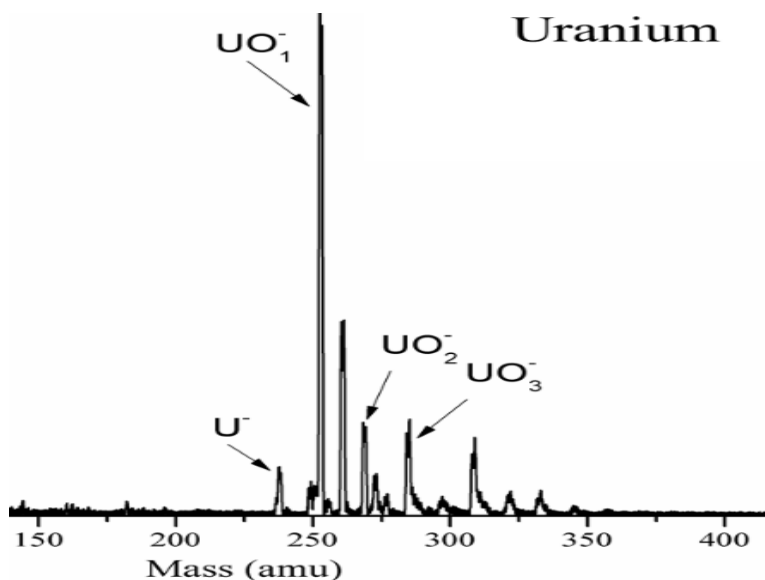


Figure III.B.1.1 Mass spectrum resulting from laser vaporization of a depleted uranium target.

The photoelectron spectrum of mass-selected uranium atomic anions was measured at two photon energies of a Nd:YAG laser and with two different types of electron energy analyzers: at the third harmonic (355 nm, 3.49 eV) using our magnetic bottle (MB) spectrometer and at the first harmonic (1064 nm, 1.16 eV) using our velocity-map imaging (VMI) spectrometer. Figures III.B.1.2 and III.B.1.3 present these spectra, respectively. Neither of these U^- spectra exhibit leakage from UH^- photoelectron spectra nor do they exhibit transitions from potentially long-lived excited U^- anion states. We have separately measured the photoelectron spectrum of UH^- and have found that its

strongest peaks are concentrated between $\text{EBE} = 0.5$ and 1.0 eV. That is a relatively quiet spectral region in both Figs. III.B.1.2 and III.B.1.3, and there is nothing above the noise level in that region, thus showing that there is no measurable leakage of UH^- into the photoelectron spectrum of U^- . In addition, our computational results (see Table III.B.1.1) predict the lowest-lying $7p$ (excited) state to lie above the ground state of U^- by 84 meV. Based on our measured value of $\text{EA}(\text{U})$, this implies a photoelectron transition at $\text{EBE} = 225$ meV. This of course is predicated on that particular excited anion state being populated and being long-lived enough to reach a photodetachment interaction region. A second excited anion state is also expected to exist above this first one, implying a photoelectron transition at an even lower EBE. Neither putative excited state transitions are apparent in our photoelectron spectra. In Fig. III.B.1.2, which exhibits lower

resolution than the spectrum in Fig. III.B.1.3, the spectral width of the main peak would obscure their presence if they were to be there, whereas in Fig. III.B.1.3, there is nothing above the noise level in the subject spectral regions, with these observations implying that excited anion transitions do not play a significant role in those spectra. For atomic anions with no electronic hot bands, the electron binding energy (EBE) at the intensity maximum of the lowest-lying EBE peak corresponds to the electron affinity (EA) of the atom, where the EA is defined as the energy difference between the ground state of the anion and the ground state of its neutral counterpart.

The electron binding energy of the fitted intensity maximum of the lowest EBE peak in Fig. III.B.1.2 is located at 0.290 eV, with this corresponding to the electron affinity of the uranium atom. Based on the instrumental resolution of our magnetic bottle analyzer at the electron kinetic energy of the lowest EBE peak and on its FWHM, we assign an error ± 0.100 eV to this measurement. Beyond the lowest EBE peak, the higher EBE peaks in this spectrum are due to photodetachment transitions from the ground state of the uranium atomic anion to the many electronic excited states of the neutral uranium atom. The previously unknown spectrum of U^- in Fig. III.B.1.2 is what the U^- photoelectron spectrum looks like over the reported EBE range and at the resolution of our magnetic bottle analyzer. The transitions observed in this spectrum are also compared with the NIST atomic levels for the uranium atom in Fig. S1 of the supplementary material. While the NIST transitions are from optical spectra, our photoelectron spectrum recovers dark states as well.

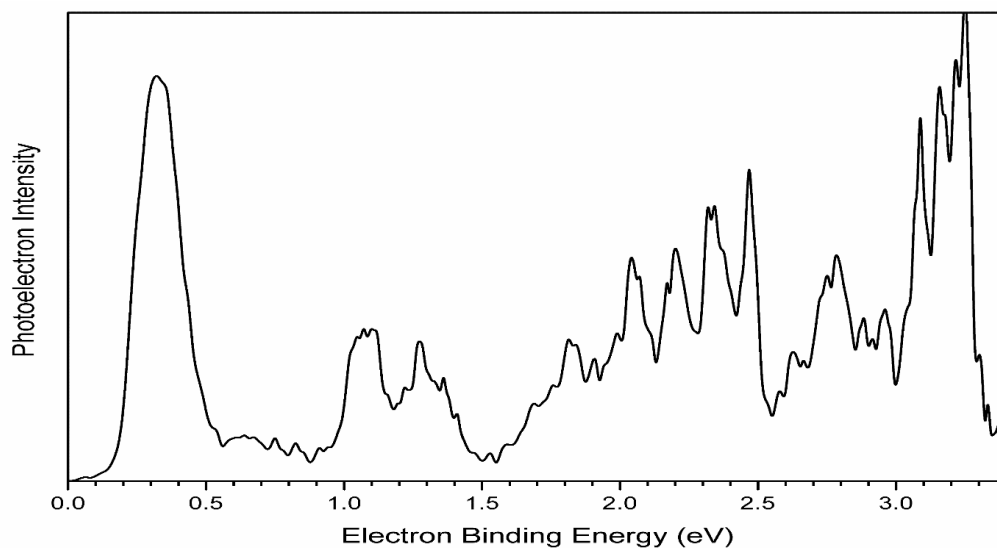
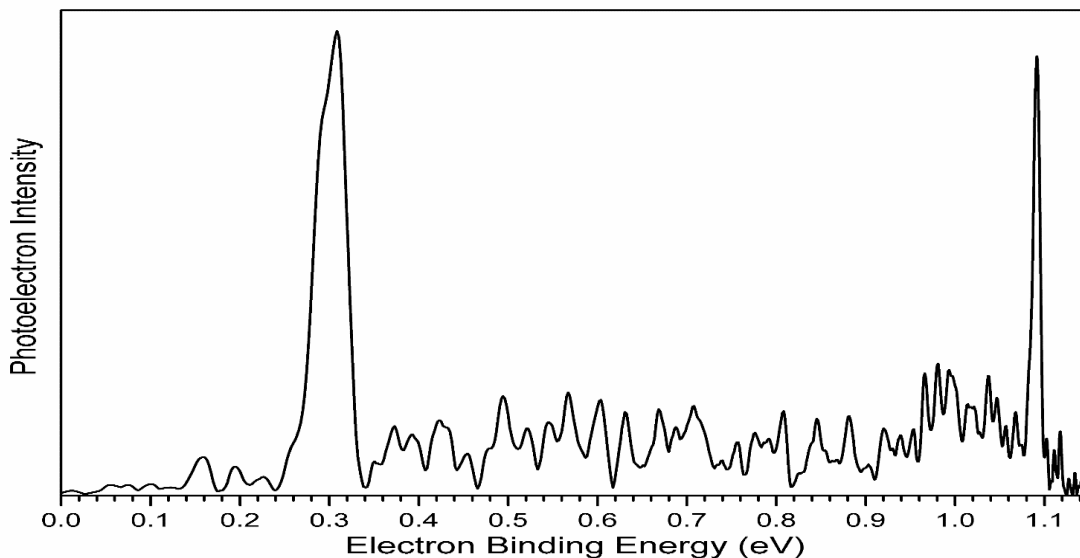


Figure III.B.1.2 Photoelectron spectrum of the uranium atomic anion (U^-) measured with the third harmonic of an Nd:YAG laser (355 nm, 3.49 eV) and our magnetic bottle (MB) electron energy analyzer.

The electron binding energy of the fitted intensity maximum of the lowest EBE peak in Fig. III.B.1.3 is located at 0.309 eV, with this corresponding to the photodetachment transition from the ground electronic state of the uranium atomic anion to the ground electronic state of the neutral uranium atom and thus to the electron affinity of the uranium atom. While the signal-to-noise ratio in Fig. III.B.1.3 is lower than that in Fig. III.B.1.2, the resolution of the VMI analyzer is significantly higher than that of the MB analyzer. Based on the instrumental resolution of our VMI electron energy analyzer and the FWHM of the lowest EBE peak, we assign an error of ± 0.025 eV to this measurement. Beyond the lowest EBE peak at $\text{EBE} = 0.309$ eV, there is a higher EBE peak at $\text{EBE} = 1.091$ eV. This is the

photodetachment transition from the electronic ground state of the uranium atomic anion to the first electronically excited state of the neutral uranium atom corresponding to an s electron detachment. While all atomic



photodetachment transitions are

Figure III.B.1.3 Photoelectron spectrum of the uranium atomic anion (U^-) measured with the first harmonic of an Nd:YAG laser (1064 nm, 1.16 eV) and our velocity-map imaging (VMI) electron energy analyzer.

inherently narrow, this peak is sharper than the origin-containing (lowest EBE) peak because instrumental resolution is better for transitions at lower electron kinetic energies. The energy difference between this well-defined peak and the lowest EBE peak is the energy splitting between the ground state of the neutral uranium atom ($^5L_6^o$), having the configuration $5f^3(^4I^o)6d7s^2$, and the $5f^3(^4I^o)6d^2(^2F)7s$ ($^7M_6^o$) excited state of the neutral uranium atom. According to NIST, CNRS, and NBS energy level tables,⁶⁴⁻⁶⁶ this energy separation is 6249 cm^{-1} or 0.775 eV . In Fig. III.B.1.3, this splitting, i.e., $1.091 \text{ eV} - 0.309 \text{ eV}$, is 0.782 eV , well within the stated error bar. One of our VMI (raw) images is shown in Figure S2 (in the Supplementary Material).

The electron affinity of the uranium atom, $\text{EA}(\text{U})$, was determined to be $0.290 \text{ eV} \pm 0.100 \text{ eV}$, using the magnetic bottle electron energy analyzer and $0.309 \text{ eV} \pm 0.025 \text{ eV}$, using the VMI electron energy analyzer. While both of these measurements are consistent with one another, the VMI determination is easily the more accurate of the two, leading to $0.309 \text{ eV} \pm 0.025 \text{ eV}$ as our reported value for the electron affinity of the uranium atom.

MRCI calculations of the electron affinities of Th and U

Table III.B.1.1 shows the results of the CMRCI+Q calculations for the electron affinities of both uranium and thorium. In each case, the ground state of the anion involves electron attachment to the 6d orbital rather than the 7p, in agreement with most previous studies. Without inclusion of spin-orbit effects, electron attachment to the 7p orbital is unstable in both cases. Clearly, the electron affinity of thorium is much larger than that of uranium, 13.5 kcal/mol (0.585 eV) vs. 3.9 kcal/mol (0.169 eV), before SO effects are accounted for. As expected, SO has the largest effect on the electron binding to the 7p orbital, which results in the 7p-attached states being stable with respect to loss of an electron. For Th^- , the $6d^27s^27p^1$ ($^4G_{5/2}^o$) state is still higher in energy than the ground $6d^37s^2$ ($^4F_{3/2}$) state by 5.8 kcal/mol (0.25 eV) at this level of theory. The previous calculations of Tang et al.²⁹ using the multi-configurational Dirac Hartree Fock (MCDHF) method predicted a much smaller energy difference of just 1.1 kcal/mol (0.048 eV). In the case of U^- , the calculations of this work predict that the $5f^36d^17s^27p^1$ ($^6M_{13/2}$) state lies higher than the $5f^36d^27s^2$ ($^6M_{13/2}^o$) by 1.9 kcal/mol (0.082 eV). From the MCDHF calculations of O'Malley and Beck, an additional 7p state of U^- , the $^6L_{11/2}$, may lie slightly below the detachment threshold, but if their relative energy between the $^6M_{13/2}$ and $^6L_{11/2}$ states (182 meV) is applied to the results of the current work, it would lie well above the threshold. At the present FC-MRCI+Q/CBS + SO level of theory, the EA values for Th and U are both smaller with respect to experiment by about 2 kcal/mol (~90 meV).

Table III.B.1.1 CMRCI+Q calculations of the electron affinities of Th and U (in kcal/mol with meV in parentheses).

Atom	Anion State	VTZ-DK+	VQZ-DK+	CBS	CBS+SO
Th	$^4F_{3/2}$ ($6d^37s^2$)	12.78	13.22	13.47	11.94 (518)
	$^4G_{5/2}^o$ ($6d^27s^27p^1$)	-1.23	-1.27	-1.29	6.12 (265)
U	$^6M_{13/2}^o$ ($5f^36d^27s^2$)	3.35	3.72	3.93	4.80 (208)

	${}^6M_{13/2} (5f^8 6d^1 7s^2 7p^1)$	-2.82	-2.90	-2.94	2.86 (124)
--	--------------------------------------	-------	-------	-------	---------------

Composite coupled cluster results for the Th and U electron affinities

The individual energy contributions to the electron affinities of both thorium and uranium, within the coupled cluster FPD scheme, are presented in Table III.B.1.2. These calculations focus only on the ground states of the atoms, neutral and anion. Overall, the contributions not involving SO coupling are remarkably similar between the two atoms. In both cases the FC-CCSD(T) electron affinities are well converged with respect to the basis set at the QZ level. Upon comparison to Table III.B.1.1, CMRCI+Q and CCSD(T) differ at their FC CBS limits by 1.1 kcal/mol (48 meV) and 1.4 kcal/mol (61 meV) for Th and U, respectively, with the CMRCI+Q values being smaller in both cases. It should be noted that the CCSD(T) calculations on U and U^- were very sensitive to the specific symmetry-broken electronic states chosen for the ROHF calculations. While the various coupled cluster diagnostics, e.g., the T_1 diagnostic (0.023 for U and 0.042 for U^-), didn't reflect strong multireference character, the resulting energies were very sensitive to these choices with resulting EAs differing by many kcal/mol. In the present calculations, the states chosen and used throughout corresponded to those giving the lowest CCSD(T) total energies with the VTZ-DK+ basis set. An additional cautionary indicator in the CCSD calculations for U was the relatively large value of two doubles amplitudes, 0.127, whereas there were no doubles amplitudes above 0.056 for any of the other atoms. Correlation of the 5s, 5p, and 5d electrons with CCSD(T) reduces the electron affinities of both Th and U by just over 1 kcal/mol (43 meV). Curiously, in the recent MCDHF calculations of Tang et al.²⁹ for the EA of thorium, where agreement with experiment to within 0.2 kcal/mol (8 meV) was presented, correlation of these electrons were not included. Hence this excellent agreement may have been somewhat fortuitous. In the present work, inclusion of spin-orbit coupling, including small effects due to the Gaunt interaction, decreases the electron affinity of thorium by about 1 kcal/mol (43 meV), while in the case of uranium, inclusion of spin-orbit coupling increases the EA by a little more than 1 kcal/mol. (43 meV). The effects of the Lamb shift is identical in both cases and raises their electron affinities by just 0.3 kcal/mol (13 meV). Valence correlation effects beyond CCSD(T) are calculated to be very modest with a well-behaved convergence for the EA of Th; the values of ΔE_T , ΔE_Q , and ΔE_P for its EA were calculated to be just -0.4, +0.7, and +0.1 kcal/mol. (-17, +30, and +4 meV), respectively. In the case of uranium, the values of ΔE_T and ΔE_Q were also calculated to be small,

−0.4 and 0.0 kcal/mol, (−17 meV and 0 meV) respectively, but the CCSDT calculations suffered from very poor convergence, particularly for the anion calculations. Convergence could not be achieved for CCSDTQ, which prevented the use of CCSDTQ(P) for this atom. In addition, while the incremental correlation energy recovery was smoothly converging in Th and Th[−] as the coupled cluster sequence increased in order, e.g., in Th[−] the values of ΔE_T , ΔE_Q , and ΔE_P were −0.79, +0.50, and −0.19 mE_h, respectively, the values of ΔE_T and ΔE_Q for U[−] were much larger at −6.05 and −7.03 mE_h, respectively. This suggests that the coupled cluster sequence for the U EA is clearly not converged.

Table III.B.1.2 Calculated contributions to the electron affinities (in kcal/mol) within the coupled cluster FPD scheme.

See Eq. (3) for details. Values in meV are given in parentheses.

Atom	E _{wCVQZ-DK+}	ΔE_{CBS}	ΔE_{CV}	ΔE_{SO}	ΔE_{Gaunt}	ΔE_{Lamb}	ΔE_T	ΔE_Q	ΔE_P	E _{FPD}	Expt.
Th	14.26	+0.29	-1.17	-1.30	+0.28	+0.28	-0.37	+0.69	+0.08	13.04	14.01 ^b
	(618)	(+13)	(-51)	(-56)	(+12)	(+12)	(-16)	(+30)	(+3)	(565)	(608) ^b
U	5.06	+0.25	-1.13	+1.14	+0.14	+0.28	-0.42	+0.01	---	5.34	7.13 ^c
	(219)	(+11)	(-49)	(+49)	(+6)	(+12)	(-18)	(+0.4)	---	(232)	(309) ^c

^a The corresponding average-of-configuration DHF values were -1.66 and +0.14 kcal/mol (−71 and +6 meV) for Th and U, respectively.

^b Photoelectron imaging value of Ref. 29, 14.0137 ± 0.0014 kcal/mol (607.692 ± 0.061 meV).

^c This work, 7.13 ± 0.58 kcal/mol (309 ± 25 meV)

The final FPD electron affinity value for thorium, 13.04 kcal/mol (565 meV), is smaller than the accurate experimental value by just under 1 kcal/mol (43 meV). Note that if the CV contribution is omitted, nearly perfect agreement with experiment is achieved (616 vs. 608 meV), which is consistent with the previous work of Tang et al.²⁹ Given the extensive correlation treatment and reliability of coupled cluster for Th/Th[−], the likely largest source of error is the treatment of SO coupling, which was carried out at the KRCI level of theory. It should be noted that correlation effects

on the SO contribution raised the electron affinity for both thorium and uranium. The final electron affinity for uranium, 5.34 kcal/mol (232 meV), is presumably also under-estimated due to a similar treatment of SO, but is also expected to suffer larger errors due to a less accurate treatment of electron correlation effects. In fact, the EA_{FPD} value of 5.34 kcal/mol (232 meV) is indeed lower than the electron affinity value that was determined experimentally in this work (7.13 kcal/mol or 309 meV) by 1.8 kcal/mol (77 meV), and this is nearly twice as large as the analogous difference for the Th EA. Similar to the Th^- case, if the CV contribution is omitted, the resulting EA (281 meV) is in much better agreement with experiment. The most accurate previous calculation of the EA of U, the relativistic MRCI calculations of O'Malley and Beck²⁸, yielded a 6d attachment EA of 260 meV (6.00 kcal/mol), which is in better agreement with the present experimental value, but as with the Th EA calculations of Tang et al.²⁹, the work of O'Malley and Beck did not correlate the 5d electrons but in addition they also neglected correlation of the 6p electrons. This could be why the latter work also incorrectly (according to this work) predicted the ground state of U^- to correspond to a 7p attachment with an EA of 373 meV (8.60 kcal/mol). Their calculations had similar problems with the EA of Th atom, predicting a 7p attachment EA of 368 meV and a 6d attachment EA of 304 meV. The latter is in error relative to the accurate experiment of Tang et al.²⁹ by a factor of 2.

Conclusions

The electron affinity of the uranium atom has been determined as $0.309 \text{ eV} \pm 0.025 \text{ eV}$ using anion photoelectron spectroscopy. Extensive MRCI calculations predict that the electron affinity corresponds to an electron attachment to the 6d orbital rather than to the 7p, which is similar to the Th atom case. Even though the composite coupled cluster method used in this work was not deemed as accurate for the EA of U as for Th, the final calculated value of 232 meV was still in better agreement with the new experimental value compared to calculations based on MRCI. The EA of U represents a significant challenge for relativistic correlation methods. The analogous coupled-cluster-based result for the EA of Th in this work, 565 meV, differed from experiment by just 43 meV, where most of the residual error is proposed to arise from incomplete recovery of SO effects.

REFERENCES

1. J. K. Gibson, *Int. J. Mass Spectrom.* **214**, 1 (2002).
2. B. Johansson, *Phys. Rev. B* **11**, 2740 (1975).
3. M. O. Krause, R. G. Haire, O. Keski-Rahkonen, and J. R. Peterson, *J. Electron Spectrosc.* **47**, 215 (1988).
4. F. David, K. Samhoun, R. Guillaumont, and N. Edelstein, *J. Inorg. Nucl. Chem.* **40**, 69 (1978).
5. R. G. Haire, *J. Alloys Compd.* **223**, 185 (1995).

6. L. Petit, A. Svane, W. M. Temmerman, and Z. Szotek, *Solid State Commun.* **116**, 379 (2000).
7. B. Johansson and H. L. Skriver, *J. Magn. Magn. Mater.* **29**, 217 (1982).
8. P. G. Huray, S. E. Nave, and R. G. Haire, *J. Less-Common Met.* **93**, 293 (1983).
9. K. Wendt, T. Gottwald, C. Mattolat, and S. Raeder, *Hyperfine Interact.* **227**, 55 (2014).
10. T. Moeller, *J. Chem. Educ.* **47**, 417 (1970).
11. N. M. Edelstein and L. R. Morss, *Radiochemistry and Nucl. Chem.*, Vol. II, 118 (2009).
12. L. R. Morss, N. M. Edelstein, and J. Fuger, *The Chemistry of the Actinide and Transactinide Elements* (Springer, Dordrecht, 2010).
13. J. J. Katz and E. Rabinowitch, *The Chemistry of Uranium* (McGraw-Hill, New York, 1951).
14. B. Villemant, in *Elements: Actinide Series in Geochemistry. Encyclopedia of Earth Science* (Springer, Dordrecht, 1998).
15. P. C. Burns and R. Finch, in *Uranium: Mineralogy, Geochemistry and the Environment* in Eds. Mineralogical Society of America, Washington, DC, 1999.
16. J. G. Hamilton, *Rev. Mod. Phys.* **20**, 718 (1948).
17. E. S. Craft, A. W. Abu-Qare, M. M. Flaherty, M. C. Garofolo, H. L. Rincavage, and M. B. Abou-Donia, *J. Toxicolo. Env. Heal. B* **7**, 297 (2010).
18. J. Marcalo and J. K. Gibson, *Handbook on the Physics and Chemistry of Rare Earths* (Elsevier, Amsterdam, 2014).
19. H. L. Skriver, O. K. Andersen, and B. Johansson, *Phys. Rev. Lett.* **41**, 42 (1978).
20. G. R. Hertel, *J. Chem. Phys.* **47**, 335 (1967).
21. W. Potzel, J. Moser, L. Asch, and G. M. Kalvius, *Hyperfine Interact.* **13**, 175 (1983).
22. S. Cotton, *Lanthanide and Actinide Chemistry* (John Wiley and Sons, Ltd., West Sussex, 2006).
23. Y. Guo and M. A. Whitehead, *Phys. Rev. A* **40**, 28 (1989).
24. S. G. Bratsch and J. J. Lagowski, *Chem. Phys. Lett.* **107**, 136 (1984).
27. K. Dinov and D. Beck, *Phys. Rev. A* **52**, 2632 (1995).
28. S.M. O'Malley and D.R. Beck, *Phys. Rev. A* **80**, 172 (2009).
29. R. Tang, R. Si, Z. Fei, X. Fu, Y. Lu, T. Brage, H. Liu, C. Chen, and C. Ning, *Phys. Rev. Lett.* **123**, 203002 (2019).
30. G. Liu, S. M. Ciorowski, and K. H. Bowen, *J. Phys. Chem. A* **121**, 5817 (2017).
31. J. Ho, K. M. Ervin, and W. C. Lineberger, *J. Chem. Phys.* **93**, 6987 (1990).
32. M. J. Travers, D. C. Cowles, and G. B. Ellison, *Chem. Phys. Lett.* **164**, 449 (1989).
33. K.R. Shamasundar, G. Knizia, and H.-J. Werner, *J. Chem. Phys.* **135**, 054101 (2011).
34. S.R. Langhoff and E.R. Davidson, *Int. J. Quantum Chem.* **8**, 61 (1974).
35. K. A. Peterson, *J. Chem. Phys.* **142**, 074105 (2015); R. Feng and K.A. Peterson, *J. Chem. Phys.* **147**, 084108 (2017).
36. M. Douglas and N. M. Kroll, *Ann. Phys.* **82**, 89 (1974).
37. M. Reiher and A. Wolf, *J. Chem. Phys.* **121**, 10945 (2004).
38. A. Karton and J. M. L. Martin, *Theor. Chem. Acct.* **115**, 330 (2006).
39. J. M. L. Martin, *Chem. Phys. Lett.* **259**, 669 (1996).
40. A. Berning, M. Schweizer, H.-J. Werner, P. J. Knowles, and P. Palmieri, *Mol. Phys.* **98**, 1823 (2000).
41. D. Feller, K. A. Peterson, and D. A. Dixon, *J. Chem. Phys.* **129**, 204105 (2008).
42. K. A. Peterson, D. Feller, and D. A. Dixon, *Theor. Chem. Acc.* **131**, 1 (2012).
43. D. A. Dixon, D. Feller, and K. A. Peterson, *Annual Reports in Computational Chemistry*, Vol. 8, 1 (Elsevier, Amsterdam, 2012).
44. D. Feller, K. A. Peterson, and D. A. Dixon, *Mol. Phys.* **110**, 2381 (2012).
45. M. Vasilu, K. A. Peterson, J. K. Gibson, and D. A. Dixon, *J. Phys. Chem. A* **119**, 11422 (2015).
46. D. Feller, K. A. Peterson, and D. A. Dixon, *Annual Reports in Computational Chemistry*, Vol. 12, 47 (Elsevier, Amsterdam, 2016).
47. G. E. Scuseria, *Chem. Phys. Lett.* **176**, 27 (1991).
48. J. D. Watts, J. Gauss, and R. J. Bartlett, *J. Chem. Phys.* **98**, 8718 (1993).
49. P. J. Knowles, C. Hampel, and H. J. Werner, *J. Chem. Phys.* **99**, 5219 (1993).
50. H.-J. Werner, P. J. Knowles, G. Knizia, F. R. Manby and M. Schütz, *WIREs Comput Mol Sci* **2**, 242–253 (2012); MOLPRO, version 2019.2, a package of *ab initio* programs, H.-J. Werner, P. J. Knowles, G. Knizia, F. R. Manby, M. Schütz, P. Celani, W. Györfy, D. Kats, T. Korona, R. Lindh, A. Mitrushenkov, G. Rauhut, K. R. Shamasundar, T. B. Adler, R. D. Amos, S. J. Bennie, A. Bernhardsson, A. Berning, D. L. Cooper, M. J. O. Deegan, A. J. Dobyn, F. Eckert, E. Goll, C. Hampel, A. Hesselmann, G. Hetzer, T. Hrenar, G. Jansen, C. Köppl,

- S. J. R. Lee, Y. Liu, A. W. Lloyd, Q. Ma, R. A. Mata, A. J. May, S. J. McNicholas, W. Meyer, T. F. Miller III, M. E. Mura, A. Nicklass, D. P. O'Neill, P. Palmieri, D. Peng, K. Pflüger, R. Pitzer, M. Reiher, T. Shiozaki, H. Stoll, A. J. Stone, R. Tarroni, T. Thorsteinsson, M. Wang, and M. Welborn, see <https://www.molpro.net>.
51. T. Fleig, J. Olsen, and L. Visscher, *J. Chem. Phys.* **119**, 2963 (2003).
 52. K. G. Dyall, *J. Chem. Phys.* **100**, 2118 (1994).
 53. J. Olsen, P. Jørgensen, and J. Simons, *Chem. Phys. Lett.* **169**, 463 (1990).
 54. DIRAC, a relativistic ab initio electronic structure program, Release DIRAC19 (2019), written by A. S. P. Gomes, T. Saue, L. Visscher, H. J. Aa. Jensen, and R. Bast, with contributions from I. A. Aucar, V. Bakken, K. G. Dyall, S. Dubillard, U. Ekström, E. Eliav, T. Enevoldsen, E. Faßhauer, T. Fleig, O. Fossgaard, L. Halbert, E. D. Hedegård, T. Helgaker, B. Helmich-Paris, J. Henriksson, M. Iliaš, Ch. R. Jacob, S. Knecht, S. Komorovský, O. Kullie, J. K. Lærdahl, C. V. Larsen, Y. S. Lee, H. S. Nataraj, M. K. Nayak, P. Norman, G. Olejniczak, J. Olsen, J. M. H. Olsen, Y. C. Park, J. K. Pedersen, M. Pernpointner, R. Di Remigio, K. Ruud, P. Sałek, B. Schimmelpfennig, B. Senjean, A. Shee, J. Sikkema, A. J. Thorvaldsen, J. Thyssen, J. van Stralen, M. L. Vidal, S. Villaume, O. Visser, T. Winther, and S. Yamamoto (see <http://www.diracprogram.org>).
 55. P. Pyykkö and L.-B. Zhao, *J. Phys. B: At., Mol. Opt. Phys.* **36**, 1469 (2003).
 56. J. Noga and R. J. Bartlett, *J. Chem. Phys.* **86**, 7041 (1987).
 57. J. D. Watts and R. J. Bartlett, *J. Chem. Phys.* **93**, 6104 (1990).
 58. T. D. Crawford and J. F. Stanton, *Int. J. Quantum Chem.* **70**, 601 (1998).
 59. S. A. Kucharski and R. J. Bartlett, *J. Chem. Phys.* **108**, 5243 (1998).
 60. M. Kallay and J. Gauss, *J. Chem. Phys.* **123**, 214105 (2005).
 61. S. A. Kucharski and R. J. Bartlett, *Theor. Chim. Acta* **80**, 387 (1991).
 62. N. Oliphant and L. Adamowicz, *J. Chem. Phys.* **94**, 1229 (1991).
 63. MRCC, A quantum chemical program suite (See also Z. Rolik, L. Szegedy, I. Ladjánszki, B. Ladóczki, and M. Kállay, "An Efficient Linear-Scaling CCSD(T) Method Based on Local Natural Orbitals," *J. Chem. Phys.* **139** (2013) 094105, as well as: www.mrcc.hu).
 64. National Institute of Standards and Technology, 2013, Handbook of Basic Atomic Spectroscopic Data, NIST Standard Reference Database 108, NIST, Gaithersburg, MD. <https://www.nist.gov/pml/handbook-basic-atomic-spectroscopic-data> (accessed Jan. 11, 2021).
 65. J. Blaise and J.F. Wyart, Selected Constants Energy Levels and Atomic Spectra of Actinides (Centre National de la Recherche Scientifique, 1992); <http://www.lac.u-psud.fr/old-lac/lac/Database/Contents.html> (accessed Jan. 11, 2021).
 66. C.C. Kiess, C.J. Humphreys and D.D. Laun, *J. Res. Nat. Bur. Stand.* **37**, 57 (1946).
 67. Q. Lu and K.A. Peterson, *J. Chem. Phys.* **145**, 054111 (2016).
 68. B.A. Finney and K.A. Peterson, *J. Chem. Phys.* **151**, 024303 (2019); *ibid* **151**, 159901 (2019).

III.B.2. Anion Photoelectron Spectroscopic and Relativistic Coupled- Cluster Studies of Uranyl Dichloride Anion, UO_2Cl_2^-

Reprinted with permission from Elsevier. *J. Mol. Spec.* 379, 111496, (2021).

Mary Marshall, Zhaoguo, Junzi Liu, Kit H. Bowen,^{a)} and Lan Cheng

Department of Chemistry, The Johns Hopkins University, Baltimore, MD 21218, USA

Abstract

A joint relativistic coupled-cluster and experimental photoelectron (PE) spectroscopic study of the uranyl dichloride anion, UO_2Cl_2^- , is reported. Sophisticated electronic-structure calculations predict the photodetachment of UO_2Cl_2^- to involve a U 5f electron and to be followed by significant geometry relaxation. Therefore, the adiabatic electron affinity (EA_a) of the uranyl dichloride neutral molecule, UO_2Cl_2 , and the vertical detachment energy (VDE) of its anion, UO_2Cl_2^- , provide valuable information about its uranium 5f orbital energies. The EA_a value was computed to be 3.15 eV. The VDE value was calculated to be 3.55 eV by augmenting the computed EA_a with a shift derived from a Franck–Condon simulation using coupled-cluster potential energy surfaces. The VDE, which corresponds to the highest intensity peak in the PE spectrum, was measured to be 3.69 ± 0.20 eV, in good agreement with the computed value. The origin transition in the PE spectrum, whose electron binding energy corresponds to the EA_a , was assigned to the feature at 3.2 ± 0.20 eV, consistent with the computed EA_a .

Introduction

The chemistry of the uranyl ion $[\text{O-U-O}]^{2+}$, an important building block in many uranium compounds, is among the central topics of actinide chemistry ^{[1], [2], [3], [4]}. For example, uranyl-containing molecules play important roles in uranium separation science. In the plutonium uranium redox extraction (PUREX) process, a standard nuclear reprocessing method, uranium is extracted as uranyl nitrate coupled to the tributylphosphate extractant ^[5]. The uranyl ion comprises two strong uranium–oxygen bonds and forms relatively weak bonds with ligands in many important uranium species, e.g., the $\text{UO}_2\text{Cl}_4^{2-}$ formal dianion in the $\text{Cs}_2\text{UO}_2\text{Cl}_4$ crystal consists of a uranyl ion weakly coupled to four chlorines. Understanding the interactions between the uranyl ion with ligands thus is of fundamental importance.

Numerous experimental and theoretical efforts ^[6-60] have been devoted to study of the uranyl ion, resulting in a better understanding of many aspects of uranyl-containing molecules. Experimental studies of electronic and vibrational spectra of UO_2Cl_2 , the target molecule of the present study, have been reported in non-aqueous solvents ^[8], in its

crystal structure ^[10], and in noble gas matrices ^[15]. Based on the measured absorption and emission spectra, the structures of UO_2Cl_2 in solvents were found to be similar to those of crystalline uranyl salts. Heaven et al. studied UO_2Cl_2 in an argon matrix, which minimally perturbs the molecule. Through laser-induced fluorescence, the lowest energy transition observed in emission spectra occurred at 20323 cm^{-1} with nearly harmonic vibrational progressions at a frequency of 840 cm^{-1} ^[15]. This is similar to transitions seen in uranyl salts in the condensed phase and in solution ^{[2], [8]}. The dominant vibrational progression is due to the U-O symmetric stretch. The O-U-O angle was found to be slightly bent, i.e., to be around 168 degree, in the normally linear UO_2^{2+} . Minor discrepancies between measured vibrational frequencies for the O-U-O symmetric bending mode and calculations of gas-phase molecules were attributed to van der Waals repulsion between the oxygen atoms and the argon matrix ^[15].

When a uranyl-containing anion differs from the corresponding neutral molecule by a uranium 5f electron, e.g., UO_2Cl_2^- is formed by adding a 5f electron to UO_2Cl_2 , the adiabatic electron affinity of the neutral molecule provides direct information about its uranium 5f orbital energies and thus is of fundamental interest. Wang and collaborators have reported the measurements of the electron affinities for uranium oxides UO_n , with $n=1-5$ ^{[23], [61], [62]}. The adiabatic electron affinity value of UO_2 was accurately determined to be $1.1688(6)\text{ eV}$ ^[62]. With two unpaired 5f electrons already present in UO_2 , however, the electron affinity of UO_2 is expected to differ substantially from those of uranyl-containing molecules. On the other hand, because of the remarkable stability of the uranyl ion, UO_3 , UO_4 , and UO_5 can in general be considered as having a uranyl ion bonded with the other oxygen atoms. The variation of the measured electron affinity values of 1.12 eV , 3.60 eV , and 4.02 eV for UO_3 , UO_4 , and UO_5 ^[23] reflect the effects of the bonding with the additional oxygen atoms on the uranyl 5f orbital energies. Wang and collaborators have also reported photoelectron spectroscopic studies of uranyl tetrahalide dianions, $\text{UO}_2\text{X}_4^{2-}$ ($\text{X} = \text{F}$ or Cl) ^[20], and uranyl trihalide anions, UO_2X_3^- ($\text{X} = \text{F}, \text{Cl}, \text{Br}, \text{or I}$) ^[21]. These photoelectron spectra provided detachment energies for the corresponding uranyl-containing systems involving electrons in the U-O bonding orbital or from the ligands.

In this paper we report a joint experimental and computational study of the photoelectron spectrum of the uranyl dichloride anion, UO_2Cl_2^- , aiming to discern the adiabatic electron affinity (EA_a) for the uranyl dichloride molecule, UO_2Cl_2 , and the vertical detachment energy (VDE) of its anion, UO_2Cl_2^- . Relativistic exact two-component coupled-cluster (CC) calculations were performed to predict the EA_a value of UO_2Cl_2 and the VDE value of UO_2Cl_2^- to guide the analysis of its complex anion photoelectron spectrum.

Experimental Details

The experiments were conducted using a laser vaporization source with our anion photoelectron spectrometer, which has described previously [63]. Briefly, a depleted uranium rod was used as the laser vaporization target. A backing gas consisting of 0.5% HCl and 0.5% O₂ in He was simultaneously expanded over the surface of the rod. The resulting anions were extracted and analyzed using a time-of-flight mass spectrometer. Fig. III.B.2.1 presents a mass spectrum showing the variety of anions that were produced by the source, comprising uranium, oxygen, and chlorine. Since the depleted uranium rod is essentially isotopically pure U-238, the isotopic pattern of chlorine assisted in assigning the anions to their corresponding mass peaks. The mass peaks at 340, 342, and 344 amu are UO₂Cl₂⁻ and follow the predicted isotopic pattern of the anion. Two other anions (UO₂Cl₂H⁻ and UCl₃⁻) also contribute to the mass spectrum in the 340 to 350 amu range.

The photoelectron spectra (PES) of UO₂Cl₂⁻ were obtained by photodetaching the 340 amu anion since it has the highest intensity. The UO₂Cl₂⁻ anions were mass selected, decelerated, and crossed with a fixed frequency photon beam, 355 nm (3.49 eV) and 266 nm (4.66 eV) Nd:YAG laser. The resultant detached electrons were energy-analyzed using a magnetic bottle energy analyzer. The time of flight spectrum is converted to electron binding energy using the Levenberg–Marquardt algorithm and calibrated against the known transitions of Cu⁻ [64]. The photodetachment process is governed by the energy-conserving relationship, $h\nu = \text{EKE} + \text{EBE}$, where EKE is the electron kinetic energy and EBE is the electron binding energy. The resolution of the energy analyzer is about 50 meV at EKE = 1 eV. The photoelectron spectra presented are the average of multiple spectra.

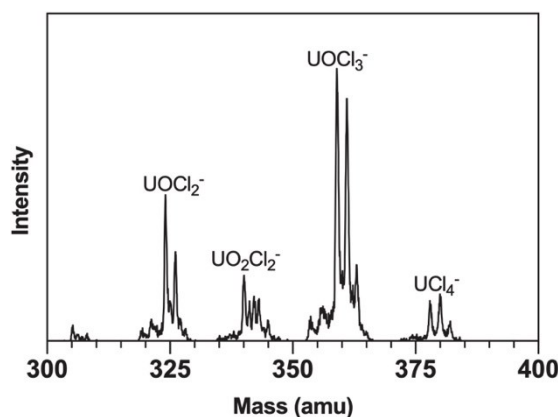


Figure III.B.2.1 The mass spectrum obtained from laser ablating a uranium rod in the presence of a 0.5% HCl and 0.5% O₂ in a He gas mixture. The UO₂Cl₂⁻ anion mass peaks occur at 340, 342, and 344 amu.

Computational Details

Given the roles of relativistic and spin-orbit effects in actinide-containing molecules and anions, calculations involving them are challenging and require high-level computational methods. In the present work, all relativistic coupled-cluster calculations were performed using the CFOUR [65], [66], [67], [68], [69], [70], [71], [72] program package. Geometry optimizations for the ground state of UO_2Cl_2 and the four lowest scalar-relativistic states of UO_2Cl_2^- were carried out at the coupled-cluster singles and doubles with noniterative triples [CCSD(T)] [73], [74] level using correlation-consistent triple-zeta (cc-pVTZ) [75], [76] basis sets. Scalar-relativistic effects were treated using the spin-free exact two-component theory in its one-electron variant (SFX2C-1e) [69], [77], [78] and cc basis sets contracted for the SFX2C-1e scheme (cc-pVXZ-X2C). The 6s, 6p, 7s, 5f electrons of U, 3s, 3p electrons of Cl, and 2s, 2p electrons of O were correlated in these calculations. SFX2C-1e equation-of-motion electron-attachment CCSD (EOMEA-CCSD) [79] calculations were also performed in the optimized structures of the anion to demonstrate the orbital composition of the unpaired electron.

The adiabatic electron affinity (EA_a) of UO_2Cl_2^- was then calculated using optimized structures for the electronic ground state of UO_2Cl_2 and UO_2Cl_2^- . SFX2C-1e-CCSD(T) calculations using uncontracted cc-pVTZ and cc-pVQZ (cc-pVTZ-unc and cc-pVQZ-unc) basis sets were carried out and the electron-correlation energies were extrapolated using a two-parameter formula [80]

$$E_{\text{corr}}[\infty Z] = E_{\text{corr}}[cc - pVXZ] - \frac{c}{X^3} \quad (1)$$

to estimate the basis-set-limit values. Since this is a detachment of a uranium 5f electron, spin-orbit (SO) coupling makes significant contribution to the detachment energy. CCSD(T)/cc-pVTZ-unc calculations in combination with exact two-component Hamiltonian [81], [82], [83] with atomic mean-field [84] spin-orbit integrals (X2CAMF) [71] were performed to obtain EA_a with non-perturbative inclusion of spin-orbit coupling. The SO correction is then obtained as the difference between X2CAMF and SFX2C-1e CCSD(T)/cc-pVTZ-unc results. The U 5d, 6s, 6p, 7s, 5f electrons, Cl 3s and 3p electrons, and O 2s and 2p electrons were correlated in these energy calculations using uncontracted basis sets, while virtual orbitals with orbital energies higher than 100 Hartree were kept frozen in the CC step. The zero-point vibrational energy (ZPE) contribution to EA_a was obtained using harmonic frequencies of UO_2Cl_2 and UO_2Cl_2^- obtained at SFX2C-1e-CCSD(T)/cc-pVTZ level by means of numerical differentiation of analytic gradients [68].

A Franck–Condon (FC) simulation of vibrational progression for the transition from the electronic ground state of UO_2Cl_2^- to that of UO_2Cl_2 was performed within the harmonic approximation at the SFX2C-1e-CCSD(T)/cc-pVTZ level. The difference between the maximal peak position of the FC spectrum and the vibrational origin transition is added to EA_a to obtain the vertical detachment energy (VDE). The computation of the FC overlap used a highly efficient implementation in the fcsquared module^[70] of the CFOUR program. The extra electron in the anion is located in a localized uranium 5f orbital, which can be well described by cc-pVTZ or cc-pVQZ basis sets. The effects of diffuse functions on the structures and energies thus are small, i.e., less than 0.005 Å for bond lengths, less than 1 degree for bond angles, and less than 0.005 eV for the adiabatic electron affinity. Therefore, we have used the cc-pVXZ, X = T, Q basis sets for uranium throughout our study.

Results and Discussion

The geometry optimization at the SFX2C-1e-CCSD(T)/cc-pVTZ level produced a C_{2v} equilibrium structure for the ground state of UO_2Cl_2 . The computed structural parameters for UO_2Cl_2^- as summarized in Table III.B.1.1 are consistent with previous computational results^{[37], [49]}. Fig. III.B.2.2 shows the four lowest electronic states of UO_2Cl_2^- and the molecular orbitals in which the unpaired electron is located. The extra electron of the UO_2Cl_2^- anion largely occupies a U 5f orbital. The presence of the additional U 5f electron introduces significant repulsion with the U-O and U-Cl bonds. Consequently, as shown in Table III.B.1.1, the U-O and U-Cl bond lengths in the anionic states are considerably longer than those in the neutral molecule. In particular, the U-Cl bond length is elongated by more than 0.15 Å. The O-U-O angle is also considerably reduced. The increase of the bond lengths is expected to weaken the U-O and U-Cl bonds. Indeed, vibrational frequencies of the UO_2Cl_2^- anion are consistently lower than those in the neutral molecule. As shown in Table III.B.1.2, the harmonic vibrational frequencies are reduced by around 10% for the symmetric U-O stretching mode and more than 20% for the symmetric U-Cl stretching mode. Even the harmonic vibrational frequency for the symmetric O-U-O bending mode is decreased by around 15%.

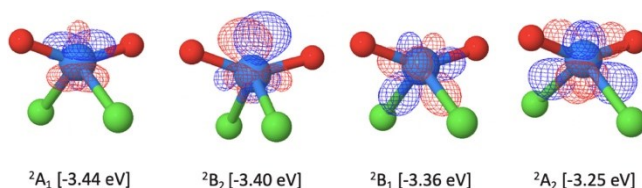


Figure III.B.2.2 Molecular orbitals in which the unpaired electrons in the lowest scalar-relativistic states of UO_2Cl_2^- are located. The O, Cl, and U atoms are colored in red, green, and cyan, respectively. The vertical electronic energy

difference with respect to the neutral molecule obtained from SFX2C-1e-EOMEA-CCSD/cc-pVTZ calculations are enclosed in the brackets.

Spin-orbit coupling tends to stabilize the 5f electron and increase the adiabatic electron affinity (EA_a). As shown in Table III.B.1.3, the SO correction to the EA_a amounts to around 0.31 eV. We mention that the basis-set error for cc-pVTZ-unc basis sets is around 0.25 eV. The computed EA_a at the SFX2C-1e-CCSD(T) level amounts to 2.582 eV for cc-pVTZ-unc basis sets, 2.727 eV for cc-pVQZ-unc basis sets, and 2.820 eV when extrapolated to estimate the basis-set-limit value. It is clearly important to take both SO correction and basis-set effects into account when conducting accurate calculations of the EA_a value of UO_2Cl_2 . The zero-point vibrational (ZPV) correction plays a relatively minor role. The ZPV contribution reduces EA_a by 0.028 eV, since the vibrational frequencies of the anion are lower than those of the neutral molecule. Altogether, these give a value of 3.153 eV for EA_a of UO_2Cl_2 . The vertical detachment energy (VDE) of $UO_2Cl_2^-$ was then obtained by adding the difference between the maximal peak position and the origin, both in the calculated FC spectrum, to the computed EA_a value. This difference, derived from Fig. III.B.2.3, has a value of 0.397 eV. The resulting computed VDE is thus 3.550 eV.

Table III.B.2.1 Structural parameters (bond lengths in Å and bond angles in degree) computed at the SFX2C-1e-CCSD(T)/cc-pVTZ level for UO_2Cl_2 and $UO_2Cl_2^-$.

		R[U-O]	R[U-Cl]	\angle [O-U-O]	\angle [Cl-U-Cl]
UO_2Cl_2	1A_1	1.755	2.531	165.8	109.5
$UO_2Cl_2^-$	2A_1	1.835	2.679	145.9	113.8
	2B_2	1.835	2.687	145.8	114.3
	2B_1	1.822	2.677	153.0	117.2
	2A_2	1.816	2.692	159.3	121.9

Table III.B.2.2 Harmonic vibrational frequencies (in cm^{-1}) computed at SFX2C-1e-CCSD(T)/cc-pVTZ level for the ground state of UO_2Cl_2 and the ground state of $UO_2Cl_2^-$.

	$UO_2Cl_2^-$	UO_2Cl_2
--	--------------	------------

a₁ (sym. Cl-U-Cl bending)	57	56
b₁ (asym. O-U-O/ Cl-U-Cl bending)	117	150
a₁ (sym. O-U-O bending)	121	206
a₂ (twisting)	193	177
b₂ (out-of-plane)	188	232
a₁ (sym. U-Cl stretching)	263	341
b₂ (asym. U-Cl stretching)	280	339
a₁ (sym. U-O stretching)	823	915
b₁ (asym. U-O stretching)	906	990

Figs. III.B.2.4(a) and b present the PES of UO_2Cl_2^- taken with a 355 nm (3.49 eV) and a 266 nm (4.66 eV) laser, respectively. The appreciable width of peak “X” ranging from 3 to 4 eV in Fig. III.B.2.4(b) signifies a significant difference between the equilibrium structures of UO_2Cl_2 and UO_2Cl_2^- . The progression observed in the photoelectron spectrum (Fig. III.B.2.4(b)) is also consistent with the vibrational progression obtained from calculations (Fig. III.B.2.3). The VDE value is the vertical photodetachment transition energy from the vibronic ground state of the anion to the electronic ground state of the neutral molecule at the geometry of its anion. This transition energy corresponds to the point of the greatest Franck–Condon vibrational overlap and is revealed in the PE spectrum by the EBE of its intensity maximum. Thus, the experimentally-determined VDE value is 3.69 eV, the EBE of the intensity maximum of the most intense peak X in the anion photoelectron spectrum shown in Fig. III.B.2.4(b). We assess an uncertainty of ± 0.20 eV. Because they are due to maximal FC overlap, experimental VDE values can be definitively determined by inspection, i.e., by locating the EBE of the intensity maximum in the ground state anion to ground state neutral photoelectron spectral band. This resulting experimentally-determined VDE value of 3.69 ± 0.20 eV is in good agreement with the computed value of 3.550 eV. Regarding the computed VDE value based on the FC simulation shown in Fig. III.B.2.3, the anharmonic contribution tends to redistribute intensities to the transitions at vibrational states with higher vibrational quantum numbers. Thus, the present FC simulation shown in Fig. III.B.2.3, which uses the harmonic approximation, leads to a slight underestimation of the actual VDE value. This is consistent with the computed value versus measured VDE values reported here.

Table III.B.2.3 The computed adiabatic electron affinity (EA_a) and vertical detachment energy (VDE) values (in eV) of $UO_2Cl_2^-$. The HF values for EA_a were obtained using the cc-pVQZ-unc basis sets. The correlation contributions were obtained using the cc-pVTZ-unc and cc-pVQZ-unc basis sets and extrapolated to estimate the basis-set-limit value.

	HF	CCSD	CCSD(T)	+SO ^a	+ZPV ^b
EA_a	3.087	2.961	2.820	3.125	3.153
VDE ^c	3.484	3.358	3.217	3.522	3.550

^a Spin–orbit corrections (difference between X2CAMF and SFX2C-1e calculations).

^b Zero-point vibrational contribution.

^c Obtained by augmenting computed EA_a with a shift of 0.397 eV derived from the Franck–Condon simulation in Fig. III.B.2.3.

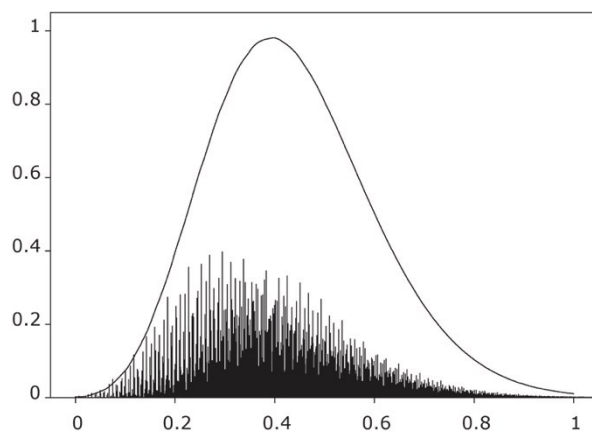


Figure III.B.2.3 Vibrational progression for the transition from the vibronic ground state of $UO_2Cl_2^-$ to vibrational states of the ground electronic state of UO_2Cl_2 obtained from Franck–Condon (FC) simulation using the harmonic approximation. The x axis denotes vibrational energies (in eV) with the origin set as the value of the origin transition. The simulation is convoluted to the experimental resolution. The broad curve is obtained by convoluting the stick spectrum with a half width at half maximum value of 0.1 eV. A value of 0.397 eV for the difference between EA_a and ADE was obtained as the shift between the threshold and the maximum peak position in this FC progression.

The electron binding energy of the origin transition in an anion photoelectron spectrum is equal to the EA_a value of the anion’s neutral counterpart. However, while the VDE value can be located by inspection of the PE spectrum, the origin transition must be assigned, and this can be challenging due to several factors. First, due to significant structural

relaxation, the origin transition of the UO_2Cl_2^- photoelectron spectrum exhibits inherently weak intensity, as clearly demonstrated in the FC simulation in Fig. III.B.2.3. Add low pre-photodetachment UO_2Cl_2^- anion intensity to the picture, and a modest signal-to-noise spectrum is the result. Next, consider the possibility of vibrational hot bands. In an ideal anion PE spectrum the EBE of the intensity threshold would reveal the origin. However, if some anion vibrational levels above $v = 0$ were to be populated, the EBE of the threshold would be slightly less than the EBE of the true origin. Laser vaporization anion sources are characterized by a competition between high temperatures due to the plasma produced in a laser strike and adiabatic cooling due to the rapid expansion of helium carrier gas. While the resulting temperature of the anions and thus the prevalence of hot bands varies considerably, some extent of hot band presence is common, making the threshold determination of the origin uncertain. While nascent anion temperatures of a few hundred degrees are often extracted from FC fits when the anions have simple structures, these are of minimal value given that the anions are not in equilibrium and thus do not conform to the Boltzmann distribution.

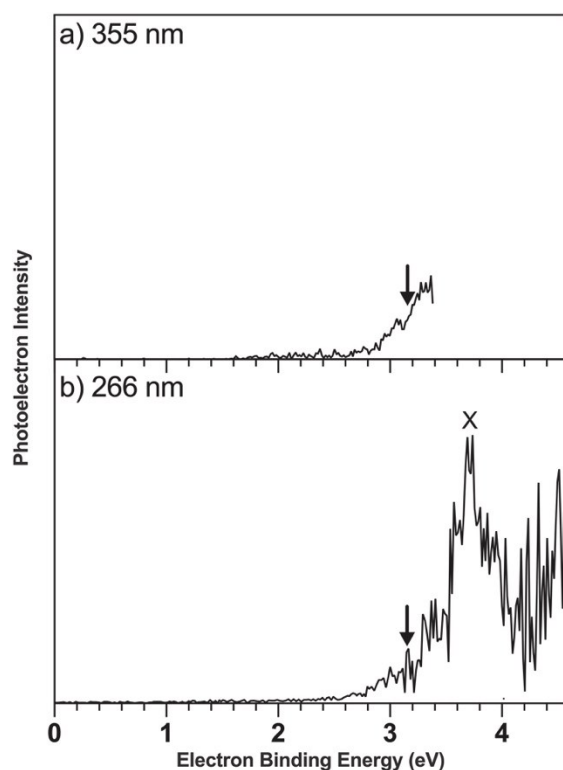


Figure III.B.2.4 The photoelectron spectra of UO_2Cl_2^- obtained using (a) the third harmonic (355 nm, 3.49 eV) and (b) the fourth harmonic of an Nd:YAG laser (266 nm, 4.66 eV). The arrows designate the position of the computed value of 3.15 eV for the adiabatic electron affinity.

The central issue in the present study is the experimental- determination of the EA_a value of UO_2Cl_2 . The origin transition is almost certainly one of the weakly discernible peaks in the PE spectrum between the hot-band-dominated threshold region and peak, X, from which the VDE value was assigned by inspection. Given the definitions of EA_a and VDE, the EA_a -determining origin transition typically sits at a lower EBE than the VDE transition by a few tenths of an eV. Given the foregoing, we assign the EA_a value of UO_2Cl_2 to be 3.2 ± 0.20 eV based of the PE spectrum of $UO_2Cl_2^-$. This same region of the spectrum is shown in Fig. III.B.2.4(a), which was measured using 355 nm photons and thus does not cover the VDE region of the spectrum. It too is consistent with this assignment. The present high-level calculations found the EA_a value of UO_2Cl_2 to be 3.15 eV and the VDE value of $UO_2Cl_2^-$ to be 3.55 eV. Experimental measurements based on the PE spectrum of $UO_2Cl_2^-$ determined EA_a value to be 3.2 ± 0.20 eV and the VDE value to be 3.69 ± 0.20 eV, both in good agreement with the computed value. All considered, we assert that our theoretically-determined and experimentally-supported value of 3.15 eV is a reliable assessment of the EA_a of UO_2Cl_2 .

Conclusion and Outlook

A joint computational–experimental study of the photoelectron spectrum of the uranyl dichloride anion, $UO_2Cl_2^-$, is reported. High-level relativistic coupled-cluster calculations predict that the photodetachment of $UO_2Cl_2^-$ involves a U 5f electron and induces significant geometry change. The electron affinity of uranyl dichloride neutral molecule, UO_2Cl_2 , thus provides information about the U 5f orbital energy in UO_2Cl_2 . In the future it would be interesting to determine electron affinities for other uranyl-containing molecules using photoelectron spectroscopy and relativistic coupled-cluster calculations, to obtain insights about the effects of ligands on the uranium 5f orbital energies of the uranyl ion.

CRedit authorship contribution statement

Mary Marshall: Collected the experiment data, Analyzed the experimental spectrum, Writing of the manuscript. Zhaoguo Zhu: Collected the experiment data, Analyzed the experimental spectrum, Writing of the manuscript. Junzi Liu: Performed calculations and analyzed the computational results, Writing of the manuscript. Kit H. Bowen: Conceptualization, Analyzed the experimental spectrum, Writing of the manuscript. Lan Cheng: Conceptualization, Performed calculations and analyzed the computational results, Writing of the manuscript.

Declaration of Competing Interest

The authors declare that they have no known competing financial interests or personal relationships that could have appeared to influence the work reported in this paper.

Acknowledgments

All computations in this work were carried out using Maryland Advanced Research Computing Center (MARCC). L. C. is indebted to John Stanton (Gainesville) for helpful discussions about Franck–Condon simulation with the harmonic approximation. The computational work has been supported by the Department of Energy, Office of Science, Office of Basic Energy Sciences, USA under Award Number DE-SC0020317 (L. C.). The experimental portion of this material is based upon work supported by the U.S. Department of Energy (DOE), Office of Science, Office of Basic Energy Sciences, Heavy Element Chemistry, USA program under Award Number, DE-SC0019317 (K.H.B).

References

- [1] R.G. Denning, *Electronic Structure and Bonding in Actinyl Ions BT - Complexes, Clusters and Crystal Chemistry*, Springer Berlin Heidelberg, Berlin, Heidelberg, 1992, pp. 215–276.
- [2] R.G. Denning, Electronic structure and bonding in actinyl ions and their analogs, *J. Phys. Chem. A* 111 (2007) 4125–4143.
- [3] P.L. Arnold, J.B. Love, D. Patel, Pentavalent uranyl complexes, *Coord. Chem. Rev.* 253 (2009) 1973–1978.
- [4] B.E. Cowie, J.M. Purkis, J. Austin, J.B. Love, P.L. Arnold, Thermal and photochemical reduction and functionalization chemistry of the uranyl dication, $[\text{U}^{\text{VI}}\text{O}_2]^{2+}$, *Chem. Rev.* 119 (2019) 10595–10637.
- [5] J. Veliscek-Carolan, Separation of actinides from spent nuclear fuel: A review, *J. Hazard. Mater.* 318 (2016) 266–281.
- [6] F.V. Stohl, D.K. Smith, The crystal chemistry of the uranyl silicate minerals, *Am. Mineral.* 66 (1981) 610–625.
- [7] C.K. Jørgensen, R. Reisfeld, *Uranyl Photophysics BT - Topics in Inorganic and Physical Chemistry*, Springer Berlin Heidelberg, Berlin, Heidelberg, 1982, pp. 121–171.
- [8] C. Görller-Walrand, S. De Houwer, L. Fluyt, K. Binnemans, Spectroscopic properties of uranyl chloride complexes in non-aqueous solvents, *Phys. Chem. Chem. Phys.* 6 (2004) 3292–3298.
- [9] R.D. Hunt, L. Andrews, Reactions of pulsed laser evaporated uranium atoms with molecular oxygen: Infrared spectra of UO , UO_2 , UO_3 , UO_2^+ , UO_2^{2+} , and $\text{UO}_3\text{-O}_2$ in solid argon, *J. Chem. Phys.* 98 (1993) 3690–3696.
- [10] J.C. Krupa, E. Simoni, J. Sytsma, N. Edelstein, Optical spectroscopic studies of uranyl chloride UO_2Cl_2 , *J. Alloys Compd.* 213–214 (1994) 471–474.
- [11] H.H. Cornehl, C. Heinemann, J. Marçalo, A.P. de Matos, H. Schwarz, The bare uranyl(2+) ion, UO_2^{2+} , *Angew. Chem., Int. Ed. Engl.* 35 (1996) 891–894.
- [12] M.J. Sarsfield, M. Helliwell, Extending the chemistry of the uranyl ion: Lewis acid coordination to a UO oxygen, *J. Am. Chem. Soc.* 126 (2004) 1036–1037.
- [13] S.P. Pasilis, J.E. Pemberton, Speciation and coordination chemistry of uranyl(VI)-citrate complexes in aqueous solution, *Inorg. Chem.* 42 (2003) 6793–6800.
- [14] P.L. Arnold, D. Patel, C. Wilson, J.B. Love, Reduction and selective oxo group silylation of the uranyl dication, *Nature* 451 (2008) 315–317.
- [15] J. Jin, R. Gondalia, M.C. Heaven, Electronic spectroscopy of UO_2Cl_2 isolated in solid Ar, *J. Phys. Chem. A* 113 (2009) 12724–12728.
- [16] P.L. Arnold, A.F. Pécharman, E. Hollis, A. Yahia, L. Maron, S. Parsons, J.B. Love, Uranyl oxo activation and functionalization by metal cation coordination, *Nature Chem.* 2 (2010) 1056–1061.
- [17] P.L. Arnold, E. Hollis, F.J. White, N. Magnani, R. Caciuffo, J.B. Love, Single- electron uranyl reduction by a rare-earth cation, *Angew. Chem., Int. Ed. Engl.* 50 (2011) 887–890.
- [18] P.L. Arnold, G.M. Jones, S.O. Odoh, G. Schreckenbach, N. Magnani, J.B. Love, Strongly coupled binuclear uranium-oxo complexes from uranyl oxo rearrangement and reductive silylation, *Nature Chem.* 4 (2012) 221–227.
- [19] R.J. Baker, New reactivity of the uranyl(VI) ion, *Chem. Eur. J.* 18 (2012) 16258–16271.
- [20] P.D. Dau, J. Su, H.T. Liu, D.L. Huang, J. Li, L.S. Wang, Photoelectron spectroscopy and the electronic structure of the uranyl tetrachloride dianion: $\text{UO}_2\text{Cl}_4^{2-}$, *J. Chem. Phys.* 137 (2012) 064315.
- [21] J. Su, P.D. Dau, Y.H. Qiu, H.T. Liu, C.F. Xu, D.L. Huang, L.S. Wang, J. Li, *Inorg. Chem.* 52 (2013) 6617–6626.
- [22] M.J. Van Stipdonk, M. d. C. Micheli, A. Plaviak, D. Martin, J.K. Gibson, Formation of bare UO_2^{2+} and NUO^+ by fragmentation of gas-phase uranyl acetonitrile complexes, *J. Phys. Chem. A* 118 (2014) 7838–7846.

- [23] J. Su, W.-L. Li, G.V. Lopez, T. Jian, G.-J. Cao, W.-L. Li, W.H.E. Schwarz, L.-S. Wang, J. Li, Probing the electronic structure and chemical bonding of mono- uranium oxides with different oxidation states: UO_x^- and UO_x ($x = 3 - 5$), *J. Phys. Chem. A* 120 (2016) 1084–1096.
- [24] M.C. Kirkegaard, J. Langford, J. Steill, B. Anderson, A. Miskowicz, Vibrational properties of anhydrous and partially hydrated uranyl fluoride, *J. Chem. Phys.* 146 (2017) 024502.
- [25] P.J. Skrodzki, M. Burger, L.A. Finney, F. Poineau, S.M. Balasekaran, J. Nees, K.R. Czerwinski, I. Jovanovic, Ultrafast laser filament-induced fluorescence spectroscopy of uranyl fluoride, *Sci. Rep.* 8 (2018) 11629.
- [26] J.H. Marks, P. Kahn, M. Vasiliu, D.A. Dixon, M.A. Duncan, Photodissociation and theory to investigate uranium oxide cluster cations, *J. Phys. Chem. A* 124 (2020) 1940–1953.
- [27] A.R. Bubas, E. Perez, L.J. Metzler, S.D. Rissler, M.J. Van Stipdonk, Collision- induced dissociation of $[\text{UO}_2(\text{NO}_3)_3]^-$ and $[\text{UO}_2(\text{NO}_3)_2(\text{O}_2)]^-$ and reactions of product ions with H_2O and O_2 , *J. Mass Spectrom.* n/a (2021) e4705.
- [28] P. Pyykkö, L.J. Laakkonen, K. Tatsumi, REX calculations. 12. iteration parameters for the 5f-element organometallics of thorium-neptunium. Geometries of ThO_2 and UO_2^{2+} revisited, *Inorg. Chem.* 28 (1989) 1801–1805.
- [29] M. Pepper, B.E. Bursten, The electronic structure of actinide-containing molecules: A challenge to applied quantum chemistry, *Chem. Rev.* 91 (1991) 719–74.
- [30] W.A. de Jong, L. Visscher, W.C. Nieuwpoort, On the bonding and the electric field gradient of the uranyl ion, *J. Mol. Struct. THEOCHEM* 458 (1998) 41–52.
- [31] S. Spencer, L. Gagliardi, N.C. Handy, A.G. Ioannou, C.-K. Skylaris, A. Willetts, A.M. Simper, Hydration of UO_2^{2+} and PuO_2^{2+} , *J. Phys. Chem. A* 103 (1999) 1831–1837.
- [32] Z. Zhang, R.M. Pitzer, Application of relativistic quantum chemistry to the electronic energy levels of the uranyl ion, *J. Phys. Chem. A* 103 (1999) 6880–6886.
- [33] Q. Wang, R.M. Pitzer, Structure and spectra of UO_2F_2 and its hydrated species, *J. Phys. Chem. A* 105 (2001) 8370–8375.
- [34] S. Matsika, R.M. Pitzer, Actinyl ions in $\text{Cs}_2\text{UO}_2\text{Cl}_4$, *J. Phys. Chem. A* 105 (2001) 637–645.
- [35] S. Matsika, Z. Zhang, S.R. Brozell, J.-P. Blaudeau, Q. Wang, R.M. Pitzer, Electronic structure and spectra of actinyl ions, *J. Phys. Chem. A* 105 (2001) 3825–3828.
- [36] D. Majumdar, K. Balasubramanian, H. Nitsche, A comparative theoretical study of bonding in UO_2^{++} , UO_2^+ , UO_2 , UO_2^- , OUCO , $\text{O}_2\text{U}(\text{CO})_2$ and UO_2CO_3 , *Chem. Phys. Lett.* 361 (2002) 143–151.
- [37] A. Kovács, R.J.M. Konings, Theoretical study of UX_6 and UO_2X_2 ($\text{X} = \text{F}, \text{Cl}, \text{Br}, \text{I}$), *J. Mol. Struct. THEOCHEM* 684 (2004) 35–42.
- [38] W.A. de Jong, E. Aprà, T.L. Windus, J.A. Nichols, R.J. Harrison, K.E. Gutowski, D.A. Dixon, Complexation of the carbonate, nitrate, and acetate anions with the uranyl dication: Density functional studies with relativistic effective core potentials, *J. Phys. Chem. A* 109 (2005) 11568–11577.
- [39] K. Pierloot, E. van Besien, Electronic structure and spectrum of UO_2^{2+} and $\text{UO}_2\text{Cl}_4^{2-}$, *J. Chem. Phys.* 123 (2005) 204309.
- [40] D. Hagberg, G. Karlström, B.O. Roos, L. Gagliardi, The coordination of uranyl in water: A combined quantum chemical and molecular simulation study, *J. Am. Chem. Soc.* 127 (2005) 14250–14256.
- [41] J.L. Sonnenberg, P.J. Hay, R.L. Martin, B.E. Bursten, Theoretical investigations of uranyl-ligand bonding: Four- and five-coordinate uranyl cyanide, isocyanide, carbonyl, and hydroxide complexes, *Inorg. Chem.* 44 (2005) 2255–2262.
- [42] E. van Besien, K. Pierloot, C. Görrler-Walrand, Electronic spectra of uranyl chloride complexes in acetone: a CASSCF/CASPT2 investigation, *Phys. Chem. Chem. Phys.* 8 (2006) 4311–4319.
- [43] M. García-Hernández, C. Willnauer, S. Krüger, L.V. Moskaleva, N. Rösch, Systematic DFT study of gas phase and solvated uranyl and neptunyl complexes $[\text{AnO}_2\text{X}_4]^n$ ($\text{An} = \text{U}, \text{Np}$; $\text{X} = \text{F}, \text{Cl}, \text{OH}$, $n = -2$; $\text{X} = \text{H}_2\text{O}$, $n = +2$), *Inorg. Chem.* 45 (2006) 1356–1366.
- [44] K. Pierloot, E. van Besien, E. van Lenthe, E.J. Baerends, Electronic spectrum of UO_2^{2+} and $[\text{UO}_2\text{Cl}_4]^{2-}$ calculated with time-dependent density functional theory, *J. Chem. Phys.* 126 (2007) 194311.
- [45] I. Infante, E. Eliav, M.J. Vilkas, Y. Ishikawa, U. Kaldor, L. Visscher, A Fock space coupled cluster study on the electronic structure of the UO_2 , UO_2^+ , U^{4+} , and U^{5+} species, *J. Chem. Phys.* 127 (2007) 124308.
- [46] G.A. Shamov, G. Schreckenbach, T.N. Vo, A comparative relativistic DFT and Ab initio study on the structure and thermodynamics of the oxofluorides of uranium(IV), (V) and (VI), *Chem. Eur. J.* 13 (2007) 4932–4947.
- [47] F. Real, A.S.P. Gomes, L. Visscher, V. Vallet, E. Eliav, Benchmarking electronic structure calculations on the bare UO_2^{2+} ion: How different are single and multireference electron correlation methods? *J. Phys. Chem. A* 113 (2009) 12504–12511.

- [48] B. Vlaisavljevich, L. Gagliardi, P.C. Burns, Understanding the structure and formation of uranyl peroxide nanoclusters by quantum chemical calculations, *J. Am. Chem. Soc.* 132 (2010) 14503–14508.
- [49] J. Su, Y.-L. Wang, F. Wei, W.H.E. Schwarz, J. Li, Theoretical study of the luminescent states and electronic spectra of UO_2Cl_2 in an argon matrix, *J. Chem. Theory Comput.* 7 (2011) 3293–3303.
- [50] F. Wei, G. Wu, W.H.E. Schwarz, J. Li, Geometries, electronic structures, and excited states of UN_2 , NUO^+ , and UO_2^{2+} : a combined CCSD(T), RAS/CASPT2 and TDDFT study, *Theor. Chem. Acc.* 129 (2011) 467–481.
- [51] P. Tecmer, A.S.P. Gomes, U. Ekström, L. Visscher, Electronic spectroscopy of UO_2^{2+} , NUO^+ and NUN : an evaluation of time-dependent density functional theory for actinides, *Phys. Chem. Chem. Phys.* 13 (2011) 6249–6259.
- [52] P. Tecmer, A. Severo Pereira Gomes, S. Knecht, L. Visscher, Communication: Relativistic fock-space coupled cluster study of small building blocks of larger uranium complexes, *J. Chem. Phys.* 141 (2014) 41107.
- [53] A. Kovács, R.J.M. Konings, J.K. Gibson, I. Infante, L. Gagliardi, Quantum chemical calculations and experimental investigations of molecular actinide oxides, *Chem. Rev.* 115 (2015) 1725–1759.
- [54] J.K. Gibson, H.-S. Hu, M.J. Van Stipdonk, G. Berden, J. Oomens, J. Li, Infrared multiphoton dissociation spectroscopy of a gas-phase complex of uranyl and 3-oxa-glutaramide: An extreme red-shift of the $[\text{o}=\text{u}=\text{o}]^{2+}$ asymmetric stretch, *J. Phys. Chem. A* 119 (2015) 3366–3374.
- [55] A.H. Greif, P. Hrobárik, J. Autschbach, M. Kaupp, Giant spin-orbit effects on ^1H and ^{13}C NMR shifts for uranium(vi) complexes revisited: role of the exchange-correlation response kernel, bonding analyses, and new predictions, *Phys. Chem. Chem. Phys.* 18 (2016) 30462–30474.
- [56] S. Zhang, F. Wang, Excitation energies of UO_2^{2+} , NUO^+ , and NUN based on equation-of-motion coupled-cluster theory with spin-orbit coupling, *J. Phys. Chem. A* 121 (2017) 3966–3975.
- [57] L. Cheng, A study of non-iterative triples contributions in relativistic equation-of-motion coupled-cluster calculations using an exact two-component hamiltonian with atomic mean-field spin-orbit integrals: Application to uranyl and other heavy-element compounds, *J. Chem. Phys.* 151 (2019) 104103.
- [58] M. Vasiliu, T. Jian, J.K. Gibson, K.A. Peterson, D.A. Dixon, A computational assessment of actinide dioxides AnO_2^{2+} for $\text{An} = \text{U}$ to Lr : The limited stability range of the hexavalent actinyl moiety, $[\text{O}=\text{An}=\text{O}]^{2+}$, *Inorg. Chem.* 59 (2020) 4554–4566.
- [59] R. Feng, E.D. Glendening, K.A. Peterson, Coupled cluster study of the interactions of AnO_2 , AnO_2^+ , and AnO_2^{2+} ($\text{An} = \text{U}, \text{Np}$) with N and CO , *Inorg. Chem.* 59 2222 (2020) 4753–4763.
- [60] O. Ordoñez, X. Yu, G. Wu, J. Autschbach, T.W. Hayton, Synthesis and characterization of two uranyl-aryl “Ate” Complexes, *Chem. Eur. J.* n/a (2020) <http://dx.doi.org/10.1002/chem.202005078>.
- [61] W.L. Li, J. Su, T. Jian, G.V. Lopez, H.S. Hu, G.J. Cao, J. Li, L.S. Wang, Strong electron correlation in UO_2^- : A photoelectron spectroscopy and relativistic quantum chemistry study, *J. Chem. Phys.* 140 (2014) 094306.
- [62] J. Czekner, G.V. Lopez, L.-S. Wang, High resolution photoelectron imaging of UO^- and UO_2^- and the low-lying electronic states and vibrational frequencies of UO and UO_2 , *J. Chem. Phys.* 141 (2014) 244302.
- [63] M. Gerhards, O.C. Thomas, J.M. Nilles, W.-J. Zheng, K.H. Bowen, Cobalt-benzene cluster anions: Mass spectrometry and negative ion photoelectron spectroscopy, *J. Chem. Phys.* 116 (2002) 10247–10252.
- [64] J. Ho, K.M. Ervin, W.C. Lineberger, Photoelectron spectroscopy of metal cluster anions: Cu_n^- , Ag_n^- , and Au_n^- , *J. Chem. Phys.* 93 (1990) 6987–7002.
- [65] J.F. Stanton, J. Gauss, L. Cheng, M.E. Harding, D.A. Matthews, P.G. Szalay, CFOUR, Coupled-Cluster techniques for Computational Chemistry, a quantum-chemical program package, With contributions from A.A. Auer, R.J. Bartlett, U. Benedikt, C. Berger, D.E. Bernholdt, S. Blaschke, Y. J. Bomble, S. Burger, O. Christiansen, D. Datta, F. Engel, R. Faber, J. Greiner, M. Heckert, O. Heun, M. Hilgenberg, C. Huber, T.-C. Jagau, D. Jonsson, J. Jusélius, T. Kirsch, K. Klein, G.M. Kopper, W.J. Lauderdale, F. Lipparini, T. Metzroth, L.A. Mück, D.P. O’Neill, T. Nottoli, D.R. Price, E. Prochnow, C. Puzzarini, K. Ruud, F. Schiffmann, W. Schwalbach, C. Simmons, S. Stopkiewicz, A. Tajti, J. Vázquez, F. Wang, J.D. Watts and the integral packages MOLECULE (J. Almlöf and P.R. Taylor), PROPS (P.R. Taylor), ABACUS (T. Helgaker, H.J. Aa. Jensen, P. Jørgensen, and J. Olsen), and ECP routines by A. V. Mitin and C. van Wüllen. For the current version, see <http://www.cfour.de>.
- [66] D.A. Matthews, L. Cheng, M.E. Harding, F. Lipparini, S. Stopkiewicz, T.-C. Jagau, P.G. Szalay, J. Gauss, J.F. Stanton, Coupled-cluster techniques for computational chemistry: The CFOUR program package, *J. Chem. Phys.* 152 (2020) 214108.
- [67] J.D. Watts, J. Gauss, R.J. Bartlett, Open-shell analytical energy gradients for triple excitation many-body, coupled-cluster methods: MBPT(4), CCSD+T(CCSD), CCSD(T), and QCISD(T), *J. Chem. Phys.* 200 (1992) 1–7.
- [68] J.F. Stanton, C.L. Lopreore, J. Gauss, The equilibrium structure and fundamental vibrational frequencies of dioxirane, *J. Chem. Phys.* 108 (1998) 7190–7196.
- [69] L. Cheng, J. Gauss, Analytic energy gradients for the spin-free exact two-component theory using an exact block diagonalization for the one-electron Dirac Hamiltonian, *J. Chem. Phys.* 135 (2011) 084114.

- [70] S.M. Rabidoux, V. Eijkhout, J.F. Stanton, A highly-efficient implementation of the Doktorov recurrence equations for Franck–Condon calculations, *J. Chem. Theory Comput.* 12 (2016) 728–739.
- [71] J. Liu, L. Cheng, An atomic mean-field spin–orbit approach within exact two- component theory for a non-perturbative treatment of spin–orbit coupling, *J. Chem. Phys.* 148 (2018) 144108.
- [72] J. Liu, Y. Shen, A. Asthana, L. Cheng, Two-component relativistic coupled- cluster methods using mean-field spin–orbit integrals, *J. Chem. Phys.* 148 (2018) 034106.
- [73] K. Raghavachari, G.W. Trucks, J.A. Pople, M. Head-Gordon, A fifth-order perturbation comparison of electron correlation theories, *Chem. Phys. Lett.* 157 (1989) 479–483.
- [74] R.J. Bartlett, J.D. Watts, S.A. Kucharski, J. Noga, Non-iterative fifth-order triple and quadruple excitation energy corrections in correlated methods, *Chem. Phys. Lett.* 165 (1990) 513–522.
- [75] K.A. Peterson, Correlation consistent basis sets for actinides. I. The Th and U atoms, *J. Chem. Phys.* 142 (2015) 74105.
- [76] T.H. Dunning Jr., Gaussian basis sets for use in correlated molecular calculations. I. The atoms boron through neon and hydrogen, *J. Chem. Phys.* 90 (1989) 1007–1023.
- [77] K.G. Dyall, Interfacing relativistic and nonrelativistic methods. IV. One- and two-electron scalar approximations, *J. Chem. Phys.* 115 (2001) 9136–9143.
- [78] W. Liu, D. Peng, Exact two-component Hamiltonians revisited, *J. Chem. Phys.* 131 (2009) 1–5.
- [79] M. Nooijen, R.J. Bartlett, Equation of motion coupled cluster method for electron attachment, *J. Chem. Phys.* 102 (1995) 3629–3647.
- [80] T. Helgaker, W. Klopper, H. Koch, J. Noga, Basis-set convergence of correlated calculations on water, *J. Chem. Phys.* 106 (1997) 9639–9646.
- [81] K.G. Dyall, Interfacing relativistic and nonrelativistic methods. I. Normalized elimination of the small component in the modified Dirac equation, *J. Chem. Phys.* 106 (1997) 9618–9626.
- [82] W. Kutzelnigg, W. Liu, Quasirelativistic theory equivalent to fully relativistic theory, *J. Chem. Phys.* 123 (2005) 241102.
- [83] M. Iliaš, T. Saue, An infinite-order two-component relativistic hamiltonian by a simple one-step transformation, *J. Chem. Phys.* 126 (2007) 64102.
- [84] B.A. Heß, C.M. Marian, U. Wahlgren, O. Gropen, A mean-field spin–orbit method applicable to correlated wavefunctions, *Chem. Phys. Lett.* 251 (1996) 365–371.

III.B.3. Au as a surrogate for F: The case of UAu_6 vs UF_6 .

(This manuscript is submitted to JACS and is under peer review)

Rachel M. Harris^{1†}, Zhaoguo Zhu^{1†}, Deepika^{2‡}, Burak A. Tufekci¹, Kirk Peterson^{3*}, Puru Jena^{2*} and Kit H. Bowen^{1*}

¹Department of Chemistry, Johns Hopkins University; Baltimore, MD 21218 USA.

²Department of Physics, Virginia Commonwealth University; Richmond, Virginia 23284 USA.

³Department of Chemistry, Washington State University; Pullman, Washington 99164 USA.

ABSTRACT: Here, anion photoelectron spectroscopy and first principles quantum chemistry are used to demonstrate to what degree Au can act as a surrogate for F in UF_6 and its anion. Unlike UF_6 , UAu_6 exhibits strong ligand-ligand, i.e., Au-Au, interactions, resulting in three low-lying isomers - two of which are distorted octahedra with the third isomer exhibiting a ring-like structure. Additionally, all the UAu_6 species have open-shell electrons, which in nearly all cases are localized on the central U atom. The electron affinity (EA) and vertical detachment energy (VDE) are measured to be 3.05 and 3.28 eV, respectively, and are in good agreement with calculations.

Main text

Uranium hexafluoride (UF_6) is the most important molecule in the nuclear industry as it is used for enriching uranium to produce fuels for nuclear reactors and fissile material for nuclear weapons. Consequently, there has been a substantial interest in understanding the chemistry of UF_6 and its derivatives. Nevertheless, a deeper understanding of the chemistry of uranium-containing molecules continues to be challenging due to their complicated electronic structures, multiple oxidation states, and strong relativistic and spin-orbit coupling effects. For example, while both UCl_6^- and UF_6^- have been studied by anion photoelectron spectroscopy and the electron affinity (EA) of UCl_6 has been measured to be 5.3 eV, UF_6^- did not photodetach^{1,2}.

Here, we adopt an alternative approach to better understand UF_6 and UF_6^- by using Au as a surrogate for F. Note that the EA of the Au atom (2.32 eV) is the highest among all metals in the periodic table; it is also one of the few metals that forms ionic bonds with metal atoms, such as Cs^3 . That Au may mimic F in UF_6 is consistent with Hoffmann's isolobal principle, which suggests that species with similar symmetry and frontier orbital energies have similar bonding and reactivity⁴. It was previously predicted by theory that Au could behave like a halogen when interacting with U in UAu_4 ^{5,6}. Recent joint experimental-theory studies on various thorium-gold anions, as well as the Au_2F molecule, have shown that indeed Au can behave very similarly to F^{7,8}. In a pilot study of UAuF trimer, we also found that Au mimics the chemistry of F (section S2, and Fig. S2 of the Supplementary Material, SM).

In the present work, a synergistic approach involving anion photoelectron spectroscopy (PES) experiments and first principles theory based on both density functional theory (DFT) and coupled cluster calculations shows that while UAu_6^- possesses some of the properties of UF_6^- , it also exhibits unique properties of its own.

The photoelectron spectra of UAu_6^- measured with 3.49 eV, 4.66 eV and 6.42 eV photons are displayed in Figure III.B.3.1. The first peak observed in the UAu_6^- spectrum has an onset around an electron binding energy (EBE) of 2.2 eV with a peak value at an EBE of 3.28 eV. In the 4.66 eV photon spectrum, this peak is seen to be split, with its higher EBE portion located at $\text{EBE} = 3.43$ eV. When there is sufficient Franck-Condon overlap between the ground state of the anion and the ground state of the neutral, and when vibrational hot bands are absent, the threshold electron binding energy (EBE) is the value of the EA. Nevertheless, since vibrational temperatures for anions are difficult to estimate, and since some degree of vibrational excitation is not uncommon, the EA value often lies between the threshold and the vertical detachment energy (VDE) value. As an approximation, we estimate the EA as that corresponding to the EBE value at $\sim 10\%$ of the rising photoelectron intensity. Focusing primarily on the 3.49 eV photon spectrum, this yields an EA value for UAu_6 of 3.05 eV. The VDE is equal to the EBE value at the lowest EBE peak's photoelectron intensity maximum and is found to be 3.28 eV for UAu_6^- .

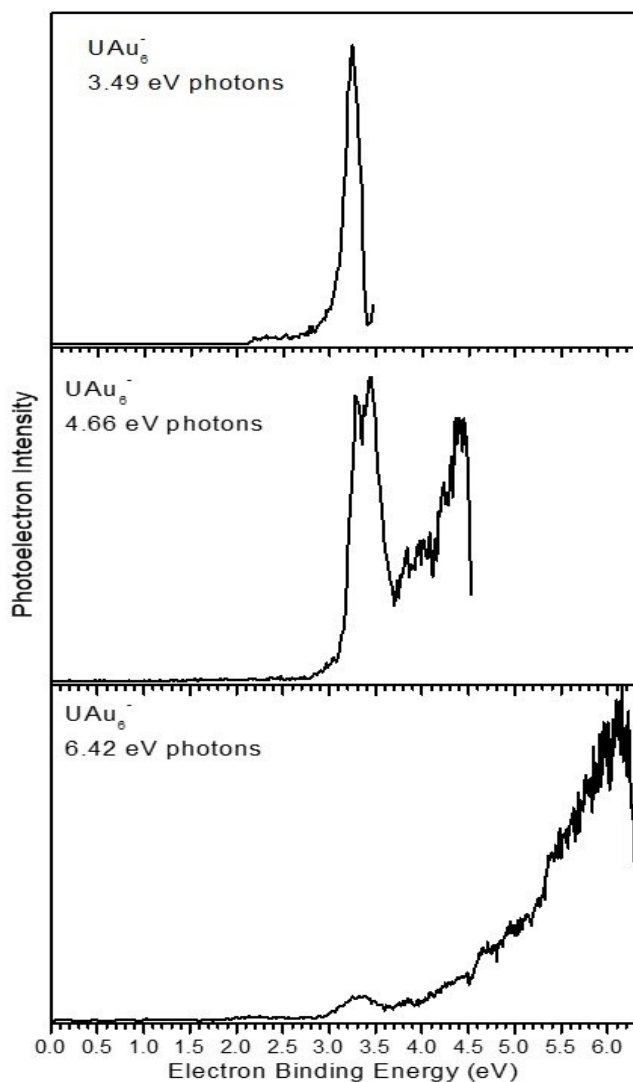


Figure III.B.3.1 Photoelectron Spectrum of UAu_6^- taken with the 3.49 eV, 4.66 eV, and 6.42 eV photons

Figure III.B.3. 2 presents the optimized geometries of the nearly degenerate neutral and anionic UAu_6 clusters. For isomer I, the six Au atoms are arranged in a ring with the U atom at its center but above its plane by 0.88 Å and 0.84 Å, respectively, for its neutral and anion geometries. (Fig. III.B.3.2a). Isomer II (Fig. III.B.3.2b) has a quasi-octahedral geometry with four Au atoms forming a rectangular configuration, while the other two Au atoms are located on opposite sides of the U atom. Isomer III (Fig. III.B.3.2c) has a butterfly-type geometry, where the U atom lies on a plane with four of the six Au atoms. The ring isomer of UAu_6^- (isomer I) is more symmetric than that of neutral UAu_6 , with the U-Au bond length contracted and Au-Au bond length expanded in the anionic cluster. These three isomers

differ in energy by at most 0.31 eV for the neutrals and 0.34 eV for the anions, which is within the accuracy of the DFT calculations. An octahedral structure for UAu_6 (Fig. S3), analogous to the equilibrium geometry of UF_6 , was calculated to be unstable with respect to distortion to isomers II and III. At the DFT optimized geometries, the same three isomers of UAu_6^- as shown in Fig. III.B.3.2 were also calculated at the CCSD(T) level of theory to be nearly degenerate, with a maximum energy difference between them of 0.53 eV (at the CCSD(T)/cc-pVTZ-PP level of theory); although the ground state corresponds to the ring type geometry (isomer I in Fig. III.B.3.2a) with isomer III lying just 0.10 eV higher in energy. A natural population analysis (NPA) showed that in all the neutral and anionic UAu_6 isomers, the U atom is positively charged. In neutral isomer I and II, all six Au atoms carry negative charge (Fig. III.B.3.2), while in neutral isomer III four Au atoms are charged negatively and two are barely positive. This is consistent with the fact that the EA of the U atom (0.31 eV) is significantly less than that of the Au atom, and thus in UAu_6 , Au atoms behave like halogens. In the anion, the charge on the U atom is decreased by nearly $\frac{1}{2}$ in the ring isomer (I), while it becomes slightly more positive in the other two isomers. In nearly all these six cases, the open shell electrons reside on the U atom as indicated by the natural spin density. The one exception is the quintet state of the neutral ring isomer, where one unpaired electron is spread over the Au atoms.

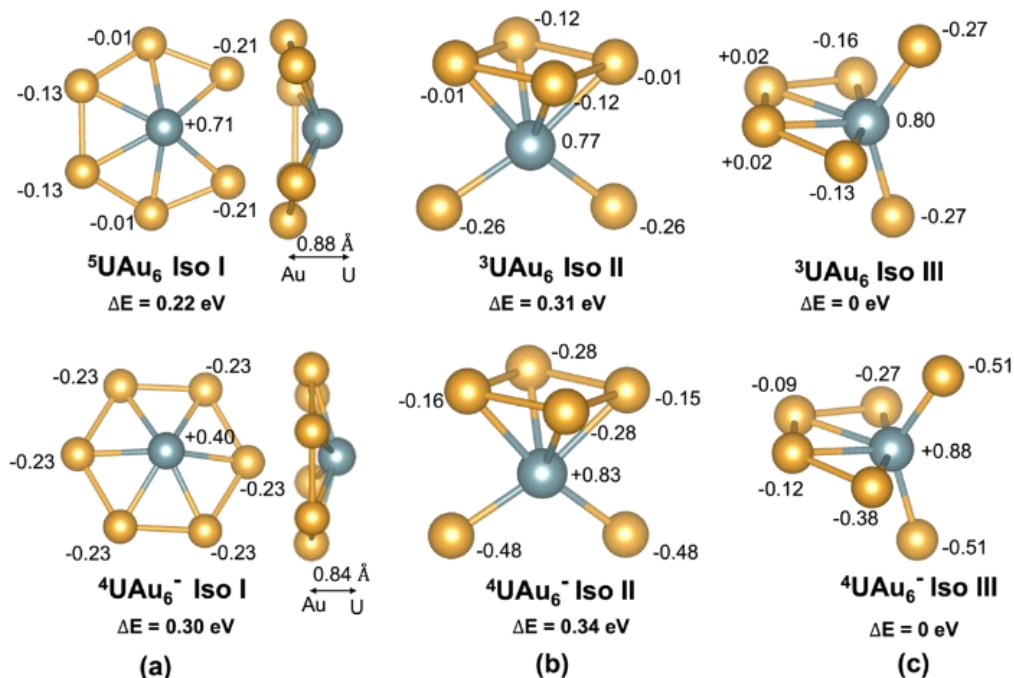


Figure III.B.3.2 Optimized ground state geometries of nearly isoenergetic isomers: (a) Ring isomer (I), (b) Quasi-

octahedral isomer (II), and (c) Butterfly isomer (III) of neutrals, i.e., UAu_6 (top row) and anions, i.e., UAu_6^- (bottom row). Relative energies, ΔE , are given at the DFT level of theory.

Comparing the theoretical EA values with experiment, the calculated VDE and EA of isomer I at the DFT level, namely, 3.18 eV and 2.99 eV, respectively, agree well with the experimental values (Table III.B.3.1). Not surprisingly, the calculated EA and VDE values of isomers II and III are also close to the experimental values. The VDE values calculated at the CCSD(T)/cc-pVTZ-PP level of theory lie slightly lower than the DFT results, with values ranging from 3.06 to 3.24 eV (the DZ values were about 0.1 eV smaller than those with TZ). These isomers are calculated to be nearly isoenergetic with very similar VDE values, and all three could be present in the spectrum shown in Figure III.B.3. 1.

Table III.B.3.1 Experimental and calculated electron affinities (EA) of UAu_6 and vertical detachment energies (VDE) of UAu_6^- clusters.

Species	EA (eV)		VDE (eV)		
	Exp.	DFT	Exp.	DFT	CCSD(T)
UAu₆	3.05		3.28		
Isomer I		2.99		3.18	3.24
Isomer II		3.04		3.34	3.06
Isomer III		3.07		3.40	3.09

The CCSD(T) results are shown using TZ basis sets.

The numbers alongside U and Au atoms represent corresponding NPA charges obtained using the NBO 7.0 program. Silver and yellow colors represent the U and Au atoms, respectively. For isomer I, top and side views are provided to visualize its 3D geometry. The superscript on the U atom represents the spin multiplicity of the cluster. The ΔE values are the relative energies with respect to the lowest energy isomer calculated with DFT.

Analogous to the bonding in UF_6 , the bonding between U and Au in UAu_6 is primarily ionic. However, there are significant differences in the electronic structures of UF_6 and UAu_6 (and their anions). While UF_6 exhibits only two-center-two-electron (2c-2e) bonds, UAu_6 exhibits 3c-2e bonds (Figs. S4-S6). In addition, UF_6 has a closed-shell singlet ground state with an octahedral structure, while UAu_6 has an open-shell ground state (quintet or triplet) with somewhat

unsymmetrical structures. The origin of these differences in the geometries can be traced to the relative bond dissociation energies (BDE) of the Au₂ and F₂ dimers. The DFT calculated Au₂ BDE of 1.96 eV (exp. 2.32 eV) is significantly larger than that of F₂, 1.61 eV (exp. 1.66 eV) with a significantly longer equilibrium bond distance, about 2.47 Å for Au₂ compared to 1.41 Å for F₂. This allows for ionic U-Au as well as Au-Au, interactions. In the octahedral geometry of singlet UAu₆ (Fig. S3), the Au-Au bond lengths are 3.87 Å, which is much longer than the calculated equilibrium distance in Au₂ (2.56 Å); hence there can be very little interaction between the Au atoms in this structure. Both isomers II and III arise from simple distortions from the octahedral geometry to allow for Au-Au interactions, and the average Au-Au distance in the three isomers of UAu₆ range from 2.72 to 2.85 Å (Table S1). Thus, the three isomers of UAu₆ can be rationalized as structures with competing U-Au and Au-Au interactions. In UF₆ the ionic U-F interaction dominates and the geometry is then determined by maximizing the numbers of U-F bonds, hence the geometry adopts a perfect O_h symmetry. In addition, the existence of strong Au-Au interactions leads to a reduction in the oxidation state of U from +6 in UF₆ to +4 in UAu₆, yielding the open-shell spin states in the latter. An important difference between UF₆ and UAu₆ that can have scientific and technological importance is that the latter is magnetic with a large magnetic moment localized at the U site. It may be possible to use UAu₆ as a building block of one dimensional ferromagnets, similar to the V₆(C₆H₆)₇ sandwich complexes which have been both predicted and experimentally confirmed^{9,10}. If so, this would be a case in which two metallic elements, that are intrinsically nonmagnetic in the bulk, give rise to a ferromagnet with constrained geometry and composition.

Realizing that Au with an outer electron configuration of [Xe]4f¹⁴5d¹⁰6s¹ has versatile chemistry in that it behaves both as a hydrogen atom and halogen atom, we used it as surrogate of F to shed additional light on UF₆. We were able to photodetach UAu₆⁻ and measure its EA and VDE to be 3.05 and 3.28, eV, respectively, making UAu₆ a pseudo-halogen. Theoretical studies based on first principles theory provided results in good agreement with experiment and showed that the bonding is dominated by ionic interaction between U and Au, similar to the bonding in UF₆. However, theory also revealed properties of UAu₆ that are very different from that of UF₆. For example, the geometry of UF₆ is an octahedron with no interaction between the F atoms while UAu₆⁻ exhibits three nearly degenerate isomers with ring, quasi-octahedral, and butterfly geometries, all having coupling between the Au atoms. An intriguing difference is that the spin multiplicity of the ring isomer of neutral UAu₆ is a quintet with a magnetic moment of 4 μ_B localized at the U site. Thus, while Au can be used as a surrogate for F, one must be aware that Au-Au interactions can cause interesting deviations from fluorine's behavior.

Author Contributions

The manuscript was written through contributions of all authors. †These authors contributed equally.

REFERENCES

- (1) Dau, P. D.; Su, J.; Liu, H. T.; Huang, D. L.; Wei, F.; Li, J.; Wang, L. S. Photoelectron Spectroscopy and Theoretical Studies of UF_5^- and UF_6^- . *J. Chem. Phys.* **2012**, *136* (19), 194304. <https://doi.org/10.1063/1.4716182>.
- (2) Su, J.; Dau, P. D.; Liu, H. T.; Huang, D. L.; Wei, F.; Schwarz, W. H. E.; Li, J.; Wang, L. S. Photoelectron Spectroscopy and Theoretical Studies of Gaseous Uranium Hexachlorides in Different Oxidation States: UCl_6^{q-} ($q = 0-2$). *J. Chem. Phys.* **2015**, *142* (13), 134308. <https://doi.org/10.1063/1.4916399>.
- (3) Heiz, U.; Vayloyan, A.; Schumacher, E.; Yeretzyan, C.; Stener, M.; Gisdakis, P.; Rösch, N. Na_xAu and Cs_xAu Bimetal Clusters: Finite Size Analogs of Sodium-Gold and Cesium-Gold Compounds. *J. Chem. Phys.* **1996**, *105* (13), 5574–5585. <https://doi.org/10.1063/1.472397>.
- (4) Hoffmann, R. Building Bridges Between Inorganic and Organic Chemistry (Nobel Lecture). *Angewandte Chemie International Edition in English*. John Wiley & Sons, Ltd October 1, 1982, pp 711–724. <https://doi.org/10.1002/anie.198207113>.
- (5) Jung, J.; Kim, H.; Kim, J. C.; Park, M. H.; Han, Y. K. Gold Behaves as Hydrogen in the Intermolecular Self-Interaction of Metal Aurides MAu_4 ($M=\text{Ti}$, Zr , and Hf). *Chem. - An Asian J.* **2011**, *6* (3), 868–872. <https://doi.org/10.1002/asia.201000742>.
- (6) Gagliardi, L. When Does Gold Behave as a Halogen? Predicted Uranium Tetraauride and Other MAu_4 Tetrahedral Species, ($M = \text{Ti}$, Zr , Hf , Th). *J. Am. Chem. Soc.* **2003**, *125* (25), 7504–7505. <https://doi.org/10.1021/ja035385a>.
- (7) Shah, A.; Banjade, H.; Long, Z. C.; Gao, Z. O.; Xu, H. G.; Zheng, W.; Jena, P. Signature of Au as a Halogen. *J. Phys. Chem. Lett.* **2022**, *13*, 4721–4728. <https://doi.org/10.1021/acs.jpclett.2c00910>.
- (8) Zhu, Z.; Marshall, M.; Bowen, K. H.; Peterson, K. A. ThAu_2^- , ThAu_2O^- , and ThAuOH^- Anions: Photoelectron Spectroscopic and Theoretical Characterization. *J. Chem. Phys.* **2022**, *156* (5), 054305. <https://doi.org/10.1063/5.0079795>.
- (9) Kandalam, A. K.; Rao, B. K.; Jena, P.; Pandey, R. Geometry and Electronic Structure of $\text{V}_n(\text{Bz})_m$ Complexes. *J. Chem. Phys.* **2004**, *120* (22), 10414–10422. <https://doi.org/10.1063/1.1738632>.
- (10) Wang, J.; Acioli, P. H.; Jellinek, J. Structure and Magnetism of $\text{V}_n\text{Bz}_{n+1}$ Sandwich Clusters. *J. Am. Chem. Soc.* **2005**, *127* (9), 2812–2813. <https://doi.org/10.1021/ja043807q>.

III.B.4. The transition from halogen-like to metallic-like bonding of gold in Uranium-Auride Clusters (U@Au_n), ($n = 3 - 7$)

(This manuscript is under preparation for submission)

Rachel M. Harris¹, Zhaoguo Zhu¹, Deepika², Burak A. Tufekci¹, Puru Jena^{2,*}, Kirk A. Peterson^{3,*}, and Kit H. Bowen^{1,*}

Affiliations:

¹ Department of Chemistry, Johns Hopkins University, Baltimore, MD 21218 USA

² Department of Physics, Virginia Commonwealth University, Richmond, Virginia 23284, USA

³ Department of Chemistry, Washington State University, Pullman, Washington 99164, USA

* Correspondence to: kbowen@jhu.edu (K.H.B) and kipeters@wsu.edu (K.A.P.)

1. Introduction

Actinide-transition metals (An-TM) bonds with a single An atom and multiple TM atoms are of fundamental interest to experimental and theoretical chemists tasked with elucidating the complicated electronic structure of such exotic complexes, especially when the TM is a coinage metal.[1-6] Theoretically early actinides, such as Uranium and Thorium, have been predicted to form planar structures in AnM_7 clusters, to eventually “superatomic” cage-like structures, in AnM_{14} , when doped within a coinage metal. The focus is primarily on describing what role these 5f electrons play in such bonds and how such multifaceted structures formed from said bonds leads to a degree of covalency amongst 5f-element complexes, a debate with both academic and industrial implications.⁷ On top of this, the similarity in energies between 5f and 6d orbitals in the actinides, and the radial extent of each, with the 6d being more diffuse, leads to a competing effect that makes proving the uniqueness of 5f orbitals more difficult.⁸ Above all however, the core reason for such difficulty has been attributed to numerous relativistic effects, primarily spin-orbit coupling, that accompany heavy elements. Such effects are the salient reasons for the cubic structure of polonium, liquid state of mercury, and the color of gold.[9,10]

With regards to gold, its pure, as well as transition-metal doped, nanoclusters have received attention in the past few decades for their catalytic activity, while also displaying a propensity for sigma aromaticity. This has been attributed to relativistic effects that can promote 5d-6s hybridization and a high degree of covalent bonding amongst gold atoms. Extensive experimental work and photoelectron spectrum of gas phase TM-doped gold clusters has also provided great insight into the idea that sigma aromaticity is clearly manifested in their highly stable planar structures. Also, similar relativistic effects happen to be an explanation for the high electron affinity of gold, and its electron acceptor

abilities, leading it to also form ionic bonds in solid-state alkali metal auride complexes. Some hypotheses, go as far as to attribute these relativistic effects to the halogen like behavior of gold.

However, sigma aromaticity does not always dominate in determining the structure of metal doped gold clusters, since the possibility of halogen mimicry in gold has been resurfaced once again in the primarily computational-driven area of actinide-gold (An-Au) clusters. The question “When does gold behave as a halogen?” was asked years ago and still to this day left with an unsatisfactory answer, with UAu_4 and ThAu_4 being the systems of choice for such consideration. This has been combatted with recent computational works with a larger Au count in An-Au clusters, which are planar and show a high degree of sigma aromaticity and has even led to an attractive name for this class of such clusters in the form of Saturnenes, for their delocalized electron ringlike orbit around the actinide atom, structurally mimicking the planet Saturn. Such computational predictions on the electronic structure of An-Au clusters have even been suggested as being potential SERS materials in biomedical applications. Superhalogens, such as ThH_5 , on the other hand have been used to describe clusters that have an electron affinity greater than chlorine. The size dependent phenomenon, as observed in the catalytic activity in pure gold clusters, can also be a contribution towards creating a linkage between sigma aromaticity and halogen mimicry in actinide- gold nanoclusters. In this work, the actinide of interest is Uranium, which when doped with gold cluster anions in the gas phase, exhibits a trend in the resulting anion photoelectron spectrum, which when coupled with computational insight, determine the onset of sigma-aromaticity in UAux- clusters when $x=6$, etc.

2. Methods

2.1 Experimental Details. When conducting anion PES, a mass-selected negative ion beam is crossed with a fixed-frequency photon beam. The resultant photodetached electrons are directed into a magnetic bottle where they are energy-analyzed. The electron binding energy (EBE) is then determined using the conservant relationship:

$$\text{EBE} = h\nu - \text{EKE} \quad (1)$$

Where EBE is the difference between the photodetached electron’s kinetic energy (EKE) and the photon energy ($h\nu$). Our apparatus consists of a laser vaporization cluster anion source, a time-of-flight mass spectrometer, a Nd:YAG photodetachment laser, and a magnetic bottle energy analyzer (cite). The magnetic bottle photoelectron spectrometer resolution is ~ 35 meV at $\text{EKE} = 1$ eV.

UAu_n⁻ clusters were generated in our apparatus using a dual-rod laser vaporization source. Rotating, translating rods of uranium and gold were independently ablated using second harmonic (nm) photons from two Nd:YAG lasers. As each metal was vaporized, a pulse of gas consisting of 10% argon in helium (80 psi) was used to induce clustering and direct the ion beam towards the extraction region. Mass spectra were obtained via time-of-flight mass spectrometry. UAu_n⁻ clusters of interest were mass-gated into an interaction region, where photoelectrons were detached using the third and fourth (355 nm and 266 nm, respectively) harmonic output of a Nd:YAG laser, as well as 193 nm photons from an excimer laser. The resulting photoelectron spectra were recorded and calibrated against the well-known atomic transitions of Cu⁻.

2.2 Computational Details. First-principles calculations are carried out using spin-polarized density functional theory (DFT) as implemented in the Gaussian 16 package¹⁰. The exchange-correlation potential was treated using the hybrid Becke, 3-parameter, Lee–Yang–Parr (B3LYP) functional along with correlation consistent polarized Valence Double- ζ (cc-pV-DZ-PP) basis set for both U and Au atoms. The relativistic effect of the core electrons in U and Au atoms are incorporated using the Stuttgart/Cologne energy-consistent (ab initio) effective core pseudopotentials with 60 core electrons (ECP60MDF). The empirical dispersions corrections are included using the Grimme's D3 damping functions¹¹. The quadratic self-consistent convergence criteria are used during the optimization process without any symmetry constraint. For each cluster, the ground state geometries of the neutral and the mono-anionic UAu_n ($n=3-7$) clusters are obtained by comparing the optimized energy of singlet, triplet, and quintet state for even electron systems and doublet, quartet, and sextet for odd electron systems. The calculated electron affinity (EA), also known as adiabatic electron affinity, is defined as the energy difference between the anion and its corresponding neutral, both at their respective ground state geometries, whereas the vertical detachment energy (VDE) is the energy difference between anion and its corresponding neutral, both at the ground state geometry of the anion. The thermodynamic stability of each cluster is confirmed by ensuring that all the vibrational frequencies are real (no imaginary component) in the studied clusters. The strength and nature of bonding in the clusters are studied using Mayer's bond order (MBO), Natural bond order (NBO), and Bader's Quantum theory of atoms in the molecule (QTAIM). The electronic structures of the clusters are analyzed by performing projected density of states (pDOS), HOMO-LUMO energy gap, and Adaptive natural density partitioning (AdNDP) analysis using the Multiwfn package¹². The pDOS analysis is performed using C-squared Population Analysis (SCPA) method proposed by Ros

and Schuit¹³ as also implemented in the Multiwfn package¹². A Lorentzian function is used to broaden the original discrete molecular orbital energy levels at full width half maxima (FWHM) of 0.5 eV.

3. Results and Discussion

The first step of our theoretical approach is to identify the geometries of the ground state and low-lying isomers of the neutral and anionic UA_n (n=3-7) clusters. A variety of techniques as outlined in the previous section are used to study the nature of bonding and their electronic structure of the ground state geometries. The electron affinities (EA) and vertical detachment energies (VDE) are calculated from the total energies of the neutral and anionic clusters and compared with the corresponding experimental values. A good agreement between theory and experiment assures the validity of the calculated geometries and electronic properties.

3.1 Photoelectron Spectra of UA_n⁻ (n= 3-7). The resulting mass spectrum of the U/Au system is displayed in Figure III.B.4.1. Pure gold clusters (Au₂⁻- Au₁₇⁻) were observed and are marked in the figure with red stars. A smaller peak 41 amu following each gold cluster peak was identified to be UA_n⁻ (where n = 3-16) and are indicated by blue hash marks in Figure III.B.4.1. Because an argon gas mixture was used as a backing gas, the possibility of argon-tagged gold clusters was addressed (LSW Cite). Argon tagging would create a mass peak 40 amu greater than its parent gold cluster, and the overlap of these argon-tagged gold cluster peaks with the uranium-gold cluster peaks could convolute the PES of the UA_n⁻ clusters. To reveal the presence of argon tagging, mass spectra were taken without the presence of uranium by simply refraining from ablating the uranium rod. Secondary argon-tagged gold cluster peaks were not observed. Additionally, PES of mass-selected UA_n⁻ clusters were taken with and without ablating the uranium rod. Without the use of the uranium rod, no spectra were observed, and thus no Ar-Au_n⁻ clusters were present. Therefore, the PES reported here are purely the result of the photodetachment of UA_n⁻.

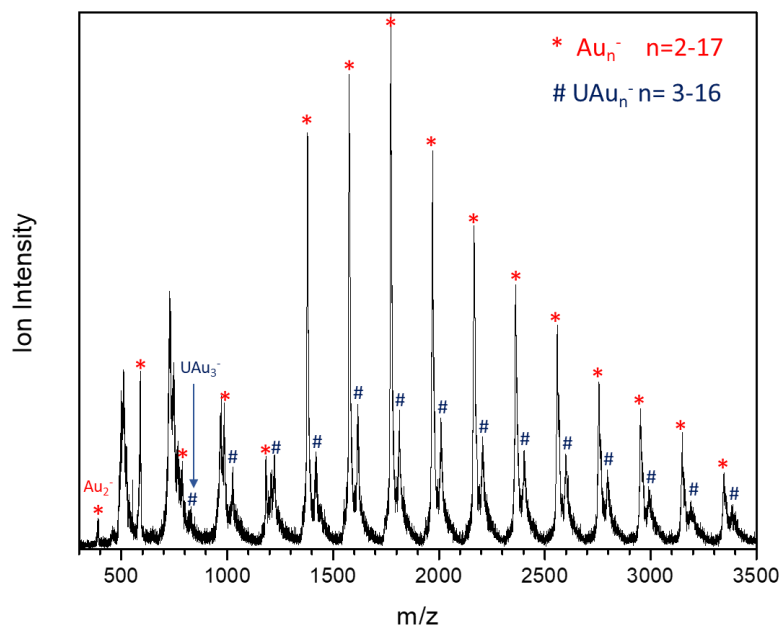


Figure III.B.4.1 Mass Spectrum resulting from laser vaporization of Au and U rods, pulsed with a 10% Ar in He gas mixture. Gold clusters are marked with a red star, starting with Au_2^- . The peaks observed 41 amu after a gold cluster peak, labelled with blue hash marks, are UAu_n^- peaks. Other peaks located in the low mass region are uranium oxides.

The photoelectron spectra of UAu_n^- ($n=3-7$) taken with 3.49 eV, 4.66 eV and 6.42 eV photons are displayed in Figure III.B.4.2. PES of other UAu_n^- clusters ($n=8-13$) are available in the SI as figures S1, S2 and S3.

- UAu_3^- 's first feature appear with an onset of 1.28 eV, with a maximum value at 1.56 eV. A second broad feature begins ~ 4.4 eV and spans to ~ 5.0 eV.
- The first feature in UAu_4^- is a broad band that begins around 2.60 eV and reaches a peak value at 3.20 eV. Two more dominant peaks, at 4.92 and 5.13 eV, are revealed at our highest photon energy.
- The UAu_5^- spectrum exhibits a very broad feature beginning ~ 1.3 eV, peaking at 3.52 eV. A higher EBE peak at 3.64 eV is also observed. Use onset of 3.24 as EA.
- The first peak observed in the UAu_6^- spectrum has an onset around 2.88 eV with a peak value observed at 3.28 eV and a second, broader feature is observed around 3.2-3.3 eV.
- The first peak observed in the UAu_7^- spectrum has an onset around 2.56 eV with a peak value observed at 3.67 eV. A second major peak is observed at 3.88.

- The UAu_8^- spectrum displays a broad feature with an onset ~ 2.97 eV.
- UAu_n^- , where $n = 9-13$ all exhibit an onset between 2.56 and 2.74 eV.
- The UAu_9^- spectrum exhibits a two small peaks at 3.29 eV and 3.99 eV.
- The UAu_{10}^- spectrum's first peak value is around 3.2 eV with a second peak observed at 3.87 eV.
- The UAu_{11}^- spectrum's first peak occurs at 3.25 eV.
- The UAu_{12}^- spectrum displays its first peak at 3.25 eV
- The UAu_{13}^- spectrum displays its first peak at 3.64 eV

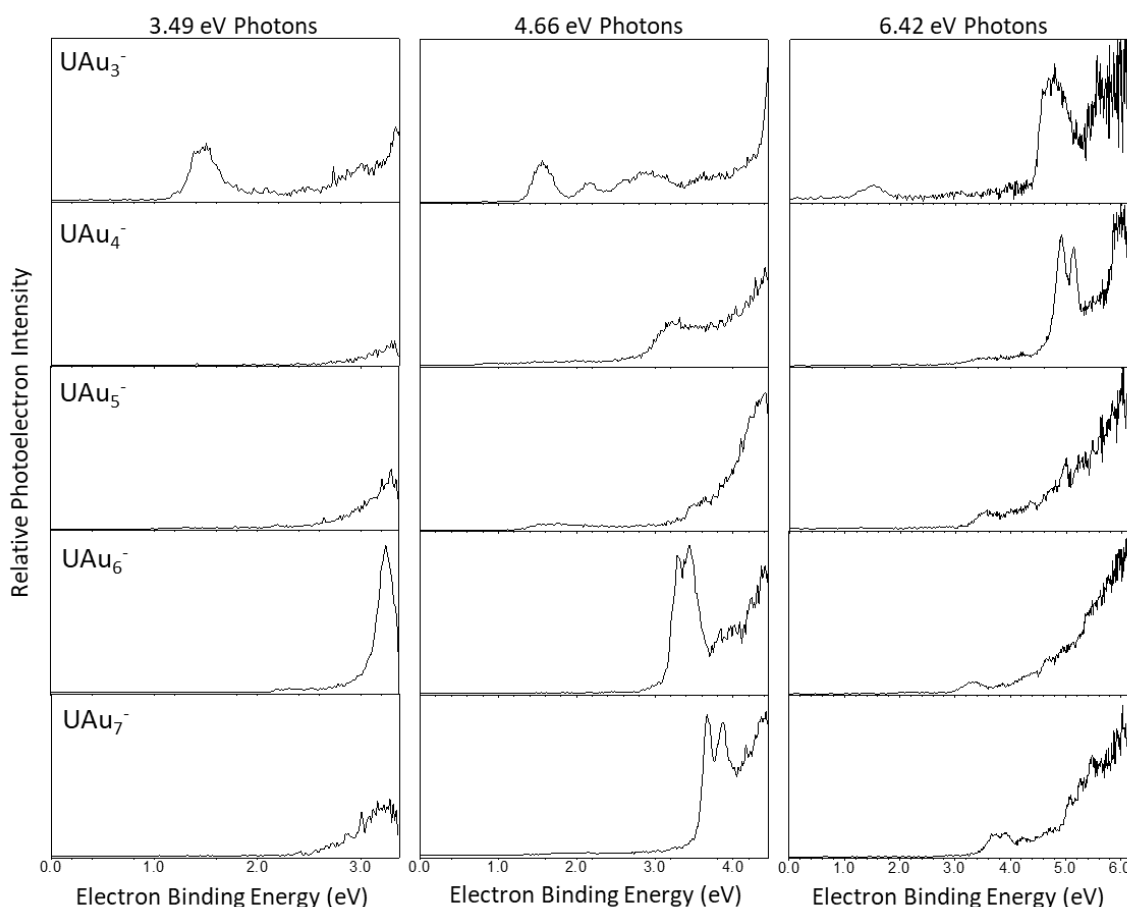


Figure III.B.4.2 Photoelectron Spectrum of UAu_n^- ($n=3-7$) taken with the third (3.49 eV) and fourth harmonic (4.66 eV) of a Nd:YAG photodetachment laser, as well as an excimer (6.42 eV) photodetachment laser.

3.1 Computational Results. The first step of our theoretical approach is to identify the geometries of the ground state and low-lying isomers of the neutral and anionic UAu_n ($n=3-7$) clusters. A variety of techniques as outlined in the previous section are used to study the nature of bonding and their electronic structure of the ground

state geometries. The electron affinities (EA) and vertical detachment energies (VDE) are calculated from the total energies of the neutral and anionic clusters and compared with the corresponding experimental values. A good agreement between theory and experiment assures the validity of the calculated geometries and electronic properties.

Equilibrium geometries of neutral and anionic clusters:

We begin our discussions with the optimized ground state geometries of neutral and anionic U@Au_n clusters ($n = 3-7$). These are shown in Figure III.B.4. 1. Both neutral and anionic UAu_3 clusters have a C_{3v} symmetry with the U-Au bond length of 2.79 Å, and 2.93 Å, respectively. The preferred spin-multiplicities of neutral and anionic UAu_3 clusters are quartet and quintet, respectively, which represent the magnetic character of the clusters. The geometries of both neutral and anionic UAu_4 are distorted and have a symmetry lower than T_d symmetry, tending more towards D_{2d} . The U-Au bond lengths in the neutral and anionic UAu_4 cluster are 2.71 Å, and 2.88 Å, respectively. Their corresponding preferred spin-multiplicities are triplet and quartet, respectively, indicating both clusters are magnetic in nature. The geometry of neutral UAu_5 , unlike those of UAu_3 and UAu_4 clusters, is significantly different from its anion, which has a D_{3h} symmetry. During the optimization of the neutral UAu_5 , the three Au atoms (i.e., Au1, Au2, and Au3) initially placed in the same plane as in its anion (with D_{3h} symmetry) move toward each other while the other two Au atoms (i.e., Au3, and Au4) initially placed out of plane also move toward each other, thus, lowering the symmetry of the neutral UAu_5 . The neutral and anionic UAu_5 clusters prefer quartet and triplet spin states, respectively, showing that they are magnetic. The U-Au bond lengths in the neutral, and anionic UAu_5 range from 2.79 - 3.25 Å, and 2.78 - 2.79 Å, respectively.

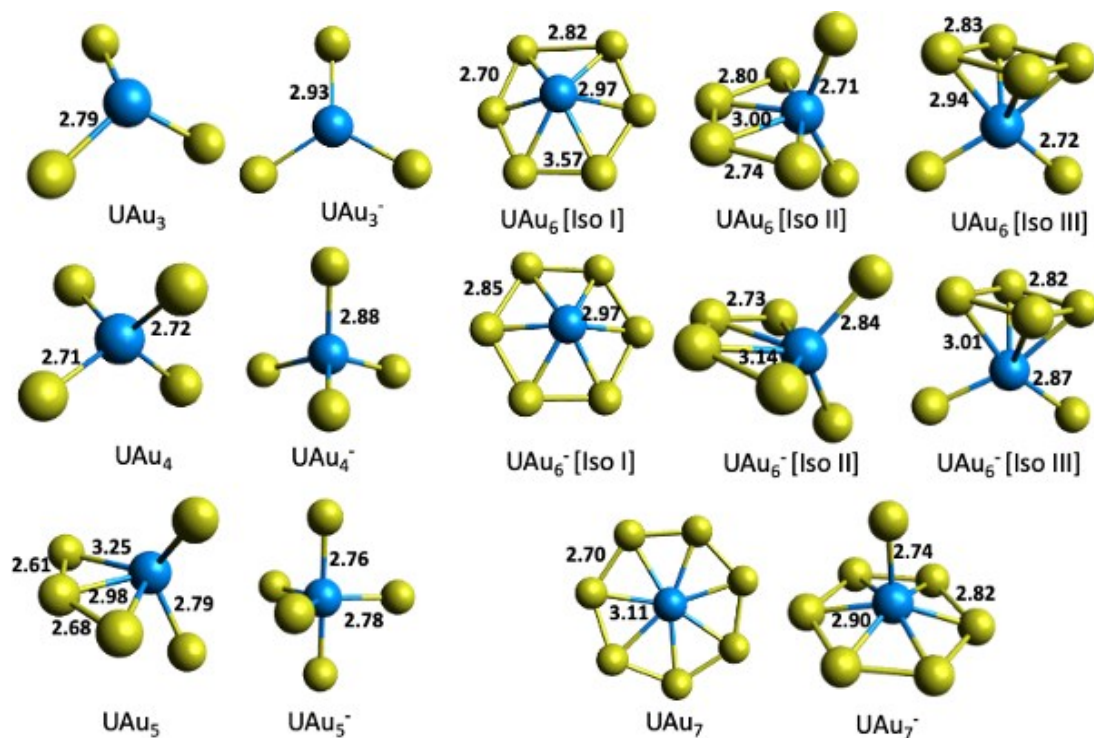


Figure III.B.4.3 Optimized ground state geometries of neutral and anionic $[UAu_n]$, $n=3-5$ at B3LYP/cc-PV-DZ-PP level of theory. Blue and metallic green spheres represent the U and Au atoms, respectively.

Nature of bonding and electronic structure of neutral and anionic clusters:

The nature of bonding and the electronic structure between U and Au atoms is studied using the calculated NBO charges on the atoms, Mayer's bond order (MBO) which signifies the bond strengths between the U and Au atoms, Adaptive Natural Density Partitioning (AdNDP) analysis, Bader's quantum theory of atom in molecules (QTAIM) analysis, Projected Density of States (pDOS) and the 3D charge density plot of the highest occupied molecular orbital (HOMO). In the following, we discuss these properties for UAu_n ($n=3-7$).

UAu_3 :

The NBO charges on U and Au in neutral UAu_3 are +1.12 e, and -0.37 e, respectively (see Table III.B.4.1, and Figure III.B.4. 2(c, d)). Charge transfer from U to Au atoms in neutral UAu_3 suggests that Au behaves more like a halogen,

a reflection of its large electron affinity. In UAu_3^- , the corresponding charges on U and Au atoms are +0.66 e, and -0.55 e, respectively. Here, a larger fraction of the electron goes to the U site as initial charge transfer from U to Au in the neutral cluster raises its oxidation state. The bond strengths between the U and Au atoms obtained from the MBO analysis are 1.22, and 1.13 in the neutral and anionic clusters, respectively. These indicate strong sigma bond between U and each Au atom (see Table III.B.4. 1). The smaller MBO values in the anionic UAu_3 is consistent with the longer and weaker U-Au bond.

The nature of bonding in UAu_3 is further analyzed using the Adaptive natural density partitioning (AdNDP) technique. The results are shown in Figure III.B.4. 2(a) and 2(b). The occupation number (ON) represents the number of electrons participating in the bond formation, with a maximum value of 2|e| per bond. In neutral UAu_3 , U possesses 3 un-paired electrons in 5f orbitals with ON of 0.99 |e|, which corresponds to three singly occupied Lewis Lone pairs. Therefore, the oxidation state of U in neutral UAu_3 is +3. Each of the 3 Au atoms in neutral UAu_3 contains doubly occupied 5 (5d) orbitals, thus contributing a total of 15 (5d)-orbitals. The corresponding ON of Au is 1.99 |e|. In addition, 3 two-center two-electron pairs (2c-2e) of neutral UAu_3 participate in the formation of 3 U-Au ionic bond with about 75 % being contributed by Au and 25 % by U. In the case of UAu_3^- , U possesses 4 un-paired electrons where 3 comes from its 5f orbitals and one from hybrid orbital consisting of 7s (63.6 %), and 6d (35.6 %) with ON of 0.99 |e|. The oxidation state of U in UAu_3^- is, thus, +4. The three 2c-2e pair with ON 1.99 |e| forming 3 U-Au bonds in UAu_3^- have ionic character with 81 % coming from Au and 19 % from U.

The nature of bonding is further confirmed using the Bader's quantum theory of atom in molecules (QTAIM) analysis. The topologies of the neutral and anionic UAu_3 clusters using the QTAIM analysis are shown in Figure III.B.4.2(c) and 2(d), respectively. The bond critical points (BCP) between two atoms within a molecule confirm the existence of a chemical bond, and the sign of the values of Laplacian of electron density ($\nabla^2\rho(r)$) at the BCP defines the nature of interaction between the corresponding atoms. The negative value of the Laplacian of electron density ($\nabla^2\rho(r) < 0$) at BCP implies covalent nature of the bond, while the positive value ($\nabla^2\rho(r) > 0$) indicates non-covalent (ionic/polar) nature. The positive values of $\nabla^2\rho(r)$ at BCP, namely, 0.12 and 0.09 au in neutral and anionic UAu_3 , respectively, further confirm the ionic nature of the bond.

To understand electronic structure of the neutral and anionic UAu_3 clusters around the Fermi level, Projected density of states (pDOS) along with the 3D charge density plot of the highest occupied molecular orbital (HOMO) are

calculated and shown in Figure III.B.4.2(e) and the inset of Figure III.B.4.2 (e), respectively. The vertical dashed lines in the pDOS for neutral and anionic UAu_3 shows the position of the HOMO energy levels (see Figure III.B.4.2(e)). The pDOS of neutral UAu_3 at HOMO energy level consists of U 5f orbital, and a very small contribution of Au 5d orbitals. This is consistent with the 3D charge density plot of HOMO. Similarly, HOMO energy level in the pDOS of UAu_3^- consists of mostly U 6d, and a small contribution of Au 6s as shown by the overlap of the corresponding orbitals at the HOMO energy level. This too is consistent with the 3D charge density plot of HOMO. As an electron is added, the HOMO energy level of UAu_3^- shifts upwards (toward higher energy states) and the corresponding HL energy gap decreases. The HL gaps in the neutral and anionic UAu_3 clusters are 2.90 eV and 1.73 eV, respectively. The above results further confirm that the additional electron preferably goes to the U atom.

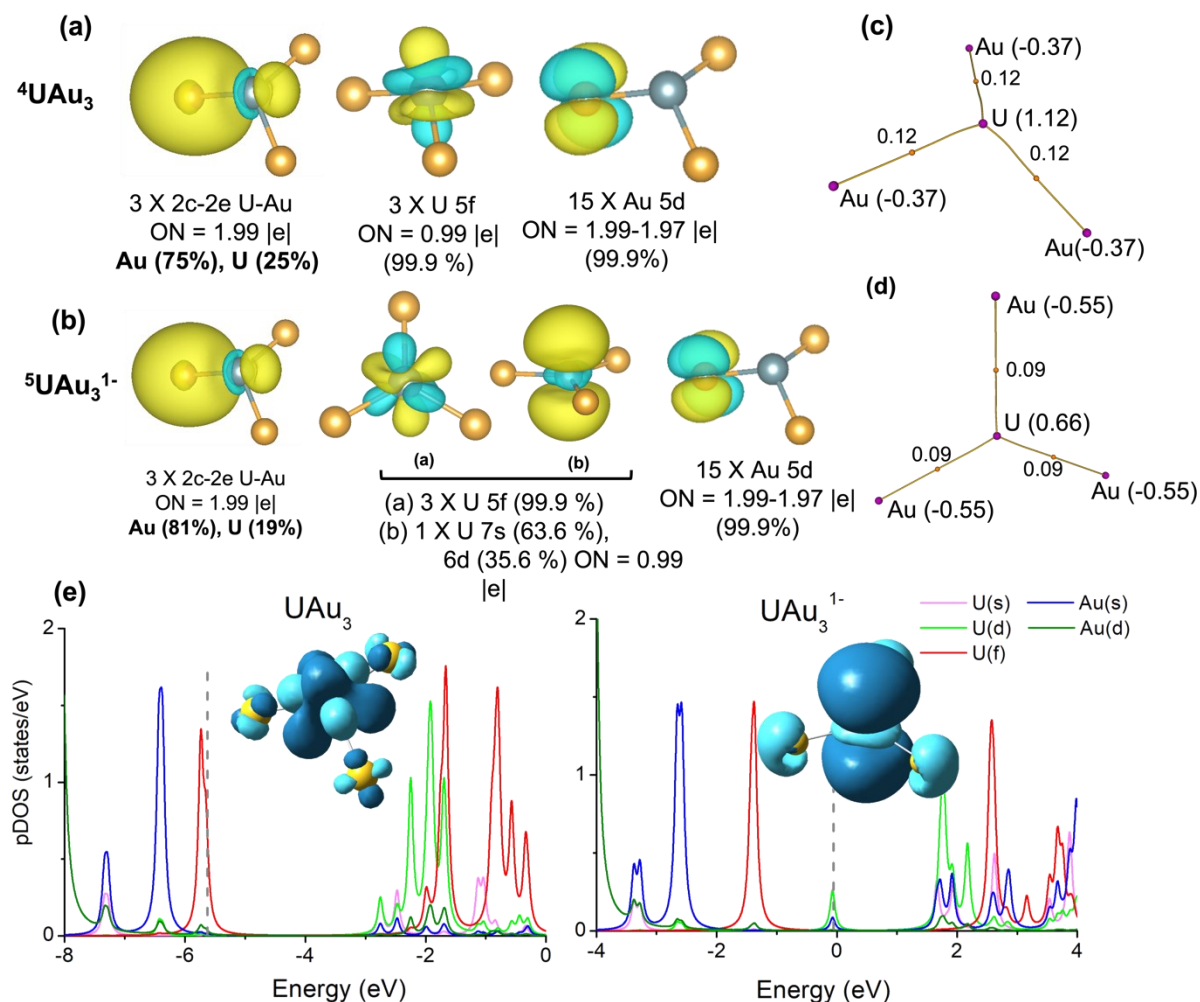


Figure III.B.4.5 Electronic structure and bonding analysis of neutral and anionic UAu_3 cluster.

(a) Adaptive natural density partitioning (AdNDP) analysis of neutral UAu_3 , and (b) UAu_3^- . (c) Bader's quantum theory of atoms in molecule (QTAIM) topology of neutral UAu_3 and (d) UAu_3^- . The pink and orange dots represent the atom centered, and bond centered critical points (BCP). The numbers at the BCP are the corresponding Laplacian electron density ($\nabla^2\rho(r)$) values (in the atomic units). The NBO charges (in units of e) are provided in the parathesis along with the atom symbols (e) Projected density of states for the neutral and anionic of UAu_3 cluster. The contribution of U(s), U(d), U(f), Au(s), and Au(d) orbitals are shown in the pink, light green, red, blue, and olive solid lines. The inset in each figure represents the 3d charge density along the HOMO energy levels. Cyan and blue colors in the HOMO represent positive and negative Isosurface charge density lobes, respectively. Yellow and blue colors in AdNDP analysis represent the charge accumulation and depletion regions, respectively. Orange and gray spheres

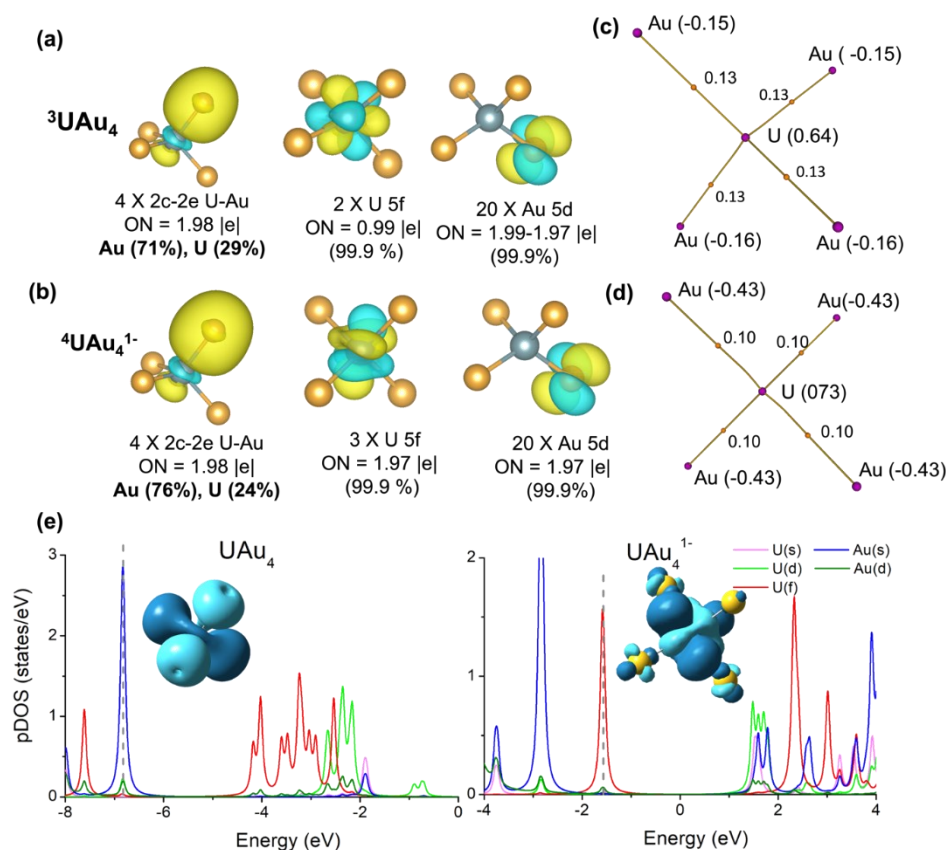


Figure III.B.4.4 Electronic structure and bonding analysis of UAu_4 cluster.

(a) Adaptive natural density partitioning (AdNDP) analysis of neutral UAu_4 , and (b) UAu_4^- . (c) Bader's quantum theory of atoms in molecule (QTAIM) topologies of neutral UAu_4 , and (d) UAu_4^- . The pink and orange dots represent the atom centered, and bond centered critical points (BCP). The number at the BCP are the corresponding Laplacian electron density ($\nabla^2\rho(r)$) values (in the atomic units). The NBO charges (in units of e) are provided in the parathesis along with the atom symbols. (e) Projected density of states for the neutral and anionic of UAu_4 cluster. The contribution of U(s), U(d), U(f), Au(s), and Au(d) orbitals are shown in the pink, light green, red, blue, and olive solid lines. The inset in each figure represents the 3d charge density along the HOMO energy levels. Cyan and blue colors in the HOMO represent positive and negative Isosurface charge density lobes, respectively. Yellow and blue colors in AdNDP represent the charge accumulation and depletion regions, respectively. Orange and gray spheres represent the Au and U atoms, respectively.

represent the Au and U atoms, respectively. Superscript in the U atom represent the spin multiplicity of the cluster.

UAu₄:

The NBO charges on U and Au atom in neutral UAu₄ are 0.64, and -0.15 (-0.16) (see Table III.4.1). Among the four Au atoms in neutral UAu₄, two Au atoms carry -0.15 e, while the other two carry -0.16 e (Figure III.B.4. 3(c)). In UAu₄⁻, on the other hand, the NBO charges on U and Au atoms are 0.73, and -0.43 e, respectively. Unlike the case of UAu₃⁻, a major fraction of the added electron in UAu₄⁻ goes to the Au atoms, causing halogen-like nature of Au in UAu₄ as we will see later the EA discussion. The corresponding MBO bond strengths are 1.34 and 1.06, confirming the strong sigma bond between the U and Au atoms, with relatively stronger bond in the neutral than in the anionic UAu₄ cluster.

The nature of chemical bonding in UAu₄ is further studied using AdNDP analysis. The results are shown in Figure III.B.4. 3(a), 3(b). In neutral UAu₄, U carries 2 un-paired electrons coming from its 5f orbitals, which correspond to two singly occupied Lewis Lone pairs with ON value of 0.99 |e|. Therefore, the oxidation state of U in neutral UAu₄ is +2. Each of the four Au atoms in the neutral UAu₄ contributes five doubly occupied 5d orbitals, creating five Lewis long pairs with ON value of 1.99-1.97 |e| (see Figure III.B.4.3(a)). Along with this, 4 two-center two-electron pairs (2c-2e) participate in the formation of 4 U-Au ionic bonds in neutral UAu₄ cluster with 71 % contribution coming from Au and 29 % from U. In UAu₄⁻, U carries 3 un-paired electrons coming from its three singly occupied 5f orbitals, which correspond to three Lewis lone pairs (see Figure III.B.4.3(b)). Therefore, the oxidation state of U in UAu₄⁻ is +3. Accordingly, four U-Au bonds formed due to 2c-2e pair with ON value of 1.98 |e| in UAu₄⁻ are ionic in character with 76 % contributed by Au and 24 % by U.

To verify further the ionic nature of U-Au bonding in UAu₄ clusters, Bader's QTAIM analysis is performed; the topologies for neutral and anionic UAu₄ clusters are shown in Figure III.B.4.3(c) and 3(d), respectively. The positive values of $\nabla^2\rho(r)$ at BCP, 0.13 au and 0.10 au for neutral and anion UAu₄ clusters, respectively confirm the ionic nature of the bond.

Next, the electronic structure around the Fermi level is analyzed using pDOS analysis and the 3D charge density plot of the HOMO for neutral and anionic UAu₄. The results are shown in Figure III.B.4.3(e) and inset of Figure III.B.4.3 (e). For neutral UAu₄, pDOS at HOMO energy level consists of mostly Au 6s orbital, which is consistent with the 3D charge density plot of HOMO. Similarly, HOMO energy level in the pDOS of UAu₄⁻ consists of mostly U 5f, and

very little of Au 5d as shown by the overlap of the corresponding orbitals (see Figure III.B.4.3 (e)). This is also consistent with the 3D charge density plot of HOMO. As the extra electron is added, the Au 6s orbitals in the pDOS of UAu_4^- near the HOMO energy level shifts upward (toward higher energy states) compared to that of the neutral state. The corresponding HL energy gap increases. The HL gaps in the neutral and anionic UAu_4 cluster are 2.62 eV and 4.29 eV, respectively. The increase in the HL gap and shifting of the participating Au 6s orbitals toward higher energy further confirm that the added electron preferentially resides on Au atom, making it behave like a halogen.

UAu₅:

The NBO charge on U in neutral UAu_5 is 0.64e while those on Au1, Au2, Au3, and Au4 are -0.24, -0.24, -0.01, -0.05, and 0.11 e, respectively. In UAu_5^- , U carries a charge of 0.05e while Au1, Au2, Au3, Au4, and Au5 carry charges of -0.20, -0.20, -0.22, -0.22, and -0.22e, respectively. Note that a larger fraction of the added electron again resides on the U atom with the remaining distributed evenly on the five Au atoms.

The strength of U-Au bond computed using the MBO analysis in the neutral UAu_5 is 1.19 for Au1 and Au2, and 0.52 for Au3, Au4, and Au5 atoms. This implies that all the Au atoms bind strongly with U. However, Au1 and Au2 have stronger bond strength than Au3, Au4, and Au5 with the U atom. The MBO for U-Au in UAu_5^- is 1.20 for Au1 and Au2, and 1.23 for Au3, Au4, and Au5. This shows nearly same bond strength of all the U-Au bond in the UAu_5^- cluster is consistent with its high symmetry.

The results of the AdNDP analysis revealing the nature of bonding in UAu_5 cluster are shown in Figure III.B.4.4(a), 4(b). In neutral UAu_5 , U atom carries 3 un-paired electrons in its 5f orbitals, which implies that U has three singly occupied Lewis Lone pairs with ON value of 0.99 |e|. Therefore, the oxidation state of U in neutral UAu_5 is +3. Along with this, in neutral UAu_5 , 3 Au atoms placed nearly in the same plane (i.e., Au1, Au2, and Au3) participate in the formation of two small rings using three-center two-electron (3c-2e) bond configuration with ON value of 1.97 |e|, corresponding to σ -aromaticity, and one ring using 3c-2e bond with ON value of 1.83 |e| corresponding to π -aromaticity, as shown in Figure III.B.4.4(a). The existence of both σ - and π -aromaticity is an interesting feature observed in UAu_5 . In UAu_5^- , all the 5 U-Au bonds are ionic in nature formed using 2c-2e pair with ON value of 1.95 |e| with 69 % contributed by Au, and 31% by U. The U atom carries 2 un-paired electrons coming from two singly occupied U 5f orbitals, which correspond to two Lewis lone pairs with ON value of 0.99 |e| (see Figure III.B.4.4(b)). Therefore, the oxidation state of U in anionic UAu_5^- is +2. To verify further the ionic nature of U-Au bonding in UAu_5

clusters, Bader's QTAIM analysis is performed, and the topologies for neutral and anionic UAu_5 clusters are examined as shown in Figure III.B.4.4(c) and 4(d), respectively. The positive values of $\nabla^2\rho(r)$ at BCP further confirm the ionic nature of U-Au bond in the UAu_5 cluster.

The electronic structure of the UAu_5 cluster around the Fermi level are analyzed using pDOS analysis along with the 3D charge density plot of the HOMO as shown in Figure III.B.4.4(e) and inset of Figure III.B.4.4 (e). For neutral UAu_5 , pDOS at HOMO energy level consists of mostly U 5f orbital, and very small amount of Au 5d, which is consistent with the 3D charge density plot of HOMO. Similarly, HOMO energy level in the pDOS of UAu_5^- consists of mostly Au 6s, consistent with the 3D charge density plot of HOMO. Comparison of the pDOS of UAu_5 and UAu_5^- near the HOMO energy level shows that Au 6s orbitals shift upward (toward higher energy states) with the addition of an electron in its neutral UAu_5 state, and the corresponding HL energy gap is increased. The HL gaps in the neutral and anionic UAu_5 cluster are 1.99 eV and 2.69 eV, respectively. The increase in the HL gap, shifting of the participating Au 6s orbitals toward higher energy, and the uniform distribution of the added electron on Au atoms in UAu_5^- further confirm that Au behaves like a halogen in UAu_5 clusters.

Electron affinities and Vertical detachment energies:

In Table III.B.4. 2, the calculated electron affinities (EA) and vertical detachment energies (VDE) of these clusters are compared with the corresponding results obtained from the photoelectron spectra. The EA and VDE of UAu_3 are 1.45 and 1.61 eV, respectively and agree well with the corresponding experimental values of 1.28 and 1.56 eV. The calculated EA and VDE for UAu_4 , namely, 2.96, and 3.39 eV, respectively, also agree well with the experimental values of 2.60, and 3.20 eV. Unlike the case of UAu_3 , the EA of UAu_4 is closer to that of the halogen atoms with Au continuing to behave like a halogen atom. This is consistent with our earlier observation that more of the added electron reside on the four electronegative Au atoms in UAu_4 . The calculated EA and VDE for UAu_5 are 2.87, and 3.84 eV, respectively. The large difference between the EA and VDE is a reflection of the significant difference in the geometries of the neutral and anionic clusters. This is also consistent with the broad PES. The calculated VDE of 3.84 eV agrees well with the experimental VDE of 3.52 eV.

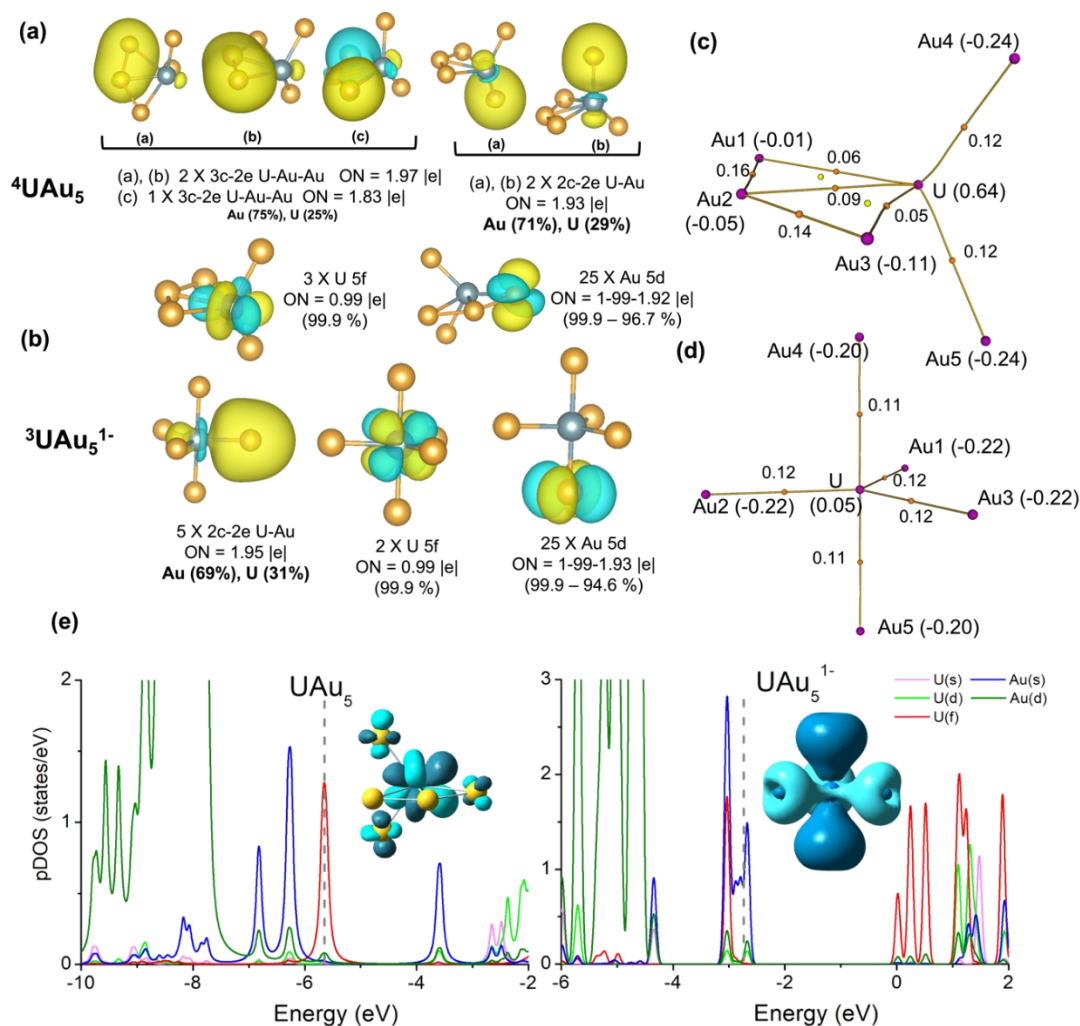


Figure III.B.4.6 Electronic structure and bonding analysis of UAu_5 cluster.

(a) Adaptive natural density partitioning (AdNDP) analysis of neutral UAu_5 , and (b) UAu_5^{1-} . (c) Bader's quantum theory of atoms in molecule (QTAIM) topology of neutral UAu_5 , and (d) UAu_5^{1-} . The pink and orange dots represent the atom centered, and bond centered critical points (BCP). The number at the BCP are the corresponding Laplacian electron density ($\nabla^2\rho(r)$) values (in the atomic units). The NBO charges (in units of e) are provided in the parenthesis along with the atom symbols. (e) Projected density of states for the neutral and anionic of UAu_5 cluster. The contribution of U(s), U(d), U(f), Au(s), and Au(d) orbitals are shown in the pink, light green, red, blue, and olive solid lines. The inset in each figure represents the 3d charge density along the HOMO energy levels. Cyan and blue colors in the HOMO represent positive and negative Isosurface charge density lobes, respectively. Yellow and blue colors in AdNDP represent the charge accumulation and depletion regions, respectively. Orange and gray spheres represent the Au and U atoms, respectively.

Table III.B.4.1 The data include the spin-multiplicity of neutral and mono-anions of UAu_n , $n = 3-7$. Also given are the singly(?) occupied Lewis lone pairs in the spin up and down state along with the natural bond order (NBO) charges

on U and Au atoms. The Mayer bond order (MBO) between the U and Au atoms, and the HOMO-LUMO gap (HL) is provided for the studied $U@Au_n$ cluster.

System	Spin-Multiplicity	Lewis LP (up, down) U Au		q(U)	q(Au)	Mayer BO U-Au	HL Gap (eV)
UAu ₃	quartet	(3,0)	(5,5)	1.12	-0.37	1.22	2.90
UAu ₄	triplet	(2,0)	(5,5)	0.64	-0.15/-0.16	1.34	2.62
UAu ₅	quartet	(3,0)	(5,5)	0.64	-0.24/-0.05	1.19/0.52	1.99
UAu ₆	quintet*	(3,0)		0.31	-0.07/-0.03		
UAu ₇	quartet	(3,0)		0.21	-0.03		
UAu ₃ ⁻	quintet	(4,0)	(5,5)	0.66	-0.55	1.13	1.73
UAu ₄ ⁻	quartet	(3,0)	(5,5)	0.73	-0.43	1.06	4.29
UAu ₅ ⁻	triplet	(2,0)	(5,5)	0.05	-0.20/-0.22	1.20/1.22	2.69
UAu ₆ ⁻	quartet	(3,0)		0.03	-0.17		
UAu ₇ ⁻	triplet	(2,0)		-0.94	-0.01/-0.07		

* The calculated EA and VDE for UAu₆ are provided for three isomers in the order of isoI/isoII/isoIII

Table III.B.4.2 Experimental and calculated electron affinities (EA) and vertical detachment energies (VDE) of UAu_n^- ($n = 3-7$) clusters.

Species	EA (eV)		VDE (eV)	
	Experimental	Theoretical	Experimental	Theoretical
UAu ₃	1.28	1.45	1.56	1.61
UAu ₄	2.60	2.69	3.20	3.39
UAu ₅	3.24	2.87	3.52	3.84
UAu ₆	2.88	2.99/3.04/3.07*	3.28	3.18/3.34/3.40*
UAu ₇	2.56	2.72	3.67	3.59

Geometry and electronic structure of $[UAu_6]^{0/1-}$

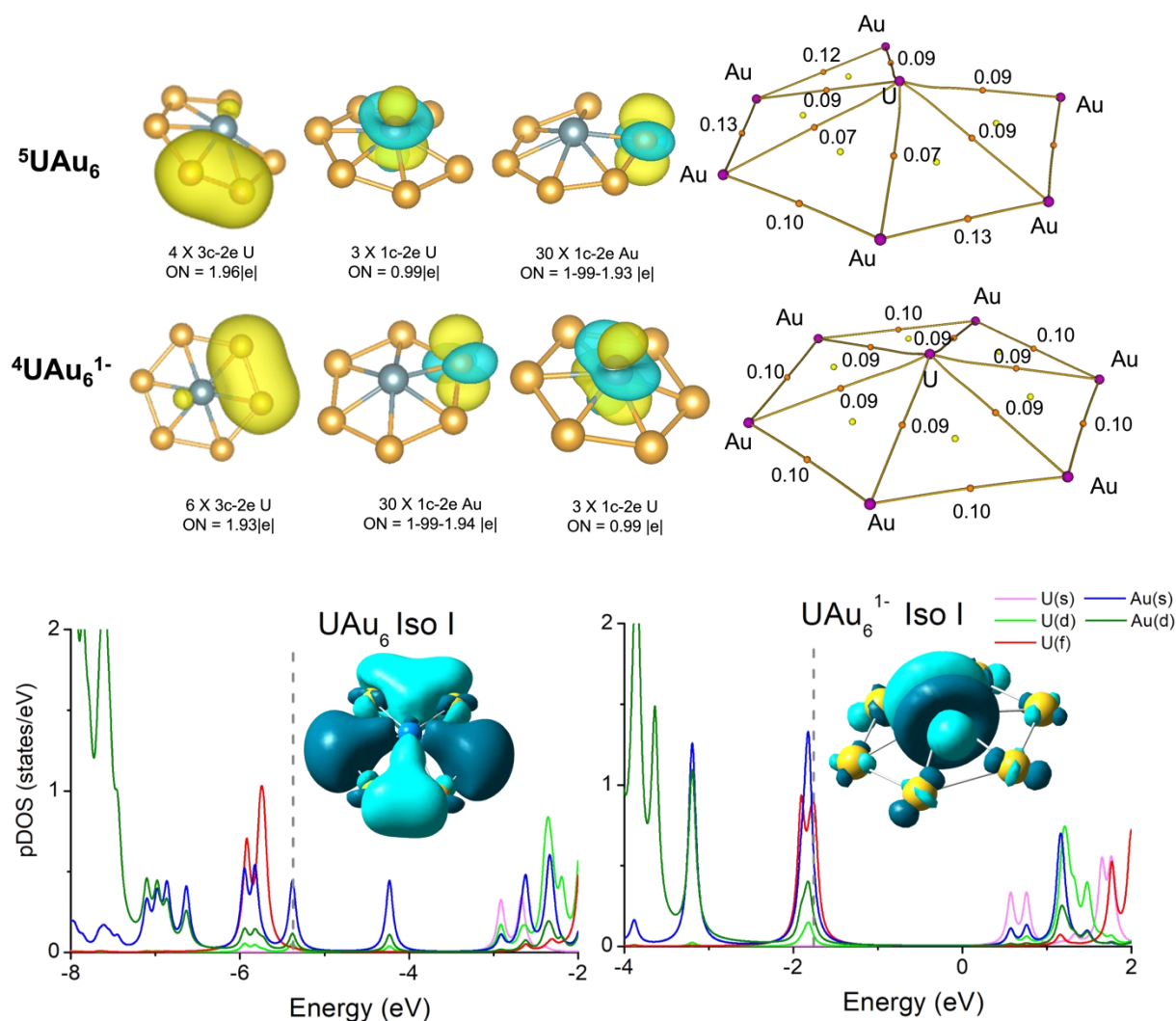


Figure III.B.4.7 Electronic structure and bonding analysis of UAu_6 cluster.

(a) Adaptive natural density partitioning (AdNDP) analysis of neutral UAu_6 , and (b) UAu_6^{1-} . (c) Bader's quantum theory of atoms in molecule (QTAIM) topology of neutral UAu_6 and (c) UAu_6^{1-} . The pink and orange dots represent the atom centered, and bond centered critical points (BCP). The number at the BCP are the corresponding Laplacian electron density ($\nabla^2\rho(r)$) values. (e) Projected density of states for the neutral and anionic of UAu_6 cluster. The contribution of U(s), U(d), U(f), Au(s), and Au(d) orbitals are shown in the pink, light green, red, blue, and olive solid lines. The inset in each figure represents the 3d charge density along the HOMO energy levels. Cyan and blue colors in the HOMO represent positive and negative Isosurface charge density lobes, respectively. Yellow and blue colors in AdNDP represent the charge accumulation and depletion regions, respectively. Orange and gray spheres represent the

Au and U atoms, respectively.

σ - aromaticity in UAu₅, UAu₆, and UAu₇ clusters

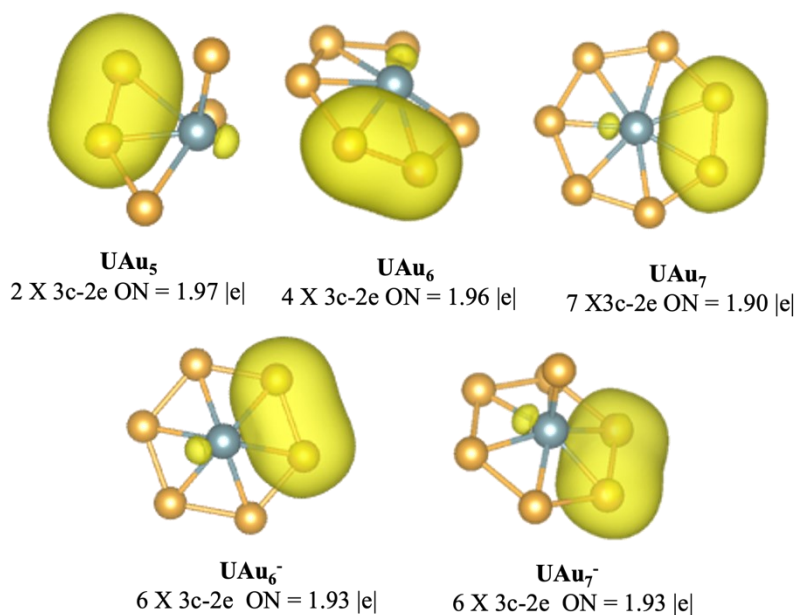


Figure III.B.4.8 AdNDP analysis on 3-centered 2-electron bonding pattern in the neutral and mono-anion of UAu_n, n= 5,6, and 7. The ON values represent the occupation number.

Author Contributions:

R.M.H., Z.Z., and B.A.T. completed the experimental photoelectron study. D., P.J. and K.A.P. performed the theoretical study. K.H.B, P.J. and K.A.P. conceived of and supervised the work.

References and Notes:

1. Zhang, P.; Liu, H.; Zou, W.; Zhang, P.; Hu S.X. Relativistic Effects Stabilize the Planar Wheel-like Structure of Actinide-Doped Gold Clusters: An@Au₇ (An = Th to Cm). *J. Phys. Chem. A* 2020, *124*, 8173-8183
2. Gao, Y.; Wang, Z. Effects of 5f-elements on electronic structures and spectroscopic properties of gold superatom model. *Chin. Phys. B* 2016, *25*, No. 083102.
3. Wang, J.; Xie, W.; Wang, J.; Gao, Y.; Lei, J.; Zhang, R.-Q.; Wang, Z. Actinide embedded nearly planar gold superatoms: structural properties and applications in surface-enhanced Raman scattering (SERS). *Phys. Chem. Chem. Phys.* 2018, *20*, 27523–27527.

4. Gao, Y.; Dai, X.; Kang, S.; Jimenez-Cruz, C.A.; Xin, M.; Meng, Y.; Han, J.; Wang, S.; Zhou, R. Structural and electronic properties of uranium-encapsulated Au₁₄ cage. *Sci Rep.* 2014, 4, 5862
5. Gao, Y.; Chen, L.; Dai, X.; Song, R.; Wang, B.; Wang, Z. A strong charge-transfer effect in surface enhanced Raman scattering induced by valence electrons of actinide elements *RSC Adv.*, 2015,5, 32198-32204
6. Wu, X.; Gao, Y.; Xie, W.; Wang, Z. Bonding properties of a superatom system with high-Z elements: insights from energy decomposition analysis *RSC Adv.*, 2020,10, 14482-14486
7. Kaltsoyannis, N. Does covalency increase or decrease across the actinide series? Implications for minor actinide partitioning. *Inorg. Chem.* 2013, 52, 3407–3413.
8. Neidig, M.L.; Clark, D.L.; Martin, R.L. Covalency in f-element complexes. *Coordination Chemistry Reviews* 2013, 257, 394-406
9. Pyykko, P. Relativistic effects in structural chemistry. *Chem. Rev.* 1988, 88, 563-594
10. Pyykko, P. Relativistic effects in chemistry; more common than you thought. *Annu. Rev. Phys. Chem.* 2012, 63, 45-64

IV. Small Molecule Activation

With diminishing natural resources, there is an ever-increasing demand for cost-effective and sustainable production of fine and commodity chemicals. The chemical process to convert small molecules such as dihydrogen (H_2), dinitrogen (N_2), dioxygen (O_2), carbon monoxide (CO), carbon dioxide (CO_2), water (H_2O), methane (CH_4) into value-added fine chemicals has been of paramount importance in industries.

Catalysis is at the center of chemistry. It is desirable to develop new catalytic methods that can permit efficient and targeted conversion of small molecules in fossil and bio-renewable feedstocks with lower energy requirements and environmental impact. Since small molecules typically involve rather inert bond(s) and are thus thermodynamically stable, valorization of small molecules requires a bond-activation step. Therefore, molecular activation is a prerequisite to catalysis.

While most catalytic reactions of small molecules occur heterogeneously, gas phase studies provide an ideal environment for probing the energetics and kinetics of a chemical process at a strictly molecular level.¹ Our anion photoelectron spectroscopy conducted in the high vacuum displays a distinct advantage in initiating and elucidating microscopic facets of molecular activation. In this chapter, I present our investigations on small molecule activation by single atomic anions and metal hydride anions via a synergetic combination of spectroscopic and computational studies.

References

1. Schwarz, H. (2017). Ménage-à-trois: single-atom catalysis, mass spectrometry, and computational chemistry. *Catalysis Science & Technology*, 7(19), 4302-4314.

IV.A. Small Molecule Activation by Single Atomic Anions

The ultimate goal in heterogeneous catalysis is to make use of each and every atom of supported (metal) catalysts, i.e. in the extreme to perform single-atom catalysis (SAC). The use of single atoms to induce activation and thus catalysis has many potential advantages. In addition to saving on the cost of expensive catalytic metals, single atom catalysts are also the ultimate single-site catalysts and as such offer the prospect of enhanced selectivity. Typical catalysts feature late transition metals. The most active transition-metal catalysts are based on Pt, Pd, Rh, Ru, Ir, Os, etc, due to their various oxidation states and ability to be a good source/sink of electrons. In this subsection IV.A, we focus on small molecule activation by single Ir and Pt anions.

In Chapter IV.A.1, evidence of water activation and splitting by single Ir anions was observed in the mass spectrum and photoelectron spectrum. Multiple isomers of the $[\text{Ir-H}_2\text{O}]^-$ complex were identified with the help of DFT calculations. NBO and ELF (Electron Local Function) analyses were conducted to study the charge and bonding characteristics of activation intermediates. Chapter IV.A.2 continues the activation study with iridium atomic and cluster anions. Hydroxylamine, a component of the well-known hydroxylammonium nitrate (HAN) ionic liquid, is a safer alternative and mimics the chemistry and performance standards of hydrazine. Upon reaction with Ir_n^- clusters, HAN loses two hydrogen atoms, and $\text{Ir}_n\text{-(NOH)}$ clusters remain.

Starting from Chapter IV.A.3 to Chapter IV.A.5, we moved on to the single platinum anions. First, we reported the selective single bond breakage by Pt^- in Chapter IV.A.3. $[\text{PtCH}_4]^-$ is shown to be H-Pt-CH_3^- by a synergy between anion photoelectron spectroscopy and quantum chemical calculations. This is the first example of methane activation by a single atomic anion. Chapter IV.A.4 expanded the study to tertiary reactions between methane, carbon dioxide, and single platinum anions. The methane activation complex, $\text{H}_3\text{C-Pt-H}^-$, reacts with CO_2 to form $[\text{H}_3\text{C-Pt-H(CO}_2)]^-$. Via a synergy between PES and calculations, mechanistic analysis reveals that both CH_4 and CO_2 are activated by the anionic Pt atom, and that the negative charge on Pt is the driving force for CO_2 insertion into Pt-H and Pt-C bonds in $\text{H}_3\text{C-Pt-H}^-$. Last, in Chapter IV.A.5, we present the CO_2 hydronation reaction in the gas phase with the presence of H_2O , platinum atoms, and electrons, which mimics the electrochemical conversion of CO_2 in the aqueous phase with Pt electrodes. A single platinum anion activates H_2O , forming H-Pt-OH^- in the first step. Next, the complex reacts with CO_2 via two different pathways to form formate or to form bicarbonate. This study provides insights into the mechanism of electrochemical conversion of CO_2 at the molecular level.

IV.A.1. Water activation and splitting by single anionic iridium atoms

(This manuscript in under preparation)

Zhaoguo Zhu, Gaoxiang Liu^{#1}, Sandra M. Ciborowski,^{#2} Yulu Cao,^{#3} Kit H. Bowen*

Department of Chemistry, Johns Hopkins University, 3400 N Charles St, Baltimore, MD, 21218 (USA) E-mail: kbowen@jhu.edu

#1 Present Address: Advanced Bioimaging Center, Department of Molecular and Cell Biology, University of California, Berkeley, Barker Hall, Berkeley, CA, 94720 (USA).

#2 Present Address: U.S. Drug Enforcement Agency, Miami, FL

#3 Present Address: Division of Chemistry and Chemical Engineering, California Institute of Technology, Pasadena, CA 91125

Abstract

Mass spectrometric analysis of the anionic products of interaction among Ir^- and water shows that the efficient generation of $[\text{Ir}(\text{H}_2\text{O})]^-$ intermediate and IrO^- product. The anion photoelectron spectra of $[\text{Ir}(\text{H}_2\text{O})]^-$, formed under different conditions, exhibit spectral features that are due to the anion-molecule complex, $\text{Ir}^-(\text{H}_2\text{O})$, and to the reaction intermediates, $[\text{H-Ir-OH}]^-$ and $[\text{H}_2\text{-Ir-O}]^-$, where one and two O-H bonds have been broken, respectively. The calculated and measured vertical detachment values (VDE) are in good agreement and thus support identification of all three types of isomers. The calculated reaction pathway shows the overall reaction $\text{Ir}^- + \text{H}_2\text{O} \rightarrow \text{IrO}^- + \text{H}_2$ is exothermic. Two minimum energy crossing points (MECPs) were located which converts the reactants between singlet and triplet potential surfaces. This study presents the first example of water activation and splitting by a single Ir anion.

Introduction

Water splitting plays a crucial role in the production of hydrogen (H_2), a promising clean and renewable energy source owing to its carbon-free emission, earth-elemental abundance, and high gravimetric energy density (approximately 142 MJ kg^{-1}). Electrolysis¹⁻³, photocatalysis^{4,5}, artificial photosynthesis^{6,7}, and thermal decomposition⁸ are the main strategies to split water. However, the scalable industrial application of water splitting is still impeded by the huge energy penalty. To reduce the high reaction energy barrier, tremendous efforts have been devoted to developing

effective and cost-efficient catalysts in different phases.⁹⁻¹¹ In recent years, single-atom catalysts (SACs)¹², especially noble-metal single-atoms catalysts (NMSACs)¹³, with atomically dispersed metal sites on different substrates, have attracted broad interest to global scholars due to their unique physicochemical properties and extreme atom utilization efficiency. Among NMSACs, Ir SACs often possess outstanding catalytical performance for water splitting.¹⁴⁻²² For instance, Ir single atoms anchored on N-doped porous carbon support with dispersed Co nanoparticles displayed the overpotential of 260 mV at 10 mA cm⁻² for the oxygen evolution reaction (OER, half-reaction in electrochemical water splitting), which is significantly smaller than that of the commercial IrO₂ (385 mV).¹⁵ Another example shows that Ir single atoms on Co_{0.8}Fe_{0.2}Se₂@Ni foam can also boost the hydrogen evolution reaction (HER), the critical half-reaction to produce H₂.¹⁶ However, the complicated environment in realistic reaction conditions is a hindrance to gain comprehensive mechanistic insight into the activation and splitting process.

Well-defined, isolated systems in the gas phase are ideal models to rule out the complex environmental perturbations. Numerous gas-phase studies of water reaction by metal atoms and clusters have provided insight into water splitting at the molecular level.²³⁻³⁷ Notably, single Ni, Pd, and Pt anions can activate water, leading to water-activated HMOH⁻ (M = Ni, Pd, Pt) and H₂MO⁻ (M = Pt) intermediates. Particularly, a single Pt anion both activate and split water forming H₂ and PtO⁻ anion products.³⁸ Inspired by previous work, we extend the metals to include Ir to provide insight in designing more Ir SACs, which may serve as alternatives to the flourishing Pt SACs. Single Ir atoms and clusters have been found to react with plenty of small molecules.³⁹⁻⁵¹ Reactivity of water (heavy water, D₂O) with single Ir cations measured at room temperature discloses that only Ir⁺(D₂O), i.e., simple D₂O solvation adducts, were observed.⁵² Nevertheless, studies on reaction between single Ir atom with water are underexplored. Herein, we utilize a combination of mass spectroscopy, anion photoelectron spectroscopy, and quantum chemistry calculations to show that single Ir anions both activate and split water.

Experimental methods

Experimental studies of [Ir(H₂O)]⁻ were conducted using a laser vaporization ion source, time-of-flight mass spectrometry, and anion photoelectron spectroscopy. Photoelectron spectrometer consists of one of several ion sources, a linear time-of-flight mass spectrometer, a mass gate, a momentum decelerator, a neodymium-doped yttrium aluminum garnet (Nd:YAG) laser for photodetachment, and a magnetic bottle electron energy analyzer having a resolution of 50 meV at EKE = 1 eV.⁵³ Photoelectron spectra were calibrated against the well-known photoelectron

spectrum of Cu^- .⁵⁴ The anions were generated using a laser vaporization source, ablating a rotating, translating metal rod with a pulsed Nd:YAG laser beam operating at a wavelength of 532 nm. Almost simultaneously, a plume of water vapor-seeded helium gas from a pulsed gas valve (backing pressure of 100 psi) was injected directly over the rod and then allowed to flow along a 3 cm tube, where reactions and cooling occurred before exiting into the high vacuum. The resulting anionic clusters were mass-analyzed by the time-of-flight mass spectrometer, and their photoelectron spectra recorded.

Computation methods

The lowest energy structures of $(\text{Ir}-\text{H}_2\text{O})^{-/0}$ systems were obtained by density functional theory (DFT)-based electronic structure calculations with the hybrid functional $\omega\text{B97x-d}$.^{55,56} The $\omega\text{B97x-d}$ functional had been tested to perform well for the IrNOH system.⁴⁵ The aug-cc-pvtz basis sets for H and O and the aug-cc-pvtz-pp basis set for Ir were used to optimize all structures.⁵⁷⁻⁵⁹ All calculations were carried out using the Gaussian 09 software package.⁶⁰ The vertical detachment energy (VDE) was obtained by subtracting the electronic energy of the neutral from anion at its anionic optimized geometry. The electronically excited states of neutral $\text{Ir}(\text{H}_2\text{O})$ were calculated using the TD-DFT method using the same functional and basis sets. Intrinsic reaction coordinate calculations were employed to check that each transition state connects two appropriate local minima. Vibrational frequency calculations were performed to check that the intermediates and transition states have zero and only one imaginary frequency, respectively. Natural population analysis (NPA) was conducted to examine the charge distribution at the $\omega\text{B97x-d}$ level using natural bond orbital (NBO) 3.1 implemented in Gaussian 09.⁶¹ NPA has been found to be satisfactory in predicting charge distributions within metal-containing clusters.^{62,63} The minimum-energy crossing points (MECPs) for the intersection of the electronic states of different spin multiplicities were searched for and located by using the method developed by Harvey et al.⁶⁴ The electron localization functions (ELF) were analyzed and plotted employing the Multiwfn program.^{65,66}

Results and discussion

The mass spectrum with water/helium mixed backing gas by using different ablation laser power are shown in figure IV.A.1.1. In the lower ablation laser power condition, only Ir^- , IrOH^- and $[\text{Ir}(\text{H}_2\text{O})]^-$ are shown in the mass spectrum. After slightly increasing the laser power, IrO^- peak also appeared, as a result of decomposition of $[\text{Ir}(\text{H}_2\text{O})]^-$. We are interested in $[\text{Ir}(\text{H}_2\text{O})]^-$ which could exist in three types of structure: (i) one is that Ir anion is solvated by a water

molecule, i.e., $\text{Ir}(\text{H}_2\text{O})$; (ii) A structure in which only one O-H bond is broken i.e., $[\text{H}-\text{Ir}-\text{OH}]^-$; (iii) the structure that two O-H bonds have been broken, i.e., $[\text{H}_2-\text{Ir}-\text{O}]^-$. In the type (i) physisorbed structure, hydrogen atoms in the water molecule only weakly interact with Ir anion. Type (ii) and (iii) anions are water-activated products resulting from one or both O-H bonds being inserted by iridium. All three types of products could possibly coexist in the ion beam.

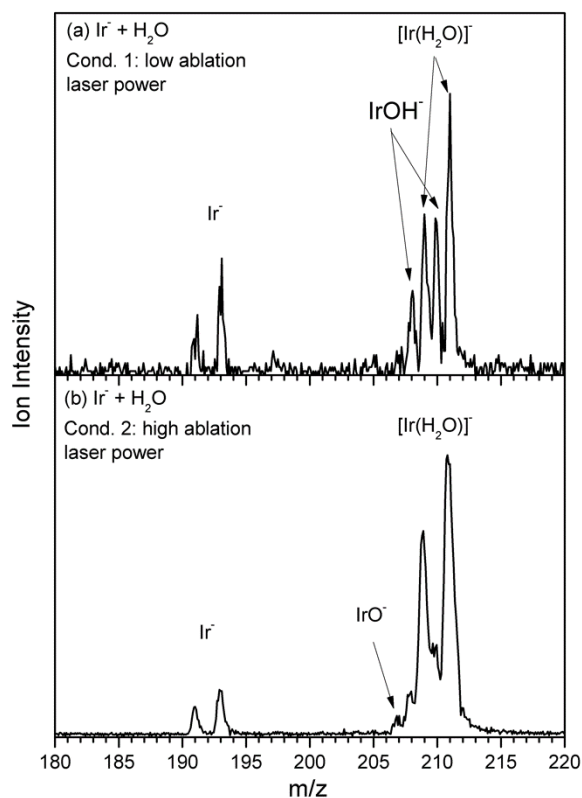


Figure IV.A.1.1 Mass spectra of Ir^- with water. Mass spectrum (a) was recorded under low ablation laser power (b) under high ablation laser power.

The photoelectron spectra were taken to distinguish these isomers. The middle and bottom panels of figure IV.A.1.2 present the anion photoelectron spectrum of $[\text{Ir}(\text{H}_2\text{O})]^-$ in low and high ablation laser power, while the spectrum of their corresponding atomic Ir anion is displayed in the top panel for comparison. Typically, when an atomic metal anion interacts weakly with another molecule, i.e., water, the photoelectron spectrum of the resulting solvated cluster anion closely resembles that of the anion alone, except for having been shifted to higher electron binding energy (EBE) and its features slightly broadened. Because the metal anion acts as the chromophore for photodetachment. Consider the photoelectron spectrum of Ir^- (figure IV.A.1.2a) and $[\text{Ir}(\text{H}_2\text{O})]^-$ (figure IV.A.1.2b). Both spectra exhibit a similar

five-peak profile. All electron binding energy peaks of $[\text{Ir}(\text{H}_2\text{O})]^-$ are all broadened and slightly shifted to the right. This great similarity between the two spectrum means solvation complex $\text{Ir}^-(\text{H}_2\text{O})$ is the major product in low laser power condition (Cond. 1). The lowest EBE peak is at 2.11 eV, determined as the vertical detachment energy (VDE) value of $[\text{Ir}-\text{H}_2\text{O}]^-$. The vertical detachment energy (VDE) is the transition energy at which the Franck-Condon overlap is at its maximum between the anion's wavefunction at the ground electronic state and that of its corresponding neutral at the geometry of the anion, i.e., these are vertical photodetachment transitions. The spectrum in the bottom panel (figure IV.A.1.1c), on the other hand, has two new peaks, which are noted by red stars. These two high EBE features at 3.25 eV and 3.85 eV strongly suggest the presence of activated isomers of $[\text{Ir}(\text{H}_2\text{O})]^-$ in higher laser ablation power condition (Cond. 2). Therefore, the spectrum at the bottom shows both features of physisorbed and chemisorbed products. However, VDEs of activated $[\text{Ir}(\text{H}_2\text{O})]^-$ are unknown since we were not able to make the activated products alone, and they may be buried in the broad peaks between 2.0-3.0 eV.

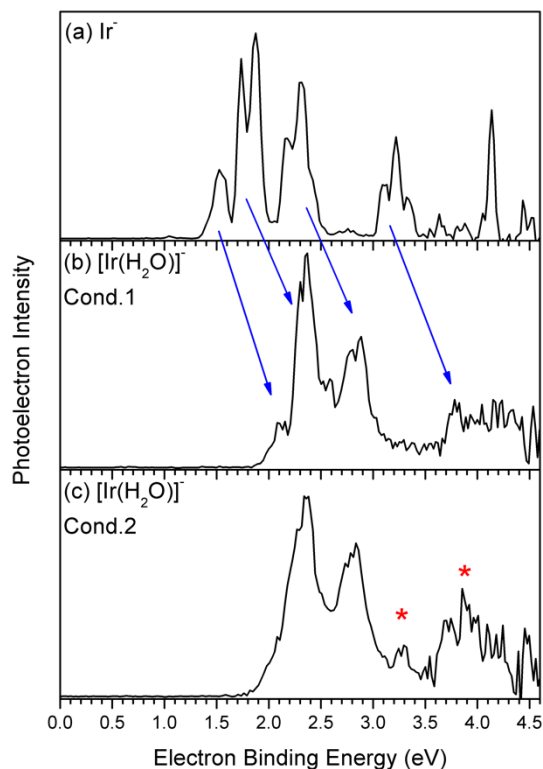


Figure IV.A.1.2. Photoelectron spectra of the atomic metal anions, Ir^- , (in the top panel) and $[\text{Ir}(\text{H}_2\text{O})]^-$ anions (in the lower panels). All of these anion photoelectron spectra were measured using the fourth harmonic (4.66 eV/photon)

of an Nd:YAG laser. Blue arrows link Ir^- peaks to the corresponding blue-shifted peaks in $\text{Ir}^-(\text{H}_2\text{O})$ anion-molecule complexes. Red dots mark additional structural isomers.

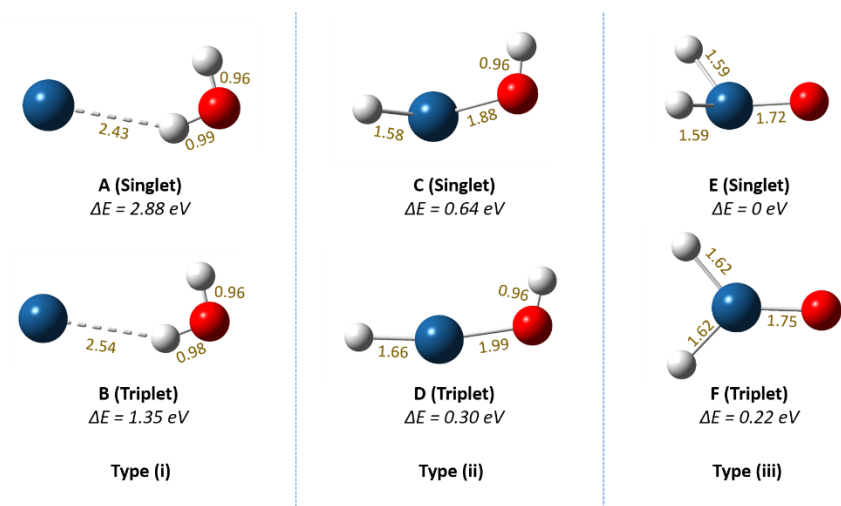


Figure IV.A.1.3 Optimized structures of $[\text{Ir}(\text{H}_2\text{O})]^-$ categorized in three types. (i) Ir anion is solvated by a water molecule; (ii) only one O-H bond is broken; (iii) two O-H bonds are broken. The relative energies of $[\text{Ir}(\text{H}_2\text{O})]^-$ and their calculated VDEs are listed below each structure. Bond lengths are also shown in each structure.

DFT calculations were carried out to find the possible intermediates formed via the reaction between Ir anion and water molecule. The optimized isomers in different spin multiplicities for these reaction intermediates are presented in Figure IV.A.1.3, along with their relative energies. We categorize all isomers into three types. Structure A and B are type (i) isomers that can be seen as an Ir⁻ anion solvated by a water molecule. The ground state of the iridium anion is a triplet with $[\text{Xe}]4f^{14}5d^86s^2$ electronic configuration, which makes the ground state of $\text{Ir}^-(\text{H}_2\text{O})$ a triplet too. The singlet solvation structure, A, is 1.53 eV higher in energy than the triplet isomer B. Both isomer A and B exhibit a planar structure. In isomer B, the bond length of the O-H bond in the water moiety is 0.96 Å and 0.98 Å, both close to that of an isolated H_2O molecule (0.96 Å). Thus, the water moiety in the isomer B remains almost intact except one O-H bond slightly elongated due to the attraction from the Ir anion. In type(ii) isomers, C and D, iridium atom is wedged into the O-H bond of water, forming an H-Ir-OH⁻ structure suggesting the water is activated, which is the first step of water splitting. Triplet isomer D is lower in energy by 0.34 eV than the singlet isomer C. The global minimum of $[\text{Ir}(\text{H}_2\text{O})]^-$, E, features two H atoms attached to the Ir atom, yielding an $\text{H}_2\text{-Ir-O}^-$ structure. Isomer E has an O-Ir- H_2 dihedral angle of 53.2°, while isomer F has a planar structure with C_{2v} symmetry. Interestingly, in type (iii) isomers,

the singlet is lower than triplet by 0.22 eV, indicating spin-crossover may take place when intermediates transform from type (ii) to type (iii).

Table IV.A.1.1 Computed VDEs for each structure from figure IV.A.1.3 and their corresponding experimental values (eV)

	Type (i)		Type (ii)		Type (iii)	
<i>Isomers</i>	A (singlet)	B (triplet)	C (singlet)	D (triplet)	E (singlet)	F (triplet)
<i>Expt. VDE</i>	2.11		N/A		N/A	
<i>Calc. VDE</i> <i>(doublet)</i>	1.19	2.72	1.67	3.01	2.31	2.54
<i>Calc. VDE</i> <i>(quartet)</i>	0.64	2.16	2.23	2.45	3.20	2.95

To verify these optimized structures, calculated VDEs from each isomer to both doublet and quartet of neutrals were compared with the experimental values. From Table IV.A.1.1, all calculated VDE values are lower than our photon energy (4.66 eV), but VDEs for isomer A (0.64 eV) and C (1.67 eV) are significantly lower than the experimental value (2.11 eV), suggesting the existence of isomer A and C in the ion beam should be excluded. Even with calculated VDE values, the complex $[\text{Ir}(\text{H}_2\text{O})]^-$ photoelectron spectra cannot be explained fully due to the dense excited states of each isomer. We further conducted TD-DFT excited-state calculations on all neutral forms of isomers at their anionic geometries. The complete list of excitation energies is provided in table S1 in the supporting information. To further confirm how each isomer contributes to the experimental spectra, we plotted the simulated density of states (DOS) spectra of isomer B, D, E, and F to compare with the experimental spectra, as shown in figure IV.A.1.4. In the DOS spectra, the first stick on the left corresponds to the ground state of the neutral, while other sticks represent the electronically excited states of the neutral. The simulated spectrum of isomer B displays two discernible bands ranging from 2.0 to 2.5 eV and 2.5 to 3.0 eV followed by three lower peaks. In the top panel of figure IV.A.1.4, the experimental spectrum collected under condition 1 is well reflected by simulated spectrum of isomer B. It suggests Ir anion solvated by a water molecule dominates the photoelectron spectrum of $[\text{Ir}(\text{H}_2\text{O})]^-$ under low ablation laser power condition. Under condition 2, however, the two new features appeared at EBE = 3.25 eV and EBE = 3.85 eV in the

spectrum suggest contributions from isomers D, F, and E, whose simulated spectra are convoluted. The highest EBE features in the simulated D, F, and E spectra are 3.4 eV, 3.0 eV, and 4.1 eV, respectively. It is possible that the new features under condition 2 can be attributed to the mixture of multiple electronic states of isomer D, E, and F. Among all isomers, isomer B resembles the experimental spectra the most in profile, indicating isomer B populates significantly more than the other three low energy isomers. Given that isomer B is 1.35 eV higher than the global minimum E, i.e., less thermodynamically favorable, one can speculate there is strong kinetic stability of isomer B.

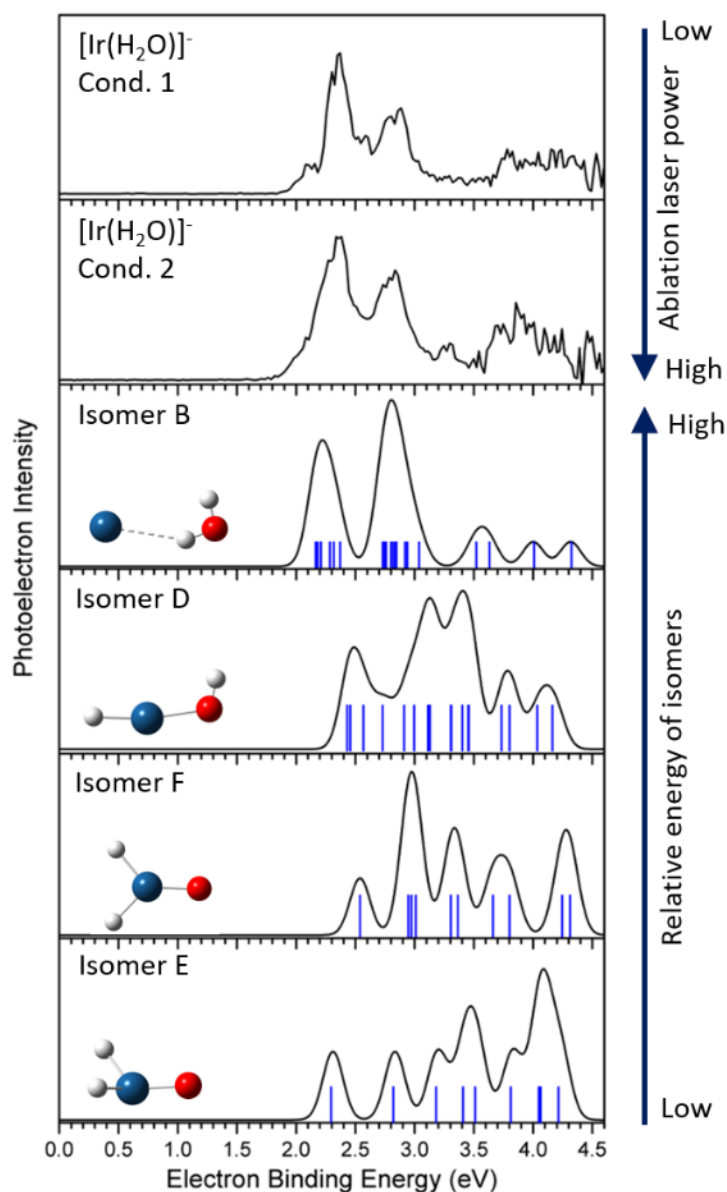


Figure IV.A.1.4 Comparison between the experimental photoelectron spectra and the simulated DOS (density of states) spectra of the low-lying isomers of $[\text{Ir}(\text{H}_2\text{O})]^-$ clusters. The simulated spectra were obtained by fitting the distribution of the transition lines with unit-area Gaussian functions of 0.2 eV full width at half maximum (FWHM). The vertical lines are the transitions obtained based on the theoretical calculated VDEs and excitation energies.

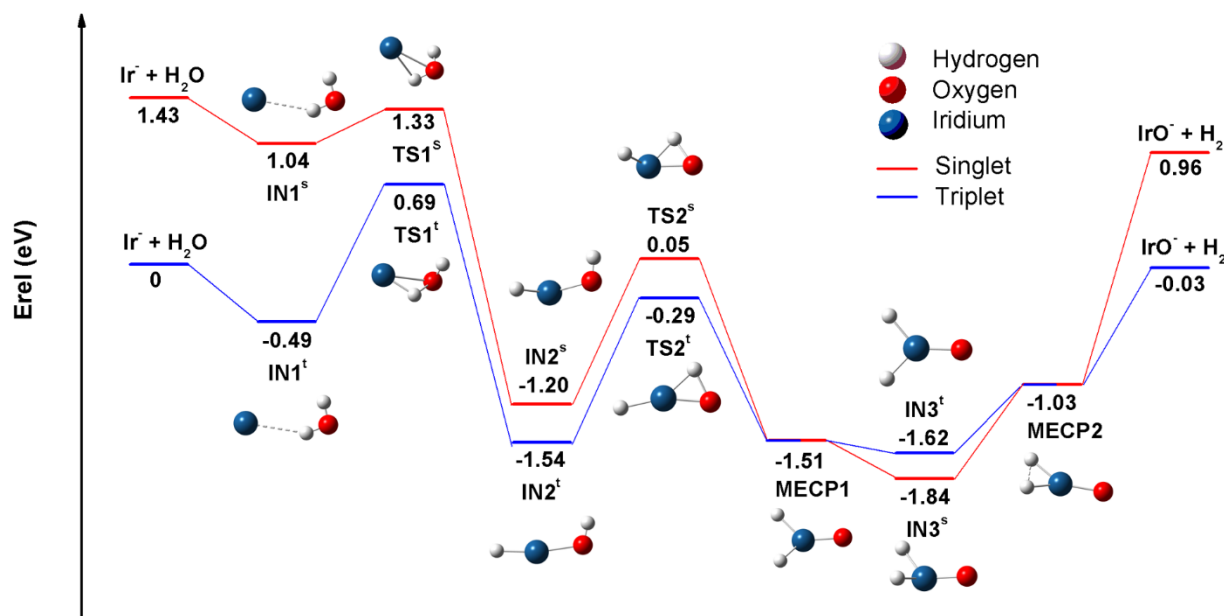


Figure IV.A.1.5 Calculated reaction pathway for H_2O with Ir anion. Energies are given in eV. The total energy of isolated Ir(triplet) and H_2O is set at 0 eV. IN for reaction intermediate, TS for transition state, and labeled with a superscript t and s, for triplet and singlet, respectively. The Minimum Energy Crossing Points (MECPs), are schematically indicated with bicolor at the crossings of the two potential energy surfaces.

The reaction path for $\text{Ir}^- + \text{H}_2\text{O}$ in both singlet and triplet multiplicities were explored to solve the uncertainty in identifying reaction intermediates and to investigate the mechanism of water splitting (Figure IV.A.1.5). **IN1^s** (isomer A) and **IN2^s** (isomer C) are not observed in the spectra due to the low VDE. Thus, reactants start from the triplet potential energy curve (blue line). The reaction between Ir anions and a water molecule is initiated via the formation of entrance channel ion-molecule complex, i.e., $\text{Ir}(\text{H}_2\text{O})$. This barrierless process forms the triplet **IN1^t**, the physisorbed adduct with a relatively long Ir-H distance (2.54 Å). In order for **IN1^t** to insert Ir anion into the O-H bond, the Ir atom needs to go beyond the H_2O plane to approach the O atom. Meanwhile, the distance of Ir-H and Ir-O is shortened to 1.59 Å and 2.35 Å, respectively, forming the Ir-H-O triangle in the first transition state **TS1^t**. **TS1^t** is

located 1.18 eV above the **IN1^t** and 0.69 eV above the entrance channel of the entire reaction. After overcoming **TS1^t**, the rupture of the first O-H bond begins to take place, and this step forming **IN2^t** is exothermic relative to **IN1^t** by 1.05 eV. The second transition state, **TS2^t**, is characterized by another hydrogen transfer from O onto Ir and is 1.25 eV above **IN2^t**. As the H atom gets close to Ir, breakage of the second O-H bond leads to **IN3^{s/t}**. This second O-H bond insertion process from **IN2^t** to **IN3^s** is also exothermic by 0.30 eV. Interestingly, **IN3^s** is lower than **IN3^t** while all other singlet **INs** and **TSs** are higher than triplets in energy. The energy inversion necessities triplet-singlet spin crossing around **IN3^{s/t}**. We searched and found two Minimum Energy Crossing Points (**MECPs**) where singlet and triplet are isoenergetic. The first **MECP1** lying between **TS2** and **IN3** has a 2.34 Å of H-H distance shorter than **IN3^t** (2.44 Å) but longer than **IN3^s** (2.10 Å). The dihedral angle of O-Ir-H₂ in **MECP1** is 25.7° between that of **IN3^t** (0°) and **IN3^s** (53.2°). The spin crossing can make both **TS2^t** to **IN3^t** and **TS2^t** to **IN3^s** pathways accessible. After passing through the **IN3^s**, the activation intermediates encounter the second **MECP2**, where the H-H distance is significantly shortened to 1.71 Å, showing an evident tendency towards H₂ + IrO⁻ products. Compared to reaction from M⁻ + H₂O to H₂ + MO⁻ (where M = Pt, Pd, Ni), which is endothermic according to the previous study,³⁸ H₂ + IrO⁻ lies 0.03 eV below the entrance channel which makes the entire reaction slightly exothermic.

Overall, the water molecule with Ir anion reaction sequentially goes through **IN1^t**, **TS1^t**, **IN2^t**, **TS2^t**, and **IN3^{s/t}** to form H₂ and triplet IrO⁻. By combining the PE spectrum and reaction mechanism study, we confirm that isomer B D E, and F of [Ir(H₂O)]⁻ coexist in the ion beam. Additionally, only **TS1^t** is higher than the entrance channel in energy along the whole pathway, which impedes the transformation from **IN1^t** (isomer B) to latter intermediates. The trapped **IN1^t** explains the domination of physisorbed adduct (isomer B) in the photoelectron spectrum under low ablation power condition (figure IV.A.1.2b). When excess energy was provided into the reaction under high ablation laser power circumstance, we began to see other chemically activated complexes (isomer D, E, and F) in the photoelectron spectrum (figure IV.A.1.2c) as well as the final product, IrO⁻, in the mass spectrum (figure IV.A.1.1b).

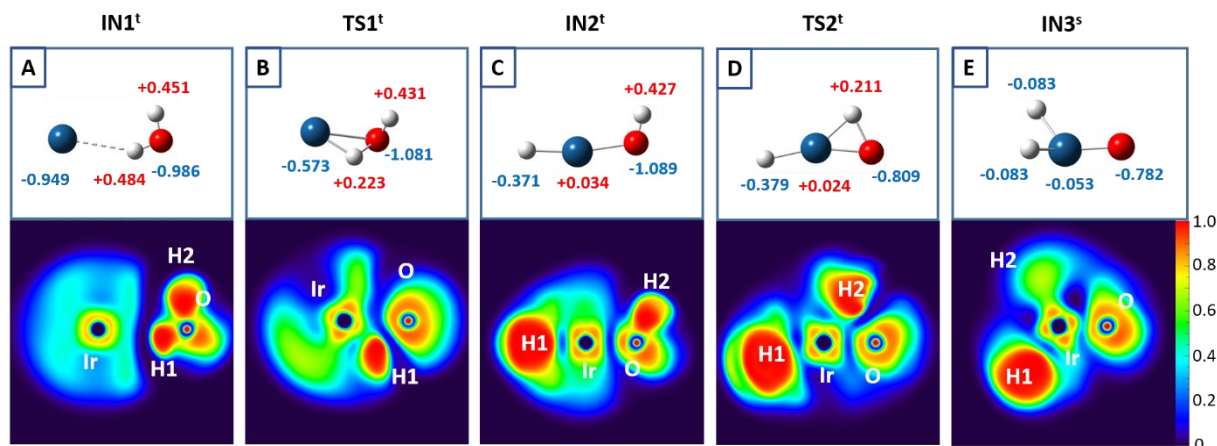


Figure IV.A.1.6 NBO net charges of all atoms in lowest intermediates and transition states in energy along the reaction pathway (upper panels). Two-dimensional electron localization functions (ELF) for the species above (lower panels). Atoms are labeled and numbered in the ELF contour. The ELF distributions are shown on the Ir-H-O plane and are described chromatically. A large ELF value means that electrons are greatly localized.

Electrons play an important role in the reduction of H₂O into H₂. Herein, we examine the net charge on every atom in critical intermediates and transition states and plot the corresponding 2-D ELF contours in figure IV.A.1.6 to study the electron flow between atoms during the water splitting reaction. In **IN1^t**, Ir stays negatively charged (-0.949 e), almost the same as a free Ir anion (-1 e). The ELF contour in the lower panel of figure IV.A.1.6A depicts electrons are localized in Ir and H₂O fragments, which are separated clearly. The dark color (low ELF value) means no covalent bond is formed between Ir and H1 atom, proving the electrostatic force governs the interaction between Ir anion and H₂O molecule. When Ir approaches the H₂O in **TS1^t**, both Ir and H experience vigorous changes in charge. Due to the identical electronegativity of Ir and H (2.2), the excess negative charge on Ir flows into the H1 atom. The moderate negative charge accumulation on O (-0.986 e to -1.081 e) from **IN1^t** to **TS1^t** is driven by the notable electronegativity difference between O (3.4) and Ir/H (2.2). From **TS1^t** to **IN2^t**, NBO analysis also shows that the net charge of the O atom is nearly unperturbed (-1.081 e ~ -1.089 e) while the net charge on Ir escalates from -0.573 e to +0.034 e along the first activation step. Thus, Ir serves as an essential electron donor when the first hydrogen transfer occurs. Unlike **IN1^t**, the ELF contours are greatly delocalized over the whole molecule in the **TS1^t** and **IN2^t** (figure IV.A.1.6a and 6b), manifesting the formation of the Ir-H1 covalent bond. In figure IV.A.1.6C, the Ir-O bond displays a patent ionic bond feature because of the low ELF values (dark color) in the middle of the Ir-O axis. To further trigger the breakage

of the second O-H bond, O starts to be a successor of Ir to provide electrons. From **IN2^t** to **TS2^t**, 0.18 e of negative charge transfer from O to H2 atom elongates and weakens the O-H bond. Meanwhile, the green color between Ir and H2 and the dark blue color between O and H2 atoms in the ELF contour (figure IV.A.1.6D) reveals the formation of the Ir-H2 bond and the cleavage of the O-H2 bond, respectively. After surmounting **TS2^t**, the net charge is evenly shared on both H atoms (-0.083 e) in **IN3^s**, close to 0 e in the neutral H₂ molecule. In figure IV.A.1.6E, the 2D contour is displayed on the H1-Ir-O plane so that the H2 atom is out of the plane. Although the ELF around the H2 atom is not fully shown on this selected plane, one can still see vaguely blue electron distributions between H1 and H2, which builds the foundation for forming an H-H bond in the H₂ molecule later.

Conclusions

To summarize, we have demonstrated that a single atomic iridium anion can both activate and split a single water molecule. Both activation intermediate, [Ir(H₂O)]⁻, and one of the reaction products, IrO⁻, were observed in the mass spectrum. Identification of multiple isomers for [Ir(H₂O)]⁻ are accomplished by a combination of anion photoelectron spectroscopy and DFT calculations. Mechanistic analysis shows that the spin crossover between singlet and triplet surfaces making two reaction channels accessible. The exothermic energetics of the overall reaction was compared to that of water reaction with single Pt/Pd/Ni anions. The NBO partial charge and ELF contour analysis reveals that Ir serves as an electron donor to activate water. This work provides insight into the nature of water activation and splitting with single Ir atom at molecular level, shedding light on the design new Ir SACs in the condensed phase.

References

1. Roger, I., Shipman, M. A., & Symes, M. D. (2017). Earth-abundant catalysts for electrochemical and photoelectrochemical water splitting. *Nature Reviews Chemistry*, 1(1), 1-13.
2. Wang, J., Cui, W., Liu, Q., Xing, Z., Asiri, A. M., & Sun, X. (2016). Recent progress in cobalt-based heterogeneous catalysts for electrochemical water splitting. *Advanced materials*, 28(2), 215-230.
3. You, B., & Sun, Y. (2018). Innovative strategies for electrocatalytic water splitting. *Accounts of chemical research*, 51(7), 1571-1580.
4. Wang, Z., Li, C., & Domen, K. (2019). Recent developments in heterogeneous photocatalysts for solar-driven overall water splitting. *Chemical Society Reviews*, 48(7), 2109-2125.
5. Wang, Q., & Domen, K. (2019). Particulate photocatalysts for light-driven water splitting: mechanisms, challenges, and design strategies. *Chemical Reviews*, 120(2), 919-985.
6. Ye, S., Ding, C., Chen, R., Fan, F., Fu, P., Yin, H., Wang, X., Wang, Z., Du, P. and Li, C., 2018. Mimicking the key functions of photosystem II in artificial photosynthesis for photoelectrocatalytic water splitting. *Journal of the American Chemical Society*, 140(9), pp.3250-3256.
7. Feng, J., Huang, H., Yan, S., Luo, W., Yu, T., Li, Z., & Zou, Z. (2020). Non-oxide semiconductors for artificial photosynthesis: progress on photoelectrochemical water splitting and carbon dioxide reduction. *Nano Today*, 30, 100830.
8. Funk, J. E. Thermochemical hydrogen production: past and present. *Int. J. Hydrog. Energy* **26**, 185–190 (2001).

9. Kudo, A., & Miseki, Y. (2009). Heterogeneous photocatalyst materials for water splitting. *Chemical Society Reviews*, 38(1), 253-278.
10. You, B., & Sun, Y. (2018). Innovative strategies for electrocatalytic water splitting. *Accounts of chemical research*, 51(7), 1571-1580.
11. Gao, C., Low, J., Long, R., Kong, T., Zhu, J., & Xiong, Y. (2020). Heterogeneous single-atom photocatalysts: fundamentals and applications. *Chemical reviews*, 120(21), 12175-12216.
12. Wang, A., Li, J., & Zhang, T. (2018). Heterogeneous single-atom catalysis. *Nature Reviews Chemistry*, 2(6), 65-81.
13. Zhang, F., Zhu, Y., Lin, Q., Zhang, L., Zhang, X., & Wang, H. (2021). Noble-metal single-atoms in thermocatalysis, electrocatalysis, and photocatalysis. *Energy & Environmental Science*, 14(5), 2954-3009.
14. Q. Wang, X. Huang, Z. L. Zhao, M. Wang, B. Xiang, J. Li, Z. Feng, H. Xu and M. Gu, *J. Am. Chem. Soc.*, 2020, **142**, 7425–7433
15. W. Lai, L. Zhang, W. Hua, S. Indris, Z. Yan, Z. Hu, B. Zhang, Y. Liu, L. Wang, M. Liu, R. Liu, Y. Wang, J. Wang, Z. Hu, H. Liu, S. Chou and S. Dou, *Angew. Chem.*, 2019, **131**, 11994–11999
16. Z. Zhang, C. Feng, C. Liu, M. Zuo, L. Qin, X. Yan, Y. Xing, H. Li, R. Si, S. Zhou and J. Zeng, *Nat. Commun.*, 2020, **11**, 1215
17. K. Jiang, M. Luo, M. Peng, Y. Yu, Y. R. Lu, T. S. Chan, P. Liu, F. M. F. Groot and Y. Tan, *Nat. Commun.*, 2020, **11**, 2701
18. J. Yin, J. Jin, M. Lu, B. Huang, H. Zhang, Y. Peng, P. Xi and C. H. Yan, *J. Am. Chem. Soc.*, 2020, **142**, 18378–18386
19. Y. Zhang, C. Wu, H. Jiang, Y. Lin, H. Liu, Q. He, S. Chen, T. Duan and L. Song, *Adv. Mater.*, 2018, **30**, 1707522
20. T. He, S. Chen, B. Ni, Y. Gong, Z. Wu, L. Song, L. Gu, W. Hu and X. Wang, *Angew. Chem.*, 2018, **130**, 3551–3556
21. Lei, Z., Cai, W., Rao, Y., Wang, K., Jiang, Y., Liu, Y., Jin, X., Li, J., Lv, Z., Jiao, S. and Zhang, W., 2022. Coordination modulation of iridium single-atom catalyst maximizing water oxidation activity. *Nature Communications*, 13(1), pp.1-10.
22. Zheng, X., Tang, J., Gallo, A., Torres, J.A.G., Yu, X., Athanitis, C.J., Been, E.M., Ercius, P., Mao, H., Fakra, S.C. and Song, C., 2021. Origin of enhanced water oxidation activity in an iridium single atom anchored on NiFe oxyhydroxide catalyst. *Proceedings of the National Academy of Sciences*, 118(36).
23. H. Zhang, H. Wu, Y. Jia, B. Yin, L. Geng, Z. Luo, K. Hansen, *Commun. Chem.* 2020, 3, 148
24. H. Zhang, M. Zhang, Y. Jia, L. Geng, B. Yin, S. Li, Z. Luo, F. Pan, *J. Phys. Chem. Lett.* 2021, 12, 1593–1600.
25. S. M. Lang, I. Fleischer, T. M. Bernhardt, R. N. Barnett, U. Landman, *Nano Lett.* 2013, 13, 5549–5555;
26. S. M. Lang, T. M. Bernhardt, D. M. Kiawi, J. M. Bakker, R. N. Barnett, U. Landman, *Angew. Chem. Int. Ed.* 2015, 54, 15113–15117;
27. S. M. Lang, T. M. Bernhardt, D. M. Kiawi, J. M. Bakker, R. N. Barnett, U. Landman, *Phys. Chem. Chem. Phys.* 2016, 18, 15727–15737.
28. M. R. Fagiani, X. Song, S. Debnath, S. Gewinner, W. Schöllkopf, K. R. Asmis, F. A. Bischoff, F. Muller, J. Sauer, *J. Phys. Chem. Lett.* 2017, 8, 1272–1277.
29. Weichman, M. L., Debnath, S., Kelly, J. T., Gewinner, S., Schöllkopf, W., Neumark, D. M., & Asmis, K. R. (2018). Dissociative water adsorption on gas-phase titanium dioxide cluster anions probed with infrared photodissociation spectroscopy. *Topics in Catalysis*, 61(1), 92-105.
30. DeVine, J. A., Abou Taka, A., Babin, M. C., Weichman, M. L., Hratchian, H. P., & Neumark, D. M. (2018). High-resolution photoelectron spectroscopy of TiO₃H₂⁻: Probing the TiO₂→H₂O dissociative adduct. *The Journal of chemical physics*, 148(22), 222810.
31. Geng, C., Li, J., Weiske, T., & Schwarz, H. (2018). Thermal O–H bond activation of water as mediated by heteronuclear [Al₂Mg₂O₅]^{•+}: Evidence for oxygen-atom scrambling. *Journal of the American Chemical Society*, 140(29), 9275-9281.
32. Chen, Y., Jin, J., Xin, K., Yu, W., Xing, X., Wang, X., & Wang, G. (2019). Infrared photodissociation spectroscopic studies of ScO (H₂O)_n= 1–3 Ar⁺ cluster cations: solvation induced reaction of ScO⁺ and water. *Physical Chemistry Chemical Physics*, 21(28), 15639-15646.
33. Jian, X., Xin, K., Hu, J., Zhang, L., Wang, X., & Wang, G. (2021). Infrared Spectroscopy of Solvation in the TaO₂⁺ Hydrolysis Reaction. *The Journal of Physical Chemistry A*, 125(23), 5054-5060.
34. Xin, K., Chen, Y., Zhang, L., Xu, B., Wang, X., & Wang, G. (2021). Infrared photodissociation spectroscopic investigation on VO⁺ and NbO⁺ hydrolysis catalyzed by water molecules. *Physical Chemistry Chemical Physics*, 23(1), 528-535.

35. Wang, M., Sun, C. X., Zhao, Y., Cui, J. T., & Ma, J. B. (2019). Efficient Liberation of Ammonia from Thermal Reaction of ScNH^+ Cations and Water. *The Journal of Physical Chemistry A*, 123(35), 7576-7581.
36. McMahon, A. J., & Jarrold, C. C. (2020). Using anion photoelectron spectroscopy of cluster models to gain insights into mechanisms of catalyst-mediated H_2 production from water. *Physical Chemistry Chemical Physics*, 22(48), 27936-27948.
37. Hou, G.L., Yang, T., Li, M., Vanbuel, J., Lushchikova, O.V., Ferrari, P., Bakker, J.M. and Janssens, E., 2021. Water Splitting by C60-Supported Vanadium Single Atoms. *Angewandte Chemie International Edition*, 60(52), pp.27095-27101.
38. G. Liu, E. Miliordos, S. Ciborowski, M. Tschurl, U. Boesl, U. Heiz, X. Zhang, S. Xantheas, K. Bowen, J. Chem. Phys. 2018, 149, 221101.
39. Schmidt, M. W.; Gordon, M. S. The Decomposition of Hydrazine in the Gas Phase and over an Iridium Catalyst. *Z. Phys. Chem.* 2013, 227, 1301–1336
40. Bussai, C.; Krüger, S.; Vayssilov, G. N.; Rösch, N. The Cluster Ir_4 and its Interaction with a Hydrogen Impurity. A Density Functional Study. *Phys. Chem. Chem. Phys.* 2005, 7, 2656–2663.
41. Krüger, S.; Bussai, C.; Genest, A.; Rösch, N. Two Hydrogen Ligands on Tetrairidium Clusters: a Relativistic Density Functional Study. *Phys. Chem. Chem. Phys.* 2006, 8, 3391–3398.
42. Balasubramanian, K.; Dai, D. Potential Energy Surfaces for $\text{Ir} + \text{H}_2$ and $\text{Ir}^+ + \text{H}_2$ Reactions. *J. Chem. Phys.* 1990, 93, 7243–7255.
43. Castillo, S.; Bertin, V.; Solano-Reyes, E.; Luna-Garcia, H.; Cruz, A.; Poulain, E. Theoretical Studies on Hydrogen Activation by Iridium Dimers. *Int. J. Quantum Chem.* 1998, 70, 1029–1035.
44. Okumura, M.; Irie, Y.; Kitagawa, Y.; Fujitani, T.; Maeda, Y.; Kasai, T.; Yamaguchi, K. DFT Studies of Interaction of Ir Cluster with O_2 , CO , and NO . *Catal. Today* 2006, 111, 311–315. (48) Ge, Y.; Jiang, H.; Kato, R.; Gummagatta, P. Size and Site Dependence of the Catalytic Activity of Iridium Clusters toward Ethane Dehydrogenation. *J. Phys. Chem. A* 2016, 120, 9500–9508.
45. Ciborowski, S.M., Buszek, R., Liu, G., Blankenhorn, M., Zhu, Z., Marshall, M.A., Harris, R.M., Chiba, T., Collins, E.L., Marquez, S. and Boatz, J.A., 2021. Study of the Reaction of Hydroxylamine with Iridium Atomic and Cluster Anions ($n=1-5$). *The Journal of Physical Chemistry A*, 125(27), pp.5922-5932.
46. Li, F. X., Zhang, X. G., & Armentrout, P. B. (2006). The most reactive third-row transition metal: Guided ion beam and theoretical studies of the activation of methane by Ir^+ . *International Journal of Mass Spectrometry*, 255, 279-300.
47. Halder, A., Liu, C., Liu, Z., Emery, J.D., Pellin, M.J., Curtiss, L.A., Zapol, P., Vajda, S. and Martinson, A.B., 2018. Water oxidation catalysis via size-selected iridium clusters. *The Journal of Physical Chemistry C*, 122(18), pp.9965-9972.
48. Li, F. X., Zhang, X. G., & Armentrout, P. B. (2005). Guided ion beam and theoretical study of the reactions of Ir^+ with H_2 , D_2 , and HD . *The Journal of Physical Chemistry B*, 109(17), 8350-8357.
49. Li, W., Wu, X., Liu, Z., Wu, H., Zhang, D., & Ding, X. (2020). C/C Exchange in Activation/Coupling Reaction of Acetylene and Methane Mediated by Os^+ : A Comparison with Ir^+ , Pt^+ , and Au^+ . *The Journal of Physical Chemistry Letters*, 11(19), 8346-8351.
50. Wheeler, O. W., Salem, M., Gao, A., Bakker, J. M., & Armentrout, P. B. (2019). Sequential activation of methane by Ir^+ : An IRMPD and theoretical investigation. *International Journal of Mass Spectrometry*, 435, 78-92.
51. Armentrout, P. B. (2017). Methane Activation by 5 d Transition Metals: Energetics, Mechanisms, and Periodic Trends. *Chemistry—A European Journal*, 23(1), 10-18.
52. Cheng, P., Koyanagi, G. K., & Bohme, D. K. (2007). Heavy water reactions with atomic transition-metal and main-group cations: gas phase room-temperature kinetics and periodicities in reactivity. *The Journal of Physical Chemistry A*, 111(35), 8561-8573.
53. Gerhards, M.; Thomas, O. C.; Nilles, J. M.; Zheng, W.-J.; Bowen, K. H. Cobalt–Benzene Cluster Anions: Mass Spectrometry and Negative Ion Photoelectron Spectroscopy. *J. Chem. Phys.* 2002, 116, 10247.
54. Ho, J.; Ervin, K. M.; Lineberger, W. C. Photoelectron Spectroscopy of Metal Cluster Anions: Cu-N , Ag-N , and Au-N . *J. Chem. Phys.* 1990, 93, 6987.
55. Chai, J.-D.; Head-Gordon, M. Systematic Optimization of Long-Range Corrected Hybrid Density Functionals. *J. Chem. Phys.* 2008, 128, 084106.
56. Chai, J.-D.; Head-Gordon, M. Long-Range Corrected Hybrid Density Functionals with Damped Atom–Atom Dispersion Corrections. *Phys. Chem. Chem. Phys.* 2008, 10, 6615–6620.
57. Dunning Jr, T. H. (1989). Gaussian basis sets for use in correlated molecular calculations. I. The atoms boron through neon and hydrogen. *The Journal of chemical physics*, 90(2), 1007-1023.

58. Kendall, R. A., Dunning Jr, T. H., & Harrison, R. J. (1992). Electron affinities of the first-row atoms revisited. Systematic basis sets and wave functions. *The Journal of chemical physics*, 96(9), 6796-6806.
59. Figgen, D., Peterson, K. A., Dolg, M., & Stoll, H. (2009). Energy-consistent pseudopotentials and correlation consistent basis sets for the 5 d elements Hf–Pt. *The Journal of chemical physics*, 130(16), 164108.
60. Frisch, M. J.; Trucks, G. W.; Schlegel, H. B.; Scuseria, G. E.; Robb, M. A.; Cheeseman, J. R.; Scalmani, G.; Barone, V.; Mennucci, B.; Petersson, G. A.; Nakatsuji, H.; Caricato, M.; Li, X.; Hratchian, H. P.; Izmaylov, A. F.; Bloino, J.; Zheng, G.; Sonnenberg, J. L.; Hada, M.; Ehara, M.; Toyota, K.; Fukuda, R.; Hasegawa, J.; Ishida, M.; Nakajima, T.; Honda, Y.; Kitao, O.; Nakai, H.; Vreven, T.; Montgomery, J. A., Jr.; Peralta, J. E.; Ogliaro, F.; Bearpark, M.; Heyd, J. J.; Brothers, E.; Kudin, K. N.; Staroverov, V. N.; Keith, T.; Kobayashi, R.; Normand, J.; Raghavachari, K.; Rendell, A.; Burant, J. C.; Iyengar, S. S.; Tomasi, J.; Cossi, M.; Rega, N.; Millam, J. M.; Klene, M.; Knox, J. E.; Cross, J. B.; Bakken, V.; Adamo, C.; Jaramillo, J.; Gomperts, R.; Stratmann, R. E.; Yazyev, O.; Austin, A. J.; Cammi, R.; Pomelli, C.; Ochterski, J. W.; Martin, R. L.; Morokuma, K.; Zakrzewski, V. G.; Voth, G. A.; Salvador, P.; Dannenberg, J. J.; Dapprich, S.; Daniels, A. D.; Farkas, O.; Foresman, J. B.; Ortiz, J. V.; Cioslowski, J.; Fox, D. J. *Gaussian 09, Revision D.01*; Gaussian, Inc.: Wallingford, CT, 2013.
61. Glendening, E. D.; Reed, A. E.; Carpenter, J. E.; Weinhold, F. *NBO Version 3.1*, 1998.
62. Wang, H.; Jae Ko, Y.; Zhang, X.; Gantefer, G.; Schnoeckel, H.; Eichhorn, B. W.; Jena, P.; Kiran, B.; Kandalam, A. K.; Bowen, K. H. The Viability of Aluminum Zintl Anion Moieties Within Magnesium-Aluminum Clusters. *J. Chem. Phys.* 2014, 140, 124309.
63. Liu, G., Zhu, Z., Marshall, M., Blankenhorn, M., & Bowen, K. H. (2021). CO₂ Activation and Hydrogenation by Palladium Hydride Cluster Anions. *The Journal of Physical Chemistry A*, 125(8), 1747-1753.
64. J N. Harvey, M. Aschi, H. Schwarz, W. Koch, The singlet and triplet states of phenyl cation. A hybrid approach for locating minimum energy crossing points between non-interacting potential energy surfaces, *Theo. Chem. Acc.* 99 (1998) 95-99.
65. Lu, T., & Chen, F. (2012). Multiwfn: a multifunctional wavefunction analyzer. *Journal of computational chemistry*, 33(5), 580-592.
66. Savin, A., Nesper, R., Wengert, S., & Fässler, T. F. (1997). ELF: The electron localization function. *Angewandte Chemie International Edition in English*, 36(17), 1808-1832.

IV.A.2. Study of the Reaction of Hydroxylamine with Iridium Cluster Anions, ($n = 1 - 5$)

Reprinted (adapted) with permission from *J. Phys. Chem. A* 2021, 125, 27, 5922-5932. Copyright 2021 American Chemical Society.

Authors: Sandra M. Ciborowski¹, Robert Buszek³, Gaoxiang Liu¹, Moritz Blankenhorn¹, Zhaoguo Zhu¹, Mary A. Marshall¹, Rachel M. Harris¹, Tatsuya Chiba¹, Evan L. Collins¹, Sara Marquez¹, Jerry A. Boatz^{2,*}, Steven D. Chambreau^{3,*}, Ghanshyam L. Vaghjiani⁴, and Kit H. Bowen^{1,*}

Abstract:

Elucidating the multifaceted processes of molecular activation and subsequent reactions gives a fundamental view into the development of iridium catalysts as they apply to fuels and propellants, e.g., for spacecraft thrusters. Hydroxylamine, a component of the well-known hydroxylammonium nitrate (HAN) ionic liquid, is a safer alternative and mimics the chemistry and performance standards of hydrazine. The activation of hydroxylamine by anionic iridium clusters, Ir_n^- ($n = 1 - 5$), depicts a part of the mechanism, where two hydrogen atoms are removed, likely as H_2 , and $\text{Ir}_n(\text{NOH})^-$ clusters remain. The significant photoelectron spectral differences between these products and the bare clusters illustrate the substantial electronic changes imposed by the hydroxylamine fragment on the iridium clusters. In combination with DFT calculations, a preliminary reaction mechanism is proposed, identifying the possible intermediate steps leading to the formation of $\text{Ir}(\text{NOH})^-$.

2. Introduction

Since the 1960s, the most often used propellants for spacecraft thrusters are comprised of hydrazine (N_2H_4) and its derivatives. Although hydrazine is effective as a monopropellant, efforts are underway to find a substitute for hydrazine compounds due to their significant hazards. Ionic liquids have been proposed as a potential alternative, due to their safer properties such as negligible vapor pressure and comparable performance as a propellant. The ability to model the performance of propulsion systems depends on a fundamental knowledge of the physical and chemical processes involved in ignition and combustion.

Liquid propellants based on nitrogen-containing compounds, including hydroxylammonium nitrate (HAN) and other ionic liquids, have shown promise in terms of effectiveness and safety¹⁻⁶. These ionic liquids also cross the boundary between monopropellants and possible use as multimode propellants, which are especially promising for high-efficiency electrospray thrusters and high-performance catalyzed (chemical) thrusters⁷. Hydroxylammonium nitrate

(HAN) was first proposed for use as a rocket propellant in the 1990's.¹ More recently, HAN-based ionic liquid (IL) formulations have been proposed to replace hydrazine as a monopropellant²⁻⁵ and for use in electric propulsion applications⁶. The numerous benefits of using HAN-based ILs over hydrazine include, for example, the reduced toxicity and respiratory hazards, higher stability with reduced explosion hazards for long-term storage, and increased performance. HAN has not been shown to be carcinogenic or mutagenic¹ and has a very low vapor pressure, whereas hydrazine has a significant vapor pressure and requires a S.C.A.P.E. apparatus for handling⁴. HAN has a low freezing point and high density, potentially enabling an increase in density specific impulse (d-Isp)⁴ with its use as a monopropellant. HAN formulations have been successfully implemented in SDS-4 (JAXA) and AF-M315E (AFRL/NASA GPIM) fueled satellites⁸. Additionally, the use of HAN in electrical propulsion applications has attracted much interest recently in the potential use in high-efficiency microthrusters⁶. In a laboratory environment, these ionic liquids can be safer to handle and are capable of mimicking the reactivity observed between catalysts and hydrazine fuels^{1,4,6,8}.

Much work has been done on the thermal decomposition and combustion mechanisms of HAN⁹⁻¹¹, but there isn't a real consensus on these mechanisms due to variety in experimental and theoretical approaches and conditions applied thus far. More importantly, the mechanism for the heterogeneous catalysis of HAN is largely unknown, and this is the focus of this work. As a protic ionic liquid, the generally accepted first step in its decomposition is the proton transfer from the hydroxylammonium cation to the nitrate anion, producing hydroxylamine (HA) and HNO₃ neutral molecules. It has been proposed that the ignition of HAN-based formulations is initiated by proton transfer leading to formation of HNO₃ and nitrogen oxides that can subsequently react with the fuel species to ignite⁵. This is consistent with a recent publication indicating the formation of NO and HNO₃ upon contact of HAN with a hot Ir catalyst⁸. HA (50% in H₂O) has been observed to decompose completely at 45-50 °C on an iridium catalyst, but no mechanism was proposed in that work¹².

In general, iridium activation of small molecules has been used successfully in Air Force applications for fuels and propellants¹³⁻²⁰. Thin coatings of iridium and its oxide make for durable engine ignition devices, rocket combustion chambers, and as a component of anodes for oxidation or splitting of methanol, ammonia, acetic acid and water, e.g., in the oxygen evolution reaction¹⁴⁻²⁰. Hydrazine decomposition is also facilitated with the use of an iridium catalyst²¹, and this mechanism has been well studied. The use of an iridium catalyst significantly improves the efficiency of

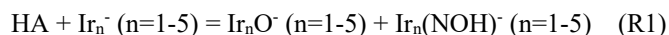
achieving activation in hydrazine, decreasing the initiation barrier from 65 kcal/mol to less than 10 kcal/mol²². This initiation comes in the way of breaking the N=N bond to create NH₂ radicals enabling the decomposition to N₂, H₂ and NH₃.

Mass spectral and photoelectron studies show that single atomic species and small ionic clusters often cause this activation, e.g., the breaking of O-H bonds in water, breaking a C-H bond in methane and altering the bond angle in carbon dioxide. These small atoms and ionic clusters can be viewed as reasonable approximations of active sites in the bulk material and as fundamental starting points to assess catalytic reactivity²³⁻³⁶. Investigating the reactivity of highly-uncoordinated small Ir_n⁺ clusters will lead to better understanding of reactive sites/reactivity at defects on bulk metal surfaces, although this study will not necessarily capture all ligands that are present on the bulk metal catalyst surface. Traditionally, studies performed by flowing the reactant gas over a pre-made surface of the catalyst or freezing the reactant gas and interacting the catalyst with its surface allow the observation of products formed from the catalysis of the small molecule, but these are complicated and expensive for current calculation methods. By focusing on isolated ionic atoms and clusters in the gas phase, individual steps and, in some cases, discernable products allow more specific details of the catalytic mechanism to be ascertained. These basic details allow for further understanding of the active sites of catalysts and provide benchmarks for contemporary calculations.

The catalytic properties of iridium have generated considerable interest in understanding the fundamental properties of iridium clusters, their interactions with other compounds and substrates, and the underlying chemistry of catalysis. Prior theoretical studies include investigations of the structures, growth patterns, and properties of bare iridium clusters³⁷⁻⁴⁰ and characterization of the low-lying excited states of Ir₂₋₈ clusters⁴¹. In addition, the fundamental interactions of iridium clusters with atomic^{42,43} and molecular^{44,45} hydrogen have been calculated. Several theoretical studies have probed the catalytic properties of iridium clusters, including correlation of catalytic activity with the cluster HOMO-LUMO gaps⁴⁶, interactions with O₂, CO, and NO⁴⁷, and dehydrogenation of ethane⁴⁸. Incorporation of iridium clusters onto alumina and magnesium oxide substrates⁴⁹ has been studied using density functional theory (DFT), including their catalytic effects on ethylene hydrogenation⁵⁰. Schmidt et al.²² used second-order perturbation theory and coupled-cluster theoretical methods to compare the decomposition of hydrazine in the gas-phase to the catalyzed decomposition by Ir₄ and Ir₆ clusters supported on an alumina substrate. DFT investigations of iridium clusters on zeolite substrates⁵¹ and their effects on hydrogen adsorption⁵²⁻⁵⁴ and migration⁵⁵⁻⁵⁷ also have been completed.

More recently, Koyasu et al.⁵⁸ conducted a combined experimental and theoretical study of the photoelectron spectroscopy (PES) of a series of anionic iridium clusters and their structural growth patterns. In addition, Lu et al.⁵⁹ refined the experimental electron affinity of atomic iridium⁶⁰ and, in a complementary follow-on theoretical paper by Barysz and Syrocki⁶¹, relativistic quantum chemical calculations were used to predict the photoelectron spectra of neutral iridium atom and its anion, including reassignment of some excited state levels.

In order to elucidate the heterogeneous catalysis mechanism, a combination of experimental and theoretical approaches are used here. Specifically, the reaction of the HA neutral with size-selected Ir_n^- ($n=1-5$) anionic clusters is probed using photoelectron spectroscopy (PES) and quantum chemical density functional theory (DFT) is used to model the potential energy surface(s) involved. Reaction 1 is proposed based on the species as detected by mass spectrometry (Figure IV.A.2.1).



Observed mass spectrometric products guide the DFT effort. Size selection of each $\text{Ir}_n(\text{NOH})^-$ ($n=1-5$) cluster is then carried out and the electron is photodetached by 266 nm photons and the energy distributions of the electrons are measured (Figure IV.A.2.2). Photodetachment thresholds and higher energy features in the PES spectra give insight into the structure of the products. The combination of determining the atomic formulas for the products from the mass spectrometer, determining possible lowest-energy structures and their vertical electron detachment thresholds from DFT calculations and computing the barriers involved on the potential energy surfaces will yield significant insight in the reaction of $\text{HA} + \text{Ir}_n^-$ ($n=1-5$) that is directly applicable to the heterogeneous catalysis process involved in HAN ignition on an iridium catalyst.

2. Methods

2.1 Experimental Details.

Anion photoelectron spectroscopy is conducted by crossing a mass-selected beam of negative ions with a fixed-frequency photon beam and energy-analyzing the resultant photodetached electrons. The photodetachment process is governed by the energy-conserving relationship: $h\nu = \text{EBE} + \text{EKE}$, where $h\nu$ is the photon energy, EBE is the electron binding (photodetachment transition) energy, and EKE is the electron kinetic energy. Our apparatus consists of a laser vaporization cluster anion source, a time-of-flight mass spectrometer, a Nd:YAG photodetachment laser, and a magnetic bottle energy analyzer⁶². The magnetic bottle photoelectron spectrometer resolution is ~ 35 meV at $\text{EKE} = 1$ eV. The fourth harmonic of a Nd:YAG laser (266 nm, 4.66 eV) was used to photodetach electrons from mass-selected

cluster iridium-NOH anions, i.e., $\text{Ir}_n(\text{NOH})^-$ ($n = 1 - 5$). The well-known atomic transitions of Cu^- were used to calibrate the photoelectron spectra⁶³.

The atomic and cluster anions of iridium were generated in a laser vaporization source. This source consisted of a rotating and translating iridium rod in a closed housing that was ablated with the focused second harmonic of a Nd:YAG laser (532 nm, 2.33 eV). After exiting the nozzle of the housing, the beam of iridium particles was crossed with a helium and hydroxylamine beam inside of a reaction cell. The generated ions were then sent through a skimmer and extracted into the time-of-flight mass spectrometer. Ions of interest were mass selected and directed into the interaction region, where electrons were photodetached with the fourth harmonic of a Nd:YAG laser (266 nm, 4.66 eV), and photoelectron spectra were recorded.

2.2 Theoretical Details.

The structures and relative energies of several isomers and electronic spin states of $\text{Ir}_n(\text{NOH})^-$ ($n=1-5$) were calculated using density functional theory (DFT) methods, with the objective of identifying the most stable species, for which the electronic vertical detachment energies (VDEs) were subsequently computed. In addition, portions of the $\text{Ir}^- + \text{NH}_2\text{OH}$ potential energy surface were mapped in order to identify plausible mechanisms of formation of the most stable $\text{Ir}(\text{NOH})^-$ species. The $\omega\text{B97x-d}$ ^{64,65} range-separated functional, which includes dispersion corrections, in combination with the def2-TZVPPD basis set^{66,67} for all atoms and the Stuttgart quasi-relativistic pseudopotential⁶⁸ for iridium were used⁶⁹⁻⁷². This pairing of functional and basis set, hereafter denoted simply as $\omega\text{B97x-d/def2}$, was selected in part since the ground state electronic configuration of atomic iridium in the neutral ($[\text{core}]5s^2 5p^6 5d^7 6s^2$) and anionic ($[\text{core}]5s^2 5p^6 5d^8 6s^2$) states are correctly predicted at this level of theory. Furthermore, the $\omega\text{B97x-d/def2}$ predicted electron affinity of 1.50 eV is in excellent agreement with the experimental value of 1.564 eV^{59,60}, lending additional confidence to the reliability of the calculated data. All structures were fully optimized and confirmed as local minima or first-order transition states via diagonalization of the mass-weighted matrix of energy second derivatives with respect to nuclear coordinates; i.e., the Hessian matrix. The minimum energy pathways connecting each transition state to reactants and products were traced using intrinsic reaction coordinate (IRC) methods^{73,74}. Relative Gibbs free energies at 298.15 K were calculated at all stationary points, with thermal and entropic corrections obtained from standard rigid-rotor, harmonic oscillator approximations⁷⁵, using harmonic vibrational frequencies scaled by a factor of 0.975⁷⁶. Restricted and unrestricted DFT calculations were performed for closed- and open-shell systems, respectively.

The relative Gibbs free energies were used in exploring the $\text{Ir}^- + \text{NH}_2\text{OH}$ potential energy surface and to identify the most stable isomers and spin states of the $\text{Ir}_n(\text{NOH})^-$ ($n=1-5$) species. In contrast, vertical detachment energies of the latter were obtained by taking the difference in electronic energies between the anionic species and the corresponding neutral with the most stable spin state at the structure of the anion.

An additional set of calculations, with the CAMQTP01 range-separated functional⁷⁷ used in place of $\omega\text{B97x-d}$, were performed to probe the electronic transition energies between the anionic and neutral forms of $\text{Ir}_n(\text{NOH})^-$ ($n=1,5$). The CAMQTP01 functional has been shown to predict accurate vertical ionization and excitation energies⁷⁷. Optimized structures of the $\text{Ir}_n(\text{NOH})^-$ ($n=1,5$) anion and neutral species were computed, using the difference in unscaled zero point energy-corrected total electronic energies to obtain adiabatic detachment energies (ADEs). In addition, VDEs were recomputed at the CAMQTP01/def2-TZVPP level, using the procedure described previously. Finally, vertical excitation energies from the optimized neutral species were computed using time-dependent density functional theory (TDDFT). All calculations were performed using the GAMESS quantum chemistry program^{78,79}.

3. Results and Discussion

3.1 Photoelectron Spectra of $\text{Ir}_n(\text{NOH})^-$.

The mass spectrum presented in Figure IV.A.2.1 resulted from the interaction of HA with the anionic iridium clusters. No intact HA molecules were observed in conjunction with the Ir_n^- clusters. Instead, the HA lost two hydrogen atoms, forming $\text{Ir}_n(\text{NOH})^-$ cluster anions, as shown in reaction R1. Iridium oxide clusters, Ir_nO^- , were also present, either resulting from the interaction with HA or oxides present on the surface of the iridium rod. To eliminate the possibility that these peaks were actually due to mass-coincident $\text{Ir}_n(\text{NH}_2)^-$ produced during the reaction, photoelectron spectra for the species 16 amu heavier than the iridium clusters were taken, both in the presence and absence of HAN in the reaction cell (see Figures S1 and S2 in the supporting information). No differences in the spectra were observed, indicating no $\text{Ir}_n(\text{NH}_2)^-$ formation.

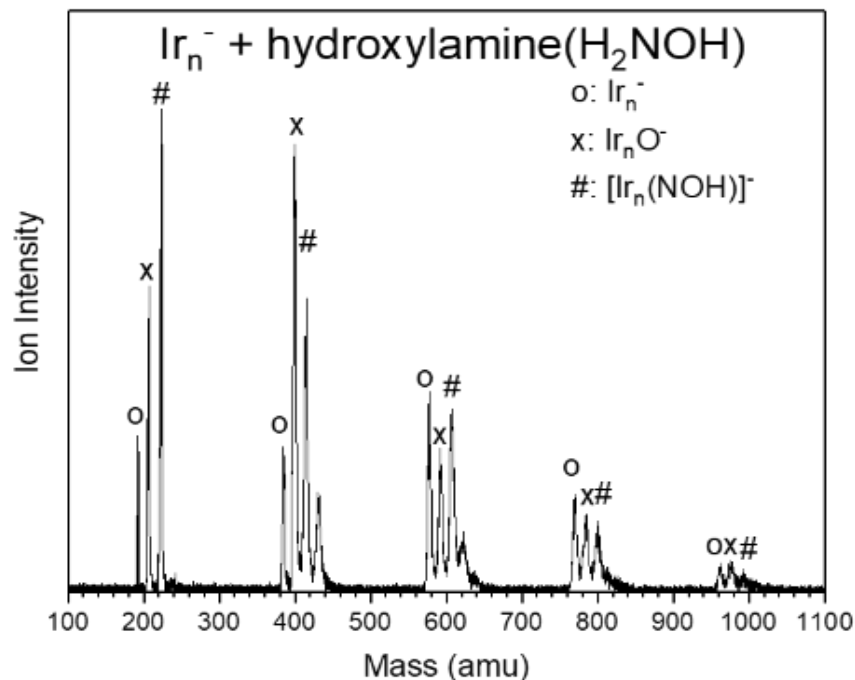


Figure IV.A.2.1 Mass spectrum of the interaction of laser-ablated anionic iridium clusters, Ir_n^- , with helium seeded with hydroxylamine (H_2NOH), resulting in a variety of Ir_n^- , Ir_nO^- , and $\text{Ir}_n(\text{NOH})^-$ clusters, indicated by o, x, and #, respectively.

Photoelectron spectra of the $\text{Ir}_n(\text{NOH})^-$ clusters ($n=1-4$) are presented in Figure IV.A.2.2. The timing of the mass gate associated with the most intense signal for the $\text{Ir}_n(\text{NOH})^-$ ($n=1,2$) species also apportioned small intensities of Ir_nO_2^- species, both then entering the interaction region during photodetachment. To differentiate between the spectra of $\text{Ir}(\text{NOH})^-/\text{Ir}_2(\text{NOH})^-$ and the spectra of the corresponding Ir_nO_2^- species, the photoelectron spectra were taken without the introduction of HA into the reaction cell and compared to the spectra obtained with HA. For $n=1$, a single peak of the combined spectrum was clearly from the dioxide: this peak was marked with a blue triangle in the spectrum (see Figures IV.A.2.2 and S3). The other peaks were substantially different from the dioxide and were clearly due to the $\text{Ir}(\text{NOH})^-$ species. For $n=2$, both spectra were normalized on to the VDE peak of Ir_2O_2^- . The Ir_2O_2^- spectrum was then subtracted from the spectrum taken in the presence of HA, producing the $\text{Ir}_2(\text{NOH})^-$ spectrum presented in Figure IV.A.2.2 (see Figure S4). It is also important to note that all spectra are substantially different from spectra of their corresponding bare iridium clusters (See Figure S6).

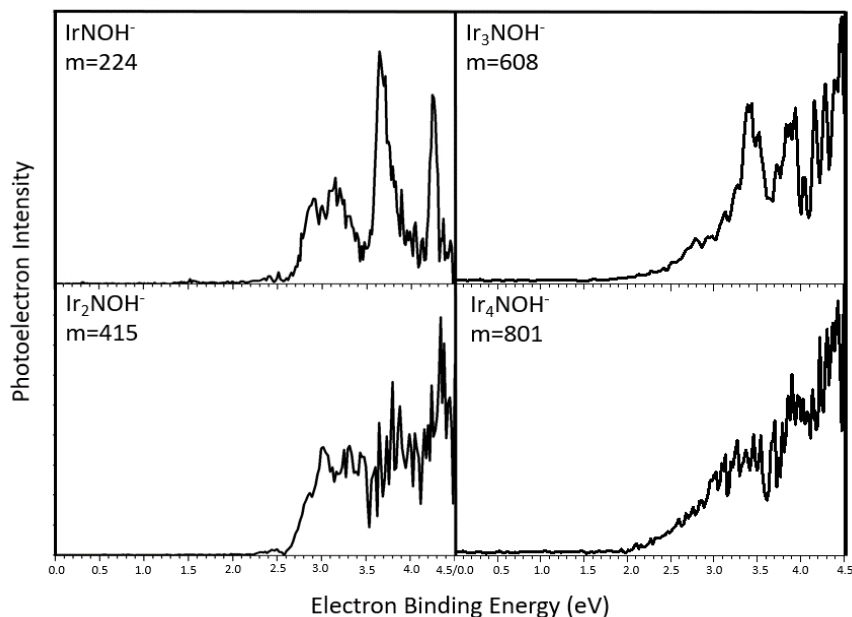


Figure IV.A.2.2 Photoelectron spectra of the $\text{Ir}_n(\text{NOH})^-$ clusters ($n = 1-4$) taken with the fourth harmonic of the Nd:YAG laser (266 nm, 4.66 eV). The marked peak in the $\text{Ir}(\text{NOH})^-$ spectrum comes from IrO_2^- .

Only $\text{Ir}(\text{NOH})^-$ shows distinguishably separated peaks, (at 2.9 eV, 3.15 eV and 4.25 eV) in its spectrum. $\text{Ir}_2(\text{NOH})^-$ starts at 2.5 eV and displays three peaks in the feature between 2.5 eV and 3.5 eV. The onset energy of the two species $\text{Ir}_3(\text{NOH})^-$ and $\text{Ir}_4(\text{NOH})^-$ is approximately 2.0 eV. Two relatively sharp peaks are observed, centered around 3.4 eV and 3.9 eV, in the photoelectron spectrum of $\text{Ir}_3(\text{NOH})^-$, while a series of peaks are seen between 3.0 eV and 3.5 eV in the spectrum of $\text{Ir}_4(\text{NOH})^-$.

Although it is difficult to determine experimentally if the strongest peak in a feature corresponds to the vertical detachment energy (VDE) or the adiabatic detachment energy (ADE)⁸⁰, we refer to these features as VDEs, which arise from the transition between the anionic state and the neutral cluster state with the largest Franck-Condon overlap. Comparison of the calculated ADEs and VDEs with the observed values, summarized in Table IV.A.2.1, shows that the theoretical VDEs are in better agreement with experiment than the ADEs, with the exception of $\text{Ir}(\text{NOH})^-$, for which the theoretical VDE and ADE are essentially the same. This suggests that the measured values correspond to VDEs. The comparison of the calculated VDE values and the measured values, shown in Table IV.A.2.1, support the assertion that the species seen in the mass spectrum are in fact $\text{Ir}_n(\text{NOH})^-$ clusters, agreeing with the predominant reaction shown in reaction R1. Additionally, the measured VDE values for $\text{Ir}_n(\text{NOH})^-$ are significantly different than

their respective bare anionic clusters. For $n=1$ to $n=3$, the difference in the VDE between $\text{Ir}_n(\text{NOH})^-$ and Ir_n^- is greater than 1 eV, and for the two largest clusters, $n=4,5$, it is greater than 0.8 eV. Large differences in the binding energy for ion-molecule interactions, as observed here, in addition to the fact that no $\text{Ir}_n(\text{NH}_2\text{OH})^-$ was found in the mass spectrum, indicate that the interaction between the iridium clusters and hydroxylamine molecules is more than simple physisorption.

Table IV.A.2.1 Measured VDEs and predicted VDEs and ADEs of $\text{Ir}_n(\text{NOH})^-$, in eV.

Species	Measured VDE	Theoretical VDE	Theoretical ADE
IrNOH^-	2.90	2.96 (a2); 3.71 (a1) ^a	2.94 (a2); 3.47 (a1) ^a
Ir_2NOH^-	3.02	3.04	2.97
Ir_3NOH^-	3.39	3.34	3.20
Ir_4NOH^-	3.46	3.47	3.19
Ir_5NOH^-	3.3 ^b	3.32(e1); 3.32(e2); 3.41(e3) ^a	3.15(e1); 3.14(e2); 3.10(e3) ^a
IrO_2^-	3.64	3.48	3.44
Ir_2O_2^-	2.63	2.81	2.19

^a See discussion and Figure IV.A.2.3.

^b See Figure S5

3.2 Theoretical Structures of Ir_n^- .

The initial set of calculations focused on identifying the most stable isomers and electronic spin states of the anionic Ir_n^- ($n=1-5$) clusters, guided by the anionic cluster calculations by Koyasu et al.⁵⁸ as well as the corresponding neutral Ir_n cluster calculations by Chen et al.⁴¹ These two studies and others³⁷⁻⁴⁰ illustrate the intrinsic challenges in theoretical characterizations of small iridium clusters, due to complicating factors such as the presence of several low-lying excited states, significant multiconfigurational character, large spin-orbit interactions and relativistic effects, etc. Consequently, the calculations presented here should not be regarded as definitive in nature, but nonetheless of sufficient reliability to provide useful insights into the observed $\text{Ir}^- + \text{NH}_2\text{OH}$ chemistry and $\text{Ir}(\text{NOH})^-$ photoelectron excitation energies.

The structures and spin multiplicities of the most stable Ir_n^- ($n=1-5$) isomers are summarized in Figure S7. The atomic iridium anion has a triplet ground state and $5d^86s^2$ valence configuration, in agreement with experiment⁵⁹. The ground state of the diatomic anion is a sextet, with the octet, quartet and doublet states higher in energy by 2.29, 0.33, and 0.65 eV, respectively. In comparison, Chen et al.⁴¹ report a $^5\Delta_g$ ground state for the neutral diatomic at CCSD(T) and MRCI levels of theory. For the $n=3$ anion, the predicted ground state is a symmetric D_{3h} ring with a multiplicity of 9. This is in contrast to the results of Koyasu et al.⁵⁸, which predict a bent (C_{2v}) isomer with a spin multiplicity of 7. However, the present calculations predict a non-symmetric ring isomer, also with a spin multiplicity of 7, which is only 0.17 eV above the D_{3h} , multiplicity=9 ground state. The most stable Ir_3^- linear $D_{\infty h}$ isomer found is a triplet, 0.69 eV above the ground state, whereas for neutral Ir_3 , Chen et al.⁴¹ report a linear $^2\Delta_g$ ground state. The $n=4$ anion has a slightly distorted planar D_{4h} structure with spin multiplicity of 8, in agreement with the predicted structure and spin multiplicity by Koyasu et al.⁵⁸ Less stable $n=4$ isomers include a planar C_{2v} $[\text{Ir}_3\text{-Ir}]^-$ and a tetrahedral cage structure, both with spin multiplicity of 8, and relative energies of 1.0 and 9.1 eV, respectively. For the $n=5$ anion, multiple cage structures and spin multiplicities from 1 to 15 were explored. The most stable isomer found has a distorted square pyramidal structure with spin multiplicity of 13, in agreement with Koyasu et al.

3.3 Theoretical Structures of $\text{Ir}_n(\text{NOH})^-$.

The next set of calculations focused on identifying the most stable isomers of $\text{Ir}_n(\text{NOH})^-$, beginning with $n=1$. The isomers considered for $n=1$ included the unfragmented molecules HN=O (bonded to Ir by either the N or O atom) and N-OH , plus all possible combinations of N,H,O fragments; i.e., N+OH , NH+O , NO+H , and N+O+H , directly bonded to Ir^- , for a total of seven types of structural isomers. For each isomer, spin multiplicities of 1, 3, and 5 were considered. In the following, the notation $\text{Ir}_n(\text{NOH})^-$ indicates the general, structural non-specific complex, whereas individual isomer structures are qualitatively described using the notation Ir(a)(b)^- to indicate that moieties "a" and "b" are directly bonded to Ir, but otherwise remain intact. For example, Ir(O)(NH)^- denotes an isomer such as O-Ir-NH .

The optimized structures of the two most stable isomers, Ir(O)(N)(H)^- and Ir(O)(NH)^- , which have nearly equal relative free energies, are shown in Figure IV.A.2.3(a1) and (a2), respectively. Additional less stable isomers are shown in Figure S8 in the SI. The isomers in Figure III.B.5.3(a1) and (a2) have a closed shell singlet ground state. The least stable isomers have unfragmented HN=O or N-OH moieties (see Figure S8), with the partially fragmented isomers Ir(NO)(H)^- and Ir(N)(OH)^- having intermediate stabilities.

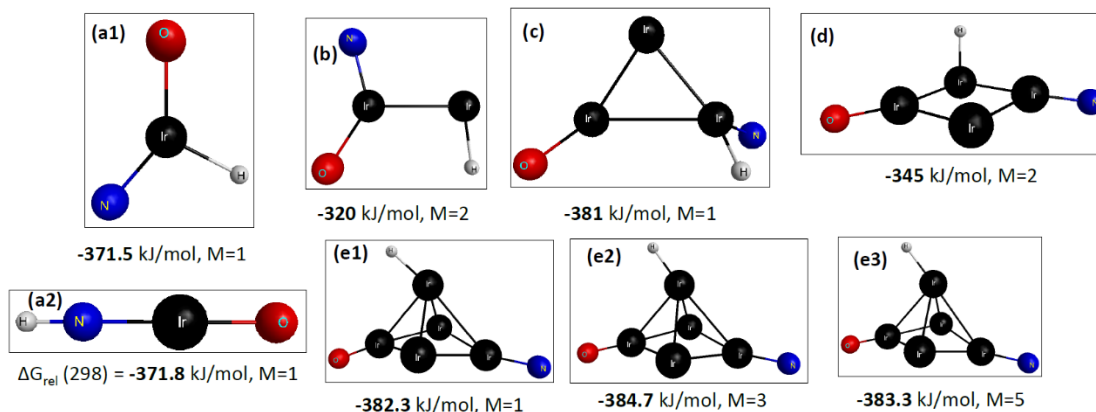


Figure IV.A.2.3 Lowest Energy Isomers of $\text{Ir}_n(\text{NOH})^-$; $n=1-5$. Free energies are at 298.15K, relative to separated $\text{Ir}_n^- + \text{NH}_2\text{OH} - \text{H}_2$; i.e., ΔG for the reaction $(\text{Ir}_n^- + \text{NH}_2\text{OH} \rightarrow \text{Ir}_n(\text{NOH})^- + \text{H}_2)$. M denotes the spin multiplicity.

A similar computational sampling of representative isomers of $\text{Ir}_2(\text{NOH})^-$ was completed, taking into account the possibility of fragments attaching to either a common Ir atom or to separate Ir atoms. In addition, spin multiplicities of 2, 4, and 6 were considered. The most stable isomer found was a fully fragmented spin-doublet $\text{Ir}_2(\text{N})(\text{O})(\text{H})^-$ species in which the O and N atoms are bonded to a common Ir atom, as shown in Figure IV.A.2.3(b). Additional isomers and the corresponding relative free energies are illustrated in Figure S9, all of which are doublets except for three spin-quartet isomers. As in the case of the $n=1$ isomers, it is generally observed that $\text{Ir}_2\text{-HNO}^-$ structures with an unfragmented HNO or ONH ligand are the least stable and partially fragmented isomers such as $\text{Ir}_2(\text{NO})(\text{H})^-$ and $\text{Ir}_2(\text{O})(\text{NH})^-$ have intermediate relative energies.

For $\text{Ir}_3\text{-NOH}^-$, a more limited sampling of representative isomers was conducted. In particular, only the cyclic form of the Ir_3^- was considered, although an extended set of spin multiplicities ranging from 1 to 9 were calculated. The most stable isomer found was a fully fragmented spin singlet $\text{Ir}_3(\text{N})(\text{O})(\text{H})^-$ structure in which the N and H atoms are bound to a common Ir, as illustrated in Figure IV.A.2.3(c). As in the $n=1$ and $n=2$ cases, the stabilities of the $\text{Ir}_3(\text{NOH})^-$ isomers generally increase with degree of HNO fragmentation, indicating that Ir-O, Ir-N, and Ir-H bonds are likely stronger than N-O, N-H, and O-H bonds. A representative subset of other isomers is shown in Figure S10. As an aside, an isomer with a bridging H atom was found (with relative free energy of -271.1 kJ/mol) and a nitrogen atom was found to insert into an Ir-Ir bond (relative free energy of -354.3 kJ/mol), reflecting the greater number of

configurational degrees of freedom associated with larger Ir_n^- clusters and possible weakening of the average Ir-Ir bond strength with increasing n .

Since the trends in relative isomer stability for $n=1-3$ discussed above indicate an energetic preference for fragmented HNO, exploration of possible isomers for the $n=4$ species was limited to partially and fully fragmented $\text{Ir}_4(\text{NOH})^-$ species, and further restricted to the planar arrangement of Ir_4^- . Spin multiplicities of 2, 4, 6, 8, and 10 were examined. The most stable isomer located is the doublet $\text{Ir}_4(\text{N})(\text{O})(\text{H})^-$ structure shown in Figure IV.A.2.3(d), in which each N, O, and H atom is bonded to a separate Ir atom. Additional, representative isomers are shown in Figure S11, which include instances of a bridging N atom.

Consideration of potential isomers of $\text{Ir}_5\text{-NOH}^-$ was restricted to the square pyramidal form of Ir_5^- and only the $\text{Ir}_5(\text{NH})(\text{O})^-$ and $\text{Ir}_5(\text{N})(\text{O})(\text{H})^-$ fragmented species. Spin multiplicities of 1 to 13 were considered, owing to the predicted ground state multiplicity of 13 for the bare Ir_5^- anion. The most stable isomer found was the $\text{Ir}_5(\text{N})(\text{O})(\text{H})^-$ triplet state structure shown in Figure IV.A.2.3(e2), although the corresponding singlet and quintet states, panels (e1) and (e3), respectively, in Figure IV.A.2.3, have similar structures and nearly the same relative energies. Additional, less stable isomers are shown in Figure S12.

3.4 Theoretical Vertical and Adiabatic detachment energies of $\text{Ir}_n(\text{NOH})^-$ ($n=1-5$).

Vertical detachment energies (VDEs) and adiabatic detachment energies (ADEs) of the $\text{Ir}_n(\text{NOH})^-$ ($n=1-5$) anions were computed using the lowest-energy structures shown in Figure IV.A.2.3. Single-point energy calculations of the corresponding neutral species were performed at the anion local minimum structures, taking the difference in electronic energies of neutral minus anion as the VDE. Multiple neutral spin states were calculated, with the smallest energy difference between neutral and anion taken as the theoretical VDE. For calculation of the ADEs, the neutral species were optimized and the ADEs were computed as the difference in zero point energy-corrected electronic energies of the anion and neutral. For $n=1$, the VDEs and ADEs of isomers (a1) and (a2) shown in Figure IV.A.2.3 were computed, due to their nearly identical relative energies. The experimental VDEs and theoretical VDEs+ADEs of $\text{Ir}_n(\text{NOH})^-$ ($n=1-5$) are summarized in Table IV.A.2.1.

For $n=1$, the calculated VDE and ADE for isomer $\text{Ir}(\text{O})(\text{NH})^-$, shown in Figure IV.A.2.3(a2), of 2.96 eV and 2.94 eV, respectively, are in excellent agreement with the measured value of 2.9 eV. In contrast, isomer $\text{Ir}(\text{O})(\text{N})(\text{H})^-$ (Figure IV.A.2.3(a1)) has a calculated VDE (ADE) of 3.71 (3.47) eV, 0.8 (0.6) eV larger than the experimental value. This

clearly suggests that isomer (a2) corresponds to the $\text{Ir}(\text{NOH})^-$ species experimentally generated. For $n=2-5$, the agreement between the measured and predicted VDEs is uniformly excellent, with differences of less than 0.1 eV. For $n=5$, VDEs for the three isomers shown in Figure IV.A.2.3, (e1), (e2), and (e3) are similar, ranging from 3.32 to 3.41 eV, with isomers (e1) and (e2) showing slightly better agreement with the measured VDE of 3.3 eV. As noted previously, for $n=2-5$ the VDEs are closer than the ADEs to the experimental data, suggesting that the measured peaks correspond to VDEs.

For comparison, the VDEs for some of the less stable isomers of $\text{Ir}_n(\text{NOH})^-$ were also computed and are shown in Figures S9-S12. For $n=2$ (Figure S9), predicted VDEs of 2.28 and 2.61 eV were obtained for two higher-energy isomers. This illustrates the sensitivity of the VDE to the isomer structure. Furthermore, the VDEs of the less stable isomers differ significantly from the observed VDE (3.02 eV), indicating that the less stable isomers are unlikely present in the experiments. Similar comments apply to $n=3-5$ (Figures S10-S12), in which the predicted VDEs of the less stable isomers are in rather poor agreement with the corresponding measured VDEs and the predicted VDEs of the most stable isomers.

The VDEs of IrO_2^- and Ir_2O_2^- were computed in a similar fashion, with values of 3.48 and 2.81 eV, respectively, and corresponding experimental values of 3.64 and 2.63 eV. While the differences between theory and experiment of 0.15 - 0.18 eV are somewhat larger than observed for the $\text{Ir}_n(\text{NOH})^-$ series of anions, the level of agreement is nonetheless acceptable.

Electronic transition energies from the anion ground state species $\text{Ir}_n(\text{NOH})^-$ ($n=1-4$) to vertical excited states of the corresponding optimized neutral were computed using time-dependent density functional theory (TDDFT) at the CAMQTP01/def2-TZVPP level, which are summarized in Table S1. For $n=1$, a single excited state energy transition below the experimental measurement limit of 4.5 eV is predicted at 3.98 eV, which is 0.27 eV lower than the highest energy peak observed in the PES spectrum shown in Figure IV.A.2.2. For $n=2$, there are three transition energies in the 3.6-4.3 eV range, all larger than the observed transitions between 2.5 and 3.5 eV in Figure IV.A.2.2. For $n=3$, there is a predicted transition energy of 3.8 eV which is near the measured transition energy at 3.9 eV. For $n=4$, there are five predicted transition energies between 3.5 and 4.5 eV, all larger than the observed transitions in the 3.0-3.5 eV range.

As seen in Table S1, the number of electronic transitions below 4.5 eV grows rapidly with increasing number of iridium atoms. This is qualitatively consistent with the complexity of the observed PES spectra of the larger $\text{Ir}_n(\text{NOH})^-$ species shown in Figure IV.A.2.2. Nonetheless, a more rigorous theoretical analysis which includes incorporation of Franck-Condon effects and consideration of vibronic transitions will be required to obtain further insights and interpretation of the measured spectra.

3.5 Formation of $\text{Ir}(\text{NOH})^-$. As shown by the experimental data, a major product of the reactions between the anionic iridium clusters Ir_n^- and hydroxylamine is $\text{Ir}_n(\text{NOH})^-$ accompanied by elimination of H_2 ; i.e., $\text{Ir}_n^{+} + \text{NH}_2\text{OH} \rightarrow \text{Ir}_n(\text{NOH})^- + \text{H}_2$. In principle, other reaction products are possible such as those listed below, with reaction free energies predicted at the $\omega\text{B97X-d/def2}$ level of theory.



In reactions (R2)-(R5) above, the predicted ground states of Ir^- , $\text{Ir}(\text{O})^-$, and $\text{Ir}(\text{H})(\text{H})^-$ are triplets, whereas $\text{Ir}(\text{O})(\text{NH})^-$ and $\text{Ir}(\text{N})(\text{H})$ are singlets. Elimination of HNO is slightly endergonic, whereas elimination of NH_3 , H_2O , and H_2 are all exergonic processes. Since (R5) is the thermodynamically favored route and also corresponds to the primary reaction products observed in the experiments, we focused our theoretical efforts on this particular reaction pathway.

In order to gain insights into the chemical processes leading to formation of $\text{Ir}_n(\text{NOH})^- + \text{H}_2$, a detailed mapping of portions of the $\text{Ir}^- + \text{NH}_2\text{OH}$ potential energy surface was undertaken. In the following, all energies are relative to separated $\text{Ir}^- (^3\text{X}) + \text{NH}_2\text{OH}$. On the triplet surface, a hydrogen-bonded complex is formed between Ir^- and NH_2OH , with a free energy of -43 kJ/mol with respect to separated $\text{Ir}^- + \text{NH}_2\text{OH}$, as illustrated in Figure IV.A.2.4(a). Additional, less stable conformers are shown in Figure S13.

Initial fragmentation of NH_2OH can occur in three primary ways, via N-H, O-H, and N-O bond scission. The corresponding products of these three processes are $\text{Ir}(\text{H})(\text{NHOH})^-$, $\text{Ir}(\text{H})(\text{ONH}_2)^-$, and $\text{Ir}(\text{OH})(\text{NH}_2)^-$, which are shown in Figure IV.A.2.4, panels (b), (c), and (d), respectively. The saddle point connecting the initial complex and the N-

H fragmentation product is shown in Figure S14, which has a barrier of 79 kJ/mol. Similarly, the saddle point for the O-H fragmentation process is shown in Figure S15, which has a smaller barrier of 56 kJ/mol.

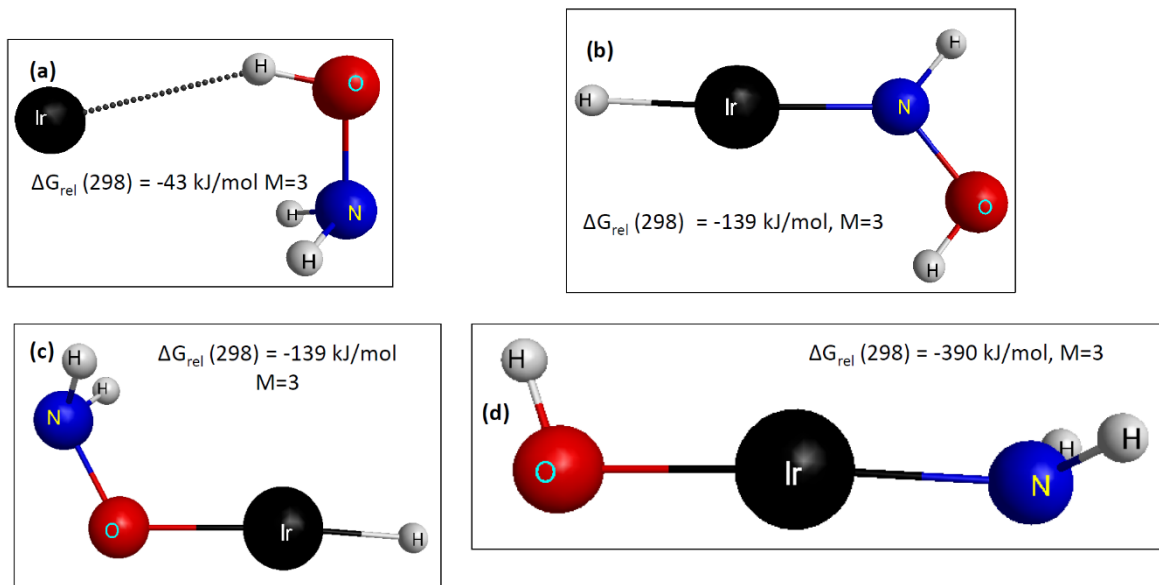


Figure IV.A.2.4 (a) Hydrogen-bonded complex between Ir^- and NH_2OH . (b) N-H fragmentation product. (c) O-H fragmentation product. (d) N-O fragmentation product. Free energies are at 298.15K, relative to $\text{Ir}^- + \text{NH}_2\text{OH}$. M denotes the spin multiplicity

Despite numerous attempts, on the triplet state surface we were unable to locate a saddle point directly connecting the initial complex and the N-O fragmentation product $\text{Ir}(\text{OH})(\text{NH}_2)^-$. However, starting from the slightly higher energy conformer of the $\text{Ir}(\text{NH}_2\text{OH})^-$ complex identified in Figure S13(d), a two-step reaction pathway leading to the N-O fragmentation product $\text{Ir}(\text{OH})(\text{NH}_2)^-$ was identified, as shown in Figure S16. The first step of the reaction, with a barrier of 28 kJ/mol, involves concerted N-O bond dissociation and transfer of an H atom from NH_2 to OH, resulting in formation of H_2O which is hydrogen-bonded in the product to the thus-formed $\text{Ir}(\text{NH})^-$ intermediate, with a relative energy of -225 kJ/mol. Since this barrier of 28 kJ/mol is smaller than that of both the N-H fragmentation process (79 kJ/mol, Figure S14) and the O-H fragmentation (56 kJ/mol, Figure S15), and hence more likely to play a key role in formation of the observed reaction products, this reaction pathway was studied in greater detail.

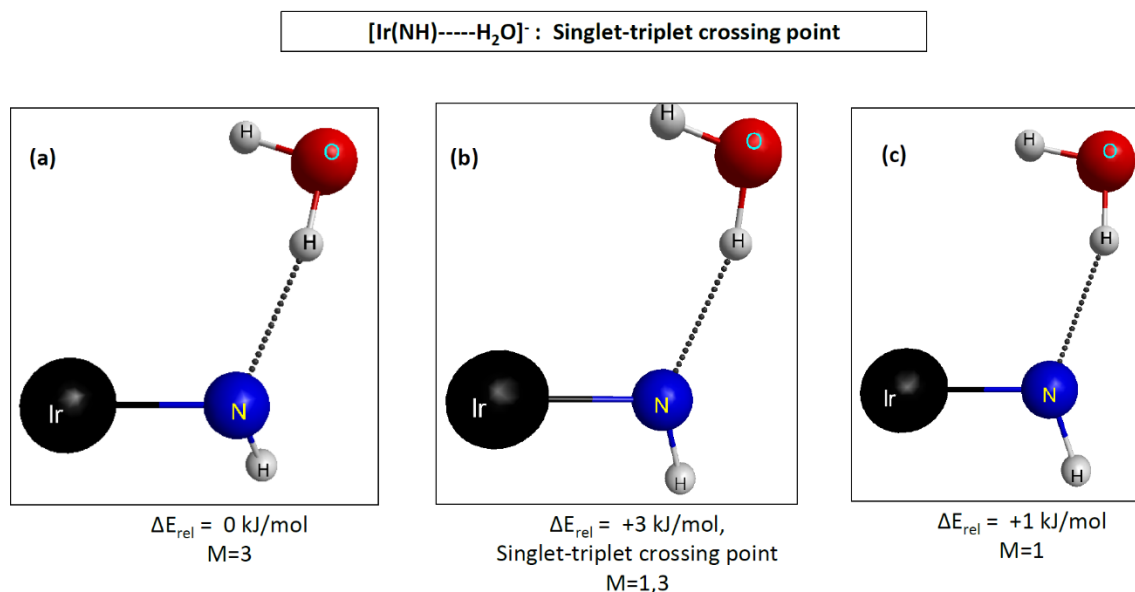


Figure IV.A.2.5 $[\text{Ir}(\text{NH})\cdots\text{H}_2\text{O}]^-$ structures at (a) the triplet state local minimum, (b) the singlet-triplet minimum energy crossing point, and (c) the singlet state local minimum. ΔE_{rel} denotes the relative electronic energies and M denotes the spin multiplicity.

The next step of this reaction pathway involves concerted dissociation of an O-H bond with the H atom reattaching to the -NH fragment and the hydroxyl moiety attaching to Ir, resulting in formation of $\text{Ir}(\text{OH})(\text{NH}_2)^-$ (Figure S16). However, it should be noted that *on the triplet state surface*, simple breaking of the hydrogen bond in the $[\text{Ir}(\text{NH})\cdots\text{H}_2\text{O}]^-$ complex to produce separated $\text{Ir}(\text{NH})^-$ and H_2O , at a relative energy of -198 kJ/mol, is energetically more favorable than crossing the second saddle point, which has a relative energy of -133 kJ/mol. However, a singlet-triplet minimum energy crossing point in close structural and energetic proximity to the triplet state $[\text{Ir}(\text{NH})\cdots\text{H}_2\text{O}]^-$ complex was located and is shown in Figure IV.A.2.5, along with the singlet and triplet state local minima. The crossing point lies only 3 kJ/mol above the triplet local minimum, suggesting that crossover to the singlet state might readily occur. On the singlet surface, the $[\text{Ir}(\text{NH})\cdots\text{H}_2\text{O}]^-$ local minimum can undergo a simple internal migration of the water molecule, with the saddle point at a relative free energy of -198 kJ/mol, followed by a nearly barrier-free transfer of an H atom from water to the Ir atom to form $\text{Ir}(\text{OH})(\text{NH})(\text{H})^-$, as illustrated in Figure S17. Finally, elimination of H_2 from $\text{Ir}(\text{OH})(\text{NH})(\text{H})^-$ to form $\text{Ir}(\text{O})(\text{NH})^-$ crosses a saddle point with a relative free energy of -161 kJ/mol, as shown in Figure S18. It should be noted that the final product, $\text{Ir}(\text{O})(\text{NH})^-$, shown in Figure IV.A.2.3(a2),

is the isomer of $\text{Ir}(\text{NOH})^-$ that has a predicted VDE (2.96 eV) in good agreement with the experimental value (2.9 eV), as discussed previously.

Figure IV.A.2.6 summarizes the key steps described above and shown individually in Figures S16-S18. Also shown on the left side of Figure IV.A.2.6 is a sequence of reaction steps, entirely on the triplet state surface, leading to formation of $\text{Ir}(\text{O})^- + \text{NH}_3$. However, this portion of the $\text{Ir}^- + \text{NH}_2\text{OH}$ potential energy surface is not discussed in detail since $\text{Ir}(\text{O})^-$ is present even in the absence of hydroxylamine.

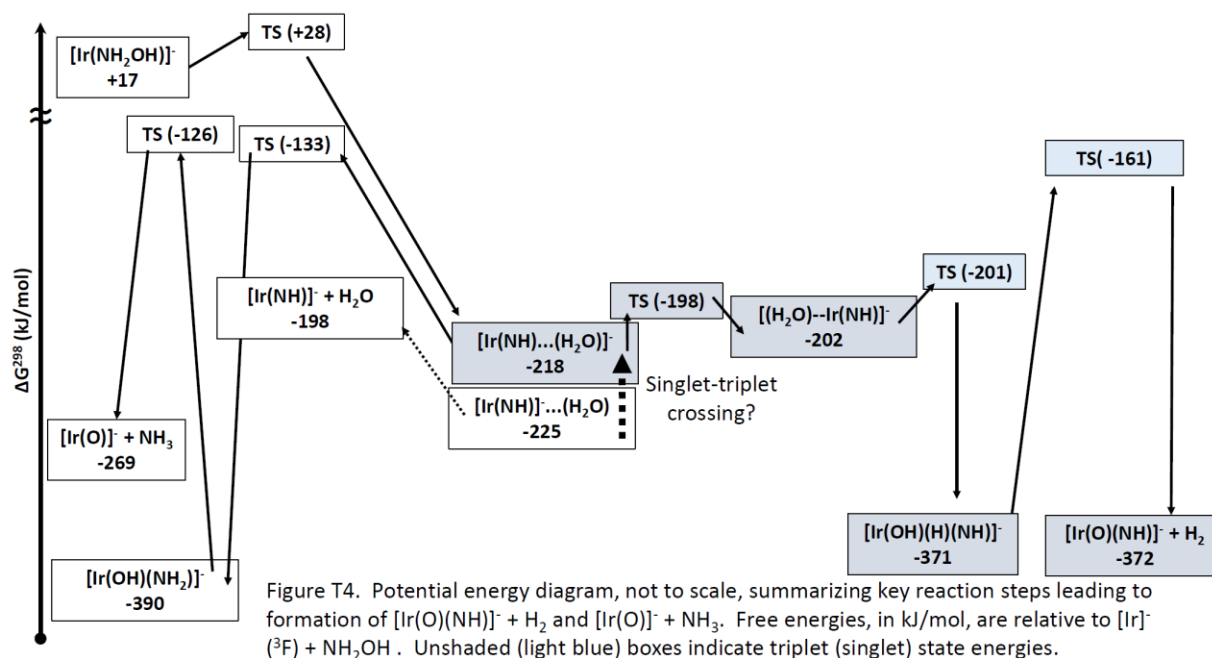


Figure IV.A.2.6 Potential energy diagram, not to scale, summarizing the key reaction steps leading to the formation of $\text{Ir}(\text{O})(\text{NH})^- + \text{H}_2$ and $\text{Ir}(\text{O})^- + \text{NH}_3$. Free energies, in kJ/mol, are relative to $\text{Ir}^- + \text{NH}_2\text{OH}$. Unshaded boxes correspond to triplet states, whereas the blue-shaded boxes are singlet states.

4. Conclusion

In this work, photoelectron spectra of mass-selected bare Ir_n^- ($n=1-5$) anionic clusters and $\text{Ir}_n(\text{NOH})^-$ ($n=1-5$) products were measured and the photoelectron VDEs were found to be in excellent agreement with DFT calculations. The reaction of Ir^- with hydroxylamine to form $\text{Ir}(\text{NOH})^- + \text{H}_2$ is proposed to proceed through a triplet to singlet crossing and is exoergic by 372 kJ/mol. This pathway could help to explain the enhanced reactivity of hydroxylamine on iridium catalysts leading to large heat release and promoting ignition of HAN-based monopropellants. The systematic

study of Ir_n^- with hydroxylamine offers a wealth of information as to the fundamental reaction mechanisms common to these heterogeneous catalytic reactions leading to combustion and ignition. Further expanding these studies to include more analogues of regularly employed fuels (hydrazines, nitrates, etc.) will give a better understanding as to the limitations of their current use in spacecraft thruster applications. This is critical in real world applications for continued design and development of the next generation fuels and catalysts, lowering the risks from exposure and explosive hazards and increasing the lifetime of the catalysts, thereby increasing the lifetime of the thrusters and spacecrafts as well.

Author Contributions:

S.M.C., G.L., M.B., Z.Z., M.A.M., R.M.H., T.C, E.L.C., and S.M. completed the experimental photoelectron study. R.B., J.A.B., and S.D.C. performed the theoretical study. K.H.B, J.A.B., and S.D.C. conceived of and supervised the work.

References:

1. Hwang, C. H.; Baek, S. W.; Cho, S. J. Experimental Investigation of Decomposition and Evaporation Characteristics of HAN-Based Monopropellants. *Combust. Flame* **2014**, *161*, 1109-1116.
2. Amariei, D.; Courthéoux, L.; Rossignol, S.; Kappenstein, C. Catalytic and Thermal Decomposition of Ionic Liquid Monopropellants Using a Dynamic Reactor: Comparison of Powder and Sphere-Shaped Catalysts. *Chem. Eng. Process.* **2007**, *46*, 165-174.
3. Amrousse, R.; Hori, K.; Fetimi, W.; Farhat, K. HAN and ADN as Liquid Ionic Monopropellants: Thermal and Catalytic Decomposition Processes. *Appl. Catal. B* **2012**, *127*, 121-128.
4. Amrousse, R.; Katsumi, T.; Azuma, N.; Hori, K. Hydroxylammonium Nitrate (HAN)-Based Green Propellant as Alternative Energy Resource for Potential Hydrazine Substitution: From Lab Scale to Pilot Plant Scale-up. *Combust. Flame* **2017**, *176*, 334-348.
5. Farshchi, M.; Vaezi, V.; Shaw, B. D. Studies of HAN-Based Monopropellant Droplet Combustion. *Combust. Sci. Tech.* **2002**, *174*, 71-97.
6. Legge, R. S. L.; Lozano, P. C. Electrospray Propulsion Based on Emitters Microfabricated in Porous Metals. *J. Propul. Power* **2011**, *27*, 485-495.
7. Schneider, S.; Hawkins, T.; Rosander, M.; Vaghjiani, G.; Chambreau, S.; Drake, G. Ionic Liquids as Hypergolic Fuels. *Energy Fuels* **2008**, *22*, 2871-2872.
8. Chambreau, S. D.; Popolan-Vaida, D. M.; Vaghjiani, G. L.; Leone, S. R. Catalytic Decomposition of Hydroxylammonium Nitrate Ionic Liquid: Enhancement of NO Formation. *J. Phys. Chem. Lett.* **2017**, *8*, 2126-2130.
9. Oxley, J. C.; Brower, K. R. In Thermal Decomposition Of Hydroxylamine Nitrate, *Proc. SPIE* **1988**, *0872*, 63-70.
10. Lee, H. S.; Thynell, S. T. Confined Rapid Thermolysis/FTIR Spectroscopy of Hydroxylammonium Nitrate. In *33rd Joint Propulsion Conference and Exhibit*; American Institute of Aeronautics and Astronautics Inc, AIAA, 1997. <https://doi.org/10.2514/6.1997-3232>.
11. Kidd, F. G.; Taylor, N. R.; Lemmer, K. M., Decomposition of Hydroxylammonium Nitrate in a Low Pressure Flowing Thermal Capillary System. *J. Molec. Liq.* **2018**, *262*, 396-404.
12. Amrousse, R.; Katsumi, T.; Itouyama, N.; Azuma, N.; Kagawa, H.; Hatai, K.; Ikeda, H.; Hori, K. New HAN-Based Mixtures for Reaction Control System and Low Toxic Spacecraft Propulsion Subsystem: Thermal Decomposition and Possible Thruster Applications. *Combust. Flame* **2015**, *162*, 2686-2692.

13. Hunt, L. B. A History of Iridium. *Platinum Metals Rev.* **1987**, *31*, 32–41.
14. Foger, K.; Anderson, J. R. Hydrocarbon Reactions on Supported Iridium Catalysts. *J. Catal.* **1979**, *59*, 325–339.
15. Vieira, R.; Bastos-Netto, D.; Ledoux, M.-J.; Pham-Huu, C. Hydrazine Decomposition over Iridium Supported on Carbon Nanofibers Composite for Space Applications: Near Actual Flight Conditions Tests. *Appl. Catal. A-Gen.* **2005**, *279*, 35–40.
16. Jiang, K.; Luo, M.; Peng, M.; Yu, Y.; Lu, Y.-R.; Chan, T.-S.; Liu, P.; de Groot, F. M. F.; Tan, Y. Dynamic Active-Site Generation of Atomic Iridium Stabilized on Nanoporous Metal Phosphides for Water Oxidation. *Nat. Commun.* **2020**, *11*, 2701.
17. Pfeifer, V.; Jones, T. E.; Velasco Vélez, J. J.; Massué, C.; Greiner, M. T.; Arrigo, R.; Teschner, D.; Girgsdies, F.; Scherzer, M.; Allan, J., et al. The Electronic Structure of Iridium Oxide Electrodes Active in Water Splitting. *Phys. Chem. Chem. Phys.* **2016**, *18*, 2292–2296.
18. Rodrigues, J. A. J.; Cruz, G. M.; Bugli, G.; Boudart, M.; Djega-Mariadassou, G. Nitride and Carbide of Molybdenum and Tungsten as Substitutes of Iridium for the Catalysts used for Space Communication. *Catal. Lett.* **1997**, *45*, 1–3.
19. Wu, W.-P.; Chen, Z.-F. Iridium Coating: Processes, Properties and Application. Part I. *Johnson Matthey Technol. Rev.* **2017**, *61*, 16–28.
20. Wu, W.-P.; Chen, Z.-F. Iridium Coating: Processes, Properties and Application. Part II. *Johnson Matthey Technol. Rev.* **2017**, *61*, 93–110.
21. Lee, S.; Fan, C.; Wu, T.; Anderson, S. L. Hydrazine Decomposition over Ir_n/Al₂O₃ Model Catalysts Prepared by Size-Selected Cluster Deposition. *J. Phys. Chem. B* **2005**, *109*, 381–388.
22. Schmidt, M. W.; Gordon, M. S. The Decomposition of Hydrazine in the Gas Phase and over an Iridium Catalyst. *Z. Phys. Chem.* **2013**, *227*, 1301–1336.
23. Castleman, A. W. Cluster Structure and Reactions: Gaining Insights into Catalytic Processes. *Catal. Lett.* **2011**, *141*, 1243–1253.
24. Asmis, K. R.; Fielicke, A. Size-Selected Clusters as Model System for Catalysis. *Top. Catal.* **2018**, *61*, 1–2.
25. Charles, E.; Sykes, H.; Christopher, P. Recent Advances in Single-Atom Catalysts and Single-Atom Alloys: Opportunities for Exploring the Uncharted Phase Space In-Between. *Curr. Opin. Chem. Eng.* **2020**, *29*, 67–73.
26. Parkinson, G. S. Single-Atom Catalysis: How Structure Influences Catalytic Performance. *Catal. Lett.* **2019**, *149*, 1137–1146.
27. Sweeny, B. C.; Ard, S. G.; Viggiano, A. A.; Shuman, N. S. Reaction of Mass-Selected, Thermalized V_nO_m⁺ Clusters with CCl₄. *J. Phys. Chem. A* **2019**, *123*, 4817–4824.
28. Ard, S. G.; Melko, J. J.; Ushakov, V. G.; Johnson, R.; Fournier, J. A.; Shuman, N. S.; Guo, H.; Troe, J.; Viggiano, A. A. Activation of Methane by FeO⁺: Determining Reaction Pathways through Temperature-Dependent Kinetics and Statistical Modeling. *J. Phys. Chem. A* **2014**, *118*, 2029–2039.
29. Sweeny, B. C.; Pan, H.; Ard, S. G.; Shuman, N. S.; Viggiano, A. A. On the Role of Hydrogen Atom Transfer (HAT) in Thermal Activation of Methane by MnO⁺: Entropy vs. Energy. *Z. Phys. Chem.* **2019**, *233*, 771–783.
30. Liu, G.; Ciborowski, S. M.; Zhu, Z.; Bowen, K. H. Activation of Hydroxylamine by Single Gold Atomic Anions. *Int. J. Mass. Spec.* **2019**, *435*, 114–117.
31. Liu, G.; Miliordos, E.; Ciborowski, S. M.; Tschurl, M.; Boesl, U.; Heiz, U.; Zhang, X.; Xantheas, S. S.; Bowen, K. Water Activation and Splitting by Single Metal-Atom Anions. *J. Chem. Phys.* **2018**, *149*, 221101.
32. Liu, G.; Ciborowski, S. M.; Zhu, Z.; Chen, Y.; Zhang, X.; Bowen, K. H. The Metallo-Formate Anions, M(CO₂)⁻, M = Ni, Pd, Pt, Formed by Electron-Induced CO₂ Activation. *Phys. Chem. Chem. Phys.* **2019**, *21*, 10955–10960.
33. Liu, G.; Zhu, Z.; Ciborowski, S. M.; Ariyaratna, I. R.; Miliordos, E.; Bowen, K. H. Selective Activation of the C-H Bond in Methane by Single Platinum Atomic Anions. *Angew. Chem. Int. Ed.* **2019**, *58*, 7773–7777.
34. Campbell, K. D.; Zhang, H.; Lunsford, J. H. Methane Activation by the Lanthanide Oxides. *J. Phys. Chem.* **1988**, *92*, 750–753.
35. Van Koppen, P. A. M.; Kemper, P. R.; Bushnell, J. E.; Bowers, M. T. Methane Dehydrogenation by Ti⁺: A Cluster-Assisted Mechanism for σ-Bond Activation. *J. Am. Chem. Soc.* **1995**, *117*, 2098–2099.
36. Sun, G.; Zhao, Z.-J.; Mu, R.; Zha, S.; Li, L.; Chen, S.; Zang, K.; Luo, J.; Li, Z.; Purdy, C., et al. Breaking the Scaling Relationship via Thermally Stable Pt/Cu Single Atom Alloys for Catalytic Dehydrogenation. *Nat. Commun.* **2018**, *9*, 4454.

37. Du, J.; Sun, X.; Chen, J.; Jiang, G. A Theoretical Study on Small Iridium Clusters: Structural Evolution, Electronic and Magnetic Properties, and Reactivity Predictors. *J. Phys. Chem. A* **2010**, *114*, 12825–12833.
38. Pawluk, T.; Hirata, Y.; Wang, L. Studies of Iridium Nanoparticles Using Density Functional Theory Calculations. *J. Phys. Chem. B* **2005**, *109*, 20817–20823.
39. Davis, J. B. A.; Shayeghi, A.; Horswell, S. L.; Johnston, R. L. The Birmingham Parallel Genetic Algorithm and Its Application to the Direct DFT Global Optimisation of IrN (N = 10–20) Clusters. *Nanoscale* **2015**, *7*, 14032–14038.
40. Zhang, W.; Xiao, L.; Hirata, Y.; Pawluk, T.; Wang, L. The Simple Cubic Structure of Ir Clusters and the Element Effect on Cluster Structures. *Chem. Phys. Lett.* **2004**, *383*, 67–71.
41. Chen, M.; Dixon, D. A. Low-Lying Electronic States of Ir_n Clusters with n = 2–8 Predicted at the DFT, CASSCF, and CCSD(T) Levels. *J. Phys. Chem. A* **2013**, *117*, 3676–3688.
42. Bussai, C.; Krüger, S.; Vayssilov, G. N.; Rösch, N. The Cluster Ir₄ and its Interaction with a Hydrogen Impurity. A Density Functional Study. *Phys. Chem. Chem. Phys.* **2005**, *7*, 2656–2663.
43. Krüger, S.; Bussai, C.; Genest, A.; Rösch, N. Two Hydrogen Ligands on Tetrairidium Clusters: a Relativistic Density Functional Study. *Phys. Chem. Chem. Phys.* **2006**, *8*, 3391–3398.
44. Balasubramanian, K.; Dai, D. Potential Energy Surfaces for Ir + H₂ and Ir⁺ + H₂ Reactions. *J. Chem. Phys.* **1990**, *93*, 7243–7255.
45. Castillo, S.; Bertin, V.; Solano-Reyes, E.; Luna-Garcia, H.; Cruz, A.; Poulain, E. Theoretical Studies on Hydrogen Activation by Iridium Dimers. *Int. J. of Quantum Chem.* **1998**, *70*, 1029–1035.
46. Feng, J.-N.; Huang, X.-R.; Li, Z.-S. A Theoretical Study on the Clusters Ir_n with n = 4, 6, 8, 10. *Chem. Phys. Lett.* **1997**, *276*, 334–338.
47. Okumura, M.; Irie, Y.; Kitagawa, Y.; Fujitani, T.; Maeda, Y.; Kasai, T.; Yamaguchi, K. DFT Studies of Interaction of Ir Cluster with O₂, CO, and NO. *Catal. Today* **2006**, *111*, 311–315.
48. Ge, Y.; Jiang, H.; Kato, R.; Gummagatta, P. Size and Site Dependence of the Catalytic Activity of Iridium Clusters toward Ethane Dehydrogenation. *J. Phys. Chem. A* **2016**, *120*, 9500–9508.
49. Chen, Y.; Huo, M.; Chen, T.; Li, Q.; Sun, Z.; Song, L. The Properties of Ir_n (n = 2–10) Clusters and their Nucleation on c-Al₂O₃ and MgO Surfaces: from ab initio Studies. *Phys. Chem. Chem. Phys.* **2015**, *17*, 1680–1687.
50. Qi, K.; Zhao, J.-M.; Wang, G.-C. A Density Functional Theory Study of Ethylene Hydrogenation on MgO- and γ-Al₂O₃-Supported Carbon-Containing Ir₄ Clusters. *Phys. Chem. Chem. Phys.* **2015**, *17*, 4899–4908.
51. Ferrari, A. M.; Neyman, K. M.; Mayer, M.; Staufer, M.; Gates, B. C.; Rösch, N. Faujasite-Supported Ir₄ Clusters: A Density Functional Model Study of Metal–Zeolite Interactions. *J. Phys. Chem. B* **1999**, *103*, 5311–5319.
52. Petrova, G. P.; Vayssilov, G. N.; Rösch, N. Density Functional Study of Hydrogen Adsorption on Tetrairidium Supported on Hydroxylated and Dehydroxylated Zeolite Surfaces. *J. Phys. Chem. C* **2007**, *111*, 14484–14492.
53. Petrova, G. P.; Vayssilov, G. N.; Rösch, N. Hydrogen Adsorption on Zeolite-Supported Tetrairidium Clusters. Thermodynamic Modeling from Density Functional Calculations. *J. Phys. Chem. C* **2008**, *112*, 18572–18577.
54. St. Petkov, P.; Petrova, G. P.; Vayssilov, G. N.; Rösch, N. Saturation of Small Supported Metal Clusters by Adsorbed Hydrogen. A Computational Study on Tetrahedral Models of Rh₄, Ir₄, and Pt₄. *J. Phys. Chem. C* **2010**, *114*, 8500–8506.
55. Petrova, G. P.; Vayssilov, G. N.; Rösch, N. Density Functional Modeling of Reverse Hydrogen Spillover on Zeolite-Supported Tetrairidium Clusters. *Chem. Phys. Lett.* **2007**, *444*, 215–219.
56. Vayssilov, G. N.; Rösch, N. Reverse Hydrogen Spillover in Supported Subnanosize Clusters of the Metals of Groups 8 to 11. A Computational Model Study. *Phys. Chem. Chem. Phys.* **2005**, *7*, 4019–4026.
57. Shor, E. A. I.; Nasluzov, V. A.; Shor, A. M.; Vayssilov, G. N.; Rösch, N. Reverse Hydrogen Spillover onto Zeolite-Supported Metal Clusters: An Embedded Cluster Density Functional Study of Models M₆ (M = Rh, Ir, or Au). *J. Phys. Chem. C* **2007**, *111*, 12340–12351.
58. Koyasu, K.; Tomihara, R.; Nagata, T.; Wu, J. W. J.; Nakano, M.; Ohshimo, K.; Misaizu, F.; Tsukuda, T. Sequential Growth of Iridium Cluster Anions based on Simple Cubic Packing. *Phys. Chem. Chem. Phys.* **2020**, *22*, 17842–17846.
59. Lu, Y.; Zhao, J.; Tang, R.; Fu, X.; Ning, C. Measurement of Electron Affinity of Iridium Atom and Photoelectron Angular Distributions of Iridium Anion. *J. Chem. Phys.* **2020**, *152*, 034302.
60. Davies, B. J.; Ingram, C. W.; Larson, D. J.; Ljungblad, U. The Electron Affinity of Iridium. *J. Chem. Phys.* **1997**, *106*, 5783–5784.

61. Barysz, M.; Syrocki, L. Theoretical Interpretation of Photoelectron Spectra of the Iridium Neutral Atom and Anion. *J. Quant. Spectrosc. Radiat. Transf.* **2020**, *255*, 107278.
62. Liu, G.; Ciborowski, S. M.; Bowen, K. H. Photoelectron Spectroscopic and Computational Study of Pyridine-Ligated Gold Cluster Anions. *J. Phys. Chem. A* **2017**, *121*, 5817-5822.
63. Ho, J.; Ervin, K. M.; Lineberger, W. C. Photoelectron Spectroscopy of Metal Cluster Anions: Cu^-_n , Ag^-_n , and Au^-_n . *J. Chem. Phys.* **1990**, *93*, 6987.
64. Chai, J.-D.; Head-Gordon, M. Systematic Optimization of Long-Range Corrected Hybrid Density Functionals. *J. Chem. Phys.* **2004**, *128*, 084106.
65. Chai, J.-D.; Head-Gordon, M. Long-Range Corrected Hybrid Density Functionals with Damped Atom-Atom Dispersion Corrections. *Phys. Chem. Chem. Phys.* **2008**, *10*, 6615-6620.
66. Weigend, F.; Ahlrichs, R. Balanced Basis Sets of Split Valence, Triple Zeta Valence and Quadruple Zeta Valence Quality for H to Rn: Design and Assessment of Accuracy. *Phys. Chem. Chem. Phys.* **2005**, *7*, 3297-3305.
67. Rappoport, D.; Furche, F. Property-Optimized Gaussian Basis Sets for Molecular Response Calculations. *J. Chem. Phys.* **2010**, *133*, 134105.
68. Andrae, D.; Häußermann, U.; Dolg, M.; Stoll, H.; Preuß, H. Energy-Adjusted ab initio Pseudopotentials for the Second and Third Row Transition Elements. *Theor. Chim. Acta* **1990**, *77*, 123-141.
69. The def2-TZVPPD basis set and stuttgart pseudopotentials were downloaded from the Basis Set Exchange (BSE) website <https://www.basissetexchange.org/>.
70. Pritchard, B. P.; Altarawy, D.; Didier, B.; Gibbs, T. D.; Windus, T. L. A New Basis Set Exchange: An Open, Up-to-date Resource for the Molecular Sciences Community. *J. Chem. Inf. Model.* **2019**, *59*, 4814-4820.
71. Feller, D. The Role of Databases in Support of Computational Chemistry Calculations. *J. Comput. Chem.* **1996**, *17*, 1571-1586.
72. Schuchardt, K. L.; Didier, B. T.; Elsethagen, T.; Sun, L.; Gurumoorthi, V.; Chase, J.; Li, J.; Windus, T.L.; Basis Set Exchange: A Community Database for Computational Sciences. *J. Chem. Inf. Model.* **2007**, *47*, 1045-1052.
73. Ishida, K.; Morokuma, K.; Komornicki, A. The Intrinsic Reaction Coordinate. An ab initio Calculation for $\text{HNC} \rightarrow \text{HCN}$ and $\text{H}^- + \text{CH}_4 \rightarrow \text{CH}_3 + \text{H}^-$. *J. Chem. Phys.* **1977**, *66*, 2153-2156.
74. Gonzalez, C.; Schlegel, H. B. An Improved Algorithm for Reaction Path Following. *J. Chem. Phys.* **1989**, *90*, 2154-2161.
75. McQuarrie, D. A. *Statistical Mechanics*; Harper & Row: New York, 1975.
76. The zero point energy scale factor of 0.975 used here is the value recommended for $\omega\text{B97x-d/def2-TZVP}$; see: Alecu, I. M.; Zheng, J.; Zhao, Y.; Truhlar, D. G. Computational Thermochemistry: Scale Factor Databases and Scale Factors for Vibrational Frequencies Obtained from Electronic Model Chemistries. *J. Chem. Theory Comput.* **2010**, *6* (9), 2872-2887.
77. Jin, Y.; Bartlett, R. J. The QTP Family of Consistent Functionals and Potentials in Kohn-Sham Density Functional Theory. *J. Chem. Phys.* **2016**, *145* (3), 34107.
78. Schmidt, M. W.; Baldridge, K. K.; Boatz, J. A.; Elbert, S. T.; Gordon, M. S.; Jensen, J. H.; Koseki, S.; Matsunaga, N.; Nguyen, K. A.; Su, S. J., et al. General Atomic and Molecular Electronic Structure System. *J. Comput. Chem.* **1993**, *14*, 1347-1363.
79. Gordon, M. S.; Schmidt, M. W. Advances in Electronic Structure Theory: GAMESS a Decade Later. In *Theory and Applications of Computational Chemistry*; Elsevier, 2005; pp 1167-1189. <https://doi.org/10.1016/B978-044451719-7/50084-6>.
80. Gozem, S.; Krylov, A. I. The EzSpectra Suite: An Easy-to-use Toolkit for Spectroscopy Modeling. *WIREs Comput. Mol. Sci.* **2021**, e1546.

IV.A.3. Selective Activation of the C-H Bond in Methane by Single Platinum Atomic Anions

Gaoxiang Liu,[†] Zhaoguo Zhu,[†] Sandra M. Ciborowski,[†] Isuru R. Ariyaratna,[‡] Evangelos Miliordos,[‡] Kit H. Bowen^{†,*}

[†]Department of Chemistry, Johns Hopkins University, Baltimore, MD 21218, USA

[‡]Department of Chemistry and Biochemistry, Auburn University, Auburn, AL 36849, USA

Reprinted with permission from John Wiley and Sons. *Angew. Chem. Int. Ed.* **58**, 7773-7777 (2019)

Abstract

Mass spectrometric analysis of the anionic products of interaction between platinum atomic anions, Pt⁻, and methane, CH₄ and CD₄, in a collision cell shows the preferred generation of [PtCH₄]⁻ and [PtCD₄]⁻ complexes and a low tendency toward dehydrogenation. [PtCH₄]⁻ is shown to be H-Pt-CH₃⁻ by a synergy between anion photoelectron spectroscopy and quantum chemical calculations, implying the rupture of a single C-H bond. The calculated reaction pathway accounts for the observed selective activation of methane by Pt⁻. This study presents the first example of methane activation by a single atomic anion.

Main text

Converting methane into high value chemicals requires it first to be chemically activated. However, because the dissociation energy of the C-H bond¹ is high, i.e., 440 kJ/mol, activation is challenging. Typically, either elevated reaction temperatures or high activity catalysts are required,²⁻³ but these inevitably compromise selectivity.⁴ Industrially, the end product of methane conversion is usually the generation of syngas, but this process consumes large amounts of energy. Clearly, it would be advantageous to functionalize methane through the selective and energy-efficient activation of the thermodynamically strong C-H bond. This goal is therefore among the greatest challenges in catalysis.

Gas-phase studies of methane activation by metal atoms and clusters have provided insight into methane functionalization at the molecular level.⁵⁻⁴² In the case of platinum the reactivities of its cationic, neutral, and anionic atoms and clusters with methane have been widely investigated.^{7,19,24-28,43-49} For its atoms, in particular, both cationic and neutral platinum atoms have been shown to activate methane, yielding both dehydrogenation and insertion

products,^{19,49} whereas anionic platinum atoms were found in FT-ICR mass spectrometric experiments to exhibit only negligible reactivity toward methane.

Here, we show that under our experimental conditions, platinum atomic anions, Pt^- , activate methane, and that due to their preference for forming the C-H insertion product, they do so with significant selectivity. Moreover, this is the first observation of methane activation by single atomic anions.

Our experimental apparatus has been described previously.⁵¹⁻⁵³ Briefly, Pt^- was prepared in a laser vaporization source and interacted with methane introduced into a collision cell downstream. No platinum cluster anions were seen under the source conditions utilized in these experiments. The resultant anionic products were identified by time-of-flight mass spectrometry. Anions of interest were mass-selected and then characterized by anion photoelectron spectroscopy, which involves crossing a mass-selected beam of anions with a fixed-frequency photon beam and energy-analyzing the resultant photodetached electrons. The photodetachment process is governed by the energy-conserving relationship, $h\nu = \text{EKE} + \text{EBE}$, where EKE is the electron kinetic energy and EBE is the electron binding (transition) energy.

Figure IV.A.3.1 presents mass spectra with or without the addition of methane. With no methane in the interaction cell, only Pt^- and weak intensities of PtC^- and PtO^- were observed (see Figure IV.A.3.1A). The formation of PtC^- and PtO^- was likely due to trace amounts of carbon and oxygen present on the platinum metal surface. When methane or deuterated methane was added to the collision cell, prominent mass series of $[\text{PtCH}_4]^-$ and $[\text{PtCD}_4]^-$ anionic complexes appeared (see Figure IV.A.3.1B and IV.A.3.1C). The presence of strong $[\text{PtCH}_4]^-$ and $[\text{PtCD}_4]^-$ ion intensities shows that Pt^- interacts efficiently with methane under our experimental conditions. The much weaker intensity peaks on the low mass side of the $[\text{PtCH}_4]^-$ or $[\text{PtCD}_4]^-$ peaks are due to PtC^- , $[\text{PtCH}_2]^-$ or $[\text{PtCD}_2]^-$. The presence of reaction products, $[\text{PtCH}_2]^-$ and $[\text{PtCD}_2]^-$, is indicative of relatively weak dehydrogenation of methane by Pt^- . By contrast, dehydrogenation and the formation of platinum-carbene complexes were the dominant outcomes of reactions between neutral and cationic platinum atoms and methane.

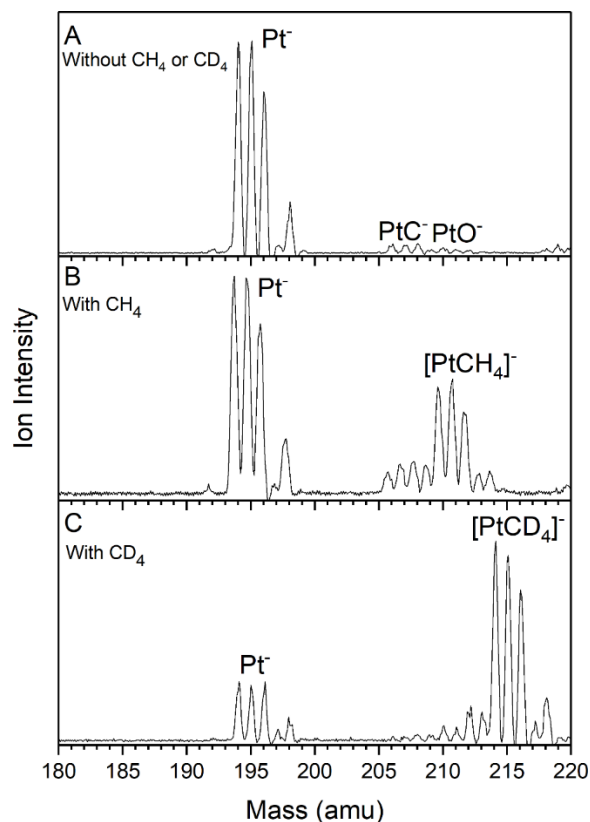


Figure IV.A.3.1 The mass spectra of Pt⁻ without methane (A), with methane (B), and with deuterated methane (C).

Figure IV.A.3.2 presents the anion photoelectron spectra of Pt⁻, [PtCH₄]⁻, and [PtCD₄]⁻, all measured with 3.496 eV photons. Figure IV.A.3.2A presents the photoelectron spectrum of Pt⁻. No transitions originating from excited-state Pt⁻ are observed, confirming that the interaction occurs between ground-state Pt⁻ and methane. The anion photoelectron spectra of [PtCH₄]⁻ and [PtCD₄]⁻ are presented in Figures IV.A.3.2B and IV.A.3.2C, respectively. Potentially, these spectra could be due to physisorbed complexes, chemisorbed species, or both. In the former case, Pt⁻ and methane would be weakly bound together to form Pt⁻(CH₄) and Pt⁻(CD₄). Typically, when an anion is solvated by another molecule, the anion photoelectron spectrum of the resulting physisorbed anionic complex closely resembles that of the anion alone, except for its spectral pattern having been shifted to higher electron binding energies (EBE) and its features slightly broadened. The photoelectron spectra of [PtCH₄]⁻ and [PtCD₄]⁻, however, bear no resemblance to the spectrum of Pt⁻, and in fact their lowest EBE peaks lie below the EBE of the lowest EBE peak in the spectrum of Pt⁻. There is no evidence that [PtCH₄]⁻ and [PtCD₄]⁻ are physisorbed complexes. In the latter (chemisorbed) case,

one or more C-H/C-D bonds would be broken, resulting in the formation of $H_n\text{-Pt-CH}_{4-n}^-$ and $D_n\text{-Pt-CD}_{4-n}^-$. Since $[\text{PtCH}_4]^-$ and $[\text{PtCD}_4]^-$ are not physisorbed complexes, the photoelectron spectra shown in Figures IV.A.3.2B and IV.A.3.2C imply that $[\text{PtCH}_4]^-$ and $[\text{PtCD}_4]^-$ are chemisorbed species. Thus, within each of these entities, methane activation has occurred; chemistry has taken place. The fact that Figures IV.A.3.2B and IV.A.3.2C have essentially identical features confirms that the chemisorption species, $[\text{PtCH}_4]^-$ and $[\text{PtCD}_4]^-$, have the same geometries and electronic structures. The anion photoelectron spectra of $[\text{PtCH}_4]^-$ and $[\text{PtCD}_4]^-$ in Figures IV.A.3.2B and IV.A.3.2C not only identify them as chemisorbed species, these photoelectron spectra also show that they possess extraordinarily rich vibronic structure. Also, the fact that $[\text{PtCH}_4]^-$ and $[\text{PtCD}_4]^-$ are chemisorbed and not just physisorbed species confirms that their strong presence in Figures IV.A.3.1B and IV.A.3.1C is the result of reactivity between Pt^- and methane, i.e., methane has been chemically activated.

The lowest EBE feature in the photoelectron spectra of both $[\text{PtCH}_4]^-$ and $[\text{PtCD}_4]^-$ has its maximum spectral intensity centered at $\text{EBE} = 1.93 \text{ eV}$. Thus, 1.93 eV is their common vertical detachment energy (VDE). The VDE is defined as the photodetachment transition energy at which the Franck-Condon overlap is at its maximum between the anion's vibrational wave function and that of its neutral counterpart with both in their ground electronic states. The other peaks in the spectra are due to vertical photodetachment transitions from the ground state anion to its neutral counterpart in its various excited electronic states, as noted above. All of the experimental, vertical photodetachment transition energies values, VPTE, are tabulated in Table IV.A.3.1.

Density functional theory (DFT) calculations were performed to find the most thermodynamically stable isomer of $[\text{PtCH}_4]^-$, which was expected to be the main contributor of the photoelectron spectrum. The energetics of the low-energy isomers were then refined at the CCSD(T) level of theory. The computational details are given in the Supporting Information (SI). Figure IV.A.3.3 presents the structures of different $[\text{PtCH}_4]^-$ isomers along with their relative energies. All energies are zero-point energy corrected. The global minimum (GM) of $[\text{PtCH}_4]^-$ features C_s symmetry and one activated C-H bond, i.e., H-Pt-CH_3^- . The physisorbed complex, $\text{Pt}^-(\text{CH}_4)$, is 0.62 eV above the GM. Two isomers corresponding to the breakage of two C-H bonds, the hydrogen-Pt-carbene complex $(\text{H}_2)\text{-Pt-CH}_2^-$ and the dihydrido-Pt-carbene complexes $\text{H}_2\text{-Pt-CH}_2^-$, are respectively 0.63 and 0.69 eV higher than the GM. Note that the H-H bond length (0.99 \AA) in $(\text{H}_2)\text{-Pt-CH}_2^-$ is significantly longer than that in the free H_2 molecule (0.74 \AA). Such elongation suggests H_2 activation due to back-donation from the Pt-CH_2^- moiety to the H_2 σ^* antibonding orbital

(Figure S2). This back-donation strengthens the interaction between H_2 and Pt-CH_2^- moieties and can lead to a high dehydrogenation energy.⁵⁴ The two structures that resulted from activating three and four C-H bonds have relative energies of 1.57 and 2.69 eV, respectively, making them unlikely to form under our experimental conditions. The isomers of $[\text{PtCD}_4]^-$ have the same structures as $[\text{PtCH}_4]^-$; their relative energies are provided in Figure IV.A.3.3 in parenthesis. To verify that the calculated GM of $[\text{PtCH}_4]^-$ describes the experimental spectrum, its VDE and VPTE values were computed at the multi-reference configuration interaction (MRCI+Q) level of theory and compared with the observed experimental values (Table IV.A.3.1). The calculated VDE and VPTE values accurately reproduce all the transitions observed in the photoelectron spectrum of $[\text{PtCH}_4]^-$, thus providing unambiguous validation of the GM structure, H-Pt-CH_3^- as the major reaction product. The GM structure may also be described as one in which a platinum atomic anion has inserted itself into one of methane's C-H bonds. Therefore, the combined results from mass spectroscopy, anion photoelectron spectroscopy, and *ab initio* quantum calculations have confirmed that atomic Pt^- readily activates methane, and that such activation process leads to H-Pt-CH_3^- with high selectivity.

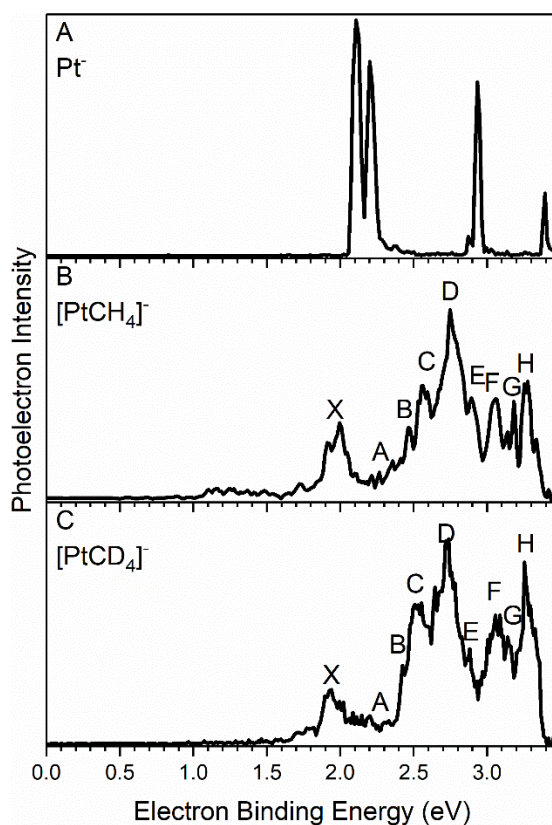


Figure IV.A.3.2 Photoelectron spectra of Pt^- (A), $[\text{PtCH}_4]^-$ (B), and $[\text{PtCD}_4]^-$ (C) all measured with 355

nm (3.496 eV) photons.

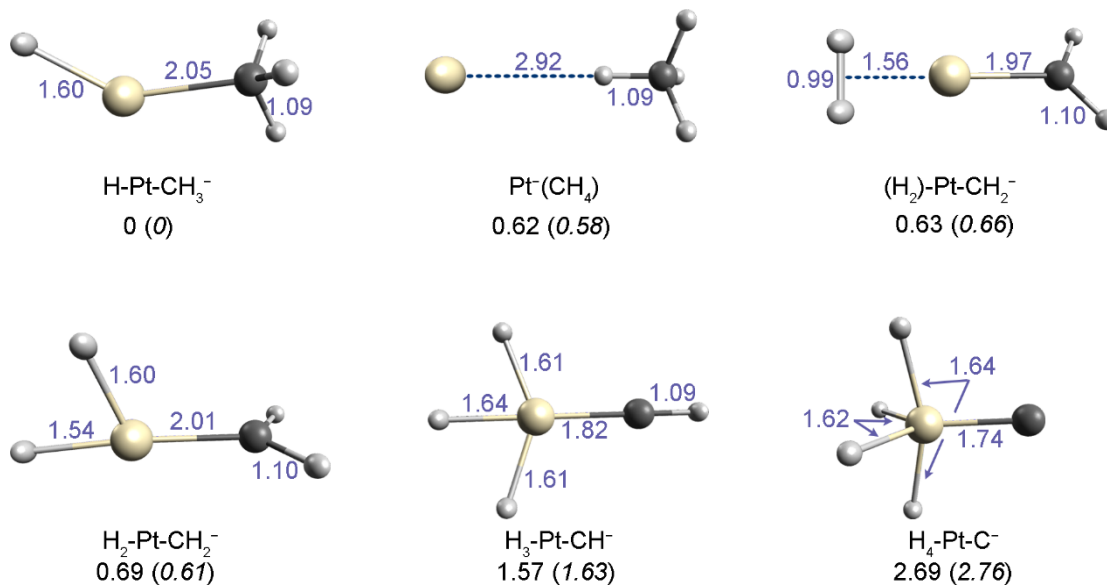


Figure IV.A.3.3 Optimized structures for [PtCH₄]⁻ and their relative energies compared to its GM. The relative energies of [PtCD₄]⁻ are shown in parenthesis. Energies are given in eV. Bond lengths are given in Å.

Table IV.A.3.1 Experimental and calculated VDE/VPTE values for the GM structure, H-Pt-CH₃⁻.

Peak	Final neutral state	VDE/VPTE (eV)	
		EXPT.	Theory ^a
X	¹ A'	1.98	1.95
A	³ A'	2.27	2.34
B	³ A''	2.46	2.52

C	$^1A'$	2.56	2.64
D	$^3A'$	2.75	2.73
E	$^3A''$	2.88	2.78
F	$^1A''$	3.07	2.99
G	$^1A'$	3.18	3.15
H	$^1A''$	3.28	3.49

^a MRCI+Q excitation energies + CCSD(T) electron affinity; see SI.

To provide mechanistic insight into the highly selective C-H bond cleavage and low dehydrogenation tendency observed when Pt^- activates methane, the reaction pathway was investigated with quantum calculations. The reaction pathway energy diagram is presented in Figure IV.A.3.4. The reaction occurs entirely on a doublet potential energy surface. Initially, CH_4 physisorbs onto Pt^- and forms the van der Waals complex **1**, $Pt(CH_4)$, with a binding energy of 0.08 eV. This solvation complex then passes over a transition state **TS1/2** in which one C-H bond is weakened and elongated. The activation barrier is 0.42 eV above local minima **1**. Such a moderate barrier can be overcome under the multi-collision conditions in the interaction cell, where translational energy is provided by collisions with the supersonically-expanded He carrier gas.¹² After overcoming **TS1/2**, Pt^- is inserted into the C-H bond and methane is activated, yielding the GM structure **2**, $H-Pt-CH_3^-$, the major activation product observed in these experiments. The activation complex would next need to overcome **TS2/3** with a barrier of 0.80 eV, in order for a second H atom to migrate from the methyl group to Pt to form **3**, $H_2-Pt-CH_2^-$. The subsequent H transfer over **TS3/5** to form $H_3-Pt-CH^-$ (structure **5**) is not favored, since it is quite endothermic with a barrier of 0.89 eV above the entrance channel. Instead, $H_2-Pt-CH_2^-$ (structure **3**) can pass over the negligible barrier of **TS3/4** to form $(H_2)-Pt-CH_2^-$ (structure **4**), where the two H atoms have combined to form a H_2 -like molecule attached to the Pt-carbene moiety. Its subsequent dissociation into H_2 and $PtCH_2^-$ is endothermic by 0.93 eV, which is consistent with the prediction⁵⁴ of a strong binding between H_2 and $Pt-CH_2^-$. The overall reaction of $Pt^- + CH_4 \rightarrow PtCH_2^- + H_2$ is thus endothermic by 0.86 eV. Note that this is significantly different from the cases of methane reacting with Pt^+ or Pt^0 , where dehydrogenation is exothermic or

only slightly endothermic.^{19,39} Our computed reaction pathway thus gives a quantitative rationale for the highly selective C-H bond cleavage and the low dehydrogenation tendency that occurs when Pt⁻ activates methane. It also explains the lack of an efficient hydrogen dissociation channel, and especially the fact that the GM, H-Pt-CH₃⁻ is trapped in a minimum on the potential energy surface, resulting in its highly selective formation.

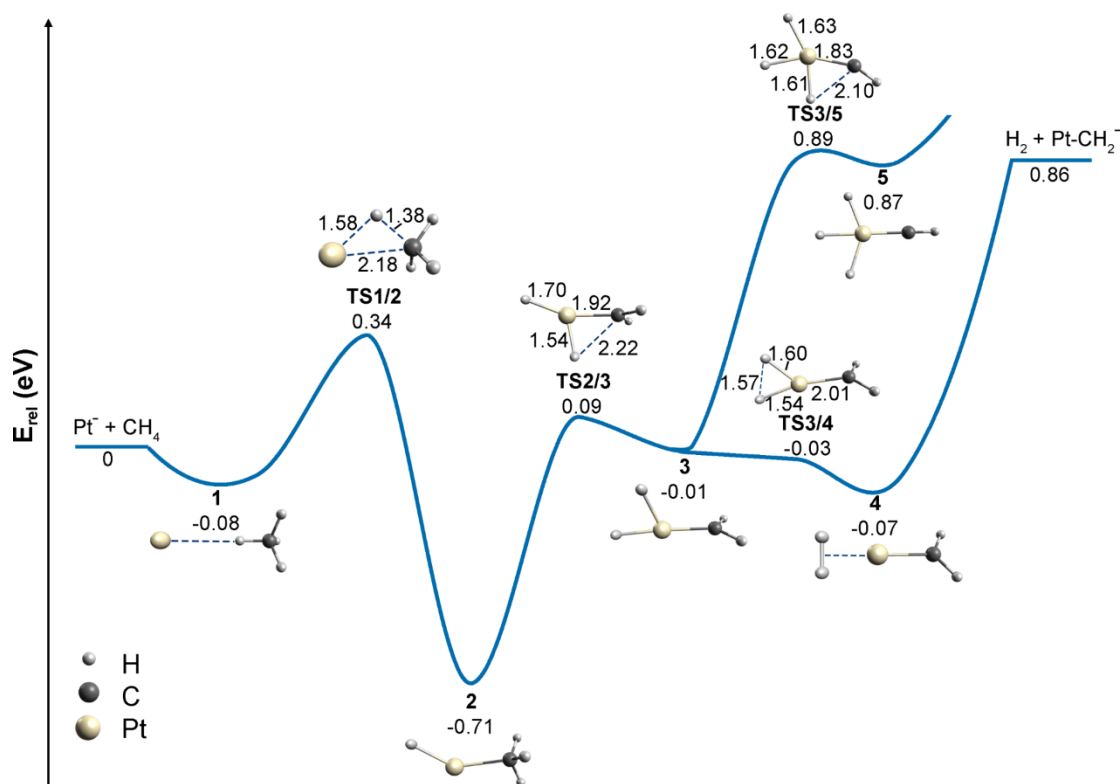


Figure IV.A.3.4 Calculated reaction pathway for methane activation by Pt⁻. Zero-point energy corrected energies are given in eV. Bond lengths of the transition states are given in Å.

The ground state of Pt⁻, ²D(6s²5d⁹), has one unpaired electron, allowing the formation of only one single σ-bond. In order for Pt⁻ to form the GM H-Pt-CH₃⁻ structure, one electron is promoted from the 5d to the 6p orbital to generate the ⁴G(6s²5d⁸6p¹) excited state with three available unpaired electrons. Two of them can couple with the unpaired electrons of the H and CH₃ fragments to form the two Pt-H and Pt-C σ-bonds. The formations of these two σ-bonds stabilizes the H(²S)/Pt(⁴G)/CH₃(²A₂) interaction, resulting in the formation of the GM. The remaining one electron

occupies a 5d-6p hybrid orbital that couples with the CH₄ anti-bonding orbital during the activation process (Figure IV.A.3.5), fulfilling the accepted donor-acceptor model for σ -bond activation.¹⁹

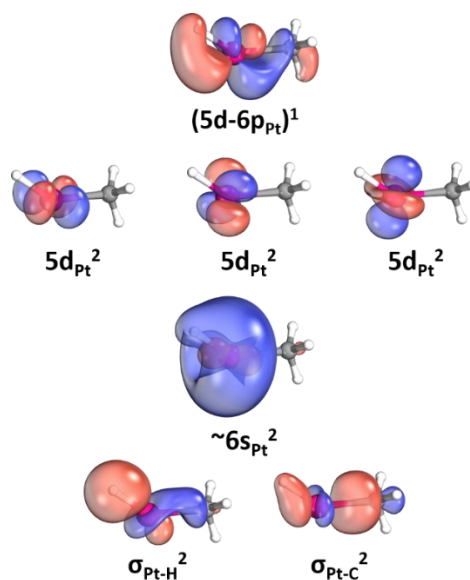


Figure IV.A.3.5 Selected molecular orbitals of the GM H-Pt-CH₃[−] depicting the Pt-C and Pt-H bonds and the nearly intact valence Pt orbitals.

To summarize, we have demonstrated that Pt[−] is able to selectively activate only one C-H bond in methane, representing the first example of methane activation by atomic anions. Mass spectrometric analysis of the reaction products between Pt[−] and CH₄ shows the preferred generation of [PtCH₄][−] and a low tendency toward dehydrogenation. [PtCH₄][−] is confirmed as H-Pt-CH₃[−] by anion photoelectron spectroscopy and quantum chemical calculation, suggesting a selective rupture of just one C-H bond. The single unpaired electrons in ground-state Pt[−] necessitates electron promotion to the 6p orbital in order to facilitate the reaction over a moderate barrier. The demonstration of methane activation by atomic anions has opened a new route for designing novel catalysts for C-H bond functionalization.

References

1. S. J. Blanksby, G.B. Ellison, *Acc. Chem. Res.* **2003**, 36, 255–263.
2. Q. Zhu, S. L. Wegener, C. Xie, O. Uche, M. Neurock, T. J. Marks, *Nat. Chem.* **2013**, 5, 104–109.
3. J. J. Spivey, G. Hutchings, *Chem. Soc. Rev.* **2014**, 43, 792–803.
4. H. Schwarz, *Angew. Chem. Int. Ed.* **2011**, 50, 10096–10115.
5. D. K. Böhme, H. Schwarz, *Angew. Chem. Int. Ed.* **2005**, 44, 2336–2354.
6. D. Schröder, H. Schwarz, *Proc. Natl. Acad. Sci.* **2008**, 105, 18114–18119.

7. J. Roithova, D. Schröder, *Chem. Rev.* **2010**, *110*, 1170-1211.
8. H. Schwarz, *Isr. J. Chem.* **2014**, *54*, 1413-1431.
9. X. L. Ding, X.N. Wu, Y. X. Zhao, S. G. He, *Acc. Chem. Res.* **2012**, *45*, 382-390.
10. Z. Luo, A. W. Castleman Jr., S. N. Khanna, *Chem. Rev.* **2016**, *116*, 14456-14492.
11. S. Zhou, J. Li, M. Schlangen, H. Schwarz, *Acc. Chem. Res.* **2016**, *49*, 494-502.
12. S. M. Lang, T. M. Bernhardt, V. Chernyy, J. M. Bakker, R. N. Barnett, U. Landman, *Angew. Chem. Int. Ed.* **2017**, *56*, 13406-13410.
13. H. Schwarz, S. Shaik, J. Li, *J. Am. Chem. Soc.* **2017**, *139*, 17201-17212.
14. Y. Zhao, Z. Li, Y. Yang, S. G. He, *Acc. Chem. Res.* **2018**, *51*, 2603-2610.
15. L. Yue, S. Zhou, X. Sun, M. Schlangen, H. Schwarz, *Angew. Chem. Int. Ed.* **2018**, *130*, 3306-3310.
16. X. Sun, S. Zhou, L. Yue, M. Schlangen, H. Schwarz, *Angew. Chem. Int. Ed.* **2018**, *130*, 6039-6043.
17. L. F. Halle, P. B. Armentrout, J. L. Beauchamp, *J. Am. Chem. Soc.* **1981**, *103*, 962-963.
18. K. K. Irikura, J. L. Beauchamp, *J. Am. Chem. Soc.* **1989**, *111*, 75-85.
19. X. Zhang, R. Liyanage, P. B. Armentrout, *J. Am. Chem. Soc.* **2001**, *123*, 5563-5575.
20. M. M. Armentrout, F. Li, P. B. Armentrout, *J. Phys. Chem. A*, **2004**, *108*, 9660-9672.
21. P. B. Armentrout, *J. Phys. Chem. A* **2006**, *110*, 8327-8338.
22. P. B. Armentrout, S. Shin, R. Liyanage, *J. Phys. Chem. A* **2006**, *110*, 1242-1260.
23. P. B. Armentrout, L. Parke, C. Hinton, M. Citir, *ChemPlusChem* **2013**, *78*, 1157-1173.
24. U. Achatz, C. Berg, S. Joos, B. S. Fox, M. K. Beyer, G. Niedner-Schatteburg, V. E. Bondybey, *Chem. Phys. Lett.* **2000**, *320*, 53-58.
25. C. Adlhart, E. Uggerud, *Chem. Commun.* **2006**, *24*, 2581-2582.
26. G. Kummerlöwe, I. Balteanu, Z. Sun, O. P. Balaj, V. E. Bondybey, M. K. Beyer, *Int. J. Mass Spectrom.* **2006**, *254*, 183-188.
27. C. Adlhart, E. Uggerud, *Chem. Eur. J.* **2007**, *13*, 6883-6890.
28. D. J. Harding, C. Kerpel, G. Meijer, A. Fielicke, *Angew. Chem. Int. Ed.* **2012**, *51*, 817-819.
29. G. Albert, C. Berg, M. Beyer, U. Achatz, S. Joos, G. Niedner-Schatteburg, V. E. Bondybey, *Chem. Phys. Lett.* **1997**, *268*, 235-241.
30. M. Citir, F. Liu, P. B. Armentrout, *J. Chem. Phys.* **2009**, *130*, 054309.
31. S. Zhou, J. Li, M. Schlangen, H. Schwarz *Angew. Chem.*, *129*, 424 - 428 (2017)
32. S. M. Lang, T. M. Bernhardt, R. N. Barnett, U. Landman, *Angew. Chem. Int. Ed.* **2010**, *49*, 980-983.
33. S. Feyel, J. Döbler, D. Schröder, J. Sauer, H. Schwarz, *Angew. Chem. Int. Ed.* **2006**, *45*, 4681-4685.
34. X. N. Wu, X. N. Li, X. L. Ding, S. G. He, *Angew. Chem. Int. Ed.* **2013**, *52*, 2444-2448.
35. Y. X. Zhao, X. N. Wu, J. B. Ma, S. G. He, X. L. Ding, *Phys. Chem. Chem. Phys.* **2011**, *13*, 1925-1938.
36. G. E. Johnson, R. Mitrić, M. Nössler, E. C. Tyo, V. Bonačić-Koutecký, A. W. Castleman Jr., *J. Am. Chem. Soc.* **2009**, *131*, 5460-5470.
37. Y. X. Zhao, Z. Y. Li, Z. Yuan, X. Li, and S. G. He. *Angew. Chem. Int. Ed.* **2014**, *53*, 9482-9486.
38. Z. Y. Li, L. Hu, Q. Y. Liu, C. G. Ning, H. Chen, S. G. He, J. Yao, *Chem. Eur. J.* **2015**, *21*, 17748-17756.
39. H. F. Li, Z. Y. Li, Q. Y. Liu, X. N. Li, Y. X. Zhao, S. G. He, *J. Phys. Chem. Lett.* **2015**, *6*, 2287-2291.
40. J. H. Meng, X. J. Deng, Z. Y. Li, S. G. He, W. J. Zheng, *Chem. Eur. J.* **2014**, *20*, 5580-5583.
41. Q. Y. Liu, J. B. Ma, Z. Y. Li, C. Zhao, C. G. Ning, H. Chen S. G. He, *Angew. Chem.* **2016**, *128*, 5854-5858.
42. Y. X. Zhao, X. N. Li, Z. Yuan, Q. Y. Liu, Q. Shi S. G. He, *Chem. Sci.* **2016**, *7*, 4730-4735.
43. D. J. Trevor, D. M. Cox, A. Kaldor, *J. Am. Chem. Soc.* **1990**, *112*, 3742-3749.
44. C. Heinemann, R. Wesendrup, H. Schwarz, *Chem. Phys. Lett.* **1995**, *239*, 75-83.
45. J. J. Carroll, J. C. Weisshaar, P. E. M. Siegbahn, C. A. M. Wittborn, M. R. A. Blomberg, *J. Phys. Chem.* **1995**, *99*, 14388-14396.
46. M. L. Campbell, *J. Chem. Soc. Faraday Trans.* **1998**, *94*, 353-358.
47. K. Koszinowski, D. Schroider, H. Schwarz, *J. Phys. Chem. A* **2003**, *107*, 4999-5006.
48. H. G. Cho, L. Andrews, *J. Phys. Chem. A* **2008**, *112*, 12293-12295.
49. M. Perera, R. B. Metz, O. Kostko, M. Ahmed, *Angew. Chem. Int. Ed.* **2013**, *52*, 888-891.
50. G. Liu, E. Miliordos, S. M. Ciborowski, M. Tschurl, U. Boesl, U. Heiz, X. Zhang, S. S. Xantheas, and K. H. Bowen. *J. Chem. Phys.* **2018**, *149*, 221101.
51. X. Zhang, G. Liu, K. H. Meiwe-Broer, G. Ganteför, K. H. Bowen, *Angew. Chem. Int. Ed.* **2016**, *55*, 9644-9647.
52. G. Liu, S. Ciborowski, K. Bowen, *J. Phys. Chem. A*, **2017**, *121*, 5817-5822.
53. G. Liu, S. M. Ciborowski, Z. Zhu, K. H. Bowen, *Int. J. Mass Spectrom.* **2019**, *435*, 114-117.
54. X. Zhang, P. Robinson, G. Gantefoer, A. Alexandrova, and K. H. Bowen, *J. Chem. Phys.* **2015**, *143*, 094307.

IV.A.4. Simultaneous Functionalization of Methane and Carbon Dioxide Mediated by Single Platinum Atomic Anions

Reprinted (adapted) with permission from *J. Am. Chem. Soc.* **142**, 21556-21561, (2020) Copyright 2020 American Chemical Society.

Gaoxiang Liu, Isuru R. Ariyaratna, Sandra M. Ciborowski, Zhaoguo Zhu, Evangelos Miliordos*, Kit H. Bowen*

Abstract

Mass spectrometric analysis of the anionic products of interaction among Pt^- , methane, and carbon dioxide shows that the methane activation complex, $\text{H}_3\text{C-Pt-H}^-$, reacts with CO_2 to form $[\text{H}_3\text{C-Pt-H}(\text{CO}_2)]^-$. Two hydrogenation and one C-C bond coupling products are identified as isomers of $[\text{H}_3\text{C-Pt-H}(\text{CO}_2)]^-$ by a synergy between anion photoelectron spectroscopy and quantum chemical calculations. Mechanistic study reveals that both CH_4 and CO_2 are activated by the anionic Pt atom, and that the successive depletion of the negative charge on Pt drives the CO_2 insertion into the Pt-H and Pt-C bonds of $\text{H}_3\text{C-Pt-H}^-$. This study represents the first example of the simultaneous functionalization of CH_4 and CO_2 mediated by single atomic anions.

Introduction

Transforming the two abundant C_1 feedstocks, methane and carbon dioxide, into functional molecules is of great interest for environmental and economic reasons. A long-sought goal has been a mutual transformation in which methane and carbon dioxide directly functionalize each other so they are simultaneously converted.¹ For example, -H and - CH_3 groups, the active species from breaking one C-H bond of methane, may respectively couple with CO_2 to form higher value products. This process, however, is rather challenging due to the high stability of both methane and carbon dioxide.² The end product of methane and carbon dioxide conversion is usually the generation of syngas by methane dry reforming, but this indirect route consumes large amounts of energy.³ Several catalysts, including metal-exchanged zeolites,⁴ Cu/Co metal oxides,⁵ and oxide-supported noble metals,⁶ have been explored for the direct mutual functionalization of methane and carbon dioxide. Nevertheless, these catalytic processes require high temperature and suffer from poor yield and selectivity. The major challenge roots in the demand for catalysts to simultaneously tackle methane activation, which is oxidative, and carbon dioxide conversion, which is reductive. Recent gas-phase studies have shown that small clusters such as CuB^+ and RhVO_3^- mediate the direct conversion of methane with carbon dioxide.⁷ Atoms in these clusters take different roles in interacting with methane or carbon dioxide, while they work cooperatively as a whole reaction site to finish the reactions. Here, we aim to further reduce

the size of the reaction site, addressing the mutual functionalization of methane and carbon dioxide mediated by single atomic anions.

We had originally been inspired by a lineage of our recent studies. In one study, we show that platinum atomic anions, Pt^- , selectively activate one C-H bond in methane to form a $\text{H}_3\text{C-Pt-H}^-$ complex. The methyl and the hydro groups are expected to be reactive to other small molecules, establishing the basis for further methane functionalization.⁸ In other studies related to CO_2 activation and hydrogenation, we demonstrate that negatively charged metal atoms, including Pt^- , activate CO_2 ,^{9,10} and that metal hydrides, especially platinum hydrides, hydrogenate CO_2 into formate.^{11,12} Based on these findings, we conceive that Pt^- is active in both the oxidative methane activation and the reductive CO_2 functionalization, and that by coupling such reactivities, Pt^- can mediate the mutual transformation of methane and carbon dioxide. In this study, we show that Pt^- breaks a methane molecule into -H and - CH_3 groups, and couples the two groups respectively with CO_2 to form formate and acetate adducts. This work represents the first example of the mutual functionalization of methane and carbon dioxide mediated by single atoms.

Results and Discussion

The mutual functionalization of methane and CO_2 starts with the selective activation of one C-H bond in methane by single platinum anions. Methane activation occurred in a laser vaporization source, where the laser ablated Pt^- reacted with methane or deuterated methane introduced into the vaporization chamber. The activation products, PtCH_4^- and PtCD_4^- , were respectively characterized by anion photoelectron spectroscopy and confirmed as $\text{H}_3\text{C-Pt-H}^-$ and $\text{D}_3\text{C-Pt-D}^-$ (Figure S1, Ref. 8). These activation products then reacted with CO_2 added into a reaction cell downstream. The resultant mass spectra show prominent mass series of $[\text{H}_3\text{C-Pt-H}(\text{CO}_2)]^-$ and $[\text{D}_3\text{C-Pt-D}(\text{CO}_2)]^-$ (Figure IV.A.4.1). Their isotopic patterns deviate from that of Pt due to mass overlaps with PtC^- or PtO^- . The formation of PtC^- and PtO^- was likely due to trace amounts of carbon and oxygen present on the platinum metal surface, or due to the carbon and oxygen existed in the laser vaporization housing which were released when interacting with the plasma. The strong ion intensities of $[\text{H}_3\text{C-Pt-H}(\text{CO}_2)]^-$ and $[\text{D}_3\text{C-Pt-D}(\text{CO}_2)]^-$ suggest an efficient interaction between CO_2 and the methane activation complexes.

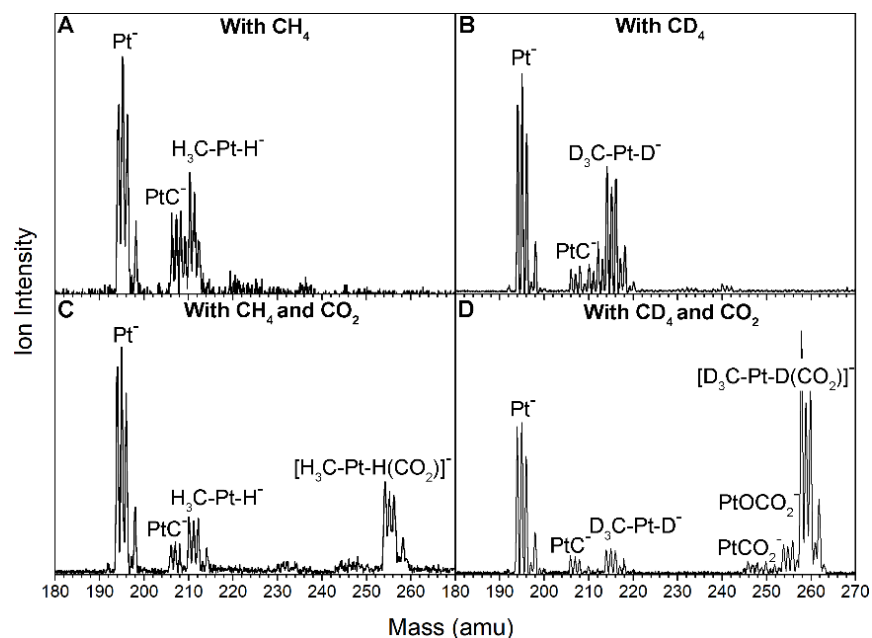


Figure IV.A.4.1 The mass spectra of Pt^- with methane (A), with deuterated methane (B), with methane and carbon dioxide (C), and with deuterated methane and carbon dioxide (D).

We then applied anion photoelectron spectroscopy to characterize $[\text{H}_3\text{C-Pt-H}(\text{CO}_2)]^-$ and $[\text{D}_3\text{C-Pt-D}(\text{CO}_2)]^-$ (Figure IV.A.4.2). The photoelectron spectra were taken at all but the lowest-mass isotopes of the interested anions, because the lowest-mass peaks may overlap with peaks of $\text{PtC}(\text{CO}_2)^-$ or $\text{PtO}(\text{CO}_2)^-$. No significant spectroscopic difference was observed among the spectra taken for the same species. Here we present a representative spectrum respectively for $[\text{H}_3\text{C-Pt-H}(\text{CO}_2)]^-$ and $[\text{D}_3\text{C-Pt-D}(\text{CO}_2)]^-$. The fact that Figure IV.A.4.2A and IV.A.4.2B have essentially identical features confirms that $[\text{H}_3\text{C-Pt-H}(\text{CO}_2)]^-$ and $[\text{D}_3\text{C-Pt-D}(\text{CO}_2)]^-$ have the same geometries and electronic structures. By examining the electron binding energies (EBE) of the spectral features, we obtain the vertical detachment energies, VDE, of these reaction products. The VDE is defined as the photodetachment transition energy at which the Franck-Condon overlap is at its maximum between the anion's vibrational wave function and that of its neutral counterpart. The feature from 2.4 to 3.0 eV is broad with its peak less discernable, suggesting contributions from multiple photodetachment transitions. The peaks at higher EBE yields VDE values of 3.41, 3.90, and 4.18 eV for $[\text{H}_3\text{C-Pt-H}(\text{CO}_2)]^-$ and $[\text{D}_3\text{C-Pt-D}(\text{CO}_2)]^-$.

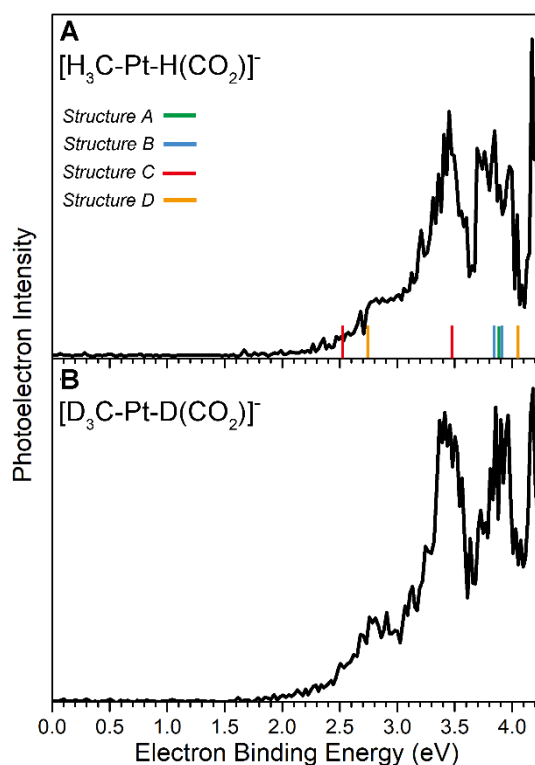


Figure IV.A.4.2 Photoelectron spectra of $[\text{H}_3\text{C-Pt-H(CO}_2\text{)}]^-$ (A) and $[\text{D}_3\text{C-Pt-D(CO}_2\text{)}]^-$ (B), both measured with 266 nm (4.661 eV) photons. The stick spectrum overlay represents the calculated VDEs of different $[\text{H}_3\text{C-Pt-H(CO}_2\text{)}]^-$ structures in Figure IV.A.4.3.

Density functional theory (DFT) calculations were performed to find $[\text{H}_3\text{C-Pt-H(CO}_2\text{)}]^-$ isomers that are possibly prepared via the reaction between $\text{H}_3\text{C-Pt-H}^-$ and CO_2 . The energetics of these isomers were then refined at the CCSD(T) level of theory. The optimized geometries for these reaction products are presented in Figure IV.A.4.3 along with their relative energies. All energies are zero-point corrected. The structures of $\text{H}_3\text{C-Pt-H}^-$ and CO_2 are also provided for reference. All $[\text{H}_3\text{C-Pt-H(CO}_2\text{)}]^-$ structures have a doublet electronic state. The global minimum of $[\text{H}_3\text{C-Pt-H(CO}_2\text{)}]^-$, **A**, features a hydro and an acetate groups respectively attached to the Pt atom, yielding a $\text{H}_3\text{CCOO-Pt-H}^-$ structure. In this structure, CO_2 inserts into the Pt-C bond of $\text{H}_3\text{C-Pt-H}^-$, and couples its carbon atom with the methyl group to form an acetate. In structure **B**, which is only 0.06 eV higher in energy than the global minimum, CO_2 wedges into the Pt-H bond of $\text{H}_3\text{C-Pt-H}^-$ to form a $\text{H}_3\text{C-Pt-OCOH}^-$, that is, CO_2 is hydrogenated to formate. In structure **C**, CO_2 is also hydrogenated, but the H atom is attached to the O atom, forming a $\text{H}_3\text{C-Pt-COOH}^-$ structure. Structure **D** is obtained by the CO_2 chemisorption onto the Pt atom in $\text{H}_3\text{C-Pt-H}^-$. In structure **D**, CO_2 is significantly bent, suggesting that CO_2 is activated on the Pt site.

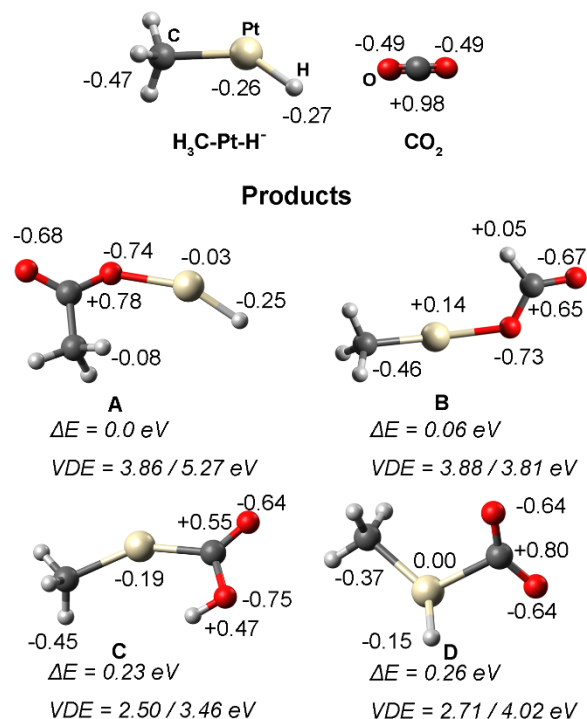


Figure IV.A.4.3 Optimized structures for $\text{H}_3\text{C-Pt-H}^-$, CO_2 , and $[\text{H}_3\text{C-Pt-H}(\text{CO}_2)]^-$. The relative energies of $[\text{H}_3\text{C-Pt-H}(\text{CO}_2)]^-$ and their calculated VDEs to singlet and triplet neutrals are shown below each structure. The Natural Bond Orbital (NBO) charge on each atom is also provided. The charge besides the methyl groups shows the total charge on $-\text{CH}_3$.

A distinct advantage for gas-phase experiments is combining experimental characterization and state-of-the-art quantum chemistry calculations to identify reaction intermediates and products, laying the foundation for a mechanistic insight into the reactions at a molecular level.¹³ To verify these calculated structures, we calculated their VDEs at the CCSD(T) level of theory and compared them with the experimental values (Figures IV.A.4.2 and IV.A.4.3). The EBE transition from 2.5 to 2.9 eV results from the photodetachment transitions of structures **C** and **D**, the calculated VDEs of which to their singlet neutrals are 2.50 and 2.71 eV, respectively. The EBE feature peaked at 3.41 eV matches the calculated VDE of structure **C** to its triplet neutral counterpart, further confirming structure **C** as one of the reaction products. Meanwhile, the EBE peak at 4.15 eV is attributed to the photodetachment transition of structure **D** to its triplet neutral. Therefore, structure **D** is also confirmed as a reaction product. Calculations on the excited states of structures **C** and **D** show that they have no transitions with photodetachment energies around 3.9 eV (Table S1), suggesting that the 3.90 eV feature is due to structures **A** and **B**. Because structures **A** and **B** both have

calculated VDEs that match the spectroscopic feature at 3.87 eV, at this point we only conclude that at least one of them exists in the reaction products.

We investigated the reaction pathway using quantum calculations to resolve the uncertainty in identifying all reaction products and to provide mechanistic insight into the synergetic methane and CO₂ functionalization (Figure IV.A.4.4). The reaction starts with the selective activation of one C-H bond in methane by Pt⁺, which has been extensively studied in our previous work.⁸ This step includes a barrier of 0.34 eV and is exothermic by 0.71 eV. The resultant H₃C-Pt-H⁻ interacts with CO₂ and binds it by forming a Pt-C bond (structure **D**). Concurrently, a total of 0.48 |e| negative charge is transferred to CO₂. Such negative charge transfer is the first step of CO₂ functionalization. Therefore, both CH₄ and CO₂ are activated on the negatively charged Pt atom. After being activated, CO₂ can insert into the Pt-C or the Pt-H bond via three different routes for further functionalization. In the route with the lowest activation barrier, CO₂ interacts with the Pt-H bond of H₃C-Pt-H⁻. The H atom transfers to the C atom while the Pt atom binds the O atom, leading to the formation of H₃C-Pt-OCOH⁻ that contains a formate moiety (Structure **B**). The transition state, **TS1**, is located 0.27 eV below H₃C-Pt-H⁻ and CO₂, which is the entrance channel for the CO₂ functionalization step under our experimental conditions¹⁴. Therefore, H₃C-Pt-H⁻ readily hydrogenates CO₂ into the formate adduct, **B**, without apparent activation barriers. CO₂ can also insert into the Pt-C bond of H₃C-Pt-H⁻ via **TS2**, where the C atom in CO₂ bonds with the C atom in the -CH₃ group. The activation barrier is 0.27 eV when compared to the energy of H₃C-Pt-H⁻ and CO₂. This route leads to H₃CCOO-Pt-H⁻ (structure **A**), a C-C coupling product featuring an acetate group. In addition,

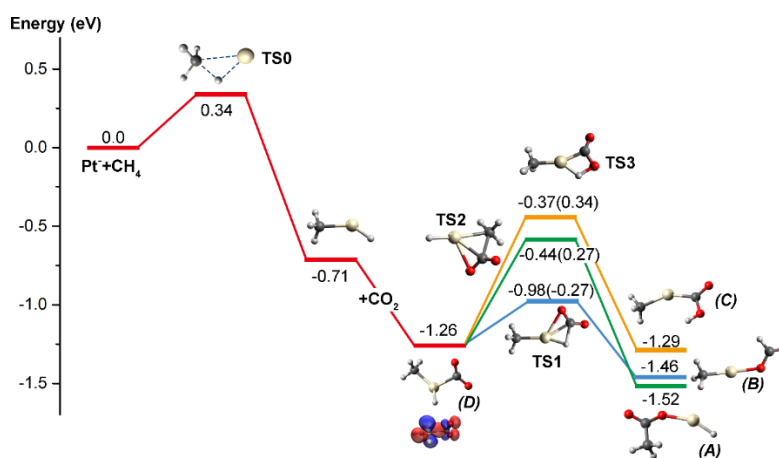


Figure IV.A.4.4 Profile of the tandem reaction between Pt⁺, CH₄, and CO₂. Zero-point corrected energies are given in eV. The numbers in parentheses indicate the activation barriers compared to the entrance channel of CO₂

functionalization.¹⁴ The letters in parentheses correspond to their labels in Figure IV.A.4.3. The potential energy surface is referenced to the total energy of isolated Pt⁻, CH₄, and CO₂.

the H atom of the Pt-H in H₃C-Pt-H⁻ can transfer to the O atom, forming another CO₂ hydrogenation product (structure **C**). The activation barrier for this route is 0.34 eV. All these barriers are accessible under our experimental conditions where excess energy is provided via multicollisions with the fastest He molecules in the Maxwell–Boltzmann distribution.¹⁵ As mentioned earlier, the spectroscopic evidence alone can confirm the existence of structures **C** and **D** as reaction products, but not structures **A** and **B**. The calculated reaction pathway helps resolve this uncertainty: both structures **A** and **B** are kinetically easier to form and thermodynamically more stable than structure **C**. Since structure **C** has been confirmed, structure **A** and **B** should also exist as reaction products. Therefore, the combined experimental and computational evidence confirms that both CO₂ hydrogenation and C-C bond coupling occur during the reaction.

When Pt⁻ activates CH₄, it is electronically excited *in situ* to the ⁴G(6s²5d⁸6p¹) state to fulfill the donor-acceptor model for σ -bond activation.^{8,13d} The negative charge on Pt reduces to -0.26|e| after distributing to the -H and the -CH₃ groups (Figure IV.A.4.3). The resultant H₃C-Pt-H⁻ activates CO₂ by donating one of the 5d electron pairs on Pt to the anti-bonding orbital of CO₂. Though a Pt-O bond is usually stronger than a Pt-C bond,¹¹ when Pt activates CO₂, the Pt/O interaction is kinetically less favorable than the Pt/C interaction due to the electrostatic repulsion between the negatively charged Pt and O atoms. When CO₂ activation is complete, all the negative charge on Pt drains to CO₂ and Pt becomes practically neutral (Figure IV.A.4.3, Structure **D**). This charge redistribution largely reduces the electrostatic repulsion between Pt and O and thus the kinetic barrier for CO₂ to be inserted into the Pt-H or the Pt-C bonds. As a result, CO₂ insertion occurs to form the more stable R-Pt-O-R' structures (Structures **A** and **B**), completing the simultaneous functionalization of CH₄ and CO₂.

Besides the reaction path we showed in this work, we also investigated other paths for the tandem reactions among Pt⁻, CH₄, and CO₂. Instead of activating CH₄ first, it is also possible to first interact Pt⁻ with CO₂ in the laser vaporization chamber, then react the prepared PtCO₂^{-8b} with CH₄ in the reaction cell. Computationally, this route is plausible (Figure S2). Experimentally, however, no spectroscopic evidence was found for CO₂ hydrogenation or C-C bond coupling products: only structure **D** and a PtCO₂⁻(CH₄) physisorbed complex were confirmed (Figure S3). This suggests that in the reaction cell, PtCO₂⁻ overcomes the first barrier to activate CH₄, but not the second one for CO₂ insertion. We think this is because the short reaction time provided by our reaction cell, which is usually on the order

of microseconds, is not enough for reactants to overcome multiple activation barriers. This route, however, may be feasible under other reaction environments such as in an ion trap. Reaction paths that involve breaking the C=O bond in CO₂ or more than one C-H bonds in CH₄ are impossible under our experimental conditions due to high kinetic barriers or low thermodynamic stability of the reaction products (Figure S2 and S4).

Conclusions

To summarize, we demonstrate for the first time that the single atomic Pt⁻ can mediate the mutual functionalization between CH₄ and CO₂. The combined mass spectrometry, photoelectron spectroscopy, and quantum chemical calculation study reveals that the CH₄ activation complex, H₃C-Pt-H⁻, interacts with CO₂ to form two hydrogenation and one C-C bond coupling products. Specifically, Pt⁻ breaks CH₄ into -H and -CH₃, activates CO₂, and couples the activated CO₂ respectively with -H and -CH₃ to form formate and acetate products. Mechanistic analysis confirms the charge redistribution as the driving force for the CO₂ insertion step. The demonstration of the simultaneous CH₄ and CO₂ functionalization by atomic anions sheds light on new routes for designing novel catalysts to utilize these two abundant C1 feedstocks.

Methods

Experimental Methods

Anion photoelectron spectroscopy is conducted by crossing a beam of mass-selected negative ions with a fixed-frequency photon beam and energy-analyzing the resultant photodetached electrons. The photodetachment process is governed by the energy-conserving relationship: $h\nu = \text{EBE} + \text{EKE}$, where $h\nu$ is the photon energy, EBE is the electron binding energy, and EKE is the electron kinetic energy. Our apparatus consists of a laser vaporization cluster anion source with an attached ligation cell, a time-of-flight mass spectrometer, a Nd:YAG photodetachment laser (operating at 266 nm), and a magnetic bottle electron energy analyzer with a resolution is ~ 35 meV at 1 eV EKE.¹⁶ Photoelectron spectra were calibrated against the well-known atomic transitions of atomic Cu⁻. The tandem reaction among Pt⁻, methane (CH₄, CD₄), and CO₂ was studied using a laser vaporization/reaction cell arrangement.¹⁷ Atomic platinum anions were generated by laser vaporization of a pure platinum foil wrapped around an aluminum rod. The resultant plasma was cooled with 5% CH₄ or CD₄ helium gas mixture delivered by a pulsed valve, having a backing pressure of 60 psig. The resulting H₃C-Pt-H⁻ or D₃C-Pt-D⁻ then traveled through a reaction cell (4-mm diameter, 5-cm length), where it encountered CO₂. CO₂ was introduced into the reaction cell by a second pulsed valve, backed by 15 psig of

pure CO₂ gas. The resulting [H₃C-Pt-H(CO)₂]⁻ and [D₃C-Pt-D(CO)₂]⁻ anionic clusters were then mass-analyzed and mass-selected by the time-of-flight mass spectrometer and their photoelectron spectra measured.

Computational Methods

All Density functional theory (DFT) calculations were performed with Gaussian 16 package.¹⁸ Geometry optimizations were carried out with the B3LYP functional and the aug-cc-pVTZ (H, C, O)^{19,20} || aug-cc-pVTZ-PP (Pt)²¹ basis sets. Stuttgart relativistic pseudopotential was employed to replace sixty inner electrons (1s²2s²2p⁶3s²3p⁶3d¹⁰4s²4p⁶4d¹⁰4f¹⁴) of the Pt atom.²¹ All geometry optimization calculations were followed by frequency calculations to verify that intermediate structures are real minima in the potential energy surface by confirming that their frequencies are real. Transition states that connect these intermediates bear only one imaginary frequency.

More accurate results were obtained by performing single point CCSD(T)²² calculations using the DFT/B3LYP optimized structures. The same basis set was applied. Zero-point energies collected from DFT/B3LYP calculations were added to the CCSD(T) energies. MOLPRO 2015²³ was used to perform all CCSD(T) calculations.

References

1. Havran, V.; Dudukovic, M. P.; Lo, C. S., Conversion of methane and carbon dioxide to higher value products. *Ind. Eng. Chem. Res.* **2011**, *50* (12), 7089-7100.
2. Gunsalus, N. J.; Koppaka, A.; Park, S. H.; Bischof, S. M.; Hashiguchi, B. G.; Periana, R. A., Homogeneous functionalization of methane. *Chem. Rev.* **2017**, *117* (13), 8521-8573.
3. (a) Shi, L.; Yang, G.; Tao, K.; Yoneyama, Y.; Tan, Y.; Tsubaki, N., An introduction of CO₂ conversion by dry reforming with methane and new route of low-temperature methanol synthesis. *Acc. Chem. Res.* **2013**, *46* (8), 1838-1847; (b) Pakhare, D.; Spivey, J., A review of dry (CO₂) reforming of methane over noble metal catalysts. *Chem. Soc. Rev.* **2014**, *43* (22), 7813-7837.
4. (a) Wang, X.; Qi, G.; Xu, J.; Li, B.; Wang, C.; Deng, F., NMR-spectroscopic evidence of intermediate-dependent pathways for acetic acid formation from methane and carbon monoxide over a ZnZSM-5 zeolite catalyst. *Angew. Chem. Int. Ed.* **2012**, *51* (16), 3850-3853; (b) Wu, J.-F.; Yu, S.-M.; Wang, W. D.; Fan, Y.-X.; Bai, S.; Zhang, C.-W.; Gao, Q.; Huang, J.; Wang, W., Mechanistic insight into the formation of acetic acid from the direct conversion of methane and carbon dioxide on zinc-modified H-ZSM-5 zeolite. *J. Am. Chem. Soc.* **2013**, *135* (36), 13567-13573; (c) Rabie, A. M.; Betiha, M. A.; Park, S.-E., Direct synthesis of acetic acid by simultaneous co-activation of methane and CO₂ over Cu-exchanged ZSM-5 catalysts. *Appl. Catal. B-Environ.* **2017**, *215*, 50-59.
5. Huang, W.; Xie, K.-C.; Wang, J.-P.; Gao, Z.-H.; Yin, L.-H.; Zhu, Q.-M., Possibility of direct conversion of CH₄ and CO₂ to high-value products. *J. Catal.* **2001**, *201* (1), 100-104.
6. (a) Wilcox, E. M.; Roberts, G. W.; Spivey, J. J., Direct catalytic formation of acetic acid from CO₂ and methane.

- Catal. Today* **2003**, 88 (1-2), 83-90; (b) Ding, Y.-H.; Huang, W.; Wang, Y.-G., Direct synthesis of acetic acid from CH₄ and CO₂ by a step-wise route over Pd/SiO₂ and Rh/SiO₂ catalysts. *Fuel Process. Technol.* **2007**, 88 (4), 319-324.
7. (a) Chen, Q.; Zhao, Y. X.; Jiang, L. X.; Chen, J. J.; He, S. G., Coupling of methane and carbon dioxide mediated by diatomic copper boride cations. *Angew. Chem. Int. Ed.* **2018**, 57 (43), 14134-14138; (b) Yang, Y.; Yang, B.; Zhao, Y. X.; Jiang, L. X.; Li, Z. Y.; Ren, Y.; Xu, H. G.; Zheng, W. J.; He, S. G., Direct Conversion of Methane with Carbon Dioxide Mediated by RhVO₃⁻ Cluster Anions. *Angew. Chem.* **2019**, 131 (48), 17447-17452; (c) Zhao, Y.-X.; Yang, B.; Li, H.-F.; Zhang, Y.; Yang, Y.; Liu, Q.-Y.; Xu, H.-G.; Zheng, W.-J.; He, S.-G., Photoassisted Selective Steam and Dry Reforming of Methane to Syngas Catalyzed by Rhodium-Vanadium Bimetallic Oxide Cluster Anions at Room Temperature. *Angew. Chem. Int. Ed.* **2020**, 59, 21216-21223.
 8. Liu, G.; Zhu, Z.; Ciborowski, S. M.; Ariyaratna, I. R.; Miliordos, E.; Bowen, K. H., Selective Activation of the C-H Bond in Methane by Single Platinum Atomic Anions. *Angew. Chem.* **2019**, 131 (23), 7855-7859.
 9. Zhang, X.; Lim, E.; Kim, S. K.; Bowen, K. H., Photoelectron spectroscopic and computational study of (M-CO₂)⁻ anions, M= Cu, Ag, Au. *J. Chem. Phys.* **2015**, 143 (17), 174305.
 10. Liu, G.; Ciborowski, S. M.; Zhu, Z.; Chen, Y.; Zhang, X.; Bowen, K. H., The metallo-formate anions, M(CO₂)⁻, M= Ni, Pd, Pt, formed by electron-induced CO₂ activation. *Phys. Chem. Chem. Phys.* **2019**, 21 (21), 10955-10960.
 11. Zhang, X.; Liu, G.; Meiwes-Broer, K. H.; Ganteför, G.; Bowen, K., CO₂ activation and hydrogenation by PtH_n⁻ cluster anions. *Angew. Chem.* **2016**, 128 (33), 9796-9799.
 12. Liu, G.; Poths, P.; Zhang, X.; Zhu, Z.; Marshall, M.; Blankenhorn, M.; Alexandrova, A. N.; Bowen, K. H., CO₂ Hydrogenation to Formate and Formic Acid by Bimetallic Palladium-Copper Hydride Clusters. *J. Am. Chem. Soc.* **2020**, 142 (17), 7930-7936.
 13. (a) Zhou, S.; Li, J.; Schlangen, M.; Schwarz, H., Bond activation by metal-carbene complexes in the gas phase. *Acc. Chem. Res.* **2016**, 49 (3), 494-502; (b) Schwarz, H.; Shaik, S.; Li, J., Electronic effects on room-temperature, gas-phase C-H Bond activations by cluster oxides and metal carbides: The methane challenge. *J. Am. Chem. Soc.* **2017**, 139 (48), 17201-17212; (c) Zhao, Y.-X.; Li, Z.-Y.; Yang, Y.; He, S.-G., Methane activation by gas phase atomic clusters. *Acc. Chem. Res.* **2018**, 51 (11), 2603-2610; (d) Armentrout, P., Activation of CH₄ by Gas-Phase Mo⁺, and the Thermochemistry of Mo- ligand Complexes. *J. Phys. Chem. A* **2006**, 110 (27), 8327-8338; (e) Green, A. E.; Justen, J.; Schöllkopf, W.; Gentleman, A. S.; Fielicke, A.; Mackenzie, S. R., IR Signature of Size-Selective CO₂ Activation on Small Platinum Cluster Anions, Pt_n⁻ (n= 4-7). *Angew. Chem.* **2018**, 130 (45), 15038-15042; (f) Johnson, G. E.; Mitric, R.; Nössler, M.; Tyo, E. C.; Bonacic-Koutecky, V.; Castleman Jr, A., Influence of charge state on catalytic oxidation reactions at metal oxide clusters containing radical oxygen centers. *J. Am. Chem. Soc.* **2009**, 131 (15), 5460-5470; (g) Deng G.; Pan S.; Wang G.; Zhao L.; Zhou M.; Frenking G., Beryllium Atom Mediated Dinitrogen Activation via Coupling with Carbon Monoxide. *Angew. Chem. Int. Ed.* **2020**, 59, 18201-18207. (g) Jian, J.; Wu, X.; Chen, M.; Zhou, M., Boron-Mediated Carbon-Carbon Bond Cleavage and Rearrangement of Benzene Forming the Borepinyl Radical and Borole Derivatives, *J. Am. Chem. Soc.* **2020**, 142, 10079-10086
 14. Under our experiment conditions where CH₄ activation and CO₂ functionalization occurred in separated cells,

$\text{H}_3\text{C-Pt-H}^-$ was sufficiently cooled when they exited the laser vaporization cell and entered the reaction cell, that is, the energy released during the exothermic CH_4 activation had dissipated before $\text{H}_3\text{C-Pt-H}^-$ interacting with CO_2 . Therefore, when calculating the activation barriers for the CO_2 functionalization step, the total energy of $\text{H}_3\text{C-Pt-H}^-$ and isolated CO_2 should be referenced. For other reactors such as ion traps, it is more reasonable to reference to the total energy of Pt^- , CH_4 and CO_2 for all steps in the reaction

15. (a) Liu, G.; Ciborowski, S. M.; Zhu, Z.; Bowen, K. H., Activation of hydroxylamine by single gold atomic anions. *Int. J. Mass Spectrom.* **2019**, *435*, 114-117. (b) Lang, S. M.; Bernhardt, T. M.; Chernyy, V.; Bakker, J. M.; Barnett, R. N.; Landman, U., Selective C-H bond cleavage in methane by small gold clusters. *Angew. Chem.* **2017**, *129* (43), 13591-13595.
16. Zhang, X.; Liu, G.; Ganteför, G.; Bowen, K. H.; Alexandrova, A. N., PtZnH_5^- , A σ -aromatic cluster. *J. Phys. Chem. Lett.* **2014**, *5* (9), 1596-1601.
17. (a) Liu, G.; Ciborowski, S. M.; Bowen, K. H., Photoelectron spectroscopic and computational study of pyridine-ligated gold cluster anions. *J. Phys. Chem. A* **2017**, *121* (31), 5817-5822. (b) Liu, G.; Miliordos, E.; Ciborowski, S. M.; Tschurl, M.; Boesl, U.; Heiz, U.; Zhang, X.; Xantheas, S. S.; Bowen, K., Communication: Water activation and splitting by single metal-atom anions. *J. Chem. Phys.* **2018**, *149* (22), 221101.
18. Frisch, M. J.; Trucks, G. W.; Schlegel, H. B.; Scuseria, G. E.; Robb, M. A.; Cheeseman, J. R.; Scalmani, G.; Barone, V.; Petersson, G. A.; Nakatsuji, H.; Li, X.; Caricato, M.; Marenich, A. V.; Bloino, J.; Janesko, B. G.; Gomperts, R.; Mennucci, B.; Hratchian, H. P.; Ortiz, J. V.; Izmaylov, A. F.; Sonnenberg, J. L.; Williams-Young, D.; Ding, F.; Lipparini, F.; Egidi, F.; Goings, J.; Peng, B.; Petrone, A.; Henderson, T.; Ranasinghe, D.; Zakrzewski, V. G.; Gao, J.; Rega, N.; Zheng, G.; Liang, W.; Hada, M.; Ehara, M.; Toyota, K.; Fukuda, R.; Hasegawa, J.; Ishida, M.; Nakajima, T.; Honda, Y.; Kitao, O.; Nakai, H.; Vreven, T.; Throssell, K.; Montgomery, J. A., Jr.; Peralta, J. E.; Ogliaro, F.; Bearpark, M. J.; Heyd, J. J.; Brothers, E. N.; Kudin, K. N.; Staroverov, V. N.; Keith, T. A.; Kobayashi, R.; Normand, J.; Raghavachari, K.; Rendell, A. P.; Burant, J. C.; Iyengar, S. S.; Tomasi, J.; Cossi, M.; Millam, J. M.; Klene, M.; Adamo, C.; Cammi, R.; Ochterski, J. W.; Martin, R. L.; Morokuma, K.; Farkas, O.; Foresman, J. B.; Fox, D. J. Gaussian, Inc., Wallingford CT, 2016.
19. Kendall, R. A.; Dunning, T. H.; Harrison, R. J. Electron Affinities of the First-row Atoms Revisited. Systematic Basis Sets and Wave Functions. *J. Chem. Phys.* **1992**, *96* (9), 6796-6806.
20. Dunning, T. H. Gaussian Basis Sets for Use in Correlated Molecular Calculations. I. The Atoms Boron through Neon and Hydrogen. *J. Chem. Phys.* **1989**, *90* (2), 1007-1023.
21. Figgen, D.; Peterson, K. A.; Dolg, M.; Stoll, H. Energy-Consistent Pseudopotentials and Correlation Consistent Basis Sets for the 5d Elements Hf-Pt. *J. Chem. Phys.* **2009**, *130* (16), 164108.
22. Raghavachari, K.; Trucks, G. W.; Pople, J. A.; Head-Gordon, M. A Fifth-Order Perturbation Comparison of Electron Correlation Theories. *Chem. Phys. Lett.* **1989**, *157* (6), 479-483.
23. Werner, H.-J. et al. see <https://www.molpro.net>.

IV.A.5. Molecular-Level Electrocatalytic CO₂ Reduction Reaction Mediated by Single Platinum Atoms

Reprinted (adapted) with permission from *Phys. Chem. Chem. Phys.*, 2022, **24**, 4226

Gaoxiang Liu^{[a]#}, Isuru R. Ariyaratna^{[b]†}, Zhaoguo Zhu^[a], Sandra M. Ciborowski^[a], Evangelos Miliordos^{[b]*}, Kit H. Bowen^{[a]*}

[a] Department of Chemistry, Johns Hopkins University, 3400 N Charles St, Baltimore, MD 21218 (USA) E-mail: kbowen@jhu.edu

[b] Department of Chemistry and Biochemistry, Auburn University, Auburn, AL 36849 (USA) E-mail: ezm0048@auburn.edu

Present Address: Advanced Bioimaging Center, Department of Molecular and Cell Biology, University of California, Berkeley, Barker Hall, Berkeley, CA 94720 (USA).

† Present Address: Department of Chemical Engineering, Massachusetts Institute of Technology, Cambridge, MA 02139, (USA).

Abstract

The activation and transformation of H₂O and CO₂ mediated by electrons and single Pt atoms is demonstrated at the molecular level. The reaction mechanism is revealed by the synergy of mass spectrometry, photoelectron spectroscopy, and quantum chemical calculations. Specifically, a Pt atom captures an electron and activates H₂O to form a H-Pt-OH⁻ complex. This complex reacts with CO₂ via two different pathways to form formate, where CO₂ is hydrogenated, or to form bicarbonate, where CO₂ is carbonated. The overall formula of this reaction is identical to a typical electrochemical CO₂ reduction reaction on a Pt electrode. Since the reactants are electrons and isolated, single atoms and molecules, we term this reaction a molecular-level electrochemical CO₂ reduction reaction. Mechanistic analysis reveals that the negative charge distribution on the Pt-H and the -OH moieties in H-Pt-OH⁻ is critical for the hydrogenation and carbonation of CO₂. The realization of the molecular-level CO₂ reduction reaction provides insights into the design of novel catalysts for the electrochemical conversion of CO₂.

Introduction

The electrocatalytic conversion of CO₂ into reduced, value-added molecules has received extensive attention for both environmental and economic reasons. While noble metal nanomaterials, such as Pt, Pd, Ru, Rh, and Ir, are mostly commonly used in electrocatalysis due to their high activity, their high cost and low natural abundance introduce major difficulties in using them for large-scale, industrial applications. Single-atom electrocatalysts that comprise

isolated active metal centers represent a promising strategy for mitigating this issue, owing to their maximum atom efficiency and unique atomic structures and electronic properties.¹⁻³ For instance, downsizing the Pt nanoparticles to single-atoms supported on substrates improves their activities toward several electrochemical reduction processes, including hydrogen evolution reaction, oxygen reduction reaction, and CO₂ reduction.^{4,5} In this study, we explore the possibility of further reducing the scale of an electrochemical reduction reaction to the molecular level. The aim is to use electrons, isolated, single noble metal atoms, water, and CO₂ molecules to achieve an electrochemical CO₂ reduction reaction (CO₂RR) that involves as few chemical entities as possible.

We selected the platinum atom as the noble metal to mediate this molecular-level electrochemical CO₂RR, a choice inspired by a lineage of our recent studies. In studies related to CO₂ activation and functionalization, we showed that the negative ions of metal atoms, including Pt⁻, activate CO₂,^{6,7} and that the activated groups on Pt atom, such as the hydro and the methyl groups, functionalize CO₂ into formate and acetate.^{8,9} In another study, we showed that while a neutral platinum atom is inert toward water, after adding an electron, a platinum anion activates a water molecule by breaking the O-H bond to form a H-Pt-OH⁻ complex.¹⁰ The hydro and the hydroxy groups in this complex are expected to be active in reacting with other small molecules. Based on these studies, we conceive that electrons endow Pt atoms with activities for both water activation and the CO₂ functionalization, and that by coupling such activities, Pt atoms can mediate a molecular-level electrochemical CO₂ reduction reaction. Here, we demonstrate that in the presence of electrons, Pt atoms break water molecules into -H and -OH groups, and respectively couple these two groups with CO₂ to form formate and bicarbonate. The overall chemical formula for this molecular-level reaction resembles that of a typical electrochemical CO₂RR on a Pt electrode. This work demonstrates the smallest scale electrochemical CO₂ reduction reaction mediated by single atoms known.

Results and Discussion

The molecular-level CO₂ reduction reaction starts with the controlled activation of one O-H bond in H₂O by single Pt atoms and electrons.¹¹ Water activation occurred in a laser vaporization source, where a laser-generated plasma containing Pt atoms and electrons interacted with water molecules introduced into the vaporization chamber. The activation product, PtH₂O⁻, was characterized by negative ion photoelectron spectroscopy and confirmed as H-Pt-OH⁻ (Figure IV.A.5.1A top panel and Figure S1). This activation product then reacted with CO₂ added into a reaction cell downstream by a second pulse valve. As all reactants were carried by supersonically expanding jets, the reaction

temperature is estimated to be on the order of several Kelvins. The duration of the reaction is around 40 ns, which is determined by the difference between the trigger timings of the second pulse valve and the time-of-flight mass spectrometer. The resultant mass spectra show prominent new peaks of reaction products at the lower mass region, while a mass series of $[\text{H-Pt-OH}(\text{CO}_2)]^-$ is observed at the higher mass region (Figure IV.A.5.1A bottom panel). Here, we focus on the species with an amu lower than 280, as these species represent the possible intermediates and products resulting from the reactions among H_2O , CO_2 , and single Pt anions. Pt clusters are not expected to contribute to these reactions. The intermediates related to reactions with Pt clusters should have the molecular formula $\text{Pt}_n(\text{H}_2\text{O})(\text{CO}_2)^-$ ($n \geq 2$) with a minimum molecular weight of 450 amu, which are beyond the scope of this work.

The peaks at the lower mass region are identified as HCO_2^- (formate), HCO_3^- , CO_3^- , and the solvation complexes of these species according to their masses and photoelectron spectra (Figure IV.A.5.1B top panel and Figure S2). For comparison, the reaction between H_2O and CO_2 with the presence of electrons only forms the $(\text{CO}_2)_n(\text{H}_2\text{O})_m^-$ solvation complexes¹¹ (Figure S3). This confirms that electrons alone will not induce chemical bond breakage or reformation in a H_2O and CO_2 gas expansion under our experimental conditions. Therefore, Pt atoms are critical for the formation of HCO_2^- , HCO_3^- , and CO_3^- . HCO_2^- and HCO_3^- are likely due to the reactions between CO_2 respectively with the -H and -OH groups in the water activation complex H-Pt-OH^- . The CO_3^- can be the result of electron-induced deprotonation of HCO_3^- , which is common for gas-phase acidic anions. The high intensities of these lower mass products suggest an efficient interaction between CO_2 and H-Pt-OH^- .

We then characterized the $[\text{H-Pt-OH}(\text{CO}_2)]^-$ reaction intermediate with negative ion photoelectron spectroscopy (Figure IV.A.5.2). The photoelectron spectra were taken at all the mass isotopes, and no significant spectroscopic difference was observed among them. The $[\text{H-Pt-OH}(\text{CO}_2)]^-$ spectrum is convolved, suggesting contributions from multiple isomers of $[\text{H-Pt-OH}(\text{CO}_2)]^-$ that coexist in the ion beam. The photoelectron spectrum consists of two subregions. The first region is relatively weak in intensity and has multiple peaks with electron binding energy (EBE) lower than 3.6 eV. This indicates that the isomers with their vertical detachment energies (VDE), which are defined as the photodetachment transition energy at which the Franck–Condon overlap is at its maximum between the anion’s vibrational wave function and that of its neutral counterpart, below 3.6 eV make up a lesser portion in the $[\text{H-Pt-OH}(\text{CO}_2)]^-$ beam. The spectral region above 3.6 eV, on the other hand, is higher in intensity, suggesting the $[\text{H-Pt-OH}(\text{CO}_2)]^-$ beam.

$\text{OH}(\text{CO}_2)]^-$ isomers with a VDE higher than 3.6 eV are the major species in the ion beam. In other words, these isomers are more stable than those with a lower VDE.

The complexity of the $[\text{H-Pt-OH}(\text{CO}_2)]^-$ photoelectron spectrum necessitates quantum chemical calculations to identify the molecular species of this reaction intermediate. A distinct advantage for studying gas-phase reactions between single atoms and molecules is the synergy between experimental characterization and high-level quantum chemistry calculations for identifying reaction intermediates and products, which lays the foundation for mechanistic insight into the reactions at a molecular level.¹² We started by performing density functional theory to search for $[\text{H-Pt-OH}(\text{CO}_2)]^-$ isomers that are possibly formed via the reaction between H-Pt-OH^- and CO_2 . The energetics of these isomers were then refined at the CCSD(T) level of theory. The optimized geometries for these reaction intermediates are presented in Figure IV.A.5.3 along with their relative energies. All energies are zero-point energy corrected. The structures of H-Pt-OH^- and CO_2 are also presented for reference. All $[\text{H-Pt-OH}(\text{CO}_2)]^-$ isomers are in a doublet electronic state. In the global minimum of $[\text{H-Pt-OH}(\text{CO}_2)]^-$, **A**, CO_2 is wedged into the Pt-H bond of H-Pt-OH^- to form a HOCO-Pt-OH^- structure, that is, CO_2 is hydrogenated to formate. In structure **B**, which is essentially isoenergetic to the global minimum, CO_2 is inserted into the O-H bond of H-Pt-OH^- , forming a H-Pt-HCO_3^- structure where CO_2 is carbonated. The bicarbonate is attached to the Pt atom via a Pt-O bond. Structures **C** and **D** are formed by the absorption of CO_2 respectively onto the Pt and O atoms in H-Pt-OH^- . In structure **C**, CO_2 exhibits a bent geometry. This suggests that CO_2 is activated, which is the first step for CO_2 to be further functionalized, upon bonding with the Pt atom. In structure **D**, on the other hand, while CO_2 also appears bent, its local charge is only slightly positive after interacting with the O atom. This suggests that charge transfer in structure **D** is minimal, and CO_2 is not activated. Based on the atomic connectivity, structure **C** is the prior step for forming structure **A**, while structure **D** is the essential step to generate structure **B**.

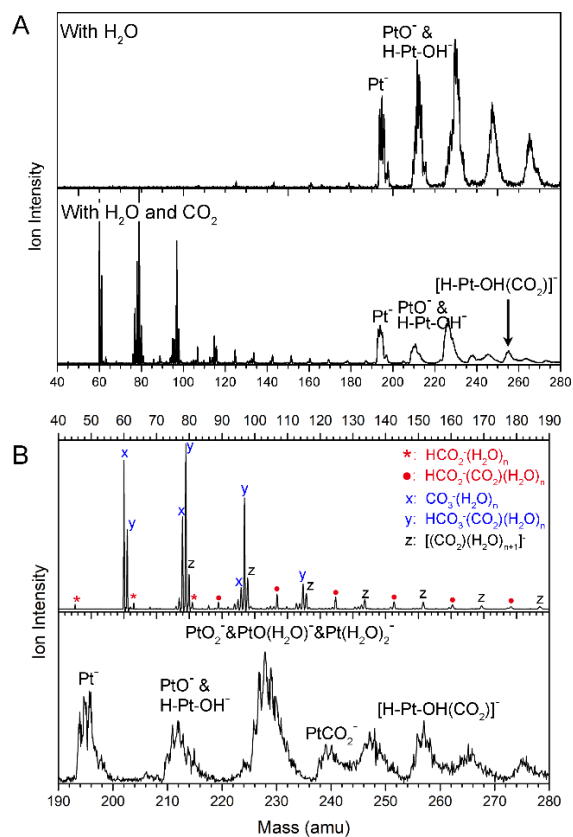


Figure IV.A.5.1 (A) Mass spectra of Pt $^-$ reacting with H $_2$ O (top panel) and with H $_2$ O and CO $_2$ (bottom panel). (B) The mass spectrum of Pt $^-$ with H $_2$ O and CO $_2$ is bisected into the lower (top panel) and higher (bottom panel) mass regions for a closer view of the reaction products.

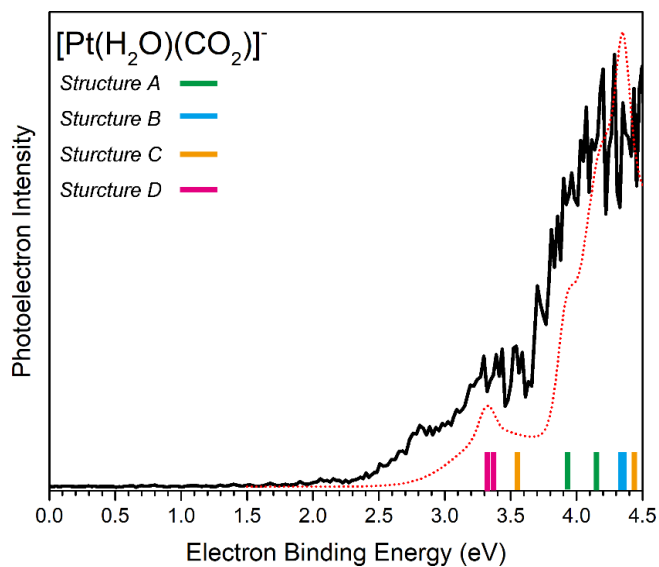


Figure IV.A.5.2 Photoelectron spectra of [H-Pt-OH(CO $_2$)] $^-$ measured with 266 nm (4.661 eV) photons. The stick

spectrum overlay represents the calculated VDEs of the different $[\text{H-Pt-OH}(\text{CO}_2)]^-$ structures in Figure IV.A.5.3.

The dotted line represents the simulated spectrum.

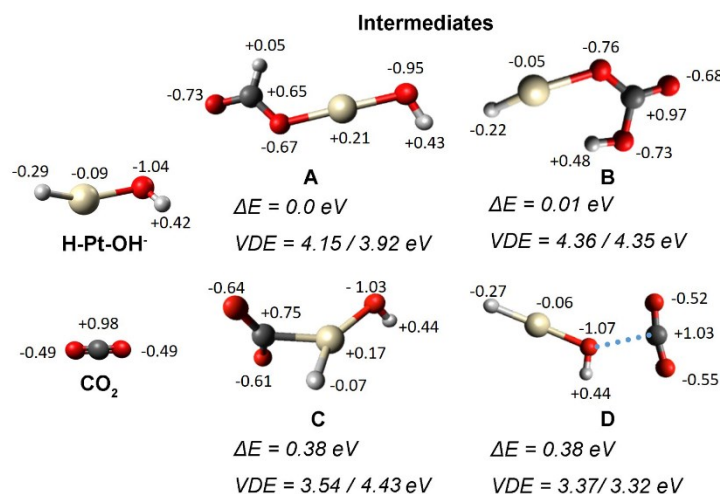


Figure IV.A.5.3 Optimized structures for H-Pt-OH^- , CO_2 , and $[\text{H-Pt-OH}(\text{CO}_2)]^-$. The relative energies of $[\text{H-Pt-OH}(\text{CO}_2)]^-$ and their calculated VDEs to singlet and triplet neutrals are shown below each structure. The Natural Bond Orbital (NBO) charge on each atom is also provided.

To verify these computationally optimized structures, we calculated their VDEs at the CCSD(T) level of theory and compared them with the experimental spectrum. The EBE transition below 3.6 eV results from the photodetachment transitions of structures **C** and **D**, whose calculated VDEs to their singlet neutrals are 3.54 and 3.37 eV, respectively. For structure **D**, its VDE to the triplet neutral, which is 3.32 eV, also falls into this EBE band. The EBE feature higher than 3.6 eV is due to the photodetachment transition of structures **A** and **B** to their corresponding singlet and triplet neutrals. The transition from structure **C** to its singlet also contributes to this EBE feature. We simulated the photoelectron spectrum based on the calculated electron affinities and VDEs (see Methods). The match between the simulated and experimental spectra indicates that structures **A**, **B**, **C**, and **D** all exist as the intermediates of the reaction between H-Pt-OH^- and CO_2 .

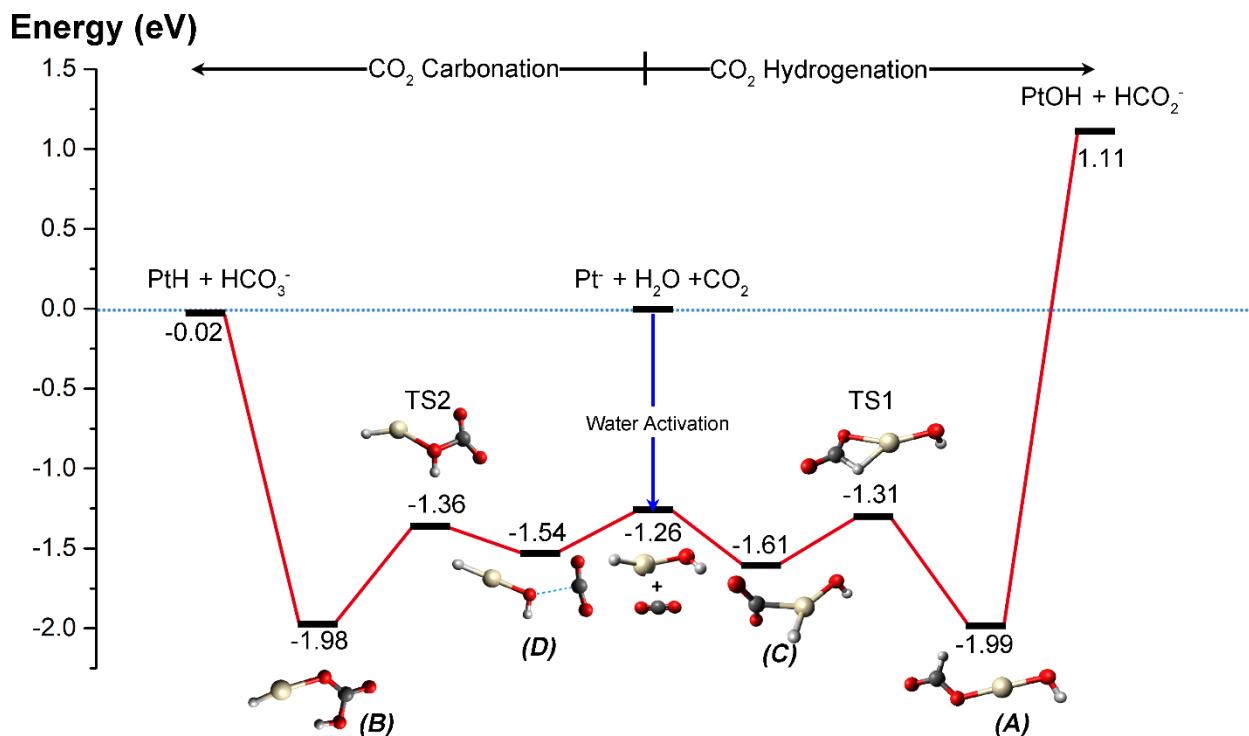
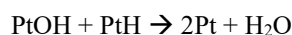
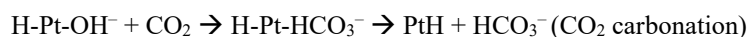
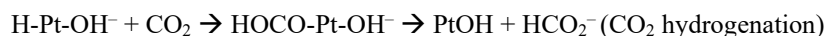
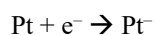


Figure IV.A.5.4 Profile of the molecular-level CO₂RR mediated by anionic Pt atoms. Zero-point corrected energies are given in eV. The letters in parentheses correspond to their labels in Figure IV.A.5.3. The potential energy surface is referenced to the total energy of isolated Pt⁻, H₂O, and CO₂.

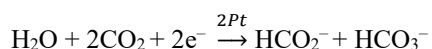
The identification of the formate and bicarbonate adducts, structures **A** and **B**, and their corresponding precursors, structures **C** and **D**, suggests two possible reaction mechanisms that are respectively responsible for the formation of the formate and the bicarbonate products observed in the mass spectra. To gain a detailed mechanistic insight into how H₂O and CO₂ are transformed on the anionic Pt atom, we investigated the reaction pathway with quantum chemical calculations (Figure IV.A.5.4). The reaction starts with the breakage of one O-H bond H₂O by Pt⁻, which has been elaborated in our previous work. This step includes a barrier of 0.51 eV and is exothermic by 1.26 eV.¹⁰ The resultant H-Pt-OH⁻ can react with CO₂ via a Pt/C interaction that leads to CO₂ hydrogenation, or an O/C interaction that results in CO₂ carbonation. The Pt/C interaction causes a 0.5|e| negative charge transfer to CO₂ and the formation of a Pt-C bond (Structure **C**). The activated CO₂ then interacts with the Pt-H bond of H-Pt-OH⁻. The H atom transfers to the C atom while the Pt atom binds the O atom, leading to the formation of HO-Pt-OCOH⁻ that contains a formate moiety (Structure **A**). The transition state, **TS1**, is located 0.05 eV below H-Pt-OH⁻ and CO₂, the reactants for the CO₂ hydrogenation step, and 1.31 eV lower than Pt⁻, H₂O, and CO₂, which is the entrance channel of the entire reaction.

Therefore, H-Pt-OH⁻ readily hydrogenates CO₂ into the formate adduct intermediate via the Pt/C interaction route. Structure **A** can further dissociate into PtOH and HCO₂⁻, accounting for the formate and formate-containing products observed in the mass spectrum. This step is endothermic, with the dissociation products 1.11 eV higher than the entrance channel. Such extra energy can be provided via multicollisions with the fastest He molecules in the Maxwell–Boltzmann distribution under our experimental conditions.¹³ It is also worth noting that H-Pt-OH⁻ may undergo a direct reaction mechanism where its -H group transfers to CO₂ to form a formate without going through the HO-Pt-OCOH⁻ intermediate (Structure **A**).^{13a, 14} For the O/C interaction route, the CO₂ wedges into the O-H bond of H-Pt-OH⁻ to form a bicarbonate adduct (Structure **B**) via **TS2**, which lies 1.36 eV below the entrance channel. This adduct can dissociate into PtH and HCO₃⁻, whose total energy is almost identical to the entrance channel. Note that the CO₂ activation intermediate, **D**, the transition state, **TS2**, and the adduct intermediate, **B**, in the CO₂ carbonation route, are respectively similar in energy as compared to their corresponding structures, **C**, **TS1**, and **A**, in the CO₂ hydrogenation route. Therefore, the carbonation and hydrogenation routes have alike energetic profiles before the dissociation of the reaction intermediates, and the higher energy of hydrogenation products accounts for the lower intensities of HCO₂⁻ related species as compared to the HCO₃⁻ related ones (Figure IV.A.5.1).

The observation of a significant amount of formate, bicarbonate, and their related products in the mass spectrum suggests a high yield of PtH and PtOH as the reaction products, though they were not directly observed due to a lack of charge. In addition, the solvation and deprotonation of formate and bicarbonate indicate noticeable interactions among the reaction products. Therefore, PtH and PtOH may react with each other to form two Pt atoms and one H₂O molecule under our experimental conditions, completing the catalytic cycle by regenerating Pt atoms. We can thus summarize all the reaction steps as follows:



By combining and balancing these steps, we proposed that the overall reaction that occurred in our experimental setup is:



Therefore, while the reactants in our setup are electrons and isolated, single atoms and molecules, the overall reaction has the same formula as a typical electrochemical CO₂ reduction reaction on a Pt electrode. We thus propose that the H₂O and CO₂ activation and conversion mediated by Pt atoms and electrons in this work represents an electrochemical CO₂ reduction reaction at the molecular level.

The neutral Pt atom is inactive to H₂O. With the addition of an excess electron, Pt⁻ activates water by breaking one of its O-H bonds to form H-Pt-OH⁻. The negative charge on Pt reduces to -0.09|e| after redistributing to the -H and the -OH groups, with the O atoms carrying the major portion of the negative charge in this water activation complex. While the negative charge on Pt in this complex is significantly lower than those observed in our previous studies, the H atom that is directly connected to Pt also contributes its negative charge when Pt interacts with CO₂. This is manifested by the decrease of the total charge on the Pt-H moiety from -0.38|e| to -0.10|e| after the CO₂ activation step. The charge on the -OH group, on the other hand, barely changes in the CO₂ hydrogenation route, suggesting that CO₂ functionalization occurs on the Pt-H moiety. The O atom in H-Pt-OH⁻ serves as another site for the initial interaction with CO₂. The negative charge on O is large (-1.04|e|), but NBO charge analysis reveals that it barely transfers to CO₂ during the O/C interaction. The carbonation occurs primarily on the -OH group, and the charge on the Pt-H moiety changes little in this route. This mechanism resembles the function of the ZnOH unit in a carbonic anhydrase.¹²ⁱ The charge analysis thus suggests that the hydrogenation and the carbonation routes proceed locally on the Pt-H and the O-H moieties, respectively, and each of the two moieties needs to possess appropriate negative charge for converting CO₂ into other species. A charge analysis shows that in neutral H-Pt-OH, the charge on the Pt-H moiety is +0.38|e|, making it unable to activate or hydrogenate CO₂ (Figure S4). Therefore, electrons play a critical role in this molecular-level electrochemical CO₂ reduction reaction, not only for enabling Pt atoms to activate H₂O activation, but also for keeping adequate negative charge on the Pt-H moiety in H-Pt-OH⁻ so CO₂ hydrogenation can occur on it.

Conclusions

To summarize, we demonstrate the activation and transformation of H₂O and CO₂ mediated by electrons and single Pt atoms. The reaction mechanism is revealed by the synergy of mass spectrometry, photoelectron spectroscopy, and quantum chemical calculations. Specifically, a Pt atom captures an electron and activates H₂O to form a H-Pt-OH⁻ complex. This complex reacts with CO₂ via two different pathways to form formate, where CO₂ is hydrogenated, or

to form bicarbonate, where CO_2 is carbonated. The overall formula of this reaction is identical to a typical electrochemical CO_2 reduction reaction on a Pt electrode. Since the reactants are electrons and isolated, single atoms and molecules, we term this reaction as a molecular-level electrochemical CO_2 reduction reaction. Mechanistic analysis reveals that the negative charge distribution on the Pt-H and the -OH moieties in H-Pt-OH^- is critical for the hydrogenation and carbonation of CO_2 . The realization of the molecular-level CO_2 reduction reaction provides new insights into the design of novel catalysts for the electrochemical conversion of CO_2 .

Methods

Experimental Methods

Anion photoelectron spectroscopy is conducted by crossing a beam of mass-selected negative ions with a fixed-frequency photon beam and energy-analyzing the resultant photodetached electrons. The photodetachment process is governed by the energy-conserving relationship: $h\nu = \text{EBE} + \text{EKE}$, where $h\nu$ is the photon energy, EBE is the electron binding energy, and EKE is the electron kinetic energy. Our apparatus consists of a laser vaporization cluster anion source with an attached ligation cell, a time-of-flight mass spectrometer, a Nd:YAG photodetachment laser (operating at 266 nm), and a magnetic bottle electron energy analyzer with a resolution is ~ 35 meV at 1 eV EKE.¹⁵ Photoelectron spectra were calibrated against the well-known atomic transitions of atomic Cu^- . The reaction among Pt^- , H_2O , and CO_2 was studied using a laser vaporization/reaction cell arrangement.¹⁶ Atomic platinum anions were generated by laser vaporization of a pure platinum foil wrapped around an aluminum rod. The resultant plasma was cooled with a water vapor seeded helium gas mixture delivered by a pulsed valve, having a backing pressure of 80 psig. The resulting H-Pt-OH^- then traveled through a reaction cell (4-mm diameter, 5-cm length), where it encountered CO_2 . CO_2 was introduced into the reaction cell by a second pulsed valve, backed by 15 psig of pure CO_2 gas. The resulting $[\text{H-Pt-OH}(\text{CO})_2]^-$ anionic cluster was then mass-analyzed and mass-selected by the time-of-flight mass spectrometer and their photoelectron spectra measured.

Computational Methods

Geometries of intermediates and transition states were optimized at the Density functional theory (DFT)/B3LYP level of theory using Gaussian16 package.¹⁷ Harmonic vibrational frequency calculations carried out at the same level of theory to confirm the existence of only real frequencies for all energy minima, and one imaginary frequency for the transition states. Frequencies were used to estimate the zero-point energy corrections for all species. More accurate

energies were obtained by performing single-point CCSD(T)¹⁸ calculations using the B3LYP geometries. Obtained zero-point energies from DFT/B3LYP were added to calculate more accurate zero-point corrected CCSD(T) energies. All CCSD(T) calculations were performed using MOLPRO 2015 package.¹⁹ For all calculations, the aug-cc-pVTZ (H, C, O)^{20,21} and aug-cc-pVTZ-PP (Pt)²² basis sets were employed. The inner 60 electrons ($1s^2 2s^2 2p^6 3s^2 3p^6 3d^{10} 4s^2 4p^6 4d^{10} 4f^{14}$) of Pt were replaced with the Stuttgart relativistic pseudopotential.²² To reproduce the photo-electron spectrum, we considered one Gaussian function for each stick of Figure IV.A.5.2. The maximum was set equal to the calculated VDE and the full-width-of-half-maximum was approximated as (VDE–EA). The latter allows the onset of the Gaussian at around the EA value. The height of the Gaussian was fit to the experimental data. VDE is calculated as the energy difference between the anionic and neutral system using the anionic optimized geometry, and EBE is the same energy difference but using the optimal structure of each species. The VDE, EBE values, and intensities are given in the SI online.

Reference

1. B. Lu, Q. Liu and S. Chen, *ACS Catal.*, 2020, **10**, 7584.
2. Y. Chen, S. Ji, C. Chen, Q. Peng, D. Wang and Y. Li, *Joule*, 2018, **2**, 1242-1264.
3. C. Zhu, S. Fu, Q. Shi, D. Du and Y. Lin, *Angew. Chem. Int. Ed.*, 2017, **56**, 13944-13960.
4. G. Gao, Y. Jiao, E. R. Waclawik and A. Du, *J. Am. Chem. Soc.*, 2016, **138**, 6292-6297.
5. X. Su, X. F. Yang, Y. Huang, B. Liu and T. Zhang, *Acc. Chem. Res.*, 2018, **52**, 656-664.
6. X. Zhang, E. Lim, S. K. Kim and K. H. Bowen, *J. Chem. Phys.*, 2015, **143**, 174305.
7. G. Liu, S. Ciborowski, Z. Zhu, Y. Chen, X. Zhang and K. H. Bowen, *Phys. Chem. Chem. Phys.*, 2019, **21**, 10955-10960.
8. X. Zhang, G. Liu, K. Meiwes-Broer, G. Ganteför and K. Bowen, *Angew. Chem. Int. Ed.*, 2016, **55**, 9644-9647.
9. G. Liu, I. R. Ariyaratna, S. M. Ciborowski, Z. Zhu, E. Miliordos and K. H. Bowen, *J. Am. Chem. Soc.*, 2020, **142**, 21556–21561.
10. G. Liu, E. Miliordos, S. M. Ciborowski, M. Tschurl, U. Boesl, U. Heiz, X. Zhang, S. S. Xantheas and K. Bowen, *J. Chem. Phys.*, 2018, **149**, 221101.
11. O. P. Balaj, C. K. Siu, I. Balteanu, M. K. Beyer and V. E. Bondybey, *Chem. Eur. J.*, 2004, **10**, 4822-4830.
12. (a) S. Zhou, J. Li, M. Schlangen, H. Schwarz, *Acc. Chem. Res.*, 2016, **49**, 494-502; (b) H. Schwarz, S. Shaik and J. Li, *J. Am. Chem. Soc.*, 2017, **139**, 17201-17212; (c) Y. X. Zhao, Z. Y. Li, Y. Yang and S. G. He, *Acc. Chem. Res.*, 2018, **51**, 2603-2610; (d) P. Armentrout, *J. Phys. Chem. A*, 2006, **110**, 8327-8338; (e) A. E. Green, J. Justen, W. Schöllkopf, A. S. Gentleman, A. Fielicke and S. R. Mackenzie, *Angew. Chem.*, 2018, **130**, 15038-15042; (f) G. E. Johnson, R. Mitric, M. Nössler, E. C. Tyo, V. Bonacic-Koutecky and A. Castleman Jr, *J. Am. Chem. Soc.*, 2009, **131**, 5460-5470; (g) G. Deng, S. Pan, G. Wang, L. Zhao, M. Zhou and G. Frenking, *Angew. Chem. Int. Ed.*, 2020, **59**, 18201-18207. (h) J. Jian, X. Wu, M. Chen and M. Zhou, *J. Am. Chem. Soc.*, 2020, **142**, 10079–10086; (i) H. Schwarz, *Coord. Chem. Rev.*, 2017, **334**, 112-123.
13. (a) G. Liu, Z. Zhu, M. Marshall, M. Blankenhorn and K. H. Bowen, *J. Phys. Chem. A*, 2021, **125**, 1747-1753.; (b) G. Liu, P. Poths, X. Zhang, Z. Zhu, M. Marshall, M. Blankenhorn, A. N. Alexandrova and K. H. Bowen, *J. Am. Chem. Soc.*, 2020, **142**, 7930-7936.; (c) G. Liu, Z. Zhu, S. M. Ciborowski, I. R. Ariyaratna, E. Miliordos and K. H. Bowen, *Angew. Chem. Int. Ed.*, 2019, **131**, 7855-7859.; (d) Lang, S. M.; Bernhardt, T. M.; Chernyy, V.; Bakker, J. M.; Barnett, R. N.; Landman, U., Selective C–H bond cleavage in methane by small gold clusters. *Angew. Chem.* 2017, **129**, 13591-13595.
14. L. X. Jiang, C. Zhao, X. N. Li, H. Chen and S. G. He, *Angew. Chem. Int. Ed.*, 2017, **56**, 4187-4191.
15. X. Zhang, G. Liu, G. Ganteför, K. H. Bowen and A. N. Alexandrova, *J. Phys. Chem. Lett.*, 2014, **5**, 1596-1601.
16. G. Liu, S. M. Ciborowski and K. H. Bowen, *J. Phys. Chem. A*, 2017, **121**, 5817-5822.

17. M.J. Frisch, G.W. Trucks, H.B. Schlegel, G.E. Scuseria, M.A. Robb, J.R. Cheeseman, G. Scalmani, V. Barone, G.A. Petersson, H. Nakatsuji, X. Li, M. Caricato, A.V. Marenich, J. Bloino, B.G. Janesko, R. Gomperts, B. Mennucci, H.P. Hratchian, J.V. Ortiz, A.F. Izmaylov, J.L. Sonnenberg, D. Williams-Young, F. Ding, F. Lipparini, F. Egidi, J. Goings, B. Peng, A. Petrone, T. Henderson, D. Ranasinghe, V.G. Zakrzewski, J. Gao, N. Rega, G. Zheng, W. Liang, M. Hada, M. Ehara, K. Toyota, R. Fukuda, J. Hasegawa, M. Ishida, T. Nakajima, Y. Honda, O. Kitao, H. Nakai, T. Vreven, K. Throssell, J. Montgomery, J.A., J.E. Peralta, F. Ogliaro, M.J. Bearpark, J.J. Heyd, E.N. Brothers, K.N. Kudin, V.N. Staroverov, T.A. Keith, R. Kobayashi, J. Normand, K. Raghavachari, A.P. Rendell, J.C. Burant, S.S. Iyengar, J. Tomasi, M. Cossi, J.M. Millam, M. Klene, C. Adamo, R. Cammi, J.W. Ochterski, R.L. Martin, K. Morokuma, O. Farkas, J.B. Foresman and D.J. Fox, Gaussian 16, Gaussian, Inc., Wallingford CT, 2016.
18. K. Raghavachari, G. W. Trucks, J. A. Pople and M. A. Head-Gordon, *Chem. Phys. Lett.*, 1989, **157**, 479–483.
19. H. J. Werner, P. J. Knowles, G. Knizia, F. R. Manby, M. Schütz, P. Celani, W. Györffy, D. Kats, T. Korona, R. Lindh, A. Mitrushenkov, G. Rauhut, K. R. Shamasundar, T. B. Adler, R. D. Amos, A. Bernhardsson, A. Berning, D. L. Cooper, M. J. Deegan, A. J. Dobbyn, F. Eckert, E. Goll, C. Hampel, A. Hesselmann, G. Hetzer, T. Hrenar, G. Jansen, C. Köppl, Y. Liu, A. W. Lloyd, R. A. Mata, A. J. May, S. J. McNicholas, W. Meyer, M. E. Mura, A. Nicklass, D. P. O'Neill, P. Palmieri, D. Peng, K. Pflüger, R. Pitzer, M. Reiher, T. Shiozaki, H. Stoll, A. J. Stone, R. Tarroni, T. Thorsteinsson, M. Wang, see <https://www.molpro.net>.
20. R. A. Kendall, T. H. Dunning and R. J. Harrison, *J. Chem. Phys.*, 1992, **96**, 6796–6806.
21. T. H. Dunning, *J. Chem. Phys.*, 1989, **90**, 1007–1023.
22. D. Figgen, K. A. Peterson, M. Dolg and H. Stoll, *J. Chem. Phys.*, 2009, **130**, 164108.

IV.B. CO₂ Hydrogenation by Metal Hydride Cluster Anions

Transforming CO₂ into reduced and value-added molecules has been a hot topic for decades due to environmental and economic reasons. However, the high stability of CO₂ molecules makes its reduction very difficult and energetically expensive. Therefore, there is an increasing demand for developing new catalysts with high efficiency and low costs. Among various catalysts, palladium-based and copper-based catalysts have shown great CO₂ hydrogenation activities. Due to the lack of direct experimental characterization of the key reaction intermediates, knowledge about the critical steps in CO₂ fixation and conversion remains limited. In this section, we present two studies on CO₂ hydrogenation by palladium hydride anions (Chapter IV.B.1) and bimetallic palladium-copper hydride anions (Chapter IV.B.2). The combined spectroscopic and computational studies revealed the mechanism of CO₂ insertion into metal hydrogen bonds at a molecular level, shedding light on designing new catalysts.

IV.B.1. CO₂ Activation and Hydrogenation by Palladium Hydride Cluster Anions

Reprinted (adapted) with permission from *J. Phys. Chem. A* **125**, 1747-1753, (2021) Copyright 2021 American Chemical Society.

Gaoxiang Liu^{#†*}, Zhaoguo Zhu[†], Mary Marshall, Moritz Blankenhorn, and Kit H. Bowen^{*}

Department of Chemistry, Johns Hopkins University, Baltimore, Maryland 21218, USA

Present address: [#]Advanced Bioimaging Center, Department of Molecular and Cell Biology, University of California, Berkeley, Berkeley, California 94720, USA

[†] *These two authors contributed equally to this manuscript*

Abstract

Mass spectrometric analysis of the anionic products of interaction between palladium hydride anions, PdH⁻, and carbon dioxide, CO₂, in a reaction cell shows an efficient generation of the PdHCO₂⁻ intermediate and isolated formate product. Multiple isomers of the PdHCO₂⁻ intermediates are identified by a synergy between negative ion photoelectron spectroscopy and quantum chemical calculations. It is shown that a direct mechanism, in which the H atom in PdH⁻ directly activates and hydrogenates CO₂, leads to the formation of the formate product. An indirect mechanism, on the other hand, leads to a stable HPdCO₂⁻ structure where CO₂ is chemisorbed onto the Pd atom.

Introduction

The catalytic conversion of CO₂ into value-added molecules using metal catalysts holds the promise for combating the greenhouse effect caused by the excess amount of CO₂ in the atmosphere. The formation of metal hydrides and the insertion of CO₂ into the metal-hydrogen bond are among the critical steps for CO₂ functionalization over metal catalysts. Comprehensive knowledge about these key steps, however, remains limited as a result of lacking direct experimental characterization on the reaction intermediates.¹⁻⁵ Especially, it is less clear how the initial CO₂ interaction with the formed metal-hydride can affect the CO₂ activation and the following CO₂ hydrogenation. Mechanistic insight into the CO₂ hydrogenation processes on the active sites is thus deemed essential for the rational design of high-efficiency catalysts for this task.

Via the synergy between the experimental characterization of reaction intermediates and quantum chemistry calculations, gas-phase studies of CO₂ reduction and hydrogenation has provided molecular-level insights into the CO₂ functionalization mechanisms.⁶⁻¹⁶ Single- and dual-metal hydrides have been studied for converting CO₂ into formate and formate complexes, shedding light on understanding the mechanisms of CO₂ hydrogenation over various

catalysts. As a well-known hydrogen absorber, palladium has been widely applied in catalytic CO₂ functionalization.¹⁷⁻
²⁰ Nevertheless, information on the reaction between palladium hydrides and CO₂ has been scarce. The present work focuses on the hydrogenation of CO₂ via reaction with the anionic palladium monohydride anion, PdH⁻. We show that depending on the atom that CO₂ initially interacts with, the reaction ends either in HPd(CO₂⁻), in which the CO₂ is activated and bonded to Pd, or in isolated Pd atom and formate, where the formate is released as a final product.

Methods

Experimental Methods

The present work utilized anion photoelectron spectroscopy (aPES) as its primary probe. The experimental technique, aPES, is conducted by crossing a mass-selected beam of negative ions with a fixed-energy photon beam and energy analyzing the resulting photodetached electrons. This technique is governed by the energy-conservation relationship, $h\nu = \text{EBE} + \text{EKE}$, where $h\nu$, EBE, and EKE are the photon energy, electron binding (photodetachment transition) energy, and the electron kinetic energy, respectively. Our photoelectron spectrometer, which has been described previously,²¹ consists of one of several ion sources, a linear time-of-flight (TOF) mass spectrometer, a mass gate, a momentum decelerator, a neodymium-doped yttrium aluminum garnet (Nd:YAG) laser for photodetachment, and a magnetic bottle electron energy analyzer. The resolution of the energy analyzer is ~ 35 meV at EKE = 1 eV. Photoelectron spectra were calibrated against the well-known photoelectron spectrum of Cu⁻.²²

The PdH⁻ anion was generated using a pulsed-arc (discharge) cluster ionization source (PACIS), which has been described in detail elsewhere.²³ During PACIS operation, a 30 μ s long, 4000 volt electrical pulse applied across the anode and the Pd sample cathode in the discharge chamber vaporizes the palladium atoms.²⁴ (The sample cathode had been prepared in a nitrogen glove box, where fresh Pd powder was firmly pressed onto a copper rod.) Almost simultaneously with the discharge, 220 psi of ultrahigh purity hydrogen gas was injected into the discharge region, where it was dissociated into hydrogen atoms. The resulting mixture of atoms, ions, and electrons then reacted and cooled as it expanded through the PACIS housing. After a small gap, this flow continued through a 15 cm long collision/reactor cell before exiting into high vacuum. To initiate the reaction between CO₂ and a mixture of PdH⁻ cluster anions, pure CO₂ was injected into the collision cell using a second pulsed valve. The resultant anions then drifted through a skimmer, through a differentially pumped region, and into the TOF region, where they were

perpendicularly extracted and mass-selected prior to photodetachment. Due to palladium's isotope pattern and the presence of multiple hydrogen atoms, photoelectron spectra were taken at all observed mass peaks.

Theoretical Methods

Computations relating to the reactions between carbon dioxide, palladium hydride anions, and the resultant products were performed using the Gaussian 09 program package.²⁵ Geometry optimizations and frequency calculations were carried out using the hybrid density functional theory (DFT) B3LYP with D3BJ empirical dispersion correction.^{26–29} Bond length of PdH^- anion optimized at B3LYP level was found to be 1.538 Å, which perfectly matches the previous result 1.538 Å at PBEPBE level.¹³ The vertical detachment energy (VDE) of the optimized structures were calculated using B3LYP DFT functional with the unrestricted Kohn–Sham solution, and then improved by single point energy calculations at the coupled cluster single-double and perturbative triple CCSD(T) level of theory.³⁰ Natural Population Analysis (NPA) was conducted to examine the charge distribution at the B3LYP level using NBO 3.1 implemented in Gaussian 09.³¹ NPA has been found to be satisfactory in predicting charge distributions within metal clusters.^{32,33} The initially estimated structures for transition states (TS) were obtained by selecting appropriate coordinates from relaxed potential energy surface scans. Vibrational frequencies were calculated to determine whether the stationary points were local minima or transition states. The intrinsic reaction coordinate (IRC) calculations were carried out to make sure that a TS connects two appropriate minima.^{34,35} The aug-cc-pwCVTZ-DK (for Pd) and aug-cc-PVTZ-DK basis sets (for C, H, O) and the second order Douglas-Kroll-Hess DKH2) scalar relativistic Hamiltonian were used throughout our computations.^{36–41}

Results and discussion

The TOF mass spectra without and with CO_2 pulsed into the reaction cell are shown in the top and bottom panel of Figure IV.B.1.1, respectively. Without CO_2 in the cell, PdH^- and PdCO^- are observed in the mass spectrum. The presence of PdCO^- is due to carbon and oxygen absorbed onto the palladium powder. Note that PdH^- is the only palladium hydride anion that is observed under this experimental condition. At higher mass, a mass series of $\text{PdH}_x\text{CO}_2^-$ appears after CO_2 is introduced into the reaction cell. We expanded this region and compared it with the simulated mass spectra of $\text{PdH}_1\text{CO}_2^-$ and $\text{PdH}_2\text{CO}_2^-$ (Figure IV.B.1.2). This comparison suggests the $\text{PdH}_x\text{CO}_2^-$ is a mixture of both $\text{PdH}_1\text{CO}_2^-$ and $\text{PdH}_2\text{CO}_2^-$. At lower mass in Figure IV.B.1.1, a peak at 45 amu can be observed after adding CO_2 into the reaction cell. Photoelectron spectroscopy confirmed this anion as the formate, HCOO^- (Figure S1). The

formation of the formate anion suggests that CO_2 is hydrogenated upon interaction with PdH^- , and that the formate product is released after the hydrogenation is complete. $\text{PdH}_1\text{CO}_2^-$, on the other hand, represents a key reaction intermediate when PdH^- hydrogenates CO_2 . Better characterization of this intermediate would help to understand the hydrogenation mechanism.

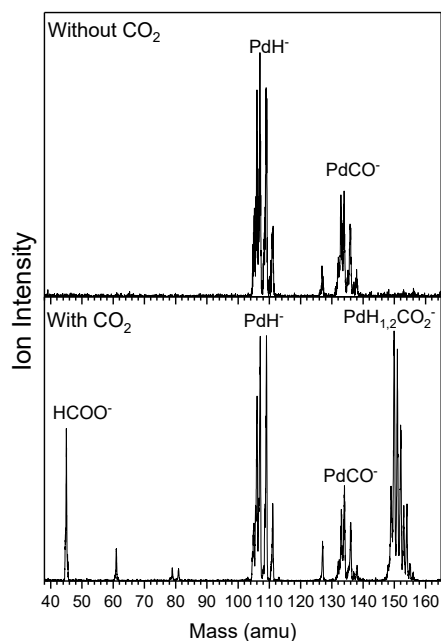


Figure IV.B.1.1 The mass spectra of anions generated by PACIS without (top panel) and with (bottom panel) CO_2 injection into the cell.

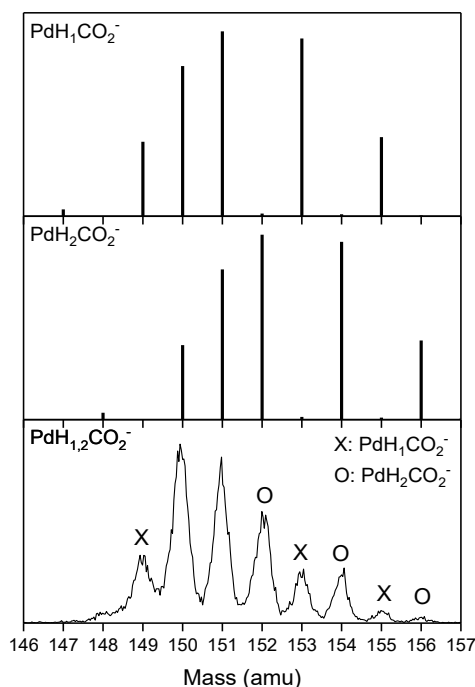


Figure IV.B.1.2 Simulated and experimental mass spectra of PdHCO_2^- and $\text{PdH}_2\text{CO}_2^-$. The peaks marked by a cross indicates peaks consisting of only PdHCO_2^- , while peaks marked with a circle indicates peaks consisting of only $\text{PdH}_2\text{CO}_2^-$.

To characterize this reaction intermediate, we identified the mass peaks that solely consist of $\text{PdH}_1\text{CO}_2^-$ (Figure IV.B.1.2), mass-selected these peaks, and performed negative ion photoelectron spectroscopy on them. The photoelectron spectrum of PdHCO_2^- taken with a 266 nm (4.66 eV) laser is presented in Figure IV.B.1.3. It shows three bands spanning from 1.5 eV to 4.5 eV. Their peak positions, 2.02, 3.34, and 4.41 eV, are respectively assigned as their vertical detachment energies (VDE). The VDE is defined as the photodetachment transition energy at which the Franck–Condon overlap is at its maximum between the anion’s vibrational wave function and that of its neutral counterpart with both in their ground electronic states.

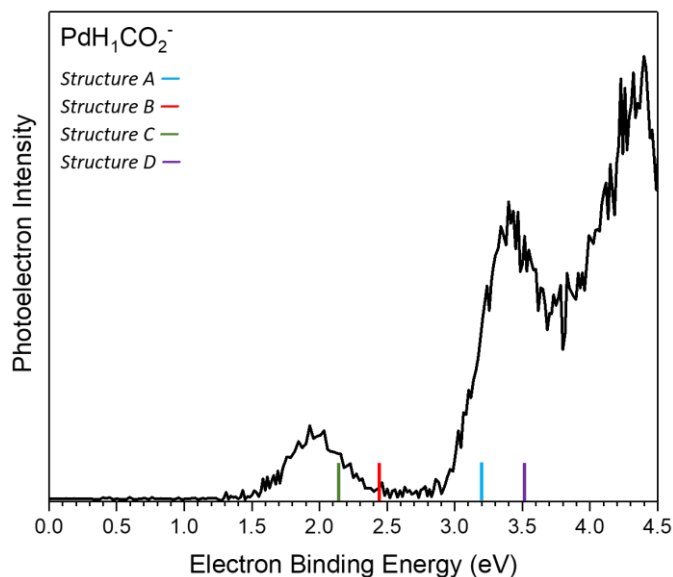


Figure IV.B.1.3 Photoelectron spectrum of PdHCO_2^- measured with 266nm (4.66 eV) photons. The stick spectrum overlay represents the calculated VDE values of the different PdHCO_2^- structures in Figure IV.B.1.4.

Figure IV.B.1.4 presents four calculated structures of PdHCO_2^- that may be made by the reaction between PdH^- and CO_2 . All structures are in their singlet states, while the triplet states are significantly higher in energy. Isomer **A** is the most stable structure. The H atom and the C atom of CO_2 bond with the Pd atom. CO_2 is significantly bent, being activated on the Pd atom. Isomers **B**, **C**, and **D** all have a formate moiety attached to the Pd. They are respectively 0.83 eV, 0.84 eV, and 1.20 eV higher in energy than isomer **A**. Isomers **B** and **C** are two conformers by rotating the longer C–O bond where the oxygen atom connects palladium. The C–H bond lengths in isomer **B** and **C** are both 1.12 Å, close to that of an isolated HCO_2^- anion (1.17 Å). Unlike other isomers which have planar geometries, structure **D** has a small Pd–H– CO_2 dihedral angle of 7.33° . The H atom in structure (isomer) **D** bridges the Pd and the C atoms.

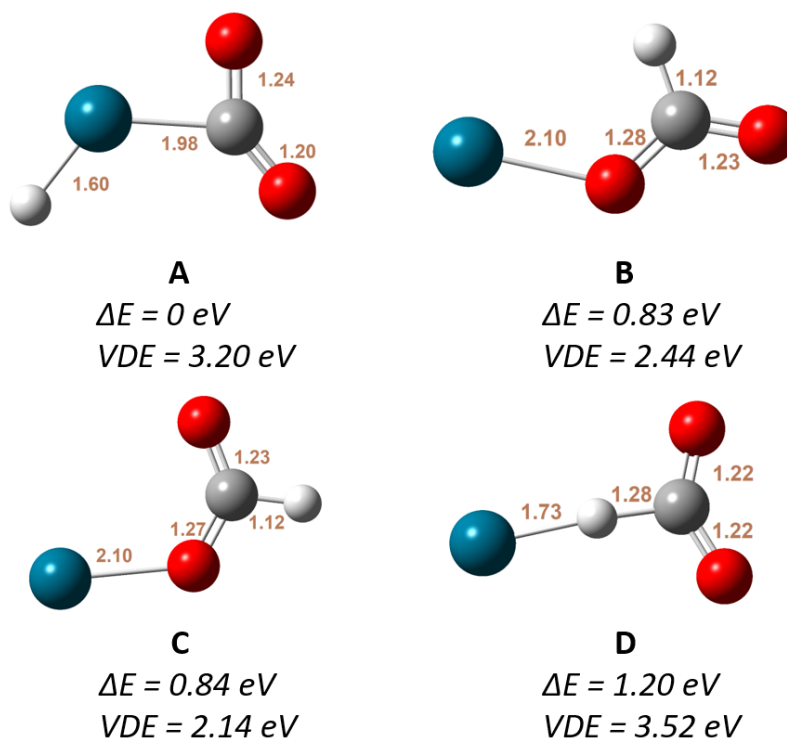


Figure IV.B.1.4 The optimized structures of PdHCO_2^- . The relative energies of PdHCO_2^- and their calculated VDEs are listed below each structure. Bond lengths are also shown in each structure.

To verify the calculated structures, we compare their calculated VDE to the experimental ones. The feature in the low EBE region (1.5 ~ 2.5 eV) of Figure IV.B.1.3 can be attributed to the photodetachment of isomer **B** and **C**. The calculated VDE values of isomers **A** and **D** are 3.20 and 3.52 eV, respectively matching the second band (3.0 ~ 3.7 eV). This band, which peaked at EBE = 3.34 eV, can also originate from a transition between the anion and the neutral excited states of structure **B** (Table S1).

The mechanism of CO_2 hydrogenation by PdH^- was investigated by quantum-chemical calculations. Figure IV.B.1.5 presents the possible reaction pathways for CO_2 activation and hydrogenation by PdH^- . For Path A, the reaction starts with the charge transfer from PdH^- to CO_2 via the interaction between Pd and C, and proceeds to **IT1** (structure **A**). The partial charge on the CO_2 moiety in **IT1** is -0.52 e, indicating that the CO_2 is significantly reduced. This CO_2 activation process is barrierless and exothermic by 1.34 eV. In order for **IT1** to convert CO_2 into formate, the H atom needs go beyond the Pd- CO_2 plane to transfer onto the CO_2 moiety. This is achieved by rotation of the single Pd-C bond that breaks planar geometry and by stretching between the H and C atom to form the Pd-H-C triangle (**TS1**). After overcoming **TS1**, the H atom connects the Pd atom and the CO_2 moiety, forming **IT2** (structure **D**). The barrier

for this step is 1.10 eV. Energetically, **TS1** is lower than **IT2** by 0.1 eV at the CCSD(T) level but 0.04 eV higher at the DFT level. This often indicates a negligible barrier (relative to **IT2**).¹² Rather than via **IT1** and **TS1**, the reaction can also proceed through the direct interaction between the H atom and CO₂ to form **IT2**, i.e. through Path B. This step is exothermic by 0.14 eV. This path represents a direct CO₂ attachment mechanism, which has been found in CO₂ hydrogenation by FeH⁻ and Cu₂H₂⁻.^{12,13} After formation, **IT2** can convert to **IT3** (structure **B**) over a very small barrier (0.01 eV). Therefore, **IT2** can easily reorient itself to **IT1** or **IT3**. As Pd approaches O, breakage of the Pd–H bond contributes to the formation of the formate moiety in intermediate **IT3**. After getting over the rotation barrier of 0.14 eV, **IT3** becomes its conformational isomer **IT4** (structure **C**). The dissociation process of intermediate **IT3/4** into the palladium atom and formate anion is endothermic by 1.05/1.04 eV. Thus, all intermediates and transition states are below the entrance channel, and the complete hydrogenation reaction is endothermic by 0.54 eV above it. This energetics makes the whole reaction accessible under the multi-collision environment in the reaction cell where excess energy is provided by colliding with the fastest-moving H₂ molecules within the Boltzman distribution.^{15,42-44}

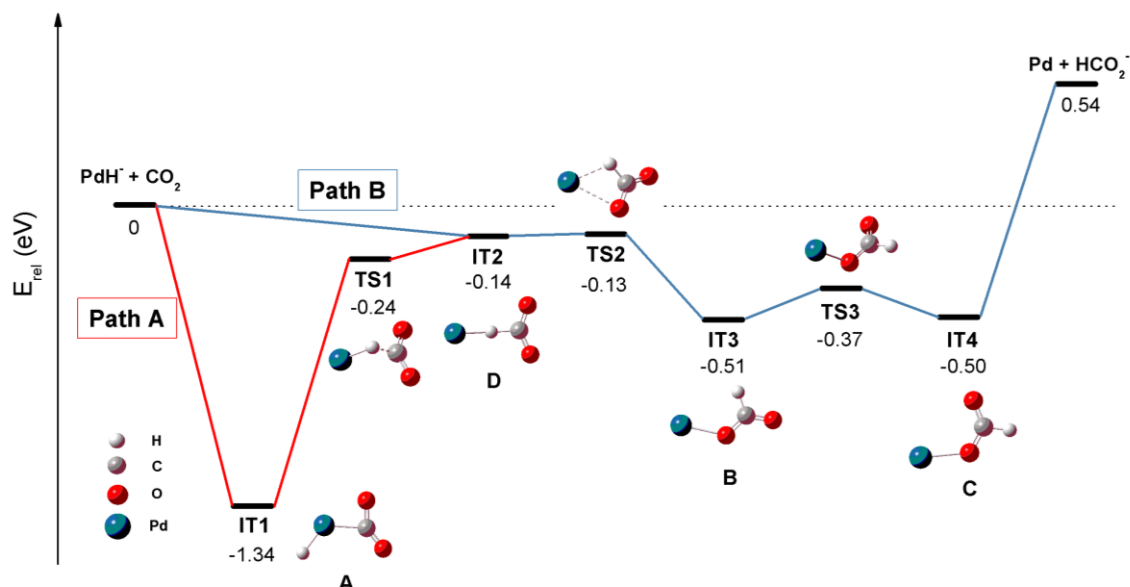


Figure IV.B.1.5 Calculated reaction pathway for CO₂ hydrogenation by PdH⁻. Zero-point energy corrected energies are given in eV. The total energy of isolated PdH⁻ and CO₂ is set at 0 eV.

Figure IV.B.1.6 maps the evolution of natural charges on different atoms/moieties of PdHCO₂⁻. Essentially, it shows that the electron required to reduce the CO₂ molecule comes from the Pd atom. From reactants to **IT1**, the charge on the CO₂ moiety (in blue) plummets by 0.512 e, indicating that CO₂ is activated in the first step of Path A. To the right

of Reactants in Figure IV.B.1.6, i.e., along path B, significant electron transfer (0.629 e) from PdH^- to the CO_2 moiety (in blue) is induced by the direct attachment of CO_2 onto PdH^- . The black line (for Pd) soars from -0.829 to -0.232 e between reactants and **IT2**, which means that the negative charge needed to reduce CO_2 mainly originates from the palladium atom as well. The downhill side of the blue line (CO_2) from Reactants to **IT3** shows that negative charge accumulates on the CO_2 moiety as the reaction proceeds. After surmounting **TS2**, the natural charge on the CO_2 moiety in **IT3** and **IT4** are -0.85 e and -0.84 e, close to the -0.94 e on CO_2 in free formate anion, revealing that CO_2 is fully activated and the hydrogenation process is complete.

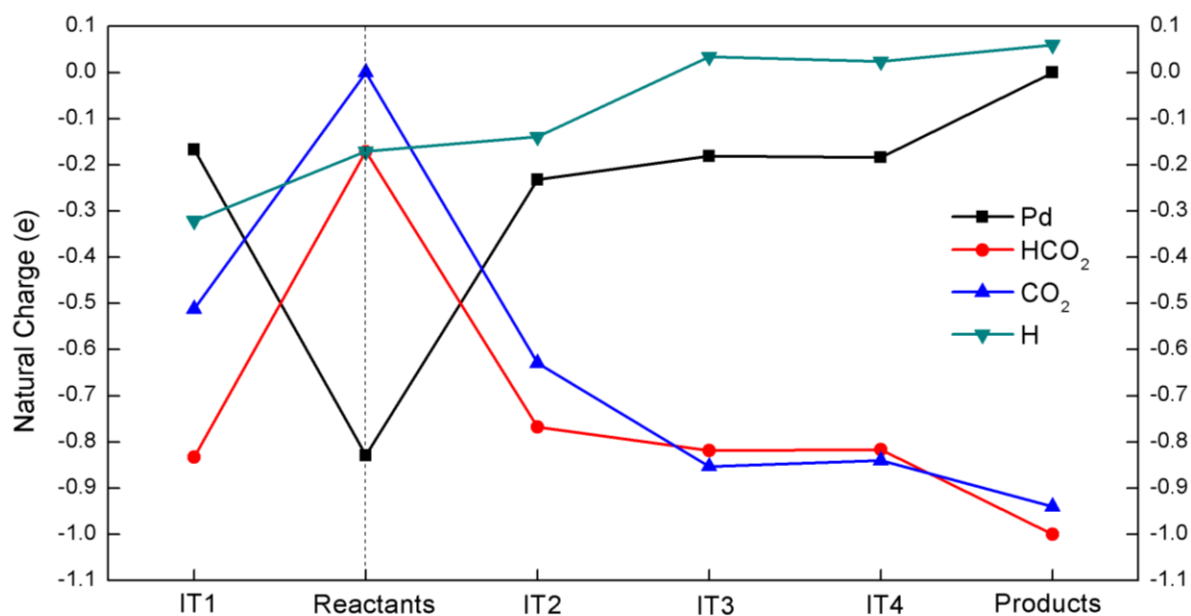


Figure IV.B.1.6 Charges on different moieties of PdHCO_2^- intermediates along the reaction pathway of CO_2 activation by PdH^- .

Additionally, hydride affinities of metal atoms provide a different perspective for the mechanism of CO_2 insertion into the metal–hydrogen bond. Considering the simplest model, M-H , bond dissociation energies (BDE) of Fe-H , Pt-H , and Pd-H are 1.63 eV, 3.44 eV, and 2.44 eV, respectively.⁴⁵⁻⁴⁷ The highest hydride affinity (3.44 eV) may account for the high barrier of CO_2 insertion into the Pt-H bond.¹¹ Moreover, the lower energy barrier of CO_2 insertion into Pd-H (1.10 eV), compared to that of Pt-H (2.84 eV), explains why CO_2 insertion is allowed in the $\text{PdH}^- + \text{CO}_2$ reaction but forbidden in the $\text{PtH}^- + \text{CO}_2$ case. In the case of FeH^- , the direct CO_2 attachment to the H atom dominates as a

result of the low Fe–H bond dissociation energy (1.63 eV). For the $\text{PdH}^- + \text{CO}_2$ reaction, on the other hand, its intermediate Pd–H BDE (2.44 eV) renders possible both an indirect and a direct hydrogenation paths (Paths A and B).

We also investigated the $\text{PdH}_2\text{CO}_2^-$ anion that appeared in the experiment. Figure IV.B.1.7 shows the photoelectron spectrum of $\text{PdH}_2\text{CO}_2^-$ anion measured with 466 nm photons, as well as the lowest-energy structures. Two broad transitions, which peaked at EBE of 3.40 and 4.34 eV, were observed in the spectrum. Thus, the VDE value for $\text{PdH}_2\text{CO}_2^-$ is 3.40 eV. The feature beyond the first peak depicts transitions from ground states of the anions to the electronic excited states of the corresponding neutrals. Optimized isomer **1** and **2** both have PdH and formate moieties, suggesting that $\text{PdH}_2\text{CO}_2^-$ is likely due to the reaction between PdH neutral molecules and formate anions. NBO analysis shows that the net charge on the Pd–H moiety is only -0.16 e in both isomer **1** and **2** structures, this indicating that $\text{PdH}_2\text{CO}_2^-$ is a $[\text{PdH}(\text{COOH})^-]$ adduct. The computed VDE values of isomer **1** and **2** are 3.32 and 3.69 eV, in agreement with the experimental result.

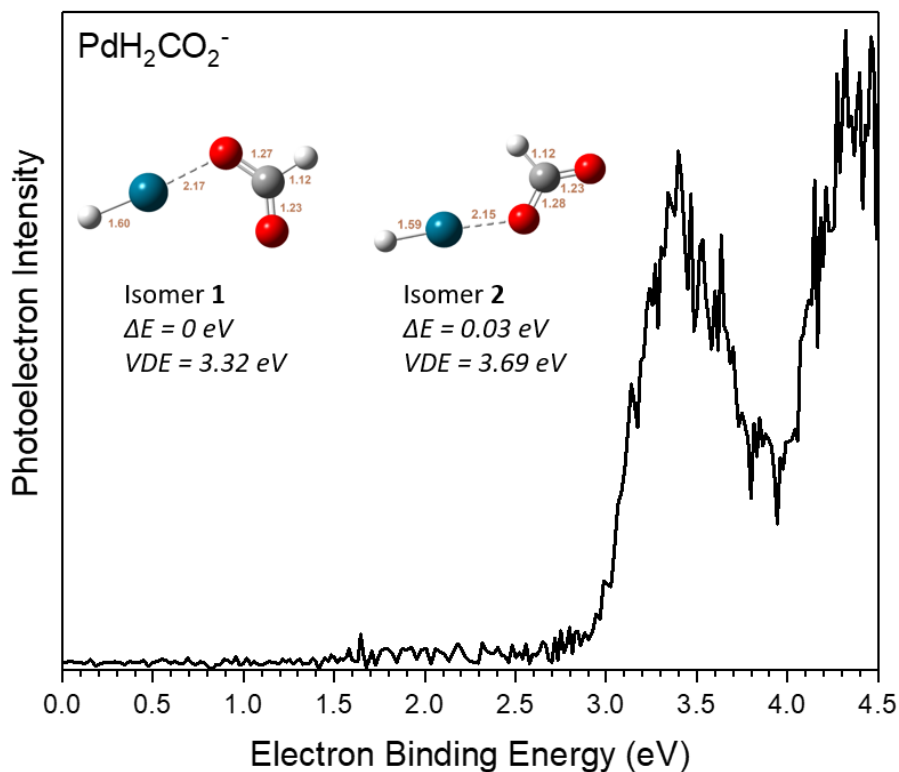


Figure IV.B.1.7 Photoelectron spectrum of $\text{PdH}_2\text{CO}_2^-$ measured with 266nm (4.66 eV) photons. Lowest energy isomeric structures are displayed for each isomer. The relative energies of $\text{PdH}_2\text{CO}_2^-$ and their calculated VDEs are listed below each structure. Bond lengths are also shown in each structure.

Conclusion

We have demonstrated that the activation of CO₂ followed by its hydrogenation can be accomplished in the gas phase by palladium hydride anions. Both the activation intermediate, PdHCO₂⁻, and the hydrogenation product, HCO₂⁻, were observed in the mass spectrum. The combination of anion photoelectron spectroscopy and quantum chemical calculation identified multiple isomers of the PdHCO₂⁻ intermediates. Mechanistic analysis reveals that direct activation of CO₂ through H-C bond formation is barrier-less and leads to the hydrogenated product, HCO₂⁻, while the attachment of CO₂ onto the palladium atom side of PdH⁻ leads to a stable H-Pd-CO₂⁻ structure. Charge analysis shows that the electron needed to activate CO₂ comes from the palladium atom. This work provides molecular-level insight into the nature of CO₂ hydrogenations with metal hydrides, shedding light on the properties of metal-based catalysis in the condensed phase.

References

1. Tang, Q.; Lee, Y.; Li, D.-Y.; Choi, W.; Liu, C. W.; Lee, D.; Jiang, D. Lattice-Hydride Mechanism In Electrocatalytic CO₂ Reduction By Structurally Precise Copper-Hydride Nanoclusters. *J. Am. Chem. Soc.* **2017**, 139, 9728–9736.
2. Zhu, S.; Jiang, B.; Cai, W.; Shao, M. Direct Observation On Reaction Intermediates And The Role Of Bicarbonate Anions In CO₂ Electrochemical Reduction Reaction On Cu Surfaces. *J. Am. Chem. Soc.* **2017**, 139, 15664–15667.
3. Mori, K.; Sano, T.; Kobayashi, H.; Yamashita, H. Surface Engineering Of A Supported Pd_{ag} Catalyst For Hydrogenation Of CO₂ To Formic Acid: Elucidating The Active Pd Atoms In Alloy Nanoparticles. *J. Am. Chem. Soc.* **2018**, 140, 8902–8909.
4. Kato, S.; Matam, S. K.; Kerger, P.; Bernard, L.; Battaglia, C.; Vogel, D.; Rohwerder, M.; Züttel, A. The Origin Of The Catalytic Activity Of A Metal Hydride In CO₂ Reduction. *Angew. Chem., Int. Ed.* **2016**, 55, 6028–6032.
5. Wang, W.; Himeda, Y.; Muckerman, J. T.; Manbeck, G. F.; Fujita, E. CO₂ Hydrogenation To Formate And Methanol As An Alternative To Photo-And Electrochemical CO₂ Reduction. *Chem. Rev.* **2015**, 115, 12936–12973.
6. Green, A. E.; Justen, J.; Schöllkopf, W.; Gentleman, A. S.; Fielicke, A.; Mackenzie, S. R. IR Signature of Size-Selective CO₂ Activation on Small Platinum Cluster Anions, Pt_n⁻ (n= 4–7). *Angew. Chem., Int. Ed.* **2018**, 57, 14822–14826.
7. Liu, G.; Ciborowski, S. M.; Zhu, Z.; Chen, Y.; Zhang, X.; Bowen, K. H. The Metallo-Formate Anions, M(CO₂)⁻, M= Ni, Pd, Pt, Formed By Electron-Induced CO₂ Activation. *Phys. Chem. Chem. Phys.* **2019**, 21, 10955–10960.
8. Liu, G.; Ariyaratna, I.; Ciborowski, S. M.; Zhu, Z.; Miliordos, E.; Bowen, K. H. Simultaneous Functionalization of Methane and Carbon Dioxide Mediated by Single Platinum Atomic Anions. *J. Am. Chem. Soc.* **2020**, 142, 51, 21556–21561.
9. Thompson, M. C.; Ramsay, J.; Weber, J. M. Solvent-Driven Reductive Activation of CO₂ By Bismuth: Switching From Metalloformate Complexes To Oxalate Products. *Angew. Chem., Int. Ed.* **2016**, 55, 15171–15174.
10. Tang, S.; Rijs, N. J.; Li, J.; Schlangen, M.; Schwarz, H. Ligand Controlled CO₂ Activation Mediated by Cationic Titanium Hydride Complexes, [LTiH]⁺ (L= Cp₂, O). *Chem. - Eur. J.* **2015**, 21, 8483–8490.
11. Zhang, X.; Liu, G.; Meiwes-Broer, K.; Gantefor, G.; Bowen, K. CO₂ Activation and Hydrogenation by Pt_{thn}⁻ Cluster Anions. *Angew. Chem., Int. Ed.* **2016**, 55, 9644–9647.
12. Jiang, L.; Zhao, C.; Li, X.; Chen, H.; He, S.-G. Formation of Gas-Phase Formate in Thermal Reactions of Carbon Dioxide with Diatomic Iron Hydride Anions. *Angew. Chem., Int. Ed.* **2017**, 56, 4187–4191.
13. Liu, Y.-Z.; Jiang, L.-X.; Li, X.-N.; Wang, L.-N.; Chen, J.-J.; He, S.-G. Gas-Phase Reactions Of Carbon Dioxide with Copper Hydride Anions Cu₂H₂⁻: Temperature-Dependent Transformation. *J. Phys. Chem. C* **2018**, 122, 19379–19384.

14. Pascher, T. F.; Oncak, M.; van der Linde, C.; Beyer, M. K. Release of Formic Acid from Copper Formate: Hydride, Proton-Coupled Electron and Hydrogen Atom Transfer All Play their Role. *ChemPhysChem* **2019**, 20, 1420–1424.
15. Liu, G.; Poths, P.; Zhang, X.; Zhu, Z.; Marshall, M.; Blankenhorn, M.; Alexandrova, A. N.; Bowen, K. H. CO₂ Hydrogenation to Formate and Formic Acid by Bimetallic Palladium–Copper Hydride Clusters. *J. Am. Chem. Soc.* **2020**, 142(17), 7930–7936.
16. McMahon, A. J.; Jarrold, C. C. Using Anion Photoelectron Spectroscopy of Cluster Models to Gain Insights Into Mechanisms Of Catalyst-Mediated H₂ Production From Water. *Phys. Chem. Chem. Phys.* **2020**, 10 <https://doi.org/10.1039/D0CP05055E>
17. Song, H.; Zhang, N.; Zhong, C.; Liu, Z.; Xiao, M.; Gai, H. Hydrogenation of CO₂ into Formic Acid Using a Palladium Catalyst on Chitin. *New J. Chem.* **2017**, 41(17), 9170–9177.
18. Qian, C.; Sun, W.; Hung, D. L.; Qiu, C.; Makaremi, M.; Kumar, S. G. H.; Wan, L.; Ghossoub, M.; Wood, T. E.; Xia, M., et al. Catalytic CO₂ Reduction by Palladium-Decorated Silicon–Hydride Nanosheets. *Nat. Catal.* **2019**, 2(1), 46–54.
19. Li, N.; Liu, M.; Yang, B.; Shu, W.; Shen, Q.; Liu, M.; Zhou, J. Enhanced Photocatalytic Performance Toward CO₂ Hydrogenation over Nanosized TiO₂-Loaded Pd under UV Irradiation. *J. Phys. Chem. C* **2017**, 121(5), 2923–2932.
20. Ma, Y.; Ren, Y.; Zhou, Y.; Liu, W.; Baaziz, W.; Ersen, O.; Pham-Huu, C.; Greiner, M.; Chu, W.; et al. High-Density and Thermally Stable Palladium Single-Atom Catalysts for Chemoselective Hydrogenations. *Angew. Chem., Int. Ed.* **2020**, 59, 21613–21619.
21. Gerhards, M.; Thomas, O. C.; Nilles, J. M.; Zheng, W.-J.; Bowen, K. H. Cobalt–Benzene Cluster Anions: Mass Spectrometry and Negative Ion Photoelectron Spectroscopy. *J. Chem. Phys.* **2002**, 116, 10247.
22. Ho, J.; Ervin, K. M.; Lineberger, W. C. Photoelectron Spectroscopy of Metal Cluster Anions: Cu–N, Ag–N, and Au–N. *J. Chem. Phys.* **1990**, 93, 6987.
23. Zhang, X.; Liu, G.; Ganteför, G.; Bowen, K. H.; Alexandrova, A. N. PtZnH₅[−], a σ-aromatic Cluster. *J. Phys. Chem. Lett.* **2014**, 5, 1596–1601.
24. Zhang, X.; Robinson, P. J.; Ganteför, G.; Alexandrova, A. N.; Bowen, K. H. Photoelectron Spectroscopic and Theoretical Study of the [HPd(η²-H₂)][−] Cluster Anion. *J. Chem. Phys.* **2015**, 143(9), 094307.
25. Frisch, M. J.; Trucks, G. W.; Schlegel, H. B.; Scuseria, G. E.; Robb, M. A.; Cheeseman, J. R.; Scalmani, G.; Barone, V.; Mennucci, B.; Petersson, G. A.; et al. *Gaussian 09*, Revision D.01; Gaussian, Inc.: Wallingford, CT, 2013.
26. Lee, C. T.; Yang, W. T.; Parr, R. G. Development of the ColleSalvetti Correlation–Energy Formula into a Functional of the Electron Density. *Phys. Rev. B* **1988**, 37, 785–789.
27. Becke, A. D. Density–Functional Exchange–Energy Approximation with Correct Asymptotic–Behavior. *Phys. Rev. A* **1988**, 38, 3098–3100.
28. Becke, A. D. Density–Functional Thermochemistry. III. The Role of Exact Exchange. *J. Chem. Phys.* **1993**, 98, 5648–5652.
29. Grimme, S.; Antony, J.; Ehrlich, S.; Krieg, H. A Consistent and Accurate Ab Initio Parametrization of Density Functional Dispersion Correction (DFT–D) for the 94 Elements H–Pu. *J. Chem. Phys.* **2010**, 132(15), 154104.
30. Raghavachari, K.; Trucks, G. W.; Pople, J. A.; Head–Gordon, M. A Fifth–Order Perturbation Comparison of Electron Correlation Theories. *Chem. Phys. Lett.* **1989**, 157(6), 479–483.
31. Glendening, E. D.; Reed, A. E.; Carpenter, J. E.; Weinhold, F. NBO Version 3.1, **1998**.
32. Wang, H.; Zhang, X.; Ko, Y. J.; Grubisic, A.; Li, X.; Ganteför, G.; Schnöckel, H.; Eichhorn, B. W.; Lee, M. S.; Jena, P.; et al. Aluminum Zintl Anion Moieties Within Sodium Aluminum Clusters. *J. Chem. Phys.* **2014**, 140, 054301.
33. Wang, H.; Jae Ko, Y.; Zhang, X.; Ganteför, G.; Schnöckel, H.; Eichhorn, B. W.; Jena, P.; Kiran, B.; Kandalam, A. K.; Bowen, K. H. The Viability of Aluminum Zintl Anion Moieties Within Magnesium–Aluminum Clusters. *J. Chem. Phys.* **2014**, 140, 124309.
34. Gonzalez, C.; Schlegel, H. B. An Improved Algorithm for Reaction–Path Following. *J. Chem. Phys.* **1989**, 90, 2154–2161.
35. Gonzalez, C.; Schlegel, H. B. Reaction–Path Following in Mass–Weighted Internal Coordinates. *J. Phys. Chem.* **1990**, 94, 5523–5527.
36. Peterson, K. A.; Figgen, D.; Dolg, M.; Stoll, H. Energy–Consistent Relativistic Pseudopotentials and Correlation Consistent Basis Sets for the 4d Elements Y–Pd. *J. Chem. Phys.* **2007**, 126(12), 124101.
37. Dunning, T. H. Gaussian Basis Sets for Use in Correlated Molecular Calculations. I. The Atoms Boron Through Neon and Hydrogen. *J. Chem. Phys.* **1989**, 90(2), 1007–1023.

38. De Jong, W. A.; Harrison, R. J.; Dixon, D. A. Parallel Douglas–Kroll Energy and Gradients in Nwchem: Estimating Scalar Relativistic Effects Using Douglas–Kroll Contracted Basis Sets. *J. Chem. Phys.* **2001**, 114(1), 48–53.
39. Kendall, R. A.; Dunning, T. H.; Harrison, R. J. Electron Affinities of the First-Row Atoms Revisited. Systematic Basis Sets and Wave Functions. *J. Chem. Phys.* **1992**, 96(9), 6796–6806.
40. Douglas, M.; Kroll, N. M. Quantum Electrodynamical Corrections to the Fine Structure of Helium. *Ann. Phys.* **1974**, 82, 89.
41. Reiher, M.; Wolf, A. Exact Decoupling of the Dirac Hamiltonian. II. The Generalized Douglas-Kroll-Hess Transformation up to Arbitrary Order *J. Chem. Phys.* **2004**, 121, 10945.
42. Liu, G.; Zhu, Z.; Ciborowski, S. M.; Ariyaratna, I. R.; Miliordos, E.; Bowen, K. H. Selective Activation of the C–H Bond in Methane by Single Platinum Atomic Anions. *Angew. Chem., Int. Ed.* **2019**, 58, 7773–7777;
43. Liu, G.; Ciborowski, S.; Bowen, K. H. Photoelectron Spectroscopic and Computational Study of Pyridine-Ligated Gold Cluster Anions. *J. Phys. Chem. A* **2017**, 121, 5817–5822.
44. Liu, G.; Miliordos, E.; Ciborowski, S. M.; Tschurl, M.; UBoesl, U.; Heiz, U.; Zhang, X.; Xantheas, S. S.; Bowen, K. H. Communication: Water activation and splitting by single metal-atom anions. *J. Chem. Phys.* **2018**, 149(22), 221101.
45. Schultz, R. H.; Armentrout, P. B. The Gas-Phase Thermochemistry of FeH. *J. Chem. Phys.* **1991**, 94(3), 2262–2268.
46. McCarthy, M. C.; Field, R. W.; Engleman, R.; Bernath, P. F. Laser and Fourier transform spectroscopy of PtH and PtD. *J. Mol. Spectrosc.* **1993**, 158(1), 208–236.
47. Tolbert, M. A.; Beauchamp, J. L. Homolytic And Heterolytic Bond Dissociation Energies of the Second Row Group 8, 9, and 10 Diatomic Transition–Metal Hydrides: Correlation With Electronic Structure. *J. Chem. Phys.* **1986**, 90(21), 5015–5022.

IV.B.2. CO₂ Hydrogenation to Formate and Formic Acid by Bimetallic Palladium-Copper Hydride Clusters

Reprinted (adapted) with permission from *J. Am. Chem. Soc.*, **142**, 7930–7936 (2020) Copyright 2020 American Chemical Society.

Gaoxiang Liu^[a], Patricia Poths^[b], Xinxing Zhang^[a], Zhaoguo Zhu^[a], Mary Marshall^[a], Moritz Blankenhorn^[a], Anastassia N. Alexandrova^{*[b]} and Kit H. Bowen^{*[a]}

[a] Department of Chemistry, Johns Hopkins University, 3400 N Charles St, Baltimore, MD, 21218, E-mail: kbowen@jhu.edu

[b] Department of Chemistry and Biochemistry, University of California, Los Angeles, 605 Charles E. Young Drive, Los Angeles, CA 90095-1569 (USA), E-mail: ana@chem.ucla.edu

Abstract: Mass spectrometric analysis of the anionic products of interaction between bimetallic palladium-copper tetrahydride anions, PdCuH₄[−], and carbon dioxide, CO₂, in a reaction cell shows an efficient generation of the PdCuCO₂H₄[−] intermediate and formate/formic acid complexes. Multiple structures of PdCuH₄[−] and PdCuCO₂H₄[−] are identified by a synergy between anion photoelectron spectroscopy and quantum chemical calculations. The higher energy PdCuH₄[−] isomer is shown to drive the catalytic hydrogenation of CO₂, emphasizing the importance of accounting for higher energy isomers for cluster catalytic activity. This study represents the first example of CO₂ hydrogenation by bimetallic hydride clusters.

Introduction

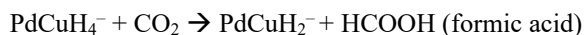
Transforming CO₂ into reduced, value-added molecules is of great interest for environmental and economic reasons. For catalytic CO₂ functionalization, bimetallic catalysts have shown improved activity and selectivity over single-component ones, as lattice engineering can be utilized to tailor the surface and electronic structures of bimetallic catalysts and thus to regulate their performance.^[1–4] The rational design of high-efficiency bimetallic catalysts demands mechanistic understanding of how the catalytic CO₂ transformation processes on the active sites. While it is well-established that the formation of metal hydrides and the insertion of CO₂ into the metal-hydrogen bond are the critical steps in CO₂ hydrogenation, comprehensive knowledge about them remains limited due to a lack of direct experimental characterization on these key reaction intermediates.^[5–9] In particular, it is less clear how the interplay between different metals can alter catalyst properties, including hydrogen and CO₂ binding sites, electronic structures, charge transfer property, and release of products, all of which influence catalytic performance.

Synergy between the experimental characterization of reaction intermediates and state-of-the-art quantum chemistry calculations enables the gas-phase studies of CO₂ reduction and hydrogenation to provide mechanistic insight into

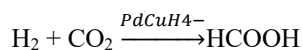
CO₂ functionalization at the molecular level.^[10-18] While single metal hydrides (e.g. Cp₂TiH⁺,^[14] PtH₃⁻,^[15] FeH⁻,^[16] and Cu_{1.2}H₂⁻^[17,18]) can convert CO₂ into formate and formate complexes, we are not aware of utilizing bimetallic hydrides for CO₂ hydrogenation. The present work focuses on the hydrogenation of CO₂ via reaction with the anionic bimetallic palladium-copper tetra-hydride cluster, PdCuH₄⁻. We selected the palladium-copper hydride because its reaction with CO₂ is an ideal model for understanding the hydrogenation process over bimetallic palladium-copper catalysts, which have shown superior CO₂ hydrogenation activity compared to single-component palladium or copper catalysts.^[19-23] We show that a metastable PdCuH₄⁻ isomer catalytically converts CO₂ to formic acid, in-line with recent theoretical predictions reporting catalysis on fluxional clusters can be driven by less stable but more active cluster isomers accessible in reaction conditions^[24-30].

Results and Discussion

PdCuH₄⁻ was prepared in a pulsed arc cluster ionization source (PACIS), which has been applied to generate various metal hydrides^[31,32]. Briefly, a ~30 μs duration, ultra-high voltage and current discharge was used to vaporize Pd and Cu powders. Almost simultaneously, high-pressure hydrogen gas was injected into the discharge region. The resulting mixture of atoms, ions, and electrons reacted to form PdCuH₄⁻, which was then collisionally cooled and carried downstream by the supersonically-expanding hydrogen gas to interact with CO₂ in a reaction cell^[15,33,34]. The resultant anionic products were identified by time-of-flight mass spectrometry. Figure IV.B.2.1 presents mass spectra with or without CO₂. With no CO₂ in the reaction cell, we observed the mass series of PdCuH₄⁻ (Figure IV.B.2.1A), and its match with the simulated isotopic pattern confirms PdCuH₄⁻ as the only palladium-copper hydride formed under our experimental conditions (Figure IV.B.2.1B). When CO₂ was added to the reaction cell, prominent mass series appeared at masses both higher and lower than PdCuH₄⁻ (Figure IV.B.2.1C). The higher-mass series is the reaction intermediate PdCuCO₂H₄⁻, which were identified by comparing the experimental and simulated isotopic patterns (Figure IV.B.2.1D). The lower-mass peaks are formate- and formic acid-containing anionic clusters. The tagging of formic acid to anionic formate made possible observation of this neutral molecule by mass spectrometry. The high summed intensity of formate and formic acid products indicates that PdCuH₄⁻ hydrogenates CO₂ efficiently. Note that the observation of formic acid suggests the reaction



yet PdCuH_2^- or other palladium-copper hydrides were absent after PdCuH_4^- reacted with CO_2 . This implies regeneration of PdCuH_4^- via H_2 absorption to PdCuH_2^- . Therefore, we proposed that the catalytic reaction



had occurred under our experimental conditions.

We then applied anion photoelectron spectroscopy to characterize PdCuH_4^- and $\text{PdCuCO}_2\text{H}_4^-$ (Figure IV.B.2.1). For PdCuH_4^- , two electron binding energy (EBE) peaks at 3.36 and 3.83 eV are assigned as the vertical detachment energies (VDE). The VDE is defined as the photodetachment transition energy at which the Franck-Condon overlap is at its maximum between the anion's vibrational wave function and that of its neutral counterpart with both in their ground electronic states. For $\text{PdCuCO}_2\text{H}_4^-$, its VDE values are 2.49, 3.93, and 4.40 eV.

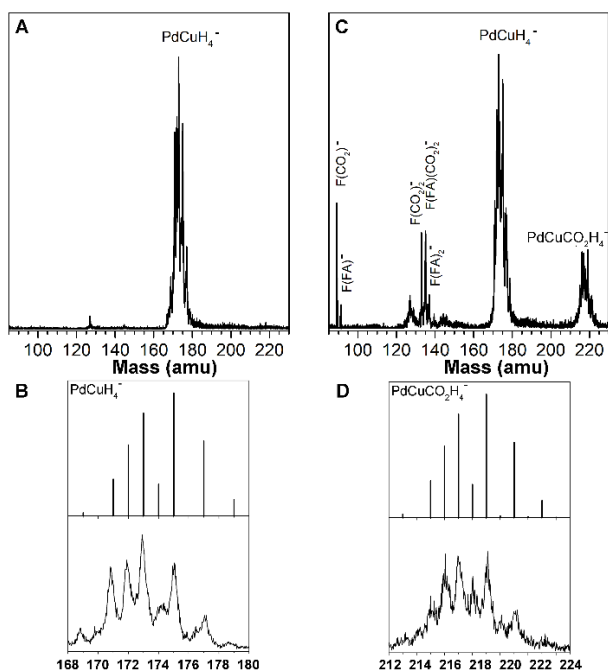


Figure IV.B.2.1 (A) The mass spectrum of PdCuH_4^- cluster anions. (B) Simulated and experimental mass spectra of PdCuH_4^- . (C) Mass spectrum of PdCuH_4^- reacting with CO_2 . (D) Simulated and experimental mass spectra of $\text{PdCuCO}_2\text{H}_4^-$. *F* indicates formate. *FA* indicates formic acid.

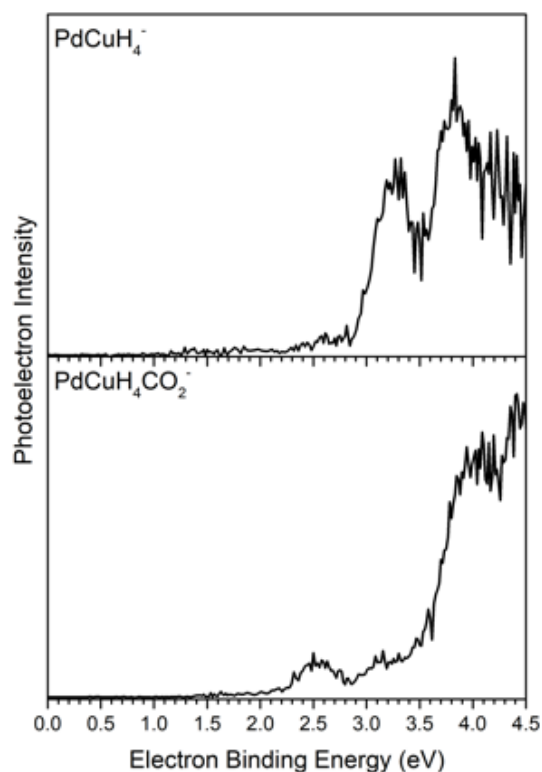


Figure IV.B.2.2 Photoelectron spectra of PdCuH_4^- (A) and $\text{PdCuCO}_2\text{H}_4^-$ (B) measured with 266 nm (4.66 eV) photons.

Figure IV.B.2.3 shows the calculated structures that are confirmed to account for the experimentally measured PES. Structure **A** and **B** are two low energy PdCuH_4^- isomers, the latter 0.46 eV higher in energy. These two structures differ only in location of one H atom – both have the same low spin state (multiplicity 1). Based on the similar charges on the metal centers across both structures, it does not appear that there is a significant change in the formal oxidation state of each metal between A and B. Structures **C**, **D**, and **E** are isomers of $\text{PdCuCO}_2\text{H}_4^-$ derived from CO_2 reacting with **A** and **B**. In structure **C**, CO_2 is inserted into the Cu-H bond of structure **A**. Structure **D**, on the other hand, is obtained by CO_2 association with the Pd and H atoms in structure **B**. Both structure **C** and **D** have a formate moiety, the latter 0.92 eV higher in energy. For structure **D**, the H atom that bridges Pd and Cu atoms can further transfer to the formate moiety, forming structure **E** with a formic acid moiety. The dissociation of structure **E** into formic acid and PdCuH_2^- , which is structure **F**, may explain the observation of formic acid in the experiment. All structures are in

their respective low-spin states. Based on the atomic charges of all of the structures, it appears that both Pd and Cu are in their 0 oxidation state throughout. The H ligands instead experience the most significant changes in charge.

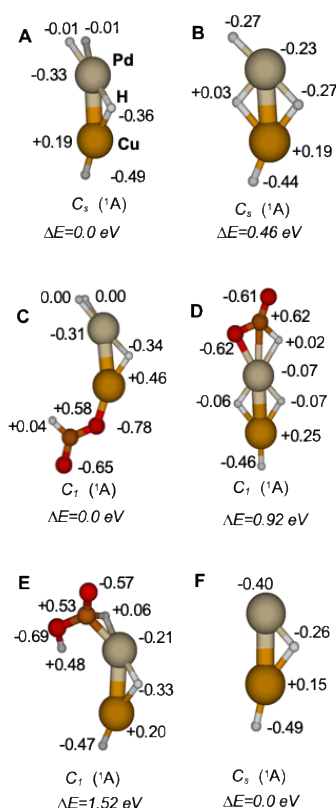


Figure IV.B.2.3 The calculated relevant lowest energy structures of PdCuH₄⁻ (A and B), PdCuCO₂H₄⁻ (C, D, and E), and PdCuH₂⁻ (F). Symmetry, spectroscopic label, and energy relative to the global minimum structure of the same stoichiometry are shown below each structure. The charge on each atom is also shown.

The verification of these calculated structures was accomplished by calculating their VDEs at the CCSD//UPBEPBE/aug-cc-pvtz+pp level of theory and comparing with the experimental values (Table IV.B.2.1). For PdCuH₄⁻, structure **A** and **B** respectively match the higher and the lower EBE feature in the experimental photoelectron spectrum. For the PdCuCO₂H₄⁻ spectrum, the feature at 4.40 eV is attributable

to structure **C**, and the feature at 3.93 eV is due to photodetachment of structure **E**. The feature at 2.49 eV does not match the calculated VDE of any PdCuCO₂H₄⁻ structure. Instead, it agrees with the calculated VDE of structure **F**. This suggests that during photodetachment, PdCuCO₂H₄⁻ was also photodissociated into PdCuH₂⁻ (structure **F**) and formic acid. The dissociation product PdCuH₂⁻ was subsequently photodetached, contributing the 2.49 eV feature in

the $\text{PdCuCO}_2\text{H}_4^-$ spectrum. This photodissociation/photodetachment phenomenon has been observed in our previous photodetachment experiment on anionic metal-hydride- CO_2 adducts.^[15] Structure **D** should be present despite having a calculated VDE beyond the range of the photodetachment laser, as structure **E** is derived from it. Therefore, the two PdCuH_4^- and three $\text{PdCuCO}_2\text{H}_4^-$ isomers were all observed experimentally. The high-energy environment in PACIS enables the formation of PdCuH_4^- clusters with different energies,^[35] which were subsequently cooled to their ground electronic states before interacting with CO_2 .

Table IV.B.2.1 Computed VDEs for each structure from Figure IV.B.2.3 and their corresponding experimental values.

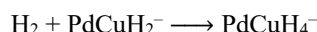
All VDE values are given in eV.

	PdCuH_4^-		$\text{PdCuCO}_2\text{H}_4^-$			PdCuH_2^-
Structure	A	B	C	D	E	F
Expt. VDE	3.83	3.36	4.40	N/A ^[a]	3.93	2.49
Calc. VDE	3.71	3.51	4.36	5.44	3.79	2.25

[a] This structure's EBE is higher than the photon energy of the photodetachment laser.

The observation of two isomers of PdCuH_4^- and their respective CO_2 insertion complexes suggests two reaction mechanisms beginning from structures **A** and **B**. Figure IV.B.2.4 presents the two calculated reaction pathways. The pathway in red is initiated by structure **A**, while the pathway in blue starts with structure **B**. When structure **A** interacts with CO_2 , CO_2 inserts into its Cu-H bond barrierlessly, forming structure **C**. This insertion step is exothermic by 1.32 eV. Structure **C**, however, is a very stable adduct, as seen by the high energy required for it to release formate as the product. The high dissociation energy of 2.38 eV according to calculations, is unlikely to occur under the multi-collision conditions in the reaction cell. Therefore, it is unlikely that the formate observed in the experiment formed via this mechanism. The reaction starting from structure **B**, on the other hand, proceeds on a smoother potential energy surface. Upon interaction, CO_2 is associated with the Pd and H atoms to form structure **D**. The transition from structure **B** to **D** is also barrierless. An H atom that bridges the Pd and Cu atoms in structure **D** subsequently transfers to the

formate moiety, forming structure **E**, with an activation barrier 0.95 eV above structure **D** or 0.09 eV above the entrance channel. The dissociation of structure **E** into PdCuH_2^- and formic acid is endothermic by 0.80 eV. Therefore, all steps on the structure **B** initiated pathway are within 0.5 eV of the entrance channel energy, making them accessible under the experimental conditions where excess energy is provided via multi-collisions with the fast-moving H_2 molecules.^[36,37] The released formic acid can deprotonate to yield formate. As mentioned earlier, the reaction does not stop at the PdCuH_2^- ion; there is no evidence of it in the mass spectrum, suggesting that in the presence of abundant H_2 in the reaction cell, the following reaction takes place:



This reaction is 0.87 eV exothermic if forming structure **A**, or 0.41 eV exothermic if leading to structure **B**. Thus, the H_2 environment readily regenerates the PdCuH_4^- clusters, completing the catalytic cycle.

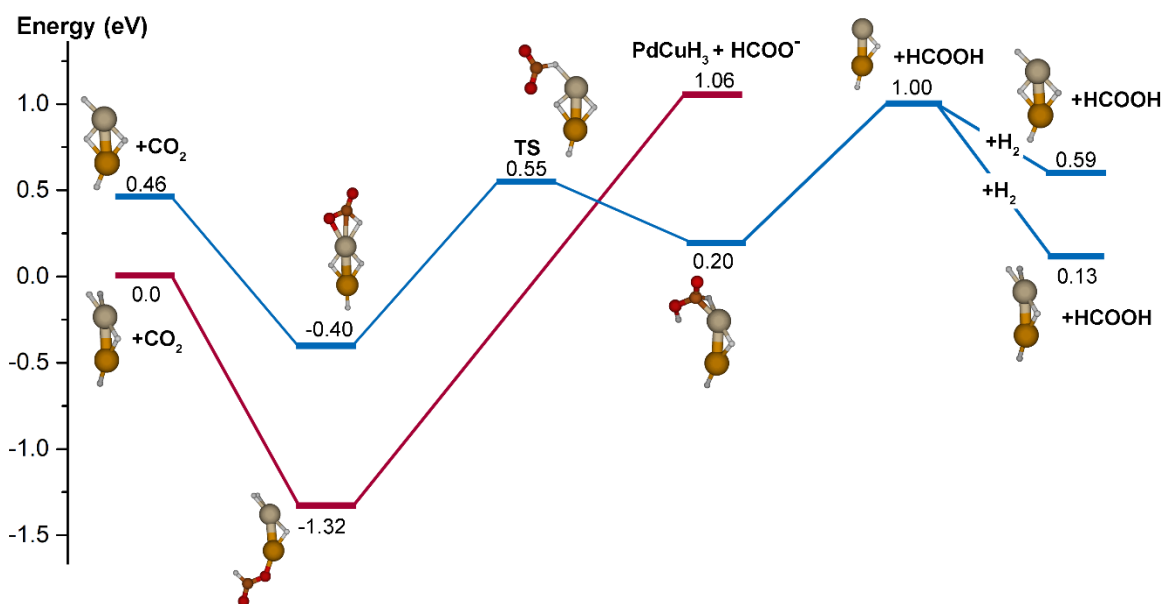


Figure IV.B.2.4 Profile for the reaction of CO_2 with PdCuH_4^- . Zero-point energy corrected energies are given in eV.

0 eV is set as the total energy of structure **A** and an isolated CO_2 .

Compared to Cu, Pd is stronger in binding H but weaker in binding O.^[5] Therefore, the structure with more H binding to Pd is more stable. Since structure **A** has one H atom that binds exclusively to Pd rather than both Pd and Cu, it is lower in energy than structure **B**. For structure **A**, however, the binding of more H exclusively to Pd inhibits the binding of CO_2 on Pd.^[38] Instead, CO_2 inserts into the Cu-H bond, forming the strong Cu-O bond (structure **C**). The high dissociation energy of the Cu-O bond prevents the release of formate product, ending this pathway in a “catalytic

deadlock”. In structure **B**, Pd is more exposed while Cu is more coordinated, which facilitates the initial CO₂ binding to the Pd atom. Since Pd has weak O binding, the formic acid moiety associates with Pd via Pd-C and Pd-H interactions, as shown in structure **E**. Dissociation of the formic acid product is thus much less endothermic with this reaction pathway. Also importantly, the Pd site becomes exposed after releasing the formic acid, and can readily absorb an H₂ molecule to complete the catalytic cycle. This result echoes recent reports emphasizing the metastable structures as the actual active sites in cluster catalysis.^[28]

The charge analysis can further rationalize the different reactivity of the two PdCuH₄⁻ clusters (Figure IV.B.2.3). The calculated atomic charges show a difference in the charge distributions in CO₂ bound to structures **A** and **B**. When CO₂ is bound to Cu, as in structure **C**, the charge difference between Cu and the formate fragment is more significant than the analogous charge difference between Pd and the formate fragment. Furthermore, Cu is positively charged, while Pd is negatively charged, so the formate moiety interacts more strongly with Cu.

Conclusions

To summarize, we have demonstrated that the bimetallic PdCuH₄⁻ clusters can convert CO₂ into formate and formic acid. Mass spectrometric analysis of the reaction products between PdCuH₄⁻ and CO₂ reveals the reaction intermediate PdCuCO₂H₄⁻, the reaction products formate and formic acid, and the regeneration of PdCuH₄⁻, completing the catalytic cycle. Different isomers of PdCuH₄⁻ and PdCuCO₂H₄⁻ are identified by anion photoelectron spectroscopy and electronic structure calculations. Mechanistic study confirms that metastable structures as the catalytic driving force. This work represents the first example of CO₂ hydrogenation by bimetallic hydride clusters, providing insight into understanding the catalytic properties of bimetallic catalysts.

Methods

Experimental Methods

The experimental technique, anion photoelectron spectroscopy, is conducted by crossing a mass-selected beam of negative ions with a fixed-energy photon beam and energy analyzing the resulting photodetached electrons. This technique is governed by the energy-conservation relationship, $h\nu = \text{EBE} + \text{EKE}$, where $h\nu$, EBE, and EKE are the photon energy, electron binding (transition) energy, and the electron kinetic energy, respectively. Our photoelectron spectrometer, which has been described previously,^[39] consists of one of several ion sources, a linear time-of-flight (TOF) mass spectrometer, a mass gate, a momentum decelerator, a neodymium-doped yttrium aluminum garnet

(Nd:YAG) laser for photodetachment, and a magnetic bottle electron energy analyzer. Photoelectron spectra were calibrated against the well-known photoelectron spectrum of Cu^- . The PdCuH_4^- anions were generated using a pulsed-arc (discharge) cluster ionization source (PACIS), which has been described in detail elsewhere.^[40] This cluster anion source has been used to generate a variety of transition metal hydride cluster anions.^[32, 41-43] It provided us with a broad range of cluster sizes and compositions. During PACIS operation, a 30 μs long, ~ 4000 volt electrical pulse applied across the anode and the mixed Pd/Cu pressed-powder cathode in the discharge chamber vaporizes the Pd and Cu atoms. Almost simultaneously with the discharge, 180 psi of ultrahigh purity hydrogen gas was injected into the discharge region, where it was dissociated into hydrogen atoms. The resulting mixture of atoms, ions, and electrons then reacted and cooled as it expanded through the PACIS housing. After a small gap, this flow then continued through a 15 cm long collision/reactor cell before exiting into high vacuum. To initiate the reaction between CO_2 and PdCuH_4^- , pure CO_2 was injected into the collision cell using a second pulsed valve. The resultant anions then drifted through a skimmer, through a differentially pumped region, and into the TOF region, where they were perpendicularly extracted and mass-selected prior to photodetachment. Due to palladium's and copper's isotope patterns and the presence of multiple hydrogen atoms, photoelectron spectra were taken at all observed mass peaks.

Computational Methods

The calculated structures presented in this work were computed using density functional theory (DFT), using the PBEPBE^[44] functional in Gaussian16^[45]. The initial structure search was performed using the LANL2DZ^[46-48] basis set, after which the lowest energy structures were further optimized using the aug-cc-pvtz+pp^[49] basis set. After geometry optimization, the energies of the anionic and neutral clusters were calculated at the CCSD^[50-53]//UPBE level to determine the vertical detachment energies (VDE) for each structure for comparison with experimental PES results. CASSCF (m,n)^[54-62] up to (14,14) was run to verify the accuracy of the single reference method. CCSD//UPBE was used rather than TD-DFT for VDE calculations due to the unreliability of the result as the functional was changed, and CCSD(T) was not used as perturbation theory failed for some structures. Only the first VDE was calculated for each structure- if there are VDE2+ peaks present in the spectrum they are not accounted for, but all peaks present in the experimental spectrum have corresponding computed VDEs. Charges on each atom were calculated using natural population analysis^[63].

References

- [1] Gilroy, K. D.; Ruditskiy, A.; Peng, H.-C.; Qin, D.; Xia, Y. Bimetallic nanocrystals: syntheses, properties, and applications. *Chem. Rev.* **2016**, *116* (18), 10414.
- [2] Kim, D.; Xie, C.; Becknell, N.; Yu, Y.; Karamad, M.; Chan, K.; Crumlin, E. J.; Nørskov, J. K.; Yang, P. Electrochemical activation of CO₂ through atomic ordering transformations of AuCu nanoparticles. *J. Am. Chem. Soc.* **2017**, *139*, 8329–8336.
- [3] Mori, K.; Sano, T.; Kobayashi, H.; Yamashita, H. Surface engineering of a supported PdAg catalyst for hydrogenation of CO₂ to formic acid: elucidating the active Pd atoms in alloy nanoparticles. *J. Am. Chem. Soc.* **2018**, *140*, 8902–8909.
- [4] Vasileff, A.; Xu, C.; Jiao, Y.; Zheng, Y.; Qiao, S.-Z. Surface and interface engineering in copper-based bimetallic materials for selective CO₂ electroreduction. *Chem* **2018**, *4*, 1809–1831.
- [5] Tang, Q.; Lee, Y.; Li, D.-Y.; Choi, W.; Liu, C. W.; Lee, D.; Jiang, D. Lattice-hydride mechanism in electrocatalytic CO₂ reduction by structurally precise copper-hydride nanoclusters. *J. Am. Chem. Soc.* **2017**, *139*, 9728–9736.
- [6] Zhu, S.; Jiang, B.; Cai, W.; Shao, M. Direct observation on reaction intermediates and the role of bicarbonate anions in CO₂ electrochemical reduction reaction on Cu surfaces. *J. Am. Chem. Soc.* **2017**, *139*, 15664–15667.
- [7] Mori, K.; Sano, T.; Kobayashi, H.; Yamashita, H. Surface engineering of a supported PdAg catalyst for hydrogenation of CO₂ to formic acid: elucidating the active Pd atoms in alloy nanoparticles. *J. Am. Chem. Soc.* **2018**, *140*, 8902–8909.
- [8] Kato, S.; Matam, S. K.; Kerger, P.; Bernard, L.; Battaglia, C.; Vogel, D.; Rohwerder, M.; Züttel, A. The origin of the catalytic activity of a metal hydride in CO₂ reduction. *Angew. Chem. Int. Ed.* **2016**, *55*, 6028–6032.
- [9] Wang, W.-H.; Himeda, Y.; Muckerman, J. T.; Manbeck, G. F.; Fujita, E. CO₂ hydrogenation to formate and methanol as an alternative to photo- and electrochemical CO₂ reduction. *Chem. Rev.* **2015**, *115*, 12936–12973.
- [10] Green, A. E.; Justen, J.; Schöllkopf, W.; Gentleman, A. S.; Fielicke, A.; Mackenzie, S. R. IR Signature of Size-Selective CO₂ Activation on Small Platinum Cluster Anions, Pt_n[–] (n = 4–7). *Angew. Chem. Int. Ed.* **2018**, *57*, 14822–14826.
- [11] Liu, G.; Ciborowski, S. M.; Zhu, Z.; Chen, Y.; Zhang, X.; Bowen, K. H. The metallo-formate anions, M(CO₂)[–], M = Ni, Pd, Pt, formed by electron-induced CO₂ activation. *Phys. Chem. Chem. Phys.* **2019**, *21*, 10955–10960.
- [12] Dodson, L. G.; Thompson, M. C.; Weber, J. M. Characterization of intermediate oxidation states in CO₂ activation. *Annu. Rev. Phys. Chem.* **2018**, *69*, 231–252.
- [13] Thompson, M. C.; Ramsay, J.; Weber, J. M. Solvent-driven reductive activation of CO₂ by bismuth: switching from metalloformate complexes to oxalate products. *Angew. Chem. Int. Ed.*, **2016**, *55*, 15171–15174.
- [14] Tang, S.; Rijs, N. J.; Li, J.; Schlangen, M.; Schwarz, H. Ligand-Controlled CO₂ Activation Mediated by Cationic Titanium Hydride Complexes, [LTiH]⁺ (L = Cp₂, O). *Chem. Eur. J.* **2015**, *21*, 8483–8490.
- [15] Zhang, X.; Liu, G.; Meiwes-Broer, K.; Ganteför, G.; Bowen, K. CO₂ activation and hydrogenation by PtHn[–] cluster anions. *Angew. Chem. Int. Ed.* **2016**, *55*, 9644–9647.
- [16] Jiang, L.; Zhao, C.; Li, X.; Chen, H.; He, S.-G. Formation of Gas-Phase Formate in Thermal Reactions of Carbon Dioxide with Diatomic Iron Hydride Anions. *Angew. Chem. Int. Ed.* **2017**, *56*, 4187–4191.
- [17] Liu, Y.-Z.; Jiang, L.-X.; Li, X.-N.; Wang, L.-N.; Chen, J.-J.; He, S.-G. Gas-phase reactions of carbon dioxide with copper hydride anions Cu₂H₂[–]: Temperature-dependent transformation. *J. Phys. Chem. C* **2018**, *122*, 19379–19384.
- [18] Pascher, T. F.; Ončák, M.; Linde, C.; Beyer, M. K. Release of Formic Acid from Copper Formate: Hydride, Proton-Coupled Electron and Hydrogen Atom Transfer All Play their Role. *ChemPhysChem* **2019**, *20*, 1420–1424.
- [19] Ma, S.; Sadakiyo, M.; Heima, M.; Luo, R.; Haasch, R. T.; Gold, J. I.; Yamauchi, M.; Kenis, P. J. A. Electroreduction of carbon dioxide to hydrocarbons using bimetallic Cu–Pd catalysts with different mixing patterns. *J. Am. Chem. Soc.* **2017**, *139*, 47–50.
- [20] Gao, D.; Zhou, H.; Cai, F.; Wang, J.; Wang, G.; Bao, X. Pd-containing nanostructures for electrochemical CO₂ reduction reaction. *ACS Catal.* **2018**, *8*, 1510–1519.
- [21] Kyriakou, G.; Boucher, M. B.; Jewell, A. D.; Lewis, E. A.; Lawton, T. J.; Baber, A. E.; Tierney, H. L.; Flytzani-Stephanopoulos, M.; Sykes, E. C. H. Isolated metal atom geometries as a strategy for selective heterogeneous hydrogenations. *Science*, **2012**, *335*, 9.
- [22] Long, R.; Li, Y.; Liu, Y.; Chen, S.; Zheng, X.; Gao, C.; He, C.; Chen, N.; Qi, Z.; Song, L.; Jiang, J.; Zhu, J.; Xiong, Y. Isolation of Cu atoms in Pd lattice: forming highly selective sites for photocatalytic conversion of CO₂ to CH₄. *J. Am. Chem. Soc.* **2017**, *139*, 4486–4492.
- [23] Bai, S.; Shao, Q.; Wang, P.; Dai, Q.; Wang, X.; Huang, X. Highly active and selective hydrogenation of CO₂ to ethanol by ordered Pd–Cu nanoparticles. *J. Am. Chem. Soc.* **2017**, *139*, 6827–6830.

- [24] Zhai, H.; Alexandrova, A. N. Fluxionality of catalytic clusters: When it matters and how to address it. *ACS Catal.* **2017**, *7*, 1905–1911.
- [25] Zandkarimi, B.; Alexandrova, A. N. *Wiley Interdiscip. Rev. Comput. Mol. Sci.* **2019**, e1420.
- [26] Sun, G.; Sautet, P. Metastable structures in cluster catalysis from first-principles: Structural ensemble in reaction conditions and metastability triggered reactivity. *J. Am. Chem. Soc.* **2018**, *140*, 2812–2820.
- [27] Zhai, H.; Alexandrova, A. N. Local fluxionality of surface-deposited cluster catalysts: The case of Pt₇ on Al₂O₃. *J. Phys. Chem. Lett.* **2018**, *9*, 1696–1702.
- [28] Jimenez-Izal, E.; Alexandrova, A. N. Computational design of clusters for catalysis. *Annu. Rev. Phys. Chem.* **2018**, *69*, 377–400.
- [29] Baxter, E. T.; Ha, M.-A.; Cass, A. C.; Alexandrova, A. N.; Anderson, S. L. Ethylene dehydrogenation on Pt₄, 7, 8 clusters on Al₂O₃: Strong cluster size dependence linked to preferred catalyst morphologies. *ACS Catal.* **2017**, *7*, 3322–3335.
- [30] Ha, M. A.; Baxter, E. T.; Cass, A. C.; Anderson, S. L.; Alexandrova, A. N. Boron switch for selectivity of catalytic dehydrogenation on size-selected Pt clusters on Al₂O₃. *J. Am. Chem. Soc.* **2017**, *139*, 11568–11575.
- [31] Li, X.; Grubisic, A.; Stokes, S. T.; Cordes, J.; Ganteför, G. F.; Bowen, K. H.; Kiran, B.; Willis, M.; Jena, P.; Burgert, R.; Schnoeckel, H. Unexpected stability of Al₄H₆: a borane analog? *Science*, **2007**, *315*, 356–358.
- [32] Zhang, X.; Liu, G.; Ganteför, G.; Bowen, K. H.; Alexandrova, A. N. PtZnH₅[−], A σ-aromatic cluster. *J. Phys. Chem. Lett.*, **2014**, *5*, 1596–1601.
- [33] Liu, G.; Ciborowski, S.; Bowen, K. Photoelectron spectroscopic and computational study of pyridine-ligated gold cluster anions. *J. Phys. Chem. A*, **2017**, *121*, 5817–5822.
- [34] Liu, G.; Zhu, Z.; Ciborowski, S. M.; Ariyaratna, I. R.; Miliordos, E.; Bowen, K. H. Selective Activation of the C–H Bond in Methane by Single Platinum Atomic Anions. *Angew. Chem. Int. Ed.* **2019**, *58*, 7773–7777.
- [35] Buendia, F.; Beltran, M. R.; Zhang, X.; Liu, G.; Buytendyk A.; Bowen, K. H. Ab initio and anion photoelectron study of Au_nRh_m (n=1–7, m=1–2) clusters. *Phys. Chem. Chem. Phys.* **2015**, *17*, 28219–28227.
- [36] Liu, G.; Ciborowski, S. M.; Zhu, Z.; Bowen, K. H. Activation of hydroxylamine by single gold atomic anions. *Int. J. Mass Spectrom.* **2019**, *435*, 114–117.
- [37] Lang, S. M.; Bernhardt, T. M.; Chernyy, V.; Bakker, J. M.; Barnett, R. N.; Landman, U. Selective C–H bond cleavage in methane by small gold clusters. *Angew. Chem. Int. Ed.* **2017**, *56*, 13406 – 13410.
- [38] Jewell, L. L.; Davis, B. H. Review of absorption and adsorption in the hydrogen–palladium system. *Appl. Catal. A* **2006**, *310*, 1–15.
- [39] Gerhards, M.; Thomas, O. C.; Nilles, J. M.; Zheng, W.-J.; Bowen, K. H. Cobalt–benzene cluster anions: Mass spectrometry and negative ion photoelectron spectroscopy. *J. Chem. Phys.* **2002**, *116*, 10247.
- [40] Zhang, X.; Wang, Y.; Wang, H.; Lim, A.; Ganteför, G.; Bowen, K. H.; Reveles, J. U.; Khanna, S. N. On the existence of designer magnetic superatoms. *J. Am. Chem. Soc.* **2013**, *135*, 4856–4861.
- [41] Zhang, X.; Robinson, P. J.; Alexandrova, A. N.; Bowen, K. H. Photoelectron spectroscopic and theoretical study of the [HPd(η²-H₂)][−] cluster anion. *J. Chem. Phys.* **2015**, *143*, 094307.
- [42] Wang, H.; Zhang, X.; Ko, Y.; Ganteför, G.; Bowen, K. H.; Li, X.; Boggavarapu, K.; Kandalam, A. Photoelectron spectroscopy of boron aluminum hydride cluster anions. *J. Chem. Phys.* **2014**, *140*, 164317.
- [43] Graham, J. D.; Buytendyk, A. M.; Zhang, X.; Collins, E.; Boggavarapu, K.; Ganteför, G.; Eichhorn, B.; Gutsev, G. L.; Behera, S.; Jena, P.; Bowen, K. H. Alanate Anion, AlH₄[−]: Photoelectron Spectrum and Computations. *J. Phys. Chem. A*, **2014**, *118*, 8158–8162.
- [44] Perdew, J. P.; Burke, K.; Ernzerhof, M. Generalized gradient approximation made simple. *Phys. Rev. Lett.* **1996**, *77*, 3865–3868.
- [45] Gaussian 16, Revision A.03, Frisch, M. J.; Trucks, G. W.; Schlegel, H. B.; Scuseria, G. E.; Robb, M. A.; Cheeseman, J. R.; Scalami, G.; Barone, V.; Petersson, G. A.; Nakatsuji, H. et al., Gaussian Inc., Wallingford, CT, **2016**.
- [46] Hay, P. J.; Wadt, W. R. Ab initio effective core potentials for molecular calculations. Potentials for the transition metal atoms Sc to Hg. *J. Chem. Phys.* **1985**, *82*, 270–283.
- [47] Wadt, W. R.; Hay, P. J. Ab initio effective core potentials for molecular calculations. Potentials for main group elements Na to Bi. *J. Chem. Phys.* **1985**, *82*, 284–298.
- [48] Hay, P. J.; Wadt, W. R. Ab initio effective core potentials for molecular calculations. Potentials for K to Au including the outermost core orbitals. *J. Chem. Phys.* **1985**, *82*, 299–310.
- [49] Peterson, K. A.; Puzarini, C. Systematically convergent basis sets for transition metals. II. Pseudopotential-based correlation consistent basis sets for the group 11 (Cu, Ag, Au) and 12 (Zn, Cd, Hg) elements. *Theor. Chem. Acc.* **2005**, *114*, 283–296.

- [50] Čížek, J. On the use of the cluster expansion and the technique of diagrams in calculations of correlation effects in atoms and molecules. *Adv. Chem. Phys.* **1969**, *14*, 35–89.
- [51] Purvis, G. D.; Bartlett, R. J. A full coupled-cluster singles and doubles model: The inclusion of disconnected triples. *J. Chem. Phys.* **1982**, *76*, 1910–1918.
- [52] Scuseria, G. E.; Janssen, C. L.; Schaefer, H. F. An efficient reformulation of the closed-shell coupled cluster single and double excitation (CCSD) equations. *J. Chem. Phys.* **1988**, *89*, 7382–7387.
- [53] Scuseria, G. E.; Schaefer, H. F. Is coupled cluster singles and doubles (CCSD) more computationally intensive than quadratic configuration interaction (QCISD)? *J. Chem. Phys.* **1989**, *90*, 3700–3703.
- [54] Hegarty, D.; Robb, M. A. Application of unitary group methods to configuration interaction calculations. *Mol. Phys.* **1979**, *38*, 1795–1812.
- [55] Eade, R. H. A.; Robb, M. A. Direct minimization in mc scf theory. The quasi-newton method. *Chem. Phys. Lett.* **1981**, *83*, 362–368.
- [56] Schlegel, H. B.; Robb, M. A. MC SCF gradient optimization of the $\text{H}_2\text{CO} \rightarrow \text{H}_2 + \text{CO}$ transition structure. *Chem. Phys. Lett.* **1982**, *93*, 43–46.
- [57] Bernard, F.; Bottoni, A.; McDouall, J. J. W.; Robb, M. A.; Schlegel, H. B. MCSCF gradient calculation of transition structures in organic reactions. *Faraday Symp. Chem. Soc.* **1984**, *19*, 137.
- [58] Frisch, M.; Ragazos, I. N.; Robb, M. A.; Bernhard Schlegel, H. An evaluation of three direct MC-SCF procedures. *Chem. Phys. Lett.* **1992**, *189*, 524–528.
- [59] Yamamoto, N.; Vreven, T.; Robb, M. A.; Frisch, M. J.; Bernhard Schlegel, H. A direct derivative MC-SCF procedure. *Chem. Phys. Lett.* **1996**, *250*, 373–378.
- [60] Siegbahn, P. E. M. A new direct CI method for large CI expansions in a small orbital space. *Chem. Phys. Lett.* **1984**, *109*, 417–423.
- [61] Robb, M. A.; Niazzi, U. *The Unitary Group Approach to Electronic Structure Computations*, CRC Press, Boca Raton, FL, **1990**.
- [62] Klene, M.; Robb, M. A.; Frisch, M. J.; Celani, P. Parallel implementation of the CI-vector evaluation in full CI/CAS-SCF. *J. Chem. Phys.* **2000**, *113*, 5653–5665.
- [63] Reed, A. E.; Weinstock, R. B.; Weinhold, F. Natural population analysis. *J. Chem. Phys.* **1985**, *83*, 735–746.

V. Superatoms

Clusters are ensembles of bound atoms intermediate, bridging the gap between molecules and macroscopic matter. Among the realm of the cluster investigations, one exciting development is the formation of strong bonds or closed electronic shells by groups of atoms can create species that react as if they were one atom. These chosen stable clusters can mimic the chemical behavior of an atom or a group listed in the periodic table, essentially functioning as “superatoms”.¹ Superaatoms include noble metal, ‘magic-number’ clusters, metal chalcogenide molecular clusters, fullerenes, Zintl ions, and clusters of boron, silicon, and aluminum.

This superatom concept originated experimentally from the study of aluminum cluster reactivity conducted in the Castleman group in 1989,² where Al cluster anions containing 13, 23, and 37 atoms were unreactive under oxygen flow, although a dramatic loss of cluster signal was readily discerned for most species. This observation was accounted for by spin conservation and shell closings at 40, 70, and 112 electrons based on a model termed Jellium.^{3,4} Al_{13} , one of the most proverbial superatoms, behaves like a Cl atom and has been characterized to bear properties respected for a superhalogen.⁵ While a Cl atom displays in total 17 electrons with the $1s^2|2s^2|2p^6|3s^2|3p^5$ configuration, the cluster Al_{13} exhibits delocalized, cluster-based s-like, p-like, and d-like orbitals with a configuration of 39 valence electrons corresponding to $1S^2|1P^6|1D^{10}|2S^2|1F^{14}|2P^5$. The similarity of the outermost layer electrons coincides with the anticipation for the mimic of halogen. Our group also has a long record of studying the Al_{13}^- .⁶ Notably, KAl_{13}^- was synthesized and characterized in the gas phase.⁷ As a prototype for ionic bonding involving intact Al_{13}^- subunits, KAl_{13} may be a stepping stone toward forming ionic, cluster-assembled materials.

Later, inspired by superhalogens (one less electron than a closed shell), the related concepts including superalkalis, super alkaline-earth metals, and magnetic superatoms spawned a wide range of pioneering studies pertaining to the understanding of factors governing the properties of clusters.⁸ It is also worth mentioning that superatomic clusters have emerged as versatile building blocks materials design.⁹ Many of these building blocks are stabilized with capping ligands. These ligands are important in that they direct self-assembly and control the coupling between clusters. With different ligands, electronic structures like electrochemical potentials are highly tunable. For each superatom as an oligomer or building block, electronic structures refer to molecular orbitals and the configuration of the electrons occupying these orbitals. Our PES technique is one of the perfect methods to probe the frontier orbitals, such as the HOMO-LUMO gap, electronically excited states, etc., which reflect of the superatoms’ intrinsic chemical

properties. In chapter V, I will present two examples of tuning the electronic structures of the cobalt sulfide clusters via ligand substitution.

References

1. Khanna, S. N., & Jena, P. (1995). Atomic clusters: Building blocks for a class of solids. *Physical Review B*, 51(19), 13705.
2. Leuchtner, R. E., Harms, A. C., & Castleman Jr, A. W. (1989). Thermal metal cluster anion reactions: Behavior of aluminum clusters with oxygen. *The Journal of chemical physics*, 91(4), 2753-2754.
3. Brack, M. (1993). The physics of simple metal clusters: self-consistent jellium model and semiclassical approaches. *Reviews of modern physics*, 65(3), 677.
4. Kappes, M. M., Radi, P., Schär, M., & Schumacher, E. (1985). Probes for electronic and geometrical shell structure effects in alkali-metal clusters. Photoionization measurements on K_xLi , K_xMg and K_xZn ($x < 25$). *Chemical physics letters*, 119(1), 11-16.
5. Bergeron, D. E., Castleman Jr, A. W., Morisato, T., & Khanna, S. N. (2004). Formation of $Al_{13}I^-$: Evidence for the superhalogen character of Al_{13} . *Science*, 304(5667), 84-87.
6. Burgert, R., Schnöckel, H., Olzmann, M., & Bowen Jr, K. H. (2006). The chlorination of the $[Al_{13}]^-$ cluster and the stepwise formation of its intermediate products, $[Al_{11}]^-$, $[Al_9]^-$, and $[Al_7]^-$: a model reaction for the oxidation of metals?. *Angewandte Chemie International Edition*, 45(9), 1476-1479.
7. Zheng, W. J., Thomas, O. C., Lippa, T. P., Xu, S. J., & Bowen Jr, K. H. (2006). The ionic $K Al_{13}$ molecule: A stepping stone to cluster-assembled materials. *The Journal of chemical physics*, 124(14), 144304.
8. Luo, Z., & Castleman, A. W. (2014). Special and general superatoms. *Accounts of Chemical Research*, 47(10), 2931-2940.
9. Doud, E. A., Voevodin, A., Hochuli, T. J., Champsaur, A. M., Nuckolls, C., & Roy, X. (2020). Superatoms in materials science. *Nature Reviews Materials*, 5(5), 371-387.

V.A.1. Tuning the Electronic Properties of Hexanuclear Cobalt Sulfide Superatoms via Ligand Substitution

Reprinted (adapted) with permission from *Chem. Sci.* **10**, 1760-1766 (2019)

Gaoxiang Liu^a, Andrew Pinkard^b, Sandra M. Ciborowski^a, Vikas Chauhan^c, Zhaoguo Zhu^a, Alexander P. Aydt^b, Shiv N. Khanna^{*c}, Xavier Roy^{*b} and Kit H. Bowen^{*a}

^a *Department of Chemistry, Johns Hopkins University, Baltimore, Maryland 21218, USA.*

^b *Department of Chemistry, Columbia University, New York, New York 10027, USA.*

^c *Department of Physics, Virginia Commonwealth University, 701 W. Grace St., Richmond, Virginia 23284, USA.*

Abstract

Molecular clusters are attractive superatomic building blocks for creating materials with tailored properties due to their unique combination of atomic precision, tunability and functionality. The ligands passivating these superatomic clusters offer an exciting opportunity to control their electronic properties while preserving their closed shells and electron counts, which is not achievable in conventional atoms. Here we demonstrate this concept by measuring the anion photoelectron spectra of a series of hexanuclear cobalt sulfide superatomic clusters with different ratios of electron-donating and electron-withdrawing ligands, $\text{Co}_6\text{S}_8(\text{PEt}_3)_{6-x}(\text{CO})_x$ ($x = 0-3$). We find that $\text{Co}_6\text{S}_8(\text{PEt}_3)_6$ has a low electron affinity (EA) of 1.1 eV, and that the successive replacement of PEt_3 ligands with CO gradually shifts its electronic spectrum to lower energy and increases its EA to 1.8 eV. Density functional theory calculations reveal that the increase of EA results from a monotonic lowering of the cluster highest occupied and lowest unoccupied molecular orbitals (HOMO and LUMO). Our work provides unique insights into the electronic structure and tunability of superatomic building blocks.

Introduction

Electron affinity and ionization energy are fundamental properties of the elements. Together they govern the interactions and bonding of close-contacting atoms and control the collective properties of solids. Because they are intrinsic to each element, however, the electron affinity and ionization energy of a given atom cannot be altered. This presents an immense synthetic challenge for the design of tunable materials as substituting atoms often leads to entirely new structures, interactions and collective behaviors.

By analogy to “atomic” building blocks, certain clusters can be used as “superatomic” building blocks for the assembly of novel materials.^{1–22} Within this context, the family of metal chalcogenide molecular clusters has recently received renewed attention for the creation of functional solids with tunable properties, including ferromagnetism, electrical conductivity, tunable optical gaps and thermal switching.^{1,7,23–32} One of the key advantages of this approach over traditional atomic solids is that the characteristics of the building blocks can be tuned pre-assembly without changing the total electron count of the superatom. Using the molecular cluster $\text{Co}_6\text{Te}_8\text{L}_6$ (L = passivating ligand) as a model system, Khanna *et al.* recently predicted theoretically that changing L from PEt_3 to CO would increase its electron affinity, in effect transforming the cluster from a superatomic alkali metal toward a superatomic halogen.^{33,34} The potential to alter the donor/acceptor property of these superatomic clusters sheds light on assembling superatomic materials with fine-tuned properties. Experimentally demonstrating this concept by measuring the electron affinity and/or ionization energy of metal chalcogenide clusters is challenging, however, because it requires bringing the charged clusters into the gas phase without damaging the inorganic core or dissociating the ligands.

In this work, we use anion photoelectron spectroscopy to probe the electron affinity (EA) and electronic structure of a series of cobalt sulfide clusters, whose ligand shells consist of differing combinations of PEt_3 and CO. The clusters $\text{Co}_6\text{S}_8(\text{PEt}_3)_{6-x}(\text{CO})_x$ are synthesized from the parent compound $\text{Co}_6\text{S}_8(\text{PEt}_3)_6$ by ligand substitution with CO. These clusters are then brought into the gas phase, where electrons are attached to form anions, using a unique infrared desorption/photoelectron-emission/supersonic helium expansion source. Mass spectrometry confirms the existence of carbonylated products with x up to 3 (*i.e.* $\text{Co}_6\text{S}_8(\text{PEt}_3)_5(\text{CO})^-$, $\text{Co}_6\text{S}_8(\text{PEt}_3)_4(\text{CO})_2^-$, and $\text{Co}_6\text{S}_8(\text{PEt}_3)_3(\text{CO})_3^-$). We find that the electron affinity and vertical detachment energy increase with the number of CO ligands, demonstrating the electronic spectral tunability of this family of superatoms. These results are further examples of the superatom concept, and an important step towards designing materials from programmable building blocks.

Methods

Synthesis

Dicobalt octacarbonyl and sulfur were purchased from Strem Chemicals. Triethylphosphine was purchased from Alfa Aesar. All other reagents and solvents were purchased from Sigma Aldrich. Dry and deoxygenated solvents

were prepared by elution through a dual-column solvent system. Unless otherwise stated, all reactions and sample preparations were carried out under inert atmosphere using standard Schlenk techniques or in a N₂-filled glovebox. While a multi-step synthesis of Co₆S₈(PEt₃)₆ has been previously reported,³⁵ we have developed an alternative one-pot approach detailed below.

Co₆S₈(PEt₃)₆. Sulfur (1.16 g, 36.25 mmol) was suspended in ~30 mL of toluene in a 200 mL Schlenk flask under N₂ atmosphere. In two separate flasks, Co₂(CO)₈ (4.12 g, 12.05 mmol) and PEt₃ (4.27 g, 36.14 mmol) were dissolved in ~20 mL of toluene. The Co₂(CO)₈ solution was added to the S suspension, followed by quick addition of the PEt₃ solution. The reaction mixture was refluxed under N₂ for 2 days. The reaction mixture was then opened to air, and hot filtered through Celite. The filtrate was cooled to room temperature and left to stand for ~3 h. Black crystals formed during that period; the resulting suspension was filtered through a fine frit and the solid was washed with toluene, and diethyl ether. The dark, black crystals were collected, dried *in vacuo*, and stored under N₂. Yield: 2.2 g (42%). MS-MALDI *m/z*⁺ calculated 1317.92; found, 1317.95.

Co₆S₈(PEt₃)_{6-x}(CO)_x. Safety note: CO is a toxic gas; this reaction can only be performed in a well-ventilated fumehood. Sulfur (0.15 g, 4.68 mmol) and Co₆S₈(PEt₃)₆ (1.00 g, 0.76 mmol) were combined in ~75 mL of toluene in a 200 mL Schlenk flask. An external bubbler was attached to the system, and the mixture was sparged with CO for 30 min. The mixture was heated to 100 °C and stirred under a CO atmosphere for 16 h. The reaction mixture was cooled to room temperature, sparged with N₂, and the solvent was removed *in vacuo*. The resulting solid was used directly without further purification.

Anion photoelectron spectroscopy

Anion photoelectron spectroscopy was conducted by crossing a mass-selected negative ion beam with a fixed energy photon beam and analyzing the energies of the resultant photodetached electrons. This technique is governed by the well-known energy-conserving relationship, $h\nu = \text{EBE} + \text{EKE}$, where $h\nu$, EBE, and EKE are the photon energy, electron binding energy (photodetachment transition energy), and the electron kinetic energy, respectively. The details of our apparatus have been described elsewhere.³⁶ Briefly, the photoelectron spectra were collected on an apparatus consisting of an ion source, a linear time-of-flight mass spectrometer for mass analysis and selection, and a magnetic-bottle photoelectron spectrometer for electron energy analysis (resolution ~35 meV at 1 eV EKE). The third harmonic (355 nm, 3.49 eV per photon) of a Nd:YAG was used to photodetach electrons

from the cluster anion of interest. Photoelectron spectra were calibrated against the well-known atomic lines of the copper anion, Cu^- .

To make the parent anions $\text{Co}_6\text{S}_8(\text{PEt}_3)_{6-x}(\text{CO})_x^-$ in the gas phase, a specialized infrared desorption/laser photoemission (IR/PE) supersonic helium expansion source is employed.³⁷ Briefly, a low power IR pulse (1064 nm) from a Nd:YAG laser hits a translating graphite bar thinly coated with the $\text{Co}_6\text{S}_8(\text{PEt}_3)_{6-x}(\text{CO})_x$ sample. Because the graphite absorbs most of the energy, a localized thermal shock lasting a few nanoseconds propels the clusters into the gas phase. Almost simultaneously, a high power pulse of 532 nm light from a second Nd:YAG laser strikes a close-by photoemitter (Hf wire), creating a shower of electrons that attach to the evaporated neutral clusters. Also, almost simultaneously, a plume of ultrahigh purity helium gas rapidly expands from a pulsed valve located slightly upstream, cooling the nascent anions and directing them into the mass spectrometer, where they are analyzed. Because the $\text{Co}_6\text{S}_8(\text{PEt}_3)_{6-x}(\text{CO})_x$ clusters are slightly sensitive to air and moisture, they are coated onto the graphite bar in a N_2 -filled glove box. The graphite bar is then enclosed inside an air-tight “suitcase” container, which is only opened under high vacuum after being transferred to the vacuum chamber.

Theoretical calculations

First-principles electronic structure calculations on the anion and neutral forms of $\text{Co}_6\text{S}_8(\text{PEt}_3)_{6-x}(\text{CO})_x$ ($x = 0-3$) clusters were carried out within density functional theory formalism. The ADF set of codes were used to perform the calculations where a PBE0 hybrid functional comprised of the PBE generalized gradient functional and 25% Hartree–Fock exchange, as proposed by Ernzerhof *et al.*, is used to incorporate exchange and correlation effects.^{38–40} The atomic wave functions are expressed in terms of Slater-type orbitals (STO) located at the atomic sites and the cluster wave functions are constructed from a linear combination of these atomic orbitals.⁴¹ A TZ2P basis set and a large frozen electron core was used. The zero-order regular approximation (ZORA) is used to include scalar-relativistic effect.^{42,43} The trial structures of the clusters were taken from the previously optimized structure of the $\text{Co}_6\text{Te}_8(\text{PEt}_3)_6$ where the Te sites were replaced by S atoms.³³ The quasi-Newton method without any symmetry restriction is used to determine the lowest energy arrangement for each trial structure of the clusters. The calculations also covered the several possible spin states for all the clusters during optimization. The adiabatic electron affinity (AEA) is calculated as the total energy difference between the anion in its ground state geometry

and the neutral cluster in its ground state geometry, while the vertical detachment energy (VDE) is given by the total energy difference between the anion in its ground state and the neutral cluster in the geometry of the anion.

Results and discussions

Fig.V.A.1.1a depicts the structure of $\text{Co}_6\text{S}_8(\text{PET}_3)_{6-x}(\text{CO})_x$. Our strategy to synthesize these clusters begins by preparing the parent compound $\text{Co}_6\text{S}_8(\text{PET}_3)_6$ on a multigram scale. To achieve this, we have developed a new approach detailed in the Methods section. Briefly, under a CO atmosphere, $\text{Co}_6\text{S}_8(\text{PET}_3)_6$ is reacted with six equivalents of S in toluene at $\sim 100^\circ\text{C}$ to partially substitute CO for PET_3 , which is trapped as SPET_3 . Using the mass spectrometry technique described below, we observe a mixture of clusters in which up to three CO ligands have been substituted for PET_3 . It is possible to separate these different species using column chromatography,³⁰ but for this study we can use the mixture of clusters without further purification.

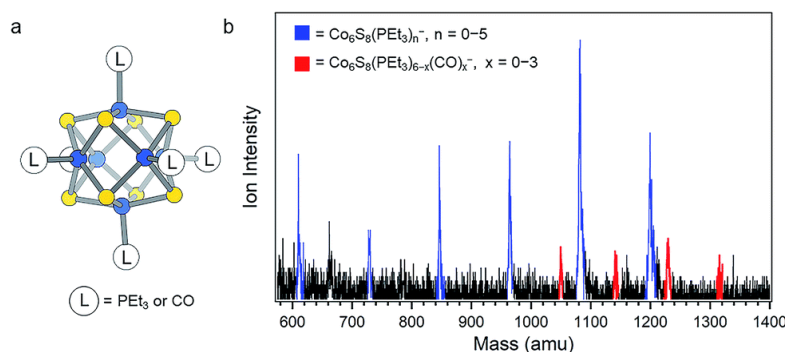


Figure V.A.1.1 (a) Structure of $\text{Co}_6\text{S}_8(\text{PET}_3)_{6-x}(\text{CO})_x$. (b) Anion mass spectrum of $\text{Co}_6\text{S}_8(\text{PET}_3)_{6-x}(\text{CO})_x^-$ generated using IR/PE anion source. This work focuses on the red peaks in the mass spectrum.

Measuring the electron affinity and electronic structure of $\text{Co}_6\text{S}_8(\text{PET}_3)_{6-x}(\text{CO})_x$ requires a negative ion photoelectron spectroscopic study on their parent anions, $\text{Co}_6\text{S}_8(\text{PET}_3)_{6-x}(\text{CO})_x^-$, in the gas phase. Common ionization methods (*e.g.* electrospray ionization and matrix-assisted laser desorption/ionization), however, fail to generate the parent anions $\text{Co}_6\text{S}_8(\text{PET}_3)_{6-x}(\text{CO})_x^-$ in the gas phase due to the effect of the solvent/matrix on neutral $\text{Co}_6\text{S}_8(\text{PET}_3)_{6-x}(\text{CO})_x$ clusters: the obtained anions are either dissociated or tagged by the solvent/matrix molecules. To make the parent anions in the gas phase, we instead employ a unique infrared desorption/photoemission (IR/PE) source as described in the Methods section. A typical anion mass spectrum of $\text{Co}_6\text{S}_8(\text{PET}_3)_{6-x}(\text{CO})_x^-$ obtained with the IR/PE source is shown in Fig. V.A.1.1b. The spectrum contains two major series of anions: $\text{Co}_6\text{S}_8(\text{PET}_3)_n^-$ ($n = 0-5$) and $\text{Co}_6\text{S}_8(\text{PET}_3)_{6-x}(\text{CO})_x^-$ ($x = 0-3$). The $\text{Co}_6\text{S}_8(\text{PET}_3)_n^-$ clusters are from the sequential dissociation of

PEt₃ from Co₆S₈(PEt₃)₆ during infrared desorption, while the Co₆S₈(PEt₃)_{6-x}(CO)_x⁻ clusters are the anions of interest in this study. Though the Co₆S₈(PEt₃)_{6-x}(CO)_x⁻ signals are weaker, their high photodetachment cross-sections allow us to collect their anion photoelectron spectra.

Fig. V.A.1.2 presents the anion photoelectron spectra of Co₆S₈(PEt₃)_{6-x}(CO)_x⁻ ($x = 0-3$) from which the adiabatic electron affinity (AEA) and vertical detachment energy (VDE) of each cluster are determined. The value of the AEA is taken to be the onset of the lowest electron binding energy (EBE) peak in the photoelectron spectrum. The VDE is the vertical transition energy from the ground state of the anion to the neutral state at the anion geometry. It is determined as the EBE value at the intensity maximum of the peak of interest, *i.e.* typically the first EBE peak. Based on the anion photoelectron spectra, the AEA values of Co₆S₈(PEt₃)_{6-x}(CO)_x are 1.1, 1.3, 1.7 and 1.8 eV for $x = 0, 1, 2, 3$, respectively, while the corresponding anion VDE values are 1.30, 1.51, 1.95 and 2.09 eV, respectively. By sequentially substituting half of the PEt₃ ligands with CO, the AEA of this superatom increases from 1.1 eV to 1.8 eV, all while maintaining the same oxidation state for the Co₆S₈ core. As a reference, the reducing agent SO₂ and oxidizing agent SO₃ have AEA values of 1.11 eV and 1.90 eV,^{44,45} respectively, where the increase in AEA is the result of the change in the S atom oxidation state. Thus, the observed changes in AEA values for the ligated superatoms are significant, given that the oxidation state of the Co₆S₈ core does not change across the ligation series: these results underscore the remarkable characteristics of the superatoms. The observed unambiguous trend of increasing AEA and VDE values with ligand substitution is a direct evidence that the electronic properties of this superatom can be tuned effectively in this way.

The tuning of the electronic properties can be further demonstrated through the spectral features located at higher electron binding energies than that of the first EBE peak. These higher EBE peaks arise from transitions from the anion ground state to various excited electronic states of the neutral cluster. The shape of these features relates to the electronic structure of the neutral clusters. While the photoelectron spectra of Co₆S₈(PEt₃)_{6-x}(CO)_x⁻

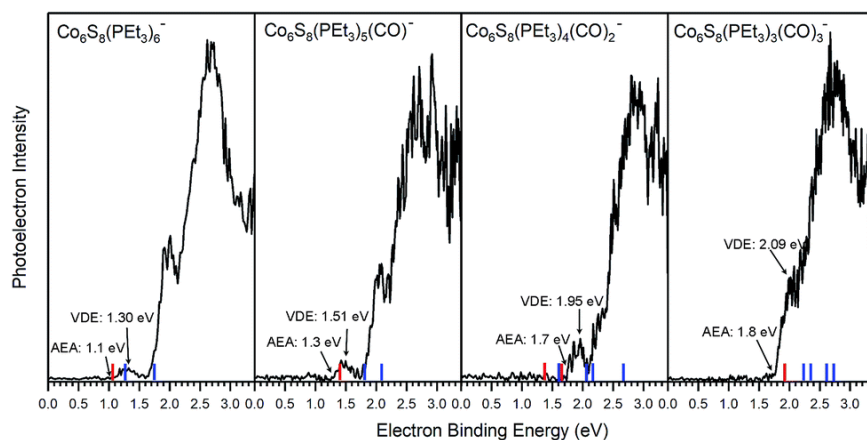


Figure V.A.1.2 Negative ion photoelectron spectra of $\text{Co}_6\text{S}_8(\text{PET}_3)_{6-x}(\text{CO})_x^-$ ($x = 0-3$) anions collected using 355 nm (3.49 eV) photons from a Nd:YAG laser. The arrows point to the experimental values of AEA and VDE; the red lines correspond to theoretical AEA, and the blue lines correspond to vertical transitions from the anion to the singlet and triplet neutral states.

shift to higher electron binding energy as x increases, the overall spectral shapes are remarkably similar, confirming that the sequential exchange of PET_3 with CO ligand leaves the essential electronic structure of $\text{Co}_6\text{S}_8(\text{PET}_3)_{6-x}(\text{CO})_x$ superatoms largely unchanged. What is changing with sequential ligation, however, is a monotonic decrease in the energies of the highest occupied and lowest unoccupied molecular orbital (HOMO and LUMO) levels, even though the gap between them remains relatively constant. This is discussed further below.

To support these experimental observations, we modeled the ground state structures of $\text{Co}_6\text{S}_8(\text{PET}_3)_{6-x}(\text{CO})_x^-$, and calculated their AEA and VDE using density functional theory formalism (Fig. V.A.1.3). In agreement with previous calculations of the $\text{Co}_6\text{Te}_8(\text{PET}_3)_{6-x}(\text{CO})_x$ system,³³ we find that the anionic clusters $\text{Co}_6\text{S}_8(\text{PET}_3)_{6-x}(\text{CO})_x^-$ have doublet spin ground states, while the neutral species have singlet spin states. For $\text{Co}_6\text{S}_8(\text{PET}_3)_4(\text{CO})_2^-$, there are two possible structures: *trans*- $\text{Co}_6\text{S}_8(\text{PET}_3)_4(\text{CO})_2^-$ and *cis*- $\text{Co}_6\text{S}_8(\text{PET}_3)_4(\text{CO})_2^-$, with the latter lower in energy by 0.20 eV. The replacement of three PET_3 ligands with CO leads to *fac*- $\text{Co}_6\text{S}_8(\text{PET}_3)_3(\text{CO})_3^-$ and *mer*- $\text{Co}_6\text{S}_8(\text{PET}_3)_3(\text{CO})_3^-$ isomers, with the latter isomer lower in energy by 0.07 eV. The small energy difference between the $\text{Co}_6\text{S}_8(\text{PET}_3)_3(\text{CO})_3^-$ isomers suggests their co-existence in the experimental beam. Table S1† contains more calculation results on neutral and anionic species.

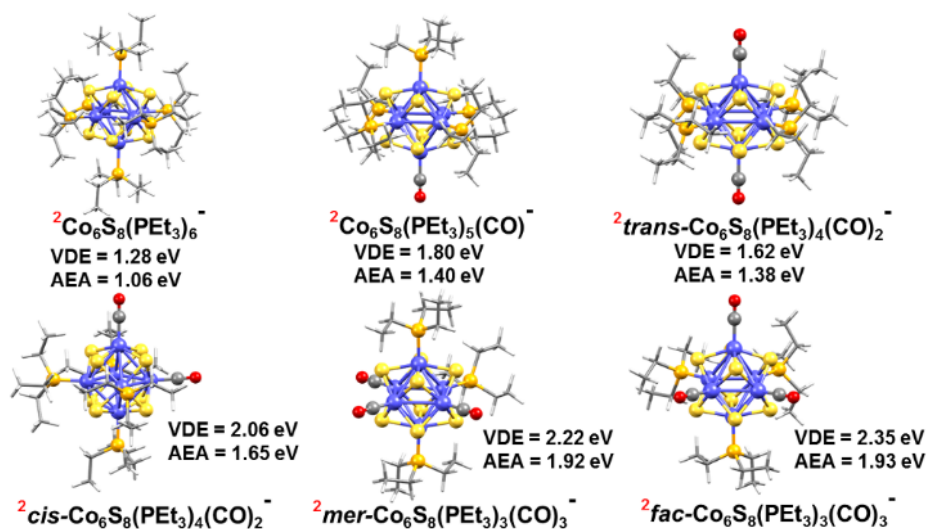


Figure V.A.1.3 Optimized ground state structure of anionic $\text{Co}_6\text{S}_8(\text{PET}_3)_{6-x}(\text{CO})_x^-$ ($x = 0-3$) clusters. The red superscript indicates the spin multiplicity ($2S+1$) of each cluster.

We modeled the electronic structure of the superatoms using the anion photoelectron spectra as fingerprints of the ground state geometry and electronic states of both the neutral and anionic clusters.⁴⁶ Three points of comparison are used to establish the theoretical ground state of the system: AEA, VDE and VDE^* . VDE and VDE^* are the vertical transitions from the anion ground state to the neutral with singlet and triplet spin multiplicity, respectively. Experimentally, VDE and VDE^* correspond to the electron binding energies of the first (lowest EBE) and second (next highest EBE) peaks in the photoelectron spectra.

Table V.A.1.1 presents both theoretical and experimental values of AEA, VDE and VDE^* for all the superatoms considered here. Using AEA, VDE and VDE^* as references to validate the computation, we observe close agreement between experimental and calculated values. The agreement between experiments and calculations is further demonstrated by including the computed values in the anion photoelectron spectra in Figure V.A.1.2. The key result is that the AEA and both VDE values increase as PET_3 ligands are successively replaced with CO. Starting with $\text{Co}_6\text{S}_8(\text{PET}_3)_6^-$, the calculated AEA, VDE, and VDE^* values of 1.06, 1.28, and 1.74 eV are close to the experimental values of 1.1, 1.30 eV, and 1.91 eV, respectively. Experimentally, the replacement of one PET_3 with a CO ligand results in a ~ 0.2 eV increase in the AEA (1.3 eV) and VDE values (1.51 and 2.05 eV), whereas the

calculated AEA (1.40 eV) and VDE values (1.80 and 2.08 eV) for $\text{Co}_6\text{S}_8(\text{PET}_3)_5\text{CO}^-$ are only slightly higher. For *cis*- $\text{Co}_6\text{S}_8(\text{PET}_3)_4(\text{CO})_2^-$ and *trans*- $\text{Co}_6\text{S}_8(\text{PET}_3)_4(\text{CO})_2^-$, the computed ground states have AEA values of 1.65 and 1.38 eV, VDE values of 2.06 and 1.62 eV, and VDE^* values of 2.66 and 2.16 eV, respectively. A comparison between the experimental and theoretical results for $\text{Co}_6\text{S}_8(\text{PET}_3)_4(\text{CO})_2^-$ confirms that this cluster is primarily the *cis*-isomer: the experimental values $\text{AEA} = 1.7$ eV, $\text{VDE} = 1.95$ eV, and $\text{VDE}^* = 2.51$ eV all agree very well with the *cis*-isomer calculations. We note that the small shoulder at 2.19 eV in the spectrum (Figure V.A.1.2) matches the calculated VDE^* of the *trans*-isomer, raising the possibility that a small amount of the *trans*-isomer is also present. For $n = 3$, both the *mer*- $\text{Co}_6\text{S}_8(\text{PET}_3)_3(\text{CO})_3^-$ and *fac*- $\text{Co}_6\text{S}_8(\text{PET}_3)_3(\text{CO})_3^-$ have similar computed AEA and VDE values that are consistent with the experimental data. Because the *mer*- and *fac*-clusters are close in energy in their neutral and anionic forms, it is very likely that they both exist in the ion beam, and that the $\text{Co}_6\text{S}_8(\text{PET}_3)_3(\text{CO})_3^-$ photoelectron spectrum contains transitions from both isomers.

Table V.A.1.1 Theoretical and experimental adiabatic and vertical detachment energies (1st and 2nd peak) of $\text{Co}_6\text{S}_8(\text{PET}_3)_{6-x}(\text{CO})_x^-$ ($x = 0-3$) clusters. The superscripts T and E indicate theoretical and experimental values, respectively.

Anionic clusters	AEA^{T} (eV)	VDE^{T} (eV)		AEA^{E} (eV)	VDE^{E} (eV)	
		VDE	VDE^*		VDE	VDE^*
$\text{Co}_6\text{S}_8(\text{PET}_3)_6^-$	1.06	1.28	1.74	1.1	1.30	1.91
$\text{Co}_6\text{S}_8(\text{PET}_3)_5(\text{CO})^-$	1.40	1.80	2.08	1.3	1.51	2.05
<i>cis</i> - $\text{Co}_6\text{S}_8(\text{PET}_3)_4(\text{CO})_2^-$	1.65	2.06	2.66	1.7	1.95	2.51
<i>trans</i> - $\text{Co}_6\text{S}_8(\text{PET}_3)_4(\text{CO})_2^-$	1.38	1.62	2.16			
<i>mer</i> - $\text{Co}_6\text{S}_8(\text{PET}_3)_3(\text{CO})_3^-$	1.92	2.22	2.71	1.8	2.09	2.67
<i>fac</i> - $\text{Co}_6\text{S}_8(\text{PET}_3)_3(\text{CO})_3^-$	1.93	2.35	2.60			

^a The superscripts T and E indicate theoretical and experimental values, respectively.

The replacement of PET_3 ligands by CO concurrently lowers the energies of the HOMO and LUMO, with the result that the HOMO-LUMO gap is essentially unchanged across the cluster series. Figure V.A.1.4a illustrates this trend for the neutral species while their absolute energy values are given in Table S1. The lowering of the HOMO and LUMO can be in part understood in terms of the vastly different ligand field effect of the cluster surface passivation: PET_3 is a strong σ -donor that increases the electron density in the core while CO is a strong π -acceptor that removes electron density from the core, thus lowering the energy of the electronic spectrum.³³ This behavior can be seen in the Figures S1 and S2 which show the one-electron energy levels of $\text{Co}_6\text{S}_8(\text{PET}_3)_{6-x}(\text{CO})_x$ ($x = 0-3$). The change in the AEA closely tracks the change in the LUMO as the electron is attached to the LUMO of the neutral. This is

illustrated in Figure V.A.1.4b, which shows the changes in the energy of the LUMO (ΔLUMO), theoretical AEA (ΔAEA^T)

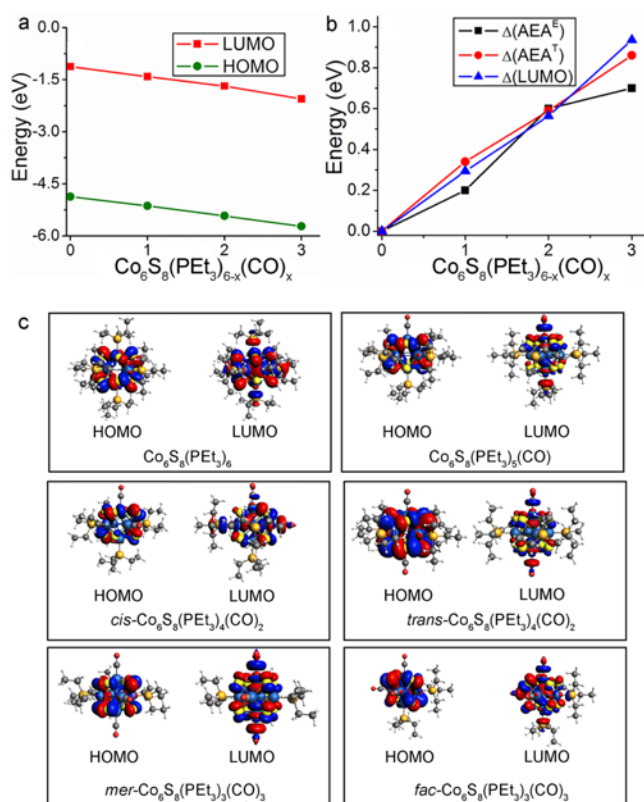


Figure V.A.1.4 (a) The absolute energy values of the HOMO and LUMO for neutral $\text{Co}_6\text{S}_8(\text{PET}_3)_{6-x}(\text{CO})_x$ ($x = 0-3$).

(b) Incremental differences in the experimental AEA values, the theoretical AEA values, and the LUMO values of $\text{Co}_6\text{S}_8(\text{PET}_3)_{6-x}(\text{CO})_x$, each with respect to $\text{Co}_6\text{S}_8(\text{PET}_3)_6$. (c) Molecular orbital iso-surfaces of the HOMO and LUMO in $\text{Co}_6\text{S}_8(\text{PET}_3)_{6-x}(\text{CO})_x$ ($x=0-3$) clusters.

And experimental AEA (ΔAEA^E) of $\text{Co}_6\text{S}_8(\text{PET}_3)_{6-x}(\text{CO})_x$ as x increases from 0 to 3. The molecular orbital iso-surfaces of the HOMO and LUMO in $\text{Co}_6\text{S}_8(\text{PET}_3)_{6-x}(\text{CO})_x$ are shown in Figure V.A.1.4c. A Mulliken population analysis of the molecular orbitals reveals that hybridization between the p-states of S and the 3d-states of Co forms the HOMO in each cluster, while the LUMO is an antibonding state comprising the $3d_z^2$ -orbital of Co and the lone pair of the ligand (PET_3/CO). An additional phenomenon combines with the traditional ligand field effect to explain the changes in AEA and VDE: PET_3 and CO form charge transfer complexes, and the induced dipoles at the cluster surface play a critical role in changing the electronic properties. As a reference, surface dipoles can either increase

or decrease the work function of metals.^{47,48} In this case, as PET_3 ligands are replaced by CO, the sign of the dipole changes and hence AEA increases as more CO are bound to the core.

Lastly, though the ionization energy of $\text{Co}_6\text{S}_8(\text{PET}_3)_{6-x}(\text{CO})_x$ is not directly measured, the successive rise in AEA and lowering of HOMO are evidence of a trend of increasing ionization energy as PET_3 is replaced by CO.

Conclusions

By combining cluster synthesis, gas-phase anion photoelectron spectroscopy, and electronic structure calculations, we have demonstrated that the electronic properties of metal chalcogenide superatomic clusters can be tuned by varying their capping ligands. While the total electron count of the closed-shell core remains unchanged, substitution of the ligands leads to a simultaneous rise or fall of the HOMO and LUMO levels, resulting in a change of the cluster donor/acceptor behavior.

These results are significant because such drastic change in the cluster properties is rarely observed in other superatomic systems. Besides changes of electron affinity and ionization potential, ligand substitution of a ligated cluster almost always results in changes of other core chemical properties such as the HOMO-LUMO gap, electron configuration, and electronic structure. For example, in phosphine-passivated gold clusters approximated by the confined nearly free electron gas model, charge transfer from the phosphine ligands results in significant changes to the core electron count and HOMO-LUMO gap.⁴⁹ The unpredictable outcome of ligand substitution can impose important challenges in designing programmable cluster building blocks. In this context, the metal chalcogenide cluster presented in this work is unique: ligand substitution can be used to tune its electron affinity and ionization potential while maintaining its HOMO-LUMO gap, electronic structure and effective electron count, thus enabling us to control its oxidative and reductive properties. Such tunability may prove crucial for applications as catalysts, semiconductor dopants, and superatomic building blocks for cluster-assembled materials. In one example, we recently showed that related clusters can be used as electron-donating or electron-accepting surface dopants for two-dimensional semiconductors, where the band structures can be controlled by the choice of ligands.^{32,50} Such dopants could also be made magnetic because of their finite spin moments.⁵¹ More broadly, our results open the door to the design of tunable functional materials from superatomic building blocks.

References

1. .A. Pinkard, A. M.Champsaur and X. Roy, *Acc. Chem. Res.*, 2018, **51**, 919-929.
2. S. A. Claridge, A. W.Castleman, S. N.Khanna, C. B. Murray, A. Sen and P. S. Weiss, *ACS Nano.*, 2009, **3**, 244–255.
3. E. G. Tulskey and J. R. Long, *Chem. Mater.*, 2001, **13**, 1149–1166.
4. S. A. Baudron, P. Batail, C. Coulon, R. Clerac, E. Canadell, V. Laukhin, R. Melzi, P. Wzietek, D. Jerome, P. Auban-Senzier and S. Ravy, *J. Am. Chem. Soc.*, 2005, **127**, 11785–11797.
5. .B. Yoon, W. D. Luedtke, R. N. Barnett, J. Gao, A. Desiredy, B. E. Conn, T. Bigioni and U. Landman, *Nat. Mater.*, 2014, **13**, 807–811.
6. J. F. Corrigan, O. Fuhr and D. Fenske, *Adv. Mater.*, 2009, **21**, 1867–1871.
7. X. Roy, C.-H. Lee, A. C. Crowther, C. L. Schenck, T. Besara, R. A. Lalancette, T. Siegrist, P. W. Stephens, L. E. Brus, P. Kim, M. L. Steigerwald and C. Nuckolls, *Science*, 2013, **341**, 157–160.
8. S. N. Khanna and P. Jena, *Phys. Rev. B.*, 1995, **51**, 13705-13716.
9. .A. W. Castleman and S. N. Khanna, Clusters, *J. Phys. Chem. C*, 2009, **113**, 2664–2675.
10. .A. C. Reber and S. N. Khanna, *Acc. Chem. Res.*, 2017, **50**, 255–263.
11. C.-H. Lee, L. Liu, C. Bejger, A. Turkiewicz, T. Goko, C. J. Arguello, B. A. Frandsen, S. C. Cheung, T. Medina, T. J. S. Munsie, R. D’Ortenzio, G. M. Luke, T. Besara, R. A. Lalancette, T. Siegrist, P. W. Stephens, A. C. Crowther, L. E. Brus, Y. Matsuo, E. Nakamura, Y. J. Uemura, P. Kim, C. Nuckolls, M. L. Steigerwald and X. Roy, *J. Am. Chem. Soc.*, 2014, **136**, 16926–16931.
12. X. Roy, C. L. Schenck, S. Ahn, R. A. Lalancette, L. Venkataraman, C. Nuckolls and M. L. Steigerwald, *Angew. Chem., Int. Ed.*, 2012, **51**, 12473–12476.
13. M. T. Trinh, A. Pinkard, A. B. Pun, S. N. Sanders, E. Kumarasamy, M. Y. Sfeir, L. M. Campos, X. Roy and X.-Y. Zhu, *Sci. Adv.* 2017, **3**, e1700241
14. V. Chauhan, S. Sahoo and S. N. Khanna, *J. Am. Chem. Soc.* 2016, **138**, 1916–1921.
15. S. N. Khanna and A. C. Reber, *Nat. Chem.*, 2017, **9**, 1151–1152.
16. .D. A. Tomalia and S. N. Khanna, *Chem. Rev.*, 2016, **116**, 2705–2774.
17. Z. Zheng, J. R. Long and R. H. Holm, *J. Am. Chem. Soc.*, 1997, **119**, 2163–2171.
18. M. Cargnello, A. C. Johnston-Peck, B. T. Diroll, E. Wong, B. Datta, D. Damodhar, V. V. T. Doan-Nguyen, A. A. Herzing, C. R. Kagan and C. B. Murray, *Nature*, 2015, **524**, 450–453.
19. M. N. O’Brien, M. R. Jones, B. Lee and C. A. Mirkin, *Nat. Mater.*, 2015, **14**, 833–839.
20. M. A. Boles and D. V. Talapin, *J. Am. Chem. Soc.*, 2015, **137**, 4494.
21. .C. L. Poyser, T. Czerniuk, A. Akimov, B. T. Diroll, E. A. Gaudling, A. S. Salasyuk, A. J. Kent, D. R. Yakovlev, M. Bayer and C. B. Murray, *ACS Nano.*, 2016, **10**, 1163–1169.
22. W.-L. Ong, S. M. Rupich, D. V. Talapin, A. J. H. McGaughey and J. A. Malen, *Nat. Mater.*, 2013, **12**, 410–415.
23. .A. Voevodin, L. M. Campos and X. Roy, *J. Am. Chem. Soc.*, 2018, **140**, 5607–5611.
24. .A. M. Champsaur, J. Yu, X. Roy, D. W. Paley, M. L. Steigerwald, C. Nuckolls and C. M. Bejger, *ACS Cent. Sci.*, 2017, **3**, 1050–1055.
25. .A. M. Champsaur, C. Mézière, M. Allain, D. W. Paley, M. L. Steigerwald, C. Nuckolls and P. Batail, *J. Am. Chem. Soc.*, 2017, **139**, 11718–11721.
26. E. S. O’Brien, M. T. Trinh, R. L. Kann, J. Chen, G. A. Elbaz, A. Masurkar, T. L. Atallah, M. V. Paley, N. Patel, D. W. Paley, I. Kyimissis, A. C. Crowther, A. J. Millis, D. R. Reichman, X.-Y. Zhu and X. Roy, *Nat. Chem.*, 2017, **9**, 1170–1174.
27. G. Lovat, B. Choi, D. W. Paley, M. L. Steigerwald, L. Venkataraman and X. Roy, *Nat. Nanotechnol.*, 2017, **12**, 1050–1054.
28. W.-L. Ong, E. S. O’Brien, P. S. M. Dougherty, D. W. Paley, C. Fred Higgs Iii, A. J. H. McGaughey, J. A. Malen and X. Roy, *Nat. Mater.*, 2017, **16**, 83–88.
29. B. Choi, J. Yu, D. W. Paley, M. Tuan Trinh, M. V. Paley, J. M. Karch, A. C. Crowther, C. H. Lee, R. A. Lalancette, X. Zhu, K. Kim, M. L. Steigerwald, C. Nuckolls and X. Roy, *Nano Lett.*, 2016, **16**, 1445–1449.
30. .A. M. Champsaur, A. Velian, D. W. Paley, B. Choi, X. Roy, M. L. Steigerwald and C. Nuckolls, *Nano Lett.*, 2016, **16**, 5273–5277.
31. .A. Turkiewicz, D. W. Paley, T. Besara, G. Elbaz, A. Pinkard, T. Siegrist and X. Roy, *J. Am. Chem. Soc.*, 2014, **136**, 15873–15876.
32. J. Yu, C. H. Lee, D. Bouilly, M. Han, P. Kim, M. L. Steigerwald, X. Roy and C. Nuckolls, *Nano Lett.*, 2016, **16**, 3385–3389.
33. V. Chauhan, A. C. Reber and S. N. Khanna, *J. Am. Chem. Soc.*, 2017, **139**, 1871–1877.
34. V. Chauhan and S. N. Khanna, *J. Phys. Chem. A*, 2018, **122** (28), 6014–6020.

35. F. Cecconi, C. A. Ghilardi, S. Midollini and A. Orlandini, *Inorg. Chimica Acta*, 1983, **76**, 183-184.
36. X. Zhang, G. Liu, G. Gantefoer, K. H. Bowen and A. N. Alexandrova, *J. Phys. Chem. Lett.*, 2014, **5**, 1596–1601.
37. A. Grubisic, H. Wang, X. Li, Y. J. Ko, S. Kocak, M. R. Pederson, K. H. Bowen and B. W. Eichhorn, *PNAS*, 2011, **108**, 14757-14762.
38. J. P. Perdew and W. Yue, *Phys. Rev. B*, 1986, **33**, 8800-8802.
39. M. Ernzerhof and G. E. Scuseria, *J. Chem. Phys.* 1999, **110**, 5029.
40. C. Adamo, *J. Chem. Phys.*, 1999, **110**, 6158.
41. E. van Lenthe and E. J. Baerends, *J. Comput. Chem.*, 2003, **24**, 1142–1156.
42. E. van Lenthe, R. van Leeuwen, E. J. Baerends and J. G. Snijders, *Int. J. Quantum Chem.*, 1996, **57**, 281-293.
43. E. van Lenthe, A. Ehlers and E. J. Baerends, *J. Chem. Phys.*, 1999, **110**, 8943.
44. M. R. Nimlos and G. B. Ellison, *J. Phys. Chem.*, 1986, **90**, 2574-2580.
45. E. W. Rothe, S. Y. Tang, G. P. Reck, *J. Chem. Phys.*, 1975, **62**, 3829.
46. P. J. Robinson, G. Liu, S. Ciborowski, C. Martinez-Martinez, J. R. Chamorro, X. Zhang, T. M. McQueen, K. H. Bowen and A. N. Alexandrova, *Chem. Mater.*, 2017, **29**, 9892-9896.
47. P. C. Rusu and G. Brocks, *J. Phys. Chem. B*, 2006, **110**, 22628-22634.
48. V. Chauhan, A. C. Reber and S. N. Khanna, *Nature Comm.*, 2018, **9**, 2357.
49. D. Mollenhauer and N. Gaston, *Phys. Chem. Chem. Phys.*, 2016, **18**, 29686.
50. A. C. Reber and S. N. Khanna, *npj Computational Material*, 2018, **4**, 33.
51. V. Chauhan, A. C. Reber and S. N. Khanna, *Phys. Chem. Chem. Phys.*, 2017, **19**, 31940-31948.

V.A.2. Ligand Effect on the Electronic Structure of Cobalt Sulfide Clusters: A Combined Experimental and Theoretical Study

Reprinted (adapted) with permission from *J. Phys. Chem. C* **123**, 25121-25127 (2019). Copyright 2019 American Chemical Society.

Gaoxiang Liu^a, Vikas Chauhan^b, Alexander P. Aydt^c, Sandra M. Ciborowski^a, Andrew Pinkard,^c Zhaoguo Zhu^a, Xavier Roy^{c,*}, Shiv N. Khanna,^{b,*} and Kit H. Bowen^{a,*}

^a Department of Chemistry, Johns Hopkins University, Baltimore, Maryland 21218, USA.

^b Department of Physics, Virginia Commonwealth University, 701 W. Grace St., Richmond, Virginia 23284, USA.

^c Department of Chemistry, Columbia University, New York, New York 10027, USA.

Abstract

Recent studies have shown that capping ligands offer a new dimension for fine tuning the properties of clusters. Here we investigate this concept by measuring the anion photoelectron spectra of a series of hexanuclear cobalt sulfide clusters, Co₆S₈, passivated by different numbers of triethylphosphine ligands, PET₃. We find that the addition of PET₃ gradually shifts the electronic spectrum of the cluster to higher energy, leading to a decrease in its electron affinity. Density functional theory calculations reveal that adding ligands demagnetize the Co₆S₈ core. The decrease in electron affinity results from a monotonic increase in the energy of the cluster lowest unoccupied molecular orbitals (LUMO). This effect is attributed to the electron donation from the ligands to the cluster core, which increases the charge density in the core region.

Introduction

Quantum confinement in small symmetric clusters can result in a grouping of electronic states into shells, leading to the formation of stable clusters with a well-defined valence. The resemblance to atomic shells has prompted the description of such entities as superatoms.¹ Utilizing these clusters as the “superatomic” building blocks for the assembly of novel materials represents a frontier in material science.¹⁻²² Within this context, the family of metal chalcogenide molecular clusters has recently received renewed attention for fabricating functional materials with tunable properties including ferromagnetism, electrical conductivity, optical gaps and thermal conductivity switching.^{2,7,23-32} One of the key advantages of such materials over traditional atomic solids is that the properties of the superatomic building blocks can be tailored pre-assembly. While the composition and structure of the cluster are

traditionally used to control the behavior of the superatomic building unit, the capping ligands have recently received attention as valuable knobs for fine tuning.^{33,34} Capping ligands can modulate the electronic characteristics of the cluster core, and direct the assembly into solid state materials.

Recently, Khanna and coworkers theoretically predicted a variety of properties that can be tuned by modifying the capping ligands of metal chalcogenide clusters. Using $\text{Co}_6\text{Te}_8\text{L}_6$ (L = capping ligand) as a model system, they have shown that changing L from PET_3 to CO increases the electron affinity of the cluster, in effect transforming it from a superatomic alkali metal to a superatomic halogen.¹⁴ Such an ability to alter the donor/acceptor behavior of the building blocks offers unique opportunity for creating materials with fine-tuned properties.³⁴ In a related study, it was predicted that the ionization energy of the Co_6Se_8 cluster can be gradually decreased by sequentially coordinating PET_3 capping ligands to its surface metal atoms.³⁵ Binding carbon monoxide (CO) ligands to the Co_6Se_8 cluster, on the other hand, results in the gradual demagnetization of the core, thus stabilizing it.³⁶ Experimentally demonstrating these predictions by measuring the electronic structures of metal chalcogenide clusters is challenging, however, because it requires bringing the charged clusters with a controlled number of ligands into the gas phase without damaging the inorganic core. Common ionization methods (e.g., electrospray ionization and matrix-assisted laser desorption/ionization) fail to generate the desirable anions in the gas phase due to the effect of the solvent/matrix on charged clusters: the obtained anions are either dehydrogenated or tagged by the solvent/matrix molecules.

We recently reported an experimental study supported by theoretical calculations establishing the tunability of the electronic properties of the cluster $\text{Co}_6\text{S}_8(\text{PET}_3)_{6-n}(\text{CO})_n$ by altering the ligand ratio.³⁸ The unique infrared desorption/laser photoemission (IR/PE) supersonic expansion source used in that work serves as the ideal tool to bring the cluster into the gas phase with different number of ligands while maintaining the core structure. Here we employ this method to investigate a series of cobalt sulfide clusters passivated with varying numbers of PET_3 ligands. The cluster $\text{Co}_6\text{S}_8(\text{PET}_3)_6$ is synthesized and then brought into the gas phase, where ligands are sequentially dissociated and electrons are attached to form anions, using the IR/PE source. Mass spectrometry confirms the existence of $\text{Co}_6\text{S}_8(\text{PET}_3)_x^-$ with x ranging from 0 to 6. We find that the electron affinity and vertical detachment energy decrease with increasing ligation, demonstrating the electronic spectral tunability of this family of superatoms.

Methods

Synthesis

Dicobalt octacarbonyl and sulfur were purchased from Strem Chemicals. PEt_3 was obtained from Alfa Aesar. All other reagents and solvents were purchased from Sigma Aldrich. Dry and deoxygenated solvents were prepared by elution through a dual-column solvent system (MBraun). Unless otherwise stated, all reactions and sample preparations were carried out under inert atmosphere using standard Schlenk techniques or in a N_2 -filled glovebox. While a multi-step synthesis of $\text{Co}_6\text{S}_8(\text{PEt}_3)_6$ has been previously reported,³⁷ we have developed an alternative one-pot approach detailed below.³⁸

$\text{Co}_6\text{S}_8(\text{PEt}_3)_6$. Sulfur (1.16 g, 36.25 mmol) was suspended in 30 mL of toluene in a 200 mL Schlenk flask. In two separate flasks, $\text{Co}_2(\text{CO})_8$ (4.12 g, 12.05 mmol) and PEt_3 (4.27 g, 36.14 mmol) were dissolved in 20 mL of toluene. The $\text{Co}_2(\text{CO})_8$ solution was added to the S suspension, followed by quick addition of the PEt_3 solution. The reaction mixture was refluxed under N_2 for 2 days. The reaction mixture was then opened to air, and hot filtered through Celite. The filtrate was cooled to room temperature and left to stand for ~ 3 h. Black crystals formed during that period; the resulting suspension was filtered through a fine frit and the solid was washed with toluene, and diethyl ether. The dark, black crystals were collected, dried *in vacuo*, and stored under N_2 . Yield: 2.2 g (42%). The characterization data are as previously published. MS-MALDI m/z^+ calculated 1317.92; found, 1317.95.

Anion photoelectron spectroscopy

Anion photoelectron spectroscopy was conducted by crossing a mass-selected negative ion beam with a fixed energy photon beam and analyzing the energies of the resultant photodetached electrons. This technique is governed by the well-known energy-conserving relationship, $h\nu = \text{EBE} + \text{EKE}$, where $h\nu$, EBE, and EKE are the photon energy, electron binding energy (photodetachment transition energy), and the electron kinetic energy, respectively. The details of our apparatus have been described elsewhere.^{39,40} Briefly, the photoelectron spectra were collected on an apparatus consisting of an ion source, a linear time-of-flight mass spectrometer for mass analysis and selection, and a magnetic-bottle photoelectron spectrometer for electron energy analysis (resolution ~ 35 meV at 1 eV EKE). The third harmonic (355 nm, 3.49 eV per photon) of a Nd:YAG was used to photodetach electrons from the cluster anion of interest. Photoelectron spectra were calibrated against the well-known atomic lines of the copper anion, Cu^- .

To make $\text{Co}_6\text{S}_8(\text{PEt}_3)_x^-$ in the gas phase, a specialized infrared desorption/laser photoemission (IR/PE) supersonic helium expansion source was employed.^{38,41} Briefly, a low power IR pulse (1064 nm) from a Nd:YAG laser hit a translating graphite bar thinly coated with the $\text{Co}_6\text{S}_8(\text{PEt}_3)_6$ sample. Because the graphite absorbed most of the energy,

a localized thermal shock lasting a few nanoseconds propelled the clusters into the gas phase. Almost simultaneously, a high power pulse of 532 nm light from a second Nd:YAG laser struck a close-by photoemitter (Hf wire), creating a shower of electrons that attached to the evaporated neutral clusters. Also, almost simultaneously, a plume of ultrahigh purity helium gas rapidly expanded from a pulsed valve located slightly upstream, cooling the nascent anions and directing them into the mass spectrometer, where they were analyzed. The $\text{Co}_6\text{S}_8(\text{PEt}_3)_6$ cluster was coated onto a graphite bar in a N_2 -filled glove box, which was then enclosed inside an air-tight “suitcase” container and opened under high vacuum after being transferred to the vacuum chamber.

Theoretical calculations

Electronic structure modeling of the anion and neutral $\text{Co}_6\text{S}_8(\text{PEt}_3)_x$ ($x = 1-5$) were carried out to understand the variation in the adiabatic and vertical detachment energies at the microscopic level. The exchange-correlation effects are included via a generalized gradient functional PBE detailed by Perdew et al.⁴² The cluster wave function is formed from a linear combination of atomic orbitals constructed from Slater-type orbitals located on the atomic sites.⁴³ A TZ2P basis set and a large frozen electron core (S:1s²2s²p⁶, Co:1s²2s²p⁶3s²p⁶, P:1s²2s²p⁶, C:1s²) are used. The calculations incorporate a zero-order regular approximation (ZORA) to include scalar-relativistic effect.^{44,45} The trial structures of the clusters are taken from the previously optimized structure of the $\text{Co}_6\text{Se}_8(\text{PEt}_3)_x$ where the Se sites are replaced by S. A quasi-Newton method without any symmetry restriction allowed a determination of the ground state of the clusters. During optimization, we investigated all possible spin states. The positive vibrational frequencies of neutral and anionic clusters established the true ground states of the clusters. Also, none of the clusters in their ground states has the spin-contamination. The adiabatic electron affinity (AEA) is calculated as the difference between the total energy between the anion in its ground state geometry and the neutral cluster in its ground state geometry, while the vertical detachment energy (VDE) is given by the total energy difference between the anion in its ground state and the neutral cluster in the geometry of the anion.

Results and discussions

Figure V.A.2.1 presents a typical mass spectrum of $\text{Co}_6\text{S}_8(\text{PEt}_3)_x^-$ obtained with the IR/PE source. The ultrashort thermal shock induced by IR laser irradiation caused the sequential dissociation of the PEt_3 ligand during the vaporization of the solid $\text{Co}_6\text{S}_8(\text{PEt}_3)_6$ sample into gas phase. $\text{Co}_6\text{S}_8(\text{PEt}_3)_x^-$ with x ranging from 0 to 6 were generated and investigated by anion photoelectron spectroscopy.

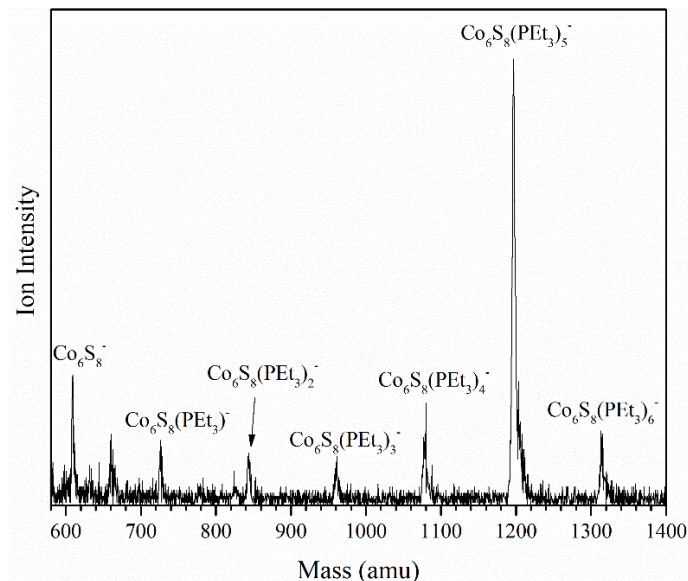


Figure V.A.2.1 Anion mass spectrum of $\text{Co}_6\text{S}_8(\text{PEt}_3)_x^-$ generated using IR/PE anion source.

Figure V.A.2.2 presents the anion photoelectron spectra of $\text{Co}_6\text{S}_8(\text{PEt}_3)_x^-$ ($x = 2-5$) collected with 355 nm (3.49 eV) 3rd harmonic laser. The spectrum of $\text{Co}_6\text{S}_8(\text{PEt}_3)_6^-$ has been published in a previous report.³⁸ Our attempts to measure the photoelectron spectra of Co_6S_8^- and $\text{Co}_6\text{S}_8(\text{PEt}_3)^-$ ($x = 0$ and 1) with a 355 nm laser were for the most part unsuccessful: for Co_6S_8^- , no photoelectron signal was observed, i.e., its AEA and VDE are above 3.49 eV, while for $\text{Co}_6\text{S}_8(\text{PEt}_3)^-$, only a small portion of its spectrum could be collected because the majority of its photoelectron spectrum lies beyond the photon energy (Figure S1). The AEA and VDE of each cluster are determined from the photoelectron spectra. The value of the AEA is taken to be the onset of the lowest electron binding energy (EBE) peak in the photoelectron spectrum. The VDE is the vertical transition energy from the ground state of the anion to the neutral ground electronic state at the anion geometry. It is determined as the EBE value at the intensity maximum of the peak of interest. Here, however, due to the large number of electronic states that can be accessed during the photodetachment process, the photoelectron spectra are convoluted. We therefore determine the VDE as the EBE of the first noticeable peak in each spectrum. Based on the anion photoelectron spectra, the AEA values of $\text{Co}_6\text{S}_8(\text{PEt}_3)_x$ are 3.0, 2.6, 2.2, 2.0 and 1.8 eV for $x = 1, 2, 3, 4$, and 5, respectively, while the corresponding anion VDE values are 3.22, 2.71, 2.44, 2.31, and 2.05 eV, respectively. We also report the VDE* values, which correspond to the transition from the anion ground state to the first electronic excited state of the neutral, as the EBE of the second noticeable peak. Their values are 3.35, 2.85, 2.45, 2.29 and 2.16 eV for $x = 1, 2, 3, 4$, and 5, respectively. By

sequentially adding PET_3 ligands to the Co_6S_8 core, the AEA and VDE of this superatom decrease systematically, which is consistent with the electron-donating nature of the PET_3 ligands.

Changes in the electronic properties of the cluster are evident in high energy spectral features above the first EBE peak. These higher EBE peaks arise from transitions from the anion ground state to excited electronic states of the neutral cluster and the shape of these features relates to the electronic structure of the neutral clusters. As x increases, the photoelectron spectra of $\text{Co}_6\text{S}_8(\text{PET}_3)_x^-$ shifts to lower electron binding energy and the overall spectral shapes change significantly. Such observation suggests a change in the electronic structure of $\text{Co}_6\text{S}_8(\text{PET}_3)_x^-$ as x changes. Note that this is different from the previous study of $\text{Co}_6\text{S}_8(\text{PET}_3)_{6-n}(\text{CO})_n^-$ where the photoelectron spectra shift to higher electron binding energy as the CO ratio increases, but the overall spectral shapes are maintained, indicating that the essential electronic structure of $\text{Co}_6\text{S}_8(\text{PET}_3)_{6-n}(\text{CO})_n$ superatoms are largely unchanged.³⁸

The structures of the anionic and neutral $\text{Co}_6\text{S}_8(\text{PET}_3)_x$ clusters were investigated by theoretical calculations. Figure V.A.2.3 shows the optimized ground state geometries of $\text{Co}_6\text{S}_8(\text{PET}_3)_x^-$, while those of the neutral species are in Figure S2. For $x = 2$ and $x = 4$, the clusters can either be *cis* or *trans* isomers. In both cases, the *trans* isomers are

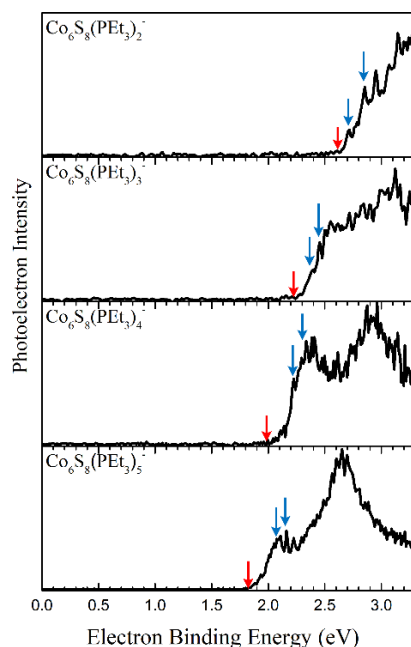


Figure V.A.2.2 Negative ion photoelectron spectra of $\text{Co}_6\text{S}_8(\text{PET}_3)_x^-$ ($x = 2 - 5$) anions collected using 355 nm (3.49 eV) photons from a Nd:YAG laser. The red arrows indicate the AEA, the blue arrows indicate the VDE and the VDE*.

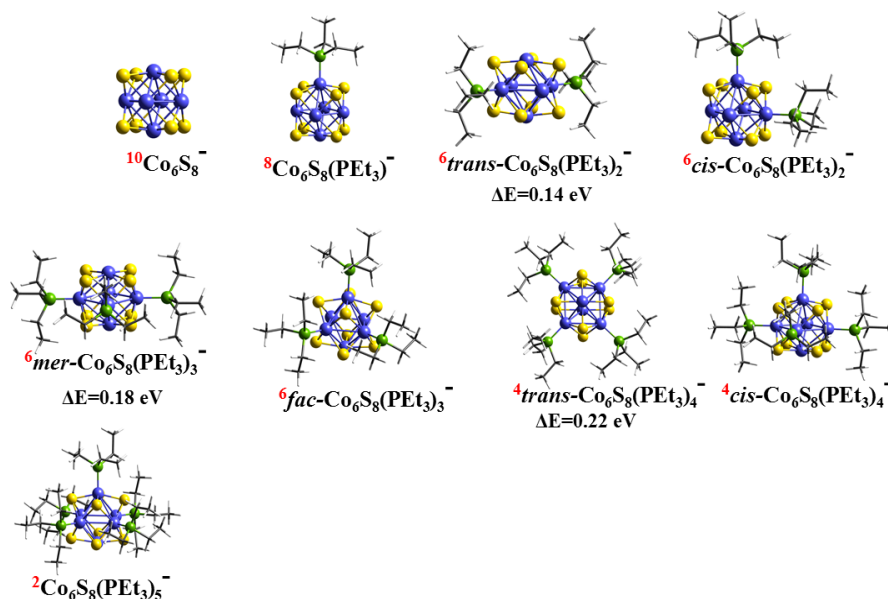


Figure V.A.2.3 Optimized ground state geometry of anionic $\text{Co}_6\text{S}_8(\text{PEt}_3)_x$ ($x = 0-5$) clusters. Superscripts in red text show the multiplicity of the clusters.

higher in energy, by ~ 0.14 and ~ 0.22 eV, respectively. A similar situation arises for the corresponding neutral clusters: the *trans* isomers are ~ 0.01 and ~ 0.25 eV higher in energy for $x = 2$ and $x = 4$ respectively. For $\text{Co}_6\text{S}_8(\text{PEt}_3)_3$, the cluster can adopt *fac* and *mer* configurations. We find that the *fac* isomer is the ground state for both anionic and neutral clusters, being lower in energy by ~ 0.18 and ~ 0.04 eV, respectively. In addition to the ligated clusters, we optimize the anionic and neutral naked Co_6S_8 core in order to complete the analysis although no photoelectron spectrum could be measured as the transitions are outside the range of measurable energies.

The key experimental finding in Figure V.A.2.2 is that the bonding of PEt_3 to the Co_6S_8 core leads to a change in the peak position and the leading edge of the spectrum. To provide insight into these variations, we calculate the VDE by taking the energy difference between the ground state of the anion and neutral cluster with the same geometry as the anion. The VDE corresponds to the first peak maximum in the photodetachment spectra and provides the most direct comparison with the experiment while an estimation of 2nd VDE is obtained by a vertical transition from the anion ground state to the neutral with next higher spin multiplicity. We also calculated the AEA, which are determined by the onset of the experimental spectra and corresponds to the energy difference between the ground states of the anion and neutral species. Finally, we examine the excited states of the neutral cluster in the anionic geometry that

correspond to the spectral features beyond the first peak. Figure V.A.2.4 compares the experimental and theoretical AEA and VDE values while Table V.A.2.1 lists the values of both the theoretical and calculated AEA and VDE. The calculated AEA and VDE of the Co_6S_8 core are 3.55 and 3.59 eV, respectively, which are in accordance with the absence of photoelectron signal when using 355 nm (3.49 eV) photon. The AEA^{T} for $\text{Co}_6\text{S}_8(\text{PET}_3)$ is 2.94 eV, agreeing with the AEA^{E} of 3.0 eV, while VDE^{E} is 3.22 eV compared to the calculated VDE^{T} of 2.98 eV. The *cis*- $\text{Co}_6\text{S}_8(\text{PET}_3)_2$ isomer has an AEA^{T} of 2.49 eV, which is slightly closer to the AEA^{E} of 2.6 eV than that of *trans*- $\text{Co}_6\text{S}_8(\text{PET}_3)_2$ (2.35 eV). Both $\text{Co}_6\text{S}_8(\text{PET}_3)_2$ isomers have VDE^{T} around 2.60 eV that are close to the VDE^{E} of 2.71 eV, suggesting the possible presence of both isomers. The AEA^{T} and VDE^{T} of *fac*- $\text{Co}_6\text{S}_8(\text{PET}_3)_3$ are 2.26 and 2.32 eV, in very good agreement with corresponding experimental values of AEA^{E} (2.2 eV) and VDE^{E} (2.39 eV), while the AEA^{T} and VDE^{T} for *mer*- $\text{Co}_6\text{S}_8(\text{PET}_3)_3$ are 2.10 eV and 2.16 eV. Both *trans*- and *cis*- $\text{Co}_6\text{S}_8(\text{PET}_3)_4$ have AEA^{T} around 2.0 eV, matching the experimental value of 2.0 eV, while the corresponding VDE^{T} (2.15 and 2.11 eV) are slightly smaller than the experimental value of 2.31 eV. In order to evaluate the dispersion effect on the calculated AEA^{T} and VDE^{T} , we also carried out calculations with Grimme dispersion corrected PBE functional.⁴⁶ Similar calculated AEA^{T} and VDE^{T} were obtained (Table S1). Overall, the calculated values are in excellent agreement with

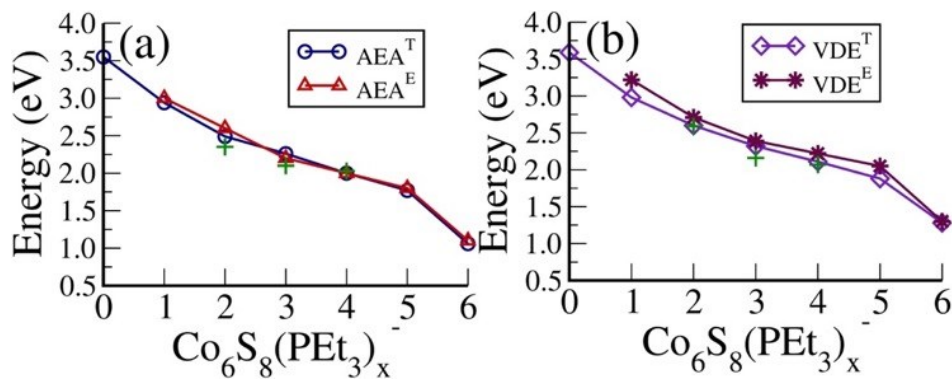


Figure V.A.2.4 The experimental and theoretical adiabatic and vertical detachment energy of $\text{Co}_6\text{S}_8(\text{PET}_3)_x$ ($x = 0 - 6$) clusters. The plus symbol (+) indicates the AEA^{T} and VDE^{T} values of cluster's isomers at $x = 2, 3$, and 5 . The results of $\text{Co}_6\text{S}_8(\text{PET}_3)_6$ are taken from Ref. 38.

experimental results, thus validating the calculations. Since the photoelectron spectra are fingerprint of the electronic structures of neutral clusters, the agreement indicates that the calculated atomic structures and the multiplicities match the ones observed experimentally.

Table V.A.2.1 Theoretical and experimental adiabatic and 1st and 2nd vertical detachment energies (VDE and VDE*) of $\text{Co}_6\text{S}_8(\text{PEt}_3)_x^-$ ($x = 0-5$) clusters.

Cluster	AEA ^E (eV)	VDE ^E (eV)		Isomers	ΔE (eV)	AEA ^T (eV)	VDE ^T (eV)	
		VDE	VDE*				VDE	VDE*
Co_6S_8^-	>3.49	>3.49	>3.49			3.55	3.59	3.96
$\text{Co}_6\text{S}_8(\text{PEt}_3)^-$	3.0	3.22	3.35			2.94	2.98	3.37
$\text{Co}_6\text{S}_8(\text{PEt}_3)_2^-$	2.6	2.71	2.85	<i>trans</i>	0.14	2.35	2.59	2.88
				<i>cis</i>		2.49	2.60	2.92
$\text{Co}_6\text{S}_8(\text{PEt}_3)_3^-$	2.2	2.39	2.45	<i>mer</i>	0.18	2.10	2.16	2.32
				<i>fac</i>		2.26	2.32	2.33
$\text{Co}_6\text{S}_8(\text{PEt}_3)_4^-$	2.0	2.22	2.29	<i>trans</i>	0.22	2.03	2.07	2.15
				<i>cis</i>		2.00	2.11	2.21
$\text{Co}_6\text{S}_8(\text{PEt}_3)_5^-$	1.8	2.05	2.16			1.77	1.88	2.09

The main result is a monotonic decrease in the AEA and VDE as ligands are successively attached to the Co_6S_8 core. Such a decrease is attributed to the fact that PEt_3 ligands are electron donors and thus increase the charge density in the core region. To support this hypothesis, we performed a Hirshfeld charge analysis (Figure S3). The cumulative charge donated from the ligands to the Co_6S_8 core gradually increases, from ~ 0.32 e in $\text{Co}_6\text{S}_8(\text{PEt}_3)$ to ~ 0.90 e in $\text{Co}_6\text{S}_8(\text{PEt}_3)_5$. The added charge affects the one-electron levels of the clusters, in particular, the HOMO and LUMO energies, which control the ionization and electron affinity. Figure V.A.2.5 presents the one-electron levels of the

neutral clusters. The values of the HOMO, LUMO and HOMO-LUMO gap for anionic and neutral clusters are given in Table S2. Note that the addition of successive ligands raises the one-electron levels, as marked by the position of the LUMO. As the position of the LUMO is raised in energy, the electron affinity of the cluster decreases since the extra electron occupies the LUMO of the neutral cluster. The largest increase in the LUMO energy occurs with the attachment of the 1st and 2nd PET_3 . Beyond $x = 2$, each additional ligand increases the LUMO by around 0.3 eV. Remarkably, we find that the ligands are not bound strongly to the cluster core: the binding energy of the first PET_3 to Co_6S_8 is 1.53 eV, and decreases to 1.38 eV for the 5th ligand.

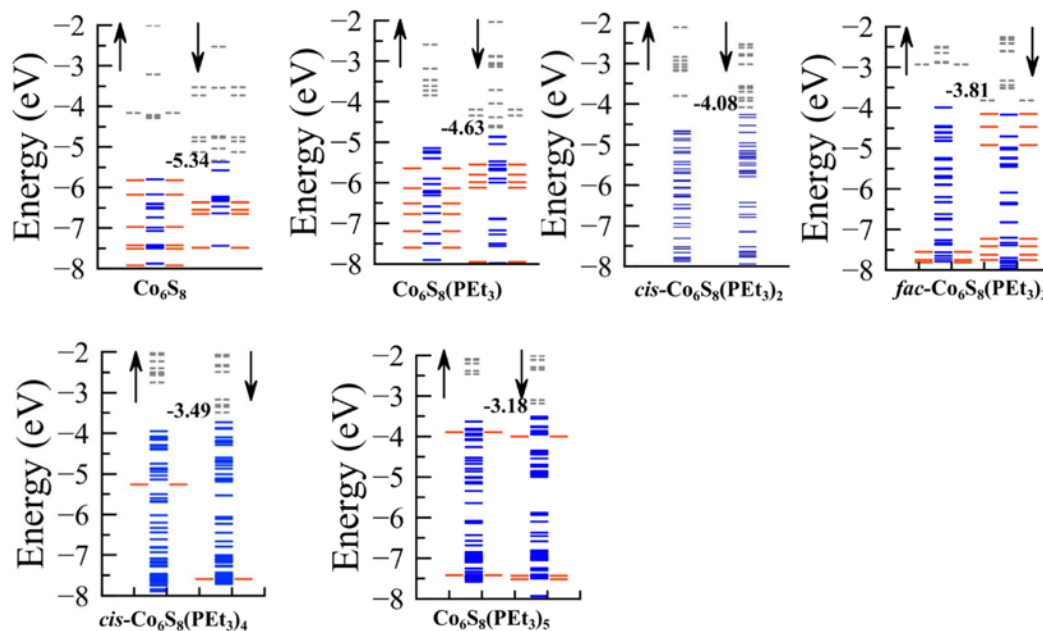


Figure V.A.2.5 One electron-energy levels of $\text{Co}_6\text{S}_8(\text{PET}_3)_x$ ($x = 0-5$) clusters. The solid blue and red bars represent the singly and doubly occupied energy levels, respectively. Unoccupied energy levels are shown by dashed gray lines. The energy of LUMO (in eV) is indicated for each cluster. The α -spin and β -spin channel are represented by up and down arrows.

Our earlier studies have shown that a complete ligation with either PET_3 or a mixture of PET_3 and CO ligands produces the lowest spin state for the $\text{Co}_6\text{S}_8(\text{PET}_3)_{6-n}(\text{CO})_n$ clusters. This contrasts drastically with the partially ligated cluster in this study: starting from the bare anionic Co_6S_8 core, with a spin multiplicity of $M = 10$, the multiplicity is reduced by 2 upon addition of a PET_3 ligand, leading to $\text{Co}_6\text{S}_8(\text{PET}_3)^-$ in an octet state. The attachment of the 2nd and 3rd PET_3 ligands produces a sextet spin state, while the bonding of the 4th and 5th ligands generates a quartet ground state. To

support these results, Figure V.A.2.6a shows the one-electron energy levels of Co_6S_8 in an octahedral symmetry. In the energy range -20 to -18 eV, there are 16 electrons accommodated in A_{1g} , T_{1u} , T_{2g} , and A_{2u} orbitals formed by s -states of S and Co sites. The remaining 86 electrons are accommodated in $T_{2g/2u}$, T_{1g}/T_{1u} , $E_{g/u}$, A_{2u} , and $A_{1g/2g}$ states in the energy range from -10 to -2 eV. A set of unoccupied T_{1g} (d_{xz} , d_{yz} , d_{xy}), T_{2u} (d_{xz} , d_{yz} , $d_{x^2-y^2}$), T_{1u} (d_{xz} , d_{yz} , d_{z^2}), and E_g (d_{z^2}) states in β -spin channel lead to a spin multiplicity $M = 11$. In addition, the E_g ($d_{x^2-y^2}$) in β -spin channel is occupied. As the LUMO is a minority spin state, addition of an electron leads to an anion with a spin multiplicity of 10. The d -orbitals in the parentheses with italics text are localized on the Co site along z -axis. Note that two d_{z^2} orbitals form a bonding E_g -type and an anti-bonding T_{1u} -type orbitals with a node along z axis. Figure V.A.2.6b shows the one-electron energy levels of Co_6S_8 with PET_3 ligand along the z -axis. Addition of PET_3 ligand breaks the octahedral symmetry and the sp -states of P combine primarily with d -states of Co to stabilize the E_g (d_{z^2}) and T_{1g} (d_{xz} , d_{yz}) states while E_g ($d_{x^2-y^2}$) state is destabilized and becomes a part (MO $^{\beta}$ -70) of unoccupied states in the β -spin channel. The E_g (d_{z^2}) states form the occupied bonding (MO $^{\alpha}$ -49, MO $^{\beta}$ -44) states with lone pair of electrons of PET_3 while corresponding unoccupied anti-bonding (MO $^{\alpha}$ -78, MO $^{\beta}$ -78) states are higher in energy. The remaining T_{2u} (d_{xz} , d_{yz} , $d_{x^2-y^2}$), T_{1u} (d_{xz} , d_{yz} , d_{z^2}) also lose their degeneracy and turn into MO $^{\beta}$ -(75,76,72) and MO $^{\beta}$ -(73,74,71), respectively. These six states along with MO $^{\beta}$ -70 and MO $^{\beta}$ -77 ($T_{1g}(d_{xy})$) lead to a reduced multiplicity $M = 9$ in the ground state of $\text{Co}_6\text{S}_8(\text{PET}_3)$. Further addition of ligands leads to a similar mixing with reduction in multiplicity.

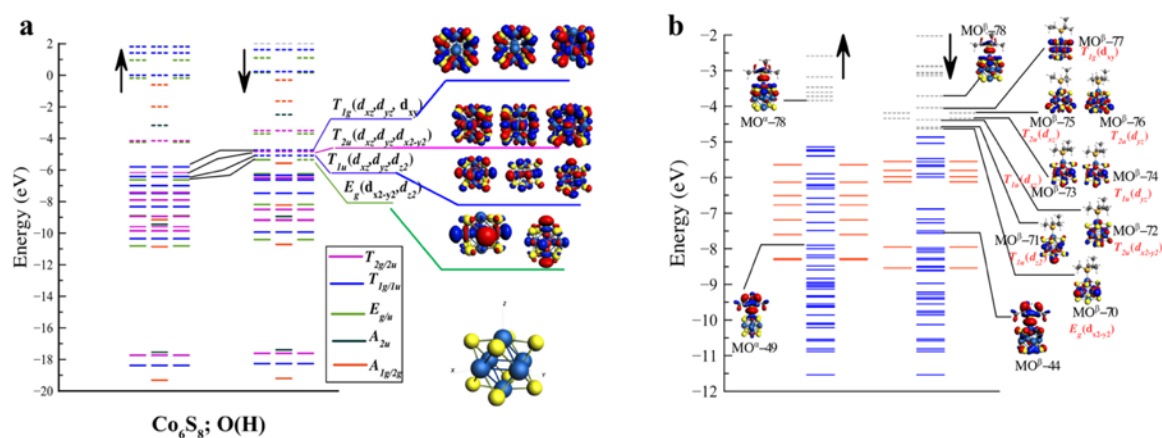


Figure V.A.2.6 (a) One-electron energy levels with their symmetry labels for Co_6S_8 in octahedron symmetry. The solid and dashes lines represent occupied and unoccupied energy levels. (b) One-electron energy levels along with their iso-surfaces for $\text{Co}_6\text{S}_8(\text{PET}_3)$. The solid blue and red bars represent the singly and doubly occupied energy levels,

respectively. Unoccupied energy levels are shown by dashed gray lines. The α -spin and β -spin channel represented by up and down arrows.

Summary

By combining inorganic cluster synthesis, gas-phase anion photoelectron spectroscopy, and electronic structure calculations, we have demonstrated that the electronic properties of metal chalcogenide clusters can be tuned by varying the number of phosphine capping ligands. The sequential addition of PET_3 to the Co_6S_8 core results in a gradual decrease of its electron affinity and a shift of its electronic spectrum to lower energy. Density functional theory calculations reveal that addition of PET_3 ligands gradually demagnetizes the Co_6S_8 core and increases its charge density. These effects stabilize the core and lift the energy of the LUMO.

References

1. Reber, A. C.; Khanna, S. N. Superatoms: Electronic and Geometric Effects on Reactivity. *Acc. Chem. Res.* **2017**, *50*, 255–263.
2. Pinkard, A.; Champsaur, A. M.; Roy, X. Molecular Clusters: Nanoscale Building Blocks for Solid-State Materials. *Acc. Chem. Res.* **2018**, *51*, 919–929.
3. Claridge, S. A.; Castleman, A. W.; Khanna, S. N.; Murray, C. B.; Sen, A.; Weiss, P. S. Dimensional Reduction: A Practical Formalism for Manipulating Solid Structures. *ACS Nano*. 2009, *3*, 244–255.
4. Tulsky, E. G.; Long, J. R. Dimensional Reduction: A Practical Formalism for Manipulating Solid Structures. *Chem. Mater.* **2001**, *13*, 1149–1166.
5. Baudron, S. A.; Batail, P.; Coulon, C.; Clerac, R.; Canadell, E.; Laukhin, V.; Melzi, R.; Wzietek, P.; Jerome, D.; Auban-Senzier, P.; Ravy, S. (EDT-TTF- CONH_2) $_6$ [$\text{Re}_6\text{Se}_8(\text{CN})_6$], a Metallic Kagome-Type Organic–Inorganic Hybrid Compound: Electronic Instability, Molecular Motion, and Charge Localization. *J. Am. Chem. Soc.* **2005**, *127*, 11785–11797.
6. Yoon, B.; Luedtke, W. D.; Barnett, R. N.; Gao, J.; Desiredy, A.; Conn, B. E.; Bigioni, T.; Landman, U. Hydrogen-bonded structure and mechanical chiral response of a silver nanoparticle superlattice. *Nat. Mater.* **2014**, *13*, 807–811.
7. Corrigan, J. F.; Fuhr, O.; Fenske, D. Metal Chalcogenide Clusters on the Border between Molecules and Materials. *Adv. Mater.* **2009**, *21*, 1867–1871.
8. Roy, X.; Lee, C. H.; Crowther, A. C.; Schenck, C. L.; Besara, T.; Lalancette, R. A.; Siegrist, T.; Stephens, P. W.; Brus, L. E.; Kim, P.; Steigerwald, M. L.; Nuckolls, C. Nanoscale Atoms in Solid-State Chemistry. *Science*, **2013**, *341*, 157–160.
9. Khanna, S. N.; Jena, P. Atomic clusters: Building Blocks for a Class of Solids. *Phys. Rev. B*. **1995**, *51*, 13705–13716.
10. Castleman, A. W.; Khanna, S. N. Clusters, Superatoms, and Building Blocks of New Materials. *J. Phys. Chem. C* **2009**, *113*, 2664–2675.
11. Lee, C. H.; Liu, L.; Bejger, C.; Turkiewicz, A.; Goko, T.; Arguello, C. J.; Frandsen, B. A.; Cheung, S. C.; Medina, T.; Munsie, T. J. S.; D’Ortenzio, R.; Luke, G. M.; Besara, T.; Lalancette, R. A.; Siegrist, T.; Stephens, P. W.; Crowther, A. C.; Brus, L. E.; Matsuo, Y.; Nakamura, E.; Uemura, Y. L.; Kim, P.; Nuckolls, C.; Steigerwald, M. L.; Roy, X. Ferromagnetic Ordering in Superatomic Solids. *J. Am. Chem. Soc.* **2014**, *136*, 16926–16931.
12. Roy, X.; Schenck, C. L.; Ahn, S.; Lalancette, R. A.; Venkataraman, L.; Nuckolls, C.; Steigerwald, M. L. Quantum Soldering of Individual Quantum Dots. *Angew. Chem., Int. Ed.* **2012**, *51*, 12473–12476.
13. Trinh, M. T.; Pinkard, A.; Pun, A. B.; Sanders, S. N.; Kumarasamy, E.; Sfeir, M. Y.; Campos, L. M.; Roy, X.; Zhu, X. Y. Distinct Properties of the Triplet Pair State from Singlet Fission. *Sci. Adv.* **2017**, *3*, e1700241

14. Chauhan, V.; Sahoo, S.; Khanna, S. N. $\text{Ni}_9\text{Te}_6(\text{PET}_3)_8\text{C}_{60}$ Is a Superatomic Superalkali Superparamagnetic Cluster Assembled Material ($\text{S}^3\text{-CAM}$). *J. Am. Chem. Soc.* **2016**, *138*, 1916–1921.
15. Khanna, S. N.; Reber, A. C. Intercalation without Altercation. *Nat. Chem.* **2017**, *9*, 1151–1152.
16. Tomalia, D. A.; Khanna, S. N. A Systematic Framework and Nanoperiodic Concept for Unifying Nanoscience: Hard/Soft Nanoelements, Superatoms, Meta-Atoms, New Emerging Properties, Periodic Property Patterns, and Predictive Mendeleev-like Nanoperiodic Tables. *Chem. Rev.* **2016**, *116*, 2705–2774.
17. Zheng, Z.; Long, J. R.; Holm, R. H. A Basis Set of Re_6Se_8 Cluster Building Blocks and Demonstration of Their Linking Capability: Directed Synthesis of an $\text{Re}_{12}\text{Se}_{16}$ Dicluster. *J. Am. Chem. Soc.*, **1997**, *119*, 2163–2171.
18. Cargnello, M.; Johnston-Peck, A. C.; Diroll, B. T.; Wong, E.; Datta, B.; Damodhar, D.; Doan-Nguyen, V. V. T.; Herzing, A. A.; Kagan, C. R.; Murray, C. B. Substitutional Doping in Nanocrystal Superlattices. *Nature*, **2015**, *524*, 450–453.
19. O'Brien, M. N.; Jones, M. R.; Lee, B.; Mirkin, C. A. Anisotropic Nanoparticle Complementarity in DNA-mediated Co-crystallization. *Nat. Mater.* **2015**, *14*, 833–839.
20. Boles, M. A.; Talapin, D. V. Many-Body Effects in Nanocrystal Superlattices: Departure from Sphere Packing Explains Stability of Binary Phases. *J. Am. Chem. Soc.* **2015**, *137*, 4494.
21. Poyser, C. L.; Czerniuk, T.; Akimov, A.; Diroll, B. T.; Gaudling, E. A.; Salasyuk, A. S.; Kent, A. J.; Yakovlev, D. R.; Bayer, M.; Murray, C. B. Coherent Acoustic Phonons in Colloidal Semiconductor Nanocrystal Superlattices. *ACS Nano*. **2016**, *10*, 1163–1169.
22. Ong, W. L.; Rupich, S. M.; Talapin, D. V.; McGaughey, A. J. H.; Malen, J. A. Surface Chemistry Mediates Thermal Transport in Three-dimensional Nanocrystal Arrays. *Nat. Mater.* **2013**, *12*, 410–415.
23. Voevodin, A.; Campos, L. M.; Roy, X. Multifunctional Vesicles from a Self-assembled Cluster-Containing Diblock Copolymer. *J. Am. Chem. Soc.* **2018**, *140*, 5607–5611.
24. Champsaur, A. M.; Yu, J.; Roy, X.; Paley, D. W.; Steigerwald, M. L.; Nuckolls, C.; Bejger, C. M. Two-Dimensional Nanosheets from Redox-Active Superatoms. *ACS Cent. Sci.* **2017**, *3*, 1050–1055.
25. Champsaur, A. M.; Mézière, C.; Allain, M.; Paley, D. W.; Steigerwald, M. L.; Nuckolls, C.; Batail, P. Weaving Nanoscale Cloth through Electrostatic Templating. *J. Am. Chem. Soc.* **2017**, *139*, 11718–11721.
26. O'Brien, E. S.; Trinh, M. T.; Kann, R. L.; Chen, J.; Elbaz, G. A.; Masurkar, A.; Atallah, T. L.; Paley, M. V.; Patel, N.; Paley, D. W.; Kyrmis, I.; Crowther, A. C.; Millis, A. J.; Reichman, D. R.; Zhu, X. Y.; Roy, X. Single-crystal-to-single-crystal Intercalation of a Low-bandgap Superatomic crystal. *Nat. Chem.* **2017**, *9*, 1170–1174.
27. Lovat, G.; Choi, B.; Paley, D. W.; Steigerwald, M. L.; Venkataraman, L.; Roy, X. Room-temperature Current Blockade in Atomically Defined Single-cluster Junctions. *Nat. Nanotechnol.* **2017**, *12*, 1050–1054.
28. Ong, W. L.; O'Brien, E. S.; Dougherty, P. S. M.; Paley, D. W.; Fred Higgs III, C.; McGaughey, A. J. H.; Malen, J. A.; Roy, X. Orientational Order Controls Crystalline and Amorphous Thermal Transport in Superatomic Crystals. *Nat. Mater.* **2017**, *16*, 83–88.
29. Choi, B.; Yu, J.; Paley, D. W.; Tuan Trinh, M.; Paley, M. V.; Karch, J. M.; Crowther, A. C.; Lee, C. H.; Lalancette, R. A.; Zhu, X.; Kim, K.; Steigerwald, M. L.; Nuckolls, C.; Roy, X. van der Waals Solids from Self-Assembled Nanoscale Building Blocks. *Nano Lett.* **2016**, *16*, 1445–1449.
30. Champsaur, A. M.; Velian, A.; Paley, D. W.; Choi, B.; Roy, X.; Steigerwald, M. L.; Nuckolls, C. Building Diatomic and Triatomic Superatom Molecules. *Nano Lett.* **2016**, *16*, 5273–5277.
31. Turkiewicz, A.; Paley, D. W.; Besara, T.; Elbaz, G.; Pinkard, A.; Siegrist, T.; Roy, X. Assembling Hierarchical Cluster Solids with Atomic Precision. *J. Am. Chem. Soc.* **2014**, *136*, 15873–15876.
32. Yu, J.; Lee, C. H.; Bouilly, D.; Han, M.; Kim, P.; Steigerwald, M. L.; Roy, X.; Nuckolls, C. Patterning Superatom Dopants on Transition Metal Dichalcogenides. *Nano Lett.* **2016**, *16*, 3385–3389.
33. Walter, M.; Akola, J.; Lopez-Acevedo, O.; Jadzinsky, P. D.; Calero, G.; Ackerson, C. J.; Whetten, R. L.; Grönbeck, H.; Häkkinen, H. A Unified View of Ligand-protected Gold Clusters as Superatom Complexes. *Proc. Natl. Acad. Sci. U. S. A.* **2008**, *105*, 9157–916.
34. Aikens, C. M. Electronic and Geometric Structure, Optical Properties, and Excited State Behavior in Atomically Precise Thiolate-Stabilized Noble Metal Nanoclusters. *Acc. Chem. Res.* **2018**, *51*, 3065–3073.
35. Reber, A. C.; Khanna, S. N. $\text{Co}_6\text{Se}_8(\text{PET}_3)_6$ Superatoms as Tunable Chemical Dopants for Two-Dimensional Semiconductors. *npj Comput. Mater.* **2018**, *4*, 33.
36. Chauhan, V.; Khanna, S. N. Strong Effect of Organic Ligands on the Electronic Structure of Metal-Chalcogenide Clusters. *J. Phys. Chem. A* **2018**, *122*, 6014–6020.
37. Ceconi, F.; Ghilardi, C. A.; Midollini, S.; Orlandini, A. One Electron Reduction of a Cobalt-sulfur Cluster. Synthesis and Molecular Structure of $[\text{Co}_6(\mu_3\text{-S})_8(\text{PET}_3)_6] \cdot \text{nthf}$. *Inorg. Chimica Acta* **1983**, *76*, 183–184.

38. Liu, G.; Pinkard, A.; Ciborowski, S. M.; Chauhan, V.; Zhu, Z.; Aydt, A. P.; Khanna, S. N.; Roy, X.; Bowen, K. H. Tuning the Electronic Properties of Hexanuclear Cobalt Sulfide Superatoms via Ligand Substitution. *Chem. Sci.* **2019**, *10*, 1760-1766.
39. Zhang, X.; Liu, G.; Gantefer, G.; Bowen, K. H.; Alexandrova, A. N. PtZnH_5^- , A σ -Aromatic Cluster. *J. Phys. Chem. Lett.* **2014**, *5*, 1596-1601.
40. Liu, G.; Ciborowski, S. C.; Bowen, K. Photoelectron Spectroscopic and Computational Study of PyridineLigated Gold Cluster Anions. *J. Phys. Chem. A* **2017**, *121*, 5817-5822.
41. Grubisic, A.; Wang, H.; Li, X.; Ko, Y. J.; Kocak, S.; Pederson, M. R.; Bowen, K. H.; Eichhorn, B. W. Photoelectron Spectroscopic and Computational Studies of the Pt@Pb_{10}^{1-} and $\text{Pt@Pb}_{12}^{1-/2-}$ Anions. *Proc. Nat. Acad. Sci.* **2011**, *108*, 14757-14762.
42. Perdew, J. P.; Yue, W. Accurate and Simple Density Functional for the Electronic Exchange Energy: Generalized Gradient Approximation. *Phys. Rev. B* **1986**, *33*, 8800-8802.
43. van Lenthe, E.; Baerends, E. J. Optimized Slater-type basis sets for the elements 1-118. *J. Comput. Chem.* **2003**, *24*, 1142-1156.
44. van Lenthe, E.; van Leeuwen, R.; Baerends, E. J.; Snijders, J. G. Relativistic Regular Two-component Hamiltonians. *Int. J. Quantum Chem.* **1986**, *57*, 281-293.
45. van Lenthe, E.; Ehlers, A.; Baerends, E. J. Geometry Optimizations in the Zero-order Regular Approximation for Relativistic Effects. *J. Chem. Phys.* **1999**, *110*, 8943-8953.
46. Grimme, S.; Ehrlich, S.; Goerigk, L. Effect of the Damping Function in Dispersion Corrected Density Functional Theory. *J. Comp. Chem.* **2011**, *32*, 1456-1465.

VI. Appendix

VI.A. Preliminary data

In this section, all the spectra that were taken by me and my partners and have not been published during my PhD career will be presented in figures. Details of experiments and interpretations will be briefly discussed.

VI.A.1. Relevant Complexes of Metal Tetraphenyl Porphyrins Studied via Photoelectron Spectroscopy

Zhaoguo Zhu, Mary Marshall, Sandra Ciborowski, Maria Dipalo, Gaoxiang Liu, and Kit H. Bowen

Introduction

Metalloporphyrins are one of the cornerstones on which the existence of life is based, and major biochemical, enzymatic, and photochemical functions depend on the special properties of a tetrapyrrolic macrocycle.[1] They transport and store oxygen in heme proteins and are building blocks in metal-organic frameworks (MOFs).[2] Anions of metal porphyrin complexes are important in many catalytic reactions.[3,4] For example, Iron tetraphenylporphyrins are prime candidates as catalysts for CO₂ reduction, which involves electron attachment to iron tetraphenylporphyrins first. Iron(0) porphyrins, which are electrochemically generated from iron(III) porphyrins by three successive one-electron reductions, undergo an electron push–pull mechanism with weak Brønsted or Lewis acids to reduce CO₂ at an overpotential as low as 220 mV (Fe-o-TMA). [5-7]

Identifying the electronic and structural properties of isolated metalloporphyrins is important for understanding their ability to transfer electrons and bind to small molecules. The electronic structure of the complexes give insight to how the small molecules are bound and/ or activated. Previous photoelectron spectroscopic experiments on metalloporphyrins, M(TPP)- (M= Fe and Ni),[8] were expanded upon to include reactions with CO₂ and O₂.

Experimental Methods

The metal tetraphenyl porphyrins were generated using a laser vaporization source. The second harmonic of a Nd:YAG laser (532 nm, 2.33 eV) ablated either an iron rod coated with 5, 10, 15, 20- tetraphenyl-21H,23H- porphine iron (III) chloride or a nickel rod coated with 5, 10, 15, 20- tetraphenyl-21H,23H- porphine nickel (II). A backing gas consisting of a gas mixture of either 5% O₂, N₂O or CO₂ in He expanded simultaneously over either the ablated coated iron rod or coated nickel rod. The photoelectron spectroscopy apparatus has been described previously.[9] Briefly, the anions generated from the laser vaporization source drift into the extraction region of the time-of-flight mass spectrometer. The anions are mass analyzed, mass selected, and decelerated. The decelerated anions are crossed with the photodetachment laser, and the photodetached electrons are energy analyzed with the magnetic bottle energy analyzer.

Anion photoelectron spectroscopy is conducted by crossing a mass-selected anion with a fixed frequency photon beam. This process is governed by the energy conserving relationship $h\nu = \text{EBE} + \text{EKE}$, where $h\nu$, EBE, and EKE are photon energy, electron binding energy, and electron kinetic energy, respectively. The third (355 nm, 3.49 eV) and fourth (266 nm, 4.66 eV) harmonics of a Nd:YAG laser were used to photodetach the anions. The magnetic bottle energy analyzer has a resolution of ~50 meV at 1 eV. The photoelectron spectra were calibrated against the well-known transitions of Cu.[10]

Experimental Results and Discussion

Three backing gases expanded over the ablated 5, 10, 15, 20- tetraphenyl-21H,23H- porphine iron (III) chloride: He, 5% CO₂ in He, and 5% O₂ in He. The resulting mass spectra is presented in (Figure VI.A.1.1). In the presence of only He, FeTPP⁻, (FeTPP)C_n⁻, and (FeTPP)Cl⁻ are present. With CO₂ seeded in the backing gas, (FeTPP)O⁻ is also generated. Upon the addition of O₂ in the backing gas, more oxygen complexes are formed, with (FeTPP)O₂⁻ the most intense.

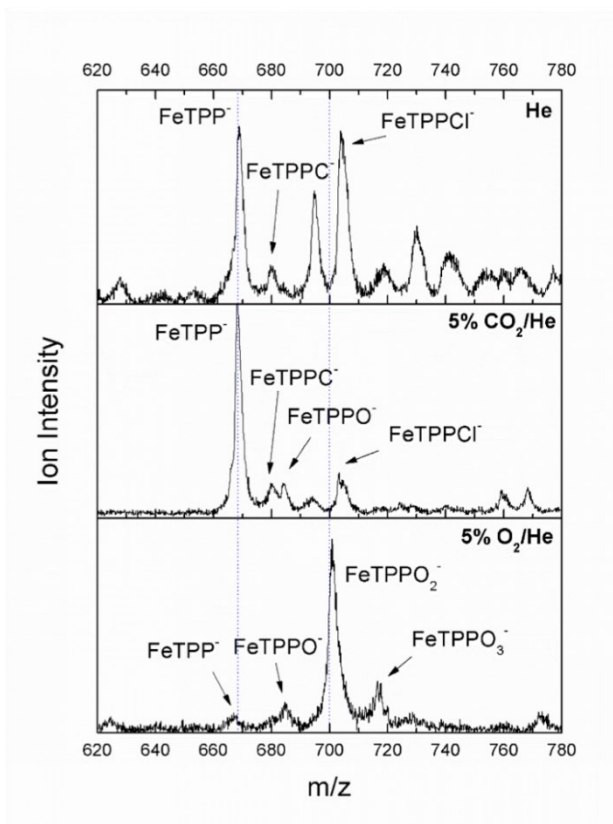


Figure VI.A.1.1: The mass spectra obtained when ablating 5, 10, 15, 20- tetraphenyl-21H,23H- porphine iron (III) chloride in the presence of He, 5% CO₂ in He, and 5% O₂ in He.

The NiTPP experiments were performed using four different backing gases: pure He, 5% N₂O in He, 5% CO₂ in He, and 5% O₂ in He. (Figure VI.A.1.2) compares the mass spectra obtained using the different backing gases. NiTPP⁻, (NiTPP)C⁻, and (NiTPP)CN⁻ are present in all experiments. (NiTPP)O⁻ was generated with 5% of an oxidizing species in the backing gas. (NiTPP)O₂⁻ was only formed with 5% O₂ in He was used as the backing gas.

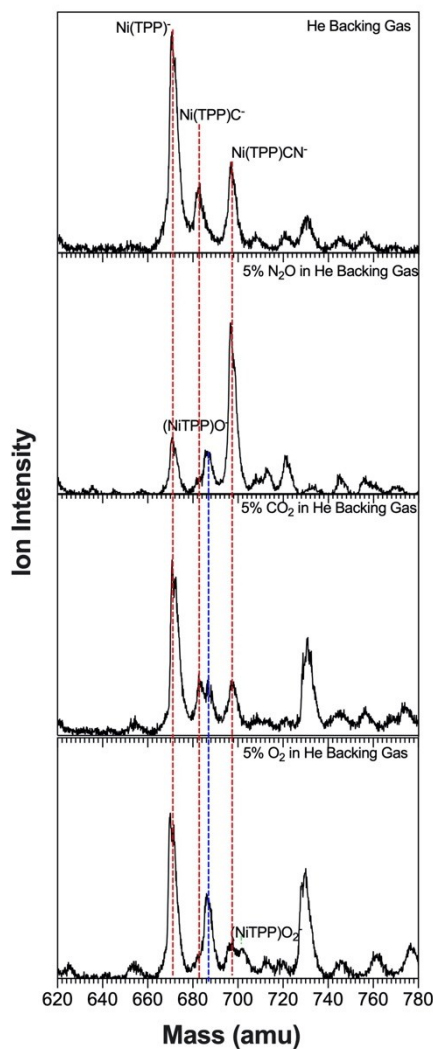


Figure VI.A.1.2 The mass spectra obtained when ablating 5, 10, 15, 20- tetraphenyl-21H,23H- porphine nickel (II) in the presence of He, 5% N₂O in He, 5% CO₂ in He, and 5% O₂ in He.

The photoelectron spectra of (FeTPP)O⁻ anions photodetached with the 3rd and 4th harmonics of a Nd:YAG laser (355 nm, 3.49 eV; 266 nm, 4.66 eV) are presented in (Figure VI.A.1.3). The electron affinity (EA) is defined as the energy difference between the anion in the ground state and the neutral in the ground state. If there is enough Franck Condon overlap, the EA is considered the onset of an anion's photoelectron spectrum. The EA of (FeTPP)O⁻ is 1.5 eV. The vertical detachment energy (VDE) is the energy difference between the ground state of the anion and higher electronic states of the neutral. The VDE is the maximum peak in the spectrum. The VDE value of (FeTPP)O⁻ is 2.0 eV. A second peak is presents itself at higher binding energy, but higher photon energy is needed to determine

the VDE value. Similarly, FeTPP^- has a VDE value of 2.0 eV, but the vertical transition to the first excited neutral state is observed in the PES at 3.1 eV.⁵

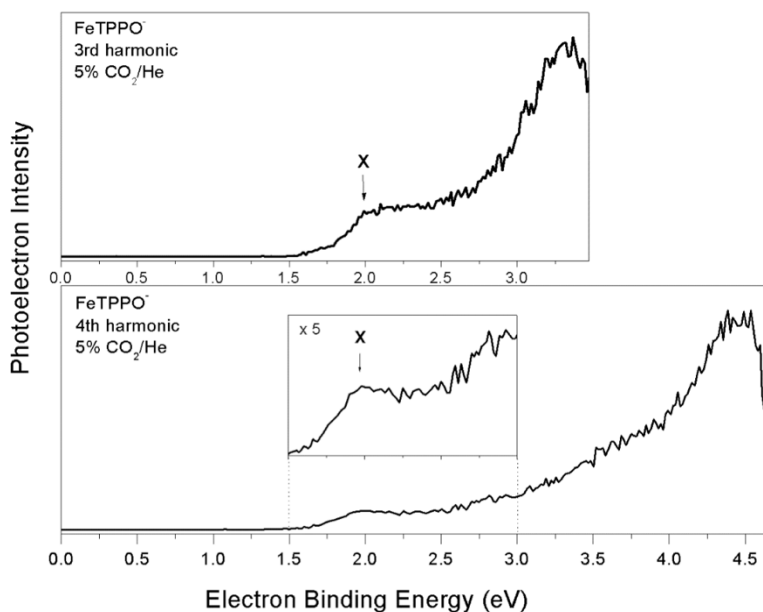


Figure VI.A.1.3 The photoelectron spectra of $(\text{FeTPP})\text{O}_2^-$ taken with the 3rd (355 nm, 3.49 eV) and 4th (266 nm, 4.66 eV) harmonics of a Nd:YAG laser.

The photoelectron spectrum of $(\text{FeTPP})\text{O}_2^-$ obtained with the 4th harmonic (266 nm, 4.66 eV) of a Nd:YAG laser is presented in (Figure VI.A.1.4). Multiple, broad peaks in the spectrum suggest O_2 becomes activated with introduced to FeTPP^- . The transition at 2.0 eV is still present. Other transitions centered at 2.8, 3.6, 3.8, and 4.3 eV are also present.

The photoelectron spectra collected from the NiTPP^- are presented in (Figure VI.A.1.4). The PES of NiTPP^- matches previously published data.⁵ The EA is 1.5 eV and the VDE value is 1.6 eV. The vertical transition to the first excited neutral state is 2.3 eV. The photoelectron spectrum changes slightly upon addition of oxygen to NiTPP^- . The EA of $(\text{NiTPP})\text{O}^-$ is shifted to 1.3 eV, and the VDE value is 1.8 eV. The vertical transition to the first excited neutral state is also 2.3 eV, but it is not as sharp of a transition. The $(\text{NiTPP})\text{O}_2^-$ anion has a EA of 1.5 eV, but there is no definitive peak to assign the VDE value to.

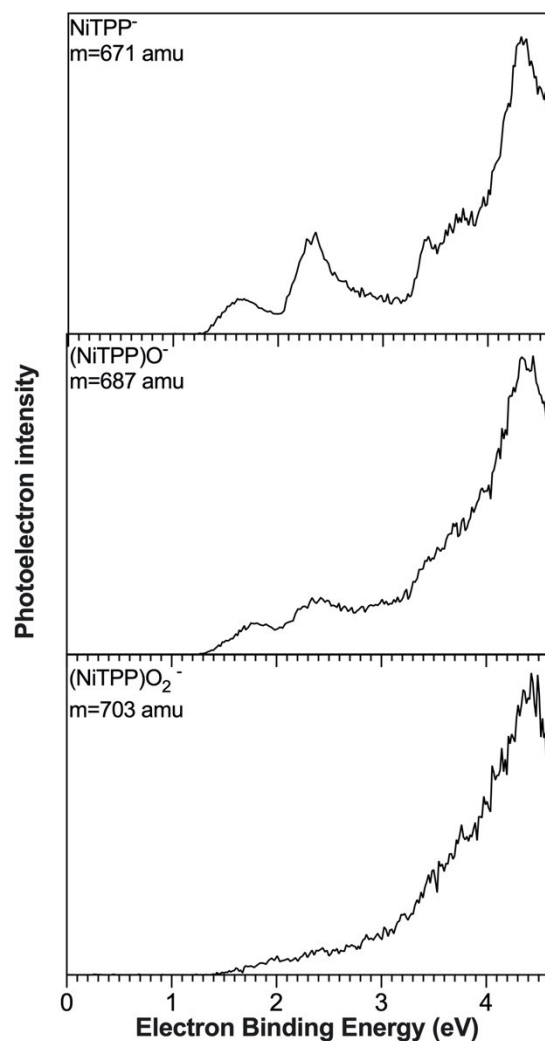


Figure VI.A.1.4 The photoelectron spectra of $(\text{NiTPP})^-$, $(\text{NiTPP})\text{O}^-$, and $(\text{NiTPP})\text{O}_2^-$ taken with the 4th (266 nm, 4.66 eV) harmonics of a Nd:YAG. Calculations are needed to confirm the EA and VDE values of the different complexes, as well as determine the connectivity.

References

1. W. R. Scheidt and C. A. Reed, *Chem. Rev.* **81**, 543 (1981).
2. B. F. Abrahams, B. F. Hoskins, and R. Robson, *J. Chem. Soc.* **113**, 3606 (1991).
3. O. Chen, S. Groh, A. Liechty, and D. P. Ridge, *J. Am. Chem. Soc.* **121**, 11910 (1999).
4. X.-S. Wang, M. Chrzanowski, C. Kim, W.-Y. Gao, L. Wojtas, Y.-S. Chen, C. P. Zhang, and S. Ma, *Chem. Commun.* **48**, 7173 (2012).

5. Bhugun, I.; L, D.; Savéant, J. M. Catalysis of the Electrochemical Reduction of Carbon Dioxide by Iron(0) Porphyrins: Synergistic Effect of Weak Brønsted Acids. *J. Am. Chem. Soc.* **1996**, *118*, 1769– 1776
6. Bhugun, I.; Lexa, D.; Savéant, J. M. Catalysis of the Electrochemical Reduction of Carbon Dioxide by Iron(0) Porphyrins. Synergistic Effect of Lewis Acid Cations. *J. Phys. Chem.* **1996**, *100*, 19981– 19985
7. Azcarate, I.; Costentin, C.; Robert, M.; Saveant, J. M. Through-Space Charge Interaction Substituent Effects in Molecular Catalysis Leading to the Design of the Most Efficient Catalyst of CO₂-to-CO Electrochemical Conversion. *J. Am. Chem. Soc.* **2016**, *138*, 16639– 16644
8. A. M. Butyendyk, J. D. Graham, and K. H. Bowen, *J. Phys. Chem. A* **119** (2015).
9. M. Gerhards, O. C. Thomas, J. M. Nilles, W. -J. Zheng, W. and K. H. Bowen, *J. Chem. Phys.* **116**, 10247 (2002).
10. J. Ho, K. M. Ervin, and W. C. Lineberger, W. C. *J. Chem. Phys.* **93**, 6987 (1990).

VI.A.2. Photoelectron Spectroscopic Study of ThPtO₂⁻ and ThPtC⁻ anions

Zhaoguo Zhu,[†] Mary Marshall,[†] Kit H. Bowen^{†,*}

[†]Department of Chemistry, Johns Hopkins University, Baltimore, MD 21218, USA

***Corresponding Author** K.H.B.: kbowen@jhu.edu

In this work, ThPtO₂⁻ and ThPtC⁻ anions were generated using a pulsed-arc (electric discharge) cluster ionization source (PACIS), which has been described in detail elsewhere. This cluster anion source has been used to generate a variety of bimetal cluster anions. During PACIS operation, a 30 μs long, 150-volt electrical pulse applied between a copper anode and the sample cathode vaporizes the sample atoms. The sample cathode was prepared in a nitrogen glove box, where a 1:1 Th:Pt powder mixture was firmly pressed into a well on top of a copper rod. To prevent contact between the thorium powder and air, a thin sacrificial layer of copper powder was pressed onto the top of the sample layer. During operation of the PACIS source and almost simultaneously with the firing of its electric discharge pulses, ~150 psi of ultrahigh purity helium gas was injected into the source's discharge region through a pulsed valve, these actions together resulting in the generation of a variety of cluster sizes and compositions. The resulting plasma, containing ions, neutrals, and electrons was cooled as it expanded through the PACIS source's housing and nozzle. The resultant anion mixture was mass-analyzed by TOF mass spectroscopy, after which the chosen mass-selected anion compositions were photodetached and their resultant electrons energy analyzed.

Results and discussions

Figure VI.A.2.1 presents the mass spectrum of cluster anions generated using a 1:1 thorium-platinum powder mixture and helium expansion gas via the PACIS source. One can observe a variety of thorium-containing cluster anions including ThO_2^{3-} , $\text{ThC}_2\text{O}_3^{3-}$, ThCuO_2^{3-} , ThPtC^- , ThPtO_2^{3-} , Th_2O^{3-} , and $\text{Th}_2\text{CuO}^{3-}$ in the mass spectrum. The contaminant elements: copper, carbon and oxygen, seen in the spectrum originated from the surface of the cathode and the surroundings in the PACIS source housing. Anions present at 439 amu and 459 amu are identified as ThPtC^- and ThPtO_2^{3-} , respectively. Both of them were mass-gated and further characterized by photoelectron spectroscopy

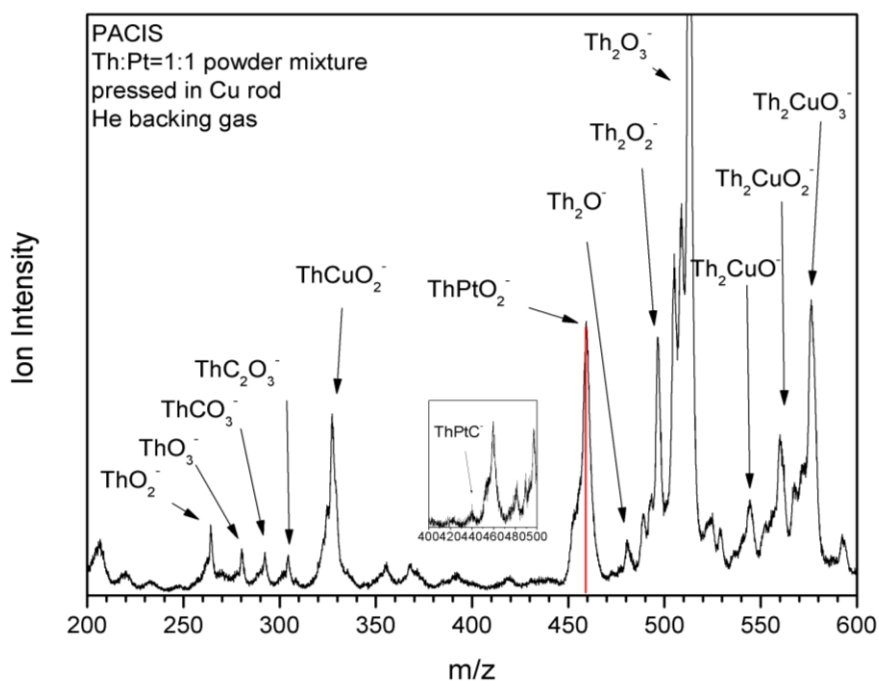


Figure VI.A.2.1 The mass spectrum of anions generated by PACIS with a 1:1 thorium-platinum powder mixture and helium gas.

with third harmonic photons (355 nm, 3.49 eV/photon) from a Nd:YAG laser.

The photoelectron spectra of ThPtC^- and ThPtO_2^{3-} are shown in Figure VI.A.2.2. In the top panel, the spectrum of ThPtC^- exhibits three bands spanning from 1.2 eV to 3.5 eV. The first band, feature X, reflects the transition from the ground electronic state of the ThPtC^- anion to that of the neutral ThPtC . The onset of this feature arises at an electron binding energy (EBE) of 1.2 eV and attains its intensity maximum at 1.50 eV. The second feature A, centered at 1.9 eV, along with the poorly resolved peaks beyond 2.3 eV represent transitions from the ground state of the anion to the various electronically-excited states of the ThPtC^- anion's neutral counterpart. The photoelectron spectrum of ThPtO_2^{3-} , shows a sharp peak X, which is centered at 1.59 eV. The fact that this peak is narrower than the lowest EBE peak in

the photoelectron spectrum of ThPtC^- suggests that the geometric structures of ThPtO_2^- and ThPtO_2 are more similar to each other than are the geometric structures of ThPtC^- and ThPtC .

The vertical detachment energy (VDE) is the photodetachment transition at which the Franck-Condon overlap between the wave function of the ground state of the anion and that of the ground state of its neutral counterpart is maximal. Thus, the VDE value corresponds to the EBE value of the intensity maximum of the lowest EBE peak. The VDE values of ThPtC^- and ThPtO_2^- are therefore 1.50 eV and 2.23 eV, respectively. The adiabatic (thermodynamic) electron affinity (EA) is the energy difference between the lowest energy state of the anion and the lowest energy state of its neutral counterpart. When sufficient Franck-Condon overlap exists between $v = 0$ of the anion and $v' = 0$ of its neutral counterpart (the origin transition) and there are no vibrational hot bands (photoelectrons from vibrationally excited anions) present, the EA value corresponds to the EBE value at the intensity threshold of the lowest EBE peak or band. We have assigned EA values by extrapolating the low EBE side of the lowest EBE bands to zero. Therefore, The EA values for ThPtC^- and ThPtO_2^- are 1.20 eV and 2.10 eV.

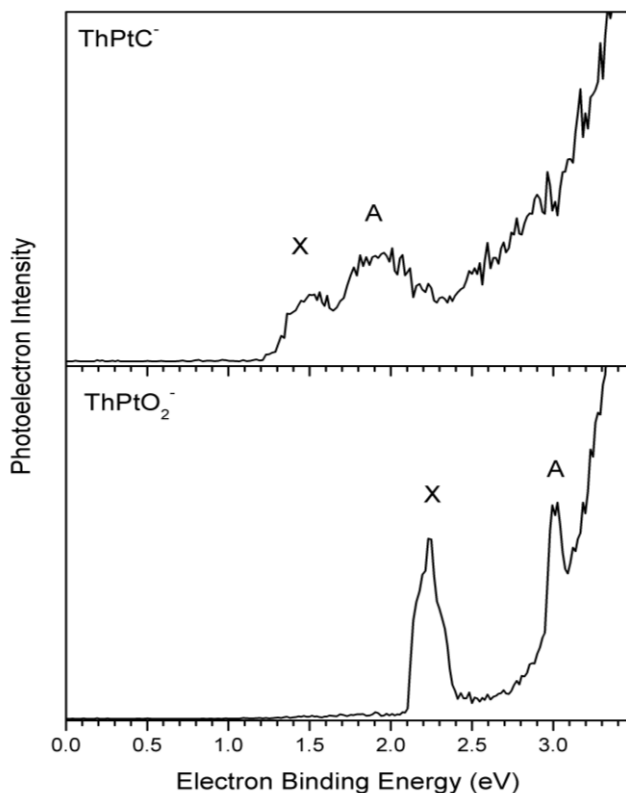


Figure VI.A.2.2 Photoelectron spectra of ThPtC^- and ThPtO_2^- measured with 3.49 eV photons.

VI.A.3. Internal Proton Transfer in the Radical Anion of Cytidine Prevents Dissociative Electron Attachment.

A Phenomenon that May Justify Different Sensitivity of Dry and Wet DNA to Electron Attachment Induced Damage

(This manuscript is not complete and waiting for inputs from collaborators. Our PES part is done.)

Lidia Chomicz-Mańka,¹ Anna Czaja,¹ Karina Fakiewicz,¹ Janusz Rak^{1*}, Karol Biernacki,² Sebastian Demkowicz,^{2*} Fahrad Izadi,³ Stephan Denifl,^{3*} Zhaoguo Zhu,⁴ Burak Ahmet Tufekci,⁴ Rachel Harris,⁴ Kit Bowen^{4*}

¹Laboratory of Biological Sensitizers, Department of Physical Chemistry, Faculty of Chemistry, University of Gdańsk, 80-308 Gdańsk, Poland

²Department of Organic Chemistry, Faculty of Chemistry, Gdańsk University of Technology, Narutowicza 11/12, 80-233 Gdańsk, Poland

³Institut für Ionenphysik und Angewandte Physik and Center for Biomolecular Sciences Innsbruck, Leopold-Franzens Universität Innsbruck, Technikerstrasse 25, A-6020 Innsbruck, Austria

⁴Department of Chemistry, Johns Hopkins University, Baltimore, Maryland 21218, United States.

*To whom correspondence should be addressed, e-mail: janusz.rak@ug.edu.pl

1. INTRODUCTION

Radiotherapy, one of the most common modality employed in cancer treatment, eliminates the cancerous cells by damaging cellular DNA. The detrimental agents are products of water radiolysis triggered by ionizing radiation that passes through patients' body during a radiotherapy session. The most abundant products of water radiolysis are hydroxyl radicals and hydrated electrons. While the former have long been considered as an efficient genotoxic agent, the role of hydrated electrons in DNA damage was questionable. Early biological experiments carried out in the 80. demonstrated that hydrated electrons might be responsible for only a small fraction of DNA deactivation initiated by radiolysis (references). However, this paradigm changed around the year 2000 due to experiments carried out in the laboratory of Leon Sanche whose group published in Science seminal resonance curves showing the formation of single (SSBs) and double (DBSs) strand breaks in the plasmid DNA bombarded under vacuum with the electrons of energy below the ionization threshold of DNA (references). This discovery resulted in a flood of papers both experimental (references) and theoretical (references) that tackled the problem of destructive interactions between

electrons and DNA. Besides exemplar works from the Sanche laboratory, one may enumerate theoretically-experimental reports from Rak Gutowski, and Bowen teams (references) which combining photoelectron spectroscopy (PES) of anions with DFT modeling explained the measured PES spectra of complexes comprising DNA components by a barrier-free proton transfer triggered by electron attachment. On the other hand, Simon's group suggested..., Leszczynski... Denifl,... Bald.....

However, it should be worth of emphasizing that few radiation chemistry papers published after 2000 demonstrated directly that in aqueous DNA solutions SSBs are not generated during radiolysis. Indeed, in a radiation chemical study devoted to the 5-bromo-2'-deoxyuridine (BrdU) labeled oligonucleotides Sanche et al. (references) showed that strand breaks are not formed in the native, non-labeled oligonucleotides when hydroxyl radicals are selectively scavenged during irradiation even for doses as large as 700 Gy (one should realize that in fractional radiotherapy of patients radiation doses do not exceed 2 Gy per a single session). Similarly. Rak et al....

The striking difference in the reactivity towards excess electrons between DNA under ultra-high vacuum and in aqueous solution might be related to proton transfer involving the initial radical anion of a nucleobase. Such suggestion results from an ab initio molecular dynamics study published recently by Kohanoff et al.

2. METHODS

2.1. Synthesis

2.2. Crossed Electron-Molecule Beam Experiments.

2.3. Photoelectron Spectroscopy Measurements.

Anion photoelectron spectroscopy is conducted by crossing a mass-selected beam of negative ions with fixed-frequency photons, followed by energy-analysis of the resulting photodetached electrons. Photodetachment is governed by the energy-conserving relationship, $h\nu = EBE + EKE$, where $h\nu$ is the photon energy, EBE is electron binding energy, and EKE is electron kinetic energy. Our anion photoelectron spectrometer has been described in detail previously.[1]

The parent anions of 5'-dCMPH were generated using a novel pulsed infrared desorption-pulsed visible photoemission anion source.[2] In the first stage of the experiment, low-power infrared laser pulses (1.17 eV/photon) from an Nd:YAG laser were used to desorb neutral 5'-dCMPH from a slowly translating graphite bar which was thinly coated

with the sample. Simultaneously, electrons were generated by visible laser pulses (another Nd:YAG laser operated at 532 nm, 2.33 eV/photon) striking a yttrium wire. At the same time, 100 psig of pure helium gas was expanded over the graphite bar and metal wire by a pulsed valve, providing a collisionally cooled jet to carry away excess energy and stabilize the resulting parent anions. The photoelectron spectrum was recorded by crossing a mass-selected beam of parent anions with a fixed-frequency photon beam (a third Nd:YAG laser operated at 355 nm, 3.49 eV/photon). The photodetached electrons were energy-analyzed using a magnetic bottle energy analyzer with a resolution of 50 meV at EKE = 1 eV. Photoelectron spectrum was calibrated against the well-known photoelectron spectrum of Cu^- . [3]

2.4. Computational Details

3. RESULTS AND DISCUSSION

3.1. Model

If proton transfer (PT) is a main factor that hinders SSB in DNA, it should be possible to demonstrate experimentally that this phenomenon does stop PT in a DNA-like species. The smallest system that has most DNA characteristics and should, in principle, undergo DEA is a nucleotide. Indeed, it possesses the phosphoester bond (the cleavage of this bond is directly responsible for a SSB in DNA), has positive electron affinity corresponding to electron attachment the π^* orbital localized on the nucleobase, and in such a system the excess electron can effectively move from the initial π^* state to the σ^* orbital of the $\text{CX}'\text{-O}$ (where $\text{X}' = 3'$ or $5'$) bond resulting in the breakage of the phosphoester bond (an equivalent of SSB). Several years ago, we published back-to-back papers employing photoelectron spectroscopy of negative anions and DFT calculations showing that in the $5'$ -nucleotide of $2'$ -deoxyadenosine electron attachment is followed by an intramolecular proton transfer to form a stable radical anion. A similar situation might be observed in pyrimidine nucleotides. Although purine nucleobases poses two condensed rings, six- and five-membered, which, at first glance suggests stereochemical closeness of the phosphate group (proton donor) and proton acceptor centers of a nucleobase in the nucleotide, pyrimidine comprising only one six-member ring could also, in principle, undergo electron attachment induced PT as indicated by the comparison of the respective distances in purine and pyrimidine nucleotides depicted in Figure 1. Thus...

3.2. Electron-Molecule Beam Experiments

3.3. Photoelectron Spectroscopy

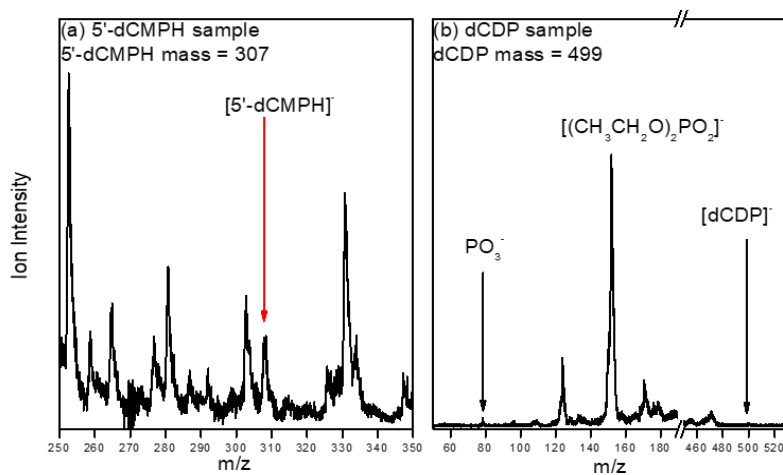


Figure VI.A.3.1 Mass spectra of (a) 5'-dCMPH, and (b) dCDP obtained by IR desorption and photoemission ion source.

Figure VI.A.3.1 shows the anionic mass spectra of 5'-dCMPH and dCDP using our pulsed IR desorption photoemission ion source. The parent anion of 5'-dCMPH with a mass to charge ratio of 307, was observed in the figure VI.A.3.1(a). Not surprisingly, after many attempts, we were not able to generate the parent anions of dCDP. The presence of $[(\text{CH}_3\text{CH}_2\text{O})_2\text{PO}_2]^-$ and PO_3^- anions suggests electron attachment caused the fragmentation of dCDP.

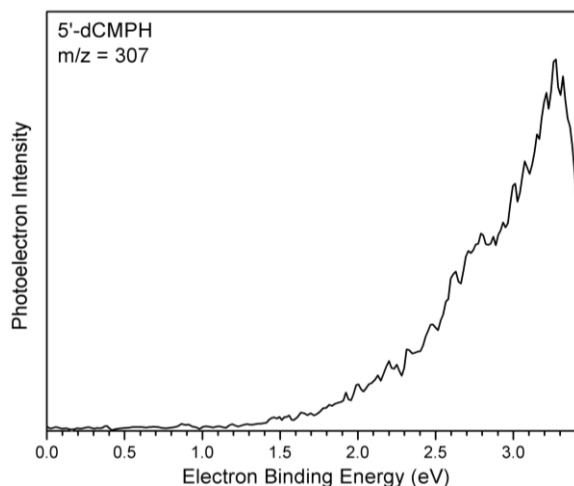


Figure VI.A.3.2 Photoelectron spectrum of 5'-dCMPH anions

The photoelectron spectrum of 5'-dCMPH recorded with 3.49 eV photons is shown in Figure VI.A.3.2. The spectrum exhibits an increasing band at the EBE scale starting from ~ 1.5 eV with a maximum of 3.27 eV. A small shoulder occurs between ~ 2.6 - 2.9 eV and peaks at ~ 2.8 eV. The broad band results from the vertical photodetachment of the excess electron from a ground vibronic state of mass-selected anions to the ground vibronic state of the resulting neutrals. The maximal photoelectron intensities correspond to the optimal Franck-Condon overlaps of the vibrational wave functions between anion and neutral ground states. This energetic quantity is the vertical detachment energy (VDE). Thus, the VDE value is determined to be 3.27 eV. The energy difference between the lowest vibrational level of the ground electronic state of the anion and the lowest vibrational level of the ground electronic state of its corresponding neutral is the adiabatic electron affinity (AEA). However, the AEA value is hard to determine explicitly due to the absence of the resolved, assignable vibrational structure and the possible presence of vibrational hot bands in the spectrum. Nevertheless, as a reasonable approximation, one can estimate the AEA as that corresponding to the EBE value at $\sim 10\%$ of the rising photoelectron intensity.[2] Therefore, from the onset of the photoelectron spectrum, the AEA for 5'-dCMPH can be estimated to be ~ 1.6 eV.

REFERENCES

1. Gerhards, M.; Thomas, O. C.; Nilles, J. M.; Zheng, W.-J.; Bowen, K. H. Cobalt-Benzene Cluster Anions: Mass Spectrometry and Negative Ion Photoelectron Spectroscopy. *J. Chem. Phys.* 2002, 116, 10247–10252.
2. Stokes, S. T.; Li, X.; Grubisic, A.; Ko, Y. J.; Bowen, K. H. Intrinsic Electrophilic Properties of Nucleosides: Photoelectron Spectroscopy of Their Parent Anions. *J. Chem. Phys.* 2007, 127, 084321.
3. Ho, J.; Ervin, K. M.; Lineberger, W. C. Photoelectron Spectroscopy of Metal Cluster Anions: Cu_n^- , Ag_n^- , and Au_n^- . *J. Chem. Phys.* 1990, 93, 6987–7002.

VI.A.4. Uranium Containing Clusters

¹ UO₂Cl₂⁻

Experimental Results

Figure VI.A.4.1 presents the mass spectrum showing the assortment of anions, consisting of uranium, oxygen, and chlorine, generated by the source. The depleted uranium rod is essentially isotopically pure U-238, so the isotopic pattern of chlorine is used to assign the anions in the mass spectrum.

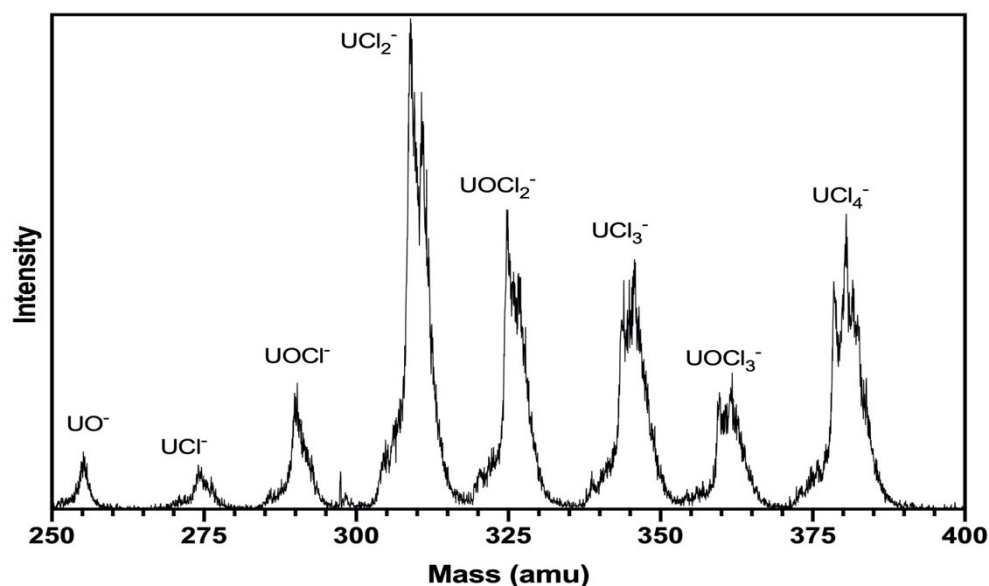


Figure VI.A.4.1 The mass spectrum obtained from ablating a depleted uranium rod in the presence of HCl and O₂.

The mass peaks at 324, 326, and 328 amu follow the predicted isotopic pattern of UOCl₂⁻. The UCl⁻ anion is observed at 273 and 275 amu, and the UCl₂⁻ anion is observed at 308, 310, and 312 amu. The UCl_n⁻ anions also follow the theoretical isotopic pattern. The photoelectron spectra of UOCl₂⁻, UCl⁻, and UCl₂⁻ were obtained by photodetaching the highest intensity mass: 324, 273, and 308, respectively.

The photoelectron spectra of UOCl₂⁻ are presented in Figure VI.A.4.2. The broad transition has an onset at 1.391 eV with a maxima at 1.968 eV. The vertical detachment energy (VDE) is the photodetachment transition at which the Franck-Condon overlap between the wave function of the ground state of the anion and that of the ground state of its

neutral counterpart is at its maxima. The VDE value corresponds to the EBE value of the intensity maxima of the lowest EBE peak. For UOCl_2^- , the VDE value is assigned to 1.968 eV.

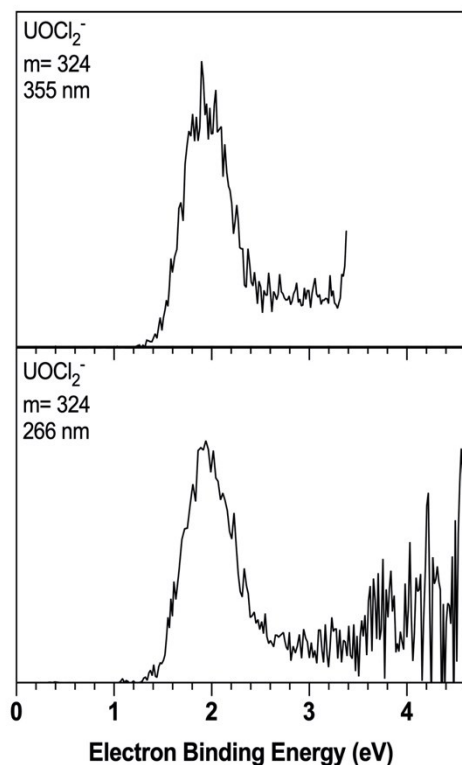


Figure VI.A.4.2 The photoelectron spectra of UOCl_2^- collected with the third (355 nm, 3.49 eV) and fourth (266 nm, 4.66 eV) harmonics of a Nd:YAG laser.

The photoelectron spectra for the UCl_n^- species are presented in Figures VI.A.4.3 and VI.A.4.4. UCl^- exhibits a broad band beginning at 0.419 eV and centered around 1.41 eV Figure VI.A.4.3. UCl_2^- presents a much sharper transition in the photoelectron spectrum Figure VI.A.4.4. The EBE onset is 0.097 eV with a maxima at 1.942 eV. The VDE value of UCl_2^- is assigned to 1.942 eV.

Continuation Needed for Publication

Theoretical calculations for all systems are needed before the experiment can be published. Dr. Lan Cheng from Johns Hopkins University, the theorist on the UO_2Cl_2^- paper, is working on the calculations for UOCl_2^- . Dr. David Dixon from University of Alabama will be providing the computation results for the UCl_n^- anions.

2 UCD_n^-

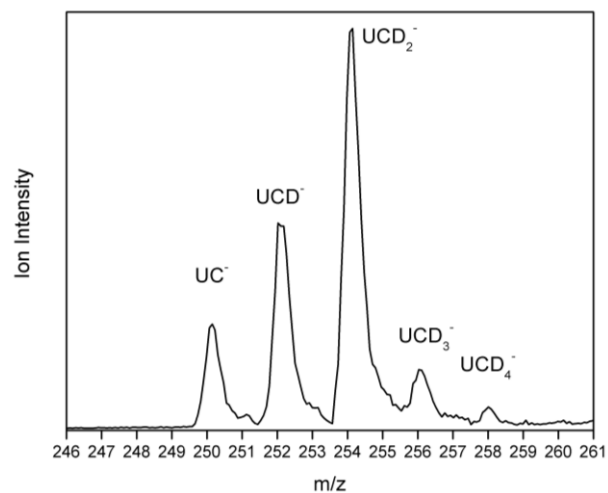


Figure VI.A.4.3 Mass spectrum of UCD_n^- , $n=0-4$.

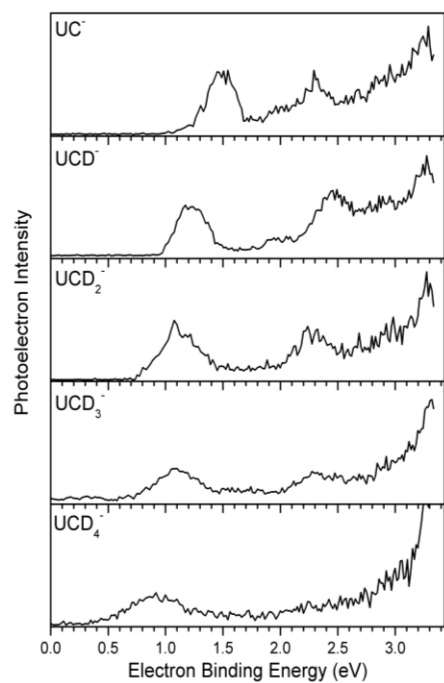


Figure VI.A.4.4 Photoelectron spectra of UCD_n^- , $n=0-4$ collected with the third (355 nm, 3.49 eV) harmonics of a Nd:YAG laser.

Experiment condition: 10% CD_4/He gas mixture in the backing pulse valve. Laser vaporization method. $\frac{1}{4}$ inch Uranium rod.

3 Argon tagging uranium clusters.

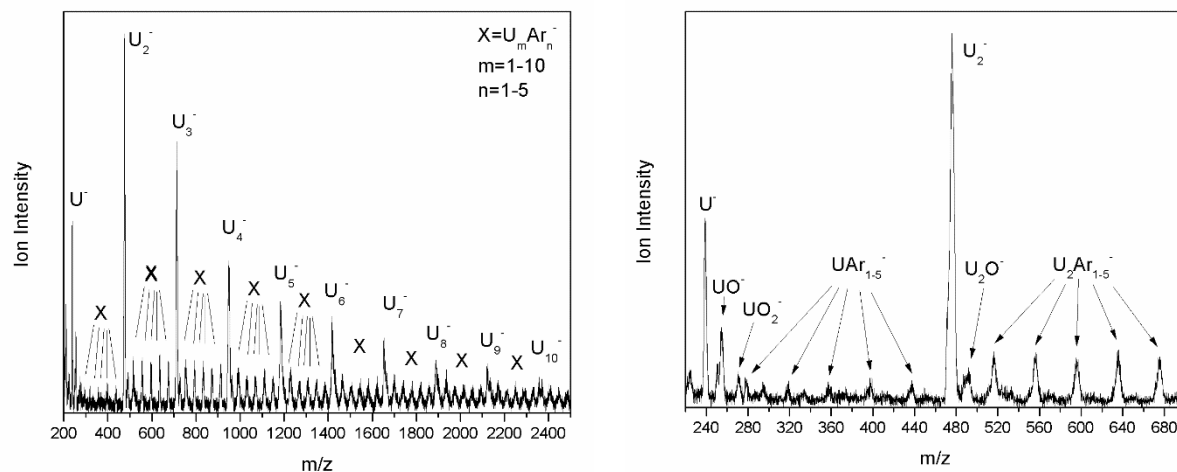


Figure VI.A.4.5 Mass spectrum of $U_mAr_n^-$. Right panel: zoomed-in view.

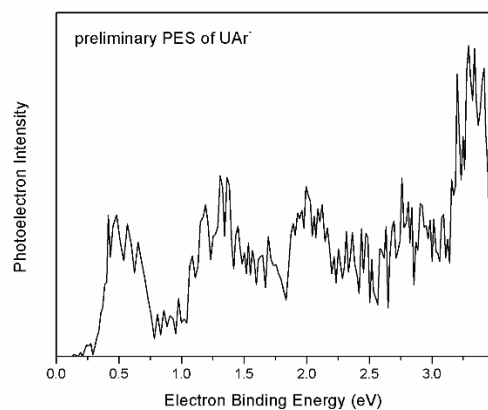


Figure VI.A.4.6 Photoelectron spectrum of UAr^- with 355 nm photons.

Here I present a preliminary PE spectrum of UAr^- . Although we did not use it in our electron affinity of uranium paper, there are still some other $U_mAr_n^-$ clusters worth trying in the future.

VI.A.5. Multiple Rydberg Anions

Zhaoguo Zhu, Mary Marshall, Evan Collins, Gaoxiang Liu, Sandy Ciborowski, Chalynette Martinez-Martinez,
Burak Tufekci, Kit H. Bowen,

Department of Chemistry, Johns Hopkins University, Baltimore, Maryland 21218, USA

Evangelos Miliordos, J.V. Ortiz

Department of Chemistry and Biochemistry, Auburn University, Auburn, AL 36849, USA

Introduction

Molecular systems containing one or more diffuse electrons have many applications in redox chemistry, catalysis, and electronics. Rydberg radicals are neutral species with a radical Rydberg electron that are only stable in their excited states and are dissociative in their ground states.¹ Herzberg discovered the first Rydberg radical, H_3 , in 1979,² and the second, NH_4 , in 1981.³ Double Rydberg anions (DRA) describe a closed-shell cation with two Rydberg-type electrons to form a negative anion, $(X^+)^{2-}$.⁴ NH_4^- was the first double Rydberg anion discovered during photoelectron studies of a hydride solvated by an ammonia, $H^-(NH_3)$. Although NH_4^- and $H^-(NH_3)$ are mass coincident, the NH_4^- anion was properly identified as a DRA. The low binding energy peak (NH_4^-) in the photoelectron spectra varied in intensity over time relative to the $H^-(NH_3)$ peak. Vibrational excitation was ruled out due to lack of a deuterium isotopic shift. Finally, the peak in the photoelectron spectrum was extremely narrow, indicating a high degree of Franck-Condon overlap with the corresponding neutral, NH_4 . Previous calculations by Ortiz and others confirmed the presence of tetrahedral NH_4^- is a stable anion geometry.⁵⁻⁹ The DRA studies were expanded to include $(N_2H_7)^-$, $(N_3H_{10})^-$, $(N_4H_{13})^-$, and $(N_5H_{16})^-$, $(N_nH_{3n+1})^-$ species. Similar to the NH_4^- experiment, the photoelectron spectrum included transition pertaining to both the DRA and solvated ammonia species. The electron binding energy (EBE) of the DRA remained relatively unaffected with the addition of more ammonia, while the solvated ammonia species steadily increased with energy.

Triple Rydberg anions (TRA) are analogous to DRA; a closed-shell, dication core with three Rydberg like electrons to create an anion. The three electrons are highly diffuse and remain relatively unaffected by the core. Ortiz proposed the anion $Mg(NH_3)_4^-$ has potential to be a TRA. This potential was exacerbated by the fact $Mg(NH_3)_4^{2+}$ was previously generated in the gas phase and photoionization and theoretical calculations have been performed on neutral $Mg(NH_3)_4$.^{10,11} Ortiz and Miliordos have investigated many systems with metal cores including main group metals and transition metals. Ammonia or crown-ethers stabilize the Li^+ , Na^+ , K^+ , Cs^+ , or Ca^{2+} centers and displace the

valence electron(s) to the periphery of the complex. The transition metals studied so far (Sc, V, Cr, Y, Mo) adopt formally a 2+ oxidation state with six ammonia ligands in the first coordination sphere; the metal s2 electrons are displaced to the periphery, residing in the second coordination sphere of the complex. The outer electrons occupy hydrogenic s, p, d, f, etc.-type orbitals, while transition metals retain also their inner d-shell.¹²⁻²² Besides metals, boron with ammonia can also form solvated electron precursors. Up to three ammonia ligands can coordinate to boron displacing two out of the three valence electrons.²³

After initial studies highlighted in this work confirmed that $\text{Mg}(\text{NH}_3)_n^-$ were indeed TRA, quadruple and multiple (>4) Rydberg anions were proposed (QRA and MRA). These systems would involve a “+n” closed- shell cationic core with n +1 delocalized Rydberg like electrons. This work highlights the many photoelectron spectroscopic experiments performed on MRA, including $\text{Mg}(\text{NH}_3)_n^-$, $\text{V}(\text{NH}_3)_n^-$, and $\text{Y}(\text{NH}_3)_n^-$. To date, heavier elements including lanthanides and actinides have not been studied theoretically. Here, we expand the systems to $\text{La}(\text{NH}_3)_n^-$, $\text{Th}(\text{NH}_3)_n^-$, and $\text{U}(\text{NH}_3)_n^-$.

Experimental Methods

A traditional laser vaporization source generated the multiple Rydberg anions. The helium carrier gas was seeded with trace amounts of NH_3 and expanded over the metal rod of interested (Mg, La, V, Y, Th, or U). The second harmonic (532 nm, 2.33 eV) of a Nd:YAG laser ablated the rotating, translating metal rod. The resulting plasma interacted with the carrier gas and supersonically expanded towards the extraction region of a time-of-flight mass spectrometer (TOF-MS). The anions of interest were mass selected, decelerated, and photodetached. The anion photoelectron spectrometer has been described in detail previously.¹²

Negative ion photoelectron spectroscopy is conducted by crossing a mass-selected anion with a fixed frequency photon beam. The photodetachment process is governed by the energy conserving relationship $h\nu = \text{EBE} + \text{EKE}$, where $h\nu$ is the photon energy, EBE is the electron binding energy, and EKE is the electron kinetic energy. The third harmonic (355 nm, 3.49 eV) of a Nd:YAG laser was used to photodetach the electrons. The detached electrons were energy analyzed using a magnetic bottle energy analyzer. The resolution of the magnetic bottle is ~50 meV at 1 eV EKE. The photoelectron spectra were calibrated using the known atomic transitions of Cu^- .¹³

Experimental Results

The mass spectrum of the $\text{Mg}(\text{NH}_3)_n^-$ series is presented in Figure VI.A.5.1. The isotopic pattern for $\text{Mg}(\text{NH}_3)_6^-$ and $\text{Mg}(\text{NH}_3)_7^-$ is clearly observed. The highest intensity peaks were photodetached. Due to an unknown contaminant, the spectrum around $\text{Mg}(\text{NH}_3)_4^-$ is convoluted. Based on the isotopic pattern, relative intensities, and contamination, the $\text{Mg}(\text{NH}_3)_4^-$ anion at mass 94 amu was photodetached.

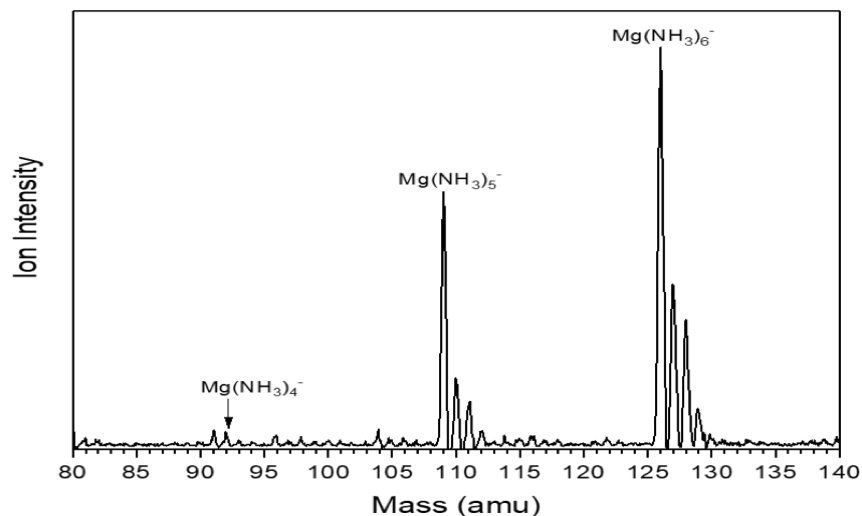


Figure VI.A.5.1 The mass spectrum obtained when ablating a Mg rod in the presence of trace amounts of NH_3 . The isotopic pattern of Mg is observed for $\text{Mg}(\text{NH}_3)_5^-$ and $\text{Mg}(\text{NH}_3)_6^-$.

The photoelectron spectra for the $\text{Mg}(\text{NH}_3)_n^-$ series are presented in Figure VI.A.5.2. All three anions have the characteristic Rydberg anion peak that remains relatively unchanged with the addition of more NH_3 . The vertical detachment energy (VDE) value of the peaks are 0.56 eV for $\text{Mg}(\text{NH}_3)_4^-$ and 0.58 eV for $\text{Mg}(\text{NH}_3)_5^-$ and $\text{Mg}(\text{NH}_3)_6^-$. There is a secondary low binding energy peak for each anion in the series: 1.12 eV, 1.11 eV, and 1.09 eV for $n=4, 5$, and 6, respectively. The VDE values are tabulated in Table VI.A.5.1.

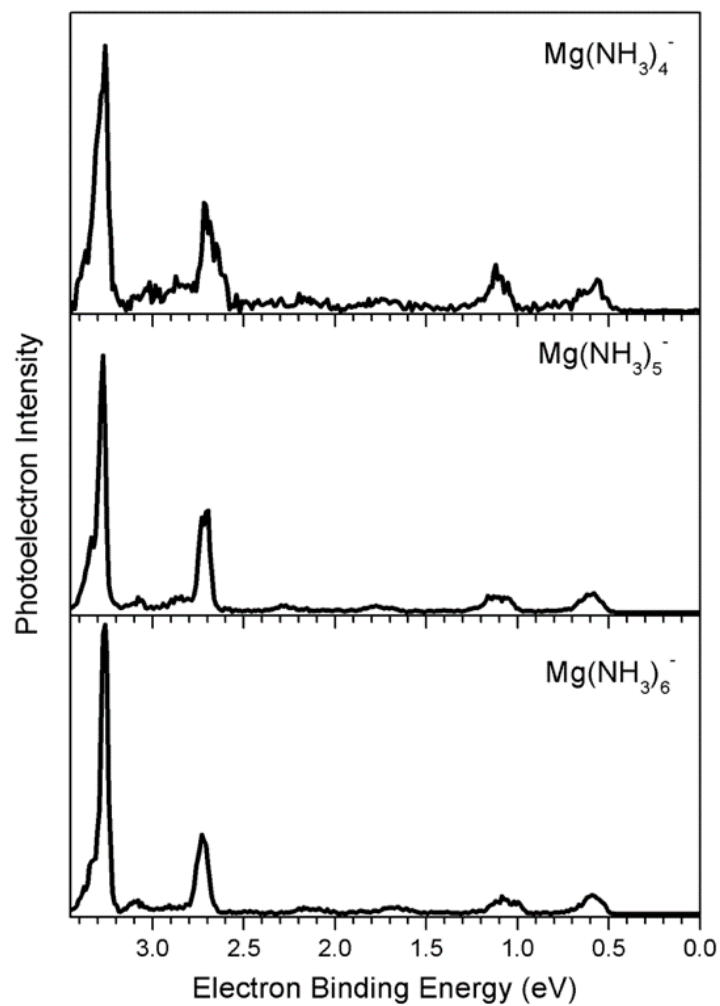


Figure VI.A.5.2 The photoelectron spectra obtained when photodetaching the TRA $\text{Mg}(\text{NH}_3)_4^-$, $\text{Mg}(\text{NH}_3)_5^-$ and $\text{Mg}(\text{NH}_3)_6^-$.

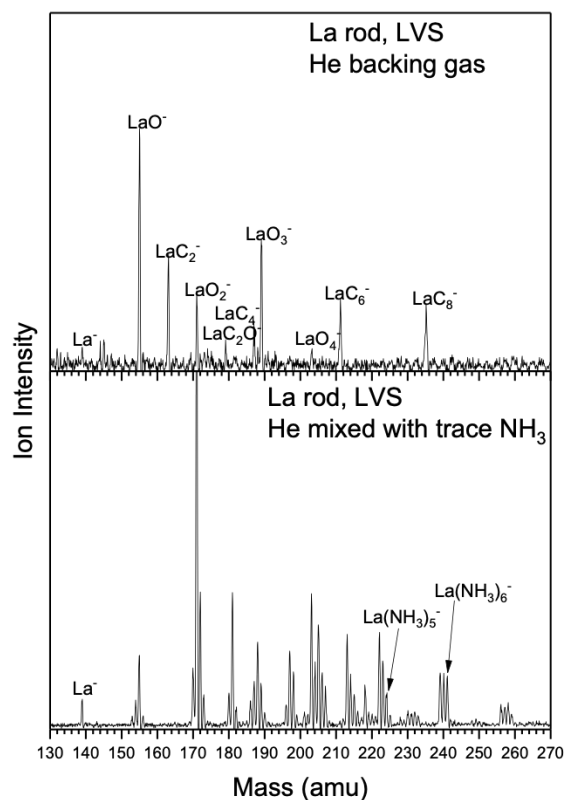


Figure VI.A.5.3 The mass spectra obtained when ablating a La rod in the presence of He (top) and trace amounts of NH_3 (bottom).

The comparison of the mass spectra obtained when ablating a La rod in the presence of solely He and trace amounts of NH_3 is presented in Figure VI.A.5.3. With only He in the backing gas, a series of lanthanum oxides were generated. In the presence of scant amounts of NH_3 , the desired $\text{La}(\text{NH}_3)_n^-$ anion series is observed, as well as LaO_n^- and dissociation products, such as $\text{La}(\text{NH}_2)(\text{NH}_3)_{n-1}^-$ and $\text{La}(\text{NH})(\text{NH}_3)_{n-1}^-$.

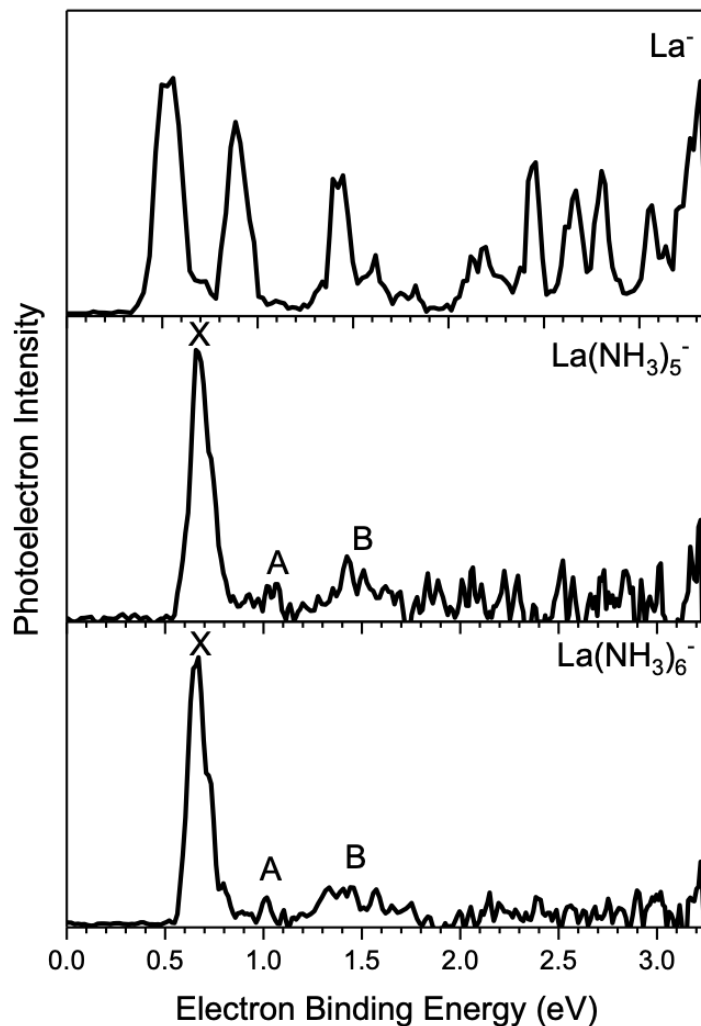


Figure VI.A.5.4 The photoelectron spectra of La^- , $\text{La}(\text{NH}_3)_5^-$, and $\text{La}(\text{NH}_3)_6^-$

The PES of La^- , $\text{La}(\text{NH}_3)_5^-$, and $\text{La}(\text{NH}_3)_6^-$ are presented in Figure VI.A.5.4. The electron affinity (EA) of La is 0.557 eV¹⁴, which is similar to the VDE value of DRA and TRA, so the PES of La^- is included as a reference. The photoelectron spectra of $\text{La}(\text{NH}_3)_5^-$ and $\text{La}(\text{NH}_3)_6^-$ are nearly identical. A strong, sharp feature at 0.66 eV is consistent with other MRA. Both anions also have transition at 1.02 eV and 1.48 eV.

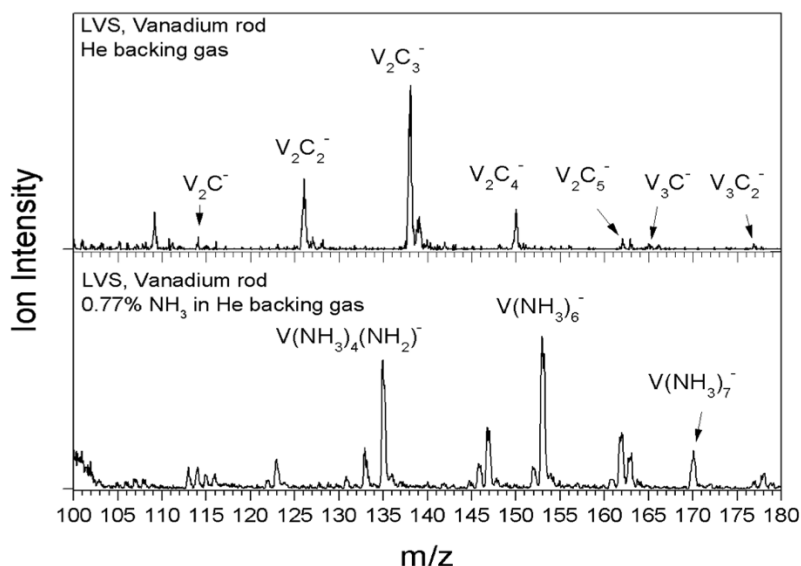


Figure VI.A.5.5 The mass spectrum obtained when ablating a vanadium rod in the presence of helium and trace amounts of NH_3 . With pure He, vanadium carbide clusters form. With trace amounts of NH_3 in the backing gas, vanadium ammonia clusters are observed.

Figure VI.A.5.5 presents the mass spectra obtained when ablating a vanadium rod with helium and with a trace amount of ammonia. The vanadium atom is mass coincidence with $(\text{NH}_3)_3$, so it is necessary to highlight the difference between vanadium clusters and addition ammonia on the vanadium. With only helium as the backing gas, there is no evidence of pure vanadium clusters, and vanadium carbide clusters are generated. Upon the addition of ammonia in the backing gas, vanadium ammonia clusters form, as well as a vanadium ammonia dissociation products.

Figure VI.A.5.6 presents the PES of $\text{V}(\text{NH}_3)_6^-$ and $\text{V}(\text{NH}_3)_7^-$. The electron affinity of $\text{V}(\text{NH}_3)_6^-$ and $\text{V}(\text{NH}_3)_7^-$ are 0.56 eV and 0.58 eV, respectively. Both anions have transitions at higher binding energy. Transitions A, B, and C in the PES of $\text{V}(\text{NH}_3)_6^-$ have a binding energy of 0.93, 1.33, and 2.37 eV, respectively. The higher binding energy transition in the $\text{V}(\text{NH}_3)_7^-$ PES is located at 1.50 eV.

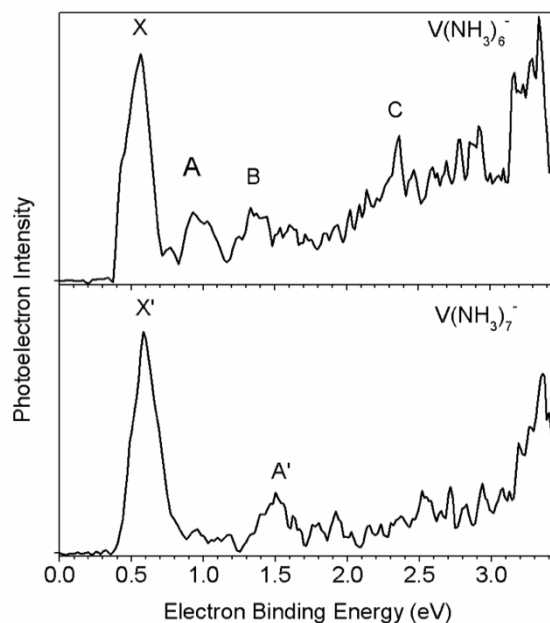


Figure VI.A.5.6 The photoelectron spectra of $V(NH_3)_6^-$ and $V(NH_3)_7^-$ obtained with the 3rd harmonic (355 nm, 3.49 eV) of a Nd:YAG laser.

The only anion present in the mass spectrum of the yttrium rod ablated in the presence of trace amounts of ammonia that did not contain pure yttrium or dissociation products was $Y(NH_3)_6^-$. The PES of $Y(NH_3)_6^-$ is presented in Figure VI.A.5.7. Similar to the other MRA, the EA is 0.66 eV. Two higher binding energy transitions are present, but, due to low resolution, the electron binding energy of the peaks is not assigned.

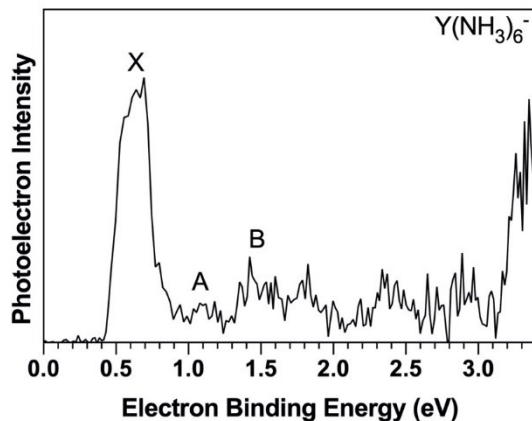


Figure VI.A.5.7 The photoelectron spectrum of $Y(NH_3)_6^-$ obtained using the 3rd harmonic (355 nm, 3.49 eV) harmonic of a Nd:YAG laser.

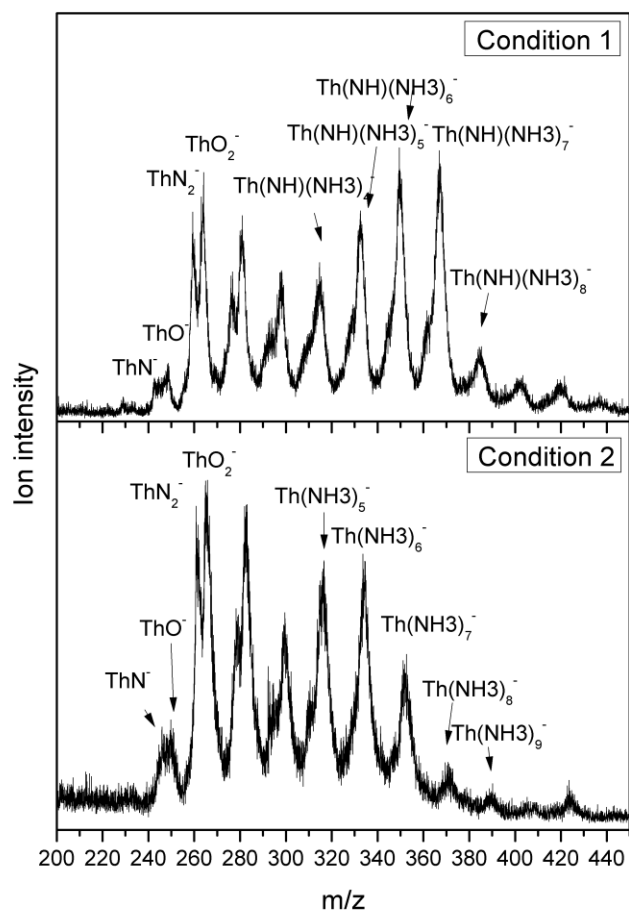


Figure VI.A.5.8 The mass spectrum obtained when ablating a U rod in the presence of trace amounts of NH_3 .

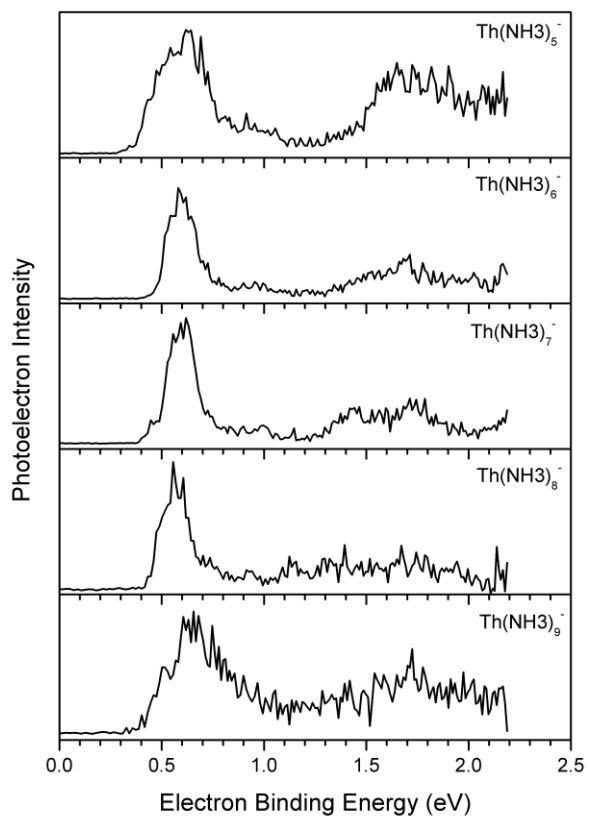


Figure VI.A.5.9 The photoelectron spectrum of $\text{Th}(\text{NH}_3)_{5-9}^-$ obtained using the 2nd harmonic (532 nm, 2.33 eV) harmonic of a Nd:YAG laser.

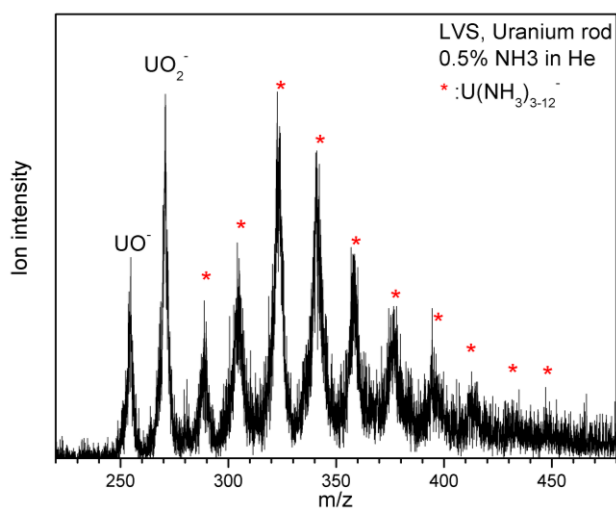


Figure VI.A.5.10 The mass spectrum obtained when ablating a U rod in the presence of trace amounts of NH_3 .

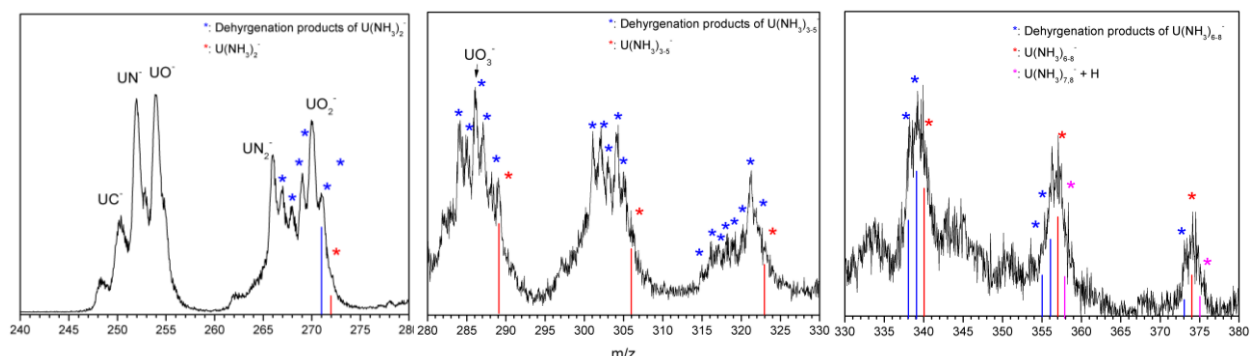


Figure VI.A.5.11 Zoomed in mass spectrum obtained when ablating a U rod in the presence of trace amounts of NH_3 .

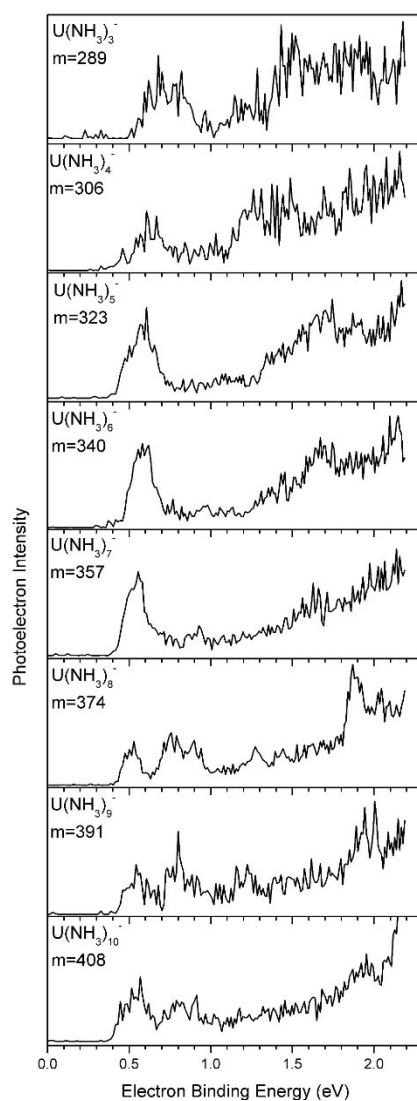


Figure VI.A.5.12 The photoelectron spectrum of $\text{U}(\text{NH}_3)_{3-10}^-$ obtained using the 2nd harmonic (532 nm, 2.33 eV) harmonic of a Nd:YAG laser.

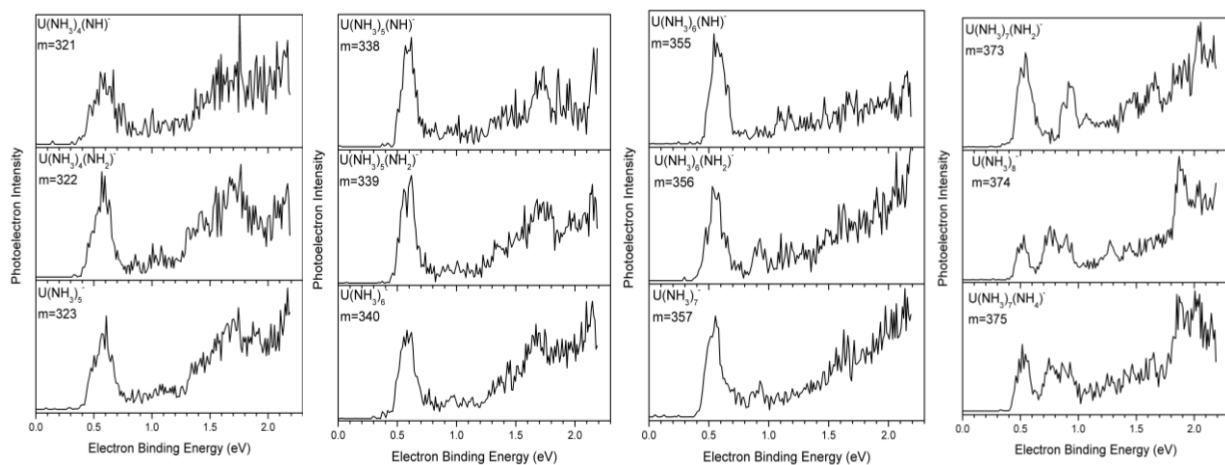


Figure VI.A.5.14 Photoelectron spectra of some dehydrogenation products and $\text{U}(\text{NH}_3)_7(\text{NH}_4)^+$.

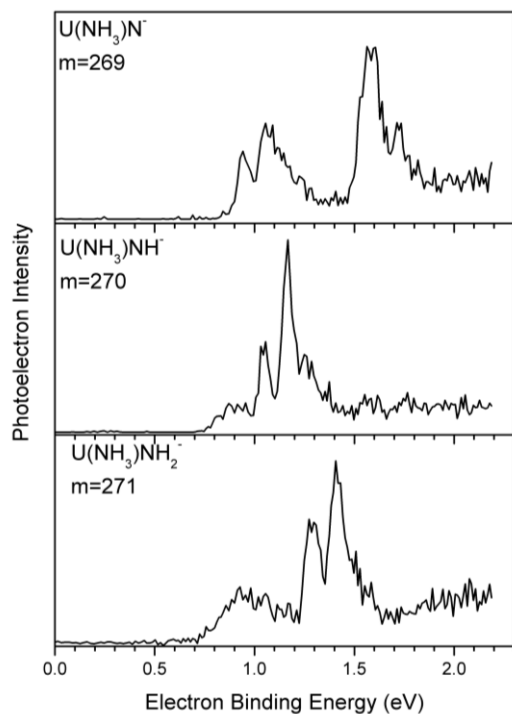


Figure VI.A.5.13 Photoelectron spectra of smaller uranium ammonia clusters.

Table VI.A.5.1 List of the VDE (eV) of the multiple Rydberg anions.

Multiple Rydberg Anion	VDE (eV)
$\text{Mg}(\text{NH}_3)_4^-$	0.56
$\text{Mg}(\text{NH}_3)_5^-$	0.58

$\text{Mg}(\text{NH}_3)_6^-$	0.58
$\text{La}(\text{NH}_3)_5^-$	0.66
$\text{La}(\text{NH}_3)_6^-$	0.66
$\text{V}(\text{NH}_3)_6^-$	0.56
$\text{V}(\text{NH}_3)_7^-$	0.58
$\text{Y}(\text{NH}_3)_6^-$	0.66
$\text{Th}(\text{NH}_3)_6^-$	0.58
$\text{U}(\text{NH}_3)_6^-$	0.57

Discussion

All multiple Rydberg systems presented have similarities to the previously published double Rydberg anions.⁴ The ammonia double Rydberg anion series exhibit a low binding energy peak between 0.415 eV and 0.472 eV. For the multiple Rydberg anions presented here, the low binding energy between is located between 0.56 eV and 0.66 eV. This indicates that the multiple Rydberg anions also have similarly delocalized and diffused states.

Similar to the DRA, the lowest binding energy peak remains relatively stable as more ammonia units are added. The electrons that occupy these states are delocalized and unaffected by changes to the composition and, thus, the structure of the anion. Preliminary calculations from Ortiz on $\text{Mg}(\text{NH}_3)_6^-$ indicate the lowest three binding energy peaks are likely from the triple Rydberg anion species. The calculated VDE values for these peaks are 0.66 eV, 0.88 eV, and 1.54 eV, respectively. The calculated VDE value of the first peak matches the experimental results; however, the other two differ slightly. Ortiz is currently improving his calculations.

Calculations for the $\text{La}(\text{NH}_3)_{5-6}^-$, $\text{V}(\text{NH}_3)_{6-7}^-$, $\text{Y}(\text{NH}_3)_6^-$, $\text{Th}(\text{NH}_3)_n^-$, and $\text{U}(\text{NH}_3)_n^-$ have not begun. While awaiting calculations on $\text{V}(\text{NH}_3)_{6-7}^-$, the present PES can be compared to the PES of V_n^- series to determine the anions contain ammonia and not pure vanadium.¹⁵ The electron affinity of V_3^- is ~1 eV and increases as more vanadium atoms are added. Based on this, the photoelectron spectra presented here are not from photodetaching V_n^- .

Transitions at higher binding energy for all the multiple Rydberg anions likely originate from photodetachment of deeper Rydberg orbitals. Further calculations are needed to determine from which orbitals they reside.

References

1. Havriliak, S. & King, H. F. Rydberg Radicals. 1. Frozen-Core Model for Rydberg Levels of the Ammonium Radical. *J. Am. Chem. Soc.* **105**, 4–12 (1983).
2. Herzberg, G. A spectrum of triatomic hydrogen. *J. Chem. Phys.* **70**, 4806 (1979).
3. Herzberg, G. Rydberg spectra of triatomic hydrogen and of the ammonium radical. *Faraday Discuss. Chem. Soc.* **71**, 165–173 (1981).
4. Xu, S.-J., Nilles, J. M., Hendricks, J. H., Lyapustina, S. A. & Bowen, K. H. Double Rydberg anions: Photoelectron spectroscopy of $\text{NH } 4 \text{ \AA}$, $\text{N } 2 \text{ H } 7 \text{ \AA}$, $\text{N } 3 \text{ H } 10 \text{ \AA}$, $\text{N } 4 \text{ H } 13 \text{ \AA}$, and $\text{N } 5 \text{ H } 16$. (2002). doi:10.1063/1.1499491
5. Gutowski, M., Simons, J., Hernandez, R. & Taylor, H. L. ‘Double-Rydberg’ molecular anions. *J. Phys. Chem.* **92**, 6179–6182 (1988).
6. Cardy, H., Larrieu, C. & Dargelos, A. An Ab initio study of the tetrahedral NH_4^- ion. *Chem. Phys. Lett.* **131**, 507–512 (1986).
7. Hirao, K. & Kawai, E. Structure and stability of $\text{H}-(\text{NH}_3)$ and $\text{H}-(\text{NH}_3)_2$. *J. Mol. Struct. THEOCHEM* **149**, 391–394 (1987).
8. Ortiz, J. V. Vertical and adiabatic ionization energies of NH_4^- isomers via electron propagator theory and many body perturbation theory calculations with large basis sets. *J. Chem. Phys.* **87**, 3557–3562 (1987).
9. Cremer, D. & Kraka, E. Theoretical determination of molecular structure and conformation. 17. On the existence of FH_2^- , OH_3^- , NH_4^- , and CH_5^- in the gas phase. *J. Phys. Chem.* **90**, 33–40 (1986).
10. Wu, B., Duncombe, B. J. & Stace, A. J. Fragmentation pathways of $[\text{Mg}(\text{NH}_3)_n]^{2+}$ complexes: Electron capture versus charge separation. *J. Phys. Chem. A* **110**, 8423–8432 (2006).
11. Elhanine, M. *et al.* Solvation of magnesium and singly ionized magnesium atoms in NH_3 clusters: Theory and experiment. *J. Chem. Phys.* **112**, 10912–10925 (2000).
12. Ariyaratna I R and Miliordos E 2021 *Phys. Chem. Chem. Phys.* **23** 20298–306
13. Ariyaratna I R, Khan S N, Pawłowski F, Ortiz J V and Miliordos E 2018 *J. Phys. Chem. Lett.* **9** 84–8
14. Ariyaratna I R, Pawłowski F, Ortiz J V and Miliordos E 2018 *Phys. Chem. Chem. Phys.* **20** 24186–91
15. Almeida N M S and Miliordos E 2019 *Phys. Chem. Chem. Phys.* **21** 7098–104
16. Almeida N M S, Pawłowski F, Ortiz J V and Miliordos E 2019 *Phys. Chem. Chem. Phys.* **21** 7090–7
17. Ariyaratna I R, Almeida N M S and Miliordos E 2019 *J. Phys. Chem A* **123** 6744–50
18. Ariyaratna I R and Miliordos E 2019 *Phys. Chem. Chem. Phys.* **21** 15861–70
19. Ariyaratna I R and Miliordos E 2020 *J. Phys. Chem A* **124** 9783–92
20. Ariyaratna I R, Pawłowski F, Ortiz J V and Miliordos E 2020 *J. Phys. Chem A* **124** 505–12
21. Khan S N and Miliordos E 2020 *J. Phys. Chem A* **124** 4400–12
22. Jackson B A and Miliordos E 2021 *J. Chem. Phys.* **155** 014303
23. Jordan, Z., Khan, S. N., Jackson, B. A., & Miliordos, E. (2022). Can boron form coordination complexes with diffuse electrons? Evidence for linked solvated electron precursors. *Electronic Structure*, **4**(1), 015001.
24. Gerhards, M., Thomas, O. C., Nilles, J. M., Zheng, W.-J. & Bowen, K. H. Cobalt–benzene cluster anions: Mass spectrometry and negative ion photoelectron spectroscopy. *J. Chem. Phys.* **116**, 10247–10252 (2002).
25. Ho, J., Ervin, K. M. & Lineberger, W. C. Photoelectron spectroscopy of metal cluster anions: Cu^- , Ag^- , and Au^- . *J. Chem. Phys.* **93**, 6987–7002 (1990).
26. Blondel, C. Comment on ‘measurement of the electron affinity of the lanthanum atom’. *Phys. Rev. A* **101**, 016501 (2020).
27. Iseda, M. *et al.* Electronic structure of vanadium cluster anions as studied by photoelectron spectroscopy. *J. Chem. Phys.* **106**, 2182–2187 (1997).

VI.A.6. Molecular-Level CO₂ Reduction Reaction Mediated by Ni and Pd Atomic Anions

(This project needs further experimental evidence. PES with higher photon energy are required. We also need input from theoretical collaborators. Miliordos's calculation cannot fully explain the experimental results.)

Zhaoguo Zhu^{[a]†}, Isuru R. Ariyaratna^{[b]†§}, Gaoxiang Liu^{[a]#}, Sandra M. Ciborowski, Evangelos Miliordos^{[b]*}, Kit H. Bowen^{[a]*}

[a] Department of Chemistry, Johns Hopkins University, 3400 N Charles St, Baltimore, MD 21218 (USA) E-mail: kbowen@jhu.edu

[b] Department of Chemistry and Biochemistry, Auburn University, Auburn, AL 36849 (USA) E-mail: ezm0048@auburn.edu

§ Present Address: Department of Chemical Engineering, Massachusetts Institute of Technology, Cambridge, MA 02139, (USA).

Present Address: Advanced Bioimaging Center, Department of Molecular and Cell Biology, University of California, Berkeley, Barker Hall, Berkeley, CA 94720 (USA).

** Corresponding authors: ezm0048@auburn.edu and kbowen@jhu.edu*

†These two authors contributed equally to this manuscript

Introduction

The catalytical conversion of CO₂ into value-added chemicals and fuels has attracted wide research interest due to the increase in the emission of CO₂, which is one of the main greenhouse gases emitted from human activities.^{1,2} Tremendous efforts in academic research and industry have been devoted to investigating photochemical and electrochemical CO₂ reduction to formate/formic acid or CO, even to methanol, using various catalysts such as transition metals and metal hydrides and transition metal complexes.³⁻⁷ Recently, single-atom catalysts (SACs) with atomically dispersed metal centers have exhibited great CO₂ reduction reaction (CO₂RR) rate due to their low-coordinated active sites and have shown the potential to minimize material usage for industrial applications.⁸⁻¹³ Among all transition metals, Ni and Pd, are the promising candidates owing to their unique electronic structures. For example, Wang and co-workers reported a single Ni atom catalyst could reduce CO₂ aqueous to CO at a high current of up to ~60 mA/mg, and the faraday efficiency was as high as 90%.¹⁴ Another study showed that ZnO supported Pd catalysts with 2 wt.% Pd loading exhibit excellent catalytic performance in the hydrogenation of CO₂ to formic acid.¹⁵

Besides the diversified catalysts in the condensed phase, which is always obscured by environmental effects, fruitful gas-phase CO₂ reduction studies have been carried out to discover mechanisms of activation and functionalization of CO₂ at a molecular level. Weber and co-workers found that single transition metal atoms (Cu, Ag, Au, Co, and Ni) can activate CO₂ and form metallo-formate anionic complexes, in which the CO₂ moieties are partially bent, bearing significant negative charge transferred from the metal anions.^{16,17} Our subsequent work using anion photoelectron spectroscopy combined with quantum chemical calculations also showed that group 10 transition metal anions, Ni⁻, Pd⁻ and Pt⁻, all activate CO₂ to form Ni(CO₂)⁻, Pd(CO₂)⁻, and Pt(CO₂)⁻, respectively.¹⁸ After activation, to form the value-added chemicals such as formate and formic acid, the hydrogenation process is necessary. A series of studies reported CO₂ could be hydrogenated by metal hydride anions, M-H⁻ (M=Fe, Co, Ni, Cu, Mn, Pd, and Pt).¹⁹⁻²⁵ Particularly, the Pd-H group in single- and dual-metal hydrides was found to play a critical role in converting CO₂ to formate and formate complexes.^{25,26} In a recent study, single platinum anions, Pt⁻, selectively activate methane and forms Pt-H hydro group and Pt-CH₃ methyl group, with the two functional groups coupling with CO₂, forming formate and acetate adducts, respectively.^{27,28} Inspired by the decisive role of the hydro-metal group in CO₂ conversion in the studies above, we conceive that the hydro group in water activation products [H-M-OH]⁻ could also react with CO₂.²⁹ Herein, we design and conduct the reactions of Pd(H₂O)⁻ and Ni(H₂O)⁻ with CO₂, and show that Pd(H₂O)⁻ can induce the hydrogenation of CO₂ to formate.

Experimental Methods

The experimental technique, anion photoelectron spectroscopy (aPES), is conducted by crossing a beam of mass-selected negative ions with a fixed-frequency photon beam and energy-analyzing the resultant photodetached electrons. The photodetachment process is governed by the energy-conserving relationship: $h\nu = \text{EBE} + \text{EKE}$, where $h\nu$ is the photon energy, EBE is the electron binding energy, and EKE is the electron kinetic energy. Our apparatus, which has been described previously, consists of a laser vaporization cluster anion source with an attached ligation cell, a time-of-flight (TOF) mass spectrometer, a Nd:YAG photodetachment laser (operating at 266 nm), and a magnetic bottle electron energy analyzer with a resolution is ~ 35 meV at 1 eV EKE.³⁰ Photoelectron spectra were calibrated against the well-known atomic transitions of atomic Cu⁻.³¹ The tandem reaction among transition metal (TM) anions, H₂O, and CO₂ was studied using a laser vaporization/reaction cell arrangement.³² Atomic Ni and Pd anions were generated by laser vaporization of a Ni rod and a Pd rod, respectively. The resultant plasma was cooled with a water vapor seeded helium gas mixture delivered by a pulsed valve, having a backing pressure of 80 psig. The resulting H-TM-OH⁻ (M=Ni

and Pd) then traveled through a reaction cell (4-mm diameter, 5-cm length), where it encountered CO₂. To initiate the CO₂ was introduced into the reaction cell by a second pulsed valve, backed by 15 psig of pure CO₂ gas. The resulting Pd(H₂O)(CO)₂⁻ and Ni(H₂O)(CO)₂⁻ anionic cluster was then mass-analyzed and mass-selected by the time-of-flight mass spectrometer and their photoelectron spectra measured.

Results and Discussion

Palladium part:

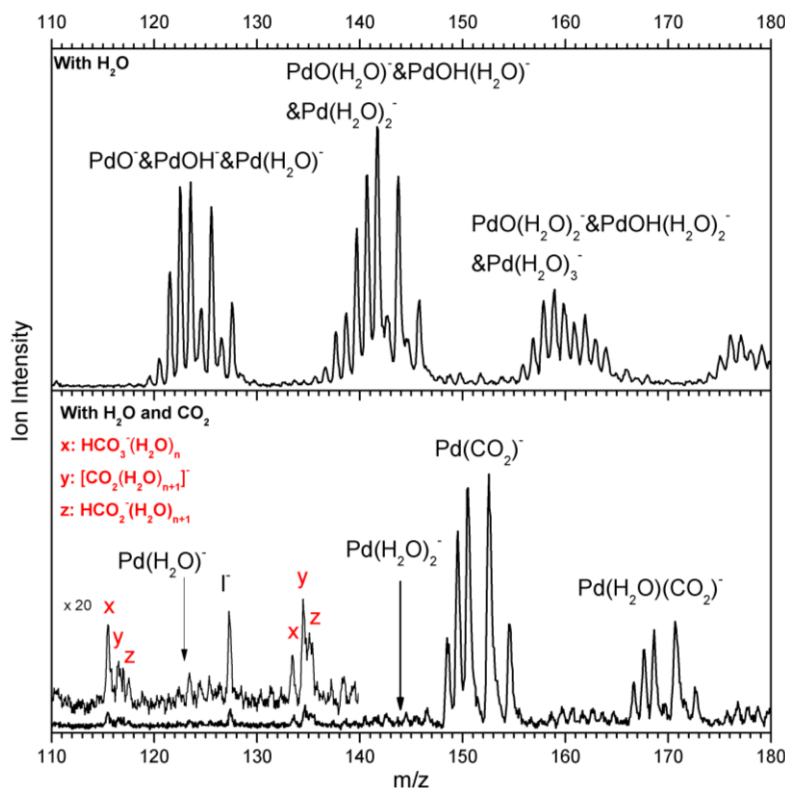


Figure VI.A.6.1 Mass spectra of Pd⁻ reacting with H₂O (top panel) and with H₂O and CO₂ (bottom panel).

The TOF mass spectra for the laser ablation generated [Pd(H₂O)]⁻ anions without and with CO₂ pulsed into the reaction cell are shown in figure VI.A.6.1. Without CO₂ in the cell, [PdO(H₂O)_n]⁻, [PdOH(H₂O)_n]⁻, and Pd(H₂O)_{n+1}⁻ (n=0-2) are observed in the top panel. Photoelectron spectrum of [Pd(H₂O)]⁻ is taken, showing both water solvation complex, Pd⁻(H₂O), and water-activated complex, [H-Pd-OH]⁻, coexist in the ion beam. Upon the interaction with CO₂ introduced into the reaction cell, at the higher mass region, two new mass series that can be assigned as Pd(CO₂)⁻ and Pd(H₂O)(CO₂)⁻ appeared in the bottom panel. Moreover, at the lower mass region, relatively weak peaks labeled with x, y, and z are identified as HCO₃⁻(H₂O)_n, [CO₂(H₂O)_{n+1}]⁻, and HCO₂⁻(H₂O)_{n+1}, respectively, according to the mass

and photoelectron spectra. The $[\text{CO}_2(\text{H}_2\text{O})_n]^-$ are products from reactions of $(\text{H}_2\text{O})_n^-$ cluster anions with CO_2 . The presence of bicarbonate solvation complexes, $\text{HCO}_3^-(\text{H}_2\text{O})_n$, is the result of the reactions between CO_2 and O-H groups in PdOH^- and water-activated complex $[\text{H-Pd-OH}]^-$. The formation of $\text{HCO}_2^-(\text{H}_2\text{O})$, formate anion solvation complexes, suggests that CO_2 is hydrogenated by $\text{Pd}(\text{H}_2\text{O})^-$, and that formate product is released after the reaction and solvated by H_2O in the reaction cell. Therefore, $[\text{Pd}(\text{H}_2\text{O})(\text{CO}_2)]^-$ is a critical reaction intermediate when CO_2 is hydrogenated by $[\text{Pd}(\text{H}_2\text{O})]^-$.

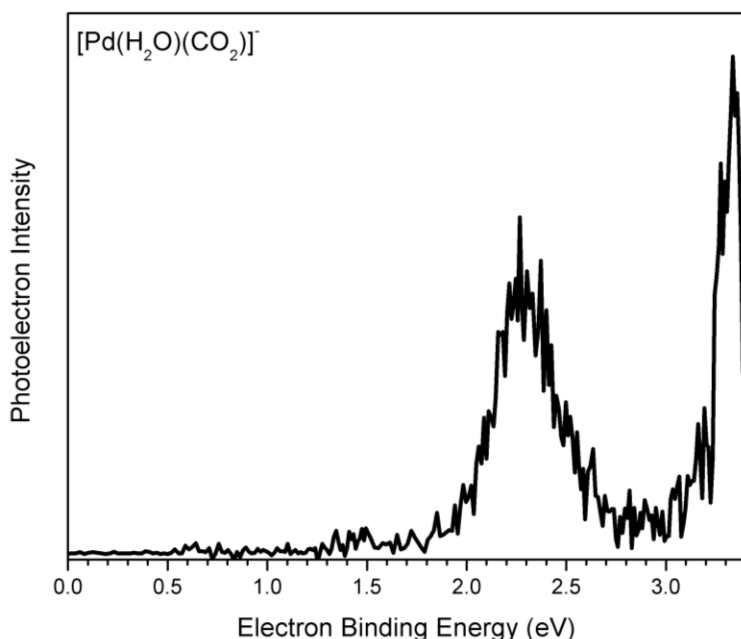


Figure VI.A.6.2 Photoelectron spectra of $[\text{Pd}(\text{H}_2\text{O})(\text{CO}_2)]^-$ measured with 355 nm (3.49 eV) photons.

To better understand the hydrogenation mechanism, we then characterize the $[\text{Pd}(\text{H}_2\text{O})(\text{CO}_2)]^-$ via anion photoelectron spectroscopy (figure VI.A.6.2). The photoelectron spectrum of $[\text{Pd}(\text{H}_2\text{O})(\text{CO}_2)]^-$ exhibits two main features. While the first broad peak spans from 1.9 eV to 2.8 eV and is centered at 2.27 eV, the second peak starts from 3.1 eV and reaches its maxima at 3.34 eV. So, 2.27 eV and 3.34 eV are assigned as their vertical detachment energies (VDE). The VDE is defined as the photodetachment transition energy at which the Franck–Condon overlap is at its maximum between the anion’s vibrational wave function and that of its neutral counterpart with both in their ground electronic states.

Nickel part:

We also studied the reactions between Ni atomic anion and H₂O and CO₂. Only with water, the mass spectrum in the top panel of figure VI.A.6.3 resembles the Pd anion result. [NiO(H₂O)_n]⁻, [NiOH(H₂O)_n]⁻, and [Ni(H₂O)_{n+1}]⁻ (n=0-2) are presented. However, unlike the Pd experiment, not only [Ni(H₂O)(CO₂)]⁻ but also [NiOH(CO₂)]⁻ was made after adding CO₂ into the reaction cell. In addition, the absence of HCO₂⁻(H₂O)_n implies the CO₂ hydrogenation process is incomplete. To further characterize the complex, anion photoelectron spectrum (figure VI.A.6.4) taken with 355 nm photons were employed to study the electronic structure of [Ni(H₂O)(CO₂)]⁻. In figure VI.A.6.4, one broad electron binding spectral band ranges from 2.5 eV and reaches its intensity maximum at 2.99 eV, with the latter number being the VDE value. After some small progressions near the crest, two discernible peaks at 3.23 eV and 3.34 eV are observed at the downhill region. The convolved spectrum suggests multiple isomers coexist in the ion beam contributing to the photodetachment process.

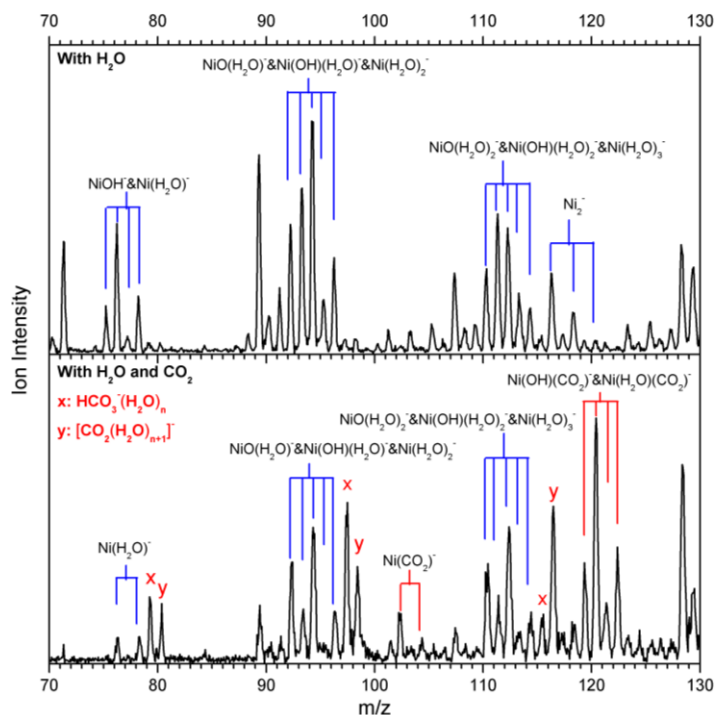


Figure VI.A.6.3 Mass spectra of Ni⁻ reacting with H₂O (top panel) and with H₂O and CO₂ (bottom panel).

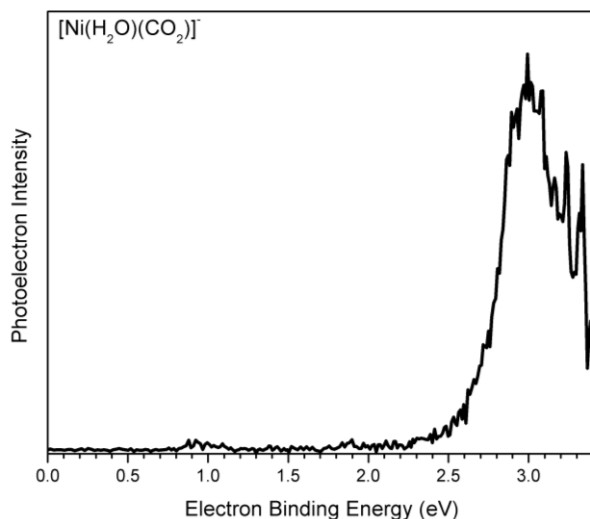


Figure VI.A.6.4 Photoelectron spectra of $[\text{Pd}(\text{H}_2\text{O})(\text{CO}_2)]^-$ measured with 355 nm (3.49 eV) photons.

References:

1. Solomon, S., Manning, M., Marquis, M., & Qin, D. (2007). *Climate change 2007-the physical science basis: Working group I contribution to the fourth assessment report of the IPCC* (Vol. 4). Cambridge university press.
2. Appel, A. M.; Bercaw, J. E.; Bocarsly, A. B.; Dobbek, H.; DuBois, D. L.; Dupuis, M.; Ferry, J. G.; Fujita, E.; Hille, R.; Kenis, P. J. A.; Kerfeld, C. A.; Morris, R. H.; Peden, C. H. F.; Portis, A. R.; Ragsdale, S. W.; Rauchfuss, T. B.; Reek, J. N. H.; Seefeldt, L. C.; Thauer, R. K.; Waldrop, G. L. Frontiers, Opportunities, and Challenges in Biochemical and Chemical Catalysis of CO₂ Fixation. *Chem. Rev.* 2013, 113 (8), 6621–6658.
3. Wang, W. H., Himeda, Y., Muckerman, J. T., Manbeck, G. F., & Fujita, E. (2015). CO₂ hydrogenation to formate and methanol as an alternative to photo-and electrochemical CO₂ reduction. *Chemical reviews*, 115(23), 12936-12973.
4. Álvarez, A., Bansode, A., Urakawa, A., Bavykina, A. V., Wezendonk, T. A., Makkee, M., ... & Kapteijn, F. (2017). Challenges in the greener production of formates/formic acid, methanol, and DME by heterogeneously catalyzed CO₂ hydrogenation processes. *Chemical reviews*, 117(14), 9804-9838.
5. Jiang, X., Nie, X., Guo, X., Song, C., & Chen, J. G. (2020). Recent advances in carbon dioxide hydrogenation to methanol via heterogeneous catalysis. *Chemical reviews*, 120(15), 7984-8034.
6. Costentin, C., Drouet, S., Robert, M., & Savéant, J. M. (2012). A local proton source enhances CO₂ electroreduction to CO by a molecular Fe catalyst. *Science*, 338(6103), 90-94.
7. Sun, L., Reddu, V., Fisher, A. C., & Wang, X. (2020). Electrocatalytic reduction of carbon dioxide: opportunities with heterogeneous molecular catalysts. *Energy & Environmental Science*, 13(2), 374-403.
8. Su, X., Yang, X. F., Huang, Y., Liu, B., & Zhang, T. (2018). Single-atom catalysis toward efficient CO₂ conversion to CO and formate products. *Accounts of chemical research*, 52(3), 656-664.
9. Tackett, B. M., Lee, J. H., & Chen, J. G. (2020). Electrochemical Conversion of CO₂ to Syngas with Palladium-Based Electrocatalysts. *Accounts of Chemical Research*, 53(8), 1535-1544.
10. Gao, D., Liu, T., Wang, G., & Bao, X. (2021). Structure Sensitivity in Single-Atom Catalysis toward CO₂ Electroreduction. *ACS Energy Letters*, 6(2), 713-727.
11. He, Q., Lee, J. H., Liu, D., Liu, Y., Lin, Z., Xie, Z., ... & Chen, J. G. (2020). Accelerating CO₂ Electroreduction to CO Over Pd Single-Atom Catalyst. *Advanced Functional Materials*, 30(17), 2000407.

12. Wang, J., Kattel, S., Hawxhurst, C. J., Lee, J. H., Tackett, B. M., Chang, K., ... & Chen, J. G. (2019). Enhancing activity and reducing cost for electrochemical reduction of CO₂ by supporting palladium on metal carbides. *Angewandte Chemie International Edition*, 58(19), 6271-6275.
13. Kwak, J. H., Kovarik, L., & Szanyi, J. (2013). Heterogeneous catalysis on atomically dispersed supported metals: CO₂ reduction on multifunctional Pd catalysts. *Acs Catalysis*, 3(9), 2094-2100.
14. Jiang, K., Siahrostami, S., Akey, A. J., Li, Y., Lu, Z., Lattimer, J., ... & Wang, H. (2017). Transition-metal single atoms in a graphene shell as active centers for highly efficient artificial photosynthesis. *Chem*, 3(6), 950-960.
15. Zhang, J., Fan, L., Zhao, F., Fu, Y., Lu, J. Q., Zhang, Z., ... & Huang, W. (2020). Zinc Oxide Morphology-Dependent Pd/ZnO Catalysis in Base-Free CO₂ Hydrogenation into Formic Acid. *ChemCatChem*, 12(21), 5540-5547.
16. L. G. Dodson, M. C. Thompson and J. M. Weber, *Annu. Rev. Phys. Chem.*, 2018, 69, 231.
17. Zhang, X.; Lim, E.; Kim, S. K.; Bowen, K. H., Photoelectron spectroscopic and computational study of (M–CO₂)[–] anions, M= Cu, Ag, Au. *J. Chem. Phys.* **2015**, 143 (17), 174305.
18. Liu, G.; Ciborowski, S. M.; Zhu, Z.; Chen, Y.; Zhang, X.; Bowen, K. H., The metallo-formate anions, M (CO₂)[–], M= Ni, Pd, Pt, formed by electron-induced CO₂ activation. *Phys. Chem. Chem. Phys.* **2019**, 21 (21), 10955-10960.
19. Zhang, X.; Liu, G.; Meiwe-Broer, K. H.; Ganteför, G.; Bowen, K., CO₂ activation and hydrogenation by PtHn[–] cluster anions. *Angew. Chem. Int. Ed.* **2016**, 55 (33), 9644-9647.
20. Jiang, L. X.; Zhao, C.; Li, X. N.; Chen, H.; He, S. G., Formation of Gas-Phase Formate in Thermal Reactions of Carbon Dioxide with Diatomic Iron Hydride Anions. *Angew. Chem. Int. Ed.* **2017**, 56 (15), 4187-4191.
21. Jiang, L. X., Li, X. N., & He, S. G. (2020). Metal-Dependent Selectivity on the Reactions of Carbon Dioxide with Diatomic Hydride Anions MH[–] (M= Co, Ni, and Cu). *The Journal of Physical Chemistry C*, 124(11), 5928-5933.
22. Huang, T., Yu, W., Cheng, J., Cong, F., Xu, B., & Wang, X. (2021). CO₂ activation by ligand-free manganese hydrides in a parahydrogen matrix. *Chemical Communications*, 57(18), 2301-2304.
23. Liu, Y. Z., Jiang, L. X., Li, X. N., Wang, L. N., Chen, J. J., & He, S. G. (2018). Gas-phase reactions of carbon dioxide with copper hydride anions Cu₂H₂[–]: Temperature-dependent transformation. *The Journal of Physical Chemistry C*, 122(34), 19379-19384.
24. Liu, Y. Z., Li, X. N., & He, S. G. (2020). Reactivity of Iron Hydride Anions Fe₂H_n[–] (n= 0–3) with Carbon Dioxide. *The Journal of Physical Chemistry A*, 124(41), 8414-8420.
25. Liu, G.; Zhu, Z.; Marshall, M.; Blankenhorn, M.; Bowen, K. H., CO₂ Activation and Hydrogenation by Palladium Hydride Cluster Anions. *J. Phys. Chem. A* **2021**, 125 (8), 1747-1753
26. Liu, G.; Poths, P.; Zhang, X.; Zhu, Z.; Marshall, M.; Blankenhorn, M.; Alexandrova, A. N.; Bowen, K. H., CO₂ hydrogenation to formate and formic acid by bimetallic palladium–copper hydride clusters. *J. Am. Chem. Soc.* **2020**, 142 (17), 7930-7936.;
27. Liu, G.; Zhu, Z.; Ciborowski, S. M.; Ariyaratna, I. R.; Miliordos, E.; Bowen, K. H., Selective Activation of the C–H Bond in Methane by Single Platinum Atomic Anions. *Angew. Chem. Int. Ed.* **2019**, 131 (23), 7855-7859.
28. Liu, G.; Ariyaratna, I. R.; Ciborowski, S. M.; Zhu, Z.; Miliordos, E.; Bowen, K. H., Simultaneous Functionalization of Methane and Carbon Dioxide Mediated by Single Platinum Atomic Anions. *J. Am. Chem. Soc.* **2020**.
29. Liu, G.; Miliordos, E.; Ciborowski, S. M.; Tschurl, M.; Boesl, U.; Heiz, U.; Zhang, X.; Xantheas, S. S.; Bowen, K., Communication: Water activation and splitting by single metal-atom anions. *J. Chem. Phys.* **2018**, 149 (22), 221101.
30. Gerhards, M.; Thomas, O. C.; Nilles, J. M.; Zheng, W.-J.; Bowen, K. H. Cobalt–Benzene Cluster Anions: Mass Spectrometry and Negative Ion Photoelectron Spectroscopy. *J. Chem. Phys.* **2002**, 116, 10247.
31. Ho, J.; Ervin, K. M.; Lineberger, W. C. Photoelectron Spectroscopy of Metal Cluster Anions: Cu–N, Ag–N, and Au–N. *J. Chem. Phys.* **1990**, 93, 6987.
32. Liu, G.; Ciborowski, S. M.; Bowen, K. H., Photoelectron spectroscopic and computational study of pyridine-ligated gold cluster anions. *J. Phys. Chem. A* **2017**, 121 (31), 5817-5822.

VI.A.7. Parent Anions of Diiodobenzene

Zhaoguo Zhu, Mary Marshall, and Burak Tufekci.

Introduction

This project was inspired by the single electron induced multiple C-I bonds breaking in ortho-diiodobenzene physisorbed on Cu(110).[1,5] Polanyi et al. has studied that the breakage of the two C-I bonds of ortho-DIB is ascribed primarily to the delocalization of charge from one I-atom to the closely neighboring one by way of overlapping antibonding orbitals. There is currently widespread interest in the electron induced reaction of physisorbed molecules.[2-5] The electron-induced reaction of pentyl bromide (PeBr) and phenyl bromide (PhBr) adsorbed on Cu(110) at 4.6 K gave a chemisorbed hydrocarbon and a Br atom product. For both reagents, PeBr and PhBr, dissociation took place via a single-electron electronic-excitation at ~2.0 eV energy to the σ^* anti-bonding orbital of the C-Br bond.

Professor Xinxing Zhang at Nankai university proposed that a single electron can cause multiple carbon-halogen bonds breaking simultaneously as well in the gas phase. His group has calculated the EA of 1,2-DIB, 1,3-DIB, and 1,4-DIB to be 0.487 eV, 0.478 eV and 0.136 eV, respectively. According to the calculated orbital diagram, the extra electron will be delocalized in the two sigma antibonding orbitals in 1,2-DIB and 1,3-DIB cases. The occupation is antibonding orbital will cause the elongation of the C-I bonds thus trigger the bond breakage. Here I present our mass spectra and PE spectra results. There is still inconsistency between experiments and theory but we also obtained some interesting spectra as byproducts of this project. My colleagues should pay more attention to this project.

Experimental methods

Parent anion of DIB was produced by a photo-emission source. Liquid form of 1,2-DIB and 1,3-DIB were put into a pulsed valve. Pulsed valve was heated past the melting point of the DIBs. 1,3-DIB was heated to 50 degree C, and 1,2-DIB was heated to 40 degree C. We tried 1,3-DIB and then 1,2-DIB. First, we were using a closed housing and then an open housing.

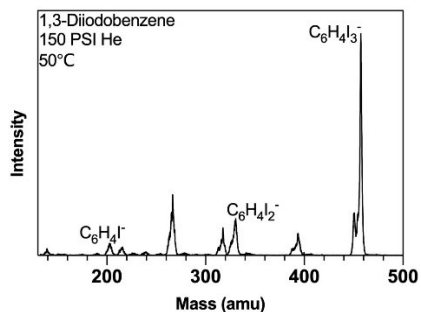


Figure VI.A.7.1 Mass spectrum of clusters generated from 1,3-DIB using a closed housing photoemission source.

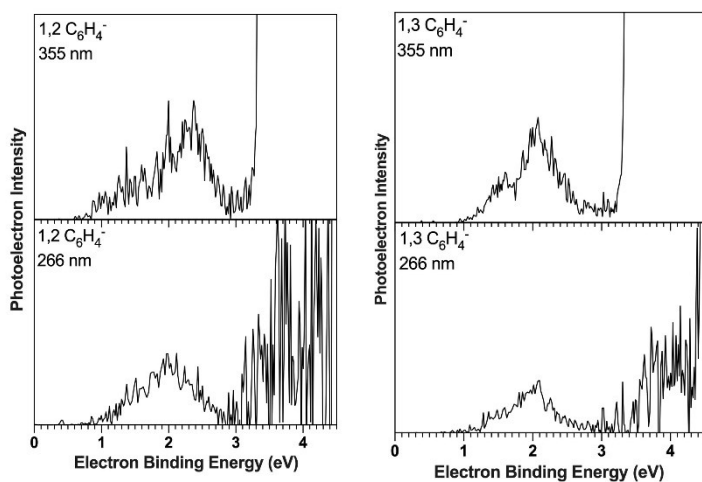


Figure VI.A.7.2 Photoelectron spectra of 1,2- C_6H_4^- and 1,3- C_6H_4^- with 355 nm and 266 nm photons.

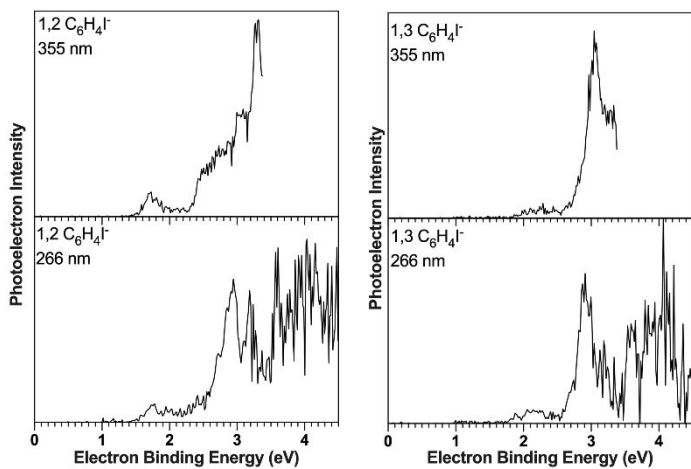


Figure VI.A.7.3 Photoelectron spectra of 1,2- $\text{C}_6\text{H}_4\text{I}^-$ and 1,3- $\text{C}_6\text{H}_4\text{I}^-$ with 355 nm and 266 nm photons.

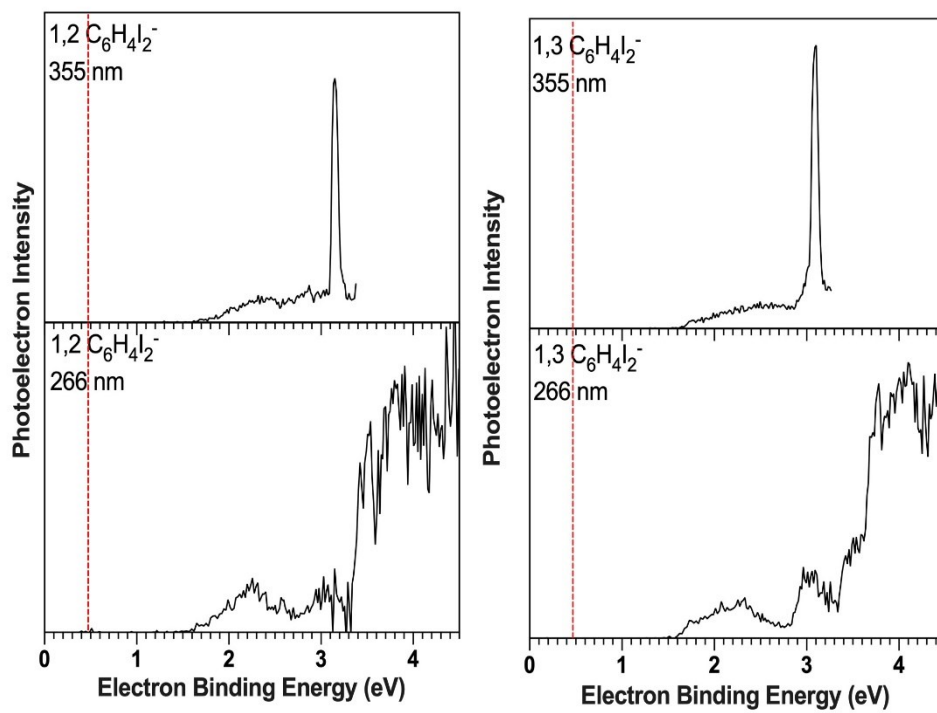


Figure VI.A.7.4 Photoelectron spectra of 1,2-C₆H₄I₂⁻ and 1,3-C₆H₄I₂⁻ with 355 nm and 266 nm photons.

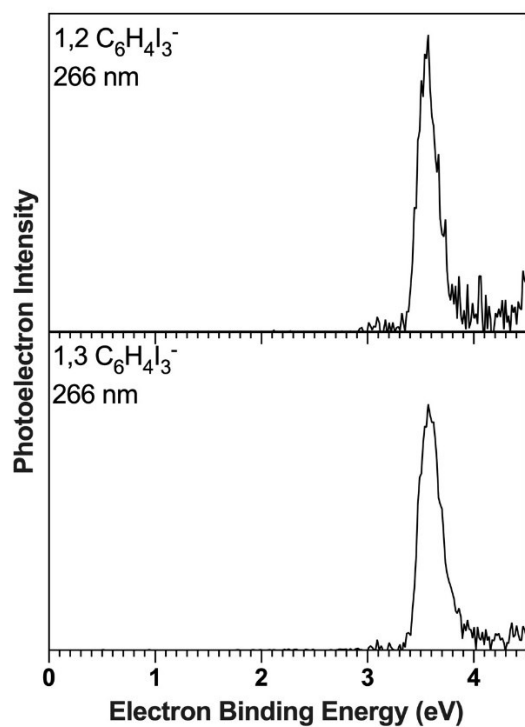


Figure VI.A.7.5 Photoelectron spectra of 1,2-C₆H₄I₃⁻ and 1,3-C₆H₄I₃⁻ with 266 nm photons.

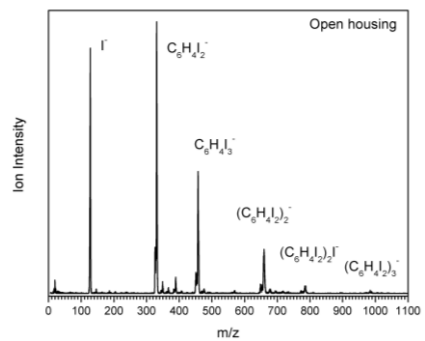


Figure VI.A.7.6 Mass spectrum of clusters generated from 1,2-DIB using an open housing photoemission source.

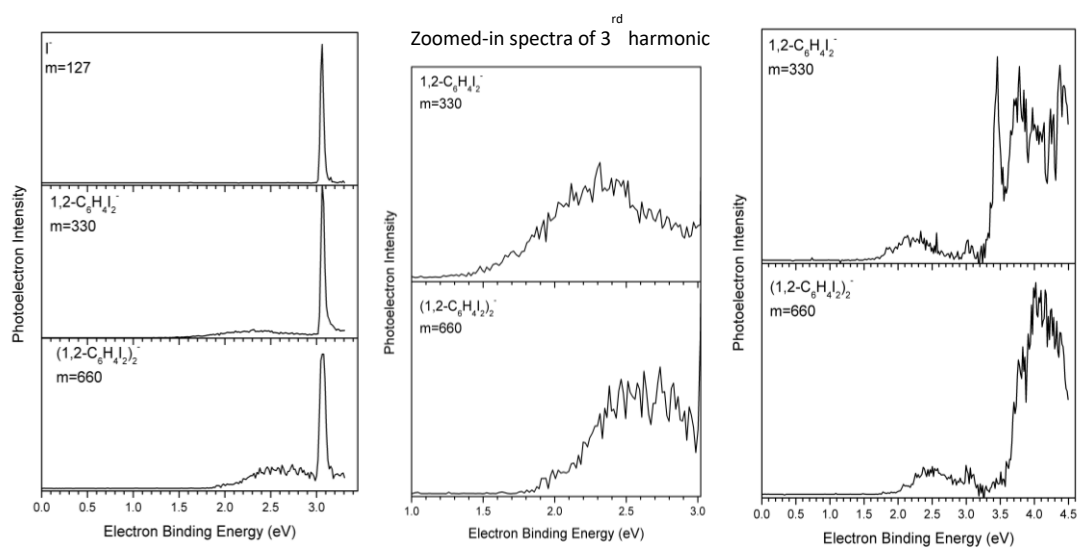


Figure VI.A.7.7 Photoelectron spectra of 1,2-C₆H₄I₂⁻ and (1,2-C₆H₄I₂)₂⁻ with 355 nm and 266 nm photons.

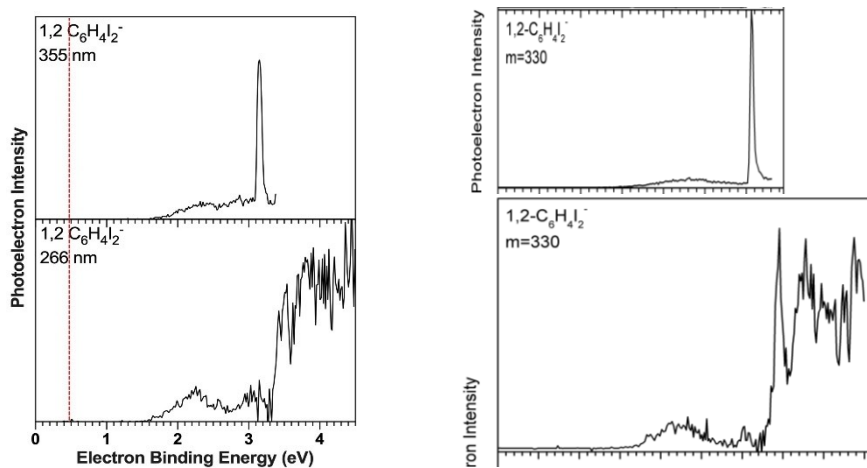


Figure VI.A.7.8 Comparison between closed housing and open housing conditions. Left: closed, right: open.

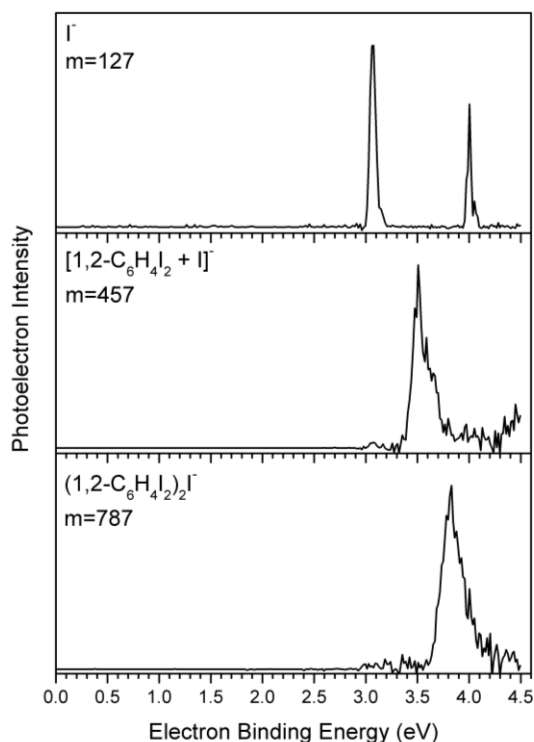


Figure VI.A.7.9 Photoelectron spectra of I^- , $1,2\text{-C}_6\text{H}_4\text{I}_3^-$, and $(1,2\text{-C}_6\text{H}_4\text{I}_2)_2\text{I}^-$ with 266 nm photons.

Results

The mass spectra we collected under closed and open housing conditions are different. As shown in the figure VI.A.7.1, We saw parent anion of 1,3-DIB, $\text{C}_6\text{H}_4\text{I}^-$, C_6H_4^- , and $\text{C}_6\text{H}_4\text{I}_3^-$. $\text{C}_6\text{H}_4\text{I}^-$ and C_6H_4^- can be seen as the fragmentation of the parent anion. They are possible electron attachment dissociation products. $\text{C}_6\text{H}_4\text{I}_3^-$ can be seen as $1,3\text{-DIB} + \text{I}^-$, or an Iodine anion surrounded by a 1,3-DIB molecule. Mass spectrum generated using 1,2-DIB is almost identical to the 1,3-DIB. figure VI.A.7.4 shows the photoelectron spectra of $1,2\text{-C}_6\text{H}_4\text{I}_2^-$ and $1,3\text{-C}_6\text{H}_4\text{I}_2^-$ with 355 nm and 266 nm photons. In the 355 nm spectra, both of them display a sharp peak around 3 eV which represents photodetachment from I^- . However, the sharp peaks disappeared in 266 nm, suggesting that the sharp transition from I^- could be due to multiphoton photodissociation process. At low EBE range, the band is broad and not well resolved so that we can only estimate the EA of compound by finding the onset of the band. Both EA of 1,2-DIB and 1,3-DIB are estimated to be 1.5 eV, which is much higher than the calculated values (*ca.* 0.5 eV). It is likely we did not see the real EA in our PE spectra.

As Xinxing suggested, we used a new open housing to do the 1,2-DIB again. Surprisingly, the intensity of the parent anions increased dramatically. Open housing can provide gentle source conditions and will not break the molecule. In the mass spectrum shown in the figure VI.A.7.6, only I⁻, 1,2-DIB anion, 1,2-DIB dimer anion, 1,2-C₆H₄I₃⁻, and (1,2-C₆H₄I₂)₂I⁻ were observed. In this case, no fragmentation was observed in the mass spectrum. We also compared the PE spectra collected under different source conditions. Spectra are similar. The peak around 3.5 eV is sharper when the anion was generated by an open housing.

Figure VI.A.7.9 shows spectra of I⁻ surrounded by different number of 1,2-DIB molecules. We can clearly see the firstly shifted to the high EBE region. It is like a solvation effect. If halogen bonds are formed in the clusters, it can be another great example of spectroscopic measurement of a halogen bond energy. Our group previously measured the Br halogen bond energy using Br⁻(CCl₃Br)_{1,2} system. This DIB system is also a direct measurement of the I halogen bond energy. [6]

Note: This project was halted for three reasons. First, the calculated data did not match our PES. Second, 1,2-DIB and 1,3 DIB are indistinguishable in terms of energy. We possibly have 1,3-DIB contamination in our 1,2-DIB experiment due some mistakes. We baked the gas line but it is hard to remove completely the I containing organic compounds in the gas cart. Third, our mass spectrum collected using gentle condition did not support Xinxing's hypothesis. However, the collection of these beautiful spectra is still a treasure box. My co-workers or other students in the lab can dig more into it. At least, the halogen bond energy is a promising project if they expand it more in the future.

References:

1. Huang, K., Leung, L., Lim, T., Ning, Z., & Polanyi, J. C. (2013). Single-electron induces double-reaction by charge delocalization. *Journal of the American Chemical Society*, 135(16), 6220-6225.
2. Timm, Matthew J., Lydie Leung, Kelvin Anggara, Tingbin Lim, Zhixin Hu, Simone Latini, Angel Rubio, and John C. Polanyi. "Contrasting efficiency of electron-induced reaction at cu (110) in aliphatic and aromatic bromides." *Journal of the American Chemical Society* 142, no. 20 (2020): 9453-9459.
3. Maksymovych, P., Sorescu, D. C., Jordan, K. D., & Yates Jr, J. T. (2008). Collective reactivity of molecular chains self-assembled on a surface. *Science*, 322(5908), 1664-1667.
4. MacLean, O., Huang, K., Leung, L., & Polanyi, J. C. (2017). Direct and delayed dynamics in electron-induced surface reaction. *Journal of the American Chemical Society*, 139(48), 17368-17375.
5. Leung, L., Lim, T., Ning, Z., & Polanyi, J. C. (2012). Localized reaction at a smooth metal surface: p-diiodobenzene at Cu (110). *Journal of the American Chemical Society*, 134(22), 9320-9326.
6. Zhang, X., Liu, G., Ciborowski, S., Wang, W., Gong, C., Yao, Y., & Bowen, K. (2019). Spectroscopic measurement of a halogen bond energy. *Angewandte Chemie International Edition*, 58(33), 11400-11403.

Curriculum Vitae

Zhaoguo Zhu

+1-4439388061 | zhuzhaoguo@outlook.com | Department of Chemistry, Johns Hopkins University, Baltimore, USA, 21218

Education

Ph.D. (candidate) in Chemistry Johns Hopkins University, Baltimore, USA	08/2016-10/2022
B. S. in Chemistry (GPA: overall:3.50/4.00, major:3.74/4.00) Nanjing University, Nanjing, China	08/2012-06/2016

Professional Experiences

Research Assistant, Johns Hopkins University	09/2017-10/2022
Teach Assistant, Johns Hopkins University	09/2016-05/2018
Research Assistant, Nanjing University	02/2014-05/2016

Honors and Awards

• Alexander Kossiakoff Award	Johns Hopkins University	2022
• Merit Student Cadre	Nanjing University	2014
• Golden Chemical Scholarship	Nanjing University	2014
• Alumni Scholarship	Nanjing University	2013

Conferences

Poster, ACS fall	Virtual	08/2020
• Photoelectron spectroscopic studies on Thorium-Gold and Thorium-Platinum containing cluster anions		
Poster, ISCAN	Richmond	11/2019
• Activation of Small Molecules by Single Metal Atomic Anions Studied via Anion Photoelectron Spectroscopy		

Publications

23. "Au as a surrogate for F: The case of UAu₆ vs UF₆" R. M. Harris, **Z. Zhu**, Deepika, B. A. Tufekci, K. A. Peterson, P. Jena and K. H. Bowen. (Accepted by JACS) (Co-first authors)
22. "Experimental and Computational Description of the Interaction of H and H⁻ with U", G. F. de Melo, M. Vasiliu, M. Marshall, **Z. Zhu**, B. Turfekci, S. Ciborowski, M. Blankenhorn, R. M. Harris, K. H. Bowen, D. A. Dixon, *J. Phys. Chem. A*, **126**, 27, 4432–4443, (2022)
21. "Molecular Properties of Thorium Hydrides: Electron Affinities and Thermochemistry", M. Vasiliu, M. Marshall, **Z. Zhu**, K. H. Bowen, D. Dixon, *J. Phys. Chem. A*, **126**, 15, 2388-2396, (2022)
20. "Molecular-Level Electrocatalytic CO₂ Reduction Reaction Mediated by Single Platinum Atoms", G. Liu, I. R. Ariyaratna, **Z. Zhu**, S. M. Ciborowski, E. Miliordos, K. H. Bowen, *Phys. Chem. Chem. Phys.*, **24**, 4226-4231, (2022)

19. "A Photoelectron Spectroscopic and Computational Study of the Deprotonated Gallic Acid and Propyl Gallate Anions", **Z. Zhu**, M. Marshall, R. Harris, E. Collins, K. H. Bowen, *J. Am. Soc. Mass Spectrom.*, **33**, 8, 1355–1361, (2022)
18. "ThAu₂⁻, ThAu₂O⁻, and ThAuOH⁻ anions: Photoelectric Spectroscopic and Theoretical Characterization", **Z. Zhu**, M. Marshall, K. Bowen, K. A. Peterson, *J. Chem. Phys.*, **156**, 054305, (2022)
17. "Interaction of Th with H^{0/+/-}: Combined Experimental and Theoretical Thermodynamic Properties" M. Vasiliu, K. A. Peterson, M. Marshall, **Z. Zhu**, B. A. Tufekci, K. H. Bowen, D. A. Dixon, *J. Phys. Chem. A*, **126**, 198-210, (2022)
16. "A Photoelectron Spectroscopic Study of Ascorbate and Deprotonated Ascorbate Anions Using an Electrospray Ion Source and a Cryogenically Cooled Ion Trap ", M. Marshall, **Z. Zhu**, R. M. Harris, E. Collins, K. H. Bowen, *J. Phys. Chem. A*, **125**, 7699-7704, (2021)
15. "Study of the Reaction of Hydroxylamine with Iridium Atomic and Cluster Anions (n = 1-5) ", S. M. Ciborowski, R. Buszek, G. Liu, M. Blankenhorn, **Z. Zhu**, M. A. Marshall, R. M. Harris, T. Chiba, E. Collins, S. Marquez, J. A. Boatz, S. D. Chambreau, G. L. Vaghijiani, K. H. Bowen, *J. Phys. Chem. A*, **125**, 5922-5932, (2021)
14. "Anion Photoelectron Spectroscopic and Relativistic Coupled-Cluster Studies of Uranyl Dichloride Anion, UO₂Cl₂⁻ ", M. Marshall, **Z. Zhu**, J. Liu, K. H. Bowen, L. Cheng, *Journal of Molecular Spectroscopy*, **379**, 111496, (2021)
13. "The Electron Affinity of the Uranium Atom", S. Ciborowski, G. Liu, M. Blankenhorn, R. Harris, M. Marshall, **Z. Zhu**, K. Bowen, K. Peterson, *J. Chem. Phys.*, **154**, 224307 (2021)
12. "CO₂ Activation and Hydrogenation by Palladium Hydride Cluster Anions", G. Liu; **Z. Zhu**; M. Marshall; M. Blankenhorn; K. Bowen, *J. Phys. Chem. A* **125**, 1747-1753, (2021) (Co-first authors)
11. "Photoelectron Spectroscopic and *Ab Initio* Computational Studies of the Anion, HThO⁻", M. Marshall; **Z. Zhu**; J. Liu; L. Cheng; K. Bowen, *J. Phys. Chem. A* **125**, 1903-1905, (2021)
10. "Simultaneous Functionalization of Methane and Carbon Dioxide Mediated by Single Platinum Atomic Anions", G. Liu, I. Ariyaratna, S. Ciborowski, **Z. Zhu**, E. Miliordos, K. Bowen, *J. Am. Chem. Soc.* **142**, 21556-21561, (2020)
9. "The Th₂O⁻, Th₂Au⁻ and Th₂AuO_{1,2}⁻ Anions: Photoelectron Spectroscopic and Computational Characterization of Energetics and Bonding", **Z. Zhu**, M. Marshall, R. Harris, K. Bowen, M. Vasiliu, D. Dixon, *J. Phys. Chem. A* **125**, 258-271, (2021)
8. "ThH₅, An Actinide-Containing Superhalogen Cluster", M. Marshall, **Z. Zhu**, R. Harris, K. H. Bowen, W. Wang, J. Wang, C. Gong, X. Zhang, *ChemPhysChem* **22**, 5-8 (2021)
7. "Magic clusters PtMg_{2,3}H₅⁻ facilitated by local σ-aromaticity", W. Wang, J. Wang, C. Gong, **Z. Zhu**, K. H. Bowen, X. Zhang, *Chemphyschem* **21**, 2388-2391, (2020)
6. "CO₂ Hydrogenation to Formate and Formic Acid by Bimetallic Palladium-Copper Hydride Clusters", G. Liu, P. Poths, X. Zhang, **Z. Zhu**, M. Marshall, M. Blankenhorn, A. Alexandrova, K. Bowen, *J. Am. Chem. Soc.*, **142**, 7930–7936 (2020)
5. "Ligand Effect on the Electronic Structure of Cobalt Sulfide Clusters: A Combined Experimental and Theoretical Study", G. Liu, V. Chauhan, A. Aydt, S. Ciborowski, A. Pinkard, **Z. Zhu**, X. Roy, S. Khanna, K. Bowen, *J. Phys. Chem. C* **123**, 25121-25127 (2019)

4. "The Metallo-Formate Anions, $M(\text{CO}_2)^-$, $M = \text{Ni, Pd, Pt}$, formed by Electron-Induced CO_2 Activation", G. Liu, S. M. Ciborowski, **Z. Zhu**, Y. Chen, X. Zhang, and K. H. Bowen, *Phys. Chem. Chem. Phys.* **21**, 10955-10960 (2019)
3. "Selective Activation of the C-H Bond in Methane by Single Platinum Atomic Anions", G. Liu, **Z. Zhu**, S. M. Ciborowski, I. R. Ariyaratna, E. Miliordos, K. H. Bowen, *Angew. Chem. Int. Ed.* **58**, 7773-7777 (2019)
2. "Activation of hydroxylamine by single gold atomic anions", G. Liu, S. M. Ciborowski, **Z. Zhu**, K. H. Bowen, *Int. J. Mass Spectrom.* **435**, 114-117 (2019)
1. "Tuning the Electronic Properties of Hexanuclear Cobalt Sulfide Superatoms via Ligand Substitution", G. Liu, A. Pinkard, S. M. Ciborowski, V. Chauhan, **Z. Zhu**, A. P. Aydt, S. N. Khanna, X. Roy, and K. H. Bowen, *Chem. Sci.* **10**, 1760-1766 (2019)

Publications (submitted or in preparation)

1. "Water Activation and Splitting by Single Anionic Iridium Atoms", Z. Zhu, G. Liu, S. M. Ciborowski, Y. Cao, R. M. Harris, K. H. Bowen, (Submitted)
2. "Photoelectron Spectroscopic and Computational Characterization of ThPtO_2^- and ThPtC^- anions", **Z. Zhu**, M. Marshall, K. Bowen, K. A. Peterson, (In preparation)
3. "Photoelectron Spectroscopic Characterization of Multiple Rydberg Anions Containing Ammonia: $M(\text{NH}_3)_n^-$, $M = \text{Mg, V, Y, and La}$ ", G. Liu, **Z. Zhu**, M. Marshall, E. Collins, K. Bowen. (In preparation)
4. "Photoelectron Spectroscopic Characterization of Multiple Rydberg Anions Containing Ammonia: $\text{Th}(\text{NH}_3)_n^-$ and $\text{U}(\text{NH}_3)_n^-$ Anions", **Z. Zhu**, M. Marshall, B. A. Tufekci, K. Bowen. (In preparation)
5. "Electronic Properties of UN and UN^- from Photoelectron Spectroscopy and Correlated Molecular Orbital Theory" G. F. de Melo, M. Vasiliu, G. Liu, S. Ciborowski, **Z. Zhu**, M. Blankenhorn, R. Harris, C. Martinez-Martinez, M. Dipolo, K. A. Peterson, K. H. Bowen, D. A. Dixon. (Submitted)
6. "A Theoretical and Experimental Study of the Spectroscopy and Thermochemistry of $\text{UC}^{+0/-}$ " G. F. de Melo, M. Vasiliu, G. Liu, S. Ciborowski, **Z. Zhu**, M. Blankenhorn, R. Harris, C. Martinez-Martinez, M. Dipolo, K. A. Peterson, K. H. Bowen, D. A. Dixon. (Submitted)
7. "The transition from halogen-like to metallic-like bonding of gold in Uranium-Auride Clusters ($\text{U}@\text{Au}_n$), ($n = 3 - 7$)" R. M. Harris, **Z. Zhu**, Deepika, B. A. Tufekci, K. A. Peterson, P. Jena and K. H. Bowen. (In preparation)
8. "Anion Photoelectron Spectroscopy and Chemical Bonding of ThSO^- and ThS_2^- " M. Marshall, **Z. Zhu**, K. Bowen, K. A. Peterson, (In preparation)
9. "HMoO and H_2MoO : Molecular Mimics for Rhodium and Platinum" G. Liu, N. Fedik, M. Marshall, **Z. Zhu**, X. Zhang, A. Boldyrev, K. H. Bowen (In preparation).